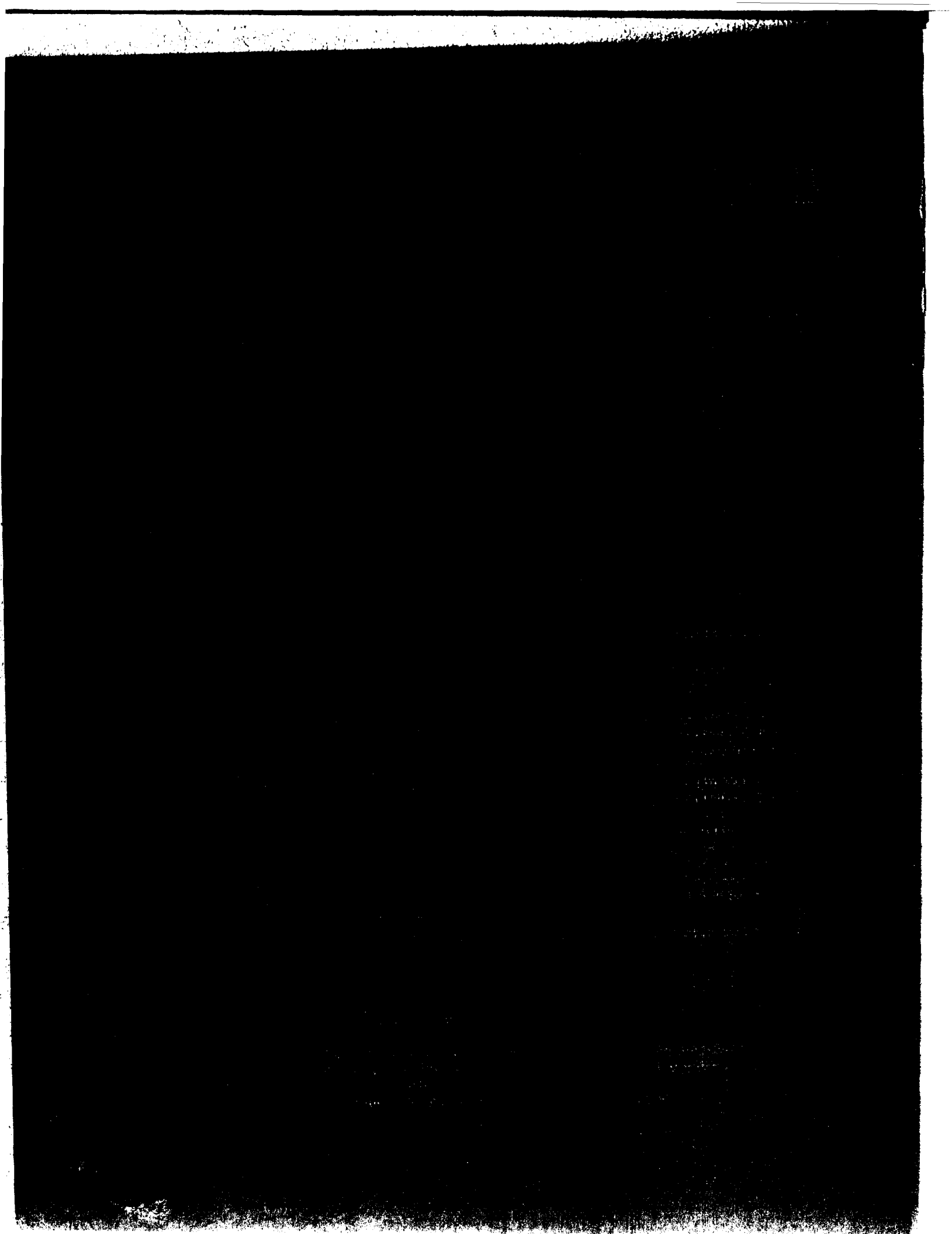


407979

R



ANL-7615

Biology and Medicine

Argonne National Laboratory
9700 South Cass Avenue
Argonne, Illinois 60439

RADIOLOGICAL PHYSICS DIVISION
ANNUAL REPORT

July 1968 through June 1969

R. E. Rowland, Division Director
P. F. Gustafson, Associate Division Director

Preceding Report
ANL-7489-July 1967 through June 1968

FROM ARCHIVES

TABLE OF CONTENTS

TOXICITY OF RADIOELEMENTS

- 1 Application of Cellulose Nitrate Films for Alpha Autoradiography of Bone
ALAN COLE, D. J. SIMMONS, HELEN CUMMINS, F. J. CONGEL, AND JACOB KASTNER
- 3 The Concentration of Radium, Thorium, and Uranium by Tropical Algae
D. N. EDGINGTON, S. A. GORDON, M. M. THOMMES, AND L. A. ALMODOVAR
- 18 Separation of Cesium and Rubidium by the Ferrocyanides of Copper, Zinc and Zirconium
D. N. EDGINGTON, M. M. THOMMES, AND L. I. HARRISON
- 25 Recovery and Modification of Radiation-Induced Division Delay in Developing Sea Urchin Eggs
PATRICIA FAILLA
- 32 The Retention of ^{133}Ba in Beagles
J. E. FARNHAM AND R. E. ROWLAND
- 38 ^{210}Pb and ^{210}Po in Wood and the Circulation of Lead in Trees
R. B. HOLTZMAN AND F. H. ILCEWICZ
- 43 The Concentration of Lead in Human Bone
R. B. HOLTZMAN, H. F. LUCAS, JR., AND F. H. ILCEWICZ
- 49 Non-Uniformity in the Retention of the Alkaline Earths in Animals and Man
ELIZABETH LLOYD
- 53 Variations in the Surface Area and Volume of Bone in Cross Sections Taken from a Single Human Rib
ELIZABETH LLOYD
- 55 Concentrations of Trace Elements in Great Lakes Fishes
H. F. LUCAS, JR., D. N. EDGINGTON, AND P. J. COLBY
- 56 Natural Thorium in Human Bone
H. F. LUCAS, JR., D. N. EDGINGTON, AND FRANK MARKUN
- 58 A Model for the Remodeling and Exchange Rate Distributions in Adult Human Bone. Preliminary Report
J. H. MARSHALL
- 76 Improved Construction of Radioactive Phantoms with Arbitrary Source Distribution
HAROLD MAY, L. D. MARINELLI, AND PAUL HESS
- 81 "Time-of-Flight" Gamma-Ray Camera of Large Dimensions
L. D. MARINELLI, G. F. CLEMENTE, I. K. ABU-SHUMAYS, AND O. J. STEINGRABER
- 87 Regularization Unfolding in Low γ -Ray Activity Measurements. I. Evaluation for One-Dimensional Scanning
G. F. CLEMENTE, L. D. MARINELLI, AND I. K. ABU-SHUMAYS
- 95 Regularization Unfolding for Two Dimensions: Progress Report
I. K. ABU-SHUMAYS
- 97 Metabolism of ^{232}Th Decay Series Radionuclides in Man and Other Animals Following Intravascular Administration of Thorotrast
R. M. PARR, H. F. LUCAS, JR., AND M. L. GRIEM
- 116 Strain Differences in the Response of the Mouse Skeleton to External Beta Irradiation
D. J. SIMMONS, R. HAKIM, AND HELEN CUMMINS
- 120 The Development and Healing of Rickets in Rats. II. Studies with Tritiated Proline
D. J. SIMMONS AND A. S. KUNIN

METEOROLOGICAL STUDIES

- 130 Chicago Air Pollution System Model Experimental Studies
J. E. CARSON
- 133 Chicago's Air Pollution Incident Control Test, Summer 1968
J. E. CARSON, R. J. VOTRUBA, AND J. W. LIN
- 135 Chicago Aircraft Sounding Program
J. E. CARSON AND D. M. NELSON
- 142 Project ITREX—A Cooperative Thunderstorm Tracer Experiment
D. F. GATZ
- 144 City of Chicago Pollution Incidents: Case Studies
D. F. GATZ AND E. W. KLAPPENBACH

- 159 Mathematical Urban Air Pollution Models
HARRY MOSES
- 160 The Use of Pyrhelimeters for Continuous Measurements of an Effective Air Pollution Mixing Depth
HARRY MOSES AND D. N. EGGENBERGER
- 167 The Tabulation Technique for Forecasting Concentrations of Urban Air Pollutants
HARRY MOSES, J. B. ANDERSON, AND D. F. GATZ

RADIATION PHYSICS

- 179 Further Studies on Fluorescence Polarization
W. R. ANDERSON AND I. B. BERLMAN
- 183 On the Fluorescence Characteristics of the *p*-Oligophenylenes and their Substituted Analogs
I. B. BERLMAN AND O. J. STEINGRABER
- 197 Total Cross Sections for Inelastic Scattering of Charged Particles by Atoms and Molecules. III. Accurate Bethe Cross Section for Ionization of Helium
MITIO INOKUTI AND Y.-K. KIM
- 197 Electro-Optical Techniques for Ultrasensitive Radiophotoluminescent Dosimetry
JACOB KASTNER, R. K. LANGS, B. A. CAMERON, MICHAEL PAESLER, AND GEORGE ANDERSON
- 197 Spectral Analysis of Thermoluminescent Glow Curves
B. G. OLTMAN, JACOB KASTNER, AND C. M. PADEN
- 198 Environmental Neutron Measurements with Solid State Track Recorders
J. H. ROBERTS, R. A. PARKER, F. J. CONGEL, JACOB KASTNER, AND B. G. OLTMAN
- 201 Permanent Damage of ${}^7\text{LiF}$ Thermoluminescent Dosimeters by Fast Neutrons
JACOB KASTNER, KEITH ECKERMAN, B. G. OLTMAN, AND PETE TEDESCHI
- 203 Ultrasonic Excitation of Thermoluminescent Lithium Fluoride
JACOB KASTNER, R. H. SELNER, C. M. PADEN, AND B. G. OLTMAN
- 204 Neutron Exposure to Lunar Astronauts
JACOB KASTNER, B. G. OLTMAN, YEHUDA FEIGE, AND RAYMOND GOLD
- 207 Inelastic-Scattering Cross Sections of Fast Charged Particles by Li^+
Y.-K. KIM AND MITIO INOKUTI
- 209 Form Factors of H^- , He , and Li^+
Y.-K. KIM
- 213 The Number of Bound States in Ion-Atom Systems
SMIO TANI AND MITIO INOKUTI
- 214 Generalized Oscillator Strengths of the Helium Atom. III. Transitions from the Ground State to the 3^1D and 4^1P States
Y.-K. KIM AND MITIO INOKUTI
- 214 Specific Primary Ionization
F. F. RIEKE AND WILLIAM PREPEJCHAL
- 218 Tables of Absorption Cross Sections, Photoionization Yields, and Photoionization Cross Sections for Several Gases
J. C. PERSON AND P. P. NICOLE
- 226 Isotope Effects in the Photoionization Yields and the Absorption Cross Sections for Ethylene and *n*-Butane
J. C. PERSON AND P. P. NICOLE
- 226 A Method for Estimating the Relative Importance of the Platzman Competitive Ionization Process from Isotope Effects in Molecular Photoionization
J. C. PERSON
- 228 The Effect of Pressure upon Ionization in Pure Rare Gases
H. A. SCHULTZ

BIO-ENVIRONMENTAL STUDIES

- 229 Behavior of Fallout ${}^{137}\text{Cs}$ in Aquatic and Terrestrial Environments
P. F. GUSTAFSON, S. S. BRAR, D. M. NELSON, AND S. E. MUNIAK
- 231 PUBLICATIONS

APPLICATION OF CELLULOSE NITRATE FILMS FOR ALPHA
AUTORADIOGRAPHY OF BONE

Alan Cole,* D. J. Simmons, Helen Cummins, F. J. Congel, and Jacob Kastner

Cellulose nitrate can be used to record the tracks of alpha particles from bone and may have some advantages over nuclear emulsions. The tracks are made visible by etching the cellulose nitrate film with NaOH and no darkroom is required. Beta rays and electrons do not produce tracks, so background fogging is eliminated. The etching process makes visible only those alpha particle tracks which penetrate the film, so the attainable resolution may be better than that of nuclear emulsions. Finally, the alpha tracks are enlarged and so may be more easily counted by a photoelectric scanner.

When an alpha particle strikes the surface of a dielectric material such as a cellulose nitrate foil and gives up more energy per unit distance along its trajectory than the critical value of the material, latent etchable tracks are produced.⁽¹⁾ The ionization and subsequent electrostatic repulsion produced by the particle creates vacancies along its path by ejecting atoms from the nitrocellulose molecules into interstitial positions. The resulting molecular fragments are more soluble than the parent molecule.⁽¹⁻³⁾ The process of recording alpha particle tracks in nitrocellulose foil by etching radiation damaged sites has been called alphagraphy. It is a simple and direct method, and because nitrocellulose films offer certain technical advantages over photographic nuclear emulsions, it has found application in health physics for dosimetry.⁽³⁾ This technique can discriminate between heavy and light charged particles, and thus the films are insensitive to electrons, thermal neutrons, or gamma irradiation. In addition, they will not fog during long term exposures, they are remarkably stable, and they can be processed (etched) in daylight and at room temperatures.

It is possible to prepare thin films of cellulose nitrate which are selectively sensitive to alpha particles which have an energy range up to 5 MeV. This suggested that the technique might be useful when high resolution autoradiographic studies are required to visualize the tissue localization of bone-seeking radioisotopes such as plutonium and radium. We will describe a method of cellulose nitrate film prepara-

tion and etching which has produced high quality autoradiographs of bone sections from mice injected intravenously with a monomeric solution of 1% sodium citrate with 90% ultrafilterable ²³⁹Pu (0.1 μ Ci).⁽⁴⁾ The animals were sacrificed 6 days after injection. The long bones obtained at autopsy were fixed in 95% alcohol, embedded undecalcified in methyl methacrylate, and were cut on a high speed rotary saw longitudinally at 100 μ . The tissue sections had been used previously to prepare contact autoradiographs using Kodak Type A autoradiographic plates, and the results of that study have recently been published by Rosenthal et al.⁽⁴⁾

We prepared a stock solution of nitrocellulose according to Benton's⁽²⁾ method: 17 g nitrocellulose† were first dissolved in a solvent composed of 5.1 g isopropyl alcohol, 4.0 g butyl alcohol, and 8 g cello-solve acetate. This solution was then dissolved in 61.9 g ethyl acetate, and 4 g dioctyl phthalate were added as a plasticizer. The mix was permitted to age for 4 days to achieve chemical equilibrium before use as an autoradiographic detector film. In practice, we diluted 25 ml of the stock solution by adding 75 ml ethyl acetate in order to obtain thin (3 μ) detector films.

Autoradiographs were prepared by simply dipping the bone sections mounted on microscope slides into the dilute cellulose nitrate solution for 10 sec. The slides were removed vertically and allowed to drain for an additional 10 sec. The underside of each slide was wiped free of the solution and the preparations were air dried horizontally overnight under a glass dish to avoid contamination with dust. The coated slides were then annealed at 70° C for 4 hr to temper the detector film as recommended by Benton,⁽²⁾ and were wrapped in aluminum foil during the exposure period. The autoradiographs were developed in a stendor dish by etching the detector films with 6.5 N NaOH at 24° C for 2 hr. Since the rate at which the hydroxyl ions attacked the radiation dam-

* Present address: Department of Anatomy, The Bowman Gray School of Medicine, Winston-Salem, North Carolina.

† Hercules Powder Co., Wilmington, Delaware; nitrocellulose RS 11.8-12.2% N₂, 5- to 6-sec viscosity, 30% isopropyl alcohol by weight.

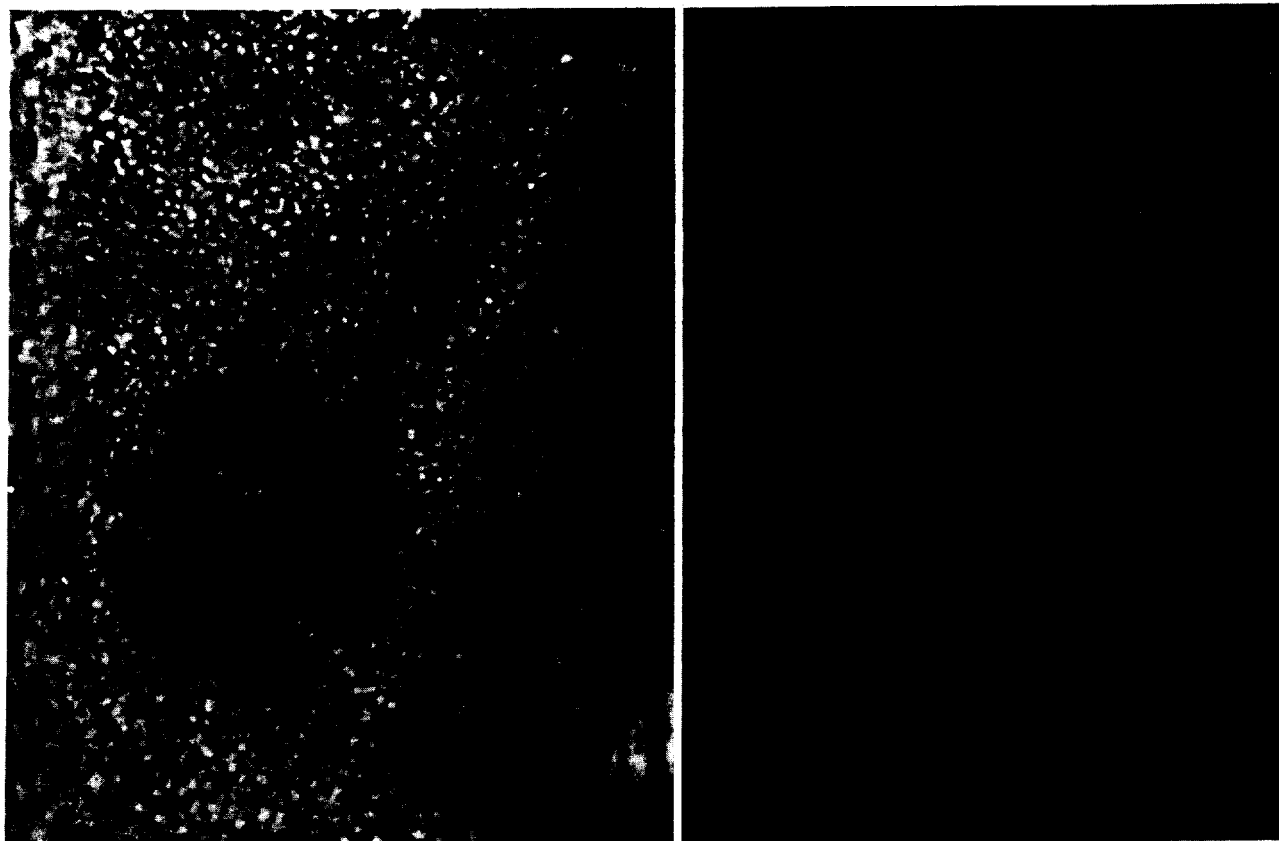


FIG. 1.—A comparison between (A) cellulose nitrate and (B) Kodak AR-10 stripping film autoradiographs of longitudinal sections from the tibia of a mouse injected with 0.1 μ Ci ionic ^{239}Pu . Both sections show alpha tracks over the endosteal surfaces of the bone. The tracks registered in the cellulose nitrate detector film after two 2-hr periods are well defined at low (100 \times) magnification. Higher magnifications (250 \times) were required to demonstrate the alpha tracks in the AR-10 emulsion.

aged sites was greater than the rate at which they attacked the bulk material (1 μ /hr), tracks were developed along the ionization paths of the alpha particles. The etching process has been described⁽²⁾ as a solid-liquid interface reaction which proceeds in two steps—the diffusion of ions from the oxidizing agent to the interface and the interface reaction. Strict control of detector film preparation is required since the etching behavior of cellulose nitrate is affected by a number of variables, such as the degree of polymerization and nitration, the plasticizer, temperature, etching time, hydroxyl concentration, and oxygen.⁽¹⁻³⁾ Daylight has not been reported to be an influencing parameter, but UV light apparently increases the etchability of detector films by decomposing the bulk material.⁽¹⁾ Since the detector films are mechanically very stable, they can withstand repeated etching. Should, for instance, an initial exposure period prove too short to develop a sufficient number of tracks, an autoradiograph may be stored and re-etched at a later time. However, while serial etching will develop new tracks registered in the detector film after each pre-

ceding etch period, the process will enlarge previously etched tracks as well and reduce the resolution of the autoradiograph somewhat.

Figure 1A shows a typical cellulose nitrate autoradiograph of bone from a mouse injected with ionic ^{239}Pu . The etched tracks, which have a conical shape and a 1 μ diameter, lie over the surface of the endosteum. Figure 2 shows a similar autoradiograph of trabecular bone. The apex of each track marks the initial damage site, and the broad end indicates where the particle emerged from or came to rest in the film. Cellulose nitrate films always show some background etch pits due to inclusion of debris during preparation and etching. But the background is never severe even after repeated etching and may be almost totally abolished by simply agitating or changing the etching solution at frequent intervals.

The resolution of the cellulose nitrate films is at least as good as, and perhaps better than, that provided by the nuclear emulsion Kodak AR-10. Figure 1B shows an AR-10 stripping film autoradiograph of an adjacent bone section exposed for an equivalent

period of time. The detection efficiency of cellulose nitrate film is not quite as high as that of nuclear emulsions because the etching process reaches only those particles which penetrate the top surface of the film (away from the bone). Since the films were 3 μ thick and the etching process removed 1-2 μ , a few tracks were missed. On the other hand, this penetration effect should increase resolution (particularly with thicker films) by etching only those alpha tracks which are more perpendicular to the plane of the film.

In summary, the cellulose nitrate method provides an alternative to autoradiography with nuclear emulsions. It does not require darkroom facilities. The alpha tracks are enlarged and more easily detectable. Background fogging is eliminated. At the expense of some decrease in efficiency one should be able to obtain better resolution than with emulsions.

REFERENCES

1. Fleischer, R. L., Price, P. B. and Walker, R. M. *Ann. Rev. Nucl. Sci.* **15**, 1 (1965).
2. Benton, E. V. U. S. Naval Radiological Defense Laboratory Report USNRDL-TR-14 (1968).
3. Becker, K. *Health Phys.* **16**, 113 (1969).
4. Rosenthal, M. W., Marshal, J. H. and Lindenbaum, A. *Diagnosis and Treatment of Deposited Radionuclides*, Symp. Richland, Washington, May 15-17, 1967. Excerpta Medica Foundation, Amsterdam, 1968, pp. 73-80.



FIG. 2.—A serially etched cellulose nitrate autoradiograph of trabecular bone from mouse, injected with 0.1 μ Ci ionic ^{239}Pu , which shows surface alpha tracks. 100 \times .

THE CONCENTRATION OF RADIUM, THORIUM, AND URANIUM BY TROPICAL ALGAE

D. N. Edgington, S. A. Gordon,* M. M. Thommes, and L. R. Almodovar†

Samples of twenty species of marine algae collected between 1961 and 1968 in Puerto Rico have been analyzed for total organic material, protein nitrogen, calcium, radium, thorium, and uranium. The results suggest that the concentration of radium, thorium, or uranium by these organisms may be controlled by two mechanisms: (1) ion-exchange or coprecipitation of the ion with the calcium carbonate matrix, or (2) complex formation with either the protein nitrogen or some other component of the organic fraction.

Concentration of radium (and possibly thorium) appears to occur by both mechanisms, the dominant one being dependent upon the division. For the *Rhodophyceae* and the highly calcified *Chlorophyceae* it is the former, and for the *Phaeophyceae* the latter. Concentration of uranium occurs by the first mechanism. This difference in behavior is consistent with the chemical forms of the ions of these elements in seawater.

* Biological and Medical Research Division.

† Department of Marine Biology, University of Puerto Rico.

INTRODUCTION

To predict the consequences of the accidental release of radionuclides from nuclear power plants it is necessary to understand the mechanisms by which stable elements are concentrated and transported within the ecosystem. Nuclear power plants, by necessity, are located close to large bodies of water for cooling purposes. Hence, aquatic organisms are among the first most likely to be affected by radionuclide release. Also, data on their natural levels of radioactivity would be useful as reference indices.

While some information is available on the concentration of various elements and radionuclides from fallout in marine organisms,⁽¹⁻³⁾ little is known concerning their distribution within species, between species, and as a function of collection site. In 1961, before the nuclear reactor "Bonus" at Punta Jiquero

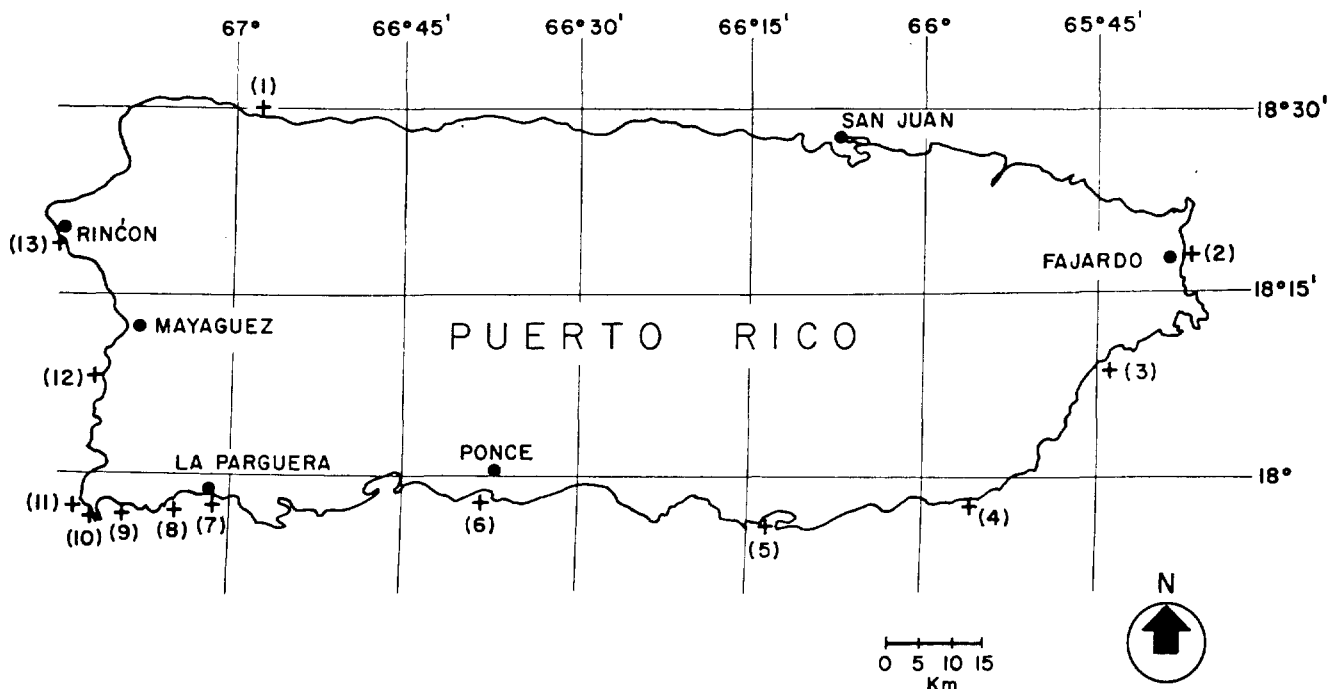


FIG. 3.—Sampling locations for the collection of algae. (1) Guajataca: rocks and surf; (2) Fajardo, Bahia Yeguas; (3) Humacao, Cayo Santiago: rocks; (4) Guardarraya: rocks; (5) Aguirre: rocks, reef in front of Central Aguirre; (6) Cayo Cardona (12 km S.W. Playa de Ponce: rocks); (7) Cayo Don Luis, La Parguera; (8) Guayacon (~3 km W. Playa La Parguera); (9) Margarita (~12 km S.W. Playa La Parguera); (10) Cabo Rojo, La Playnela (East); (11) Cabo Rojo, Punta Aquila (West); (12) Punta Arenas; (13) Rincon: rocks, surf; (14) Culebra (not included on map).

near Rincon on the northwest coast of Puerto Rico went critical, a series of samples of different species of marine algae were collected from sites around the island (Figure 3). These samples, together with several additional collections made in 1967 and 1968, have been analyzed for (1) the naturally-occurring alpha particle emitters, radium (^{226}Ra), thorium (^{232}Th) and uranium (^{238}U); (2) three components representative of the total mass of the organism, total organic material, protein nitrogen, and calcium; (3) trace elements including cadmium, chromium, cobalt, copper, indium, gallium, iron, and arsenic; and (4) the gamma radioactivity from both naturally-occurring as well as fallout isotopes. In this paper we shall discuss the relationships between the natural levels of radium, thorium, or uranium with protein nitrogen and calcium carbonate.

METHODS

Algae Samples

Algal samples were collected from thirteen different locations around the coast of Puerto Rico and on the island of Culebra which is 38 km east of Fajardo (Figure 3).

The algal samples were rinsed briefly in fresh water as soon as possible after collection, drained, and dried under forced draft at 100°C to constant weight. They

were then ground in a Wiley mill to a 20-mesh powder.

The different species of algae collected and their sites of collection are listed in Table 1. (For the coding of the sites of collection see Figure 3.)

Radium

Radium was determined using the radon emanation method described by Lucas.⁽⁴⁾ Twenty-gram samples of the algae were suspended in dilute nitric acid to decompose any carbonates present and then digested with aliquot portions of concentrated nitric acid until the evolution of oxides of nitrogen ceased. A siliceous residue was found after digestion of almost all of the samples. This residue was removed by filtration, dried, and weighed. The filtrate was diluted to approximately 200 ml with radium-free water and transferred to the emanation flask for radon analysis. The total radium concentration in these samples varied between 0.2 and 2 pCi (approximately 1-10 cpm ^{222}Rn).

Thorium and Uranium

Thorium, uranium, and other trace elements were determined by the neutron activation methods of Edgington and Lucas.^(5, 6) One-gram samples of the algal powder were ashed by low temperature oxida-

TABLE 1. IDENTIFICATION OF SAMPLES AND SUMMARY OF RESULTS OF ANALYSES

Division and species	Sample No.	Collection		Soluble fraction	Organic, g/g	Nitrogen, mg/g	Calcium, g/g	Radium, pCi/g	Thorium, µg/g	Uranium, µg/g
		Date	Site							
CHLOROPHYTA										
<i>Halimeda opuntia</i>	3	1961	8	1.000	0.260	5.460	0.300	0.020		1.240
	21	1961	10	0.996	0.060	2.200	0.320	0.060		1.850
	39	1961	6	0.984	0.080	2.560	0.330	0.050	0.100	1.770
	44	1961	5	0.989	0.430	2.560	0.250	0.020	0.220	0.680
	49	1961	12	0.941	0.050	2.580	0.360	0.030		1.280
	54	1961	14	0.973	0.070	2.460	0.320	0.030		1.750
	75	1968	9	0.978	0.060	3.300	0.310	0.070	0.090	1.620
	80	1968	10	0.973	0.100	3.300	0.306	0.040		1.470
	85	1968	12	0.956	0.080	3.400	0.291	0.110	0.070	1.460
				<i>N</i>	9	9	9	9	4	9
				\bar{X}	0.132	3.091	0.310	0.048	0.120	1.458
				σ_x	0.043	0.329	0.010	0.010	0.034	0.121
<i>Penicillus capitatus</i>	10	1961	9	0.907	0.310	5.900	0.275	0.080	0.120	1.650
	20	1961	10	0.968	0.260	10.400	0.236	0.030	0.075	1.580
	57	1961	14	0.990	0.340	11.400	0.202	0.020	0.110	1.600
	74	1968	9	0.970	0.180	8.700	0.231	0.030		1.700
	79	1968	9	0.928	0.140	5.900	0.285	0.060	0.080	1.690
	84	1968	12	0.852	0.190	5.900	0.275	0.080	0.070	1.650
					<i>N</i>	6	6	6	6	5
				\bar{X}	0.237	8.033	0.251	0.050	0.091	1.645
				σ_x	0.032	1.017	0.013	0.011	0.010	0.019
<i>Aurainvillea rawsoni</i>	61	1961	14	0.756	0.140	13.500	0.110	0.110		1.000
	65	1961	11	0.808	0.090	4.000	0.027	0.120	0.270	0.970
	67	1961	10	0.975	0.130	6.400	0.200	0.050	0.280	1.590
	69	1967	4	0.487	0.150	6.500	0.150	0.200	0.390	0.280
	72	1967	3	0.840	0.150	7.500	0.243	0.140	0.160	1.380
				<i>N</i>	5	5	5	5	4	5
				\bar{X}	0.132	7.580	0.146	0.124	0.275	1.044
				σ_x	0.011	1.588	0.037	0.024	0.047	0.224
<i>Ulva latuca</i>	14	1961	10	0.917	0.490	8.300	0.003	0.010		0.100
	37	1961	6	0.945	0.400	12.900		0.020	0.050	0.210
	40	1961	4	0.947		25.200		0.010		
<i>Cyrtospira barbata</i>	16	1961	11	0.996	0.240	7.200	0.204	0.010	0.060	1.270
	30	1961	1	0.937	0.210	7.900	0.393	0.030		1.460
<i>Caulerpa racemosa</i>	11	1961	7	0.981	0.460	16.000	0.084	0.050	0.130	0.370
<i>Codium isthmocladium</i>	29	1961	13	0.945	0.490	9.700	0.002	0.040		0.130
RHODOPHYTA										
<i>Laurencia papillosa</i>	5	1961	12	0.853	0.360	8.200	0.120	0.060		0.450
	17	1961	11	0.876	0.430	7.900	0.190	0.060	0.080	0.240
	33	1961	1	0.919	0.480	11.460	0.060	0.020	0.160	0.300
	45	1961	5	0.801	0.300	7.390	0.110	0.040	0.150	0.660
	59	1961	14	0.944	0.400	11.640	0.110	0.150		0.510
	63	1961	14	0.990	0.430	15.160	0.070	0.050		0.300
				<i>N</i>	6	6	6	6	3	6
				\bar{X}	0.400	10.292	0.110	0.063	0.130	0.410
				σ_x	0.030	0.857	0.026	0.019	0.025	0.080

TABLE 1.—Continued

Divison and species	Sample No.	Collection		Soluble fraction	Organic, g/g	Nitrogen, mg/g	Calcium, g/g	Radium, pCi/g	Thorium, $\mu\text{g/g}$	Uranium $\mu\text{g/g}$
		Date	Site							
<i>Gracillaria cornea</i>	26	1961	13	0.986	0.560	6.840	0.040	0.030	0.090	0.250
	27	1961	13	0.954	0.570	9.180	0.030	0.010		0.210
	28	1961	13	0.997	0.270	13.580	0.010	0.010		0.180
	34	1961	1	0.997	0.520	10.760	0.010	0.010		0.100
				N	4	4	4	4	1	4
				\bar{X}	0.480	10.090	0.023	0.015	0.090	0.185
				σ_x	0.071	2.026	0.015	0.011		0.039
<i>Acanthopora specifera</i>	6	1961	7	0.951	0.430	11.460	0.150	0.060	0.620	0.470
	42	1961	5	0.768	0.230	12.000	0.140	0.090		0.630
	56	1961	14	0.919	0.170	8.120	0.100	0.030		0.610
	70	1967	3	0.984	0.270	10.200	0.070	0.190		0.720
				N	4	4	4	4	1	4
				\bar{X}	0.275	10.445	0.115	0.092	0.620	0.607
				σ_x	0.090	0.864	0.033	0.031		0.152
<i>Hypnea musciformis</i>	12	1961	10	0.928	0.430	17.300	0.003	0.110	0.020	0.240
	25	1961	13	0.880	0.450	15.900	0.009	0.020		0.300
	38	1961	6	0.930	0.430	20.600	0.009	0.020		0.240
				N	3	3	3	3	1	2
				\bar{X}	0.437	17.933	0.007	0.050	0.020	0.270
				σ_x	0.069	3.275	0.026	0.063	0.000	0.000
<i>Digenia simplex</i>	22	1961	10	0.900	0.410	5.900	0.140	0.050	0.300	0.630
	31	1961	1	0.776	0.340	11.500	0.158	0.030		0.620
	73	1967	11	0.882	0.480	6.500	0.173	0.140		0.400
				N	3	3	3	3	1	3
				\bar{X}	0.410	7.967	0.157	0.073	0.300	0.550
				σ_x	0.030	5.422	0.061	0.030		0.043
<i>Bryothamnion triquetrum</i>	23	1961	13	0.854	0.450	7.500	0.167	0.040		0.070
<i>Ceramium nitens</i>	7	1961	7	0.957	0.590	14.120	0.020	0.030	0.070	0.190
<i>Galaxaura cylindrica</i>	24	1961	13	0.962	0.200	6.000	0.256	0.020		0.850
<i>Spyridia filamentosa</i>	41	1961	5	0.872		10.200	0.087	0.040		
PHAEOPHYTA										
<i>Dictyota divaricata</i>	2	1961	9	0.984	0.290	8.280	0.130	0.070	0.160	1.140
	43	1961	5	0.703	0.110	7.940	0.110	0.080		2.140
	55	1961	14	0.959	0.220	3.800	0.330	0.100		1.940
	68	1961	4	0.643	0.270	5.400	0.160	0.120		0.200
	71	1967	2	0.928	0.230	7.400	0.120	0.090		0.130
				N	5	5	5	5	2	5
				\bar{X}	0.224	6.564	0.170	0.092	0.145	1.266
				σ_x	0.030	1.141	0.047	0.021		0.265
<i>Padina gymnospora</i>	9	1961	9	0.907	0.300	5.700	0.151	0.080	0.155	0.780
	18	1961	10	0.919	0.200	3.500	0.234	0.040	0.085	1.150
	35	1961	6	0.877	0.300	6.500	0.130	0.050	0.120	1.030
	60	1961	14	0.905	0.380	8.800	0.098	0.100	0.240	0.650
	81	1968	10	0.938	0.330	5.200	0.153	0.070		0.640
	86	1968	12	0.836	0.340	5.500	0.192	0.060	0.340	0.700
				N	6	6	6	6	5	6
				\bar{X}	0.308	5.867	0.160	0.067	0.188	0.825
				σ_x	0.029	0.757	0.020	0.014	0.034	0.139

TABLE 1.—Continued

Division and species	Sample No.	Collection		Soluble fraction	Organic, g/g	Nitrogen, mg/g	Calcium, g/g	Radium, pCi/g	Thorium, μ g/g	Uranium, μ g/g
		Date	Site							
<i>Sargassum polyceratum</i>	4	1961	7	0.992	0.360	8.600	0.040	0.100	0.130	0.440
	15	1961	10	0.981	0.380	11.200	0.031	0.080		
	32	1961	1	0.928	0.500	14.000	0.044	0.080		0.430
	48	1961	12	0.970		9.400	0.061	0.150		
	53	1961	14	0.970		8.800	0.080	0.090		
				N	3	5	5	5	1	2
				\bar{X}	0.413	10.400	0.051	0.100	0.130	0.435
				σ_x	0.063	1.842	0.039	0.013		0.000
<i>Turbinaria turbinata</i>	19	1961	10	0.997	0.310	8.200	0.024	0.110	0.220	0.610
	62	1961	14	0.850		17.100	0.007	0.130		
				N	1	2	2	2	1	1
				\bar{X}	0.310	12.650	0.015	0.120	0.220	0.610
				σ_x	0.000	0.000	0.000	0.000		0.000

tion with ionized oxygen.* Samples of the ash were then irradiated in the Argonne National Laboratory CP-5 reactor, along with suitable standards. The integrated neutron flux was approximately 5×10^{16} n/cm². After irradiation the samples were dissolved in concentrated hydrochloric acid and fractionated by passage through an anion exchange column. The daughter products, ²³³Pa and ²³⁹Np from the ²³³Th and ²³⁹U, produced by neutron irradiation were eluted from the column and assayed by gamma-ray spectroscopy.

Calcium

Calcium was determined by atomic adsorption spectrophotometry.⁽⁷⁾ The determinations were made on the same solutions used for radium analysis.

Protein Nitrogen

Protein nitrogen was determined by the micro Kjeldahl method. One-hundred-milligram samples of the algae were suspended in 5% trichloroacetic acid and allowed to remain overnight at 4° C. The precipitate was washed by centrifugation with the trichloroacetic acid and then oxidized with concentrated sulfuric acid and hydrogen peroxide. After partial neutralization of the digestion mixture, the nitrogen content was determined colorimetrically using Nessler's reagent.⁽⁸⁾

Total Organic Matter

The total organic matter content was estimated from the loss in weight during the low temperature

oxidation with ionized oxygen. The oxidation of organic matter is presumed to be the major contributor to the loss of weight, but it must be recognized that the oxidation of various inorganic compounds, i.e., bromides and iodides, may also occur and contribute to the loss in weight.

RESULTS AND DISCUSSION

The results of the analyses for (1) total organic material, (2) the concentration of nitrogen precipitated by trichloroacetic acid (as an index of protein content), (3) calcium, (4) radium, (5) thorium, and (6) uranium are given in Table 1 together with other data pertinent to the identification of the individual algal samples. The first three of these analyses are representative of the major chemical components of the algae.

Calcium is considered a major component because, of the ten divisions into which algae have been classified, five contain members which lay down appreciable concentrations of calcium carbonate.⁽⁹⁾ Three of the five divisions, the green algae (*Chlorophyta*), the brown algae (*Phaeophyta*) and the red algae (*Rhodophyta*) are represented in the samplings made in this study. For *Chlorophyta* the calcareous algae belong to the families of the order Siphonales—the Dasycladaceae (*Cympolia*) and the Codiaceae (*Halimeda opuntia* and *Penicillus capitatus*). On the other hand *Padina gymnospera* is the sole representative of the *Phaeophyta* which calcifies, and for the *Rhodophyta* there was a single collection of *Galaxaura cylindrica* which is highly calcified. The results from the analysis of a limited series of samples of seawater and sand are given in Table 2. The analytical results presented

* Tracerlab Low Temperature Asher, Model LTA 600, Large Sample Assembly.

in Tables 1 and 2 are, for almost all the different algal samples, averages of replicate determinations on the same large (20 g) sample for radium and calcium, and on different small (< 1 g) samples for total organic content, nitrogen and the neutron activation analysis experiments, which generally were in agreement to better than $\pm 10\%$.

In almost all of the algal samples an insoluble off-white residue remained after wet oxidation or dissolu-

tion of the product of low temperature oxidation nitric or hydrochloric acid. These residues were found to be soluble in hydrofluoric acid and were, therefore, in all probability hydrated silicates. This residue was filtered off and weighed. All analytical results have been normalized to the soluble weight, and the fraction of each sample which dissolved is shown in Table 1. The insoluble residue generally accounts for less than 10% of the gross weight; for most of the

TABLE 2. ANALYSIS OF WATER, SAND, AND THREE SPECIES OF ALGAE COLLECTED FROM THREE DIFFERENT LOCATIONS

Location	Material	Soluble fraction	Ca, g/g	Ra, pCi/g	U, $\mu\text{g/g}$	Ra/Ca	U/Ca
Cajo Margarita (9)	Water	1.00	3.9×10^{-4}	7.2×10^{-5}	3×10^{-3} (a)	0.18	7.6
	Sand	0.984	0.30	0.039	1.68	0.13	5.3
	<i>Halimeda opuntia</i>	0.978	0.31	0.073	1.62	0.24	5.2
	<i>Penicillus capitatus</i>	0.970	0.23	0.034	1.70	0.15	7.4
	<i>Padina gymnospora</i>	—	—	—	—	—	—
Cabo Rojo (10)	Water	1.00	4.4×10^{-4}	1.3×10^{-4}	3×10^{-3} (a)	0.29	6.8
	Sand	0.780	0.32	0.072	1.08	0.22	3.4
	<i>Halimeda opuntia</i>	0.973	0.31	0.045	1.48	0.15	4.8
	<i>Penicillus capitatus</i>	0.928	0.28	0.060	1.69	0.21	5.9
	<i>Padina gymnospora</i>	0.938	0.15	0.067	0.64	0.44	4.2
Punta Arenas (12)	Water	1.00	3.5×10^{-4}	4.1×10^{-5}	3×10^{-3} (a)	0.12	8.7
	Sand	0.554	0.25	0.086	0.59	0.34	2.4
	<i>Halimeda opuntia</i>	0.956	0.29	0.08	1.46	0.37	5.0
	<i>Penicillus capitatus</i>	0.852	0.28	0.080	1.65	0.29	6.0
	<i>Padina gymnospora</i>	0.836	0.19	0.060	0.70	0.31	3.6

(a) From Ref. 15.

TABLE 3. RESULTS OF REGRESSION ANALYSIS

Correlation	All algae			<i>Chlorophyta</i>			<i>Rhodophyta</i>			<i>Phaeophyta</i>		
	R	f	P	R	f	P	R	f	P	R	f	P
Organic with												
Nitrogen ^(a)	0.57	64	0.001	0.60	26	0.001	0.15	23	—	0.65	15	0.01
Calcium ^(a)	-0.66	63	0.001	-0.57	25	0.005	-0.42	23	0.05	-0.51	15	0.05
Radium ^(a)	-0.23	64	—	-0.40	26	0.05	-0.17	23	—	-0.09	15	—
Thorium ^(a)	-0.12	33	—	-0.15	16	—	-0.67	8	—	-0.60	9	—
Uranium ^(a)	-0.77	62	0.001	-0.69	26	0.001	-0.73	22	0.001	-0.73	14	0.005
Nitrogen with												
Radium ^(a)	-0.09	69	—	-0.19	27	—	-0.06	24	—	0.43	18	0.10
Radium ^(b)	-0.14	56	—	-0.18	22	—	-0.19	19	—	0.69	15	0.005
Thorium ^(a)	-0.09	33	—									
Uranium ^(a)	-0.54	62	0.001	-0.46	26	—	-0.34	22	—	0.29	14	—
Calcium with												
Nitrogen ^(a)	-0.69	67	0.001	-0.56	25	0.005	-0.65	24	0.001	0.80	18	0.001
Nitrogen ^(b)	-0.69	55	0.001	-0.67	21	0.001	-0.60	19	0.01	0.82	15	0.001
Radium ^(a)	-0.10	67	—	-0.17	25	—	0.19	24	—	-0.40	18	—
Radium ^(b)	-0.02	54	—	-0.08	21	—	0.51	19	0.001	-0.81	15	0.001
Thorium ^(a)	-0.22	32	—									
Uranium ^(a)	0.76	61	0.001	0.77	25	0.001	0.56	22	0.01	0.50	14	0.10
Uranium ^(b)	0.77	50	0.001	0.83	21	0.001	0.62	18	0.05	0.31	12	—

(a) All data taken.

(b) Selected data. Individual data point dropped if $\bar{X} - 3\sigma < X < \bar{X} + 3\sigma$ for each species.

samples it was less than 5%. Silicification appears to be associated particularly with the yellow-green algae, the *Chrysophyta*⁽¹⁰⁾. Thus the residue might derive, in part, from epiphytic diatoms.⁽¹¹⁾ The insoluble residues might also represent mechanically entrapped contaminants. It would be expected that those algae which have a mat- or sponge-like structure, and which grow where there is considerable suspended material of land origin, would show the greatest degree of such entrapment. It is of interest, therefore, that the spongy *Aurainvillea rawsoni* shows the greatest degree of variation in insoluble residue, its soluble fraction varying between 0.98 and 0.48 for different samples. *Laurencia papillosa* and *Dictyota divaricata* also show a large variation in their soluble fractions.

The degree of contamination by silica would also depend on the nature of the bottom sediments where the algae are growing. The importance of this factor may be inferred from the variability in the values of the analyses for calcium and insoluble matter in the samples of sand from different locations (Table 2). Even the limited sampling represented by Table 2

shows that, depending on collection location, the sand can consist of from 60% to 90% of calcium carbonate and other acid soluble components. It may be further noted from the data in Table 2 that the concentrations of radium, uranium, and calcium in sand are very similar to those reported for the samples of *Halimeda opuntia* or *Penicillus capitatus* (Table 1 also). This is consistent with the observations that the sands in the region of collection are made up largely of the mineral residues of calcareous organisms, particularly *Halimeda*.⁽¹²⁾ Thus, it is possible that calcareous contamination might have contributed to the extent of variance found for some of the analyses.

For those species where samples were collected in sufficient number in 1961 and again in 1967 or 1968, there were no significant differences between the two groups in their concentrations of calcium, radium, uranium or nitrogen. An insufficient number of samples from each location precludes an evaluation of the effect of the environment at each collection site or of location dependent differences for the various spe-

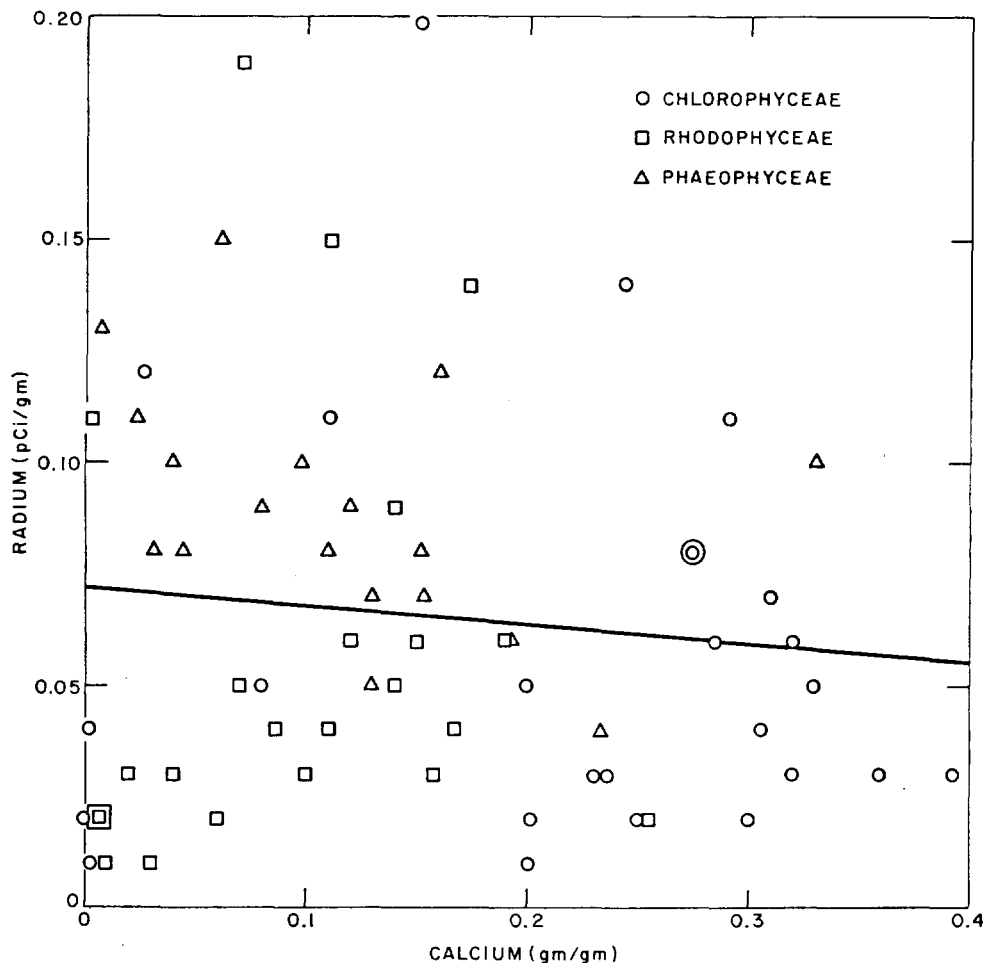


FIG. 4.—The variation in the concentration of radium with the degree of calcification of the algae

cies collected. However, samples of *Halimeda opuntia*, *Penicillus capitatus* and *Padina gymnospora*, and contiguous water and sand, were collected at three different sites in 1968. Some analytical data for these samples are summarized in Table 2. Cajo Margarita (9) and Cabo Rojo (10) are close to each other on the southwest coast and Punta Arenas (12) is on the west coast of the island (Figure 3). From these analytical values, the concentrations of calcium and radium appear to be lower on the west coast of the island than at the two locations on the southwest coast. Surprisingly, as is shown by the values of the $[Ra]/[Ca]$ ratio, samples of all three species of algae and sand at Punta Arenas concentrate radium preferentially to calcium from sea water by a factor greater than two, while on the southwest coast there is, in general, no concentration or even a discrimination. It may be noted further from the values of the $[U]/[Ca]$ ratio there is a discrimination against uranium by all of the three species investigated, as well as by sand, at these collection sites.

In addition to measuring the concentration of cal-

cium in these samples, the total content of organic material and protein nitrogen were also determined. From all these data an attempt has been made to understand the apparently complex relationship which govern the concentration of radium, thorium and uranium by these algae. To this end regression analysis of the analytical data has been made and correlation coefficients calculated. The values of the correlation coefficients R , the number of degrees of freedom f and the probability P of there being no correlation in each case are tabulated in Table 3 according to phyta and for the complete sample. In the case of some of the correlations the values before and after the rejection of suspect data are recorded.

When the degree of calcification increases, the proportion of organic matter in the organism should decrease. Regression analysis of the analytical data confirms this proposition (Table 3); the correlation coefficients of -0.66 ($f = 63$) for total organic material and -0.69 ($f = 67$) for protein nitrogen with calcium are both highly significant when considering all algal samples. Analysis of the data according to

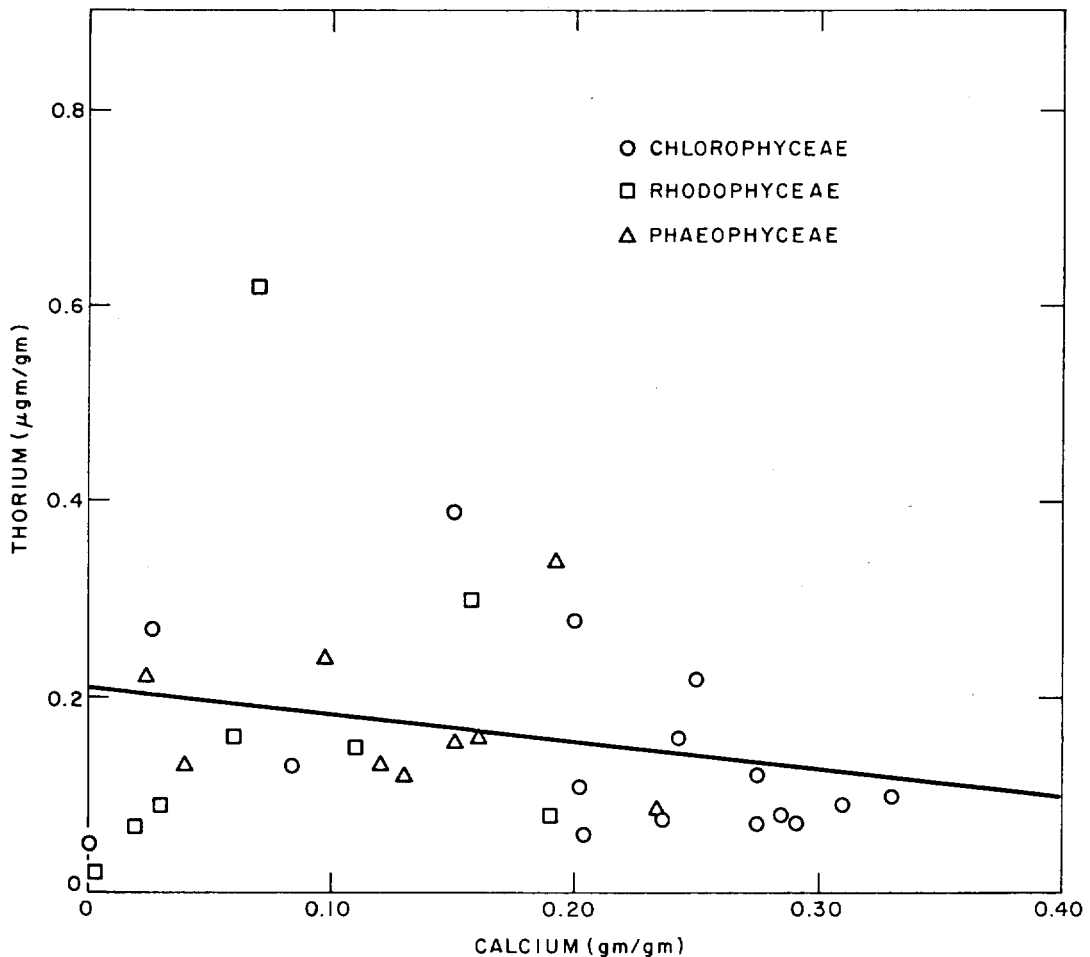


FIG. 5.—The variation in the concentration of thorium with the degree of calcification of the algae

phyta does not alter the significance of the correlation.

As might be expected, the correlation between protein nitrogen and total organic material was also highly significant ($R = 0.57$ for $f = 64$). However, if the regression analysis is carried out according to phyta, the correlation for *Chlorophyta* and *Phaeophyta* is highly significant while there is no correlation for the *Rhodophyta*.

In all of the species of algae analyzed in this study calcium carbonate is laid down and normally retained as the orthorhombic crystalline form aragonite, which, while being metastable under many conditions, is the most common modification in warm tropical waters.⁽¹³⁾ The exchange or coprecipitation of radium or uranyl ions with calcium in the aragonite lattice is possible because there should be neither steric problems nor restrictions on the formation of solid solutions due to ionic size (particularly at the extremely low concentrations of these two ions). Therefore it would be expected that either of these two ions (Ra^{++} or UO_2^{++}) could act as a tracer for calcium

and that their concentration in the organism would be directly proportional to its calcium content. Although there is no biological evidence of this in a calcium carbonate system, there are many instances of radium localization at sites where calcification occurs in the bones of animals. Inferences have been made concerning calcium metabolism on the basis of this localization.⁽¹⁴⁾ There is, thus, the widely held belief that radium may be used as a tracer for calcium at least in the apatite (calcium phosphate) system. Similarly, while data for uranium metabolism are relatively scarce, the uranyl ion is found in all natural apatite deposits. In the case of thorium and its ions, whose solution chemistry under the conditions of pH and salinity found in seawater is complex, it is uncertain whether any thorium would be present in an ionic form to act as a tracer for calcium.

The relationships between radium, thorium, and uranium with calcium are shown in Figures 4 to 6. The lines drawn through the experimental data were derived from the regression analyses for each set of data. These analyses (Table 3) show that (1) there

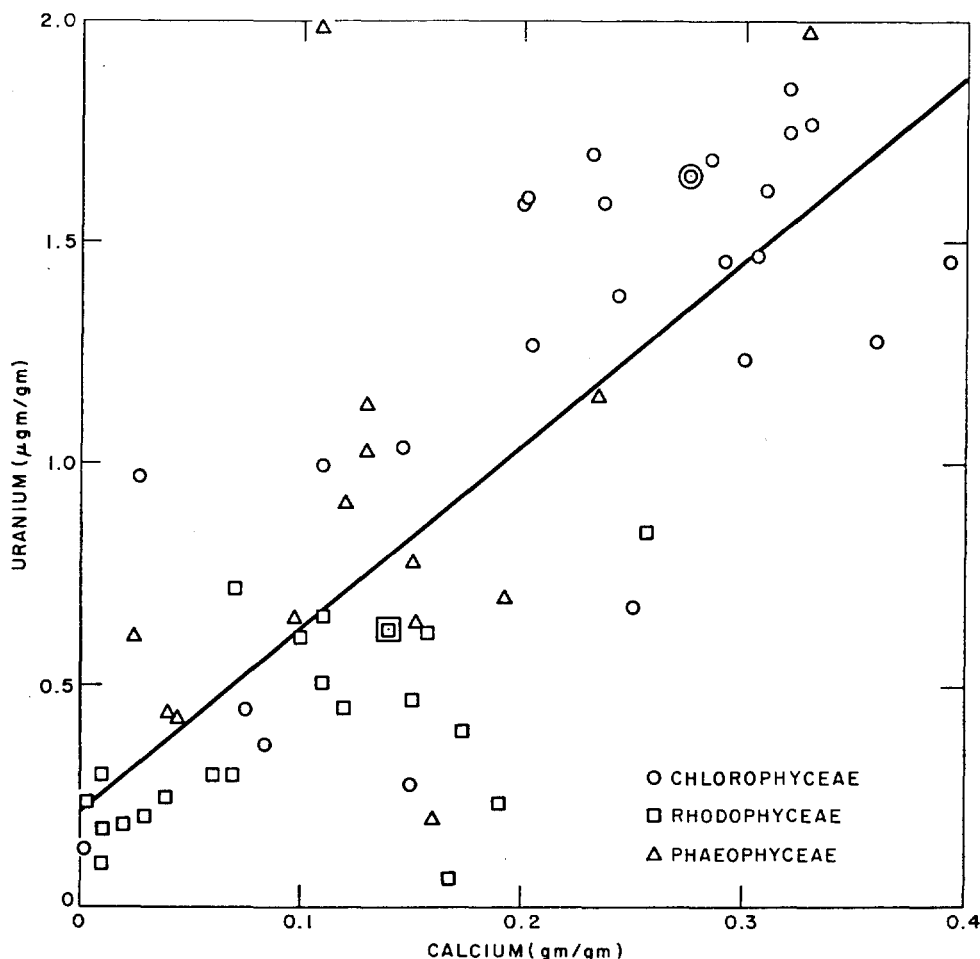


FIG. 6.—The variation in the concentration of uranium with the degree of calcification of the algae

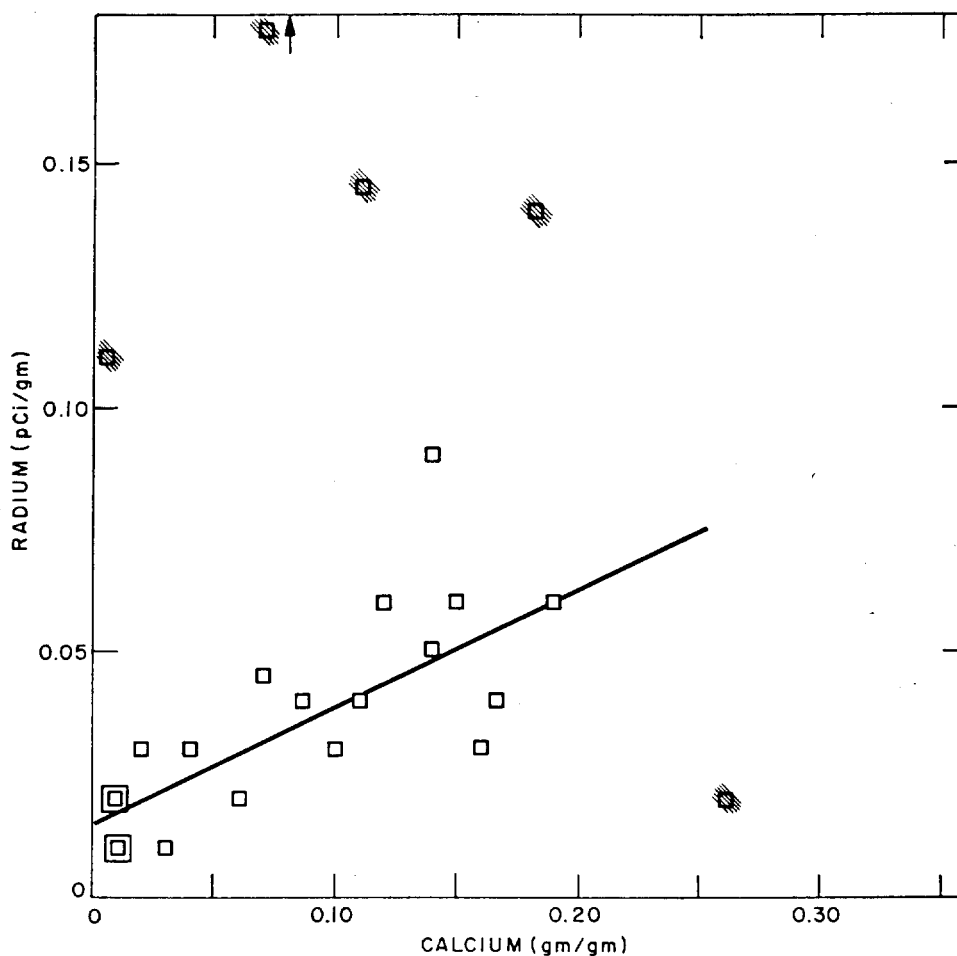


FIG. 7.—The variation in the concentration of radium with the degree of calcification for the *Rhodophyceae*

is no correlation between radium or thorium and calcium; the calculated values of the correlation coefficient were not significantly greater than zero; (2) the correlation between uranium and calcium is highly significant ($P < 0.001$). The result for radium is very surprising.

Since there was no direct relationship between radium or thorium and the calcareous material, regression coefficients for all algae were then calculated for their correlation with the concentration of protein nitrogen. The results are found in Table 3 and show that there is no direct relationship with protein nitrogen for radium or thorium. There is, however, a highly significant inverse correlation with protein nitrogen for uranium ($P < 0.001$), but this, of course, follows from the strong inverse correlation between calcium and protein nitrogen.

From a careful examination of the data shown in Figure 4 for the relationship between the concentrations of radium and calcium in these algae, it appeared that regression analysis according to phyta might lead to meaningful correlations being found.

Regression analysis of all of the data for each of the three phyta did not lead to calculated values of the correlation coefficient which were significantly greater than zero ($P > 0.1$). However, if all of the results which are not included within the limits $\bar{X} \pm 3\sigma$ (where \bar{X} and σ refer to any analytical parameter for each separate species) are rejected, then highly significant correlation coefficients ($P < 0.001$) are found for the *Rhodophyceae* and *Phaeophyceae*, but the correlation coefficient for the *Chlorophyceae* is still not significant.

The experimental values of concentrations of radium and calcium for the *Rhodophyceae* and *Phaeophyceae* are shown in Figures 7, and 8, respectively. The data points which are hatched are those which were rejected in the second regression analysis. This analysis clearly demonstrates differences according to phyta for the concentration of radium with increasing calcification. The concentration of radium, on the one hand, increases with increasing degree of calcification in the *Rhodophyceae* ($R = 0.51$), is completely variable in the *Chlorophyceae*, and on the other hand de-

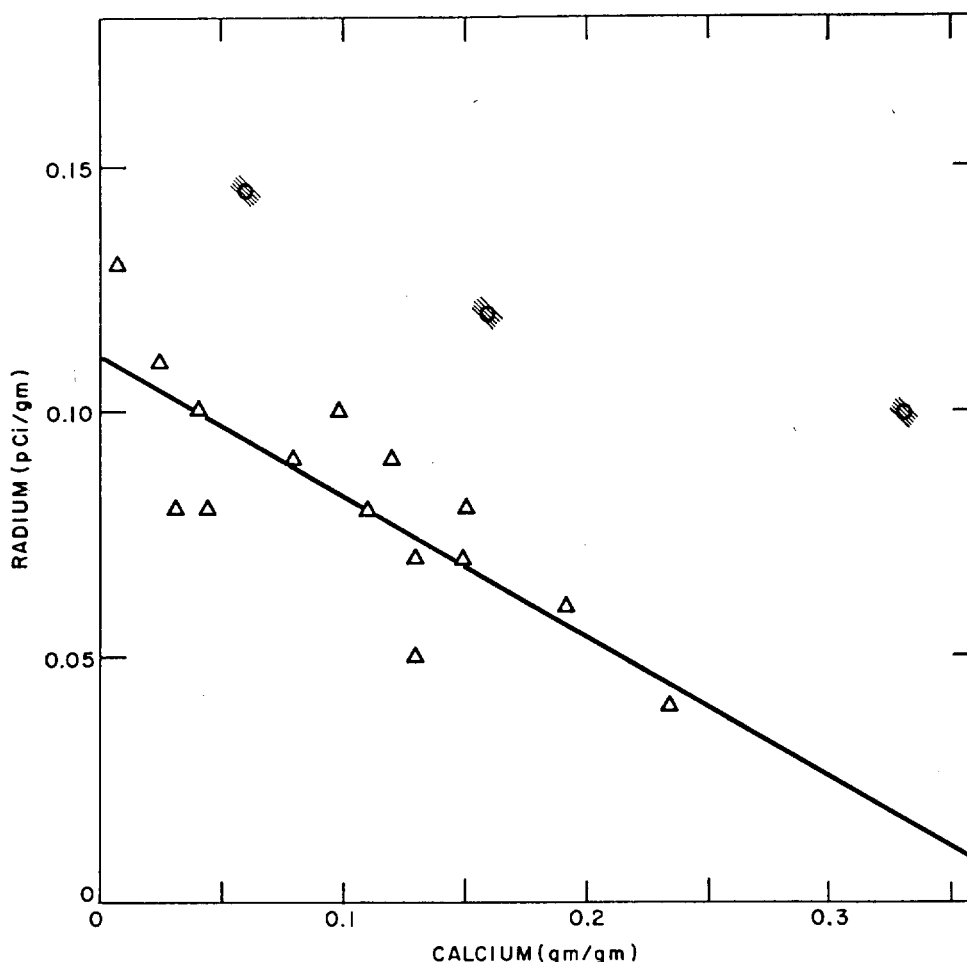


FIG. 8.—The variation in the concentration of radium with the degree of calcification for the *Phaeophyceae*

creases with increasing degree of calcification in the *Phaeophyceae* ($R = 0.81$).

A similar analysis was performed for the relationship between the concentrations of radium and protein nitrogen. The values of the correlation coefficients for the *Chlorophyceae* and *Rhodophyceae* were not significantly greater than zero ($P > 0.1$).

However, for the *Phaeophyceae*, where there was a significant inverse correlation between radium and calcium, the value of the correlation coefficient ($R = 0.69$) was significant ($P < 0.1$) when all the experimental data were considered, and highly significant ($P < 0.005$) when selected data were taken. Therefore, the concentration of radium by *Phaeophyceae* is directly dependent on the concentration of protein nitrogen in the algae. The data and regression line are shown in Figure 9.

As the thorium data were not sufficiently numerous, further regression analysis was not applied. However, splitting of the data into subsets according to phyta did not alter the conclusion that the concentration of uranium in these algae increases with increasing cal-

cification and decreasing protein content, except perhaps in the case of *Phaeophyceae*.

The lack of significant correlations for the *Chlorophyceae* between the concentrations of radium and calcium or protein nitrogen may derive, in part, from the fact that the sampling within this division was biased toward those species which are highly calcified (*Halimeda opuntia* and *Penicillus capitatus*). The deposition of radium in these two species is probably entirely due to coprecipitation with calcium carbonate, as the concentration of organic material, particularly in the former species, is very low. If this is the case, then the $[Ra]/[Ca]$ ratio (pCi/g) should be a constant. The $[Ra]/[Ca]$ ratio should increase with decreasing content of inorganic material in the organism if radium is being complexed by the organic fraction.

A comparison of the average values of the analytical data for these two species is shown in Table 4. From these values it can be seen that, while total concentration of calcium in *Penicillus capitatus* is 25% less than in *Halimeda opuntia*, and the concentration of total organic material or protein nitrogen

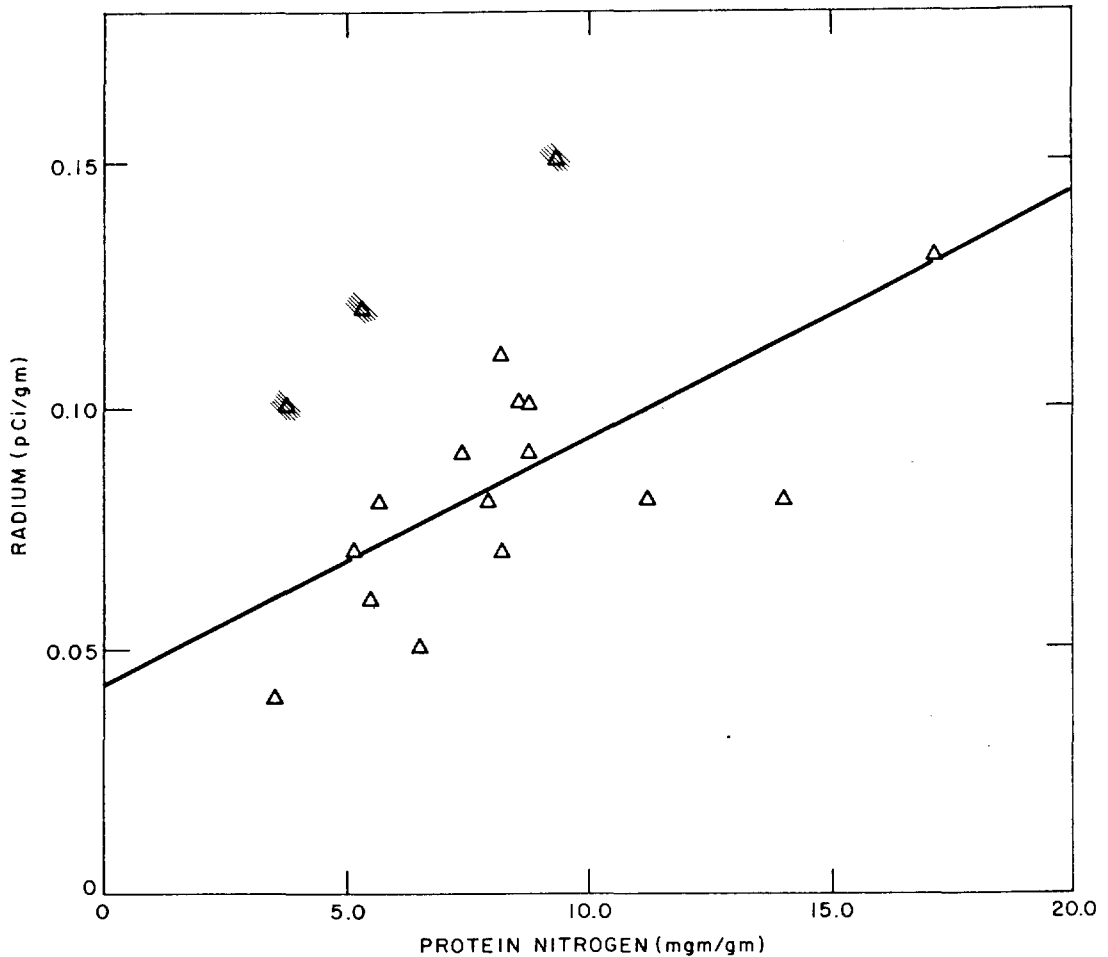


FIG. 9.—The variation in the concentration of radium with the concentration of protein nitrogen for the *Phaeophyceae*

TABLE 4. AVERAGE VALUES FOR THE ANALYSIS OF TWO MEMBERS OF THE DIVISION *Chlorophyta*

Species	Total organic, g/g	Protein nitrogen, ng/g	Calcium, g/g	[Ra]/[Ca], pCi/g
<i>Halimeda opuntia</i> (n = 6)	0.07 ± 0.01	2.73 ± 0.19	0.324 ± 0.018	0.145 ± 0.022
<i>Penicillus capitatus</i> (n = 5)	0.24 ± 0.05	8.46 ± 1.13	0.244 ± 0.014	0.188 ± 0.043
			t_{calc}	2.02
			$t_{0.5} (f = 9)$	2.26

is approximately 300% greater, there is no significant difference in the value of the [Ra]/[Ca] ratio in these two species on the basis of Student's *t* test.

The variations in the [M]/[Ca] ratio for radium, thorium and uranium with increasing degree of calcification for all samples are shown in Figures 10, 11 and 12. The ordinate at the left of each figure gives the [M]/[Ca] ratio in seawater. The [Ra]/[Ca] ratio for seawater was obtained from the data in Table 2, and those for [Th]/[Ca] and [U]/[Ca] from the data on cal-

cium in the same table and from published values for thorium (0.05 ng/ml) and uranium (3 ng/ml).⁽¹⁵⁾ These ratios are: [Ra]/[Ca] = 0.20 pCi/g; [Th]/[Ca] = 0.18 μ g/g; [U]/[Ca] = 7.5 μ g/g.

Concentration of radium relative to calcium from seawater occurs in all but the most highly calcified species, *Halimeda opuntia* (Figure 10); when the algae contain less than 50% calcium carbonate, the concentration factor varies between 5 and 100, with most species of algae having values between 2 and 40. Sim-

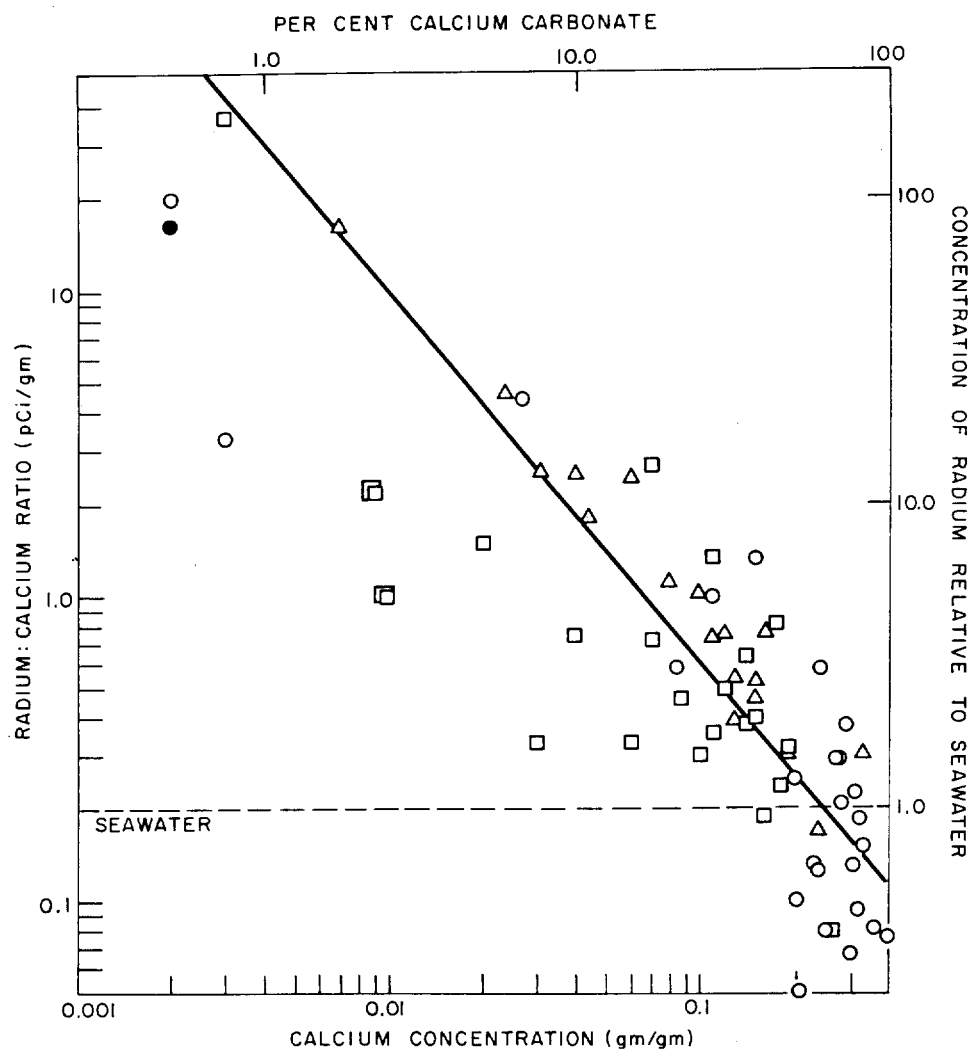


FIG. 10.—The variation in the $[Ra]/[Ca]$ ratio with the degree of calcification of the algae

ilarly, the concentration factors for thorium (Figure 11) are always greater than 1.0 and are higher than those found for radium. In contrast, the concentration factors for uranium relative to calcium from seawater are most frequently less than 1.0 (Figure 12), but do increase slowly to a maximum of 10.0 when the algae contain less than 10% calcium carbonate.

From these data it may be concluded that there are two mechanisms involved in the concentration of radium, thorium, and uranium by these algae. These are (1) ion exchange or coprecipitation of the ion with the calcium carbonate matrix, and (2) some form of complex formation with either the protein nitrogen or some other component of the organic fraction.

The concentration of radium and thorium appears to be related more to the latter than the former since in general the $[M]/[Ca]$ ratio increases with decreasing concentration of calcium carbonate in the organism. In the case of radium, the variation in the $[Ra]/[Ca]$

ratio is very obviously dependent on phyta (Figure 10). We have already considered in detail the behavior of the highly calcified members of the *Chlorophyceae* and concluded that there the concentration of radium is due to mechanism (1). Similarly, it has been shown that members of the *Rhodophyceae* concentrate radium proportionally to their calcium content (Figure 7), but their $[Ra]/[Ca]$ ratios are significantly higher than those, for example, of *Halimeda opuntia*, which suggests that some of the radium is being complexed by the organic fraction of the organism. The concentration of radium by the *Phaeophyceae* has been shown to be proportional to the concentration of protein nitrogen and is, therefore, largely fixed by organic complexation.

The behavior of radium is consistent with its chemical properties in seawater. Under normal conditions in seawater radium is almost certainly present as its free ion because, as its concentration is so low

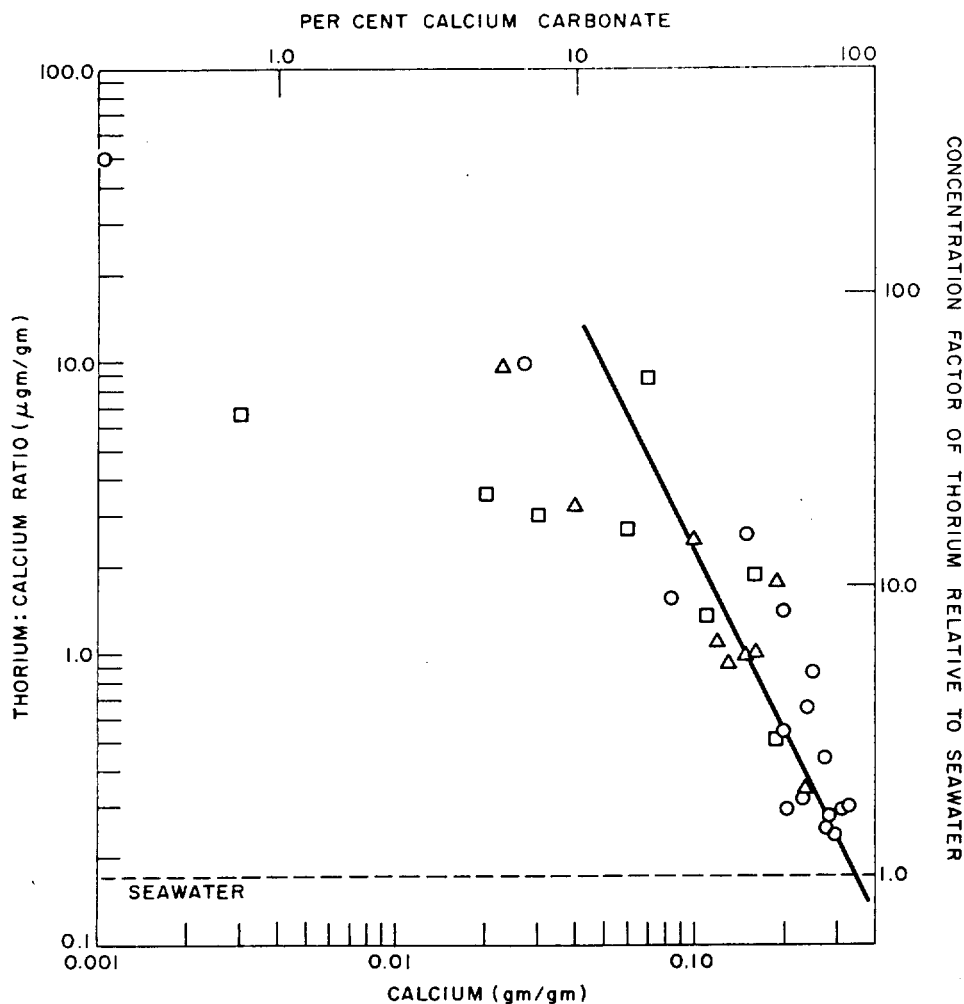


FIG. 11.—The variation in the $[Th]/[Ca]$ ratio with the degree of calcification of the algae

($10^{-7} \mu\text{g}/\text{l}^{(15)}$), there is no question of the solubility product being exceeded for RaCO_3 , or $\text{Ra}(\text{OH})_2$.

The behavior of thorium appears to parallel that of radium. The greater rate of increase in the value of $[Th]/[Ca]$ ratio with decreasing calcium content in the organism as compared to that for radium (Figures 10 and 11) is in agreement with the greater stability of thorium complexes with organic ligands over those of radium. However, the picture is not as simple as this, as it is highly unlikely that the free thorium ion (Th^{4+}) exists at the pH of seawater,⁽¹⁶⁾ and therefore the organism is concentrating thorium either as a hydrated oxide or a charged colloidal particle.

On the other hand, the results for uranium suggest that the effect of the organic fraction on the complexation of uranium is secondary to the coprecipitation or ion exchange with the calcium carbonate matrix. This difference in behavior between uranium and radium is entirely consistent with the differences in the be-

havior of these two ions in seawater. Unlike radium, at the pH, $p\text{CO}_2$ and E_H of seawater, uranium is most likely to occur as the anionic species $[\text{UO}_2(\text{CO}_3)_3]^{4-}$.⁽¹⁷⁾ Therefore, while radium is available for either complexing by the organic fraction or coprecipitation in the inorganic fraction, the uranyl ion, being in the anionic form, is not readily available for the formation of organic complexes, unless they are much more stable than the carbonate complex. Uranium is, therefore, coprecipitated as the anionic carbonate with calcium carbonate (or undergoes an anion exchange reaction) in those species of algae in which calcification occurs. When the fraction of calcium carbonate is low, then the formation of organic complexes becomes more important.

The differences in behavior found in the concentration of radium by members of the three phyta studied are of considerable interest, particularly as the trend to a greater concentration of radium in the least cal-

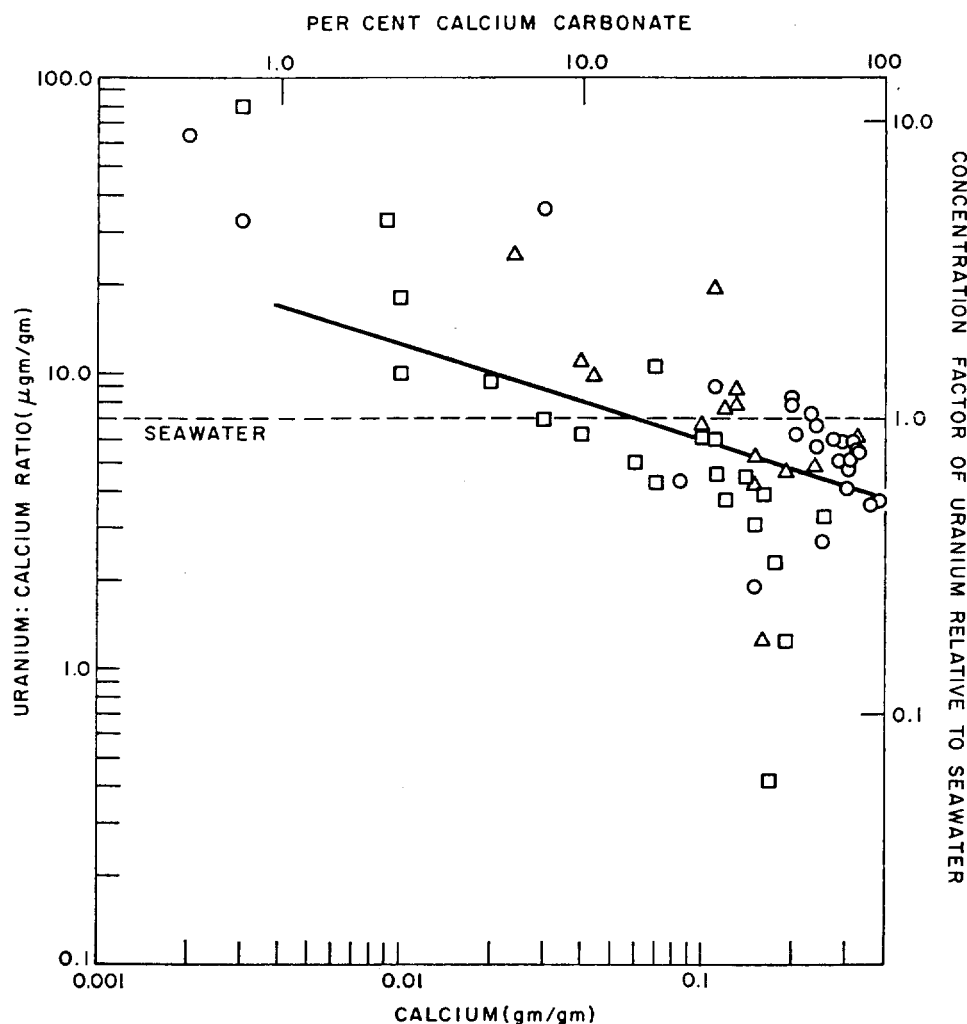


FIG. 12.—The variation in the [U]/[Ca] ratio with the degree of calcification of the algae

cified of the organisms is in direct contrast to the discrimination found for strontium in various freshwater algae.⁽¹⁸⁾ It would be particularly desirable to extend this study to include the other Group II elements, magnesium, strontium, and barium in order to ascertain whether the behavior found in the case of radium is peculiar to that element. Generally, those organisms which have a high [Sr]/[Ca] ratio also have high [Ra]/[Ca] ratios.⁽¹⁹⁾ In addition it would be interesting to include in this more extended study samples of the family *Cryptonemiales*, the coralline red algae, which even though they are tropical organisms, deposit calcium carbonate as the stable rhombohedral calcite.⁽²⁰⁾ In the argonitic *Halimeda opuntia* the concentration of strontium carbonate is 1.3%,⁽²¹⁾ while in the calcitic red algae its concentration is only 0.35%.⁽²²⁾ The reverse situation is true for the concentration of magnesium.⁽²¹⁾ This behavior is the result purely of ionic size. Substitution of larger

ions for calcium in the calcite lattice is limited by the steric factors of a close packed lattice.

REFERENCES

1. Bowen, H. J. M. *Trace Elements in Biochemistry*. Academic Press, London, 1966, pp. 68-73.
2. Mauchline, J. and Templeton, W. L. *Oceanog. Mar. Biol. Ann. Rev.* **2**, 229 (1964).
3. Vinogradov, A. P. *Sears Found. Mar. Res.*, Memoir No. 2 (1953).
4. Lucas, H. F. *Rev. Sci. Instr.* **28**, 680 (1957).
5. Edgington, D. N. *Int. J. Appl. Rad. Isotopes* **18**, 11 (1967).
6. Lucas, H. F. and Edgington, D. N. *Modern Trends in Activation Analysis*, Ed. DeVoe, J. R. National Bureau of Standards Special Publ. No. 312 (1969), p. 1207.
7. *Analytical Methods for Atomic Absorption Spectrophotometry* Perkin-Elmer, Norwalk, Conn., 1968.
8. Lindner, R. C. *Plant Physiol.* **19**, 76 (1944).
9. Morris, I. *An Introduction to the Algae*, Hutchinson & Co., London, 1967, p. 10.
10. Lewin, J. C. *Silicification. Physiology and Biochemistry of Algae*, Ed. R. A. Lavin. Academic Press, New York 1962.

11. Aleem, A. A. *J. Ecol.* **38**, 75 (1950).
12. van Overbeek, J., personal communication.
13. Revelle, R. and Fairbridge, R. *Geol. Soc. America, Memoir* **67** 1, 239 (1957).
14. Marshall, J. H. *J. Theoret. Biol.* **6**, 386 (1964).
15. Bowen, H. J. M. *Trace Elements in Biochemistry*, Academic Press, London, 1966, p. 19.
16. Hietanen, S. and Sillen, L. G. *Acta Chem. Scand.* **13**, 533 (1959).
17. Blake, C. A., Coleman, C. F., Brown, K. B., Hill, D. G., Lowrie, R. S., and Schmitt, J. M. *J. Am. Chem. Soc.* **78** 5978 (1956).
18. Fuller, W. H. and Hardecastle, J. E. *Soil Sci. Soc. Am. Proc.* **31**, 772 (1967).
19. Koczy, F. F. and Titze, H. *J. Marine Res.* **17**, 302 (1958).
20. Lowenstam, H. A. *J. Geol.* **62**, 284 (1954).
21. Emery, K. O., Tracey, J. I., and Ladd, H. S. U. S. Geol. Survey Prof. Paper 260A (1954).
22. Thomson, T. G. and Chow, T. J. *Papers in Marine Biology and Oceanography, Suppl. to Deep Sea Res.* **3**, 20 (1955).

SEPARATION OF CESIUM AND RUBIDIUM BY THE FERROCYANIDES OF COPPER, ZINC, AND ZIRCONIUM

*D. N. Edgington, M. M. Thommes, and L. I. Harrison**

The suitability of several metal ferrocyanides for ion exchange separation of cesium and rubidium has been studied. Both cesium and rubidium are satisfactorily absorbed on zinc ferrocyanides and could be recovered in separate fractions by elution with solutions of nitrate ion. Zirconium ferrocyanide absorbs cesium strongly and is well suited to concentrate cesium when subsequent elution is not required, e.g., to separate fallout ^{137}Cs from sea water. Copper ferrocyanide absorbs both cesium and rubidium strongly, but is of little value in analysis because of difficulties in elution of adsorbed species.

Extensive measurements of the concentration of radioactive ^{137}Cs in the biosphere have been made in order to understand more fully the behavior of this fission product in terrestrial and aquatic environments, as well as in man. While most elements are discriminated against with increasing trophic level, Gustafson has shown that the ratio of ^{137}Cs to potassium increases in the aquatic environment.⁽¹⁾ Folsom has measured the concentration of this radionuclide and stable cesium in salt water fish⁽²⁾ and sea water.⁽³⁾ Recently, Edgington and Lucas have shown that there is also an increase in rubidium concentration with increasing trophic level in freshwater fish.⁽⁴⁾ It would be interesting to know whether stable cesium exhibits the same increase in concentration with trophic level as its radioactive isotope.

In order to determine the concentration of cesium in water and biota, its separation by ion exchange and solvent extraction has been extensively studied.⁽⁵⁾ On the other hand, very little has been published concerning the separation of rubidium. Because solvent extraction and anion exchange processes are not effective for univalent cations, much attention has been focused on the development of cation exchange materials for their separation. Such an exchanger would be useful for concentrating trace

amounts of these elements in the biota for analysis: measurement of ^{137}Cs from fallout, and the separation of radioactive cesium and rubidium from mixtures of nuclides produced by neutron activation of biological or other samples.

For these purposes it is desirable to use a cation exchanger which will not only concentrate trace amounts of cesium and rubidium, but will also allow them to be eluted as well with a high percentage of recovery. The organic ion exchangers, Dowex 50W-X12, sodium form,⁽⁶⁾ and Amberlite IR-100,⁽⁷⁾ have been used, but they require large columns and are time consuming in operation. Many highly insoluble inorganic compounds have also been investigated. The compounds of zirconium,⁽⁸⁾ the heteropoly acids,⁽⁹⁻¹¹⁾ ammonium phosphomolybdate,⁽¹⁰⁻¹³⁾ and various cobaltcyanides^(14, 15) and ferrocyanides (hexacyanoferrates)^(14, 16-19) have been shown to have exchange properties for cesium and rubidium. The ferrocyanides have a high specificity in particular for cesium, but have to be destroyed using the concentrated sulfuric acid to get the cesium back into solution. Therefore, the present study is being conducted in order to obtain a greater understanding of the ion exchange behavior of the zinc, copper, and zirconium ferrocyanides, and to evaluate their usefulness as exchangers for ion exchange chromatography of these two elements.

METHODS AND MATERIALS

Analytical grade reagents were used in the following preparations.

Preparation of Heavy Metal Ferrocyanides

Zinc ferrocyanide was prepared as described by Kourim, Rais and Million,⁽¹⁷⁾ but on a larger scale. Eight hundred milliliters of 0.1 M potassium ferro-

* ANL-CSUI Honor Student, Spring, 1969.

cyanide were added dropwise to 2500 ml of 0.1 *M* zinc nitrate while stirring. The resulting fine precipitate of the ferrocyanide was allowed to digest for one to two hours in a boiling water bath, and after cooling to room temperature, was filtered through a sintered glass funnel. The precipitate was washed with ammonium nitrate, then distilled water, and dried at 110° C for 4 hr. The resulting solid was ground in a mortar, the fraction between 40 and 200 mesh being collected.

Copper and nickel ferrocyanides were prepared in a similar manner using 167 ml of 0.1 *M* potassium ferrocyanide and 500 ml of 0.1 *M* copper or nickel nitrate.

Samples of copper and zirconium ferrocyanides (less than 0.25- μ mesh) were also obtained from T. R. Folsom at the Scripps Institute of Oceanography for investigation.

Solutions of Radioactive Nuclides

Cesium-137 was obtained from an IAEA standard cesium solution containing 25.79 μ Ci/ml. The concentration of cesium was approximately 7.3×10^{-6} *M*.

Rubidium-86 was prepared by irradiating 10 mg of spectrographic grade rubidium chloride* in the Juggernaut reactor. After irradiation, the material was dissolved in 7 ml of water so that the rubidium concentration was 1.2×10^{-2} *M*.

Determination of Distribution Coefficients (K_D)

Distribution coefficients for copper, zinc, and zirconium ferrocyanides were measured in the following manner. One-tenth gram aliquot portions of the inorganic ion exchanger were weighed into two dram (7 ml) polyethylene flip-top vials (Olympic Plastics). Five milliliters of the required aqueous phase were added, followed by a 50- μ l aliquot of the radioactive nuclide (^{137}Cs or ^{86}Rb). Blanks were prepared to measure the total activity added to the vials by following the same procedure, only omitting the exchanger. If the K_D was known to be very large, smaller amounts of the exchanger were taken. The maximum concentrations of rubidium and cesium in the final solution used were 1.4×10^{-4} *M* and $<10^{-7}$ *M*, respectively.

The vials were shaken overnight on a rotary shaker. The two phases were then allowed to separate, and the supernatant aqueous phase was filtered through 0.45- or 0.8- μ Millipore filters. Four milliliters of the filtrate were pipetted and made up to 5 ml with distilled water into 2-dram polyethylene flip-top vials. These samples, as well as the blanks, were

counted using a 3" x 2" NaI(Tl) crystal. The counts were recorded on a scaler, and the gamma-ray spectrum was accumulated on a 400-channel pulse height analyzer.

The counts per gram of exchanger were calculated from the difference between the total counts in the aqueous phase after equilibration and the total activity added initially. The distribution coefficients for the tracer between the inorganic ion exchanger and the aqueous phase were calculated from

$$K_D = \frac{\text{counts/g of exchanger}}{\text{counts/ml of aqueous phase}}$$

Kinetics of Attainment of Equilibrium

The rate of attainment of equilibrium of the ion exchanger with the cesium ions was determined by measuring the apparent distribution coefficient after different times of shaking.

Stability of the Inorganic Ion Exchangers

A procedure similar to that used for the measurement of the distribution coefficients was employed to determine the stability of zinc and ferrocyanides in strong acid, except that no radioactivity was added. The aqueous phases were subjected to analysis by atomic absorption spectroscopy for iron and zinc. The techniques used were as described in the Perkin-Elmer 303 atomic absorption spectrophotometer manual for these two elements.

Column Experiments

A water slurry of the exchangers was prepared so the fines could be decanted. Ion exchange columns were made by packing a 7-cm length of polyethylene tubing, 0.6 cm diameter, with about 3 cm of the slurry under gravity. Ten milliliters of water were spiked with a known concentration of cesium, rubidium, or both, and passed through the column at a constant rate of 1 ml/min by means of a polystaltic pump. The eluate from the column was collected and counted to check the efficiency of adsorption of the cesium or rubidium. Then, 10 ml of a selected eluent were passed through the column at a rate of 1 ml/min. Fifty-drop fractions (1.5 ml) were collected and then counted. The columns were regenerated by passing water through them.

RESULTS AND DISCUSSION

The ion exchange properties of the ferrocyanides of zinc, copper, and zirconium have been investigated in this study. Distribution coefficients were measured for the partition of cesium and rubidium between several different solutes and these ferrocyanides. The stabil-

* Obtained from Johnson Matthey Company.

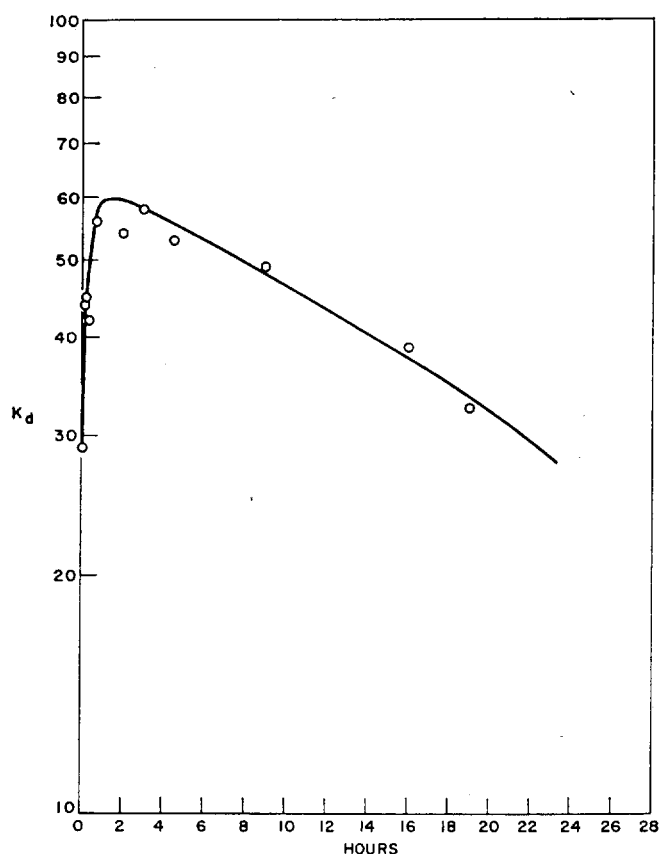


FIG. 13.—Rate of attainment of equilibrium in the partition of cesium between zinc ferrocyanide and nitric acid.

ity in strong acid and the rate of attainment of exchange equilibrium of the zinc ferrocyanide were also determined. The results obtained will be discussed separately for each of these inorganic ion exchange materials.

Zinc Ferrocyanide

Rate of Attainment of Ion Exchange Equilibrium.—The rate of attainment of equilibrium for the partition of cesium between zinc ferrocyanide and 4 *M* nitric acid was determined. The results are shown in Figure 13. The value of the distribution coefficient (K_D) increases to a maximum after shaking for 45 min and then decreases slowly thereafter with longer equilibration times. The decrease at longer times is probably due either to surface decomposition of the inorganic exchange material by the acid or to a competitive reaction with the hydrogen ions from the acid.

Stability of Zinc Ferrocyanide.—In order to determine the stability of the zinc ferrocyanide in the presence of various eluants likely to be employed in the separation of rubidium and cesium, a series of experiments was set up to determine the concentrations of

zinc and iron found in the solute after equilibration for 16 hr.

Table 5 shows the concentration of zinc and iron found in solution after 1 g of zinc ferrocyanide has been equilibrated with 1 ml of the appropriate aqueous phase. The average concentrations of iron in the nitric acid solutions were approximately equal. However, the concentration of dissolved zinc in the nitric acid solutions was ten times the concentration of the iron, while for ammonium nitrate solutions, the concentration was four times as great. Assuming that the molecular formula of the precipitated zinc ferrocyanide is $Zn_2Fe(CN)_6$, then the concentration of zinc should be twice that of the iron. The zinc ferrocyanide was originally precipitated using a 50% excess zinc in order to aid complete precipitation of the ferrocyanide. It is highly probable that the precipitated material would accumulate excess zinc ions by adsorption or occlusion and that it is these ions that are being preferentially dissolved. The even greater concentration of zinc in solution under acid conditions may be due also to a competitive reaction between zinc and hydrogen ions.

TABLE 5 CONCENTRATIONS OF IRON AND ZINC IN VARIOUS SOLUTIONS AFTER 1 G OF ZINC FERROCYANIDE HAS BEEN EQUILIBRATED WITH 1 ML OF THE APPROPRIATE AQUEOUS PHASE

Molarity	HNO ₃ , g/ml	NH ₄ NO ₃ , g/ml
<i>Concentration of zinc</i>		
1		8.9×10^{-3}
2	1.75×10^{-2}	8.9×10^{-3}
3	1.95×10^{-2}	8.3×10^{-3}
4	2.1×10^{-2}	9.9×10^{-3}
5		8.3×10^{-3}
6	2.2×10^{-2}	9.1×10^{-3}
7	1.75×10^{-2}	8.8×10^{-3}
8	1.69×10^{-2}	8.6×10^{-3}
9	1.72×10^{-2}	8.6×10^{-3}
Average Molarity	1.88×10^{-2} $1.44 \times 10^{-1} M$	8.9×10^{-3} $6.8 \times 10^{-2} M$
<i>Concentration of iron</i>		
1		9.5×10^{-4}
2	2.9×10^{-3}	2.1×10^{-3}
3		4.2×10^{-3}
5	1.7×10^{-3}	
6		2.9×10^{-3}
7	3.1×10^{-3}	7.4×10^{-4}
8	1.7×10^{-3}	1.8×10^{-3}
9	2.1×10^{-3}	1.7×10^{-3}
Average Molarity	2.3×10^{-3} $4.1 \times 10^{-2} M$	2.0×10^{-3} $3.6 \times 10^{-2} M$

Distribution Coefficients.—The distribution coefficients for cesium and rubidium are shown in Figure 14. The distribution coefficients reported for the partition of cesium and rubidium between water and zinc ferrocyanide are in agreement with those previously reported by Gorenc and Kosta.⁽¹⁵⁾

Using nitric acid, the distribution coefficients for cesium range from 9160 at zero acid concentration to 1.5 with 9 *M* acid, and for rubidium from 2520 at zero acid concentration to 1.8 with 9 *M* acid. The distribution coefficients for rubidium are much lower than those for cesium in dilute acid (up to 4 *M*). At concentrations of acid greater than 4 *M*, the differences between the distribution coefficients for cesium and rubidium become much smaller, and for 9 *M* acid, are minimal.

When ammonium nitrate is used in place of nitric acid in the aqueous phase, the distribution coefficients for cesium decrease from 9160 to 3.2 at 9 *M*, and for rubidium, from 2520 to 0.9. The distribution coefficients for the two elements are widely separated at all ammonium nitrate concentrations.

The Separation of Rubidium and Cesium Using Columns of Zinc Ferrocyanide.—Ion exchange columns of zinc ferrocyanide were prepared as described in the section on methods. The columns were loaded with cesium or rubidium by passing 10 ml of water spiked with ¹³⁷Cs or ⁸⁶Rb through the column. The eluant was checked for residual activity, and in all cases greater than 99% of the activity was adsorbed.

According to the results presented in Figure 14, a separation of rubidium and cesium should be possible. Rubidium may be eluted first with 2 *M* ammonium nitrate or 3 *M* nitric acid and then cesium with 9 *M* ammonium nitrate or 9 *M* nitric acid. The results of such experiments are shown in Figures 15 and 16. The rubidium was quantitatively desorbed using either 2 *M* ammonium nitrate or 3 *M* nitric acid with little or no contamination due to cesium. While 91% of the cesium was eluted using 9 *M* nitric acid, only 68% was removed using 9 *M* ammonium nitrate.

Copper Ferrocyanide

Distribution Coefficients.—The distribution coefficients for the partition of cesium and rubidium between copper ferrocyanide and aqueous solutions of nitric acid or ammonium nitrate are shown in Figure 17.

In the nitric acid system, the values of the distribution coefficients for rubidium show a very noticeable initial decrease from 1590 at zero acid concentration to 34 with 1 *M* acid, and then continue to drop to a value of 0.14 with 9 *M* acid. The value of the distribu-

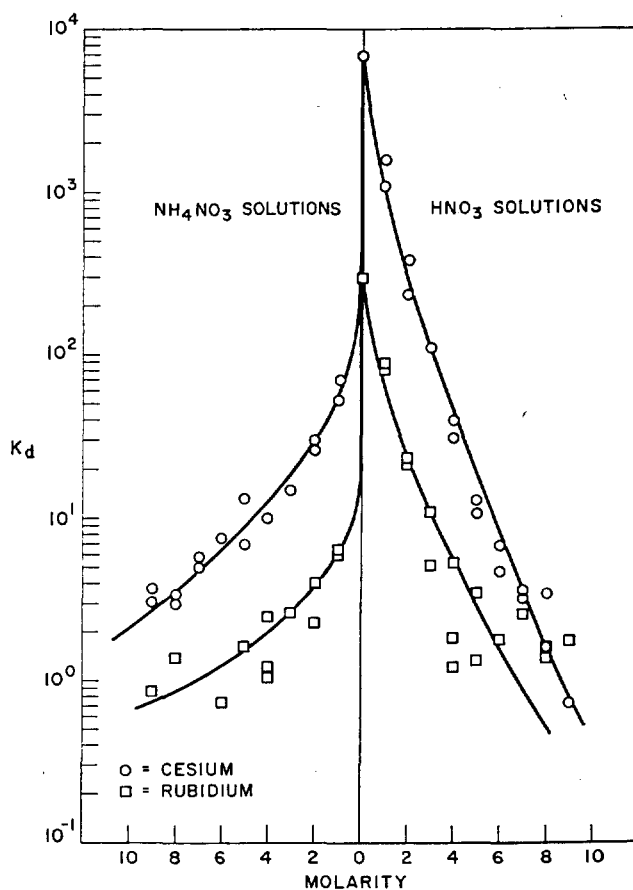


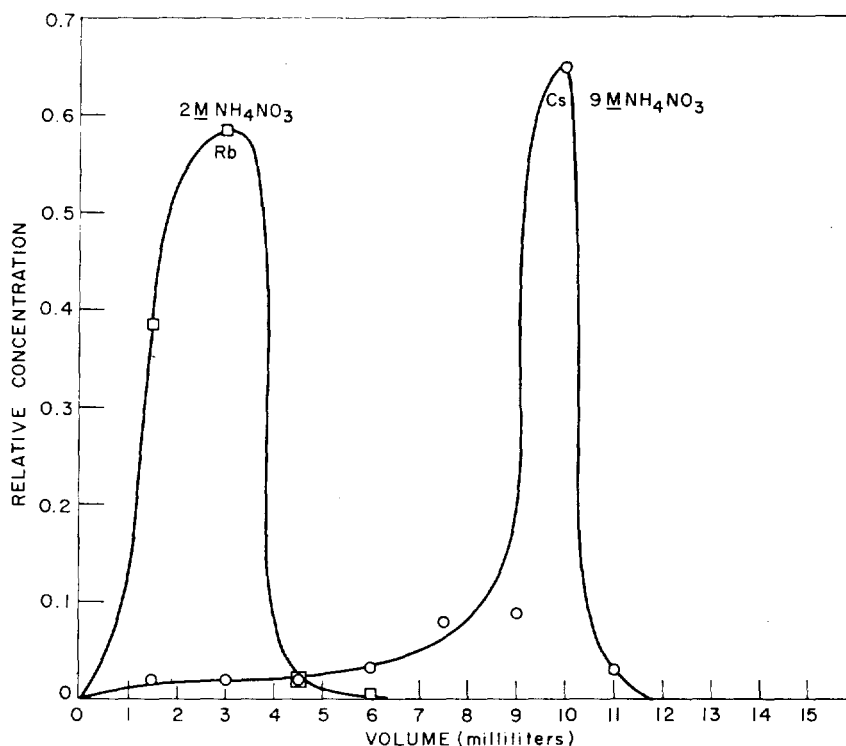
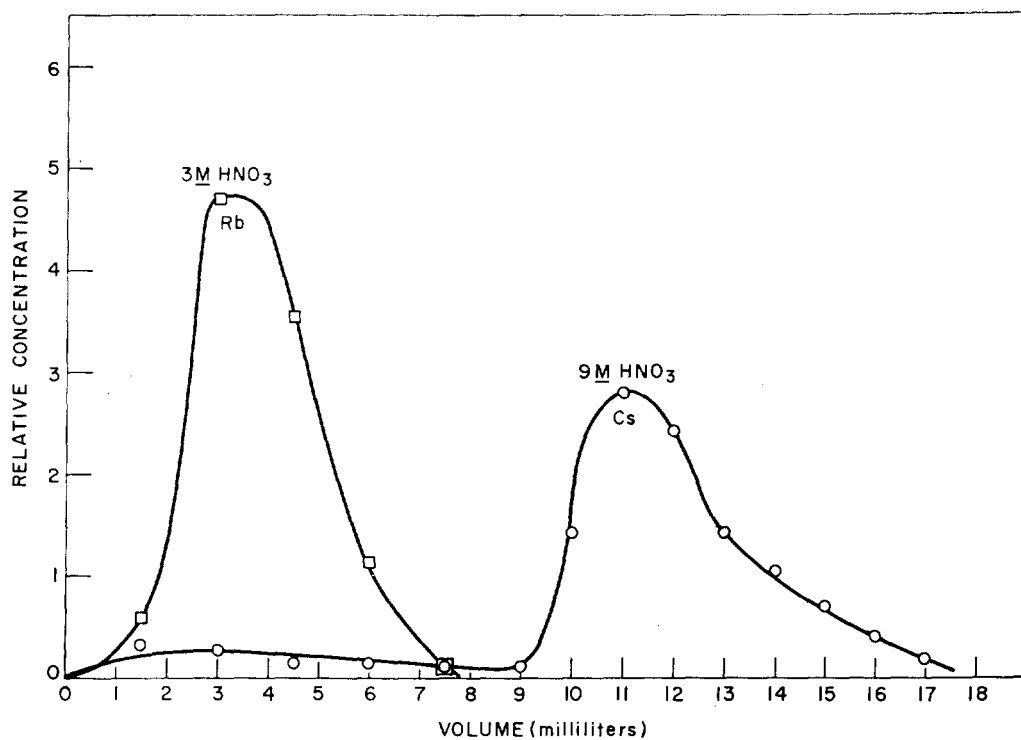
FIG. 14.—Distribution coefficients for the partition of cesium and rubidium between zinc ferrocyanide and nitric acid or ammonium nitrate (cf. Figures 17 and 19).

tion coefficients for cesium decreases from 38,100 at zero concentration to 5.9 with 8 *M* acid.

Using ammonium nitrate the values of the distribution coefficient for rubidium decrease from 1590 at zero ammonium nitrate concentration to 2.8 with 9 *M* ammonium nitrate. Similar experiments with cesium give values of K_D which are extremely high, decreasing from 38,100 to 116 with 9 *M*.

The behavior of the copper ferrocyanide prepared in this study was compared to that found for a sample of this exchanger obtained from Folsom. Distribution coefficients for the partition of cesium between ammonium nitrate solutions and the two copper ferrocyanides were compared. The material prepared for this study gave values of K_D which were twice as large as those obtained using the material prepared by Folsom. This difference will probably be found to be due to variations in the method of preparation and is most likely connected with the concentration of copper in the precipitating solution.

Separation of Cesium and Rubidium Using Copper Ferrocyanide.—From these values of the distribution coefficient it may be predicted that a good separation



FIGS. 15 AND 16.—Separation of rubidium and cesium using columns of zinc ferrocyanide

of rubidium from cesium may be obtained using either nitric acid or ammonium nitrate as an eluant, but because the values of K_D for cesium remain large, even at the highest concentration of the eluents tested, the recovery of cesium from the column is

likely to be poor. However, under acid conditions, this exchanger tends to coalesce and not allow the passage of the eluent through the column, so elution curves were obtained using only ammonium nitrate (Figure 18). Rubidium is eluted with 6 *M* ammonium nitrate,

but there appears to be a little contamination with cesium.

Zirconium Ferrocyanide

Distribution Coefficients.—The distribution coefficients for the partition of cesium and rubidium between zirconium ferrocyanide and aqueous solutions of ammonium nitrate and nitric acid are shown in Figure 19.

Using nitric acid, the values of the distribution coefficient decrease from 3143 at zero acid concentration to 1.8 with 9 M acid. The rubidium is not at all strongly adsorbed, and the values of distribution coefficients decrease from 23.8 at zero acid concentration to 0.56 with 9 M acid. The differences between the distribution coefficients for cesium and rubidium for every acid concentration are large.

Similarly, there is a very sharp drop in the distribution coefficients for cesium from 3143 at zero NH_4NO_3 concentration to 123 with 2 M ammonium nitrate, and then a gradual decrease to 17 for 9 M. The distribution coefficients for rubidium decrease from 23.8 at zero ammonium nitrate concentration to 0.95 at 8 M ammonium nitrate and show poor reproducibility.

The value of the distribution coefficient of 23.8 for the partition of rubidium between water and zirconium ferrocyanide is lower by a factor of almost one hundred for other heavy metal ferrocyanides investigated.

Separation of Cesium and Rubidium from Columns of Zirconium Ferrocyanide.—The short ion exchange

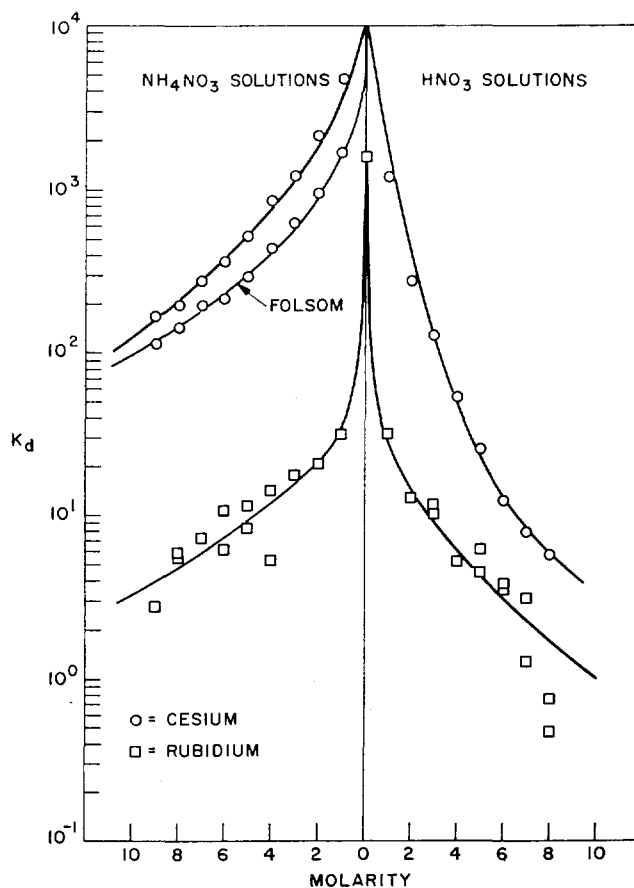


FIG. 17.—Distribution coefficients for partition of cesium and rubidium between copper ferrocyanide and nitric acid or ammonium nitrate.

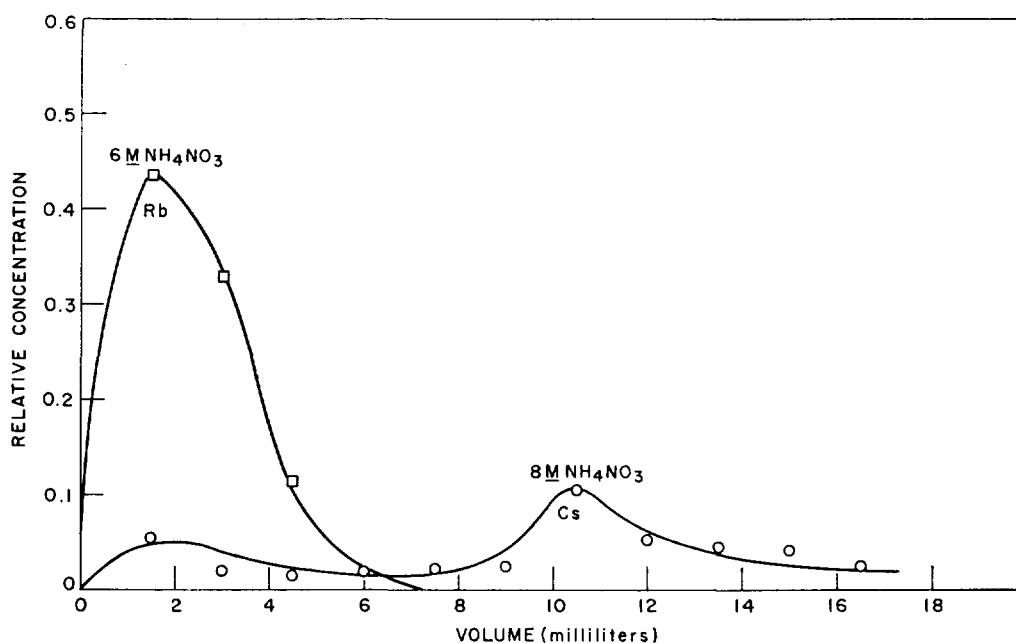


FIG. 18.—Separation of rubidium and cesium using copper ferrocyanide

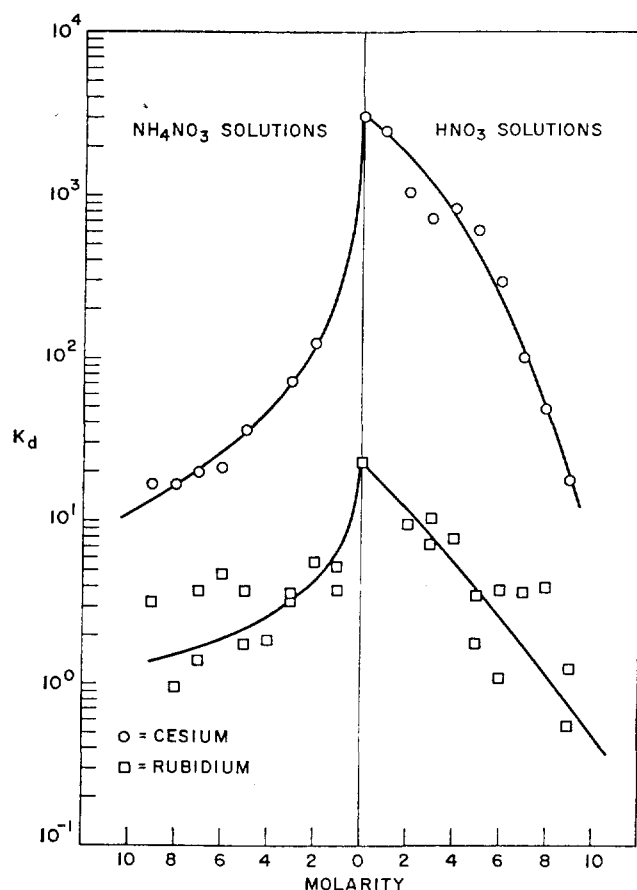


FIG. 19.—Distribution coefficients for the partition of cesium and rubidium between zirconium ferrocyanide and ammonium nitrate and nitric acid.

columns of zirconium ferrocyanide adsorbed greater than 99% of the cesium but a maximum of only 46% of rubidium from the spiked water solutions. The adsorbed rubidium was readily eluted with 6 *M* nitric acid, but the cesium could be only partially eluted using 9 *M* acid.

Zirconium ferrocyanide is therefore the most specific of the exchangers examined for the concentration of cesium, but is of little value for the separation of rubidium because of the low value of K_D for this ion.

SUMMARY

The ion exchange behavior of several heavy metal ferrocyanides has been investigated. The ferrocyanides have shown varying degrees of stability in the eluents studied. Zinc ferrocyanide and zirconium ferrocyanide were stable in nitric acid and ammonium nitrate. Copper ferrocyanide was attacked in the ion exchange columns by nitric acid, but was stable in ammonium nitrate. According to the values of K_D for the three ferrocyanides, the separation of rubidium from cesium is feasible in each case, but the re-

covery of cesium is highly dependent on the particular ferrocyanide used.

These predictions were confirmed by the column experiments. Zinc ferrocyanide was found to be the best exchange medium for the separation and recovery of cesium and rubidium. Using 2 *M* ammonium nitrate or 3 *M* nitric acid, the adsorbed rubidium could be completely recovered from a zinc ferrocyanide column. Cesium could then be eluted from the column with either 9 *M* nitric acid or 9 *M* ammonium nitrate.

Zirconium ferrocyanide was an excellent exchange material for the concentration of cesium since total adsorption occurred and the cesium could not be eluted effectively. Rubidium, however, was poorly adsorbed by the material and could be readily eluted. Likewise, copper ferrocyanide adsorbed cesium strongly, and it could be eluted only with great difficulty. Rubidium was effectively adsorbed and separated from cesium on copper ferrocyanide columns using ammonium nitrate as eluent.

Zirconium ferrocyanide, because of the high values of its distribution coefficient K_D and values of its distribution coefficients for cesium under all conditions is ideally suited to concentrate fallout ^{137}Cs from seawater. The ^{137}Cs adsorbed on columns of zirconium ferrocyanide can be counted directly and the concentration of the radionuclide determined. Other radionuclides will not interfere since the ferrocyanide is specific for the alkali metals and because the activity of other long-lived nuclides such as ^{40}K is known to be equal to or less than that of cesium. Similarly, copper ferrocyanide concentrates cesium and rubidium but is of little value in analysis because of the difficulties encountered in elution of adsorbed species.

Cesium and rubidium, on the other hand, can be quantitatively recovered from as well as concentrated by zinc ferrocyanide. Zinc ferrocyanide is, therefore, an ideal material for the preconcentration of rubidium and cesium before analysis. Trace amounts of cesium and rubidium may be concentrated on columns of this exchanger from large volumes of natural waters and then determined after removal from the column by neutron activation with a minimum of contamination from nuclides other than those of zirconium or iron. Zinc ferrocyanide can also be used to separate these alkali metals from mixtures of other elements in biological samples.

REFERENCES

1. Gustafson, P. F., Brar, S. S., and Muniak, S. E. *Nature* **211**, 843 (1966).
2. Folsom, T. R., Young, D. R., and Sreekn Moran, C. Scripps Institute of Oceanography, unpublished data.
3. Folsom, T. R., Feldman, C., and Rains, T. C. *Science* **144**, 538 (1964).

4. Edgington, D. N. and Lucas, H. F., Jr. Radiological Physics Division, Argonne National Laboratory, unpublished data.
5. Yamagata, N. U. S. Atomic Energy Commission Report NP-15366 (1965).
6. Wester, P. O., Brune, D. and Samsahl, K. *Int. J. Appl. Radiation Isotopes* **15**, 59 (1964).
7. Smales, A. A. and Salmon, L. *Analyst* **80**, 37 (1955).
8. Amphlett, C. B., McDonald, L. A., Burges, J. S., and Maynard, J. C. *J. Inorg. Nucl. Chem.* **10**, 69 (1959).
9. Krttil, J. *J. Inorg. Nucl. Chem.* **19**, 298 (1961).
10. Krttil, J. and Kourim, V. *J. Inorg. Nucl. Chem.* **12**, 367 (1960).
11. *Ibid.*, p. 370.
12. Yamagata, N., Iswashimia, K., and Tajima, E. *J. Radiat. Res. (Tokyo)* **4**, 30 (1962).
13. Prout, W. E., Russell, E. R., and Groh, H. J. *J. Inorg. Nucl. Chem.* **27**, 473 (1965).
14. Langford, J. C. U. S. Atomic Energy Commission Report HW-49668 (1967).
15. Gorenc, B. and Kosta, L. *Z. Anal. Chem.* **223**, 410 (1966).
16. Mohanrao, G. J. and Folsom, T. R. *Analyst* **88**, 105 (1963).
17. Kourim, V., Rais, J., and Million, B. *J. Inorg. Nucl. Chem.* **26**, 1111 (1964).
18. Schuly, W. W. and McKenzie, T. R. U. S. Atomic Energy Commission Report TID-7517 (1955).
19. Watari, K., Imai, K., and Izawa, M. *J. Nucl. Sci. Technol.* **4**, 190 (1967).

RECOVERY AND MODIFICATION OF RADIATION-INDUCED DIVISION DELAY IN DEVELOPING SEA URCHIN EGGS*

Patricia Failla

Treatment of fertilized sea urchin eggs with a number of agents that prolong the normal cell division cycle permits recovery during the prolongation period from division delay caused by previous irradiation of one or both gametes. Treatment with several of these agents has also been shown to modify the subsequent response of fertilized eggs to radiation. Some implications of the results in the elucidation of the recovery process are discussed.

Virtually all dividing cells exposed to sufficient doses of ionizing radiation exhibit division delay. Developing sea urchin eggs are an excellent material in which to study this effect for a number of reasons. First, a remarkable natural synchrony of the initial divisions greatly facilitates experimental procedures. Second, since this material has long been a favorite of embryologists and molecular biologists, extensive morphological and biochemical information is readily available. Third, the eggs are rugged and can tolerate treatments that mammalian cells cannot. Finally, there is the opportunity to compare the reactions of irradiation of almost pure nuclear material (sperm), nucleus and cytoplasm (eggs) or a developing diploid system (fertilized eggs or zygotes). The criterion of radiation damage under consideration, therefore, is the delay in the time of first division of fertilized sea urchin eggs after one or both gametes have been irradiated. The magnitude of this radiation-induced cleavage delay, however, can be altered both before and after fertilization. It is this aspect that will be emphasized.

Henshaw^(1, 2) showed over 30 years ago that the division delay resulting from the irradiation of un-

fertilized eggs could be reduced by increasing the interval between irradiation and fertilization. Postponement of fertilization of normal eggs with irradiated sperm, however, had no such effect. This suggested that some cytoplasmic constituent was involved in this type of recovery. More recently, a postfertilization recovery from division delay has been demonstrated in both irradiated eggs and sperm.⁽³⁻⁵⁾ During the study of this recovery process modification of radiation-induced division delay itself has been achieved.

The postfertilization recovery process involves a prolongation of the first division cycle by various chemical or physical means during which the radiation effect on either egg, sperm or zygote diminishes. The experimental protocol is outlined schematically in Figure 20. On lines 2 and 4 the sperm is depicted as irradiated, resulting in radiation-induced division delays of D and D' , respectively. On lines 3 and 4 a chemical or physical agent is applied to the fertilized egg inducing a prolongation of the division cycle which serves as a recovery period. If D' is less than D , recovery is said to have occurred during the time R . By using agents which are known to interfere with specific cellular activities, the influence of this interference or inhibition on the recovery process can be investigated and the process itself better characterized.

While studying the influence of various agents on the recovery process, it was decided to ascertain which portion of the cell cycle was being prolonged. That, is, although the agents are applied for various intervals soon after fertilization, they may produce a delay in a later portion of the cell cycle. This is the case with radiation: no matter when the gametes or fertilized eggs are irradiated, the radiation-induced

* Presented in part at the Fifty-fourth Scientific Assembly and Annual Meeting of the Radiological Society of North America, Chicago, Illinois. December 1-6, 1968.

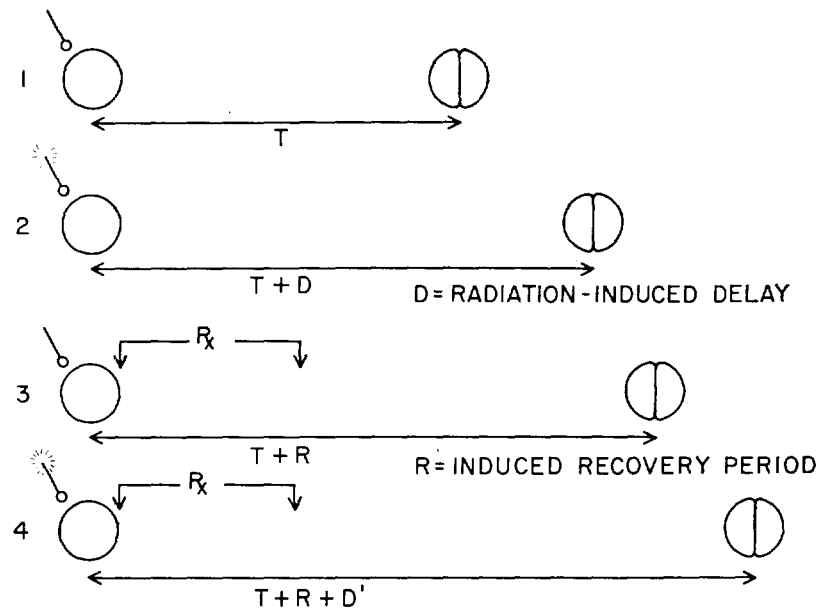


FIG. 20.—Schematic experimental protocol. T represents the normal control cell division time, D the delay because of radiation exposure of the sperm, R the prolongation of normal control cell division cycle by treatment of fertilized egg with physical or chemical agent, and D' the radiation-induced delay after such treatment.

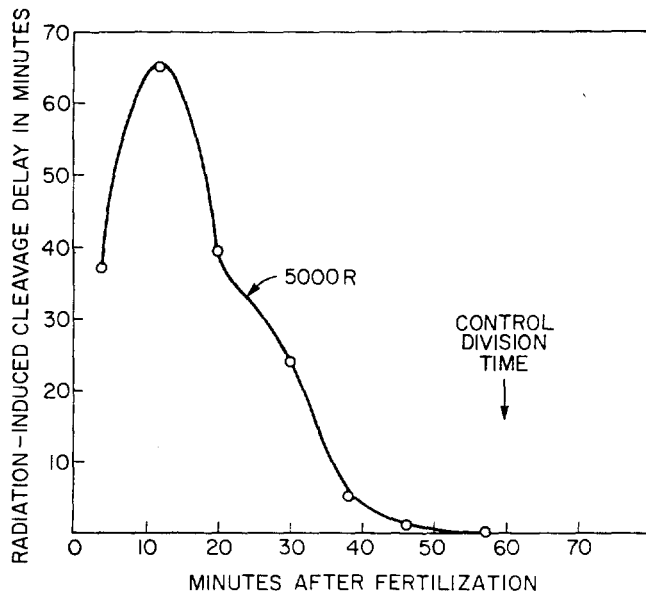


FIG. 21.—The sensitivity to radiation-induced cleavage delay as a function of the time during the first cell cycle the *Arbacia* zygotes are irradiated with 5000 R.

division delay occurs in early prophase. If the zygote is irradiated after this time, no delay is evident until the second division cycle. This can be seen in Figure 21 which depicts the variation in the amount of division delay produced by a dose of radiation as a function of the time during the first cell cycle that the zygotes are irradiated. For *Arbacia punctulata* zygotes the radiation insensitive portion of the cycle begins about 15 min before division. The character-

istic shape of this radiation sensitivity curve suggested its use in determining the time of action of the agents. If the chemically-induced mitotic delay takes place during the time of treatment, then it would be expected that the radiation sensitivity curve of the drug-treated zygotes would be shifted in time to the right by an amount equivalent to the treatment period or its induced delay. Therefore, the fertilized eggs or zygotes were treated with a number of agents and then exposed to radiation. The changes in shape and position of the sensitivity curves indicated that different agents acted at different times. It was also found that treatment with several agents modified the subsequent response of the system to radiation. This effect will be called modification and should be distinguished from protection which implies that the agent is present at the time of irradiation. A study of this type should give some insight into the types of reactions and cellular activities that are responsible for the variation of radiation response during the cell cycle.

MATERIALS AND METHODS

Two species of sea urchin have been used, *Arbacia punctulata*,* and *Lytechinus pictus*.† The animals are maintained in two 25-gallon refrigerated aquaria which recirculate artificial sea water (Instant

* Supplied by the Marine Biological Laboratory, Woods Hole, Massachusetts or Glendle Noble, Panama City, Florida

† Supplied by Pacific Biomarine Supply Co., Venice, California.

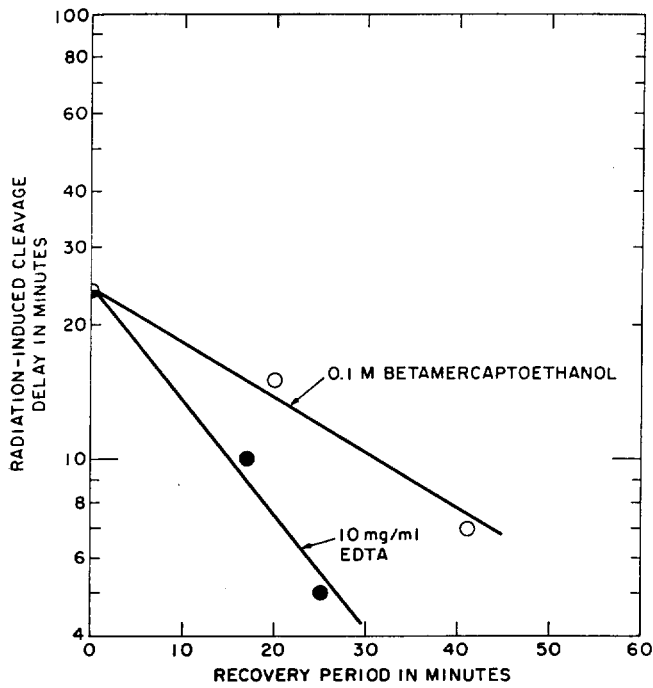


FIG. 22.—Decrease in cleavage delay in *Arbacia* sperm exposed to 7200 R as a function of the time the control cell division cycle is prolonged by treatment of the zygote with either beta mercaptoethanol or EDTA.

Ocean†) continuously through a calcareous filtrant spread over the bottom of the tank.

Gametes are procured by injection of 0.5 M KCl or by electrical stimulation of the animals with an alternating potential of about 8 volts. The fertilized eggs develop in either Instant Ocean or natural sea water at room temperature. The radiation doses are delivered by a ^{137}Cs gamma source at a dose rate of about 1200 R/min.

Since the first division of fertilized sea urchin eggs is so remarkably synchronous, estimation of the time when 50% of the eggs have cleaved is made visually under low magnification. This time can generally be determined to within ± 1 min. Hence, cleavage delays are good to about ± 2 min.

RESULTS

Previous publications⁽³⁻⁶⁾ have described the effects of prolonging the control cell division cycle by temporary exposure of fertilized eggs to nitrogen, D_2O , sodium azide, Colcemid, ribonuclease, or 0°C on the radiation-induced cleavage delay. When the cell cycle is prolonged by treatment with all these agents except low temperature, there is a decrease in the radiation-induced cleavage delay. Recovery is, therefore, said to have occurred during the time the cycle is prolonged. No significant reduction in the radia-

tion-induced division delay is evident, however, when the cell cycle time is extended by incubation of the fertilized eggs at 0°C or any temperature lower than normal. Two other agents, EDTA and beta mercaptoethanol, have now been used which prolong the cycle and also permit recovery to take place. Figure 22 shows the effect of treating the same gametes with these agents. At the concentrations used, EDTA appears to be more effective, probably because of less interference with activity required for recovery or a difference in time of action. These agents are listed in Table 6 along with the others and their assumed modes of action. That recovery has been observed with all these agents except temperature must indicate that the temperature coefficient of the recovery process is similar to that applying to extension of the cell cycle. Additional evidence is provided by the observation that the magnitude of the radiation-induced division delay in any one experiment is independent of the temperature (between 8°C and room temperature) at which the fertilized eggs develop.⁽⁵⁾

In order to define the time of action of the agents listed in Table 6, their effects on the radiation sensitivity curve (Figure 21) were determined. The

TABLE 6 EFFECT OF VARIOUS AGENTS ON CELL DIVISION CYCLE

Agent inducing prolongation of division cycle	Effect on radiation-induced cleavage delay	Interpretation
0 to 15.5°C	$D' \approx D$	No recovery when division period prolonged by reduced temperature.
N_2	$D' < D$	Aerobic metabolism not required for recovery.
D_2O	$D' < D$	Rigidification of mitotic apparatus does not interfere with recovery.
Puromycin (+ N_2)	$D' \leq D$	Recovery not wholly dependent on protein synthesis.
NaN_3	$D' < D$	Aerobic metabolism not required for recovery.
Colcemid	$D' < D$	Interference with spindle formation does not interfere with recovery process.
Ribonuclease	$D' < D$	Surface effect? Does not interfere with recovery.
EDTA	$D' < D$	Complexing of divalent cations? Does not interfere with recovery.
Beta mercaptoethanol	$D' < D$	Interference with aster and spindle development does not block recovery process.

D = Radiation-induced cleavage delay.

D' = Radiation-induced cleavage delay after treatment with agent inducing recovery period.

† Supplied by Aquarium Systems, Inc., Wickliffe, Ohio.

agents were applied to the zygotes for a 20- to 30-min time period shortly following fertilization. The zygotes were subsequently irradiated at different times in the cell cycle—in some cases during the treatment period. A comparison of the radiation sensitivity curves of treated and untreated zygotes for the agents tested is given below.

Figure 23 shows the effect of treating *Lytechinus* zygotes for twenty minutes with $10^{-4} M$ ribonuclease after fertilization. The solid curve depicts the response of control zygotes to irradiation with 5000 R at the times indicated on the abscissa. The dashed curve depicts the response of zygotes to the same dose of radiation after the ribonuclease treatment. The solid and dashed arrows represent the division times of the unirradiated control and treated zygotes; thus, a 20-min treatment with ribonuclease delayed the unirradiated cell division time by about 18 min. The response curve for the drug-treated zygotes resembles closely that of the untreated ones and appears to be shifted in time only by the approximate length of the treatment time. This would be expected if the treatment with ribonuclease delayed the cell progression process only during the time of application and did not affect the system's subsequent response to radiation. Figure 24 shows similar results when *Arbacia* zygotes are temporarily immersed in 99.8% deuterated sea water.

On the other hand, Figure 25 depicts the radiation response of *Arbacia* zygotes after a 30-min treatment with $2.5 \times 10^{-3} M$ sodium azide. Again, the reactions

responsible for the shape of the response curve appear to be delayed principally during the time of treatment, but in this case the magnitude of radiation response is appreciably less during and after the treatment. A similar result is shown in Figure 26 for treatment with 0.1 M beta mercaptoethanol. There is possibility, however, that even though in each case the fertilized egg suspension was rinsed, enough chemical remained to protect some critical structures from the action of the radiation.

As shown in Figure 27, treatment with EDTA (mg/ml) of *Arbacia* zygotes appeared to protect zygotes both before and after application. In this instance, however, the prolongation of the cell division period seemed to occur in the latter part of the cycle—after the chemical was apparently removed by dilution. A similar, but less dramatic, result was observed when colchicine was used. This is shown in Figure 28 which depicts treatment of the same zygotes in morning and afternoon experiments with two different colchicine concentrations. Only the lower concentration was protective. The super-imposition of the control curves in the two experiments, however, illustrates the precision of the measurements. However, again the complete removal of the chemical from sensitive structures by the rinsing process was not assured or tested, and, therefore, the reduction in radiation effect observed might be the result of protection of relevant entities by the chemical present during and after the treatment period.

It is felt that the action of nitrogen is immediate

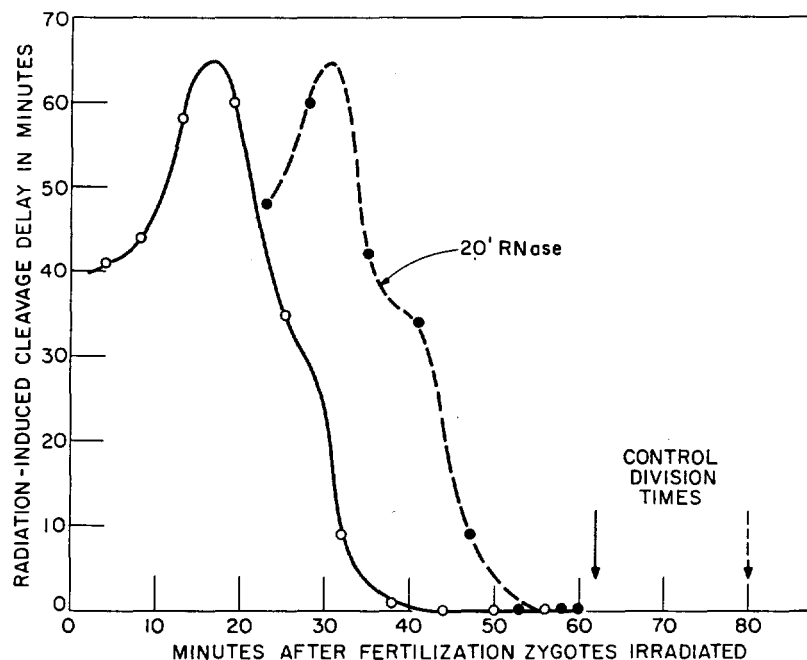


FIG. 23.—The sensitivity to radiation-induced cleavage delay as a function of the postfertilization time *Lytechinus* zygotes are irradiated. The dashed curve shows the effect of treatment with $10^{-4} M$ ribonuclease for 20 min right after fertilization.

appear
treat-
diation
treat-
r treat-
is the
h case
chem-
s from

TA (10
ect the
his in-
ivision
he cy-
ed by
as ob-
wn in
ne ga-
th two
lower
ion of
wever,
How-
micals
s was
ion in
f pro-
resent

diate,

i.e., it enters and leaves the cell in strict conformity to its concentration in the medium at any time. Therefore, the effect of nitrogen on the response curve was tested. The results are shown in Figure 29. The reduction in radiation response after the bubbling of nitrogen through the cell suspension has ceased and air has been readmitted can only mean then that the system has been modified in its response to radiation. It can be envisioned that some reactions, sensitive to radiation, have proceeded and perhaps have been completed during the anaerobic period. Therefore, they may no longer be as vulnerable to exposure to radiation. These reactions, however, do not seem to be those that determine the shape of the response curve. Only the magnitude, therefore, and not the shape of the radiation response curve is altered by the absence of oxygen.

Figures 30 and 31 show the results of similar experiments involving prolongations of the cell cycle time by temporary reductions of temperature. A lowering of the normal ($\sim 22^\circ\text{C}$) development temperature, even by less than 10°C , postponed the processes determining the characteristic shape of the radiation response curve but did not modify the magnitude of the response. Since the difference in control egg division times was appreciably less than the treatment time, however, these reactions appear to have proceeded more rapidly than normal once the system was returned to control temperatures. Again, therefore, certain activity must have been possible during the period of reduced temperature which permitted the more rapid rate of completion of the cell cycle once

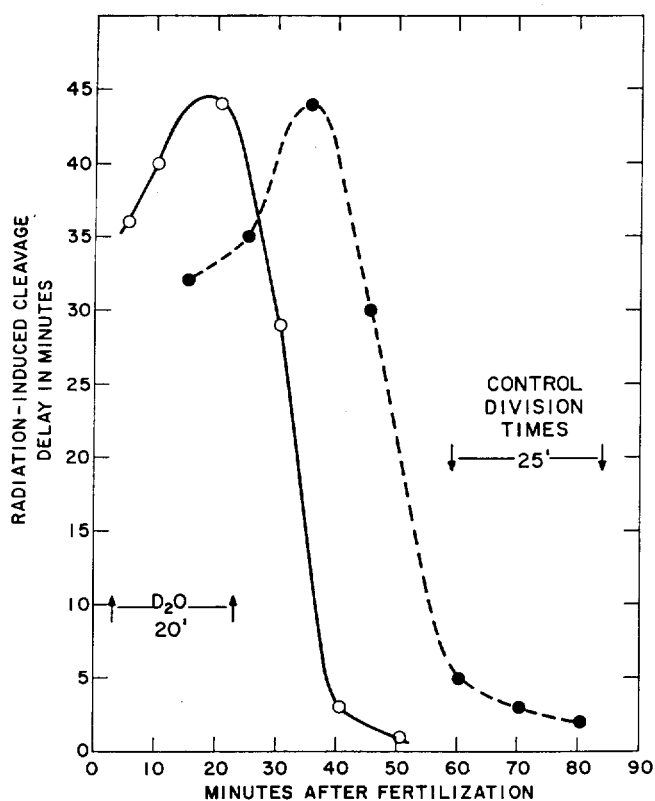


FIG. 24.—The sensitivity to radiation-induced cleavage delay as a function of the postfertilization time *Arbacia* zygotes are irradiated. The dashed curve shows the effect of immersion in 99+% deuterated sea water for 20 min right after fertilization.

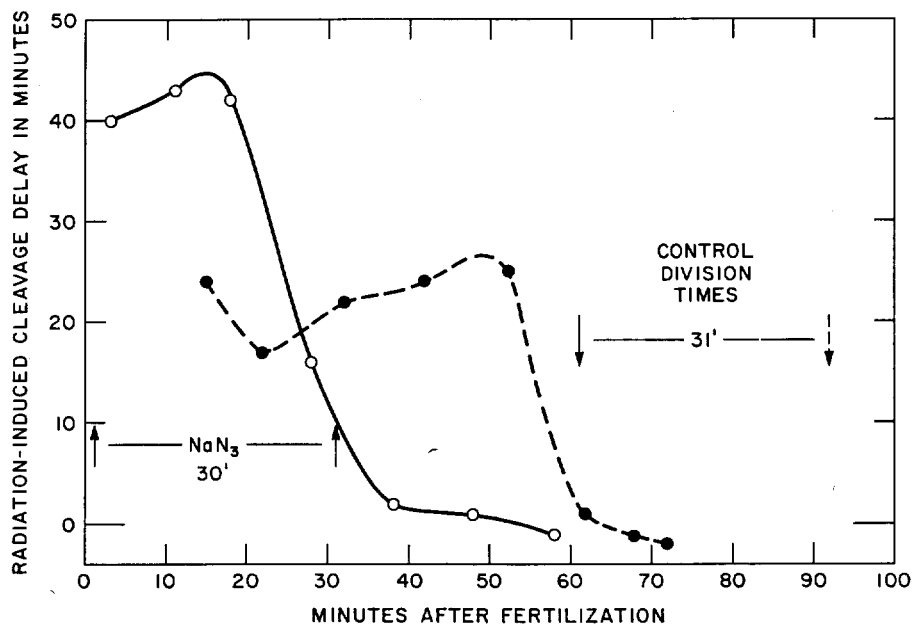


FIG. 25.—The sensitivity to radiation-induced cleavage delay as a function of the postfertilization time *Arbacia* zygotes are irradiated. The dashed curve shows the effect of treatment with $2.5 \times 10^{-3} M$ sodium azide for 30 min right after fertilization.

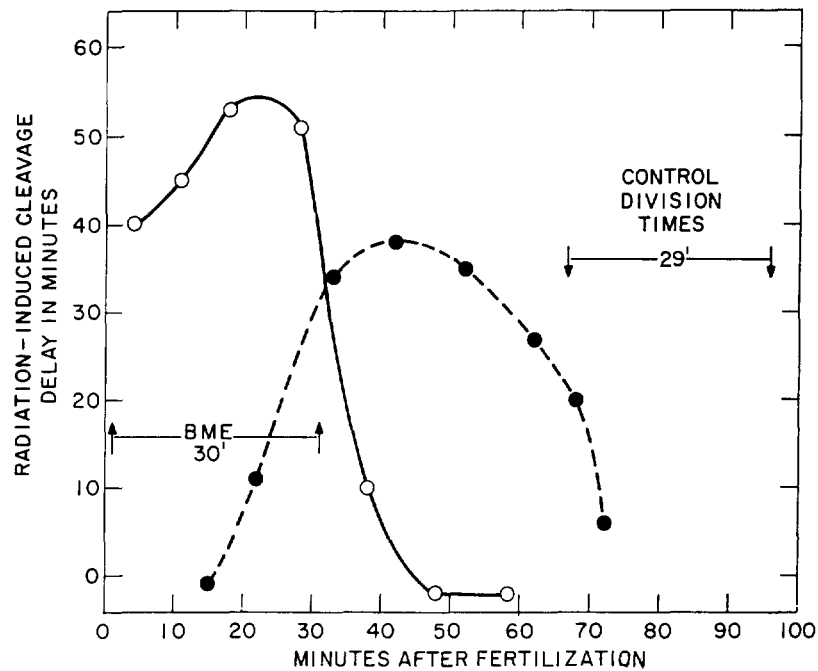


FIG. 26.—The sensitivity to radiation-induced cleavage delay as a function of the postfertilization time *Arbacia* zygotes are irradiated. The dashed curve shows the effect of treatment with 0.1 M beta mercaptoethanol for 30 min right after fertilization.

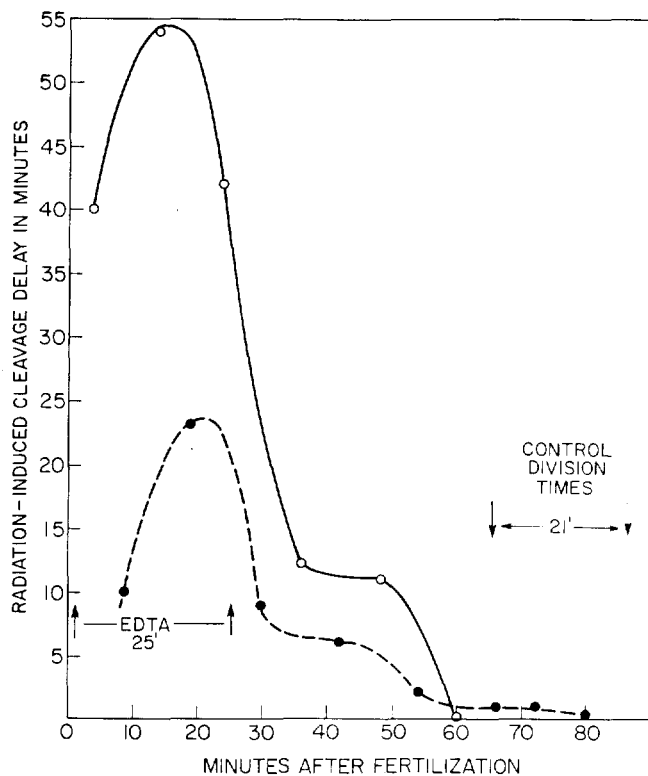


FIG. 27.—The sensitivity to radiation-induced cleavage delay as a function of the postfertilization time *Arbacia* zygotes are irradiated. The dashed curve shows the effect of treatment with 10 mg/ml EDTA for 25 min right after fertilization.

normal temperatures were restored. The reactions responsible for the shape of the radiation curves, therefore, are inhibited by reduced temperature, interference with oxidative metabolism, treatment with ribonuclease, D_2O , and beta mercaptoethanol. They do not appear responsive, however, to the action of EDTA or colchicine. EDTA treatment, and to a lesser degree colchicine treatment, nevertheless, slow down later reactions, protect while present and alter subsequent responses to radiation. Hopefully, similar experiments with other agents will help to shed new light on the mechanisms associated with the radiation response of developing sea urchin egg systems.

DISCUSSION AND SUMMARY

Recovery from radiation-induced division delay in sea urchin eggs has been shown to occur when the normal cell division time is extended by temporary treatment with a number of agents, except the lowering of temperature. The recovery mechanism, therefore, is felt to have approximately the same temperature coefficient as the general processes leading to cell division. Considering the interpretations of the actions of the agents so far used, it can be inferred that interference with aerobic metabolism, protein synthesis or mitotic apparatus development does not block this recovery process. The actions of ribonuclease and EDTA are not so well defined. Ribonuclease is reported to bind to the cell surface and perhaps inhibit cleavage nonenzymatically by inter-

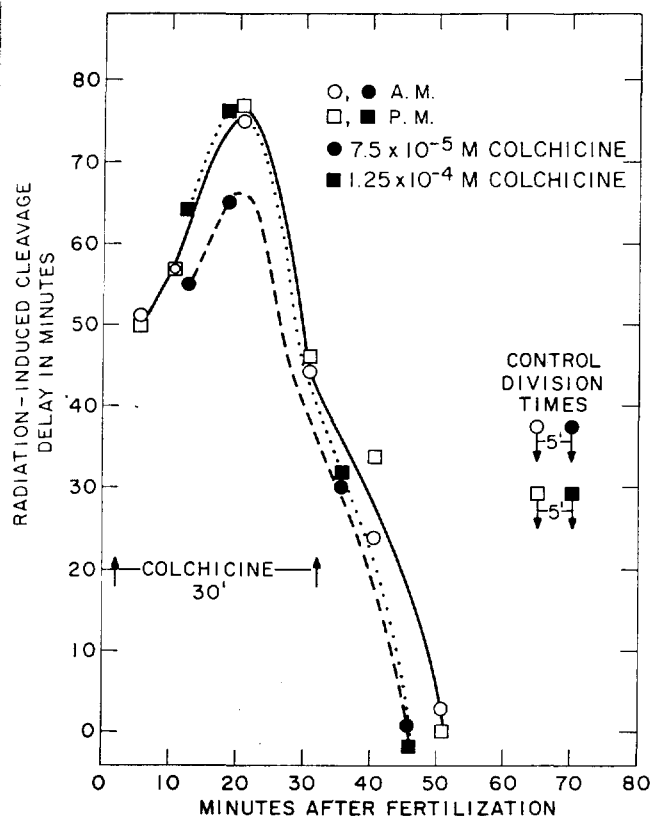


FIG. 28.—The sensitivity to radiation-induced cleavage delay as a function of the postfertilization time *Arbacia* zygotes are irradiated. The open circles and squares represent experiments on the same control gametes in the morning and afternoon, respectively. The solid curve is drawn through these symbols. The dashed curve shows the effect of treatment with $7.5 \times 10^{-5} M$ colchicine for 30 min right after fertilization, while the dotted curve shows the effect of $1.25 \times 10^{-4} M$ colchicine treatment for 30 min right after fertilization.

acting as a basic protein with the cell surface.⁽⁷⁾ The chelating activity of EDTA is presumed responsible in some way for its action. As discussed in last year's report,⁽⁶⁾ comparisons of recovery rates under the action of these various agents tends to implicate some metabolic activity in the recovery process. One indication is that more recovery generally occurs during extensions of the cell division period induced by physico-chemical agents like D_2O , colchicine, and EDTA than during comparable time periods induced by metabolic inhibitors.

From analysis of the variations in radiation response curves as a function of the time during the cell cycle that fertilized eggs are exposed, a "modification" effect of certain of the agents has been uncovered. Thus, the radiation response of zygotes that have been treated with sodium azide, beta mercaptoethanol, nitrogen, and EDTA is less than their untreated counter-parts. Since this reduced response is observed at times when the agent is not present dur-

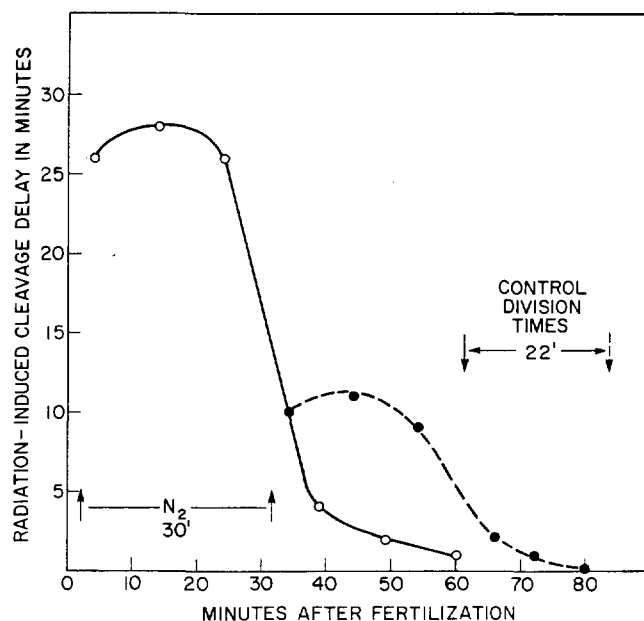


FIG. 29.—The sensitivity to radiation-induced cleavage delay as a function of the postfertilization time *Arbacia* zygotes are irradiated. The dashed curve shows the effect of treatment with nitrogen for 30 min right after fertilization.

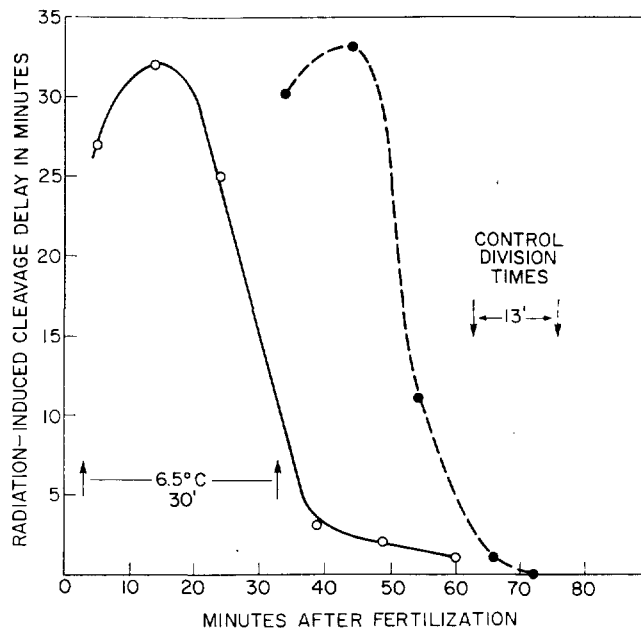


FIG. 30.—The sensitivity to radiation-induced cleavage delay as a function of the postfertilization time *Arbacia* zygotes are irradiated. The dashed curve shows the effect of incubation at $6.5^\circ C$ for 30 min right after fertilization.

ing exposure, it cannot be the usual type of protection afforded, for example, by hypoxia. Therefore, the phenomenon has been termed modification. In a similar experiment, puromycin treatment, on the other hand, has been shown by Rustad and Burchill⁽⁸⁾ to sensitize fertilized *Arbacia* eggs to subsequent radia-

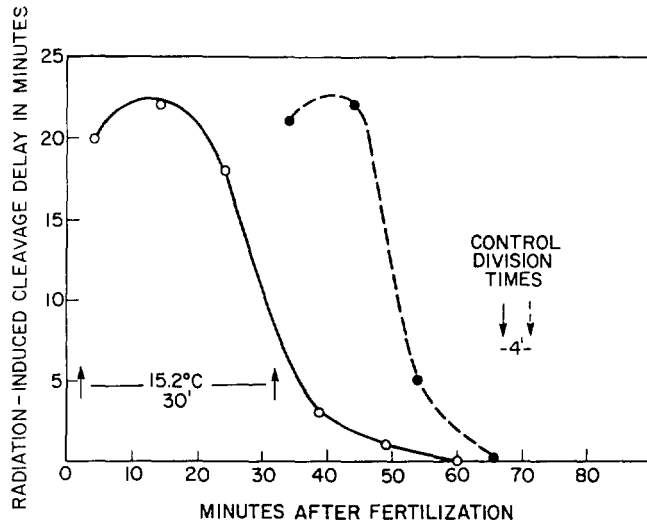


Fig. 31.—The sensitivity to radiation-induced cleavage delay as a function of the postfertilization time *Arbacia* zygotes are irradiated. The dashed curve shows the effect of incubation at 15.2° C for 30 min right after fertilization.

tion treatment. It is hoped that further study of the effects of various agents on the recovery and modification processes will lead to a better understanding not only of the processes themselves, but also of the underlying radiation response.

Mitotic or division delay in mammalian cells also varies as a function of the time during the generation cycle irradiation takes place. The subject has been reviewed recently by Sinclair.⁽⁹⁾ The form of response appears similar to that found with sea urchin eggs in that the maximum delay occurs when the cells are irradiated during the period of DNA synthesis, *S*. For cells not irradiated in *S*, the principal

portion of the division delay after moderate doses expressed as a block in *G*₂. More detailed comparison will not be made here. It appears evident, however, that work on the naturally synchronized cell system of dividing sea urchin eggs is pertinent to the problem of division delay in irradiated mammalian cells.

The assistance of Regina Rigoni in carrying out these studies is gratefully acknowledged.

REFERENCES

1. Henshaw, P. S. Further Studies on the Action of Roentgen Rays of the Gametes of *Arbacia punctulata*. *Am. Roentgenol.* **43**, 899-993 (1940).
2. Henshaw, P. S. Studies of the Effect of Roentgen Rays on the Time of First Cleavage in Some Marine Invertebrate Eggs. I. Recovery from Roentgen-Ray Effects in *Arbacia* Eggs. *Am. J. Roentgenol.* **27**, 890-898 (1932).
3. Failla, P. Recovery from Radiation-Induced Delay in Cleavage in Gametes of *Arbacia punctulata*. *Science* **134**, 1341-1342 (1962).
4. Failla, P. Recovery from Division Delay in Irradiated Gametes of *Arbacia punctulata*. *Radiat. Res.* **25**, 331-336 (1962).
5. Failla, P. Division Delay in Irradiated Gametes of Sea Urchins. Argonne National Laboratory Radiological Physics Division Annual Report, July 1966 through July 1967. ANL-7360, p. 78.
6. Failla, P. Division Delay and Recovery in Irradiated Sea Urchin Gametes. Argonne National Laboratory Radiological Physics Division Annual Report, July 1967 through June 1968. ANL-7489, p. 13.
7. Cormack, D. H. Site of Action of Ribonuclease during Inhibition of Egg Cleavage. *Nature* **209**, 1364-1365 (1966).
8. Rustad, R. C. and Burchill, B. R. Radiation-Induced Mitotic Delay in Sea Urchin Eggs Treated with Puromycin and Actinomycin D. *Radiat. Res.* **29**, 203-210 (1966).
9. Sinclair, W. K. Cyclic X-Ray Responses in Mammalian Cells *In Vitro*. *Radiat. Res.* **33**, 620-643 (1968).

THE RETENTION OF ¹³³Ba IN BEAGLES

J. E. Farnham and R. E. Rowland

Barium, like the other alkaline earths, is a bone-seeking element. These studies, which started some ten years ago, were designed to examine the whole-body retention and the plasma clearance of Ba¹³³ in beagles of various ages, with the aim of comparing these parameters with the values found for calcium, strontium, and radium. This is the final report of this study.

INTRODUCTION

The retention of barium in the skeleton and in the blood, like that of the other alkaline earths, is of interest because it is closely related to the calcium metabolism of bone.⁽¹⁻⁶⁾ Knowledge of the differences and similarities in the metabolism of barium and calcium

should elucidate the normal processes of skeletal metabolism. Furthermore, the chemical similarity of barium and radium insures that extending our meager knowledge of barium metabolism will contribute to our understanding of the toxicity of radium in man and animals.

In June of 1959 we began a long-term study to measure the whole-body retention of ¹³³Ba in two beagle dogs over a period of several years. Progress data have been given in three earlier reports.^(5, 7, 8) Subsequently we have injected three additional beagle dogs with the ¹³³Ba isotope to measure the short-term uptake and retention of barium, and to measure the rad

chemical distribution of the ^{133}Ba in various bones and types of bones (cortical vs. trabecular) throughout the dog skeleton.

This barium isotope was chosen because 1) it has a long half-life of 7.2 years and is excellently suited for long-term retention studies, 2) the radiation dose from it is minimal (^{133}Ba decays by electron capture and no beta particles are emitted), and 3) quantitative measurements are easily made by means of scintillation counters, that is, gamma counters for whole-body retention data, and liquid scintillation counters for blood, fecal, and chemically ashed samples.

MATERIALS AND METHODS

Each animal was given an intravenous injection of ^{133}Ba in the form of BaCl_2 in 0.075 N HCl, with a

TABLE 7. INJECTION OF DOGS WITH ^{133}Ba

Dog	Age at injection	Weight at injection, kg	^{133}Ba injected, μCi	Sacrifice time, days from injection
A22B	8 m	7.2 kg	6.1	3113
576	≈ 4 yr	10.1 kg	10.0	1508
156	6.5 yr	≈ 7.2 kg	10.5	7
A22C	9.25 yr	10.0 kg	300	7
A22D	9.5 yr	12.5 kg	314	7

TABLE 8. RETENTION OF BARIUM TRACER

Days after injection	Fractional retention				% injected dose/g calcium			
	576	A22B	A22C	A22D	576	A22B	A22C	A22D
0	1	1	1	1	0.667	0.952		1.03
1			0.895	0.791			0.978	0.818
2			0.747	0.680			0.816	0.703
3			0.636	0.513			0.695	0.531
4			0.518	0.443			0.566	0.458
5			0.460	0.369			0.503	0.382
6			0.409	0.323			0.447	0.334
7			0.354	0.295			0.387	0.305
20	0.491	0.667			0.327	0.635		
27	0.464	0.647			0.309	0.616		
34	0.427	0.589			0.285	0.561		
41	0.420	0.588			0.280	0.561		
48	0.418	0.610			0.279	0.581		
83	0.371	0.509			0.247	0.485		
139	0.332	0.460			0.221	0.438		
188	0.307	0.401			0.205	0.382		
293	0.252	0.361			0.168	0.344		
363	0.224	0.352			0.149	0.335		
454	0.213	0.319			0.142	0.335		
693	0.173	0.280			0.115	0.267		
995	0.153	0.291			0.102	0.277		
1002	0.157	0.303			0.105	0.289		
1499	0.128	0.264			0.085	0.251		
3113	—	0.206				0.196		

TABLE 9. BARIUM: BLOOD SPECIFIC ACTIVITY

Time, days	Percent injected dose/mg calcium			
	576	A22B	A22C	A22D
0.021	—	—	3.26×10^{-1}	2.58×10^{-1}
0.042	2.83×10^{-1}	2.73×10^{-1}	2.65×10^{-1}	2.12×10^{-1}
0.098	—	—	2.03×10^{-1}	1.70×10^{-1}
0.167	—	—	1.35×10^{-1}	1.19×10^{-1}
0.25	1.17×10^{-1}	6.31×10^{-2}	1.17×10^{-1}	9.57×10^{-2}
0.313	—	—	9.5×10^{-2}	8.43×10^{-2}
1	5.15×10^{-2}	1.76×10^{-2}	4.61×10^{-2}	3.13×10^{-2}
2	2.04×10^{-2}	8.83×10^{-3}	2.51×10^{-2}	1.82×10^{-2}
3	1.18×10^{-2}	3.59×10^{-3}	1.39×10^{-2}	1.04×10^{-2}
4	—	—	9.26×10^{-3}	7.23×10^{-3}
5	—	—	6.37×10^{-3}	4.40×10^{-3}
6	—	—	5.06×10^{-3}	2.39×10^{-3}
7	3.80×10^{-3}	1.66×10^{-3}	4.02×10^{-3}	1.75×10^{-3}
14	1.10×10^{-3}	6.28×10^{-4}		
1002-1091	—	8.60×10^{-6}		
1100-1195	7.40×10^{-6}	—		
1450-1550	4.65×10^{-6}	—		
1765-1865	—	3.50×10^{-6}		

stable barium level of 10 mg/ml of solution. The injection materials were neutralized with NaOH immediately before injection. The age and weight of each dog at the time of injection, the quantity of ^{133}Ba injected, and the time of sacrifice are listed in Table 7.

Samples of venous blood were obtained at frequent intervals on the day of injection and periodically thereafter for plasma clearance studies. Separate urine and fecal samples were collected from each animal on the days indicated in Table 10. No fecal or blood samples were collected from Dog 156.

Preparations of samples and analyses were as follows:

Whole-Body Retention

The body burdens of the two long-term retention animals were measured in a steel room of the Division of Biology and Medicine by placing a 5" x 4" NaI(Tl) crystal, connected to a multichannel analyzer, in a reproducible position with respect to each dog. Immediately after the intravenous injections of the isotope, each animal was counted so that the original count included all of the injected activity. All subsequent counts were expressed as a fraction of the original count. Also, for calibration purposes, an aliquot of the original injection solution, sealed in a glass vial, was counted in a reproducible position immediately after each dog was counted. The retention, expressed as percent of injected dose per gram of total skeletal calcium, and the plasma specific activity, expressed as percent of injected dose per milligram of plasma calcium, are tabulated in Tables 8 and 9 and

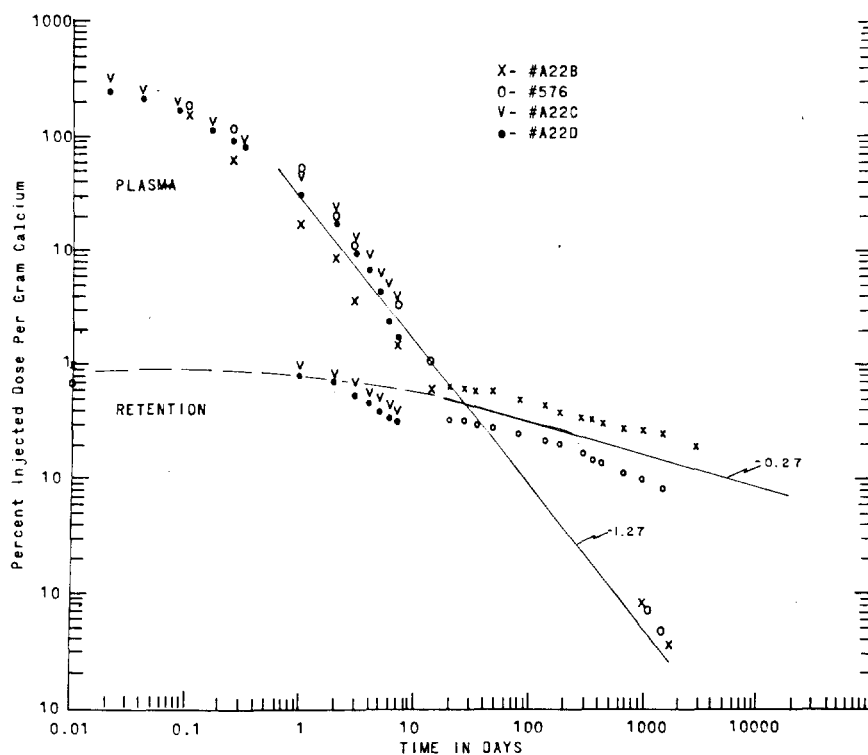


FIG. 32.—The ^{133}Ba plasma specific activity and the whole-body retention of this isotope in four beagles plotted as a function of time after intravenous injection.

are both shown in graphical form in Figure 32. The 3113-day ^{133}Ba retention point for Dog A22B was obtained from radiochemical analysis of the entire skeleton.

The values listed in Table 8 and plotted in Figure 32 are expressed as percent of injected dose per gram of skeletal calcium. It has been assumed that the total skeletal calcium in Dogs 576 and A22B was 1.5% of their respective total body weights:⁽⁹⁾ 150 g calcium for Dog 576 and 105 g calcium for Dog A22B. The total skeletal calcium in Dogs A22C and A22D was measured. The values of the total skeletal calcium in these two dogs were 91.5 g for Dog A22C and 96.7 g for Dog A22D. These stable calcium determinations on both plasma and the complete skeletons were made on a Perkin-Elmer atomic absorption spectrophotometer by the method described in their handbook.⁽¹⁰⁾

Seven days before sacrifice (3106 days after the ^{133}Ba injection) Dog A22B, at age 9.2 years, was injected with 2081 μCi of high specific activity ^{45}Ca as part of a kinetic study.⁽¹¹⁾ At about the same time, its two littermates were also injected intravenously with tracers: Dog A22C received 300 μCi ^{133}Ba and Dog A22D received both 423 μCi of ^{45}Ca and 315 μCi of ^{133}Ba . The dogs were maintained in separate activity cages for one week, during which time periodic blood samples and daily fecal and urine samples were collected. Data from the analysis of these specimens per-

mitted us to compare ^{45}Ca and ^{133}Ba retention blood curves of Dog A22B at 8 months of age vs. years of age. All four of the above mentioned curves are plotted on log-log scale in Figure 33.

Plasma Clearance

Three-milliliter samples of heparinized (0.02–0.05 ml of heparin) whole blood from Dogs A22B and 576 were sealed in glass vials and counted in a NaI well counter. The ^{133}Ba standard vial was counted in the same manner. The concentration determination of ^{133}Ba for the last four observations were made in pooled samples of plasma. The plasma was collected over periods of about three months by taking approximately 150 ml of whole blood from the appropriate dog every two weeks, separating the plasma, and storing it until a sufficient quantity had been obtained for gamma-ray analysis. The final collected volumes were wet ashed with 2 N HCl and concentrated down to 3-ml volumes, which were sealed in glass vials for comparison with earlier samples. At sacrifice a terminal blood sample of 300 ml was taken from Dog 576. The observed values are listed in Table 9 as percent of injected dose per milligram of calcium and plotted in Figure 32 as percent injected dose per gram calcium.

The ^{133}Ba content in the blood plasma from Dogs A22C and A22D was measured using liquid scintillation techniques. Aliquots of plasma separated from

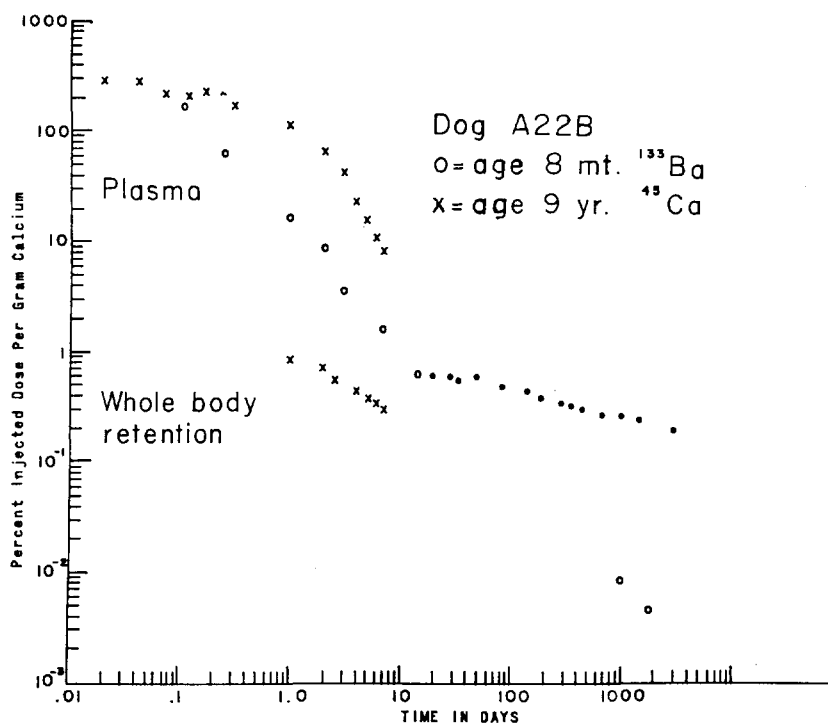


FIG. 33.—The plasma specific activity and the whole body retention of ^{133}Ba and ^{45}Ca given intravenously into a single beagle dog, but at two widely different ages. ^{133}Ba was administered when the animal was 8 months of age and ^{45}Ca when the animal was 9.2 years of age.

3 ml samples of whole blood were dissolved in liquid scintillation vials using hydroxide of hyamine and 10 ml each of absolute ethanol and scintillation solution. The vials were then counted against aliquots of the ^{133}Ba injection solution (dissolved in the same manner as the plasma) in a Packard Tri-Carb liquid scintillation spectrometer system, Model 3002. Quenching was controlled by gain adjustments and observations of the spectrum shift through simultaneous two-channel counting with one narrow and one wide window opening. These observed values are also listed in Table 9 and plotted in Figure 32.

Urine Samples

Urine samples were wet ashed with concentrated HNO_3 and then diluted up to volume in volumetric flasks. Three-milliliter aliquots from each sample taken from Dog 576 or A22B were sealed in a glass vial and counted in the same NaI(Tl) well counter that was used for the plasma clearance studies. Smaller aliquots of the wet ashed urine samples from Dogs A22C and A22D were transferred to liquid scintillation vials and counted in the liquid scintillation counter.

Fecal Samples

All fecal samples were placed in separate porcelain crucibles, heat dried, ashed overnight in a 600°C

muffle furnace, dissolved in concentrated HNO_3 , transferred to volumetric flasks, and diluted to volume. Aliquots from the prepared samples from the appropriate dog were either sealed in glass vials and gamma counted in the well counter or dissolved in liquid scintillation solution and counted in the liquid scintillation spectrometer. All fecal and urinary excretion rates (percent of injected dose per day) are summarized in Table 10.

Bone Determinations

The bone specimens were air dried, weighed, placed in separate preweighed crucibles, ashed overnight in a muffle furnace at 750°C , reweighed to determine the ash weight of each sample, dissolved in 2 N HCl, and then transferred to volumetric flasks. Five long bones (a femur, tibia, humerus, radius, and ulna) from Dog 576 and the left femur from each of the other dogs were cut into five pieces, which were coded as proximal end, proximal shaft, mid-shaft, distal shaft, or distal end prior to weighing and ashing. As was done with the other samples, appropriate aliquots were either sealed in glass vials and counted in the well counter or dissolved in scintillation solution and counted in the liquid scintillation counter. The observed values, listed in Table 11, were calculated by comparison with the standards made from the original injection solution.

RESULTS AND DISCUSSION

Barium-133 emits two strong gamma rays, one at 81 keV and one at 360 keV, as well as other less intense gamma rays. It was of interest to note that the shape of the spectrum as recorded by this particular NaI(Tl) crystal, remained unchanged throughout the

TABLE 10. EXCRETION DATA

Sample	Day	Percent injected dose ^{133}Ba				Percent injected dose ^{45}Ca	
		576	A22B	A22C	A22D	A22D	A22B
Feces	1	—	—	0.386	0.541	0.883	0.609
	2	—	—	8.599	2.289	2.868	10.060
	3	3.17	—	7.191	5.315	6.065	12.672
	4	1.28	0.439	8.708	10.599	14.174	12.930
	5	1.16	0.298	2.495	3.552	5.430	10.067
	6	—	0.118	2.560	3.429	11.891	4.027
	7	—	—	2.666	1.158	2.969	2.020
Urine	1	—	—	8.406	16.374	0.816	1.110
	2	—	—	3.785	4.130	0.045	1.461
	3	2.78	—	2.742	4.466	0.377	0.657
	4	0.85	0.270	1.389	1.842	—	0.624
	5	1.05	0.377	1.540	2.302	1.781	0.555
	6	—	0.162	0.806	2.026	0.285	0.619
	7	—	—	1.030	0.876	0.327	0.284
Feces/ urine	1	—	—	0.046	0.03	1.08	0.55
	2	—	—	2.27	0.55	63.73	6.89
	3	1.14	—	2.62	1.19	16.09	19.29
	4	1.51	1.62	6.27	5.75	—	20.72
	5	1.10	0.79	1.62	1.54	3.05	18.14
	6	—	0.72	3.18	1.69	41.7	6.51
	7	—	—	2.59	1.32	9.08	7.11

TABLE 11. ^{133}Ba CONCENTRATIONS IN VARIOUS BONES (PERCENT INJECTED DOSE PER GRAM ASH)

	576 (1508 days from injection)	156 (7 days from injection)	A22D (7 days from injection)	A22C (7 days from injection)	A22B (3113 days from injection)
Femur					
Proximal epiphysis	0.040	0.089	0.154	0.201	—
Proximal metaphysis	0.025	0.043	0.155	0.150	—
Proximal epiphysis plus proximal metaphysis	0.035	0.070	0.155	0.166	0.103
Mid-shaft	0.018	0.042	0.057	0.065	0.075
Distal metaphysis	0.026	0.039	0.153	0.134	—
Distal epiphysis	0.046	0.095	0.146	0.212	—
Distal metaphysis plus distal epiphysis	0.039	0.075	0.149	0.181	0.079
Tibia	0.032	0.047	0.070	0.086	0.086
Humerus	0.030	0.072	0.126	0.152	0.086
Radius	0.031	0.042	0.057	0.081	0.106
Ulna	0.035	0.044	0.069	—	0.091
Lumbar vertebra	0.033	0.095	0.094	0.116	0.052
Total femur	0.035	0.068	0.133	0.152	0.083

period of observation, namely from minutes to after injection. This indicates that the effective sorption and scattering of the gamma radiation was essentially the same after the isotope was deposited within the bone as it was when the isotope was in the blood. Thus, in this case, the technique of recording an original burden measurement immediately after injection and before any excretion has taken place is valid as the 100% point, and the spectrum thus obtained may be compared directly to any later spectrum even though the location of the isotope within the bone is not the same at later times.

Figure 32 indicates that the retention of ^{133}Ba in these animals is not exactly described by a simple exponential function.⁽¹²⁾ It is clear that the plot of retention versus time does not yield a straight line on log-log coordinates; this is particularly true for the older dogs.

It should be noted that the plasma concentration of ^{133}Ba shown in Figure 32 has been expressed in the same units as the retention. This type of plot shows the relationship between the specific activity of the plasma and that of the skeleton.

A straight line can be drawn through the plasma concentration points from day 2 to day 7 or day 14 of the data from three of the animals. Dog A22D, however, indicates a definite departure from a straight line during this time interval. The values for the interval between 1000 and 1900 days (See Dogs A22B and A22C) indicate that the plasma concentration did not continue to fall as rapidly during the entire exposure period. The significant point is that by 1000 days after the isotope administration the plasma specific activity is a factor of fifty below that of the skeleton. The shape of these blood curves on the log-log plot is typical

other data and relates well to Marshall's power function model.⁽¹³⁾

In Table 12 the measured retention and plasma clearance are expressed as power functions where t is in days. The coefficient of the retention function was obtained by extending the straight line which fits the interval between 2 and 14 days to the day 1 intercept. The experimental slopes (the b term in the power function $R_t = at^{-b}$) were measured from the data shown in Figure 32.

It should be noted that "crossover," the time at which the specific activity of the blood drops below that of the skeleton, occurred between 14 and 100 days. An average slope has been drawn for the plasma and retention curves shown in Figure 32 to indicate a "crossover" point.

The fecal and urinary excretion rates, summarized in Table 10, indicate a general decrease in the urinary excretion rate with time after injection, whereas the fecal excretion rate may have a peak somewhere between 2 and 4 days. The peak in the fecal excretion rate could be due entirely or in part to a fecal delay.

Table 11 tabulates the ^{133}Ba concentrations, as percent of injected dose per gram of ash, of various bones and segments of bones. It is probably not meaningful to compare the actual quantity of ^{133}Ba retained in the dogs because of their different ages, since Decker, et al.⁽¹⁴⁾ have shown a marked difference in retention with age. However, the specific activity, in terms of percent of injected dose per gram of ashed bone segment relative to the specific activity of the whole bone, is probably a significant quantity to compare between the animals. Thus, in Table 13, we have compared the relative ^{133}Ba retention of bone segments and whole bones at short times and long times after injection. A ratio greater than one indicates more activity per gram of ash in the bone segment than in the bone as a whole. A ratio less than one indicates the opposite. At seven days after injection the trabecular bone of the proximal and distal epiphyses has a specific activity two or three times that of the cortical bone of the mid-shaft. This suggests a reactivity or turnover rate of trabecular bone that is two to three times that of cortical

TABLE 12. PLASMA RETENTION AND CLEARANCE OF ^{133}Ba

Dog	Age	Measured retention, fraction of injected dose	Measured plasma concentration, % of injected dose/ml plasma
A22B	8 m	1.30 $t^{-0.23}$	$1.76 \times 10^{-3} t^{-1.27}$
576	4 yr	1.00 $t^{-0.31}$	$5.15 \times 10^{-3} t^{-1.48}$
A22C	9 yr	0.98 $t^{-0.59}$	$4.61 \times 10^{-3} t^{-1.47}$
A22D	9.5 yr	0.82 $t^{-0.67}$	$3.13 \times 10^{-3} t^{-1.83}$

bone. One, therefore, expects that trabecular bone would eventually lose activity more rapidly than cortical bone so that the ratio of the specific activity of trabecular segments to that of a whole bone should decrease with time after injection. A slight decrease is shown by 1508 and 3113 days, but the effect is surprisingly small.

Thus, the analysis of tracer content in segments of various bones suggests that, while changes are occurring, these changes are not rapid. Even four and nine years after the isotope administration those bones or portions of bone usually considered to turn over rapidly still contain relatively high specific activity levels when they are compared to the regions of compact cortical bone where the turnover is known to be low.

SUMMARY

The whole-body retention, plasma clearance, and bone deposition of ^{133}Ba have been measured in beagle dogs. The ^{133}Ba retention by these animals is clearly not well described by a single power function, but does relate well to Marshall's theory of alkaline earth metabolism. No attempt has been made to fit these data with a series of exponential functions.

The plasma clearance studies indicate a steep slope of the barium blood curve when compared to normal calcium blood curves. This steep slope is typical of all barium, radium and strontium data that we have examined, but we have yet to appreciate its significance. The excretion rates show a general decrease with time after injection.

The analysis of the tracer content in various bones and segments of bones suggests that, even several years

TABLE 13. RATIO OF SPECIFIC ACTIVITIES OF FEMUR SEGMENTS TO SPECIFIC ACTIVITY OF ENTIRE FEMUR

Femur bone segment	Dog 576 1508 day	Dog A22B 3113 day	Dog 156 7 day	Dog A22C 7 day	Dog A22D 7 day	Avg. 7-day value	Avg. 7 day/ 1508 day
Proximal epiphysis	1.15	—	1.31	1.32	1.16	1.26	1.10
Proximal shaft	0.706	—	0.63	0.99	1.17	0.93	1.32
Proximal epiphysis plus shaft	0.998	1.24	1.04	1.09	1.17	1.10	1.10
Mid-shaft	0.523	0.90	0.61	0.47	0.50	0.53	1.01
Distal shaft	0.734	—	0.57	0.88	1.15	0.87	1.19
Distal epiphysis	1.31	—	1.39	1.39	1.10	1.29	0.98
Distal shaft plus epiphysis	1.117	0.95	1.11	1.19	1.12	1.14	1.02

after the isotope administration, trabecular bone which is usually considered to turn over rapidly still contains high amounts of activity as compared to cortical bone.

REFERENCES

1. Bauer, G. C. H., Carlsson, A., and Lindquist, B. A Comparative Study on the Metabolism of Ba¹⁴⁰ and Ca⁴⁵ in Rats. *Biochem. J.* **63**, 535 (1956).
2. Bligh, P. H. and Taylor, D. M. Comparative Metabolism of Strontium and Barium in the Rat. *Biochem. J.* **87**, 612 (1963).
3. Harrison, G. E., Carr, T. E. F., and Sutton, A. Distribution of Radioactive Calcium, Strontium, Barium, and Radium Following Intravenous Injection into a Healthy Man. *Int. J. Radiat. Biol.* **13**, 235 (1967).
4. Moore, W., Jr. Comparative Metabolism of Ba¹³³ and Ca⁴⁵ by Embryonic Bone Grown *in Vitro*. *Radiat. Res.* **21**, 376 (1964).
5. Rowland, R. E. Retention and Plasma Clearance of the Alkaline Earth Elements. Argonne National Laboratory Radiological Physics Division Semiannual Report, July through December 1959, ANL-6104, pp. 34-47.
6. Stover, B. J., Atherton, D. R., and Arnold, J. S. Comparative Metabolism of Ca⁴⁵ and Ra²²⁶. *Proc. Soc. Exptl. Biol. Med.* **94**, 268 (1957).
7. Rowland, R. E. The Retention of Barium-133 in Beagles. Argonne National Laboratory Radiological Physics Division Semiannual Report, January through June 1962. ANL-6646, pp. 113-115.
8. Farnham, J. E. and Rowland, R. E. The Retention of Barium-133 in Beagles. Argonne National Laboratory Radiological Physics Division Annual Report, July 1964 through June 1965. ANL-7060, pp. 70-73.
9. Van Dilla, M. A., Stover, B. J., Floyd, R. L., Atherton, D. R. and Taysum, D. H. Radium (Ra²²⁶) and Lead (Pb²¹⁰) Metabolism in Dogs. *Radiat. Res.* **8**, 417 (1957).
10. *Analytical Methods for Atomic Absorption Spectrometry*. Perkin-Elmer Co., Norwalk, Connecticut, 1966.
11. Ellsasser, J. C., Farnham, J. E., and Marshall, J. H. Comparative Kinetics and Autoradiography of Ca⁴⁵ and Sr⁹⁰ in Ten-Year-Old Beagle Dogs. Argonne National Laboratory Radiological Physics Division Annual Report, July 1967 through June 1968. ANL-7489, p. 24.
12. Norris, W. P., Tyler, S. A., and Brues, A. M. Retention of Radioactive Bone-Seekers. *Science* **128**, 456 (1957).
13. Marshall, J. H. Theory of Alkaline Earth Metabolism. The Power Function Makes Possible a Simple Comprehensive Model of Skeletal Systems. *J. Theor. Biol.* **6**, 386 (1964).
14. Decker, C. F., Kaspar, L. V., and Norris, W. P. The Retention of Strontium Metabolism with Age in the Beagle. *Radiat. Res.* **23**, 475 (1964).

¹⁰Pb AND ²¹⁰Po IN WOOD AND THE CIRCULATION OF LEAD IN TREES

R. B. Holtzman and F. H. Ilcewicz

Measurements of ²¹⁰Pb and ²¹⁰Po concentrations in tree rings from four 100-year-old trees were made in order to estimate the rates of radial translocation. Decrease of the concentration of the ²¹⁰Pb with a 21.4-year half-life showed that there is little circulation of lead in hickory heartwood more than 20 years old. In oak there appears to be little circulation in wood less than 5 years old, but this conclusion is less reliable because of the low concentration of the ²¹⁰Pb and the presence of ²²⁶Ra. The concentrations of the ²¹⁰Po correlated fairly well with those of the ²¹⁰Pb. Preliminary measurements of the stable lead concentrations did not show increased uptake in recent times. However, more detailed studies on the ²¹⁰Pb and stable lead concentrations are needed to determine the value of the heartwood of trees as a temporal record of lead contamination of the environment.

In recent years the concentration of ²¹⁰Pb, a naturally-occurring radionuclide with a 21.4-year half-life, has been used for age determination of materials such as snow⁽¹⁾ and lead in artists' paints,^(2, 3) and as a tracer for stable lead in rain.⁽⁴⁾ As a time-dependent tracer it could also be useful in estimating the temporal distribution of lead over the last century.

Despite the generally acknowledged increase in contamination of man's environment by lead over the last century or more, many of the quantitative aspects are uncertain, such as the rates of change of this contami-

nation in the biosphere in general and in man in particular. Environmental levels of lead in the past can be obtained from contemporary measurements, which, however, are scarce, often of low sensitivity and accuracy, and not easily compared to present day measurements. Another possibility is the measurement of lead in relics of the past which are uncontaminated by present day lead. Thus, Chow and Patterson⁽⁵⁾ and Jaworowski⁽⁶⁾ have measured lead in glacial cores. Jaworowski also determined lead in bone from ancient gravesites.⁽⁶⁾ Similarly, Ault et al.⁽⁷⁾ have looked at the lead concentrations and isotopic composition in a set of 3 tree rings covering a 30-year period. This type of sampling may be useful in estimating the amount of lead contamination in trees in different environments and possibly the change in contamination over many years, if one assumes that the trees absorb a measurable amount of the additional lead either through the roots or leaves.

This use of trees depends on the stabilization of lead concentration within a few years of formation of the wood. Although the heartwood does contain living cells, the arguments on metabolism of Stewart⁽⁸⁾ indicate that radial transport of materials in heartwood

unlikely. However, metabolites do travel along the ray tracheids, tritiated water enters heartwood, and in softwoods fission products are found in wood formed prior to the existence of bomb fallout.⁽⁹⁾

This paper reports on the use of ²¹⁰Pb tracer to estimate the rates of radial translocation of lead in trees. Also measured was ²¹⁰Po, which gives an indication of the transport of this nuclide. These nuclides occur in nature and are derived from the ²³⁸U chain which decays to ²²⁶Ra and then through a chain of short-lived daughters to ²¹⁰Pb, which has a 21.4-year half-life. This nuclide then decays to 5-day ²¹⁰Bi and finally to

¹³⁸-day ²¹⁰Po. Because of their different chemistries and because the radioactive rare gas intermediate, ²²²Rn, may be easily translocated, the ²¹⁰Pb moves through the biosphere independently of its predecessors. Although the origins of the stable and radioactive lead in the tree may differ, one would expect that after entry their metabolic behaviors would be similar, if not identical. Thus, if we assume no circulation, no excretion, and that the input rates are constant, the ²¹⁰Pb concentration would decrease with its 21.4-year radioactive half-life as one goes from the younger to the older wood (outer rings toward the center).

TABLE 14. ²¹⁰Pb, ²¹⁰Po AND ²²⁶Ra CONCENTRATIONS IN HICKORY

Sample number and direction	Age of ring, years	Mean age, years	²¹⁰ Pb, pCi/g dry	²¹⁰ Po, pCi/g dry	Ratio ²¹⁰ Po/ ²¹⁰ Pb	²²⁶ Ra, pCi/g dry
1 S	Bark	0	0.233 ± 0.014	0.192 ± 0.021	0.83 ± 0.10	
2 S	1-2	1.5	0.157 ± 0.017	0.329 ± 0.029	2.09 ± 0.29	0.265 ± 0.016
3 S	3-4	3.5	0.214 ± 0.019	0.192 ± 0.026	0.90 ± 0.15	0.082 ± 0.009
4 S	5-6	5.5	0.261 ± 0.024	0.202 ± 0.042	0.77 ± 0.17	
5 S	7-8	7.5	0.221 ± 0.017	0.176 ± 0.023	0.80 ± 0.12	
6 S	9-11	10.0	0.184 ± 0.017	0.239 ± 0.025	1.29 ± 0.18	
7 S	12-14	13.0	0.207 ± 0.017	0.238 ± 0.032	1.15 ± 0.18	
8 S	15-16	15.5	0.192 ± 0.017	0.280 ± 0.027	1.46 ± 0.19	
9 S	17-18	17.5	0.221 ± 0.017	0.269 ± 0.026	1.22 ± 0.15	
10 S	19-20	19.5	0.268 ± 0.020	0.170 ± 0.026	0.63 ± 0.11	
11 S	21-23	22.0	0.269 ± 0.018	0.238 ± 0.025	0.88 ± 0.11	
12 S	24-25	24.5	0.266 ± 0.022	0.254 ± 0.040	0.95 ± 0.17	
13 S	26-27	26.5	0.271 ± 0.021	0.196 ± 0.027	0.72 ± 0.12	
14 S	28-29	28.5	0.250 ± 0.020	0.227 ± 0.043	0.91 ± 0.19	
15 S	32-34	33.0	0.208 ± 0.017	0.221 ± 0.03	1.06 ± 0.20	
16 S	35-37	36.0	0.240 ± 0.019	0.081 ± 0.03	0.34 ± 0.16	
17 S	38-39	38.5	0.143 ± 0.018	0.266 ± 0.043	1.86 ± 0.38	
18 S	40-41	40.5	0.178 ± 0.019	0.157 ± 0.042	0.88 ± 0.26	
19 S	42-43	42.5	0.202 ± 0.019	0.164 ± 0.043	0.81 ± 0.22	
20 S	44-45	44.5	0.142 ± 0.017	0.216 ± 0.042	1.52 ± 0.34	
21 S	46-47	46.5	0.179 ± 0.019	0.110 ± 0.042	0.62 ± 0.24	
22 S	48-49	48.5	0.058 ± 0.011	0.076 ± 0.026	1.31 ± 0.51	
23 S	50-51	50.5	0.167 ± 0.018	0.146 ± 0.041	0.87 ± 0.26	
24 S	52-53	52.5	0.138 ± 0.018	0.194 ± 0.044	1.41 ± 0.37	
25 S	54-55	54.5	0.124 ± 0.017	0.146 ± 0.041	1.18 ± 0.37	
26 S	56-57	56.5	0.103 ± 0.014	0.126 ± 0.035	1.22 ± 0.38	
27 S	58-59	58.5	0.119 ± 0.016	0.146 ± 0.041	1.22 ± 0.38	
28 S	60-61	60.5	0.092 ± 0.013	0.104 ± 0.033	1.14 ± 0.40	
29 S	62-63	62.5	0.080 ± 0.012	0.125 ± 0.031	1.56 ± 0.44	
30 S	62-67	65.0	0.085 ± 0.010	0.086 ± 0.017	1.01 ± 0.23	
31 S	64-65	64.5	0.087 ± 0.013	0.077 ± 0.031	0.88 ± 0.38	
32 S	70-73	71.5	0.069 ± 0.010	0.064 ± 0.026	0.92 ± 0.39	
33 S	73-77	75.0	0.055 ± 0.009	0.071 ± 0.023	1.29 ± 0.47	
34 S	77-80	78.5	0.051 ± 0.008	0.039 ± 0.021	0.76 ± 0.42	
ENE	78	78.0	0.053 ± 0.007	0.036 ± 0.012	0.69 ± 0.24	
ENE	79	79.0	0.045 ± 0.007	0.042 ± 0.012	0.93 ± 0.30	
ENE	80	80.0	0.061 ± 0.007	0.048 ± 0.012	0.79 ± 0.22	
35 S	84-86	85.0	0.035 ± 0.007	0.086 ± 0.021	2.15 ± 0.63	
36 S	88-92	90.0	0.050 ± 0.008	0.046 ± 0.021	0.92 ± 0.44	
37 S	90-95	92.5	0.086 ± 0.010	0.082 ± 0.017	1.03 ± 0.23	
38 Center	100	100.0	0.057 ± 0.008	0.073 ± 0.014	1.28 ± 0.32	
				Mean	1.11 ± 0.34 (S.D.)	

The measurements of ^{210}Pb , ^{210}Po , and stable lead were made on four trees 100 to 120 years old, cut in 1966 on the grounds of Argonne National Laboratory, which is in a rural-suburban area about 25 miles southwest of the Chicago Loop. These were a hickory (*Carya cordyformis*), a black oak (*Quercus velutina*) and two white oaks (*Quercus alba*). A cross section of each trunk 12 to 18 inches in diameter and 18 inches thick was cut about 6 feet above the ground. A fifth tree, a 30-year-old elm from a nearby suburban street, was also examined for stable lead.

TABLE 15. ^{210}Pb AND ^{226}Ra CONCENTRATIONS IN BLACK OAK

Sample number and direction	Age of ring, years	Mean age, years	^{210}Pb , pCi/g dry	^{226}Ra , pCi/g dry
1 S	1-7	4.0	0.0580 ± 0.0061	0.0081 ± 0.0022
E	1-10	5.5	0.0722 ± 0.0067	
N	1-10	5.5	0.0746 ± 0.0065	
2 S	14-18	16.0	0.0351 ± 0.0054	0.0097 ± 0.0035
3 S	23-25	24.0	0.0244 ± 0.0046	
4 S	32-35	33.5	0.0189 ± 0.0038	0.0008 ± 0.0031
5 S	42-46	44.0	0.0185 ± 0.0039	
6 S	52-56	54.0	0.0311 ± 0.0045	
E	53-57	55.0	0.0180 ± 0.0037	
N	52-58	55.0	0.0306 ± 0.0044	
7 S	63-67	65.5	0.0202 ± 0.0037	
8 S	72-76	74.0	0.0045 ± 0.0018	
9 S	83-84	83.5	0.0078 ± 0.0023	
10 S	88-90	89.0	0.0070 ± 0.0022	
E	90-94	92.0	0.0111 ± 0.0028	
N	88-95	91.5	0.0049 ± 0.0018	
11 S	96-99	97.5	0.0134 ± 0.0032	

The wood from 2 to 5 adjacent rings was removed by a power drill, the bit of which had been carefully washed and used in the wood several times before samples were taken. Only this particular bit was used. The drillings were dried 8 hr at 110° C, weighed, and wet ashed in nitric and perchloric acids. (The samples in which only stable lead was measured were dried at 500° C.). The solutions were converted to 0.5 N and the ^{210}Po daughter of the ^{210}Pb was plated on a silver disk by heating 6 to 8 hr at 95° C, after which the ^{210}Po was alpha counted. The solutions were stored 4 months or more to allow the ^{210}Po to grow after which they were replated and counted. The amounts of both ^{210}Po and ^{210}Pb present were calculated from the Bateman equations for radioactive growth and decay.⁽¹⁰⁾ Stable lead was estimated by the spectrophotometric dithizone extraction method. The errors of measurement for stable lead were a 5% (standard deviation) and for ^{210}Pb and ^{210}Po errors based on counting statistics at the 90% level of confidence are given in the data.

The results are presented in Tables 14 to 17. Given are the concentrations of the ^{210}Pb and ^{210}Po in terms of pCi/g dry wood, the ratios of these values in a group of rings and the respective ages of these rings in the trees. Some values of ^{226}Ra concentration are given. Because of the large errors in the ^{210}Po determinations in the black oak, only the ^{210}Pb concentrations are given in Table 15. The directional representations (N, S, E, W, and ENE) of the radii along which samples were taken are relative and not necessarily actual directions in the living tree.

TABLE 16. ^{210}Pb , ^{210}Po AND ^{226}Ra CONCENTRATIONS IN WHITE OAK I

Sample number and direction	Age of ring, years	Mean age, years	^{210}Pb , pCi/g dry	^{210}Po , pCi/g dry	Ratio $^{210}\text{Po}/^{210}\text{Pb}$	^{226}Ra , pCi/g dr
1 S	1-7	4.0	0.108 ± 0.008	0.112 ± 0.078	1.03 ± 0.72	0.0142 ± 0.00
W	1-7	4.0	0.089 ± 0.008	0.127 ± 0.079	1.42 ± 0.89	
N	2-9	5.5	0.085 ± 0.008	0.010 ± 0.075	0.11 ± 0.88	
2 S	14-18	16	0.055 ± 0.006	0.088 ± 0.054	1.61 ± 1.00	0.0107 ± 0.00
3 S	22-27	24.5	0.040 ± 0.005	0.102 ± 0.049	2.52 ± 1.26	0.0249 ± 0.00
4 S	33-37	35.0	0.030 ± 0.004	0.069 ± 0.040	2.31 ± 1.37	0.0176 ± 0.00
5 S	43-48	45.5	0.037 ± 0.004	0.022 ± 0.042	0.59 ± 1.13	0.0172 ± 0.00
6 S	52-56	54.0	0.028 ± 0.004	0.038 ± 0.037	1.22 ± 1.36	
W	52-57	54.5	0.029 ± 0.005	0.009 ± 0.048	0.33 ± 1.67	
N	51-55	53.0	0.023 ± 0.004			
7 S	59-64	61.5	0.028 ± 0.004	0.022 ± 0.038	0.76 ± 1.35	
8 S	69-73	71.0	0.026 ± 0.004			
9 S	79-83	81.0	0.014 ± 0.003	0.016 ± 0.033	1.17 ± 2.39	
10 S	85-87	86.0	0.016 ± 0.004	0.012 ± 0.034	0.72 ± 2.14	
11 S	89-93	91.0	0.013 ± 0.003	0.024 ± 0.035	1.83 ± 2.71	
12 S	96-98	97.0	0.017 ± 0.004			
W	94-97	95.5	0.013 ± 0.003	0.020 ± 0.031	1.53 ± 2.48	
N	93-96	94.5	0.023 ± 0.004	0.012 ± 0.041	0.52 ± 1.80	
				Mean	1.18 ± 0.70 (S.D.)	

TABLE 17. ^{210}Pb , ^{210}Po AND ^{226}Ra CONCENTRATIONS IN WHITE OAK II

Sample number and direction	Age of ring, years	Mean age, years	^{210}Pb , pCi/g dry	^{210}Po , pCi/g dry	Ratio $^{210}\text{Po}/^{210}\text{Pb}$	^{226}Ra , pCi/g dry
1 S	1-7	4.0	0.059 ± 0.007	0.090 ± 0.039	1.53 ± 0.69	0.0116 ± 0.0025
1 W	1-7	4.0	0.052 ± 0.006	0.027 ± 0.034	0.51 ± 0.66	
N	1-7	4.0	0.058 ± 0.006	0.030 ± 0.037	0.52 ± 0.64	
2 S	13-17	15.0	0.032 ± 0.004	0.030 ± 0.023	0.95 ± 0.74	0.0154 ± 0.0023
3 S	22-29	25.5	0.037 ± 0.004	0.0067 ± 0.023	0.20 ± 0.69	
4 S	33-38	35.5	0.030 ± 0.004	0.039 ± 0.025	1.32 ± 0.85	
5 S	43-48	45.5	0.026 ± 0.004	0.041 ± 0.023	1.55 ± 0.90	
6 S	52-55	53.5	0.022 ± 0.003	0.036 ± 0.020	1.63 ± 0.94	
W	53-58	55.5	0.037 ± 0.005			
N	53-58	55.5	0.025 ± 0.004	0.006 ± 0.022	0.25 ± 0.87	
7 S	59-63	61.0	0.022 ± 0.003	0.020 ± 0.020	0.94 ± 0.92	
8 S	70-74	72.0	0.030 ± 0.004	0.018 ± 0.022	0.60 ± 0.75	
9 S	79-82	80.5	0.027 ± 0.003	0.017 ± 0.020	0.63 ± 0.76	
10 S	90-93	91.5	0.025 ± 0.003	0.002 ± 0.020	0.11 ± 0.79	
11 S center	100	(101)	0.024 ± 0.004	0.013 ± 0.021	0.52 ± 0.88	
W	99-103	101	0.029 ± 0.003	0.006 ± 0.021	0.21 ± 0.73	
N	99-103	101	0.020 ± 0.003	0.043 ± 0.021	2.10 ± 1.11	
				Mean	0.85 ± 0.61 (S.D.)	

The fractional errors of the ^{210}Pb data range from about 5 to 20% and of the ^{210}Po from 10 to 20% in the hickory and 50% and upwards in the oaks. These large errors in the oak data were caused by the low activities in these trees and by the long (1 year) interval between acquisition of the specimens and analysis.

Although Students' *t*-test shows the mean ratio of 1.11 ± 0.34 (S.D.) in the ^{210}Po to ^{210}Pb concentrations in hickory to be significantly greater than 1.00 ($P < 0.025$), it is still very close to unity. For the white oaks these means of 1.18 ± 0.70 and 0.85 ± 0.61 for I and II, respectively, are not significantly different than unity, indicating that the ^{210}Po follows the ^{210}Pb in the tree.

The results of the ^{210}Pb analyses versus age of the wood are shown on semilogarithmic plots in Figures 34 to 37. The ^{210}Pb concentrations in hickory (Figure 34) are constant in the 20 outer rings or even increase, presumably because the ^{210}Pb circulates. After this time the concentration drops off with a 21-year half-life, as shown by the close correspondence of the data points with the line representing the half-life of the ^{210}Pb . That the concentrations are fairly constant within a ring can be seen from the agreement among the circles representing values within a ring (or set of rings) along one radius of the tree, and the squares and triangles representing values along other radii. The bark, despite exposure to dust and weather, shows no higher concentration of ^{210}Pb than does the adjacent wood.

The curves for the three oak trees are less spectacular and less uniform. The black oak data shown in Figure 35 do not fit the 21-year half-life nearly as well

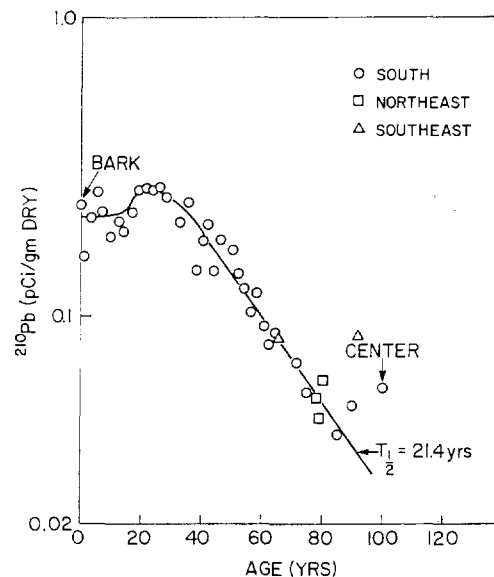


FIG. 34.—Variation of ^{210}Pb specific activity with age of wood in hickory.

as do those of the hickory. The fit of the data for White Oak I is poorer, and for White Oak II poorer yet, as shown by the upper sets of data points in Figures 36 and 37. The tendency to level off with age indicates either that 10 to 30% of the ^{210}Pb circulates in these trees, that the early uptake of this nuclide was greater than the more recent, or that a "background" of ^{210}Pb is continuously being produced by parent nuclides, ^{226}Ra or ^{222}Rn , present in the wood. Thus, if values of 0.010 and 0.015 pCi/g are subtracted from each of the data points for White Oak I and White Oak II, respectively, the points fall more nearly with a

21-year half-life as shown in the lower curves of Figures 36 and 37.

Preliminary measurements of ^{226}Ra concentration in a few samples from each of the trees as given in Tables

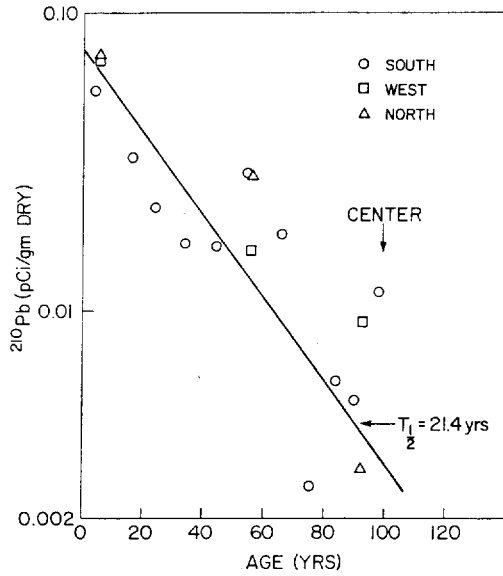


FIG. 35.—Variation of ^{210}Pb specific activity with age of wood in black oak.

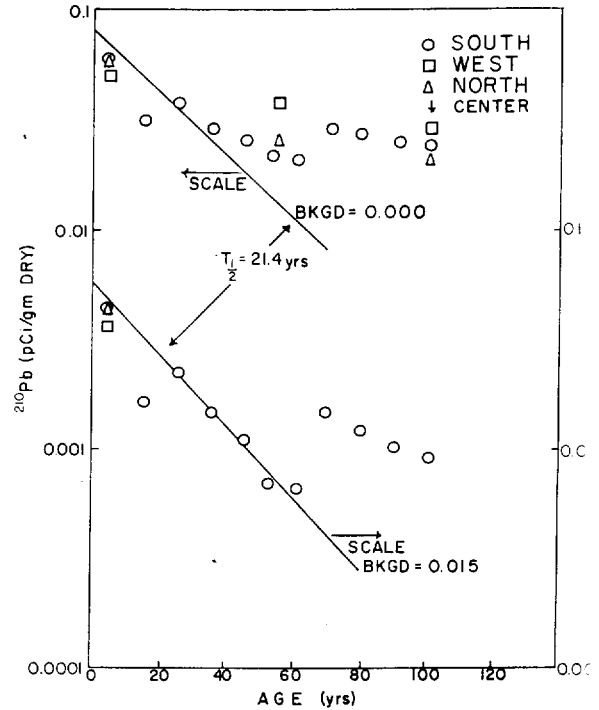


FIG. 37.—The upper curve shows variation of ^{210}Pb activity with age of wood in White Oak II. The lower is the same with a constant background of 0.015 pCi ^{210}Pb subtracted (see text).

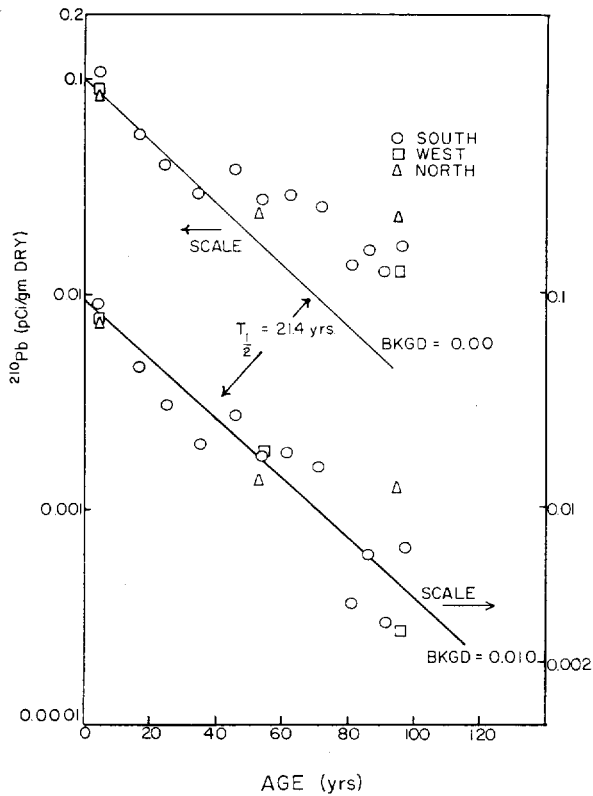


FIG. 36.—The upper curve shows variation of ^{210}Pb specific activity with age of wood in White Oak I; the lower one is these data with a constant background of 0.010 pCi ^{210}Pb /g subtracted (see text).

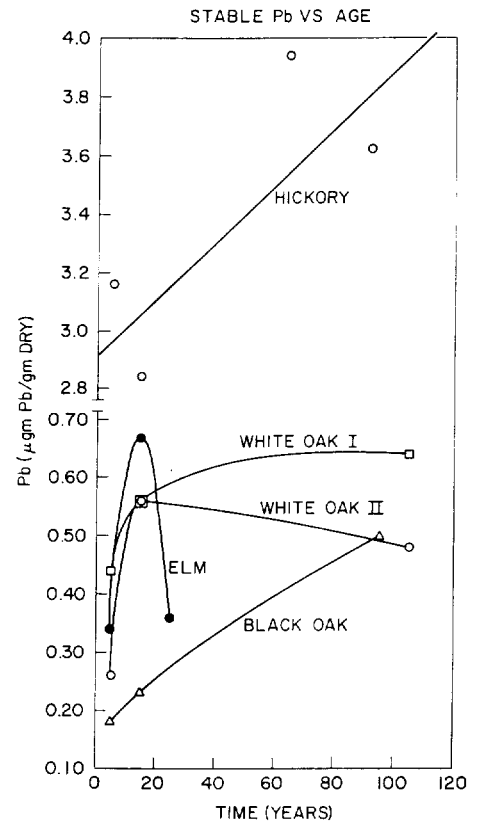


FIG. 38.—The variations in concentrations of stable lead in the various trees with age.

14 to 17 support the values of "background" concentrations chosen in these calculations. Measurements are in progress to estimate further the ^{226}Ra content and also to assess the emanation rate of the ^{222}Rn daughter from the wood, which determines the fraction of the ^{226}Ra forming ^{210}Pb in the wood.

Since these results indicate that the circulation of lead in heartwood is small after a certain time, if any significant portion of the lead was derived either from direct atmospheric uptake or from increased concentration in the soil from atmospheric fallout, the wood might show the effects of changes in exposure over the years. Some measurements of the stable Pb concentration in these trees made by Dr. Ter Haar are shown in Figure 38.⁽¹²⁾ Although environmental lead may be increasing, the few points available indicate a lower concentration of stable lead in trees in more recent times. This effect may be caused by the weighting of the data by the low values in the outer rings (near $t = 0$), which because of metabolic activity may be unrepresentative of the remainder of the wood. Also, as the tree ages and roots become deeper, the availability to the trees of stable lead may decrease relative to that of ^{210}Pb . Thus, increased lead in the atmosphere and soil over the years may not be available to the wood, and so the effects are not seen in this type of measurement.

Both the ^{226}Ra and stable lead data are consistent with those of the ^{210}Pb (^{210}Po) in that the concentrations in the hickory are much higher than in the other woods by factors of 2 to 10. The reasons for these variations are unknown, but they could be caused by basic metabolic differences, the higher ash content of the hickory, or to differing environmental levels to which our particular specimens were exposed. The latter case seems unlikely since one would not expect all three materials to increase simultaneously.

In summary, the decrease of the ^{210}Pb concentration with a 21.4-year half-life shows there is little circulation of lead in hickory heartwood more than 20 years old, while in oak there is little circulation even in wood less than 5 years old (but with less certainty). The uncertainties in these conclusions are caused by the

low concentration of ^{210}Pb and the presence of ^{226}Ra in the oaks. The ^{210}Po does not appear to circulate, either. Decreased, rather than increased, concentration of stable lead in recent times is evidenced by these data. However, more detailed measurements are necessary to check this point.

REFERENCES

1. Crozaz, G. and Langway, C. C., Jr. Dating Greenland Firn-Ice Cores with Pb-210. *Earth and Planetary Science Letters* **1**, 194-196 (1966).
2. Keisch, B., Feller, R. L., Levine, A. S., and Edwards, R. R. Dating and Authenticating Works of Art by Measurement of Natural Alpha Emitters. *Science* **155**, 1238-1241 (1967).
3. Keisch, B. Dating Works of Art through the Natural Radioactivity: Improvements and Applications. *Science* **160**, 413-414 (1968).
4. Ter Haar, G. L., Holtzman, R. B., and Lucas, H. F., Jr. Lead and Lead-210 in Rainwater. *Nature* **216**, 353-355 (1967).
5. Murozumi, H., Chow, T. J., and Patterson, C. Concentrations of Common Lead in Greenland Snows. U. S. Atomic Energy Commission Report NYO-3450-1 (1966), pp. 213-215.
6. Jaworowski, Z. Stable Lead in Fossil Bones. *Nature* **217**, 152-153 (1968).
7. Ault, W. U., Senechal, R. G., and Erlebach, W. E. Isotopic Composition as a Natural Tracer of Lead in Man's Environment. Paper presented at American Chemical Society Meeting, Minneapolis, Minnesota, April 15, 1969.
8. Stewart, C. M. Excretion and Heartwood Formation in Living Trees. *Science* **153**, 1068-1074 (1966).
9. Adams, W. H., Christenson, C. W., and Fowler, E. B. Relationship of Soil, Plant and Radionuclide. *Radioactive Fallout, Soils, Plants, Foods, Man*, Ed. Eric. B. Fowler. Elsevier Publishing Company, Amsterdam, 1965, pp. 46-49.
10. Holtzman, R. B. Measurement of the Natural Contents of RaD (Pb^{210}) and RaF (Po^{210}) in Human Bone—Estimates of Whole-Body Burdens. *Health Phys.* **9**, 385-400 (1963).
11. Assoc. of Official Agricultural Chemists. *Official Methods of Analysis of the Association of Official Agricultural Chemists*. Washington, D. C., 1965, pp. 369-370.
12. Ter Haar, G. L., The Ethyl Corporation. Personal communication.

THE CONCENTRATION OF LEAD IN HUMAN BONE

R. B. Holtzman, H. F. Lucas, Jr., and F. H. Ilcewicz

The concentration of lead in bone from humans whose ages ranged from newborn to 85 years was found to increase with age at a rate of $0.6 \mu\text{g} (\text{g ash})^{-1} \text{yr}^{-1}$ and to be $8.7 \mu\text{g} (\text{g ash})^{-1}$ at birth. These results corroborate previous reports of increases up to age 30, and they show a continuing and similar increase in the group over 35 years of age. This rate represents an increase in skeletal content of about $4 \mu\text{g}/\text{day}$, which is about 1%

of the daily intake. The biological half-life of lead implied from the data from this study ranges from 70 to 90 years and is longer than previously reported. The concentrations of lead in the group over 30 apparently consisted of two normally-distributed populations, which may reflect differences in the cigarette smoking habits of the subjects. Further studies are required to more accurately evaluate the effects of smoking

and to determine whether the accumulation of lead in adults simply reflects a long biological half-life or is caused by changing levels of intake of lead.

INTRODUCTION

Lead, because of its wide commercial application, ubiquity in the environment, and high toxicity, has probably been the subject of more toxicological studies than any other single substance. Consequently, the toxicity is well known for high levels of acute and chronic exposure to lead. Patterson⁽¹⁾ and Hardy⁽²⁾ are very concerned about a possible health hazard to persons not occupationally exposed to lead, since in urban areas, the average lead concentration in blood is as high as one-third to one-half that at which symptoms of toxicity may be clinically apparent following an acute exposure.⁽³⁾

Despite extensive toxicological, metabolic, and environmental studies,⁽²⁾ much still remains to be learned about the metabolic parameters of this element and its distribution in man and the environment. There is also disagreement about the variation of lead in man as a function of age, residence history, and occupation in other than industrial exposure to this element.⁽⁴⁾

Part of the controversy on the toxicity of lead concerns the ability of the body to compensate for increased intake levels, that is, the tendency for excretion rates of lead to approach asymptotically those of intake.^(1, 4) The change in lead content of the human body as a function of age may, therefore, be a sensitive method of assessing the degree of this compensation.

In recent work by Nusbaum et al.⁽⁵⁾ the lead concentration in calvarium and rib bone from subjects in the Los Angeles area was slightly higher for subjects over 20 years of age than below. Above 30 years of age the concentration did not appear to change. The lead concentration in lung, bone, kidney, pancreas, liver, and aorta was shown by Schroeder and Balassa's analyses of Tipton's data⁽⁶⁾ to increase up to ages of at least 30-40 years. More recently Schroeder and Tipton⁽⁷⁾ reported that the concentrations of lead and calcium in aortas increased with age, and that the lead concentration increased faster than calcium. Horiuchi et al.⁽⁸⁾ in Japan found a similar increase in rib, vertebra, and femur up to age 40, and the concentrations of lead and calcium in the various bones were correlated at the 0.05 level of significance. They estimated that the total body lead content increased from about 78 mg in adolescence to about 131 mg at age 50. The similarity between these estimates and the 111-mg total body content⁽⁹⁾ estimated from the data of Tipton et al.⁽¹⁰⁾ and more recent estimates of 131 mg by Tipton and Schroeder⁽⁷⁾ indicates a similarity between the U. S.

and Japanese populations. However, there is still a question about the total mass of soft tissue at the time of sampling of the wet bone in the Japanese study.

This increase of skeletal lead content with age applies, as stated by Schroeder and Tipton,⁽⁷⁾ the body is not in a steady state with respect to lead. Thus, the human body retains a portion of all lead ingested. Thus, the increase in lead content of about 50 mg in 30 years (Horiuchi) represents a retention of about 4 $\mu\text{g}/\text{day}$, or about 1% of the 400 μg in daily.^(9, 11) This low level of retention is well within the experimental error of most metabolic balance studies. Accumulation could be due to the long biological half-life of lead in the skeleton or to changes in diet and smoking habits on reaching adulthood. Smokers, as shown by Nusbaum et al.,⁽⁵⁾ may increase skeletal lead by as much as 30%.

Corroboration of increases in skeletal lead with age is shown in previously reported data of ²¹⁰Pb, a naturally-occurring radioactive nuclide with a 22-year half-life, which is also ubiquitous in humans and the environment.⁽¹²⁾

The purpose of this study is to determine the lead concentration in bone from a large number of people for whom age, sex and residential histories were available. Occupational histories were also available for 85 of the 105 subjects.

EXPERIMENTAL METHOD

The bone samples were obtained during normal clinical or autopsy procedures. No two samples were from the same subject, and the cause of death or basis for surgery was known. None are believed to have been occupationally exposed to lead.

Lead concentration was also determined in teeth from 29 other subjects from Chicago and neighboring regions of Illinois. These teeth were pooled in groups of 2 to 4 teeth each.

The concentration of lead was determined by the spectrophotometric method of Ilciewicz et al.⁽¹³⁾ In this method the bone is ashed 8 hr at 600° C and dissolved in 9 M HCl at a concentration of up to 10 mg/ml. After extraction with triisooctylamine to remove interfering elements, mainly iron, the lead is determined from the absorbance at a wave length of 271 m μ . Comparison of dry-ashed with identical wet-ashed specimens showed no loss of lead due to heating or to the solvent extraction procedure. Because of the variability of bone weights, as discussed elsewhere, the high likelihood of lead being associated with the mineral fraction of bone, the concentrations are given as a function of the ash weight of bone.⁽¹⁴⁾ The overall analytical errors are estimated to be less than 5%.

RESULTS AND DISCUSSION

The concentrations of lead in the various specimens in units of $\mu\text{g/g}$ bone ash, along with the age of the subject are presented in Table 18. The specimens are tabulated by bone type, i.e., rib, vertebra and cortical (femur and tibia), and by sex from subjects without known bone disease ("normal" bone). In addition, data from a previously published paper are included for uninvolved cortical bone (femur or tibia) from subjects with osteogenic sarcomas ("sarcoma" bone).⁽¹⁵⁾

The concentration is plotted as a function of age of the subject in Figure 39. The linear least squares line is shown for each group. For the "normal" cases the equation is

$$Y = (3.6 \pm 4.3) + (0.60 \pm 0.09)t$$

and for the "sarcoma" cases

$$Y = (8.6 \pm 2.7) + (0.37 \pm 0.08)t,$$

where Y is the lead concentration ($\mu\text{g/g}$ ash) and t is the age in years.

The variation of the lead content of different bones with age was evaluated and the coefficients of the linear least squares fits to the data are summarized in Table 19. The linear fit was chosen as the simplest to describe the data; no significant improvement of the variance was given by a second order function ($P > 0.05$),⁽¹⁶⁾ except in "normal" female vertebra ($P < 0.05$).

The zero intercepts, A , (concentration at birth) ranged from -2 to $13 \mu\text{g/g}$ ash with large standard deviations. At the 5% levels of significance or better, only 2 groups, sarcoma "all" and sarcoma "female," had intercepts significantly greater than zero ($P < 0.01$). However, a mean value of $8.7 \mu\text{g/g}$ ash was obtained for bone from three stillbirths and a 6-month-old child. This is consistent with the data of Horiuchi et al.⁽⁸⁾ who found the lead concentration of fetal bone to increase with age from $0.5 \mu\text{g/g}$ ($3 \mu\text{g/g}$ ash if the wet-to-ash ratio in fetal bone is 6) in a 5-month fetus to $1.5 \mu\text{g/g}$ ($9 \mu\text{g/g}$ ash) at 10 months. Schroeder and Tipton (their Table 5)⁽⁷⁾ found less than $4 \mu\text{g/g}$ ash in bone in their 0-to-1-year old subjects (apparently the detection limits of their measurements). The apparently negative intercept in the normal cortical bone is consistent with that of Horiuchi et al.⁽⁸⁾ for femur bone.

The slopes of the regression curves of the various data groups are significantly greater than zero ($P < 0.01$), except for female rib ($P \approx 0.07$). The slopes of the lines for the different groups are not significantly different from that of the total "normal" of $0.60 \mu\text{g}$ ($\text{g ash})^{-1} \text{yr}^{-1}$, except those of the female rib and "sarcoma" subjects which are significantly lower ($P <$

TABLE 18. CONCENTRATION OF LEAD IN BONE ASH AS A FUNCTION OF AGE OF SUBJECT

Rib ^(a)		Vertebra ^(a)		Cortical ^(a)		Cortical ^(b)	
Age, yr	Concentration, $\mu\text{g Pb/g ash}$	Age, yr	Concentration, $\mu\text{g Pb/g ash}$	Age, yr	Concentration, $\mu\text{g Pb/g ash}$	Age, yr	Concentration, $\mu\text{g Pb/g ash}$
Male							
0	16.9	0.5	8.5	8	3.9	9	7.0
3	< 1.0	28	24.7	13	3.3	12	3.5
8	3.6	28	35.5	14	12.6	13	7.3
27	23.2	44	19.4	19	2.8	13	7.5
30	11.0	53	61.2	20	4.0	16	7.6
32	15.4	57	47.9	42	38.9	17	30.5
36	13.2	59	41.9	48	37.2	17	13.0
37	19.5	71	41.6	49	24.0	23	17.7
37	25.5			53	34.5	27	13.7
37	39.4			56	43.5	32	16.3
38	19.7			59	79.3	44	17.3
38	7.7			61	31.5	47	31.8
41	59.4			65	96.5	58	50.0
42	57.2			66	30.8	59	38.6
44	50.8			72	43.3	63	19.0
48	25.8			85	40.5	64	33.9
59	49.6					67	28.2
68	48.1					68	33.4
74	21.7						
Female							
8	7.2	0	6.0	13	6.2	7	22.5
18	9.7	0	3.5	61	22.2	11	3.6
25	15.0	9	12.2	72	33.8	12	14.7
32	16.6	34	28.8			12	18.1
32	25.7	46	44.3			14	14.7
34	13.2	55	67.2			15	24.7
35	8.4	65	65.2			15	16.9
37	13.5	65	82.5			15	16.4
38	21.6	85	60.5			23	24.0
40	17.9	85	18.3			30	19.6
41	22.5					46	25.9
42	24.1					47	10.1
43	13.0					50	22.0
46	56.9					62	40.0
49	16.5						
65	13.4						
68	25.6						

(a) Subjects having no known bone disease.

(b) Subjects having osteogenic sarcoma.

0.01 and < 0.025 , respectively). However, these differences appear to result from an excess of high values at the younger ages. If the zero intercept, A , is fixed at zero, the slopes of the regression lines are no longer significantly different.

That the slopes are not zero is also shown by the significant correlation coefficients in Table 19 of about 0.5 to 0.7. While bone from female rib increases at only about one-half the rate of male rib, this difference is not significant ($P \approx 0.10$). The slope for "normal" male cortical bone appears to be different from that

TABLE 19. LINEAR REGRESSION PARAMETERS FOR VARIOUS DATA GROUPINGS OF LEAD CONCENTRATION IN BONE

Type (No. of samples)	Linear regression coefficients		Correlation coefficient, r	Maximum probability, $r = 0$
	Intercept	Slope		
	$A \pm \text{S.D.}, \mu\text{g Pb (g ash)}^{-1}$	$B \pm \text{S.D.}, \mu\text{g Pb yr}^{-1} (\text{g ash})^{-1}$		
All samples (105)	4.9 ± 2.9	0.552 ± 0.065	0.70	0.0005
Normal				
All (73)	3.63 ± 4.13	0.605 ± 0.089	0.62	0.0005
Cortical, M + F (19)	-1.70 ± 9.48	0.709 ± 0.183	0.71	0.0005
Trabecular, M + F (54)	5.53 ± 4.63	0.562 ± 0.103	0.64	0.0005
Vertebra, M + F (18)	11.04 ± 7.73	0.600 ± 0.151	0.67	0.005
Rib, M (19)	7.06 ± 7.98	0.536 ± 0.194	0.45	=0.025
Rib, F (17)	8.25 ± 7.67	0.276 ± 0.187	0.33	0.10
Osteogenic sarcoma (cortical)				
All (32)	8.62 ± 2.67	0.371 ± 0.078	0.69	0.0025
Male (32)	4.47 ± 3.96	0.456 ± 0.094	0.77	0.005
Female (14)	13.15 ± 3.56	0.248 ± 0.115	0.50	0.05
Other data				
Horiuchi et al. ^(a)	-0.65	0.61	—	—
Schroeder and Tipton ^(b)				
Rib, 0-49 yr	(0.00) ^(c)	1.03 ± 0.10	—	—
Rib, 0-69 yr	9.3 ± 9.8	0.59 ± 0.26	—	—

(a) Reference 8.

(b) Reference 7, Table 5.

(c) Forced zero intercept.

for the "sarcoma" bone, but it is not significant at the 5% level of confidence. The concentration of lead in bone of female sarcoma cases increases more slowly than "normal" cortical bone ($P < 0.05$) and is essentially identical to the "normal" female rib bone.

The lead concentration for subjects over age 30 shows a similar increase with age. For "normal" subjects the rate of increase is $b = (0.56 \pm 0.17) \mu\text{g Pb g}^{-1} \text{ yr}^{-1}$, and for the "sarcoma" cases, $b = (0.50 \pm 0.21) \mu\text{g Pb g}^{-1} \text{ yr}^{-1}$.

The rate of increase of concentration estimated in "normal" bone of about $0.6 \mu\text{g g}^{-1} \text{ yr}^{-1}$ bone ash, is equivalent to the $0.37 \mu\text{g g}^{-1} \text{ yr}^{-1}$ in wet bone (femur) found by Horiuchi et al.⁽⁸⁾ if one assumes that femur has about 60% ash content.⁽¹⁴⁾ Schroeder and Tipton's data in their Table 6 give estimated rates by weighted least squares analysis of $1.03 \mu\text{g g}^{-1} \text{ yr}^{-1}$ in the 0-49 year group and $0.59 \text{ g}^{-1} \text{ yr}^{-1}$ in the 0-69 group (Table 19). Their higher values may be caused by some high measurements in the 40- to 59-year group which range to $265 \mu\text{g g}^{-1}$. The yearly increases observed by Horiuchi, et al.⁽⁸⁾ and in this study amount to an accumulation in "normal" subjects of about 1.9 mg of lead per year in a "Standard Man" with 2600 g of total skeletal ash. The estimated total skeletal lead of 96 mg in a "Standard Man," aged 50, in this study, compares favorably with the 92 mg of skeletal lead from a previous report⁽⁹⁾ and a little less favorably with the 110

TABLE 20. CONCENTRATION OF LEAD IN TEETH.

No.	Mean age, ^(a) yr	No. of teeth in pool	Pb, $\mu\text{g/g ash}$
1	4	2	9.6
2	6	3	2.9
3	24	4	21.4
4	26	4	17.2
5	43	4	40.5
6	44	4	22.7
7	62	4	21.9
8	64	4	14.2
Mean (ages 4-6)			6.3
Mean (ages 24-64)			23.0 ± 9.2 (S.D.)

(a) Mean of age at time of tooth extraction.

mg of Schroeder and Tipton based on their measurements of 43 ppm of ash and 2600 g of skeletal ash.

Unlike that in bone, the lead concentration in teeth did not increase with age after the second decade shown in Table 20, the concentration appears to level off at $23 \pm 9 \mu\text{g/g ash}$, which is equivalent to that reached in bone at about age 27. The constant concentration is to be expected because of the greatly reduced mineral metabolism in the teeth of adults. The low values in the deciduous teeth are consistent

the significant but low concentrations observed in bone from fetuses and young children.

The validity of the confidence limits depends on the statistical distribution of the data. The total data and the subgroupings given in Table 19 were normally distributed as shown by a cumulative probability test. However, since the concentration increases with age, the distribution could be biased by the sample age distribution, that is, by the number of samples from younger subjects relative to those from older ones. This age effect was removed by testing the distribution of the residuals (the deviations of the data points from the least squares line). A histogram for all 105 samples is given in Figure 40. A best-fit gaussian curve for these data is shown by the solid line. The distribution of the deviation from the least-squares line appears to be skewed and a 2-gaussian-fit reduces the variance ($P < 0.10$). This skewness is attributed, at least in part, to the additional lead intake by smokers.⁽⁵⁾ The effect of smoking on lead content of bone would be most apparent in subjects over 30 years of age. The histogram for these 41 trabecular "normal" cases is given in Figure 41. The solid lines represent two normal curves. These two curves give a significant variance reduction ($P < 0.05$) over a single normal curve. The smaller curve, centered on $+11.2 \mu\text{g/g}$ ash represents 29% of the total area. This value, while lower than the 44% of the smokers in the adult population (above 17 years

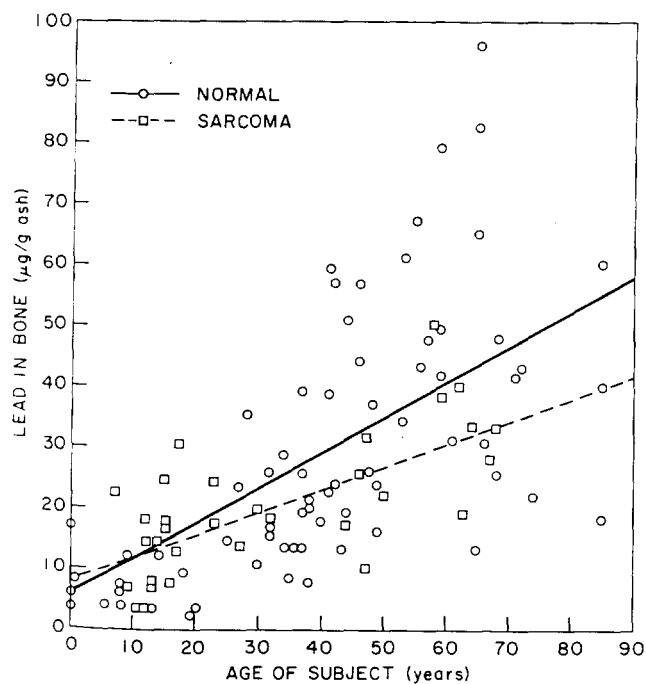


Fig. 39.—Concentration of lead in human bone ash versus age of subjects for "normal" and "sarcoma" cases. Lines are linear least squares fit to the data.

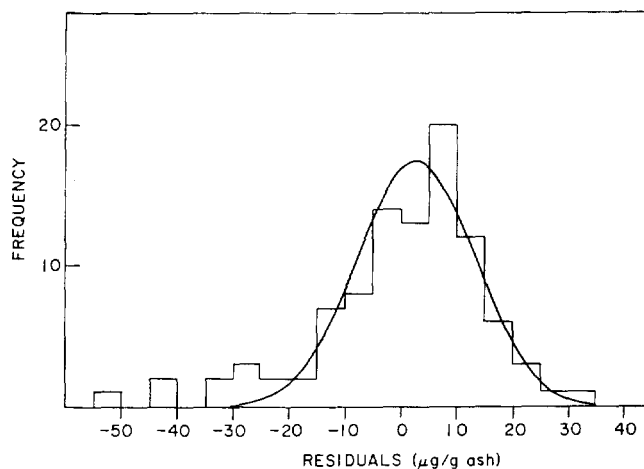


Fig. 40.—Deviation of lead concentration from least squares fit for all data. Gaussian fit of the distribution is also given.

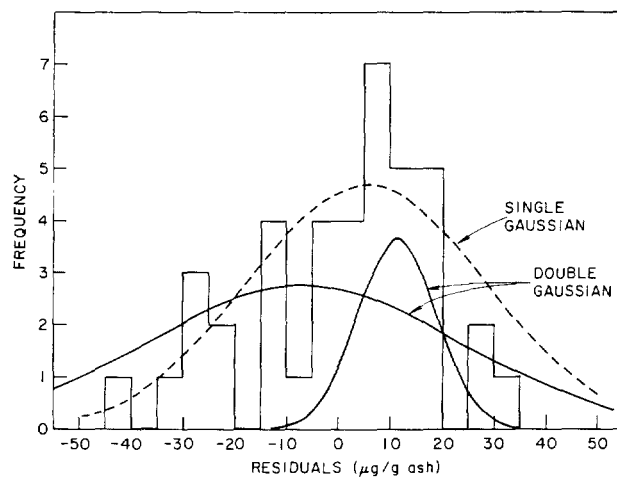


Fig. 41.—Deviations of lead concentrations from least squares fit for "normal" cases over 30 years of age. Best fit for 2 gaussians also shown.

of age), is comparable to the fraction of those smoking more than 11 cigarettes per day.⁽¹⁷⁾

If one assumes the exponential model of mineral metabolism given in the ICRP Report,⁽¹¹⁾ and that lead intake is constant over the lifetime, the body should reach equilibrium within a period of time equal to several half-lives of lead in the skeleton. Thus, from the previously estimated biological half-life of about 15 years,⁽⁹⁾ the content should level off at about 50 years. This value of the half-life is inconsistent with the data. The slopes of the linear regression curves derived for the concentration versus age data for specimens from people above 30 years of age are very similar to those of the whole group, but with larger variances. However, these slopes are still significantly greater than zero ($P < 0.01$).

The half-life of lead in the body can be estimated if

one assumes that the half-life and rates of intake and excretion are constant. A single exponential model leads to the equation

$$C = C_{\infty}(1 - e^{-\lambda t}), \quad (1)$$

where C_{∞} is the skeletal concentration of lead at long times, λ is the decay constant (0.693/half-life), and t is the time in years. An iterative procedure to estimate the parameters of the above equation (Davidon's variable metric minimization)⁽¹⁸⁾ gives a half-life of 71 ± 12 years and a content at long times of $91 \pm 13 \mu\text{g/g}$ ash for the "normal" subjects. This half-life is substantiated to some extent in data on ^{210}Pb excretion rates in radium dial painters in which the biological half-life (which would appear to apply to stable lead, also) is about 57 years.⁽¹⁹⁾

The increase in stable lead with age is also consistent with previously published data on ^{210}Pb in 128 samples from about 100 subjects from an unexposed midwestern U. S. population.⁽¹²⁾ A linear regression of the variation of specific activities in pCi $^{210}\text{Pb/g}$ bone ash with age t was

$$Y = (0.068 \pm 0.024) + (0.0015 + 0.004)t. \quad (2)$$

The rate of increase is significant ($P < 0.005$), although as with stable lead in subjects over 30 years of age, the coefficient was smaller and not significant at the 5% level, in agreement with the data of Hunt et al.⁽²⁰⁾ For the radioactive lead this decrease in slope is probably caused by the radioactive decay half-life of 21.4 years, which limits the effective (observed) half-life in the body to a maximum of about 15 years.

Although the half-life estimated here is similar to that found previously, the large variances are a strong indication of the necessity for further examination of the assumptions, particularly those of constant intake, and of the model itself. Thus, the intake of Pb may vary drastically at various times in life or with social change. A particularly large increase may occur in the late teens, because of an increased exposure to cigarette smoke and auto exhaust. Smoking alone may increase the intakes of stable lead by 30%⁽⁵⁾ and of ^{210}Pb by 100%.⁽²¹⁾

In contrast to the possible increased exposure to young adults, a decreased exposure above age 70 seems likely. The fraction of male smokers drops from 55.9% in the 17 to 44-year group to 28.4% in the over 65-year group. For women, an even greater reduction in the percent smoking is observed.⁽¹⁷⁾ This means that persons reaching the older ages would be partially selected by smoking habit from a lower lead intake group. This selectivity would result in the reduced number of high values at the older ages as shown in Figure 39, and as noted by others.⁽⁵⁻⁸⁾

CONCLUSION

The data presented here on both stable lead and ^{210}Pb are consistent with those of Horiuchi et al. and of Schroeder and Tipton⁽⁷⁾ and demonstrate an increase in the skeletal concentration of lead with age. This increase requires that 1% of the daily intake be permanently bound by bone, and indicates that the body is in equilibrium with environmental lead. The soft tissue concentrations of lead were constant with age in U.S. subjects.^(7, 8) In contrast, Schroeder and Tipton showed a positive correlation between skeletal and soft tissue concentrations in U.S. subjects. Thus, the skeletal lead may not be toxic and bone may be a detoxifying "sink" in cases of lead poisoning,⁽²⁾ and skeletal concentration is an indication of the total body exposure. Smoking appears to increase the daily intake of lead. Since the percentage of the human population exposed is lowest in the very young and the very old, smoking will affect the correlation between age and the concentration of lead in the bone. Further studies of this nature combined with extensive, well-controlled metabolic balance studies are indicated. In particular, the lead concentrations in bone from smokers and non-smokers need further investigation.

REFERENCES

1. Patterson, C. C. Contaminated and Natural Lead Environments in Man. *Arch. Environ. Health* **11**, 34 (1965).
2. Hardy, H. L. What is the Status of Knowledge of the Effect of Lead on Identifiable Groups in the Population. *Clin. Pharmacol. Therap.* **7**, 713-722 (1966).
3. The Working Group on Lead Contamination. *Survey of Lead in the Atmosphere of Three Urban Communities*. Public Health Service Publication No. 999-AP-12.
4. Kehoe, R. A. The Metabolism of Lead in Man in Health and Disease. (The Harben Lectures, 1960). *J. Roy. Soc. Public Health Hyg.* **24**, 81-121, 129-143, 177-203 (1960).
5. Nusbaum, R. E., Butt, E. M., Gilmour, T. C., and DiDio. Relation of Air Pollutants to Trace Metals in Bone. *Arch. Environ. Health* **10**, 227-232 (1965).
6. Schroeder, H. A. and Balassa, J. J. Abnormal Trace Metals in Man: Lead. *J. Chronic Diseases* **14**, 408-425 (1961).
7. Schroeder, H. A. and Tipton, I. H. The Human Burden of Lead. *Arch. Environ. Health* **17**, 965-978 (1966).
8. Horiuchi, K., Horiguchi, S., and Suekane, M. Studies on the Industrial Lead Poisoning. I. Absorption, Transportation, Deposition and Excretion of Lead. 6. Lead Contents in Organ-Tissues of the Normal Japanese. *Osaka City Med. Journal* **5**, (1), 41-70 (1959).
9. Holtzman, R. B. Critique on the Half-Lives of Lead and RaD in the Human Body. Argonne National Laboratory Radiological Physics Division Semiannual Report, July through December 1960. ANL-6297, pp. 67-80.
10. Tipton, I. H., Steiner, R. L., Foland, W. D., Cook, M. Bowman, D. K., McDaniel, K. K., Fentress, S. D.,

- Foland, J. M. U. S. Atomic Energy Commission Reports, ORNL-CF-56-3-60 (1956), ORNL-CF-57-2-3 (1957), ORNL-CF-57-2-4 (1957), ORNL-CF-57-11-33 (1957),
11. International Commission on Radiological Protection, Committee II on Permissible Dose for Internal Radiation (1959) (ICRP). *Health Phys.* **3**, 1 (1960).
 12. Holtzman, R. B. Measurement of the Natural Contents of RaD (Pb^{210}) and RaF (Po^{210}) in Human Bone—Estimates of Whole-Body Burdens. *Health Phys.* **9**, 385 (1963).
 13. Ilcewicz, F. H., Holtzman, R. B., and Lucas, H. F., Jr. Rapid Spectrophotometric Method for the Determination of Lead in Bone Ash. *Anal. Chem.* **36**, 1132-1135 (1964).
 14. Holtzman, R. B. Desirability of Expressing Concentrations of Mineral-Seeking Constituents of Bone as a Function of Ash Weight. *Health Phys.* **8**, 315-319 (1962).
 15. Lucas, H. F., Jr., Holtzman, R. B., and Dahlen, D. C. Radium-226, Radium-228, Lead-210, and Fluorine in Persons with Osteogenic Sarcoma. *Science* **144**, 1573-1575 (1964).
 16. Snedecor, G. W. and W. G. Cochran. *Statistical Methods*. The Iowa State University Press, Ames, Iowa, 1967, Sixth Ed., pp. 453ff.
 17. National Center for Health Statistics. Cigarette Smoking and Health Characteristics. United States July 1964-June 1965. U. S. Department of Health, Education, and Welfare, Public Health Service. Public Health Service Publication No. 1000-Ser. 10, No. 34 (May, 1967), p. 2.
 18. Davidon, W. C. Variable Metric Method for Minimization. Argonne National Laboratory Report ANL-5990 (Rev. 2) (1966); also ANL Computer Library Program C-183.
 19. Holtzman, R. B. and Lucas, H. F., Jr. Unpublished data.
 20. Hunt, V. R., Radford, E. P., Jr., and Segall, A. Comparison of Concentrations of Alpha-Emitting Elements in Teeth and Bones. *Int. J. Radiat. Biol.* **7**, 277-287 (1964).
 21. Holtzman, R. B. and Ilcewicz, F. H. Lead-210 and Polonium-210 in Tissues of Cigarette Smokers. *Science* **153**, 1259-1260 (1966).
 22. Harvey, S. C. Heavy Metals—Lead. *The Pharmacological Basis of Therapeutics*, Ed. L. S. Goodman and A. Gilman. The Macmillan Company, New York, 1965, Third ed., pp. 943-975.

NON-UNIFORMITY IN THE RETENTION OF THE ALKALINE EARTHS IN ANIMALS AND MAN*

Elizabeth Lloyd

In order to summarize some of the experimental information on which the model of bone turnover being developed for the ICRP must be based, measurements of the uptake and loss of Ca^{45} , Sr^{90} , and Ra^{226} in different bones and in different parts of bone of rabbits, dogs, and man are reviewed.

^{226}Ra in Different Human Bones

In man the pattern of distribution of radium in individual bones as a function of time after intake appears to be somewhat similar to that shown above for the rabbit. Figure 43 shows a linear-linear plot of the concentration of ^{226}Ra in different human bones. This graph summarizes the data available from the MIT studies on human radium.⁽¹⁾ There is a wide spread in the different values for different bones, and for the sake of clarity, the individual points have been omitted here. Figure 44 shows a typical spread of the experimental values for the vertebrae where a straight line on a log-linear plot appears to give a slightly better fit to the data than the linear-linear plot in Figure 43.

In Figure 43 the results have been further subdivided to show the difference in persons who were exposed before age 20 and those exposed after 20 years of age. The duration of exposure varied from 0.1 year to 31 years, but 18 out of 24 cases had a duration of exposure less than 5 years. In addition, it is probable that even in the cases having a long duration of exposure, the most significant exposure took place in the earlier years before more strict regulations were imposed. Figure 44 does, however, show a larger spread in the values for the cases which were exposed at age greater than 20 years. This is in agreement with the findings of Fletcher et al.⁽²⁾ from ^{90}Sr fallout studies.

RETENTION IN TRABECULAR BONE AND CORTICAL BONE VS. WHOLE SKELETON

^{90}Sr in Different Rabbit Bones

The alkaline earths are taken up in different concentrations in different bones. In general, trabecular bone appears to take up more radioisotope than cortical bone but releases it faster. Figure 42 shows the specific activity of ^{90}Sr in different bones in the adult rabbit relative to the mean value for the whole skeleton at different times after a single intravenous injection. This shows about a fivefold difference in the specific activity of the lumbar vertebrae compared with the midportion of the tibia at 10 min after injection. This difference drops to about a factor of two at 460 days when both portions of bone approach the mean values for the whole skeleton.

* This is a synopsis of a contribution made as a member of the ICRP Committee on the Local Retention Function of Bone-Seeking Isotopes.

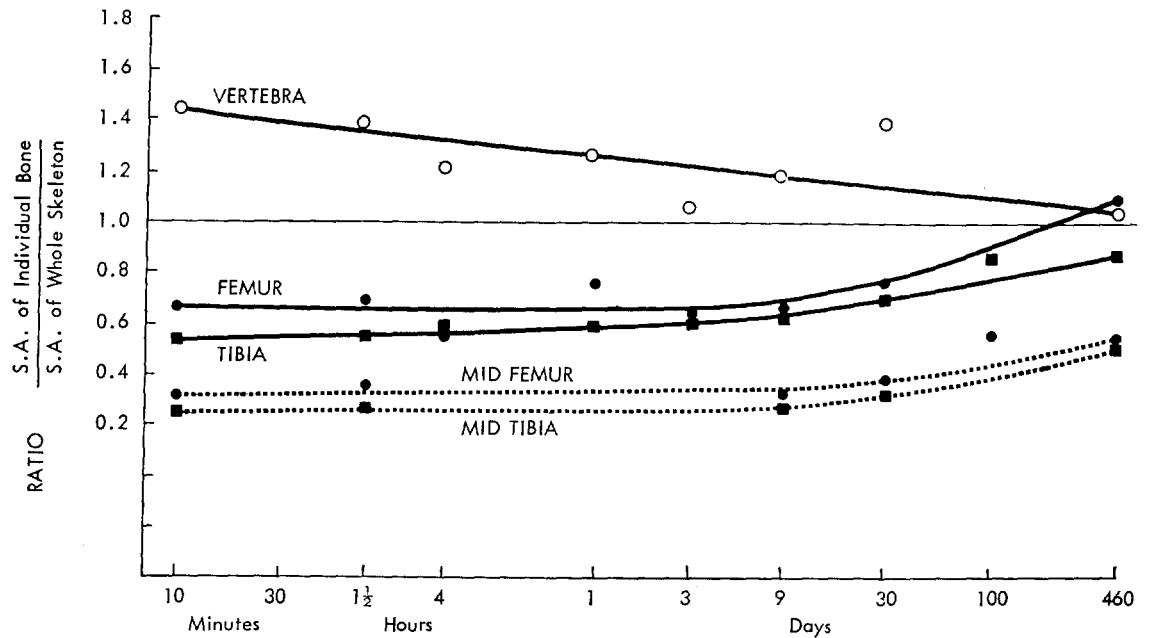


FIG. 42.—The specific activity of ^{90}Sr in different bones of the adult rabbit relative to the total skeleton after a single venous injection.

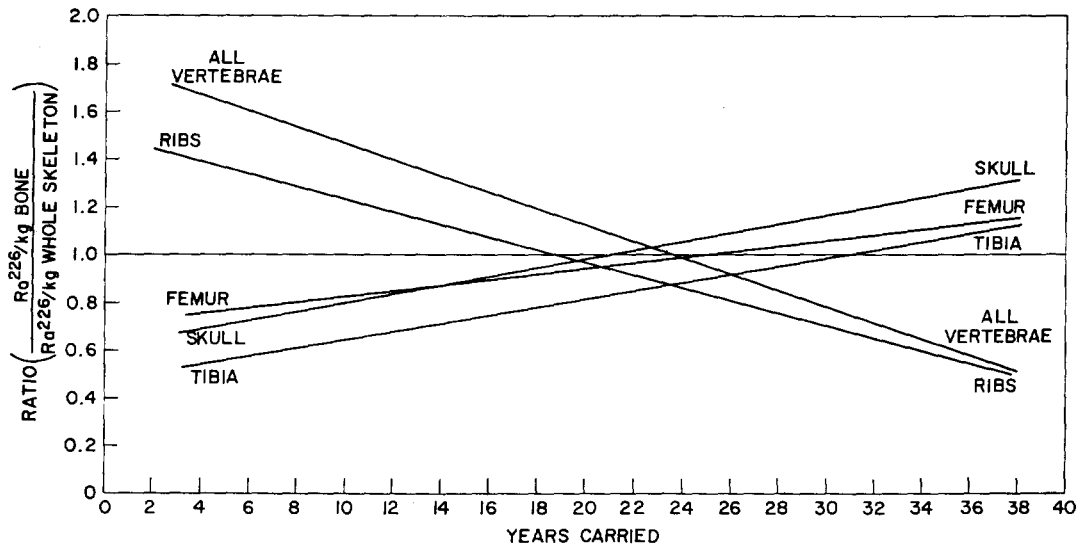


FIG. 43.—Concentration of ^{226}Ra in different human bones relative to the total skeleton

RATIO OF THE SPECIFIC ACTIVITY IN THE DIFFUSE COMPONENT TO THAT OF THE WHOLE BODY

Loss of Radioisotopes as Seen Microscopically

Two theories are currently considered to explain the loss of activity from bone, (1) resorption, i.e., the removal of bone by osteoclasts and (2) the loss of activity by exchange with the extracellular fluids. Bone formation, and by inference bone resorption rates, have been well documented by tetracycline labeling techniques. The rate of loss by exchange process is, how-

ever, much more difficult to quantitate. In Figure 47 I have tried to document what is known about loss of activity by the exchange process. There are main components of uptake of the alkaline earth seen in autoradiographs of bone, (1) a hotspot component usually associated with areas of bone growth and (2) a diffuse component which refers to label throughout the whole volume of the bone. These components have been studied separately to evaluate the loss of activity by exchange. The short-term uptake on bone surfaces is ignored in these studies.

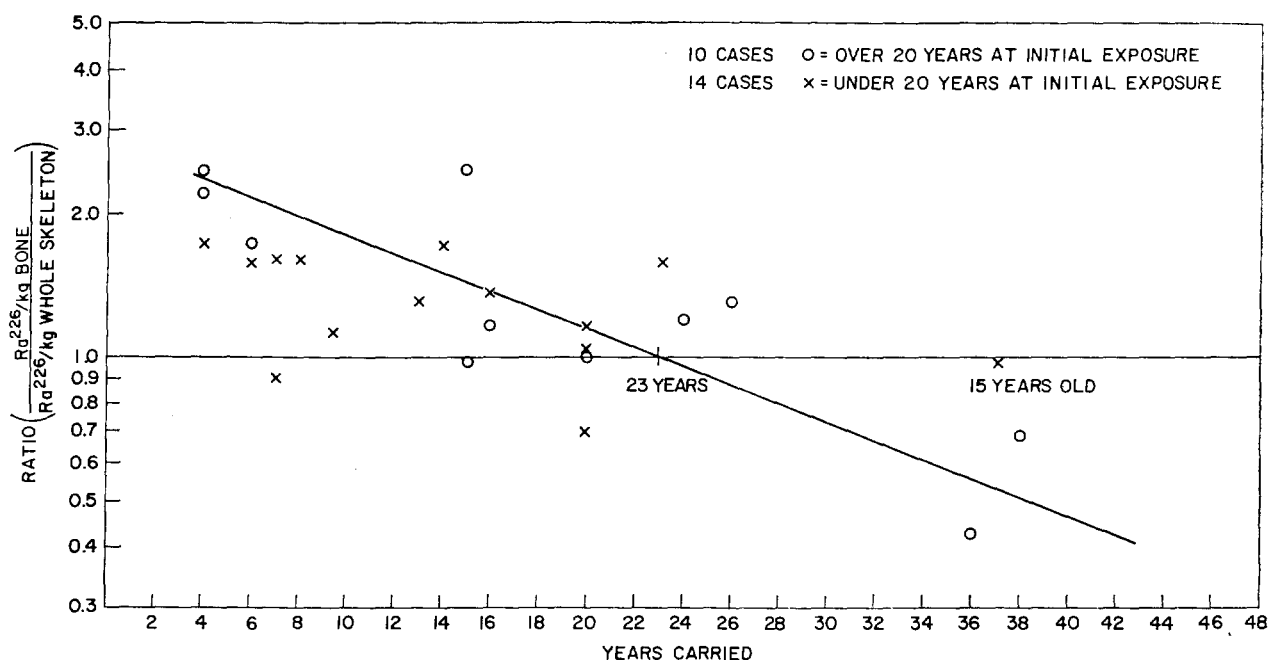


FIG. 44.—Difference in concentration of ^{226}Ra in persons exposed before and after age 20

Figure 45 shows the results obtained by Sears et al.⁽³⁾ in the vertebrae of high-level radium dogs which were sacrificed serially at different times after injection. There would appear to be no significant difference in the rate of fall of the hotspots and the diffuse activity. Likewise, two other studies in dogs with ^{226}Ra ⁽⁴⁾ and ^{45}Ca ⁽⁵⁾ failed to show any significant difference between the loss from the hotspots and from the diffuse label of the cortex of the tibia between one month and one year after injection. However, the loss in the whole-body retention between these two times was less than 40%.

Figure 46 shows a similar plot for ^{45}Ca as observed for hotspots and diffuse uptake for rabbits.⁽⁶⁾ The values shown here suggest a lower rate of loss of activity from the hotspots compared with the diffuse. Between 3 days and 100 days the loss in activity was about a factor of 4 for the hotspots and a factor of 10 for the diffuse. Figure 47 gives the best values we have been able to obtain for the human data. Here the loss in the hotspot activity over a period of 25 years is a factor of 3.6, while that for the diffuse is a factor of 10 over the same period for the mid-cortex of the tibia. The values plotted for the hotspots at short times after injection were calculated from the injected dose assuming that the hotspots in the bone were formed at the same concentration as the $^{226}\text{Ra}/\text{g Ca}$ in the blood. This was found to be true for dogs.⁽⁴⁾ Recently, the diffuse label was shown to be 0.48 and 0.35 of the uniform label

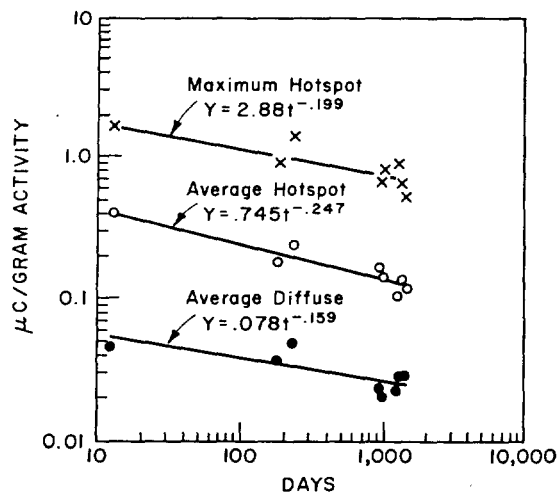


FIG. 45.—Diminution of ^{226}Ra in canine vertebrae

in two radium cases studied at 140 days and 400 days after injection of radium,⁽⁷⁾ compared to an average value of 0.43 found for about 20 cases at 25 years after injection.⁽⁸⁾ This suggests that the diffuse level in the tibial cortex divided by the uniform label for the whole skeleton does not change appreciably with time.

There would appear to be some doubt as to whether the diffuse label and the hotspot levels vary between different bones. All the animal work^(3, 6, 9) would suggest that the diffuse level found in the vertebrae is about a factor of two higher than that found in the mid-shaft of the tibia at short times after injection.

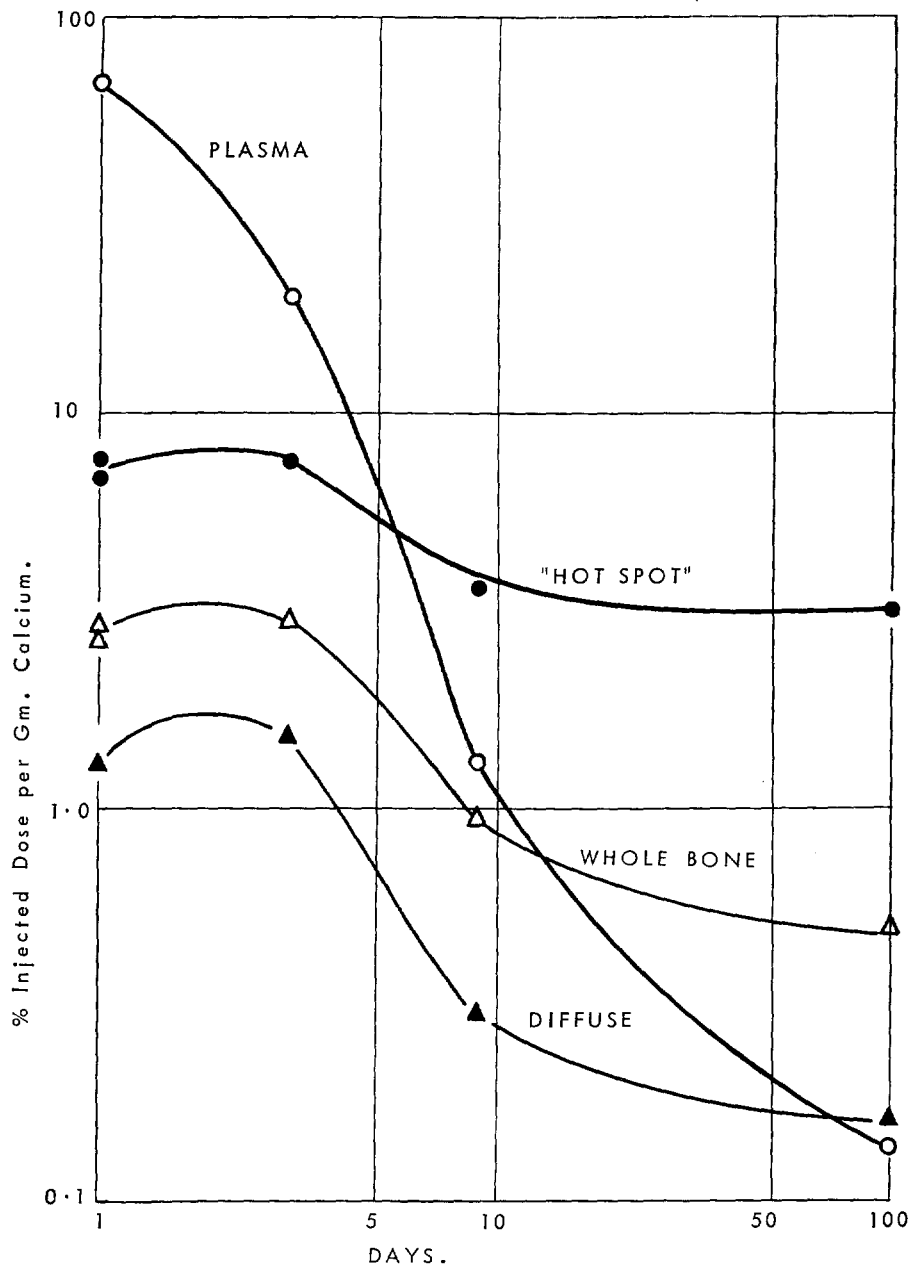


FIG. 46.—Diminution of ⁴⁵Ca in rabbit vertebrae

At long times, however, the high level Ra dogs continued to show the same difference, while the ⁴⁵Ca rabbits showed a much higher loss of diffuse label from the vertebra than from the tibia, in parallel with the loss in activity from the individual bone, not from the skeleton as a whole.

In the human radium cases, the quantitative autoradiographic data on bones other than the cortex of the long bones, is insufficient to draw any conclusions re-

garding any difference in either the diffuse or hot activity between different bones or the pattern of activity with time. A study along these lines is in progress in our laboratory. However, since the concentration in the cortex of the tibia bears a much more constant ratio to the average skeletal concentrations than any other bone studied (Figure 42), the use of the diffuse activity in this site as an index for total skeletal retention would appear to be a good choice.

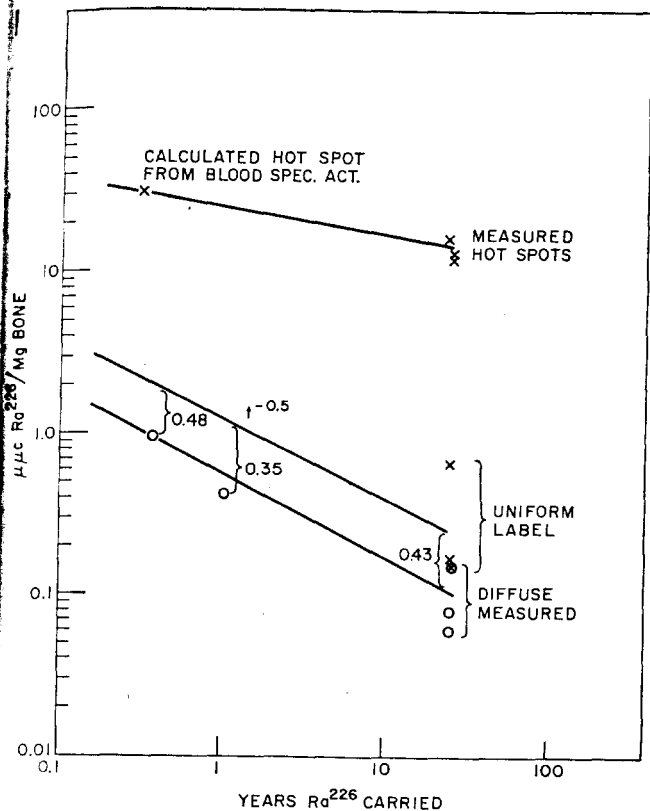


Fig. 47.—Summary of data on ^{226}Ra in human bone

REFERENCES

1. Evans, R. D. Radium and Mesothorium Poisoning and Dosimetry and Instrumentation Techniques in Applied Radioactivity. MIT Annual Progress Report MIT-952-2 (May 1965).
2. Fletcher, W., Loutit, J. F., and Papworth, D. G. Interpretation of Levels of Strontium-90 in Human Bone. *Brit. Med. Journal* **2**, 1225-1230 (November 1966).
3. Sears, K. A., Jee, W. S. S., and Mays, C. W. Radium Dosimetry, University of Utah, College of Medicine, Department of Anatomy, Radiobiology Division, Semiannual Report, COO-226 (1962).
4. Rowland, R. E. Microscopic Metabolism of Ra^{226} in Canine Bone and its Bearing on the Radiation Dosimetry of Internally Deposited Alkaline Earths. *Radiat. Res.* **15** (1), 126-137, (1961).
5. Marshall, J. H. Measurements and Models of Skeletal Metabolism. *Mineral Metabolism*, Ed. C. Comar and F. Bronner, in press.
6. Lloyd, E. Quantitative Autoradiography of Ca^{45} in Bone. *Calcified Tissues* (University of Liege) **31**, 381-390 (1965).
7. Rowland, R. E. Unpublished data (1969).
8. Rowland, R. E. and Marshall, J. H. Radium in Human Bone: The Dose in Microscopic Volumes of Bone. *Radiat. Res.* **11**, 299-313 (1959).
9. Ellsasser, J. C., Farnham, J. E., and Marshall, J. H. Comparative Kinetics and Autoradiography of Ca^{45} and Ba^{133} in Ten-Year-Old Beagle Dogs; The Diffuse Component Distribution throughout the Skeleton. To be published

VARIATIONS IN THE SURFACE AREA AND VOLUME OF BONE IN CROSS SECTIONS TAKEN FROM A SINGLE HUMAN RIB

Elizabeth Lloyd

The human rib is a convenient site for bone biopsy and is often used to obtain estimates of skeletal mineralization or radioisotope uptake. It is not generally appreciated how much the character of a rib varies along its length. An automatic film scanning system (CHLOE) is used to demonstrate the

changes in surface-to-volume ratio which one finds in a single human rib.

Our interest in the surface area and volume of cross sections of bone was aroused by the fact that some

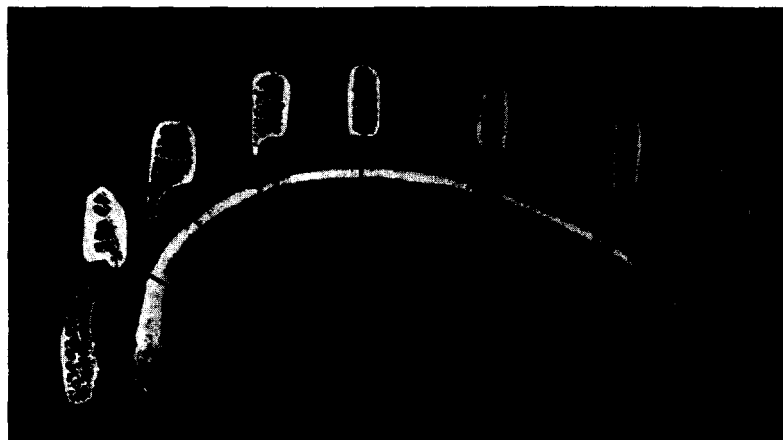


Fig. 48.—Microradiographs of cross sections of the sixth rib

hotspot
of loss
ress in
in the
atio to
other
level
would

TABLE 21. PERIMETER AND AREA OF CROSS SECTIONS OF BONE TAKEN FROM DIFFERENT POSITIONS ALONG THE LENGTH OF A HUMAN RIB

Section number	Bone area, cm ²	Bone perimeter, cm	P/A, cm/cm ²
Sternal end			
8	0.16	28	176
9	0.18	29.3	163
10	0.13	25.1	193
11	0.14	24.9	178
13	0.11	19.4	176
15	0.13		
17	0.10	16.5	165
19	0.13	15.2	117
20	0.10	14.8	148
21	0.12	15.2	127
22	0.13	14.0	108
25	0.13	17.3	135.5
26	0.14	14.9	106.2
28	0.14	15.1	107.8
30	0.16	12.8	80.6
31	0.16	13.1	
34	0.16	14.7	92.0
35	0.17	14.5	85.0
38	0.16	15.1	94.4
39	0.16	14.7	92.1
42	0.18	14.8	82.0
43	0.18	13.3	73.8
45	0.22	17.1	77.7
46	0.21	16.7	79.4
49	0.20	16.4	82
50	0.20	16.8	84
52	0.23	20.0	87
53	0.21	19.7	94
55	0.24	19.8	82.5
56	0.24	19.6	81.5
60	0.36	15.5	43
61	0.36	14.8	41
63	0.34	12.9	38
64	0.33	12.9	39
66	0.27	14.8	55
68	0.27	18.1	67
72	0.25	21.0	84

bone-seeking isotopes such as ²³⁹Pu and ²⁴¹Am deposit specifically on bone surfaces. Calculations of the relative toxicity of these isotopes compared with those which deposit throughout the whole volume of bone (such as ²²⁶Ra) must include a factor for the surface/volume ratio. As part of this study, which was designed to make representative sampling throughout the whole skeleton, a single rib of a cadaver was studied at 40 different positions along its length. In view of the fact

that the rib has been used extensively as a repetitive site for removal of biopsy material in the study of bone diseases,⁽¹⁻⁴⁾ the variations noted along its length would appear to be of considerable interest.

The sixth rib was first cut into seven segments along its length, each segment being about 4.5 cm long. Sections 100 μ thick were cut from each end of the segments. These were x-rayed using a high contrast film so that the bone appeared clear on a black ground. This type of microradiograph (as opposed to the more conventional type which shows different shades of gray corresponding to different mineral contents) greatly facilitated the definition of bone surfaces for quantitation of bone area and surface length using the automatic scanner. The scanning device⁽⁵⁾ was the same as that used previously.^(6,7) The bone area and length and the bone area were determined from the number and length of line segments generated on the film. A full description of the method is given elsewhere.

Figure 48 demonstrates the appearance of microradiographs of the cross sections of bone taken at the junction of each of the 7 segments. It is interesting to note that close to the costal cartilage junction, the cortex is very thin and this encloses a large number of very fine trabeculations. About 5 cm from the vertebral end the cortex is very much thicker and the trabeculations are fewer and coarser. Values for the cross-sectional area, together with the surface length or perimeter of each of the bone sections studied, are given in Table 21. Values of perimeter/area are also given. Values for the representative bone sections taken at 4.5 cm intervals are also shown in Figure 49. In Table 21 the numbers of the sections listed start with number 1 taken from the sternal end of the rib and range to number 72 taken from the vertebral end. The bone area changes from 0.10 cm² to 0.36 cm², while the perimeter changes from 12.9 cm to 29 cm. The bone area is greatest about 5 cm from the vertebral end where the cortex is thickest. The perimeter is small at this position giving a value of 43 cm/cm² for perimeter/area compared with a value about 5 times greater obtained for a section taken close to the sternal end.

CONCLUSION

The variation both in the thickness of the cortex and in the size and number of the trabeculations at different positions along the length of a single rib underlines the need for caution in comparing biopsy material taken from different subjects. In particular, biopsy samples taken at positions as close as 1 cm apart have been shown to vary by as much as 15%. This could easily lead to an erroneous diagnosis of osteoporosis in a normal subject if extreme care is not taken to en-

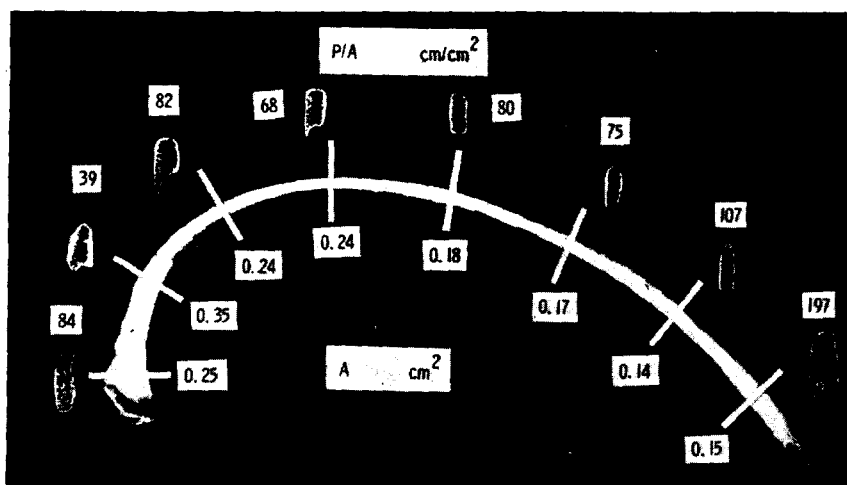


FIG. 49.—Values for area and perimeter are for the bone shown in Figure 48

that the biopsy sample is taken from the same site as the control samples.

REFERENCES

1. Barer, M. and Jowsey, J. Bone Formation and Resorption in Normal Human Rib. *Clin. Orthoped.* **52**, 241-247. (1967).
2. Frost, H. M. Measurement of Human Bone Formation by Means of Tetracycline Labeling. *Can. J. Biochem. Physiol.* **41**, 31-42 (1963).
3. Sedlin, E. D., Frost, H. M., and Villanueva, A. R. Variations in cross-section area of rib cortex with age. *J. Gerontol.* **18**, 9-13 (1963).
4. Sedlin, E. D., Villanueva, A. R., and Frost, H. M. Age Variations in the Specific Surface of Howship's Lacunae as an Index of Human Bone Resorption. *Anat. Rec.* **146**, 201-205 (1963).
5. Hodges, D. Applied Mathematics Division Tech. Memo No. 61 (1963).
6. Lloyd, E., Marshall, J. H., Butler, J. W., and Rowland, R. E. A Computer Programme for Automatic Scanning of Autoradiographs and Microradiographs of Bone Sections. *Nature* **211**, 661-662 (1966).
7. Lloyd, E., Rowland, R. E., Hodges, D., and Marshall, J. H. Surface-to-Volume Ratios of Bone Determined by Computer Analysis of Microradiographs. *Nature* **218**, 365-366 (1968).

CONCENTRATIONS OF TRACE ELEMENTS IN GREAT LAKES FISHES*

H. F. Lucas, Jr., D. N. Edgington, and P. J. Colby†

The concentration of up to 14 trace elements has been determined in whole fish and fish liver samples obtained from Lake Michigan, Lake Superior, and Lake Erie. The mean concentrations in 19 whole fish samples from three species of fish were as follows: uranium (3 ppb), thorium (6 ppb), cobalt (28 ppb), cadmium (94 ppb), arsenic (16 ppb), chromium (1 ppm) and copper (1.3 ppm). The mean concentration of 40 liver samples from 10 species of fish were as follows: uranium (~2 ppb), thorium (≤ 2 ppb), cobalt (40 ppb), copper (9 ppm), zinc (30 ppm), bromine (0.4 ppm), arsenic (30 ppb), and cadmium (0.4 ppm). In addition, the following ele-

ments were observed in most of the samples: antimony (5-100 ppb), gold (2-5 ppb), lanthanum (1-20 ppb), rhenium (0.5-5 ppb), rubidium (0.06-4 ppm), and selenium (0.1-2 ppb).

Variations in trace element concentration with species and collection site have been found. Uranium and thorium content varies with species, but not for the same species from different lakes. The trace elements, copper, cobalt, zinc, and bromine, have a nearly constant concentration in all samples studied. In contrast, the concentration of cadmium, arsenic, and chromium was interspecies and for some species interlake dependent. The neutron activation, radiochemical group separation, and computer processing of complex gamma-ray spectra technique has proved to be a powerful and rapid method for the analysis of many trace elements in fish.

* Abstract of paper presented at the Twelfth Conference on Great Lakes Research, Ann Arbor, Michigan, May 1969, and submitted for publication.

† U. S. Bureau of Commercial Fisheries, P.O. Box 640, Ann Arbor, Michigan.

NATURAL THORIUM IN HUMAN BONE

H. F. Lucas, Jr., D. N. Edgington, and Frank Markun

The ^{232}Th concentration in rib bone from 38 humans ranged from <0.1 to 72 ng/g ash. Values increased with age and were fitted by the expression

$$Y = (0.16 \pm 0.02)T,$$

where Y is the ^{232}Th concentration in ng/g bone ash and T is the age in years. Evaluation of retention of the ^{226}Ra produced by decay of ^{232}Th is not feasible because direct intake of naturally-occurring ^{226}Ra is too large.

INTRODUCTION

The measurement of thorium in normal, non-industrially exposed humans is required for the evaluation of its radiological hazard. Studies with dogs have shown that the ^{224}Ra daughter of ^{228}Th is essentially completely retained by bone.⁽¹⁾ If one assumes that ^{226}Ra produced by the decay of ^{232}Th is similarly retained, then the radiation dose to the bone would be higher than that previously assumed. In addition, the metabolism of thorium under natural environmental conditions is needed for the evaluation of its toxicity. Edgington has reviewed present knowledge and finds many questions unanswered.⁽²⁾ The purpose of this study was to determine the concentration of thorium in samples of human bone taken at surgery or autopsy.

EXPERIMENTAL METHOD

The samples were obtained through the interest and courtesy of many physicians as part of a survey of the natural radium content of human bone. All samples selected for this study were rib bone and were obtained at the time of either surgery or autopsy. The residence, age, sex, and occupation of each patient was recorded in almost all cases. On receipt at Argonne National Laboratory, these samples had been scraped to remove soft tissue, dried at 110°C , and stored at -10°C until prepared for thorium assay.

All samples were ashed for 16 hr at 600°C in quartz crucibles. Weighed aliquots were transferred to 10-mm OD \times 10-cm-long quartz tubes.* These tubes were sealed with a crushed aluminum foil plug. Thorium standards ($5.5\ \mu\text{g}$) were aliquoted into the quartz tubes, evaporated to dryness under a heat lamp, and sealed in the same manner as the bone samples. Four bone samples plus standards were combined in a single irradiation can. All samples were irradiated in the isotope tray of the Argonne CP-5

* "Spectrasil," Thermal American Fused Quartz Co., Montville, New Jersey.

reactor for 24 hr at a flux of about 2×10^{12} sec, and then allowed to cool for about 7 days.

The samples and standards were washed the quartz irradiation tubes with about 9 ml HCl. Less than 1% of the ^{233}Pa activation remained in the vial. Four sets of duplicate standards were run, and the average deviation of the mean of each set ranged from 2.7 to 4.7%, an average of 3.6%. The reproducibility of the standard was acceptable and indicates that the neutron flux was quite uniform.

The bone samples were dissolved in 10 ml HCl to which several drops of 30% hydrogen peroxide and 0.1 g aluminum nitrate were added. The reagents reduce chromium to its trivalent state and complex any fluoride ion present in the sample. The solution was heated for several minutes in a water bath to insure complete dissolution of the sample. The sample was then transferred to a column of Dowex 1-X8 anion exchange resin (100 mesh), 1/2 in diameter by 35 cm long. The ^{233}Pa activation product of ^{232}Th is quantitatively retained on the column under these conditions.

Cations and weakly bound anions are eluted with 90 ml 9 M HCl.⁽³⁾ The ^{233}Pa was then eluted with four 10-ml portions of 4 M HCl 0.3 M HF, and the fractions were collected directly in counting tubes. Approximately 90% of the ^{233}Pa was obtained in the second and third fractions. The amount of ^{233}Pa in both samples and the standards was determined by counting with a 4" \times 2" NaI (TI) crystal, an ND-120 multichannel analyzer, and an iterative least squares computational method.^(4, 5) This method has been found to be very sensitive and is not affected by small amounts of other radionuclides present in the sample.^(6, 7) The amount and concentration of ^{233}Pa were determined from the ratio of decay-corrected counting rates of ^{233}Pa in the sample to that in the standards. The standard deviation of the result is determined by the standard method from the counting statistics and the deviation between duplicate standards.

DISCUSSION

The ^{232}Th concentration in bone from 38 individuals is summarized in Table 22. The concentration ranges from ≤ 0.1 to 72 ng/g ash. However, the highest value was observed in bone from an individual who had a 40-year occupational exposure to th

TABLE 22. Th IN HUMAN BONE ASH

Age, years	Sex	Weight, g ash	²³² Th, ng/g ash	Age, years	Sex	Weight, g ash	²³² Th, ng/g ash
3	U	0.51	0.9 ± 0.2	54	M	0.72	14.8 ± 0.4
3	M	0.44	1.9 ± 0.2	55	M	0.64	20.2 ± 0.3
8	M	0.26	≤0.2	55	M	0.64	2.9 ± 0.2
11	M	0.47	0.4 ± 0.2	60	M	0.41	9.2 ± 0.8
12	F	0.85	≤0.1	62	M	0.44	14.1 ± 0.7
25	F	0.28	12.2 ± 1.9	64	M	0.69	13.1 ± 0.5
27	M	0.74	9.9 ± 0.5	65	F	0.53	4.1 ± 0.2
29	F	0.50	1.9 ± 0.4	68	F	0.59	22.3 ± 0.6
36	M	0.46	5.8 ± 0.2	70	M	0.46	3.4 ± 0.4
37	F	0.68	1.7 ± 0.2	72	F	0.48	3.4 ± 0.3
41	M	0.61	2.1 ± 0.2	73	M	0.75	13.1 ± 0.5
41	U	0.49	1.7 ± 0.3	78	M	0.68	22.4 ± 0.4
42	M	0.55	1.1 ± 0.2	78	F	0.33	42.4 ± 1.5
43	F	0.41	9.9 ± 0.5	79	F	0.24	≤0.2
44	F	0.37	5.8 ± 0.3	79	F	0.36	72.2 ± 1.2
49	M	0.69	6.5 ± 0.4	80	M	0.50	4.0 ± 0.4
51	F	0.30	7.5 ± 0.6	87	U	0.40	27.7 ± 0.9
52	F	0.51	6.7 ± 0.4	90	F	0.46	30.5 ± 0.8
53	M	0.66	5.2 ± 0.4	91	M	0.91	5.9 ± 0.2

dust. This individual operated a commercial movie projector where the carbon electrodes contain thoria and ceria to improve the actinic quality of the light source.

The ²³²Th concentration in normal human bone ash has been reported as 10 ng/g ash by Petrow and Strehlow⁽⁸⁾ for a composite sample from individuals whose ages were "largely adult." In addition, Picer and Strohal⁽⁹⁾ report 23 ng/g ash for a single sample for which the age is not given. These values agree well with the range of concentration found in this study.

The variation of the ²³²Th concentration with age is shown in Figure 50. The simplest function to describe the increasing concentration with age was assumed to be linear, and the solid line is that obtained by the least squares analysis. The equation for this line is:

$$Y = (0.16 \pm 0.02)T \quad (1)$$

where Y is the ²³²Th concentration in ng/g bone ash and T is the age in years.

The distribution of the deviation from the least squares line was skewed like that found for lead, which was attributed to an increased level of exposure by smokers compared to non-smokers.⁽¹⁰⁾ A careful inspection of Figure 50 will show that 14 results fall unusually close to the dashed line, having a slope $Y = 0.05T$. This slope is one-third that of the solid line. The cause of this grouping is not known and will require additional information such as dust inhalation exposure and smoking histories.

The possibility of determining the retention of ²²⁶Ra produced by the decay of ²³²Th in bone was evaluated. The maximum ²³²Th concentration of 72

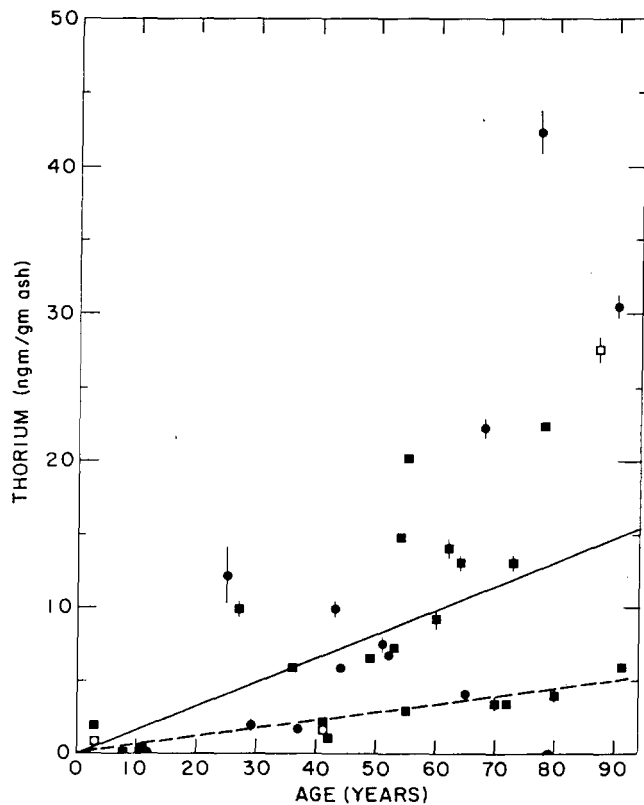


FIG. 50.—Variation of thorium concentration in human bone ash with age. ●, female; ■, male.

ng/g ash was found in a 79-year-old woman who lived in Canton, Illinois, for 57 years. This city obtained water from deep sandstone aquifers for many years.⁽¹¹⁾ Unfortunately, the wells were sealed so that samples could not be obtained. However, the

^{226}Ra content of water from similar deep wells in this area ranges from 5 to 10 pCi/liter.⁽¹²⁾ The ^{226}Ra content of the bone from this high thorium case was 0.087 ± 0.025 pCi/g ash which correlates well with that expected for exposure to this level of radium.⁽¹³⁾ The ^{228}Ra concentration in these deep well waters is similar to that of the ^{226}Ra .⁽¹⁴⁾ Thus, the ^{228}Ra concentration in the bone of this patient will exceed that of ^{232}Th and the retention of ^{228}Ra produced by ^{232}Th decay cannot be determined from this sample.

All other ^{232}Th results are less than 40 ng/g ash—or 4 fCi/g ash. By neglecting the increase of thorium with age and assuming a quantitative retention of ^{228}Ra produced by thorium decay, the maximum ^{228}Ra concentration would be equal to that of ^{232}Th or 4 fCi/g ash. This level of ^{228}Ra is equal to or less than that obtained directly from food and water so that retention of ^{228}Ra produced by the decay of ^{232}Th cannot be determined from these cases.⁽¹⁵⁾

The retention of ^{228}Ra produced in situ can probably be determined from industrial workers since some of these have been exposed to thorium dusts at a very much higher level than the normal person.⁽¹⁶⁾ If possible, lung, liver, spleen, and bone samples should be obtained.

REFERENCES

1. Stover, B. J., Atherton, D. R., Buster, D. S., and Keller, N. Metabolism of the ^{238}Th Decay Series in Adult Beagle Dogs. II. $^{234}\text{Ra}(\text{ThX})$, $^{214}\text{Pb}(\text{ThB})$, and $^{214}\text{Bi}(\text{ThC})$. Research in Radiobiology, U.S. Atomic Energy Commission Report COO-119-231 (1964), pp. 110-172.
2. Edgington, D. N. Thorium and Uranium in the Natural Environment: A Review of Present Knowledge. Argonne National Laboratory Radiological Physics Division Annual Report, July 1964 through June 1965. ANL-7060, pp. 73-76.
3. Edgington, D. N. The Estimation of Thorium and Uranium at the Submicrogram Level in Bone by Neutron Activation. *Int. J. Appl. Radiat. Isotopes* **18**, 11-18 (1967).
4. Parr, R. M., and Lucas, H. F., Jr. A Rigorous Least Squares Analysis of Complex Gamma-Ray Spectra with Partial Compensation for Instrumental Stability. *IEEE Nucl. Sci.* **NS-11**(3), 349 (1964).
5. Lucas, H. F., Jr. Computer Program for Assay of C Mixtures of Gamma-Emitting Radionuclides. National Laboratory Radiological Physics Division Annual Report, July 1964 through June 1965, ANL-746-50.
6. Edgington, D. N., and Lucas, H. F., Jr. Neutron Activation Analysis of Samples of Biological and Environmental Interest: Evaluation of the Method. Argonne National Laboratory Radiological Physics Division Annual Report, July 1966 through June 1967, ANL-7360, pp. 1-10.
7. Lucas, H. F., Jr. and Edgington, D. N. Computer Analysis of Gamma-Ray Spectra. *Proc. 1968 Int. Conf. on Trends in Activation Analysis*, October 7-11, 1968, J. R. DeVoe. NBS Special Publ. No. 312 (1968), pp. 1207-1214.
8. Petrov, H. G., and Strehlow, C. D. Spectrophotometric Determination of Thorium in Bone Ash using Actinometer. *Anal. Chem.* **39**, 265-267 (1967).
9. Picer, M. and Strohal, P. Determination of Thorium and Uranium in Biological Materials. *Anal. Chim. Acta* **131-136** (1968).
10. Holtzman, R. B., Lucas, H. F., Jr., and Ilciewicz, J. The Concentration of Lead in Human Bone. This Report is available from the National Library of Medicine, Washington, D.C.
11. Public Ground-Water Supplies in Illinois. Illinois Water Survey, Bull. No. 40.
12. Emrich, G. H. and Lucas, H. F., Jr. Geologic Occurrence of Natural ^{226}Ra in Ground Water in Illinois. *Bull. Geol. Assoc. Sci. Hydrology (Holland)* **8**, 5-19 (1963).
13. Lucas, H. F., Jr. Correlation of the Natural Radioactivity of the Human Body to that of Its Environment: I. Measurement and Retention of ^{226}Ra from Food and Water. Argonne National Laboratory Radiological Physics Division Semiannual Report, January through June 1960. ANL-6199, pp. 55-66.
14. Krause, D. P. ^{228}Ra (Mesothorium 1) in Illinois Waters. Argonne National Laboratory Radiological Physics Division Semiannual Report, January through June 1960. ANL-6049, pp. 51-52.
15. Stehney, A. F., Radioisotopes in the Skeleton: Naturally Occurring Radioisotopes in Man. *Symp. on Radioisotopes in the Biosphere*, Ed. R. S. Caldecott and L. A. S. Center for Continuation Study, University of Minnesota, Minneapolis, 1960, pp. 366-381.
16. Albert, R., Klewin, P., Fresco, J., Harley, J., Harriand Eisenbud, M. Industrial Hygiene and Medicine in a Thorium Refinery. *Arch. Ind. Health* **11**, 242 (1955).

A MODEL FOR THE REMODELING AND EXCHANGE RATE DISTRIBUTIONS IN ADULT HUMAN BONE. PRELIMINARY REPORT*

J. H. Marshall

The International Commission of Radiological Protection (ICRP) has requested information concerning the turnover

* This analysis was performed in connection with the work of the (ICRP) International Commission of Radiological Protection Task Group on the Local Retention Functions of Bone Seekers.

times of bone-seeking radioisotopes in different kinds of human bone tissue. Maximum permissible doses to bone heretofore been calculated assuming a uniform distribution. ICRP would now like to calculate doses separately for cortical and trabecular bone, for bone volumes, and for bone surface. The following model is being developed in order to organize what experimental data are available and to provide such

formation. It represents an extension of the power function model and takes explicitly into account the microscopic mechanisms of tracer deposition and removal.

INTRODUCTION

In order to calculate the radiation dose to various parts of bone tissue from internally deposited radionuclides, one needs to know their pattern of uptake and retention within the skeletal system. Appropriate data for man are scarce, so that existing estimates of the doses within bone have been based either on the assumption of a uniform distribution of the radionuclide or on an observed ratio which relates the activity in newly-formed bone to the specific activity of the diet. It is the purpose of this report to go more deeply into the subject and to see whether our accumulating knowledge of the mechanisms of skeletal metabolism and the retention of radionuclides can be put to use in the construction of a quantitative bone model.

The primary interest will be in the bone-volume-seekers, the alkaline earth radioisotopes of calcium, strontium, barium, and radium, because they are most closely related to the metabolism of bone itself. The pattern of uptake of the bone-surface-seekers, the rare earths and actinides, can probably be related to that of the alkaline earths through the surface/volume ratios of bone.⁽¹⁾

A Glossary of terms appears at the end of this report. An analysis of the pertinent measurements in bone will appear in a forthcoming publication.⁽²⁾ A short description of metabolic mechanisms and their possible relation to osteosarcoma induction are given in Reference 3.

Abstract of Model

Data bearing directly on the dose rate distribution within human bone as a function of time are scarce. Therefore, our approach is to construct a model of bone remodeling which is flexible enough to fit existing data and yet not so complicated that its parameters cannot be independently compared with experiment. The model is an extension of the modified power function model and encompasses the microscopic mechanisms and the dose distribution within bone.

For the present, the model is limited to the description of adult human bone. It considers the skeleton to be made up of essentially two kinds of bone, cortical bone and trabecular bone. To each kind of bone it assigns a turnover rate or apposition-resorption rate. This determines the amount of tracer activity in the intense hotspots. The turnover rate of cortical bone also determines the time constant of the final exponential in the overall retention function. Under the assumption that this remodeling by apposition-resorption

in one kind of bone is random as to location, it then specifies the distribution of local bone ages within that kind of bone. Using an expression for augmentation rate versus local bone age derived from numerous experiments in animals and man, it calculates the distribution of augmentation rates and the overall augmentation rate for each kind of bone. This determines the distribution of activity not connected with apposition.

The apposition rate and the augmentation rate for each kind of bone are then added to give the kinetic A-value or addition rate, which can be directly compared with measurements of total tracer uptake in human bone. The power function or multi-exponential part of the whole-body retention curve is associated with the process of diminution in both hotspots and the diffuse component. The final exponential term in the retention function, which is characteristic of age-invariant systems, is associated (as mentioned above) with the resorption rate in cortical bone. The model is somewhat overdetermined, which means that internal consistency is obtained only for certain sets of input parameters. Fortunately, these appear to include the best estimates of the actual values of the various parameters from direct measurements.

SUMMARY OF BACKGROUND INFORMATION

Data for Man

- (a) The concentration of ⁹⁰Sr in different parts of bone as a result of fallout.
- (b) Radioisotope kinetics in man using ⁴⁵Ca, ⁴⁷Ca, ⁸⁵Sr, ¹³³Ba, ²²³Ra and ²²⁶Ra.
- (c) Quantitative autoradiography of ²²⁶Ra and ⁴⁵Ca.
- (d) The concentration of ²²⁶Ra in different bones relative to that in the whole skeleton from autopsies and exhumations of radium patients.
- (e) Tetracycline labeling of human bone followed by ultraviolet microscopic analysis of biopsy or autopsy material.
- (f) Microradiographic analysis of formation and resorption surface.
- (g) Whole-body counting or radioisotope retention over long periods of time.
- (h) Histological survey of normal bone for resorption surfaces and osteoid seams.
- (i) Surface-to-volume ratios of cortical and trabecular bone in different locations.
- (j) Measurements of the amount of trabecular and cortical bone in different locations.
- (k) Measurements of the composition of trabecular and cortical bone.
- (l) Ratio of ²²⁵Ra/²²⁶Ra in normal human bone, cortical and trabecular.

(m) Measurements of the tracer content of soft tissue.

Data for Animals

- (a) Radioisotope kinetics.
- (b) Quantitative autoradiography.
- (c) Ratios of uptake in different bones and parts of bone.
- (d) Tetracycline labeling of dogs, cats, and rabbits.
- (e) Whole body retention functions for dogs and rabbits.
- (f) Surface to volume ratios for bone from dogs.

MODEL OF THE SKELETAL METABOLISM OF THE ALKALINE EARTHS

1. *Basic Postulates*

Macroscopic—(a) The retention function is either a modified power function or a sum of many exponential terms. (When available, both forms should be quoted.)

(b) The retention function for adult man is practically independent of the age at injection after age 25* (age-invariance postulate).

(c) There is no long-term discrimination between alkaline earth elements in transfers between blood and bone (postulate of no discrimination). (This postulate is needed only to derive the final exponential from the early plasma clearance. If one takes a value of λ from other information, it is not required.)

(d) The rate of excretion of activity from the body at any time is proportional to its current concentration in the blood plasma (excretion postulate).

Microscopic—(e) Calcium transfer between blood and bone can be completely described by four processes: apposition, resorption, augmentation, and diminution. Apposition and resorption are the osteoblastic and osteoclastic processes which affect local bone volume. Augmentation and diminution include all the processes of calcium transfer which take place in existing bone in the absence of apposition and resorption.

(f) Diminution includes both the calcium transferred from bone to blood by diffusion (long-term exchange) and that transferred by Bélanger's osteolysis. Augmentation includes the calcium transferred from blood to bone both by diffusion (long-term exchange) and by secondary mineralization. The rate of secondary mineralization in a given volume of bone is its augmentation rate minus its diminution rate.

(g) The total rate of long-term uptake of calcium in the skeleton, the kinetic A -value or addition rate,†

* An onset of osteoporosis of about 1%/year after age 50 is characteristic of the general population, but this can be simply superimposed on the predictions of the present model.

† A -values have long been called accretion rates in the literature, but this is a misnomer.

is equal to the sum of the apposition rate and the diminution rate. It is found experimentally that microscopic volume of bone in which apposition is occurring, the apposition rate measured by tetracycline labeling agrees with the value of A_5 measured for that volume by calcium kinetics. A_5 refers to the value of A at 5 days after injection. Augmentation rate is defined as the value of A_5 for a volume of bone in which there is no apposition. (See Reference 2 for complete development of these observations and definitions.)

(h) Augmentation rates may depend to some extent upon the metabolic state of the skeletal system as a whole—the data on this point are not yet conclusive. However, the main determinant of the augmentation rate of a given volume of bone is the age of that bone. If the bone has been formed recently (within the last few years), it will have a much higher augmentation rate than if it had been formed many years ago. It is, therefore, a distribution of augmentation rates throughout a given region of bone which depends upon the distribution of local bone ages within that region. And the distribution of local bone ages depends upon the rate of apposition-resorption.

(i) The data obtained so far for the augmentation rate as a function of local bone age in experimental animals and two men⁽⁴⁾ can be well represented by the expression

$$Aug_5 = 30t^{-0.7} \quad t > 0.2 \text{ year,} \ddagger$$

where Aug_5 is the kinetic A -value calculated 5 days after tracer injection for bone in which the apposition rate is zero (no bone formation taking place), given in percent per year, and t is the local bone age in years. For ages (t -values) between about 0.2 year and 1 year, Aug_5 represents mainly secondary mineralization. For t -values greater than 1 year, secondary mineralization is largely complete and Aug_5 represents mainly diffusion of calcium into fully calcified bone. Diffusion *in* is balanced by a corresponding diminution or diffusion *out*. This augmentation-diminution continues throughout the life of the bone. In normal adult animals and normal man it appears to represent the greater part of the calcium transfer between blood and bone.

(j) In a given region of adult human bone, such as the cortex of a long bone, the spatial distribution of apposition and resorption sites is assumed to be random. (One uses this postulate to calculate the age distribution of bone volumes, given the turnover rate λ and the age of the subject.) This assumption of randomness could

‡ A complete list of terms and definitions will be found at the end of this article.

independently verified by observing the overlapping of
 aversian systems in bone of known age and remodeling
 rate. A truly random process would produce a distribu-
 tion of bone generations shown in Figure 51. (See
 section on the generation distribution of remodeling
 bone.)

2. Derived Relationships

(a) It follows from postulates 1(b), 1(c), and 1(d)
 that the area under the curve of the specific activity of
 the body between the time of injection and infinite
 time is equal to the area under the curve of specific
 activity of the blood plasma versus time.

(b) This area is simply $q/\eta k$, where q is the activity
 injected and ηk is the rate of excretory plasma clearance
 expressed as grams of calcium per day (liters per day
 times the calcium content per liter).

(c) This requirement of area together with the early
 retention curve determines the time constant of the final
 exponential which is characteristic of age-invariant
 systems. If the system is age-invariant, then a tracer
 following a single injection must eventually reach trans-
 ient equilibrium: a state in which the tracer concentra-
 tions differ in different compartments, but all decrease
 in proportion to the same exponential function of
 time.⁽⁵⁾

3. New Associations

(1) (a) Observation and theory show that the removal
 of tracer activity from bone by diminution (diffusion)
 can be represented quite closely by the power function.
 At short and intermediate times after tracer intake,
 power function retention in bone existing at the time of
 intake can result from diffusion of tracer in cylindrical
 geometry around canaliculi.⁽⁶⁾ In bone formed shortly
 after intake and in existing bone at long times after
 intake, power function retention can result from the
 decrease of the coefficient of diffusion with local bone
 age.

(b) On the other hand, in an age-invariant system
 the removal of tracer activity by resorption of bone
 could not produce power function or multi-exponential
 retention unless there were an extremely wide distribu-
 tion of the turnover times of bone in different parts of
 the skeleton. Bone turnover times that differed by four
 or five orders of magnitude in different locations would
 be required to produce the sort of power function or
 multi-exponential function that is observed for skeletal
 retention. The ratio between the fastest and the slowest
 turnover by apposition-resorption is probably not
 greater than four or six. Therefore, the effect of resorp-
 tion should be associated only with the final one or
 possibly two exponential terms. The earlier terms (or
 the power function part of retention) should be associ-

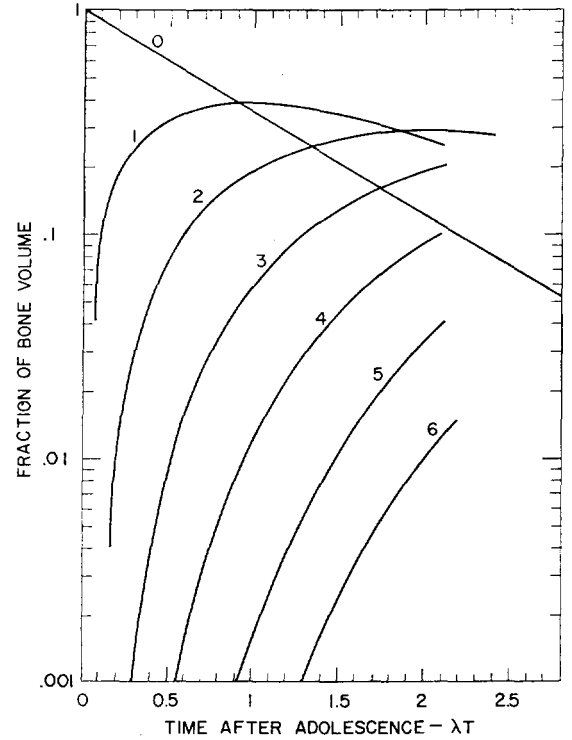


FIG. 51.—The distribution of generations within a region of bone that has been remodeling at the rate λ in locations governed entirely by chance (osteons) for a period of time T since the original formation of the skeleton (assumed to occur at the age of adolescence). Figures from Table 28. These predictions, if verified, could be used to verify the applicability of the assumption of randomness in local regions of remodeling.

ated with diminution. In view of the little data on this point, we assume that the diminution of activity from hotspots and from the diffuse component is the same so that the specific activities of individual hotspots and the diffuse component decrease in parallel with the power function part of the whole-body retention curve.

4. Bone Model

(a) Let us assume that there are two classes of bone, cortical bone and trabecular bone, each with its own rate of turnover by apposition-resorption. Let the rate of cortical turnover be λ (in units of time^{-1}). Then let the rate of trabecular turnover be $\sigma\lambda$. σ probably is of the order of 4 to 6. Let the fraction of the skeleton that is trabecular be τ , and the fraction that is cortical be $1 - \tau$ (fraction by calcium content). τ is probably about 0.2.

(b) Then it is easy to show that when an injected tracer has finally equilibrated within this skeletal system, practically no activity remains in the trabeculae. The skeletal activity is almost wholly in the slowly-turning-over cortex so that it is the turnover time of

the cortex which determines the time constant of the final exponential of the system as a whole. (See section on justification for equating the final exponential rate constant λ in the retention function with the rate of apposition-resorption in cortical bone.)

(c) Sections 2(c), 3(b) and 4(b) can now be combined to relate the final exponential of the modified power function or multi-exponential model directly with the rate of apposition-resorption in cortical bone.

(d) A corollary to 4(c) is that the retention curves of all the alkaline earth elements in adult man must have the same time constant for their final exponential. This is a reasonable possibility in view of existing data. This time constant must also agree with the best estimates of cortical turnover in man by the method of tetracycline labeling.

(e) Now the turnover rates λ and $\sigma\lambda$ determine the amount of new bone that is being formed in the cortex and in trabeculae at the time of tracer intake. Therefore, they determine the amount of activity in intense hotspots. The distribution of this activity among osteons growing at different rates is treated in the section on detailed uptake in osteons.

(f) If we assume that the rates of turnover have been constant and that the remodeling has been random as to location in each kind of bone, then λ and $\sigma\lambda$ determine the distribution of bone ages within the cortex and the trabeculae, respectively. Knowing these distributions one can calculate the augmentation rate for cortex and trabeculae (see the section on age distribution of augmentation rates). Knowing both the augmentation rates and the apposition rates, one can then add them to obtain the addition rates or A -values for cortical and trabecular bone and for the skeleton as a whole. These A -values determine the tracer uptake; they must agree with direct measurements of A -values by kinetic studies.

(g) The relative uptake of tracer in cortical and trabecular bone is also determined by the area requirement for age-invariant systems [2(a)]: the area under the trabecular curve of specific activity must equal the area under the cortical curve. The final exponential for trabeculae has already been specified to be σ times that for cortex (and body). Therefore, with a retention function of the type

$$\epsilon^b(t + \epsilon)^{-b} e^{-\sigma\lambda t} \quad (2)$$

the area requirement determines the relative uptake in trabeculae as compared to cortex once σ has been agreed upon.

(h) Sections (f) and (g) give independent values for the ratio of tracer uptake in trabeculae as compared to cortex. They must agree for the macroscopic model to be consistent with the microscopic model.

(i) Finally, having determined the tracer uptake in trabeculae, the tracer uptake in the cortex is determined by the requirement that the total tracer uptake equal that for the body as a whole with which calculation was started.

(j) The effect of soft tissue uptake is still to be treated.

5. Results

This new bone model provides a solution for outstanding problems in the literature:

(a) It shows that one can reconcile the low bone turnover (a few percent/year) measured by cyclone labeling with the high rate of long-term uptake (15%/year) measured by calcium kinetic difference between the two rates is shown by the fact that to be produced both by the diffuse component and by a wide distribution of augmentational hotspots. The uptake of activity in fully calcified regions which are—due to remodeling—much younger than the skeleton as a whole.

(b) It shows that the measurements of “bone turnover” from ^{90}Sr uptake in fallout-labeled skeletons are much lower than calcium kinetic measurements because the latter are calculated only about five years after injection, whereas the fallout measurements pertain to an average residence time of several decades after intake in a system for which the apparent residence time increases with the period of the observations.

(c) The model demonstrates that it is possible to construct a system which is age-invariant in retention measurements of the whole-body retention of injected tracer in spite of the fact that the individual microscopic bone volumes are not age-invariant because their local rates of augmentation and diminution decrease as bone ages. The rates of resorption and apposition in the adult human skeleton, however, are just sufficient to keep creating enough new bone to maintain the rates of augmentation and diminution in the skeleton as a whole at constant levels throughout most of adult life (see Figure 52). The model is, therefore, macroscopically steady state but microscopically non-steady state.

The osteoblasts and osteoclasts, through their continuous production of new bone, produce a homeostasis in the calcium metabolism of the skeletal system as a whole, in spite of the aging of the individual units of bone of which it is made.

(d) The model finally explains how it is possible to have a very low ratio of the diffuse to uniform uptake and at the same time to have more than half of the kinetic A -value produced by the process of diffuse uptake in existing, fully-mineralized bone. We recognize

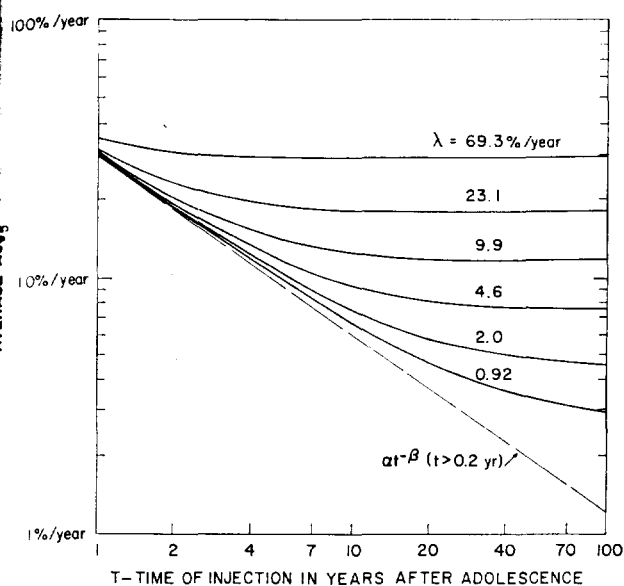


Fig. 52.—The calculated value of the average augmentation rate (λ) in a region of bone that has been subject to random remodeling at the rate λ for a period of time T since the original formation of the skeleton (assumed to occur at the age of adolescence). Figures from Table 27.

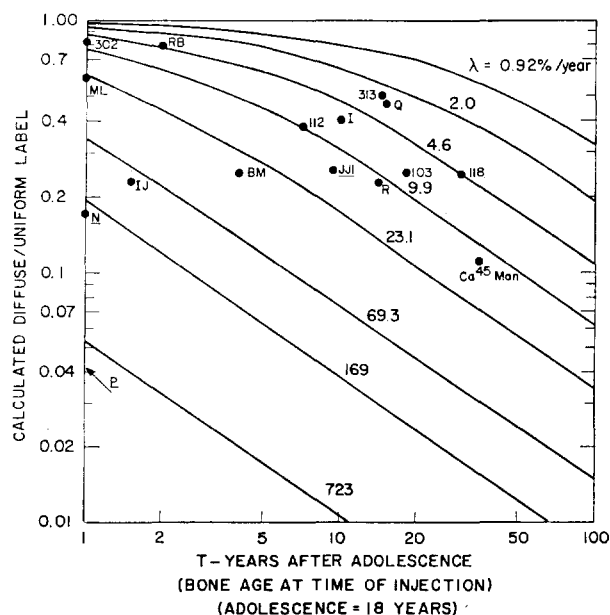


Fig. 53.—The calculated ratio of the diffuse specific activity to the uniform label (average specific activity) for a region of bone that has been remodeling randomly at the rate λ for a time T after adolescence. The diffuse specific activity referred to here is assumed to be that deposited by the augmentation rate of the original, unremodeled bone which is of age T . The total activity of the bone is the sum of this diffuse activity, the activity in hotspots in newly-forming bone, and the augmentational hotspots in bone of age less than T that has been formed by remodeling since adolescence.

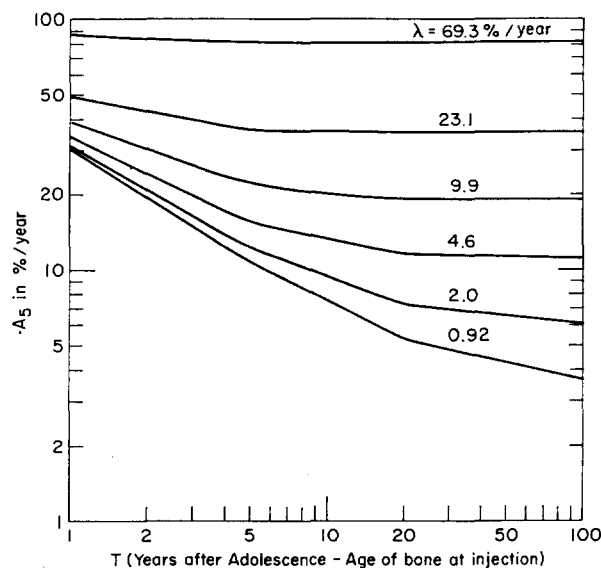


Fig. 54.—Calculated values of A_5 as a function of λ and T . The total activity represented by A_5 is the sum of the diffuse activity in original bone (aged T), the activity in newly forming hotspots ($75\% \lambda$), and the activity in augmentational hotspots. Figures from Table 27.

uptake determine uptake must which the to be evaluated for several low rate of and by tetra form calcium netics. The the mode ent and by spots, the as of bone nger than bone turn skeleton measurement five days measurements eral year parent reser e observa possible to respect to of an individual riant be imination tion and ever, are bone to minution roughout is, there copically heir con neostasis tem as a units of ssible to rm label f of the usion in ize the

diffuse component as a low level, relatively uniform, long-term uptake of activity in existing bone. In men who take in their activity at an advanced age the distribution of bone ages within their skeleton is much wider than in 15- to 25-year-old men and in 1- to 3-year-old dogs, which have provided most of our autoradiographs. The volume of bone originally laid down during skeletal growth has been reduced by resorption to a small fraction of the skeleton, but it is this bone with its low augmentation rate that we have probably associated with the diffuse component. In sites that have been remodeled since adolescence there is younger bone with higher augmentation rates. The most intense hotspots still correspond to sites of apposition at the time of tracer intake, but there should now be many hotspots of intermediate intensity which are not associated with current bone formation or secondary mineralization. These augmentational hotspots have not previously been identified, but the above calculations show that they should contain a third or a half of the total activity in a skeletal system receiving its tracer activity at an advanced age. The specific activities of some of these augmentational hotspots could be as high as ten times the specific activity of the diffuse uptake in the remnant of adolescent bone. Figures 53 and Figure 54 show that this realization solves a long standing discrepancy in our approach. It is important now to locate these augmentational hotspots experimentally by combined ^{45}Ca and tetracycline labeling in older animals and man.

DETAILED UPTAKE OF ACTIVITY IN FORMING HAVERSIAN SYSTEMS

Continuous or Multiple Injection

Several experiments have verified that the deposition of alkaline earth activity in forming haversian systems occurs at the specific activity of the blood plasma at the time of that formation.

Therefore, a knowledge of the average specific activity of the plasma during the period of tracer intake yields the specific activity of the new bone formed during the same period. An observed ratio has been used for this estimate heretofore, but the observed ratio method does not take into account the dilution of the blood plasma with unlabeled calcium transferring from bone to blood for a considerable period of time after the start of the continuous tracer intake. Furthermore, the observed ratio method is not intimately connected with the mechanisms of calcium transfer to and from the blood plasma, since it is expressed as a product of discrimination factors for urine, feces, and bone—mechanisms which in fact are in parallel, not in series.

A more powerful method for this particular calculation follows from the excretion postulate (basic postulate 1(d) above, and postulate I of Reference 5). If you know the shape of the retention curve R for a radioisotope in the body following a single injection, then the curve of the plasma specific activity versus time is given by the time derivative of this function together with the rate of excretory plasma clearance, ηk . If you know the curve of plasma specific activity following a single injection, then you can derive that for plasma specific activity following the start of continuous tracer intake simply by taking the time integral of the single injection curve. This procedure yields the simple result that the specific activity of the plasma under continuous tracer intake is

$$S_c = (\dot{q}/\eta k)(1 - R_s), \quad (3)$$

where

- \dot{q} = the rate of tracer introduction into the blood
- ηk = the rate of excretory plasma clearance in grams of calcium per day (equivalent)
- S_c = the plasma specific activity at any time t after the start of the continuous tracer intake and the specific activity of bone formed at this time
- R_s = the whole-body retention of the tracer at the same time t after a single injection.

This useful result depends only upon the excretion postulate and upon the assumption of a steady state over a relatively short period of time. It is well verified by experiment. This equilibrium value of S_c for a given \dot{q} depends only upon the rate of excretory plasma clear-

ance, ηk , values of which are available for the earth elements in man and many animals.

Single Injection

Tetracycline labeling in dogs and cats⁽⁷⁻⁹⁾ and labeling in a dog⁽¹⁰⁾ have shown that haversian in the process of their formation lay down bone at a linear apposition rate that decreases in proportion to the current size of the haversian canal. To a good approximation this may be expressed

$$dr/dt = -\beta r,$$

where r is the radius of the canal as a function of time and β is the fractional rate of closure in units of t^{-1} . Marshall found $\beta = 0.03 \pm 0.01 \text{ day}^{-1}$ in an adult dog. Lee found β values of 0.04, 0.03, and 0.026 in dogs of age 3 months, 1 year, and >1 year, respectively. Manson and Waters in experiments on dogs and cats found that the data on osteon growth were well represented by

$$r_1 = k r_2,$$

where r_1 is the radius of the first label and r_2 is that of the second label.

Expression (5) is consistent with expression (4) because the solution of (4) yields

$$r_2 = r_1 e^{-\beta t_{12}},$$

where t_{12} is the time interval between the labels. It follows that

$$k = e^{-\beta t_{12}}.$$

Manson and Waters found β values of 0.044 and 0.035 day^{-1} in cats of age 9 months and 2.5 years, respectively, and β values of 0.055 and 0.045 day^{-1} in two adult dogs.

These expressions imply that the individual osteon lays down bone more rapidly in the early stages of osteon formation when the canal is large than it does in later stages as the canal closes. In addition, there is the fact that the canal surface area, and, therefore, the number of osteoblasts decrease in direct proportion to canal radius so that the mass of bone being laid down per unit of time decreases as the square of the radius. The amount of calcium being laid down in a forming haversian system per unit length as a function of time is then

$$g = \rho \frac{d(\text{Area})}{dt} = \rho \left(2\pi r \frac{dr}{dt} \right),$$

where

- g = grams of calcium per day per cm length of bone
- r = radius of canal as a function of time
- ρ = grams calcium per cm^3 of new bone.

Substituting (4) into (8)

$$g = \rho(2\pi\beta r^2) = 2\pi\rho\beta r_0^2 e^{-2\beta t}, \quad (9)$$

where r_0 = the radius of the resorption cavity or cement line of the osteon. When the osteon canal is closed to its final radius, r_f , growth stops so that

$$r_f = r_0 e^{-\beta t_h}, \quad (10)$$

where t_h = the time necessary for the formation of a haversian system. Therefore,

$$t_h = \frac{1}{\beta} \log_e (r_0/r_f). \quad (11)$$

For values $r_0 = 100$ microns, $r_f = 10$ microns, $\beta = 0.03 \text{ day}^{-1}$, the time necessary for the formation of an osteon is $t_h = 11$ weeks, and the average apposition rate, dr/dt , is 1.2 microns/day.

The number of forming osteons per unit area of bone, N , is then

$$N = nt_h, \quad (12)$$

where n = the number of osteons which start forming per unit area per unit time. Then the fraction of the bone volume which turns over per unit time is λ (the same λ used above for the rate of cortical turnover), where

$$\lambda = n\pi(r_0^2 - r_f^2). \quad (13)$$

From these relations one can calculate the number of forming osteons per unit area of bone for a given bone turnover rate.

The distribution of tracer uptake in these forming osteons for a single injection then follows from the consideration that the uptake in a given osteon is proportional to the rate at which calcium is being laid down in that osteon [g from expression (9)]. Furthermore, if we assume that the turnover rate λ has been constant for at least the osteon formation time t_h , then the number of osteons with a growth rate between g and $g + dg$ will be proportional to the length of time dt spent in this interval of growth rate by a single osteon. Differentiating expression (9) with respect to time,

$$dg = -2\pi\rho\beta^2 r_0^2 e^{-2\beta t} = -2\beta g dt \quad (14)$$

$$dt = -\frac{dg}{2\beta g}. \quad (15)$$

Then the number of osteons per unit area with growth rates between g and $g + dg$ is

$$\frac{dN}{dg} = \left| \frac{ndt}{dg} \right| = \frac{n}{2\beta g}. \quad (16)$$

The long-term activity deposited in growing osteons is given by

$$H = gI, \quad \text{where } I = \int_0^t S dt \quad (17)$$

and where H is the activity per unit length deposited in an osteon with growth rate g and t is the time after injection (diminution of this activity produces a peak value of H at a relatively short time after injection). Furthermore, I reaches its final value for relatively short times t . Therefore, the growth rate g does not have time to change very much during the major part of the tracer uptake. The value of t used here is not critical—it should be the order of a week.

Then the distribution of hotspot intensities due to the process of osteon formation is given by

$$\frac{dN}{dH} = \frac{n}{2\beta H} = \frac{\lambda}{2\beta H\pi(r_0^2 - r_f^2)}, \quad (18)$$

where

$$H_{\max} = g_{\max}I = 2\pi\rho\beta r_0^2 I$$

$$H_{\min} = g_{\min}I = 2\pi\rho\beta r_f^2 I.$$

The normalization of this distribution is correct because one may integrate (18) over the range from H_{\min} to H_{\max} and obtain expression (12) above. This distribution of hotspot intensities following a single injection of tracer is hyperbolic in that it depends upon H^{-1} . The basis for this calculation is well established experimentally because both expression (4) and (17) have been verified by direct experiments in dogs and cats, the latter for both ^{45}Ca and ^{226}Ra . However, it would be most interesting to obtain direct verification of expression (18) by measuring the dose distribution from ^{45}Ca in a dog old enough for an equilibrium population of growing osteons to have been established.

Note that a convenient expression for the time integral of the plasma specific activity S after a single injection is given by the excretion postulate:

$$I = \int_0^t S dt = (q/\eta k)(1 - R), \quad (19)$$

where q is the amount of activity injected,

ηk is the excretory plasma clearance,

I is the time integral of S from injection until time t , and

R is the whole-body retention of the isotope at the same time t .

The curve of whole-body retention can, therefore, be used to indicate how closely I has approached its final value for infinite time. (Note the similarity between expressions (19) and (3), both derived from the excretion postulate and well verified by experiment.)

BONE SURFACE EXCHANGE

The initial deposition of the alkaline earth elements within hours after injection is similar to that of the bone-surface-seekers. Tracer leaving the blood rapidly transfers to all bone surfaces near blood vessels. This phenomenon has recently been investigated by Rowland⁽¹¹⁾ using ⁴⁵Ca in adult dogs and rabbits.

It is important to emphasize the difference between bone surface and bone crystal surface. From *in vitro* experiments with bone crystals in water one learns that the initial uptake of ⁴⁵Ca *in vitro* is by exchange with the calcium atoms at the surfaces of bone crystals. However, this is *not* an adequate description of what happens *in vivo*, although it is often so stated in the literature. *In vivo*, only the bone crystals which lie at bone surfaces take any part in the short-term exchange of calcium. These crystals at bone surfaces constitute only about 0.1% of all the bone crystals in the body. The rest (99.9%) are buried within the organic matrix with very little water so that it takes a considerable time for ⁴⁵Ca to reach them by diffusion from the blood (from days for the crystals nearest canaliculi to perhaps years for those furthest removed⁽⁶⁾). The bone surfaces involved in this early exchange are the endosteal and periosteal surfaces of cortical bone, the walls of haversian and volkmann canals, and the surfaces of trabeculae. Bone surface exchange must, therefore, be carefully evaluated (particularly for isotopes such as ²²⁴Ra which have a short half-life) because the cells lining bone surfaces appear to be a prime target for osteosarcoma induction.

Our information about this component of skeletal metabolism comes from two sources: Rowland's experiments on dogs and rabbits with ⁴⁵Ca, and alkaline earth kinetics for times shortly after injection. Rowland found by quantitative autoradiography and blood curve analysis that the amount of calcium involved in the exchange at bone surfaces was equivalent to that which lies within 2000 Å of each bone surface. The same depth was determined for dogs and rabbits. Whether all crystal calcium within 2000 Å of each bone surface is involved or only the calcium at crystal surfaces within a depth of 10,000 Å (1 micron) of each bone surface cannot be determined from the autoradiographs. However, the total amount of calcium involved is about 0.1% of the body calcium (this follows from the figure 2000 Å times the surface-to-volume ratio for the human skeleton, 42 cm²/cm³, measured by Lloyd⁽¹⁾).

The difference between the exchange in dogs and rabbits is a question of time scale: the exchangeable ⁴⁵Ca activity reached a maximum in dogs about 15 hr after injection, while that in rabbits reached a maxi-

mum about 2 hr after injection. If the modified function model, $R = \epsilon^b(t + \epsilon)^{-b}$, is fitted to Rowland's data for plasma specific activity, the value of ϵ for rabbits is 1.6 hr and that for the dogs is 12 hr. Analysis of the power function model⁽⁵⁾ showed that ϵ is equal to E_0/A_0 and hence to the turnover time of the initial pool. This relation, together with the correspondence between the value of ϵ and the time of maximum exchangeable activity in the dogs and rabbits, shows that the power function parameter ϵ is very closely associated with the time of maximum tracer uptake at bone surfaces. We would like more data on this, particularly in man, but it seems reasonable to use the best estimates of the ϵ -values for the alkaline earths in adult man (0.18 day for radium, 0.26 day for strontium, and 2.5 days for calcium) with the assumption that the maximum activity at bone surfaces due to exchange is proportional to ϵ .

The size of this initial pool by kinetics of the alkaline earths in dogs and man is about $E_0 = 0.25\%$ of the body calcium. This is somewhat larger than Rowland's measurement of the size of the bone surface pool. The difference is probably due to the fact that the initial pool of calcium is located in soft tissue. Heaney⁽¹²⁾ estimates that 60% of the short-term calcium pool in man is soft tissue, which fits Rowland's measurement and the kinetic measurement very well. The exact behavior of the heavier alkaline earths at bone surface exchange is still a matter for conjecture. Ellsasser's⁽¹³⁾ measurements of barium uptake in dogs indicate that at least up to about a week after injection barium and radium may be preferentially deposited on bone surfaces by a factor of two or more over calcium. This needs further investigation.

If we assume that Rowland's figure of 2000 Å is applicable to all the alkaline earths in man, then we can use the area rule [2(a), (b), (c)] to calculate the dose to bone surfaces due to this short-term exchange.

In a steady state system with no discrimination between blood and bone, the continuous introduction of activity into the blood at a constant rate would produce equality between the specific activity in the plasma and the calcium in the exchangeable pool at bone surfaces. Therefore, after a single injection the time integral of the plasma specific activity S and the pool specific activity V from the time of injection to time infinity are equal:

$$\int_0^{\infty} V dt = \int_0^{\infty} S dt = q/\eta k,$$

in which the third quantity, $q/\eta k$, follows from equation (19). The dose accumulated at the bone surfaces due to this exchangeable activity is then directly related to the number of microcurie-days per cm² of

surface, D , where

$$D = \Delta \rho \int_0^{\infty} V dt \quad (21)$$

$$= (2 \times 10^{-5} \text{ cm})(0.5 \text{ g}_{\text{Ca}}/\text{cm}^3)q/\eta k,$$

where $\Delta = 2000 \text{ \AA} = 2 \times 10^{-5} \text{ cm} =$ the measured equivalent depth of the pool

$$\rho = 0.5 \text{ g}_{\text{Ca}}/\text{cm}^3 = \text{the calcium content per unit volume of bone.}$$

Therefore, if we assume that the 2000 \AA figure measured for ^{45}Ca in rabbits and dogs applies equally well to human bone for the different alkaline earths, then

$$D = (10^{-5} \text{ g}_{\text{Ca}}/\text{cm}^2)q/\eta k \quad (22)$$

is the microcurie-days per cm^2 of bone surface. This may be compared to the average dose to bone as a whole calculated from the time integral of body specific activity B , because the latter is also given by $\int_0^{\infty} B dt = q/\eta k$:

$$\begin{aligned} \text{Average dose to bone in } \mu\text{Ci-days/g}_{\text{bone}} \\ = (0.25 \text{ g}_{\text{Ca}}/\text{g}_{\text{bone}})q/\eta k. \end{aligned} \quad (23)$$

In order to convert expression (22) to the average dose to soft tissue within 40μ of the bone surface (applicable to alpha particles):

$$\begin{aligned} \text{Soft tissue surface dose} \\ = \frac{1}{2} \frac{10^{-5} \text{ g}_{\text{Ca}}/\text{cm}^2(q/\eta k)}{40 \mu (10^{-4} \text{ cm}/\mu)(1 \text{ g}/\text{cm}^3)}. \end{aligned} \quad (24)$$

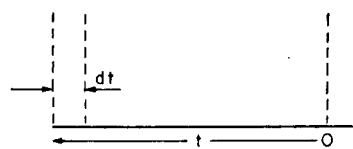
Therefore,

$$\begin{aligned} \frac{\text{Exchangeable surface dose to soft tissue}}{\text{Average bone dose to hard tissue}} \\ = \frac{0.00125}{0.25} = 0.005, \end{aligned}$$

which was obtained by dividing expression (24) by expression (23). Therefore, this initial surface dose due to the rapidly exchanging calcium on bone surfaces is very small (0.5% for typical alpha particles) compared to the lifetime doses from long-lived isotopes to the skeleton as a whole. This intense short-term uptake on bone surfaces may be of importance, however, in the case of ^{224}Ra , which has a half-life of only 3.64 days and hence can never accumulate the long-term dose to the skeleton.

THE AGE DISTRIBUTION OF AUGMENTATION RATES

1. Assume that a region of bone has a random resorption-apposition rate of λ (time $^{-1}$)



2. Then the amount of new bone formed in time dt is λdt .

3. After a time t , $e^{-\lambda t}$ of this new bone will remain unremodeled, so the fraction of the bone, df , with age between t and $t + dt$ is

$$df = \lambda e^{-\lambda t} dt. \quad (25)$$

4. Then

$$f = \int_0^{\infty} \lambda e^{-\lambda t} dt = -e^{-\lambda t} \Big|_0^{\infty} = 1$$

is the total amount of bone in the region. \therefore The normalization is correct.

5. If at adolescence all the bone is essentially new bone, and if the time since adolescence is T , then the age distribution of bone as a function of T is

$$\frac{df}{dt} = \lambda e^{-\lambda t} + [e^{-\lambda T} \text{ with age } T], \quad (26)$$

$$(0 \leq t \leq T)$$

where t is bone age from 0 to T .

6. Then

$$f = \int_0^T \lambda e^{-\lambda t} dt + e^{-\lambda T} = -e^{-\lambda t} \Big|_0^T + e^{-\lambda T} = 1. \quad (27)$$

\therefore Normalization is again correct.

7. From the data given by Marshall⁽⁴⁾ one can express augmentation rates as a function of bone age:

$$Aug_5 = \alpha t^{-\beta}, \quad (28)$$

where $\alpha = 30$

$$\beta = 0.70$$

Aug_5 is in %/year, and

t is the age of the bone in years.

8. Then the augmentation rate of the tissue as a whole is found by summing the local augmentation rates weighted by the fraction of bone in each age group:

$$Aug_5 \text{ for whole region} = \int_0^T Aug_5(t) df. \quad (29)$$

$$9. \quad Aug_5 = \alpha \lambda \int_0^T t^{-\beta} e^{-\lambda t} dt + \alpha T^{-\beta} e^{-\lambda T}. \quad (30)$$

10. From the calculations of the incomplete gamma function by Rowland and Leuer,⁽¹⁴⁾ one can pick out values for the integral in step 9. Table 23 gives the values for the integral $\int_0^T t^{-0.7} e^{-\lambda t} dt$ and Table 24 the values for $T^{-0.7} e^{-\lambda T}$.

TABLE 23. VALUES FOR THE INTEGRAL $\int_0^T t^{-0.7} e^{-\lambda t} dt$

λ, yr^{-1}	0.693	0.231	0.099	0.046	0.020	0.0092
$T_{1/2}, \text{yr}$	1	3	7	15	35	75
T, yr						
0.2	1.919	2.010	2.037	2.047	2.053	2.055
1	2.889	3.163	3.259	3.298	3.318	3.326
2	3.176	3.716	3.918	4.019	4.067	4.086
5	3.327	4.330	4.862	5.127	5.282	5.346
10	3.339	4.574	5.475	6.023	6.349	6.513
20	3.339	4.639	5.852	6.815	7.514	7.839
50	3.339	4.643	5.983	7.412	8.873	9.761
100	3.339	4.643	5.987	7.518	9.484	11.04

TABLE 24. VALUES FOR $T^{-0.7} e^{-\lambda T}$

λ, yr^{-1}	0.693	0.231	0.099	0.046	0.020	0.0092
$T_{1/2}, \text{yr}$	1	3	7	15	35	75
T, yr						
1	0.500	0.794	0.906	0.955	0.980	0.991
2	0.154	0.388	0.505	0.561	0.591	0.604
5	0.010	0.102	0.198	0.258	0.293	0.310
10	0.0002	0.0198	0.074	0.126	0.163	0.182
20	—	0.0012	0.0170	0.0490	0.0823	0.1022
50	—	—	0.00046	0.0065	0.0238	0.0408
100	—	—	—	0.00040	0.0054	0.0159

TABLE 25. λ TIMES TABLE 23 + TABLE 24

λ, yr^{-1}	0.693	0.231	0.099	0.046	0.020	0.0092
$T_{1/2}, \text{yr}$	1	3	7	15	35	75
T, yr						
1	2.50	1.52	1.23	1.11	1.05	1.02
2	2.35	1.25	0.893	0.746	0.672	0.642
5	2.32	1.10	0.679	0.494	0.399	0.359
10	2.31	1.08	0.616	0.403	0.290	0.242
20	2.31	1.07	0.596	0.362	0.233	0.174
50	2.31	1.07	0.593	0.347	0.201	0.131
100	2.31	1.07	0.593	0.346	0.195	0.117

11. Therefore, Aug_s for the region as a whole is given by α times Table 25.

12. *Conclusions* (a) For reasonable remodeling rates the average augmentation rate is almost independent of the time since adolescence over the major portion of the human life-span. For example, for a resorption-apposition rate of $\lambda = 4.6\%/year$ the augmentation rate would be within the limits $11.8 \pm 1.3\%/year$ from $T = 8$ years to $T = \infty$, or from say age 25 onwards.

(b) If we let $T = 40$ years, the local augmentation

rate of 40-year-old bone would only be 2.2%. However, only 16% of the region of bone would have this low a rate. Very likely, it would be considered as the diffuse component. The rest of the bone volume would contain a distribution of bone ages and the augmentation rates of the younger members of this distribution would far outweigh those of the older members.

(c) We, therefore, have a successful quantitative description of the continual creation of enough bone to provide an overall augmentation rate practically independent of age. This is true for the stasis of the adult skeleton due to remodeling.

(d) Therefore, it is consistent to consider the adult skeleton as age-invariant with respect to the injected tracer, even though individual bone elements are aging and their local augmentation rates are decreasing with their increasing age.

(e) If we assume that the dependence of the augmentation rate upon bone age which we used for dogs, step 7, can be used for bone in man of the same age, then it follows that an apposition-resorption rate of 4.6%/year implies an augmentation rate of 11%/year. The sum of these two rates is about 15.6%/year, which is the observed A_s value for normal man.

(f) Therefore, about 70% (11/15) of the long tracer activity would be associated with augmentation and only 30% (4.6/15) with apposition. This augmentation activity would not, however, be obviously associated with a uniform diffuse component but instead be located in bone only a few years old and with intensities perhaps as much as 10 times the diffuse activity apparent in 40-year-old bone.

(g) The age distribution (step 5) insures that $\lambda T \ll 1$, as it is for young adult dogs, then there would be a large area of bone with a relatively uniform diffuse component. However, for older dogs and man the distribution of local augmentation rates is much more varied. One expects blotchy autoradiographs as we found in ^{45}Ca in man, with what uniform diffuse activity they represent only a small fraction of the overall augmentation rate.

Improvement on Step 7

Because bone less than 0.2 year old (about the time to form a human haversian system) is in the immediate neighborhood of bone formation, it would be more accurate to use the formula for augmentation rate with a lower limit of 0.2 year. Bone younger than 0.2 year would then not contribute to augmentation but would be included in apposition. (See Table 2)

Then Figure 52 is α times Table 26.

The exclusion of bone less than 10 weeks of age

TABLE 26. λ TIMES (TABLE 23 LESS THE VALUE IN TABLE 23 FOR 0.2 YEAR) + TABLE 24

T, yr	λ, yr^{-1}					
	0.693	0.231	0.099	0.046	0.020	0.0092
1	1.17	1.06	1.03	1.01	1.01	1.00
2	1.03	0.78	0.691	0.652	0.631	0.623
5	0.99	0.638	0.478	0.400	0.358	0.340
10	0.98	0.612	0.414	0.309	0.249	0.223
20	0.98	0.608	0.395	0.268	0.192	0.155
50	0.98	0.608	0.391	0.253	0.160	0.112
100	0.98	0.608	0.391	0.252	0.154	0.099

the augmentation rates, but the reduction is only about 30% in the region of interest.

A-Value and Augmentation Rate

(a) Figure 52 gives augmentation rates (A_{ug_5}) vs. λ and T excluding bone younger than 10 weeks (0.2 year).

(b) Therefore, it does not include apposition but does include secondary mineralization.

(c) Since new bone is only 75% mineralized, the apposition rate in mass per unit mass per unit time is 75% λ .

(d) $A_5 = A_{ug_5} + 75\% \lambda$.

The diffuse component will be understood as the tracer uptake in the original bone laid down at adolescence. It is therefore bone of age T years and its local augmentation rate is $A_{ug_5} = \alpha T^{-\beta}$.

The ratio $\frac{\text{Diffuse}}{\text{Uniform label}} = \frac{\text{Local } A_{ug_5} \text{ (adolescent bone)}}{A_5}$

The curves in Figure 53 show diffuse/uniform label versus T and λ , taken from Table 27. Figure 54 shows A_5 versus λ and T taken from Table 27.

Conclusion

(a) The ratio diffuse/uniform label for a given remodeling rate should decrease as the age of the person at the time of tracer intake increases. This trend is confirmed by the radium cases of Rowland and Marshall¹⁶¹ with one exception (case IJ). (See Figure 53.)

(b) For a given age at injection, the higher the remodeling rate the lower the diffuse/uniform ratio. Dogs N (age 1 year) and P (age 3 months) fit the prediction very well.

(c) For animals injected at the older ages, quite low diffuse/uniform ratios are found, but the fraction of the A -value due to augmentation stays over 50%. (Figure 55).

The ⁴⁵Ca dog JJ1 (age 10 years) should have a diffuse-uniform ratio = 0.25. The value 0.167 was

observed. About 56% of A_5 was augmentation (theoretically).

The 51-year-old man with ⁴⁵Ca examined in 1958 has a blood curve consistent with $A_{5/c} = 18.6\%/year$. Therefore he is plotted in Figure 53 at $T = 33$ years and a diffuse/uniform label of $(2\%/year)/(18.6\%/year)$ or 0.107. This corresponds to $\lambda = 12\%/year$ and

TABLE 27. VALUES OF PARAMETERS CALCULATED FROM THE MICROSCOPIC MODEL

	T, yr	$\lambda, \%/yr$					
		69.3	23.1	9.9	4.6	2.0	0.92
$A_{ug_5}, \%/yr$	1	25.0	32.0	31.5	30.5	30.0	30.0
	5	29.5	19.0	14.4	12.0	10.8	10.3
	20	29.5	18.2	11.8	8.1	5.8	4.6
	100	29.5	18.0	11.7	7.6	4.6	3.0
$A_5, \%/yr$	1	87.0	49.3	38.9	34.0	31.5	30.7
	5	81.5	36.3	21.8	15.5	12.3	11.0
	20	81.5	35.5	19.2	11.5	7.3	5.3
	100	81.5	35.3	19.1	11.1	6.1	3.7
$A_{ug_5}/A_5, \%$	1	40	65	81	90	95	98
	5	36	52	66	77	88	94
	20	36	51	61	70	79	87
	100	36	51	61	68	75	81
% original bone left	1	50	79	91	96	98	99
	5	3.1	31	61	79	90	96
	20	—	1.0	14	40	67	83
	100	—	—	—	1	14	40
Diffuse/uniform label	1	0.34	0.61	0.77	0.88	0.95	0.98
	5	0.119	0.27	0.45	0.63	0.79	0.88
	20	0.045	0.104	0.192	0.32	0.50	0.70
	100	0.015	0.034	0.062	0.108	0.196	0.323

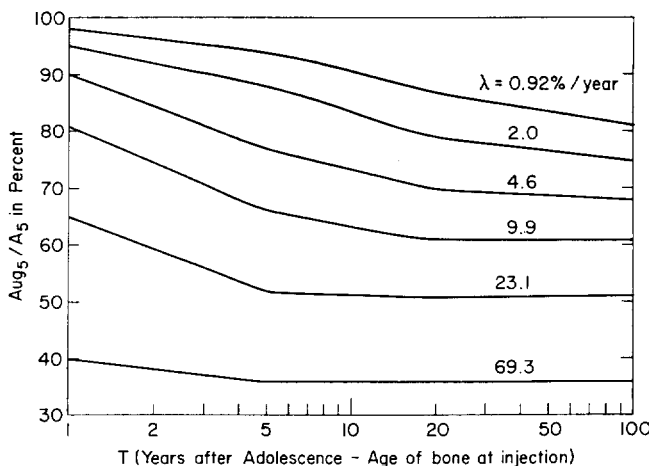


FIG. 55.—The calculated percentage of the total kinetic A-value (A_5) that is due to augmentation (A_{ug_5}) rather than to the deposition of activity in newly-forming bone. Figures from Table 27.

$A_{ug_5} = 13\%/year$ or $A_5 = 22\%/year$. Despite his low ratio of diffuse/uniform label of 0.11, about 55% of the A -value is augmentation according to Table 27.

(d) The assumption of random remodeling together with an augmentation rate which depends solely on the age of each bone volume element ($30t^{-0.7}\%/year$, where t is bone age in years) leads to a bone model which answers a number of outstanding questions.

(1) For remodeling rates of about 4%/year or greater, there can be age-invariance of tracer retention over most of the adult life-span in spite of the local decrease of augmentation rate with bone age.

(2) The ratio diffuse/uniform label is seen to depend both on remodeling rate and on age at tracer intake.

(3) For older dogs and men it is clear that the ratio diffuse/uniform label can be as low as 0.1 in spite of the fact that over half the value of A_5 is due to augmentation. The calculation that a significant fraction of A_5 can be in augmentational hotspots removes what had appeared to be a serious discrepancy between data and model.

Therefore, it would be most interesting to obtain experimental verification of the high fraction of A_5 that should be due to augmentational hotspots in older animals. This experiment should involve both ^{45}Ca and double tetracycline labeling of an older dog or man.

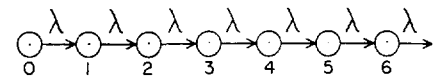
THE GENERATION DISTRIBUTION OF REMODELING BONE

The assumption of random remodeling can be tested by examining microradiographs for the presence of overlapping haversian systems. If the remodeling rate is a constant, λ (years^{-1}) and if remodeling occurs at locations governed entirely by chance, then at a time T after adolescence there should be volume fractions of bone versus generation as shown in Figure 51 and Table 28. Generation 0 is the original bone formed during growth, generation 1 is once remodeled bone, etc.

TABLE 28. FRACTION OF THE BONE VOLUME OCCUPIED BY EACH GENERATION OF BONE

Bone generation	λT				
	0	0.2	0.6	1	2
0	100%	82%	55%	37%	13%
1	0%	17%	34%	37%	28%
2	0%	1%	10%	19%	28%
3	0%	0%	1.5%	6%	19%
4	0%	0%	0.1%	1%	9%
5	0%	0%	0%	0.1%	3%
6	0%	0%	0%	0%	1%

This table summarizes Figure 51 which was derived iteratively on a calculator from the series



which is identical to radioactive series decay. The constant λ is the same for each bone fraction, so the Bateman equations break down.

For the case in radioactive series decay in which successive λ 's are equal, Evans⁽¹⁷⁾ shows that the first daughter would peak at $\lambda T = 1$. From this it appears likely that the second daughter would peak at $\lambda T = 2$, etc. Furthermore, although the calculation of Figure 51 is slightly in error, the amount of generation 0 bone should equal that of generation 1 at $\lambda T = 1$ when 1 peaks, and generation 2 should equal generation 1 at $\lambda T = 2$ when the amount of generation 2 peaks, etc. Table 28 has been adjusted to show these relations.

Note that if $\lambda = 4.6\%/year$, $\lambda T = 2$ would be at $T = 43$ years or about age 60, and 1% of the volume would be sixth generation bone.

Perhaps a more likely situation would be $\lambda = 1\%/year$ observed at $\lambda T = 1$ or 50 years after adolescence or age about 68 years. In this case, perhaps generations 0-3 would be detectable, with generation 0 occupying 6% of the volume. (One generation would be fourth generation bone.)

Careful microradiographic observation of the distribution of overlapping haversian systems might show whether this model of random remodeling is valid. If the distribution of generations is not as wide as Table 28 predicts—that is, if the required proportions of higher generations of bone are not found in practice—then resorption is not random but favors older bone. If true, this would be an important finding for bone dosimetry and for an understanding of the biological signal which calls for resorption at a particular location in adult bone not subjected to a changing pattern of

TURNOVER AND SURFACE-TO-VOLUME RATIO

Can the Ratio of Trabecular Turnover to Cortical Turnover be Related to the Respective Surface-to-Volume Ratios?

This would be an attractive hypothesis for bone because it would imply that an osteoblast or osteoclast does not know whether it is on a surface of cortical bone or of trabecular bone. The fraction of bone on the apposition surface and resorption surface would be the same everywhere (provided there was no characteristic stress which called for adaptive remodeling).

Jowsey's observations of surface activity in di-

TABLE 29. SUMMARY OF JOWSEY'S DATA ON BONE SURFACE IN ADULT HUMAN BONE

	Percent of total bone surface	
	Formation	Resorption
Rib	2.6	4.6
Anterior iliac crest	3.3	7.0
Femur midshaft	2.8	3.9
Avg.	2.9 ± 0.4 (S.D.)	5.2 ± 1.6 (S.D.)

TABLE 30. TURNOVER RATES OF DIFFERENT BONES USING TABLE 29 FOR FORMATION SURFACE

	Surface/volume, cm/cm ²	Formation surface, %	Turnover rate, %/year	Turnover ratios
<i>Cortical bone</i>				
Mid-femur	30	2.8	2.5	1
<i>Trabecular bone</i>				
Femur head	75	2.9 ^(a)	6.4	2.6
Thoracic vertebra	90	2.9 ^(a)	7.6	3.0
Lumbar vertebra	90	2.9 ^(a)	7.6	3.0
Rib	90	2.6	6.8	2.7

(a) Average value from Table 29.

locations are pertinent here.⁽¹⁸⁾ The data in Table 29 are the average values for normal human bone for ages 35, 45, 55, and 65 taken from Jowsey's graphs in the above reference. (There appears to be very little change with age in this age range.)

Although the values are somewhat larger in the very trabecular iliac crest, very little error will result from the assumption of equal fractional areas, particularly for formation.

The volume turnover rates are, therefore, almost proportional to the respective surface-to-volume ratios.

Lloyd⁽¹⁾ has found the surface-to-volume ratios in human bone listed in Table 30.

The right hand column shows the respective turnover rates based on the formation surface from Table 29 and a linear apposition rate of $0.8 \mu/\text{day}$. Lee⁽⁹⁾ has

found that linear apposition rates are the same in trabeculae as in the cortex of dogs of different age. For

adult dogs they average $1 \mu/\text{day}$. Villanueva et al.⁽¹⁹⁾ report a linear apposition rate of $0.8 \pm 0.3 \mu/\text{day}$ (S.D.)

for a series of adult human ribs.

Typical Calculation

If we use the values for femur midshaft from Jowsey and Lloyd and the apposition rate of $0.8 \mu/\text{day}$ from Frost:

$$2.8\% (30 \text{ cm/cm}^2) (0.8 \mu/\text{day})(365 \text{ days/year})(10^{-4} \text{ cm}/\mu) = 2.5\%/\text{year} \text{ (turnover rate of the femur midshaft).} \quad (31)$$

Conclusion

The ratios between these turnover rates in different bones are quite close to those observed in the ⁹⁰Sr measurements in man. Apparently the ratio of the surface-to-volume ratios gives a reasonable estimate of the ratio of trabecular-to-cortical turnover. In addition, Lloyd's surface/volume ratios together with Jowsey's formation surface and Frost's mean apposition rate lead to acceptable absolute values of the turnover rates. It would be most valuable, therefore, to have more measurements of the surface/volume ratio in different bones both in dog and in man.

Note on Linear Resorption Rate

Note that if resorption proceeded at the same $0.8 \mu/\text{day}$ as does apposition, and if the iliac crest had a surface/volume ratio of 90 cm/cm^2 , then Table 29 indicates that the anterior iliac crest would lose bone mass at the rate of $9.7\%/\text{year}$. Over each 10-year period 60% of the bone would be lost. However, Jowsey observes no more than a 10% loss of bone from the posterior iliac crest over a 40-year period. This suggests that the high values for resorption surface in Table 29 do not indicate an imbalance between the

volume rates of apposition and resorption. Perhaps the effective linear resorption rate is only about $0.4 \mu/\text{day}$.

MATHEMATICAL SUMMARY OF MACROSCOPIC MODEL

1. The whole-body retention function is either

Case (a) A power function followed by an exponential

$$R = \epsilon^b(t + \epsilon)^{-b} \quad t \leq t_y \quad (32)$$

$$R = (\epsilon^b t_y^{-b} e^b) e^{-bt/t_y} \quad t \geq t_y \quad (33)$$

Case (b) A power function times an exponential

$$R = \epsilon^b(t + \epsilon)^{-b} e^{-\lambda t} \quad (34)$$

Case (c) A series of exponentials.

2. In any case, the total area under the retention curve is given by $c/\eta k$ (which follows from the model of the skeletal metabolism of the alkaline earths, postulates 1(b), 1(c), 1(d)). This assumes that the system is age-invariant with no long-term discrimination between blood and bone.

3. From step 2 it follows that for cases (a) and (b) in Step 1:

$$\text{Case (a)} \quad \frac{t_y}{t_x} = (1 - b)^{1/1-b} (t_x/\epsilon)^{b/1-b} \quad (35)$$

$$\text{Case (b)} \quad \lambda = \left[\frac{\Gamma(2 - b) \eta k \epsilon^b}{(1 - b) c} \right]^{1/1-b}$$

4. The final exponential in case (b) has a lower rate constant than case (a), which allows a choice as to the best fit for data. (a) leads to $\lambda \cong b/t_y = 2.5\%/year$ for Ca, Sr and Ra in man. (b) produces a common $\lambda \approx 1.5\%/year$ for approximately the same input data.

★ From this point on, consider only case (b)—the power function times an exponential.

5. The average specific activity of the body is then

$$B = \frac{q}{c} \epsilon^b (t + \epsilon)^{-b} e^{-\lambda t} \quad [\text{case (b)}]. \quad (37)$$

6. We associate λ in Step 5 with the turnover rate of cortical bone by apposition-resorption.

7. Then if the apposition-resorption rate of trabecular bone is σ times that of the cortical bone, the specific activity of trabecular bone is

$$V_T = (\sigma^{1-b}) \frac{q}{c} \epsilon^b (t + \epsilon)^{-b} e^{-\sigma \lambda t}, \quad (38)$$

where the first bracket (σ^{1-b}) normalizes the whole expression for V_T so that

$$\int_0^\infty V_T dt = \int_0^\infty B dt = \int_0^\infty S dt = q/\eta k. \quad (39)$$

This is another application of the area rule. It determines the initial uptake of activity in the trabeculae once σ has been chosen.

8. Now the ratio of trabecular specific activity to body specific activity, V_T/B , may be compared with data for radium in man and ^{90}Sr in man:

$$\frac{V_T}{B} = \sigma^{1-b} e^{-\lambda(\sigma-1)t}. \quad (40)$$

9. Expression (40) is exponential so that V_T/B can be plotted as a straight line vs. time since tracer intake on semilogarithmic graph paper. (See Lloyd's report on radium in man.⁽²⁰⁾)

10. The time at which V_T crosses and starts falling below B is

$$t_z = \frac{(1 - b) \log_e \sigma}{\lambda(\sigma - 1)} \quad (V_T = B). \quad (41)$$

11. Lloyd's plot of the MIT radium vertebrae is fitted by

$$\text{(a)} \quad \sigma^{1-b} = 2.9 \quad (\text{left hand intercept})$$

$$t_z = 23 \text{ years}$$

$$\text{For radium, } b = 0.5, \text{ so } \sigma = 8.4$$

$$\lambda = 0.63\%/year$$

An equally good fit would be

$$\text{(b)} \quad \text{If } \sigma^{1-b} = 2.0, \text{ then } \sigma = 4.0$$

$$\lambda = 1.45\%/year$$

$$t_z = 23 \text{ years}$$

(c) From the considerable spread in the data one can only conclude that λ is the order of 1%/year.

12. For case (b) above, the power function times exponential, the effective rate constant for radium at a time t after radium intake is $[(1/R)(dR/dt)]$

$$\lambda_{\text{effective}} = \lambda + \frac{b}{t + \epsilon}$$

For $t = 35$ years

$$\lambda = 1\%/year \quad \lambda_{\text{effective}} = 2.4\%/year$$

$$b = 0.5$$

This agrees with Keane and Evans'⁽²¹⁾ measurement of the average rate constant in 20 radium samples some 30 to 40 years after intake.

13. If the fraction of the skeleton (by weight) that is trabecular is designated by τ , the ratio of the specific activity of cortical bone to the body is given by

$$\frac{V_c}{B} = \frac{1 - \tau \sigma^{1-b} e^{-\lambda(\sigma-1)t}}{1 - \tau}$$

This expression insures that the sum of the cortical and trabecular activity always equals the total activity [compare (40) and (43)]. It fits the plot for human radium quite well.

The expressions above for V_T , V_c , and B are for radium in man in Figure 56.

JUSTIFICATION FOR EQUATING FINAL EXPONENTIAL RATE CONSTANT λ WITH CORTICAL APPosition-RESORPTION

From expression (42) it is clear that at very long times after injection the power function (and the exponential) can be neglected and λ is the dominant term.

1. Consider the behavior of the parallel compartments, which a number of bone compartments exchange calcium directly with the blood plasma. A particular compartment, i , has specific activity, V_i , calcium and calcium transfer rate (due to apposition-resorption), a_i . The behavior of V_i is given by

$$c_i \frac{dV_i}{dt} = -a_i(V_i - S),$$

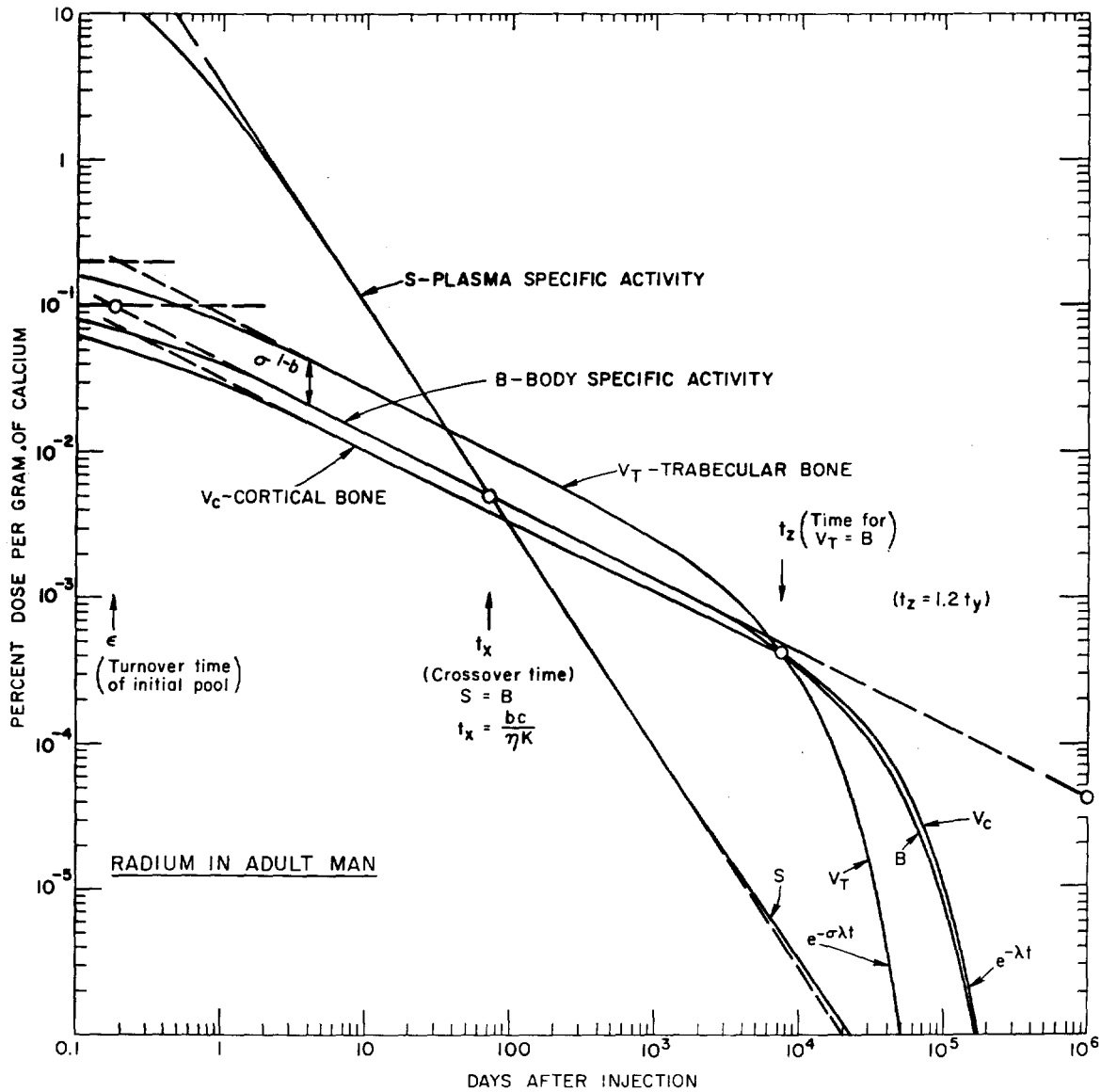


FIG. 56.—Summary of the macroscopic model. Curves show the body specific activity B , the plasma specific activity S , the specific activity of cortical bone V_c , and the specific activity of trabecular bone V_T as given by the model. The parameter values are chosen to approximate the behavior of radium in normal adult man: $b = 0.5$, $\epsilon = 0.18$ day, $\eta k = 7$ g calcium per day, $\sigma = 4$ (the ratio of the turnover rates of trabecular and cortical bone), $\tau = 0.2$ (the fraction of trabecular bone in the skeleton), and $c = 1000$ g calcium (body calcium). The given values of b , ϵ , and ηk lead to the prediction that the final exponential rate will be 1%/year (assuming age-invariance and no long-term discrimination), and this rate has been taken as the turnover rate of cortical bone by apposition-resorption. Note that the areas under all four curves from time zero to time infinity are equal to each other and equal to $q/\eta k$, where q is the activity injected (100% dose) and ηk is the excretory plasma clearance in grams of calcium per day.

where S is the specific activity of the plasma, the central compartment.

2. Now when transient equilibrium following a single injection is finally reached,

$$V_i = V_{ie} e^{-\lambda t} \tag{45}$$

$$S = S_e e^{-\lambda t} \tag{46}$$

where V_{ie} and S_e are the compartment and plasma specific activities at the beginning of the equilibrium

period, which is here taken as $t = 0$, and λ is the final exponential rate constant of the model as a whole.

3. Then

$$\frac{dV_i}{dt} = -\lambda V_{ie} e^{-\lambda t} = \lambda V_i \tag{47}$$

so

$$-c_i \lambda V_i = -a_i (V_i - S) = -a_i V_i + a_i S \tag{48}$$

$$a_i V_i - c_i \lambda V_i = a_i S \tag{49}$$

$$V_i - \frac{c_i}{a_i} \lambda V_i = S \quad (50)$$

$$V_i(1 - \lambda/\lambda_i) = S \quad (51)$$

$$\boxed{\frac{V_i}{S} = \frac{1}{1 - \lambda/\lambda_i}}, \quad (52)$$

where $\lambda_i = \frac{a_i}{c_i}$ = the rate of apposition-resorption for compartment i .

4. Now if λ_i refers to trabecular bone, we can write

$$\lambda_i = \sigma \lambda$$

or

$$\frac{V_\tau}{S_e} = \frac{\sigma}{\sigma - 1}. \quad (53)$$

5. The ratio of S/B , plasma to body specific activities, at transient equilibrium follows from the relations

$$S = S_e e^{-\lambda t} \quad (54)$$

$$B = B_e e^{-\lambda t} \quad (55)$$

and the excretion postulate

$$q \frac{dR}{dt} = -\eta k S, \quad (56)$$

where $qR/c = B$.
Then

$$q \frac{dB}{dt} = cdB/dt = -\lambda c B = -\eta k S \quad (57)$$

so

$$\boxed{\left(\frac{S}{B}\right)_e = \frac{\lambda c}{\eta k}} \quad (58)$$

which is the ratio of plasma to body specific activities at final transient equilibrium.

6. Therefore,

$$\left(\frac{V_\tau}{B}\right)_e = \left(\frac{V_\tau}{S}\right)_e \left(\frac{S}{B}\right)_e = \frac{\sigma}{\sigma - 1} \left(\frac{\lambda c}{\eta k}\right). \quad (59)$$

For $\lambda = 1.5\%/year$
 $c = 1000 \text{ gCa}$
 $\eta k = 7 \text{ gCa/day (70 liters/day)}$
 $\sigma = 4$

for radium in man

$$\left(\frac{V_\tau}{B}\right)_e = 0.0078.$$

In other words, if trabeculae have a turnover rate of 4

times that of the final rate constant λ , then at equilibrium their specific activity would be 1% that of the skeleton as a whole.

7. Cortical specific activity at transient eq must be

$$\left(\frac{V_c}{B}\right)_e = 1.248,$$

assuming $\tau = 0.2$ (20% trabecular, 80% cortical)

8. Substituting the above into (52) and using (55)

$$\left(\frac{V_c}{S}\right)_e = \left(\frac{V_c}{B}\right)_e \left(\frac{B}{S}\right)_e = 1.248 \left(\frac{\eta k}{\lambda c}\right) \frac{1}{1 - \lambda/\lambda_c}$$

where λ_c is the rate constant of cortical bone (apposition-resorption).

9. For the parameters listed in step 6

$$1.248 \left(\frac{(7 \text{ gCa/day})(365 \text{ days/year})}{(1.5\%/year)(1000 \text{ gCa})} \right) = \frac{1}{1 - \lambda/\lambda_c}$$

$$\frac{1}{1 - \lambda/\lambda_c} = 212.6$$

$$1 - \lambda/\lambda_c = 0.0047$$

$$\text{Radium in man } \boxed{\lambda/\lambda_c = 0.995},$$

the ratio of the body's final exponential λ to position-resorption rate in cortical bone.

10. Therefore, λ_{cortex} is within 1/2% of λ if the two can be equated without significant error

11. In general

$$\boxed{\frac{\lambda}{\lambda_c} = 1 - \frac{(1 - \tau)}{\frac{\eta k}{\lambda c} - \tau \left(\frac{\sigma}{\sigma - 1}\right)}}$$

For calcium, with

$$\eta k = 0.3 \text{ gCa/day}$$

$$\lambda = 1.5\%/year$$

$$c = 1000 \text{ gCa}$$

$$\tau = 0.2$$

$$\sigma = 4$$

$$\frac{\lambda}{\lambda_c} = 0.886 \quad (11\% \text{ difference}).$$

Even 11% is still negligible in view of our uncertainty about λ .

CONNECTION WITH THE MICROSCOPIC MODEL

1. The final exponential of the macroscopic model, we have associated with the apposition-resorption rate in cortical bone.

2. Knowing the latter, we know the amount of activity in hotspots a few weeks after injection. The total activity involved in new bone formation and secondary mineralization in cortical bone is

$$A_{HC} = \lambda c(1 - \tau)I \quad (66)$$

where $c(1 - \tau)$ is the amount of cortical calcium λ is the fraction being renewed per unit time I is the time integral of plasma specific activity.

3. From expression (19),

$$I = \int_0^t S dt = \frac{q}{\eta k} (1 - R). \quad (67)$$

4. The asymptote of the integral at $t = \infty$ is

$$I_\infty = q/\eta k. \quad (68)$$

5. Therefore,

$$A_{HC} = q \left(\frac{\lambda c}{\eta k} \right) (1 - \tau) \quad (69)$$

6. Similarly, the total activity involved in bone formation in trabecular bone is

$$A_{HT} = q \left(\frac{\lambda c}{\eta k} \right) \sigma \tau \quad (70)$$

7. From the section on osteon formation, one can calculate the average hotspot intensity and the distribution.

8. Knowing both the total activity and the hotspot activity, one obtains the activity not connected with bone formation. This calculation must then agree with the direct calculation of the overall augmentation rate in the section on osteon formation.

9. Expressions (69) and (70) give the fraction of the injected activity which deposits in hotspots due to bone formation. They do not give the fraction of the retained activity (the current body burden) in hotspots. If hotspots show little diminution for a month or so, then the two figures can be quite different. The diminution in hotspots at times shortly after injection requires further experimental investigation. Also, the effect of soft tissue uptake has not yet been included.

CONCLUSION

The preliminary model outlined above promises to provide a framework into which the data listed in the summary of background information can be fitted. One must now attempt to find the best parameters for

normal man, keeping in mind that the macroscopic and microscopic models must be internally consistent.

List of Symbols

Capital letters indicate functions of time since tracer injection.

A_{ugs}	Augmentation rate, the kinetic A -value calculated 5 days after injection for bone in which there is no apposition.
R	Fractional retention of tracer in body.
S	Plasma specific activity.
S_c	Plasma specific activity under continuous tracer intake.
\dot{q}	The rate of tracer intake into blood.
r	Radius of osteon canal.
β	Fractional rate of closure of osteon canal.
g	Mass of calcium per unit length of osteon being laid down per unit time.
ρ	Grams calcium per cm^3 of bone.
t_h	Time for forming an osteon.
N	Number of forming osteons per unit area of bone (not a function of time).
n	Number of osteons per unit area of bone which start forming per unit time.
H	Activity per unit length of osteon.
I	The time integral of S from 0 to t .
V	Specific activity of some compartment in bone.
D	Microcurie-days per cm^2 of bone surface.
Δ	Depth of Rowland's exchange on bone surface.
f	A volume fraction of bone.
T	The time since skeletal formation (a person's age minus about 18 years).
α, β	Used to express augmentation rate as a function of bone age.
A_t	Kinetic A -value calculated at time t .
t_v	Equilibration time for model in which a power function is followed by an exponential [Case (a)].
V_i	Specific activity of i^{th} compartment.
c_i	Calcium content of i^{th} compartment.
a_i	Calcium transfer rate of i^{th} compartment.
V_{i0}	V_i at beginning of period of transient equilibrium.
S_0	S at beginning of period of transient equilibrium.
A_{HC}	Activity in bone formation hotspots in cortical bone.
A_{HT}	Activity in bone formation hotspots in trabecular bone.
B	Body specific activity ($\mu\text{Ci}/\text{gCa}$).
V_T	Trabecular specific activity.
V_c	Cortical specific activity.
q	Activity injected.
c	Body calcium.
ϵ	Turnover time of initial pool (days).

- b Power function slope (due to diminution).
 λ Rate constant of final exponential (turnover rate of cortical bone).
 ηk Excretory plasma clearance in g_{Ca}/day (liters/day times g_{Ca}/liter).
 t_x Crossover time (the time at which body specific activity B equals plasma specific activity S).
 k Endogenous excretion rate (g_{Ca}/day).
 σ Ratio of the turnover rates of trabecular to cortical bone (by apposition-resorption).
 t_z Time at which falling $V_T = B$ (crossover of trabecular and body specific activity).
 τ Fraction of skeleton that is trabecular bone (by calcium content).

REFERENCES

- Lloyd, E., Rowland, R. E., Hodges, D., and Marshall, J. H. Surface-to-Volume Ratios of Bone Determined by Computer Analysis of Microradiographs. *Nature* **218**, 365 (1968).
- Marshall, J. H. Measurements and Models of Skeletal Metabolism. *Mineral Metabolism*, Ed. C. Comar and F. Bronner. Academic Press, New York, 1969, Vol. III, pp. 1-122.
- Marshall, J. H. The Retention of Radionuclides in Bone. *Delayed Effects of Bone-Seeking Radionuclides*, Ed. C. W. Mays, W. S. S. Jee, R. D. Lloyd, B. J. Stover, J. H. Dougherty, and G. N. Taylor. University of Utah Press, Salt Lake City, 1969, pp. 7-25.
- Marshall, J. H. Microscopic Metabolism of Calcium in Bone. *Bone as a Tissue*, Ed. K. Rodahl, J. T. Nicholson, and E. M. Brown, Jr. McGraw-Hill, New York, 1960, pp. 144-155.
- Marshall, J. H. Theory of Alkaline Earth Metabolism. The Power Function Makes Possible a Simple but Comprehensive Model of Skeletal Systems. *J. Theoret. Biol.* **6**, 386 (1964).
- Marshall, J. H. and Onkelinx, C. Radial Diffusion and Power Function Retention of Alkaline Earth Radioisotopes in Adult Bone. *Nature* **217**, 742 (1968).
- Manson, J. D. and Waters, N. E. Maturation Rate of the Osteon of the Cat. *Nature* **200**, 489 (1963).
- Manson, J. D. and Waters, N. E. Assessment of Osteon Maturation Rate in the Dog. *Arch. Oral Biol.* **12**, 1577-1591 (1967).
- Lee, W. R. Appositional Bone Formation in Canine: A Quantitative Microscopic Study Using Tetraalkylammonium Markers. *J. Anat. (London)* **98**, 665 (1964).
- Marshall, J. H., Rowland, R. E., and Jowsey, J. Microscopic Metabolism of Calcium in Bone, I-V. *Radiat. Environ. Biophys.* **1**, 197-270 (1959).
- Rowland, R. E. Exchangeable Bone Calcium. *Am. J. Physiol.* **203**, 233 (1966).
- Heaney, R. P. Evaluation and Interpretation of Kinetic Data in Man. *Clin. Orthoped.* **31**, 153 (1961).
- Ellsasser, J. C., Farnham, J. E., and Marshall, J. H. Comparative Kinetics and Autoradiography of ^{137}Ba in Ten-Year-Old Beagle Dogs. Argonne National Laboratory Radiological Physics Division Report, July 1967 through June 1968. ANL-7489, p. 1.
- Rowland, R. E. and Leuer, C. J. An Evaluation of a Complete Gamma Function Over a Range of Biologically Significant Values. Argonne National Laboratory Radiological Physics Division Semiannual Report, June 1961. ANL-6398, pp. 24-35.
- Rowland, R. E., Marshall, J. H., and Jowsey, J. Calcium in Human Bone: The Microradiographic Approach. *Radiat. Res.* **10**, 323 (1959).
- Rowland, R. E. and Marshall, J. H. Radium in Bone: The Dose in Microscopic Volumes of Bone. *Radiat. Res.* **11**, 299 (1959).
- Evans, R. D. *The Atomic Nucleus*, McGraw-Hill, New York, 1955, p. 479.
- Jowsey, J., Kelly, P. J., Riggs, B. L., Bianco, A. J., D. A., and Gershon-Cohen, J. Quantitative Radiographic Studies of Normal and Osteoporotic Bone. *J. Bone Joint Surg.* **47-A**, 785 (1965).
- Villanueva, A. R., Ramser, J. R., Frost, H. M., A. R., Frame, B., and Smith, R. W. Tetracycline Quantitative Measurements of the Tissue and Dynamics in 10 Cases of Osteoporosis. *Clin. Orthoped.* **203**, 203 (1966).
- Lloyd, E. Non-Uniformity in the Retention of the Alkaline Earths in Animals and Man. This report.
- Keane, A. and Evans, R. D. Massachusetts Institute of Technology Report 952-5, Part II (1968), p. S10.

IMPROVED CONSTRUCTION OF RADIOACTIVE PHANTOMS WITH ARBITRARY SOURCE DISTRIBUTION*

Harold May, L. D. Marinelli, and Paul Hess

The substitution of beads or pellets instead of liquids is proposed for the convenient loading of radioactive phantoms. An analysis of the general problem suggests that mixtures of active and inactive beads are perhaps most immediately convenient, whereas the use of loaded lattices offers simplification and use of a "library" of simulated and economical "organs."

* Presented orally at the 14th Annual Meeting of the Health Physics Society, June 8-12, 1969, Pittsburgh.

INTRODUCTION

A wide variety of devices has been used to simulate the human body and its internal organs for the purpose of calibrating the response of radiation detection equipment. This variety is primarily the result of varying requirements upon the accuracy with which the phantoms must simulate the dimensions and atomic properties of the body.

be duplicated. There is considerably less variety in choice of materials employed. While rice, sugar, or similar granular materials are frequently used to simulate the uncontaminated body, it is the almost universal custom to employ aqueous solutions when radioactivity is to be incorporated therein. For intensive and varied use, a phantom containing radioactive liquid has several practical disadvantages, namely the ever-present danger of leakage, which may lead to contamination of expensively shielded detectors and enclosure, and the inconvenience of cross contamination between different isotopes used within the phantom itself. The latter counsels the use of short-lived materials, and the additional labor that their use entails. These problems increase in importance with the complexity in detail of the phantom.

Less hazardous and tedious manipulation may be obtained by incorporating the desired radioelement into beads of suitable size. These may be poured from storage container to phantom many times with quantitative transfer. While they are still subject to accidental spillage, recovery and salvage are considerably simplified. We have recently investigated the practicality of such a system, and present here a progress report on some of its advantages and problems.

PREPARATION OF BEADS

Radioactive microspheres of either ceramic or plastic material are available from the 3M Company in sizes ranging from 10 to 150 micrometers.⁽¹⁾ On special order, they supplied us with much larger plastic spheres, $725 \pm 70 \mu$ in diameter. Specific activities normally produced range from 0.1 to 30 Ci/g. These activity levels are not compatible with our intended use, but, again by special request, we obtained spheres loaded with cesium-137 and cobalt-60 at approximately $1.3 \mu\text{Ci/g}$.

The spheres are much too small to handle individually or to locate if accidentally spilled (about 5000/g); therefore, we obtained nylon beads 5.5 mm diameter with a 1-mm hole drilled to the approximate center of each. (The indentation will hold about 20 microspheres.) A fixed number of spheres were placed in each cavity and sealed in place with a drop of low-viscosity epoxy cement. A vacuum pickup device, adjusted to accept a fixed number of spheres, devised by Mr. E. Fudala of the Radiological Physics Division staff shop, greatly simplified the loading procedure. Figure 57 illustrates beads held in a simple polyethylene jig while being loaded and sealed. Beads were loaded with each isotope at two specific activity levels, and each lot was sprayed with paint of a distinctive color to guard against accidental admixture and to facilitate retrieval if inadvertently dropped.

STANDARDIZATION

When liquid sources are used, a uniform distribution automatically results. With discrete beads, one must either (1) assay each bead separately, identify it uniquely, and sum the total activity in a given source, or (2) determine the mean activity level of the beads and their distribution about that value. We chose the latter course for obvious reasons.

One hundred microspheres were counted repetitively (a different sample each time) with a total of 58 samples; a few additional runs were made with only 10 or 20 microspheres, i.e., single beads. Table 31 summarizes the results.

Data are expressed as net counts per minute in the entire photopeak, as detected by a 17.8-cm diameter by 8.9-cm thick NaI crystal and single channel analyzer. Sources were placed in accurately reproducible geometry on the crystal face.

The first loading of beads was carried out using microspheres from the top of the container. The absolute activity level was about 30% greater than that inferred from the assay supplied by the 3M Company. We speculated that perhaps the discrepancy might be due to nonuniform labeling of the plastic resin spheres, which were then insufficiently intermixed and randomized during subsequent processing and shipping. Hence we sampled spheres taken from the midplane and bottom of the container and noted significant differences, though nothing like 30% (see lines 4 and 5 Table 31). The large values of chi squared indicated that the samples tested do not represent a normal distribution. We observe that many spheres are in actuality more like half-spheres, with a smaller fraction of intermediate shapes. It has been suggested that allowing the spheres to roll down a slightly inclined plane would separate those with large flat surfaces and hence improve the uniformity, and we intend to try this.

With this activity level, filling a liver or kidney entirely with source beads results in an inconveniently large total activity. The remedy is to use the required number of active beads, diluted with additional non-radioactive ones. For economy, the latter may be of Lucite instead of nylon. As a practical matter, we think it likely that not more than 100 active spheres will usually suffice for a given requirement. The number actually used may well be determined by the statistical distribution in space required to simulate a uniform distribution, rather than by the precision in total activity.

The mean density of close-packed beads is about 0.7 g/cm^3 . For accurate simulation of the larger organs, where self-absorption may be appreciable, fine granules could be added to increase the density to unity.



FIG. 57.—Loading radioactive beads

TABLE 31. STATISTICS OF Cs¹³⁷ MICROSHERES

Sample		n	\bar{t} , min	Counting rate, cpm	S.D.	χ^2
Location	No. of beads					
Top	100	58	10	11,930 \pm 180	1634	
Top	20	10	13	11,850 \pm 179	346	
Top	10	9	6	12,070 \pm 218	201	
Middle	100	10	10	12,690 \pm 140	155	
Bottom	100	11	10	12,450 \pm 240	523	

n = No. of samples counted.

\bar{t} = mean counting time per sample.

About 25 radioelements are available from the 3M Company in microsphere form. For short-lived isotopes, it would seem entirely feasible to load the nylon beads with any desired stable element and produce the desired activity in situ by neutron irradiation. We have not investigated this possibility in detail as yet.

ANALYSIS

The usefulness of a phantom is solely dependent on its imitating the relevant dimensions and shape of the body and of the radioactive organ, and on correctly locating one within the other. Obviously, the detector (customarily a single or multiple NaI crystal, possibly collimated) must be placed identically with respect to the body and the phantom. If we are concerned with calculating the burden of a single individual with precision, the uncertainties arising from natural variations in size and location must all be recognized as these are upon the patient's age, race, and *habitus*. But these considerations are common to any calibration procedure.

As a preliminary to studying the statistical properties of many sources, an analysis was attempted of the minimum number and optimum spatial positions of discrete beads that are required to simulate a uniformly active organ to any stated degree of accuracy.

problem is illustrated in Figure 58. Consider a linear shaped element of an extended radioactive mass or organ, imbedded in the body. The length of this element is $2l$, its center is the point P . Let the detector be at a distance a from the center. The radioactive segment lies at a depth t within absorbing, but nonradioactive tissue. The analysis assumes that the angles mutually subtended by the source and detector are relatively small, so that variations in response with deviations in path direction from the line joining their midpoints may be neglected. Keep in mind that the task at hand is not to calculate the crystal response exactly, but to estimate how spatially uniform the distribution of spheres must be so as to simulate satisfactorily the response of an extended uniform source identically placed.

We assume the attenuation to be exponential. This implies that the detector response should be restricted to the "photopeak" region. As illustrated, the effects of scattering within adjacent volume elements of the organ may be appreciable, and the absorption coefficient to be used must be chosen accordingly.

The relative reading, in arbitrary units, produced by a point source at the center, P is

$$R_P = \frac{KQ_0e^{-\mu(l+t)}}{a^2}, \quad (1)$$

where Q_0 is the source strength and K a constant relating to detector efficiency, whereas that produced by a linear source of equal strength and length $2l$ will be

$$R_e = \frac{KQ_0e^{-\mu(l+t)}}{2la^2} \int_{-l}^{+l} \frac{e^{\mu x} dx}{(1-x/a)^2}. \quad (2)$$

Solution of the integral is given by Evans.⁽²⁾ The denominator is expanded in a series, and integration term by term readily follows. For the case where μl is appreciably less than unity, so that higher terms in μl may be discarded, a particularly simple expression

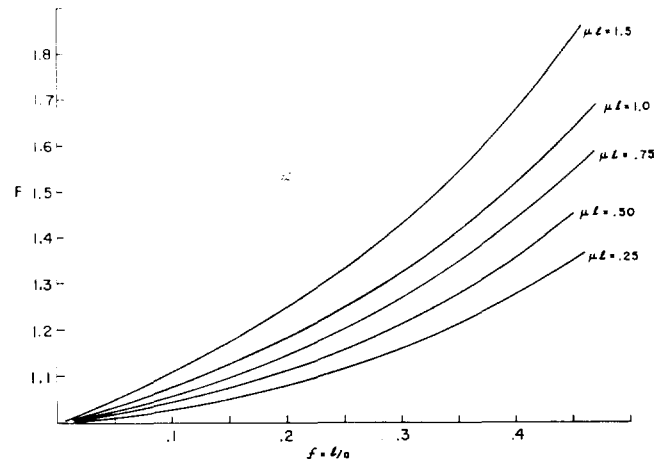


Fig. 59.—Efficiency factor F vs. $1/a$

results. The normalized response factor F , namely the ratio of the response R_e from an extended source to R_P , is given by

$$F = R_e/R_P = \frac{1}{(1-f^2)} + \mu l(2/3 f + 4/5 f^3 + 6/7 f^5 + \dots), \quad (3)$$

where $f = l/a$. F may also be thought of as the factor by which the point source strength must be increased in order to obtain a response equal to that of the extended segment of total strength Q_0 . Note that exponential terms in thickness t disappear, being common to both numerator and denominator.

Equation (2) can also be integrated exactly within the range of approximation where $e^{\mu x} = 1 + \mu x$, with the following result

$$F' = \frac{1}{1-f^2} + \frac{\mu l}{2f^2} \left(\log \frac{1-f}{1+f} + \frac{2f}{1-f^2} \right), \quad (4)$$

where in order for $e^{\mu x}$ to differ by less than 10%, μx is restricted to values less than about 0.5.

Values of the factor F as calculated from equation (3) are plotted vs. the parameter $f = l/a$ in Figure 59. The values assumed for μl in the three upper curves are well outside the range for which the approximation is valid. The point of this figure is that if one wants to represent an extended line source (and by extension, the whole organ) by only one point source at the center to within an accuracy of, say, 10%, the acceptable range in values of μl and l/a is quite restricted.

The correct value of the exponential integral may be calculated to a much closer approximation if additional terms [equation (2)] are retained and the simplifying assumptions avoided.* In Figure 60 the values of

* The resulting solution to 16 terms, including the parameters of μl and l/a to the sixth power, is given by Evans.⁽²⁾

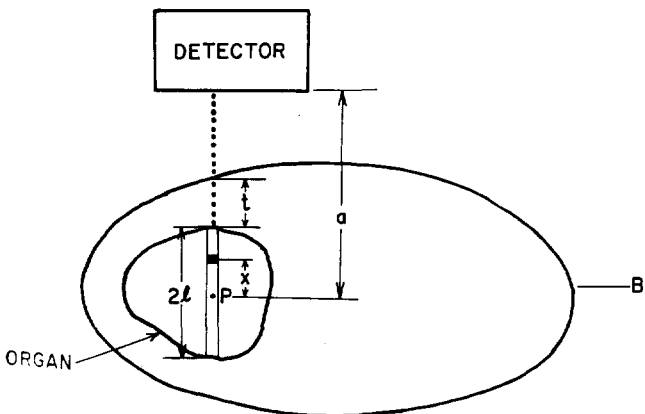


Fig. 58.—Geometry of organ depth location in whole-body counting.

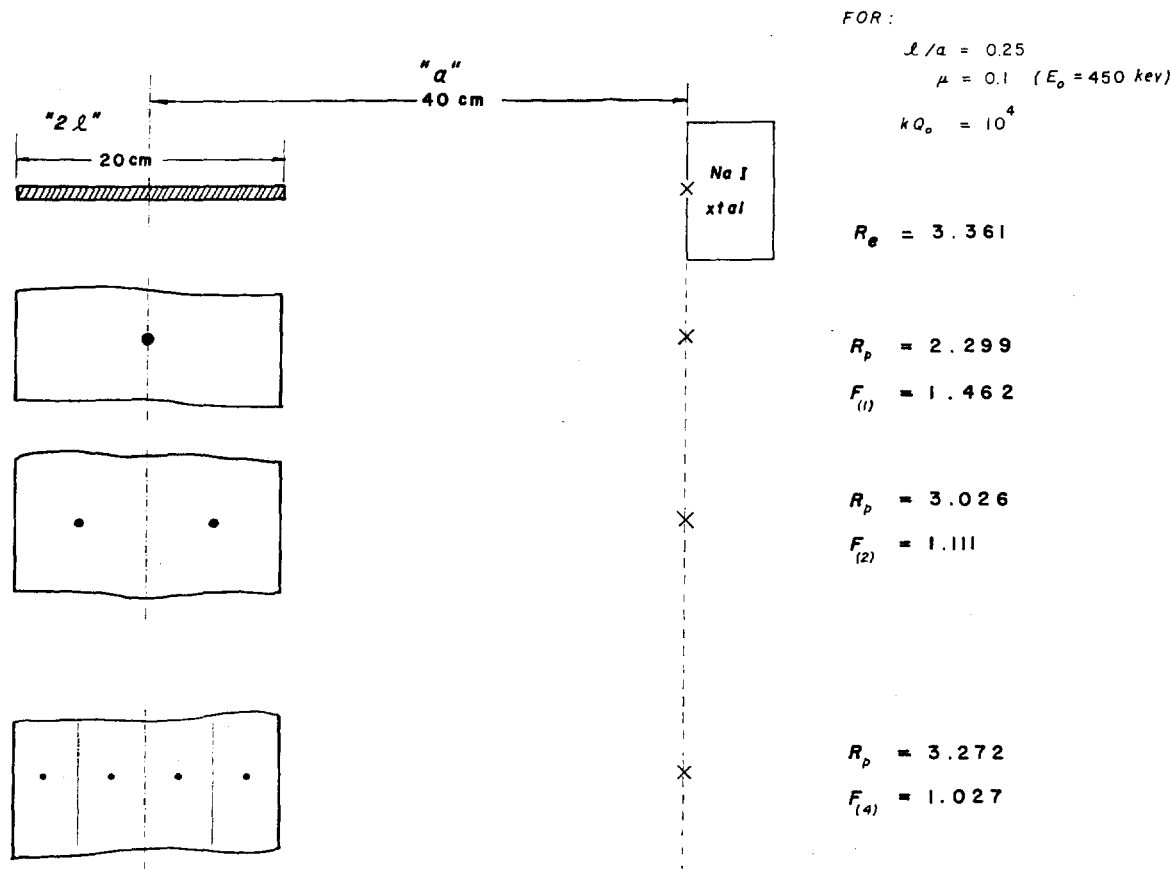


FIG. 60.—Comparison of single, double, and quadrupole point source approximations to a uniform line source

R_e thus obtained, for a choice of parameters typical of many counting systems, is compared with the response of one-, two-, and four-point sources having equal total intensity and distributed symmetrically. It is found that two sources result in a response which is 11% low, three sources (not illustrated)—5%, and four sources—2.7%. There is one big drawback. The point source nearest the detector contributes 56% of the total response for four sources, and the first two contribute 82%. They must, therefore, be located accurately at the designated places, but of course in many phantom systems this is impractical, if not impossible.

On the other hand, one might envision a phantom system in which a uniform distribution within any selected organ, or indeed any arbitrary activity distribution, could be simulated by a set of equal point sources located at uniquely determined points of a three-dimensional grid or coordinate system. A computer program permitting a systematic investigation of organ size, shape and composition based upon such a concept has been reported by Snyder et al.⁽³⁾

We are inclined to believe that a more useful approach is to determine the most probable response and the statistical distribution about the mean resulting

from successively large numbers of points located randomly. One might try to do this empirically by placing a sufficient number of beads in a suitable enclosure, shaking them up thoroughly, and observing the resultant count rate. The question of what constitutes "sufficient number," and what is the distribution function would then be evaluated from a large number of repeated trials. A more sophisticated approach would involve Monte Carlo simulation by computer. Investigation of the properties of an ensemble of sources along these lines is continuing.

In conclusion, an alternate system for the safe handling of small amounts of radioactivity into phantoms has been described. We feel that the method has improved flexibility (being capable of simulating about any arbitrarily chosen source configuration) and safety. Further analysis of the random spatial distribution assumed by multiple sources, and the resulting detector response in realistic, three-dimensional coordinates is necessary in order to realize its full potential.

REFERENCES

1. Grotenhuis, I. M. Properties and Uses of Radiating Spheres. *Radioactive Pharmaceuticals*, Ed. G. A. Anderson, p. 115. McGraw-Hill, New York, 1964.

et al. U. S. Atomic Energy Commission Report CONF-651111 (1966), pp. 205-209.
 2. Evans, Robley D. and Evans, Richard O. Studies of Self-Absorption in Gamma-Ray Sources. *Rev. Mod. Phys.* **20**, 305-326 (1948).

3. Snyder, W. S., Ford, Mary R., and Warner, G. G. Effect of Size, Shape, Composition, and Density of Body Organs on the Absorption of Gamma Rays from a Uniform Source in an Organ. U. S. Atomic Energy Commission Report ORNL-4316 (October 1968) p. 274.

"TIME-OF-FLIGHT" GAMMA-RAY CAMERA OF LARGE DIMENSIONS

L. D. Marinelli, G. F. Clemente, I. K. Abu-Shumays,* and O. J. Steingraber

The localization of low levels of radioactivity by means of time-of-flight techniques is possible if resolutions of the order of 5 cm are tolerated. A survey is given of the optical, electronic, and mathematical problems involved.

An economical instrument, capable of measuring *in vivo* distributions of the order of 0.01 μ Ci of γ -ray activity, obviously would prove useful in monitoring internal contamination in neutron radioactivation analysis *in vivo* and perform, over large areas, some of the tasks performed by the several γ -ray cameras available today. In the case of K^{40} , with an instrumental efficiency of 7%, the expected average counting rate would be of

ure 61. A collimator grid whose cubic septa have lumina from 25 to 100 cm^2 will cover the array. To the ends of these rods there are optically coupled fast photomultipliers (P.M.) connected in turn to fast subnanosecond circuits that measure the time elapsed between the two signals generated by a single scintillation in the anodes of the corresponding P.M. pair.

At the present, the measurement of subnanosecond intervals has become a fine art whose techniques can be used to advantage.⁽²⁾ The time "jitters" Δt of these fast measurements or, equivalently, the spatial resolution $W_{1/2}$ of our system, depends on identical factors, except

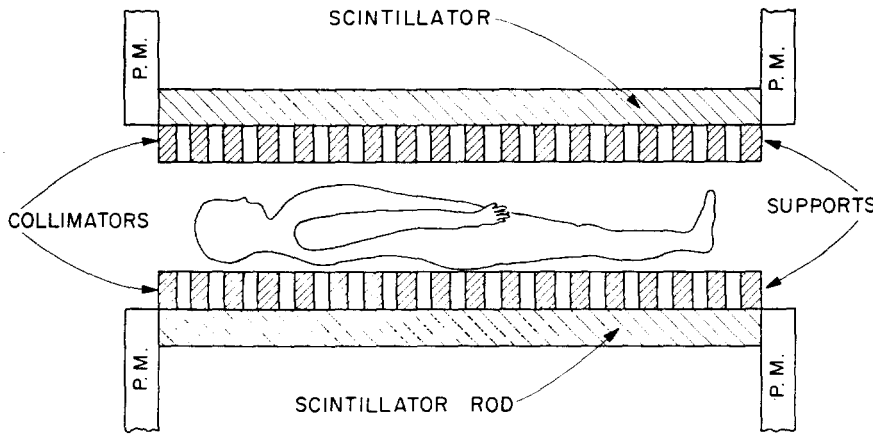


FIG. 61.—Outline of γ -ray camera

the order of 0.2 counts/ cm^2 /min; hence, in the presence of a comparable background, statistical errors of the order of 10% would require a counting rate of about 20 cpm for $\frac{1}{2}$ hr. Obviously at these levels one cannot gain good statistical information on activity spread over areas much smaller than 100 cm^2 , and this only with the most efficient visualization systems available, such as the autofluoroscope.⁽¹⁾

In order to reduce the number of photomultipliers used, we have thought of utilizing prismatic plastic fluorescent rods of 2" \times 2" cross section, one or two meters long and encircling the subject as shown in Fig-

that in our case the photons from each scintillation reach the photocathodes through different path lengths and that, in effect, the effective decay time of the photocathode burst is lengthened. The dispersion in a long fluorescent rod can be represented by a roughly Gaussian distribution described by

$$W_{1/2} = \Delta t \cdot f(L) \propto (N_0 f(c))^{-1/2} f(\tau_1 \tau_2) f(r) f(L),$$

where $W_{1/2}$ is the FWHM of the distribution of the time intervals Δt obtained with a rod irradiated by a fixed point source finely collimated;

N_0 is the number of photons arriving at the photocathode;

* Applied Mathematics Division.

located at
 by placing
 enclosure,
 g the re-
 stitutes a
 ion func-
 umber of
 ch might
 . Investi-
 f source
 safe load-
 phantom
 has both
 ting just
 ion) and
 al distri-
 resulting
 al coord-
 ontial
 ig Micro-
 Andrews

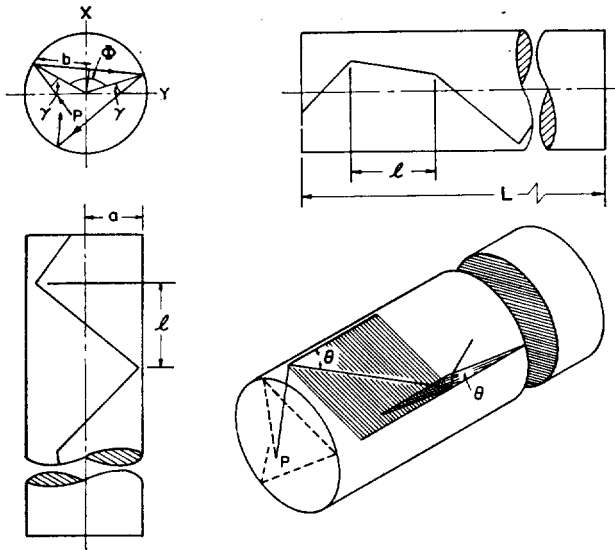


FIG. 62.—Orthogonal projections and perspective trace of skew path of light ray in cylindrical rod.

- $N_0 f(c)$ is the number of photoelectrons released therefrom;
- $f(\tau_1 \tau_2)$ is a function of the rise and decay time of the fluor;
- $f(r)$ is the effect of the dispersion in the total electron transit time in the phototube and of the fraction of each pulse utilized;
- $f(L)$ is the effect of the dispersion of the light photons traveling through the rod.

It is possible to explain some of the experimental results obtained if we recall the analysis of Potter⁽³⁾ on the conduction of light through optical fibers. In a cylindrical or square rod of length L , the length of either a skew or meridional ray is proportional to $L/\cos \theta$, θ being the angle between the ray and the axis or a line parallel to it. A meridional ray will stay in the same plane, whereas a skew ray (Figure 62) will, in general, spiral down the rod keeping, however, the angle $\theta = \text{constant}$ and the path length equal to $L/\cos \theta$. These relationships obtain irrespective of the magnitude of the cross section.

Since the rays emitted along the larger θ 's will arrive later, and the emission is isotropic, it can be shown that the instantaneous flux density will decrease as the square of their transit time measured in units of the transit time of the axial ray.⁽⁴⁾ If one trips the circuits with a smaller and smaller fraction of the pulse, one selects predominantly the rays traveling the shortest paths; hence the time per unit axial distance decreases, but the spatial resolution ($W_{1/2}$) remains unchanged. Hence, if one shifts a collimated point source along the rod, the number of cm per channel of the TAC* remains insensitive to the fraction r of the pulse that is utilized,

* Time-amplitude converter.

but the ratio of picoseconds/cm does not (Figure 63). As far as linearity of time vs. axial path, the rod is excellent (Figure 64), but the counting efficiency cpm/ μCi decreases by about 10% toward the end of the rod for reasons not entirely understood, but likely related to absorptive, reflective and coupling losses, the sum of which is not constant as the section occurs throughout the rod. This variation in efficiency is inconvenient but unavoidable, since ultimately, its equivalent will be met sooner or later in a study concerning the human body, where the detector efficiency will vary because of the unequal thickness encountered throughout the length and width of the body.

From this point on we will not consider displacement errors but consider instead that, once one identifies the distribution of scintillation in the rods surrounding the body, one must consider which experimental parameters contribute most to information concerning the distribution of the radioactivity in the body. This problem of folding is essentially stated by the Fredholm equation of the first kind or by its equivalent matrix equation which, in the presence of experimental error, yields approximate solutions of what are considered "ill-posed" problems.

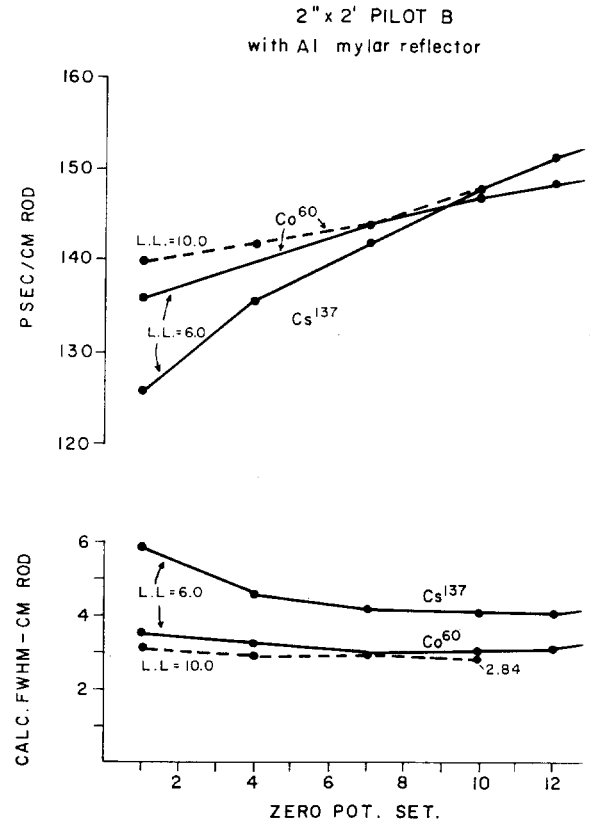


FIG. 63.—Top, transit time per axial unit distance; bottom, spatial resolution as a function of fraction of pulse utilized.

Figure 63) problems." We consider here the one-dimensional case
 the result is which is expressed as follows

$$\int_a^b K(x,x') f(x') dx' = g(x) + \epsilon(x)$$

where $f(x')$ is the unknown distribution of radioactivity

per unit length of the body. The kernel $K(x,x')$ is the counting rate registered by the scintillator at x due to the presence of an "ideal unit point source" situated at x' . We assume that it can be determined very accurately for practical purposes by prolonged measurements over appropriate inanimate phantoms containing relatively intense sources.

$g(x)$ is the counting rate detected at the position x and is subject to both statistical and experimental error. $\epsilon(x)$ stands for the error whose limits are known from knowledge of $g(x)$, although its actual value is unknown. No detail can be given here of the methods of solving this equation for $f(x')$ once $K(x,x')$ and $g(x)$ are given.⁽⁵⁾ In practice, the physical problem is further complicated by the fact that the amounts of radioactivity sought in the human body are unusually small. Hence, careful study must be devoted to the selection of response kernels of width most appropriate to optimize the amount of needed information.

Experimentally our experience was gained with a film source (~ 0.7 mm width) consisting of a fine catheter ~ 200 cm long filled with uniform Cs^{137} microspheres of about 0.2 nCi and shaped as a sequence of sinusoidal waves of varying frequency and extending about 60 cm. The detector was either a 3" diameter NaI crystal with three collimators or a cylindrical rod 2" diameter and 60 cm long covered by lead bricks separated from spaces ranging from 1 to 5 cm, as indicated in Figure 61.

The results concerning $W_{1/2}$, namely the effect of the kernel width on the solution $f(x')$, are illustrated in Figure 65. As were all our results, they were obtained by the smoothing technique, described elsewhere⁽⁵⁾ and programmed in a 3600 computer. Our $f(x')$, the true distribution, is shown by the solid line; our calculated solu-

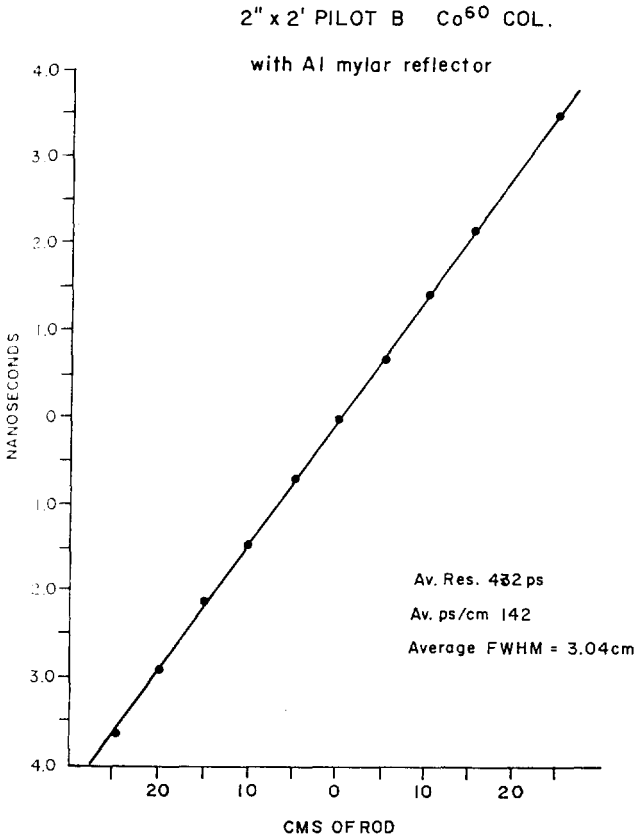


Fig. 64.—Proportionality between distance and transit time

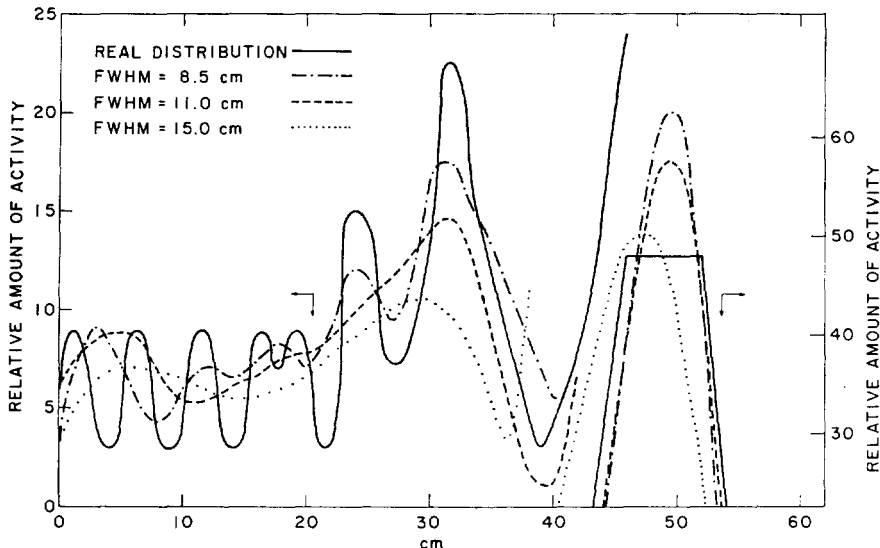


Fig. 65.—Influence of kernel resolution on detail of $f(x')$

tion, obtained by taking readings every 2 cm, shows the advantages of the narrower collimation yielding a $W_{1/2} = 8.5$ cm vis-a-vis 11 and 15 cm respectively. It is seen that except for the area of the distribution between 15–21 cm, the calculations could be considered satisfactory, since the errors in $f(x')$ are not more than a few times those introduced in $g(x)$. (Note that the tangible error at $x' < 10$ cm is due to having failed to include $g(x)$ readings for $x < 0$, namely those beyond the spatial limits of the distribution).

Before proceeding further, we must recall that even if we had perfect photomultipliers and instantaneous

Interval on $f(x)$ (cm)	Integrated Activity on $f(x)$			Experimental Value of the Activity $\pm 3\%$ (μCi)
	Percent Error			
	FWHM = 15.0 cm $h = 2$ cm	FWHM = 11.0 cm $h = 2$ cm	FWHM = 8.5 cm $h = 2$ cm	
0-14	1.1 ~22	1.0 ~11	0.9 ~0	0.9
14-44	3.2 ~10	2.7 ~7	3 ~3.5	2.9
44-54	4.2 ~10	4.8 ~2	4.6 ~2	4.7

FIG. 66.—Influence of kernel resolution on accuracy of integral values of $f(x')$ over 0–14, 14–44 and 44–54 cm of extended source.

scintillations, the spatial resolution would be limited by: (a) the dispersion due to the rod, (\approx of its length);⁽⁶⁾ (b) the length of the luminescent track; and (c) the energy interval of the Compton electrons chosen for counting. The choice of the will be the result of a compromise since the resolution will be the result of a compromise since the resolution affected inversely by the square root of the gamma energy (that is the number of light photons per scintillation), whereas the statistical information is proportional to the $1/2$ power of the number of scintillations.

It is not unlikely that the choice will also depend on whether detail of the function $f(x')$, or accuracy of the integral $\int_a^b f(x') dx'$, is considered the more important information as far as the ultimate medical purpose is concerned. An illustration of what may happen is shown in Figure 66 where the information given by the peaking curves is gathered in terms of radioactivity intervals of 14, 30, 10 cm, to simulate dimensions of some organs within the body. It is seen that as the activity is sought over intervals larger than the errors drop sharply within acceptable limits.

A parameter of some practical importance is the interval h along $g(x)$ at which readings are taken. Figure 67 shows the effects of intervals between 1 and 4 cm shown for a resolution of 8.5 cm; it is seen that as the detail is concerned $h = 2$ cm is best in this case. In larger experiments with a resolution of 15 cm (Fig:

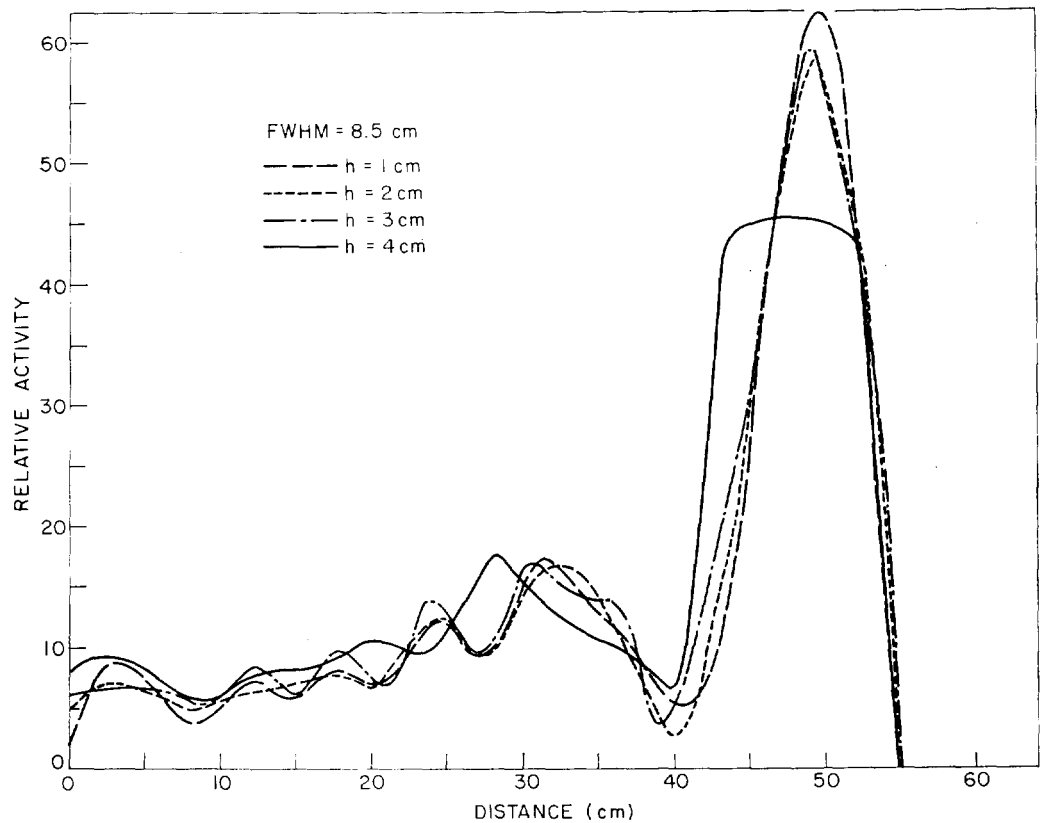


FIG. 67.—Effect of h on details of $f(x')$ with $W_{1/2} = 8.5$ cm

be limited
rod, ($\approx 2-3$
inescent el
the Compt
of the lat
e resolution
e gamma-r
per scintill
proportion
ions.
so depend
accuracy of
re importa
al purpose
pen is giv
y the prec
ivity with
dimensions
at once t
n the $W_{1/2}$
imits.
ce is the
ken. In Fi
nd 4 cm a
hat as far
ase. In sim
(Figure 6)

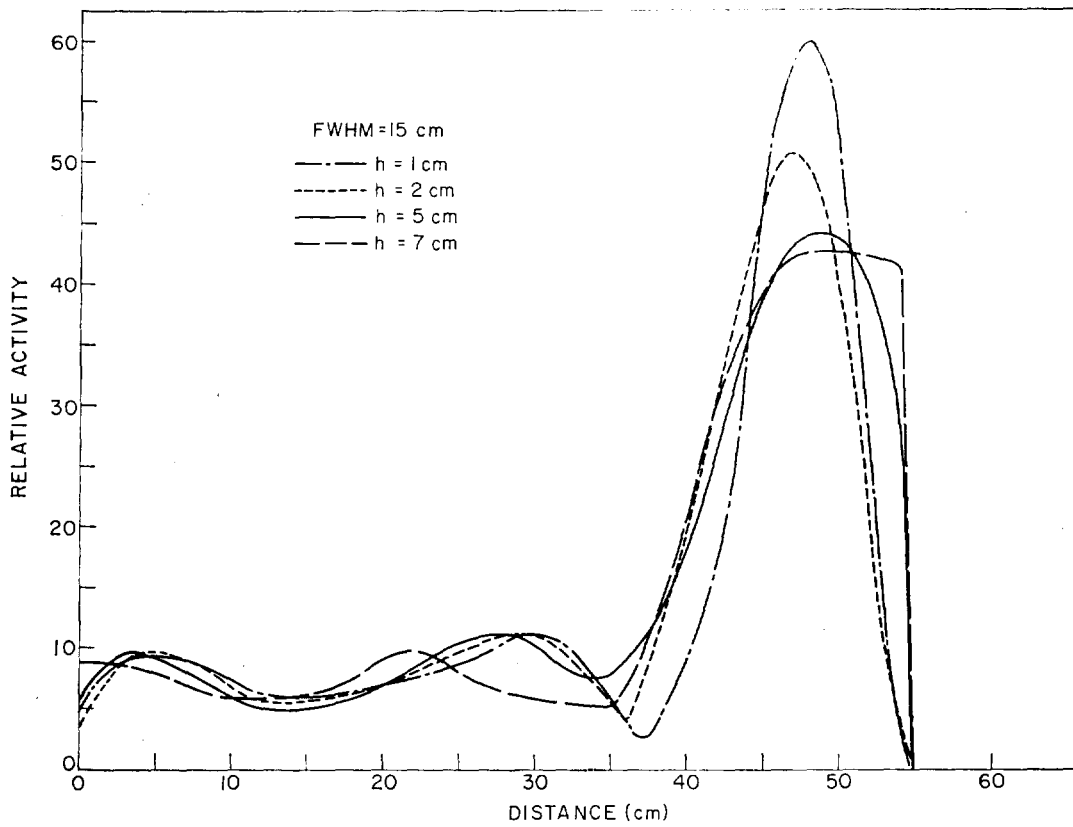


FIG. 68.—Effect of h on details of $f(x')$ with $W_{1/2} = 15$ cm

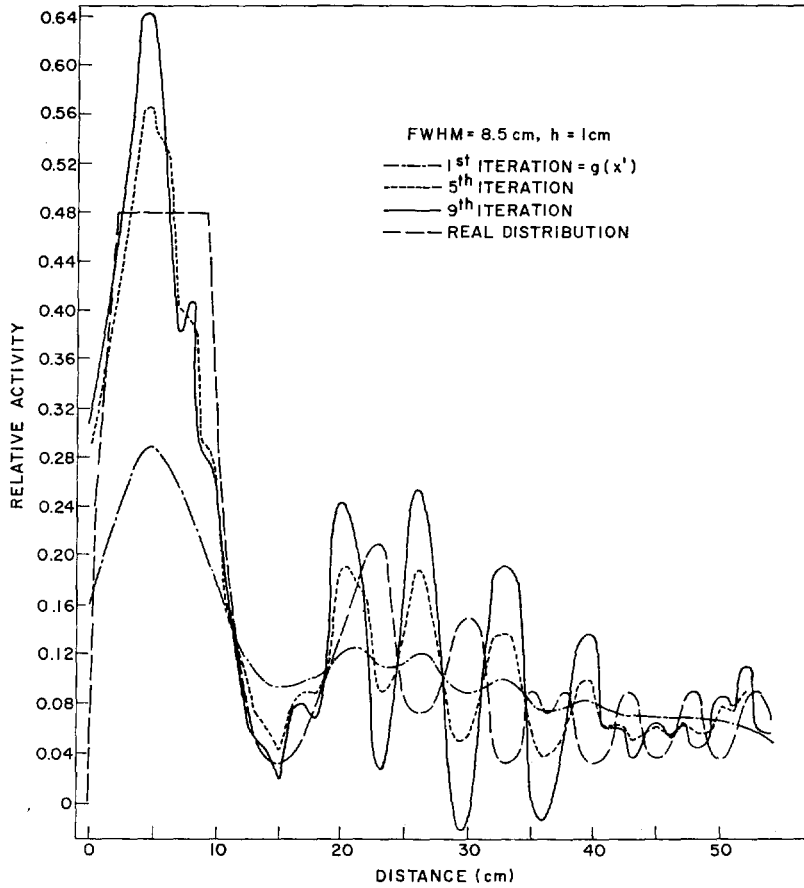


FIG. 69.—Effect of iteration techniques on $f(x')$ solutions

TABLE 32. $W_{1/2}$ VALUES OBTAINED UNDER VARIOUS CONDITIONS OF COLLIMATION, DEPTH, AND SOURCE-TO-ROD DISTANCES

Distance between two consecutive lead bricks, collimator width, cm	Absorber thickness, cm	Distance between source and rod, cm	Pilot Y 2 in. × 2 ft		Pilot B 2 in. × 2 ft	
			Resolution, (a) cm	Efficiency, (b) 10 ³ cpm/μCi	Resolution, (a) cm	Efficiency, (b) 10 ³ cpm/μCi
No collimation	0.0	0.0	10.5	—	8.5	—
3.0	0.0	10.5	8.8	—	6.3	—
3.0	0.0	14.5	8.8	2.8	6.3	—
3.0	0.0	18.5	8.8	—	6.3	—
3.0	2.0	12.5	8.8	—	6.3	3.8
3.0	4.0	14.5	8.8	—	6.3	—
3.0	8.0 ^(c)	18.5	9.2	1.3	6.3	1.3
5.0	0.0	10.5	9.2	—	8.0	9.0
5.0	0.0	14.5	9.2	—	8.0	—
5.0	0.0	18.5	9.2	3.5	8.0	—
5.0	2.0	12.5	9.2	5.5	8.0	6.8
5.0	4.0	14.5	9.4	4.5	8.0	5.2
5.0	8.0	18.5	10.0	2.5	8.0	2.9
1.0	0.0	10.5	—	—	5.3	1.5

(a) Cs¹³⁷ point source.

(b) Cs¹³⁷ 54 cm long distribution.

(c) 7.5 cm of polyethylene + 0.5 cm of plaster of Paris "tissue."

of Figure 69 show that the solution can lead to generated peaks and valleys and that their location be seriously misplaced.

Preliminary results with cylindrical plastic rods collimated with sources at realistic depths are shown in Table 32; from the few experiments made we conclude that the resolutions attainable simulated clinical conditions are of the order of less and that the results obtained with the same dimensional source are similar to those obtained with crystal.

With larger prismatic rods, but without effort to improve the ensuing crude light piping, the resolution of the kernel gets worse (Table 33); hence, one is limited with present technology to 5- x 5-cm rods about 100-cm length. It must be noted, however, that faster and more transparent scintillators and more sensitive P.M.'s are already available and that better conditions are expected.

It is our intention, however, to investigate further mathematical and collimation problems with a two-dimensional camera by using a set of six square rods 2 feet in length to look at constructional details of a practical model capable of dealing with a two-dimensional phantom. The actual construction of this type is well under way.

TABLE 33. EFFECT OF ROD CROSS SECTION DIMENSION ON RESOLUTION OF PILOT B ROD^(a)

Rod dimensions, cm	Resolution, cm	Resolution, ρsec	Rod dimensions, cm	Resolution, cm	Resolution, ρsec
5 dia. × 61 L, round	Co = 3.2	460	5 dia. × 91 L, round	Co = 3.9	530
	Cs = 4.3	630		Cs = 5.1	700
			5 × 5 × 91 L, square	Co = 4.6	630
				Cs = 6.0	820
		5 × 10 × 91 L, rectangular with light pipe	Co = 7.5	960	
			Cs = 9.0	1170	
		10 × 10 × 91 L, square with light pipe	Co = 8.7	1175	
			Cs = 10.4	1400	

(a) All wrapped in black paper.

not much could be done by varying h ; within the intervals considered, $h = 5$ cm seems the best. We conclude provisionally, that h should be around $\frac{1}{3} W_{1/2}$, but recognize that more experimentation is needed on this point.

A preliminary inquiry has been made on the possible success of the iterative method of solving Fredholm's equation for the distribution considered above. Results

REFERENCES

1. Bender, M. A. The digital autofluoroscope, *Medical isotope Scanning*, Intern. Atomic Energy Agency, V 1964, Vol. 1, pp. 391-399.
2. Ogata, A., Tao, S. J., and Green, J. H. Recent developments in measuring short time intervals by time-to-amplitude converters. *Nucl. Inst. Methods*, **60**, 141-150 (1968).
3. Potter, R. J. A theoretical and experimental study.

ical fibers, Univ. of Rochester Institute of Optics Report NYO-9033 (April 1960), p. 6-46.

Post, R. F. Resolving time of scintillation counters, *Nuclear Electronics* **10** (6), 56-58 (June 1952).

Marinelli, L. D., Clemente, G. F., Abu-Shumays, I. K., and Steingraber, O. J. Localization of radioactivity *in vivo* by photon time-of-flight techniques. Argonne National

Laboratory Radiological Physics Division Annual Report, July 1967-June 1968, ANL-7489, pp. 1-12.

6. Marinelli, L. D., Clemente, G. F., Abu-Shumays, I. K., and Steingraber, O. J. Localization of scintillations in gamma ray cameras by time-of-flight techniques: Linear resolutions attainable in long fluorescent rods. *Radiology* **92**, 167 (January 1969).

REGULARIZATION UNFOLDING IN LOW γ -RAY ACTIVITY MEASUREMENTS. EVALUATION FOR ONE-DIMENSIONAL SCANNING

G. F. Clemente, L. D. Marinelli, and I. K. Abu-Shumays*

The problem of converting the spatial distribution of the counting rate of a scanning 3" NaI crystal to the distribution of radioactivity in the object being studied involves solution of a Fredholm equation of the first kind. Precision of the results is studied as a function of the physical parameters used in the measurements.

INTRODUCTION

We have reported elsewhere^(1, 2) on various methods for the quantitative determination of the distribution of low level activity in man. We wish here to study, in more detail, one such competitive method, the regularization unfolding method, and specifically, its application to a representative experimental model to be described below. We will analyze the effect of the experimental parameters on the accuracy of the regularization unfolding of low activity scanning data. A comparison of some of our results with results using the usual iterative method^(3, 4) favors the regularization unfolding^(5, 6).

The unfolding problem can be formulated by the following Fredholm equation of the first kind

$$g'(x') = g(x') + \epsilon(x') = \int_a^b f(x) K(x, x') dx \quad (1)$$

where $f(x)$ is the unknown distribution of activity, $g'(x')$ the hypothetically exact and $g(x')$ the actual spectrum or response of the detector, $\epsilon(x')$ the statistical and experimental error superimposed on $g(x')$, and the kernel $K(x, x')$ the point response function.

For simplicity, the present treatment is restricted to one dimension. We start with a known distribution $f(x)$, calibrate (i.e., measure the response kernel by using point sources of known activity), measure the spectrum $g(x')$ corresponding to $f(x)$ and try to reproduce the known distribution $f(x)$ by using the regularization unfolding method.

The distribution of activity $f(x)$ consisted of a polyethylene catheter 0.034" I.D., 270 cm long filled with

Applied Mathematics Division.

radioactive (Cs^{137}) microspheres (≈ 0.725 mm in diameter); the source configuration (54 cm long) consisted of nearly sinusoidal waves of 5-cm amplitude and of varying frequencies set on a light Lucite bar. The total activity ($1.07 \pm 3\% \mu\text{Ci}$) of the distribution was calibrated by proper comparison with the activity ($0.127 \mu\text{Ci}$) of the point source used to obtain the point response function $K(x, x')$.

Measurements of the spectrum $g(x')$ were carried out by taking measurements at various intervals over a single distribution of activity, using a 3" x 3" NaI crystal with different collimators placed in a low background lead well. The crystal was restricted to move on a straight line parallel to the long axis of the distribution $f(x)$.

This paper considers the influence of the following parameters on the calculated distribution $f(x)$: A. previous knowledge of the total radioactivity C which is the integral of the distribution $f(x)$; B. the full width at half maximum (FWHM) of the point response kernel (equivalent to the resolution radius of the collimator); C. the experimental and statistical error superimposed on $g(x')$; D. the quadrature approximations or, equivalently, the interval h between two consecutive readings of $g(x')$; and E. the usefulness of extending the measurements of $g(x')$ beyond the range of the distribution $f(x)$, and thus increasing the information content of $g(x')$. We will proceed to describe the method we used to solve for the distribution $f(x)$. This method has been programmed for the IBM 360 by Mrs. Alice B. Meyer and one of the authors (IKA).

MATHEMATICAL OUTLINE OF THE UNFOLDING PROCEDURE

If one eliminates $\epsilon(x')$ from Eq. (1), the result is a mathematically "ill-posed problem." The measurement $g(x')$ is relatively insensitive to fictitious (positive-negative) distributions f' for which

$$\int_a^b K(x, x') f'(x) dx = \epsilon'(x'),$$

where ϵ' is a distribution whose amplitude is of the order of the magnitude of error in the measurement of $g(x')$. In other words, small errors in $g(x')$ may be amplified to such an extent that the exact solution of Eq. (1) [deleting $\epsilon(x')$] becomes physically meaningless.

Eq. (1) is usually approximated by a linear system of equations, or equivalently, a matrix equation. The interval (a,b) is subdivided into n parts $a = x_1 < x_2 \cdots < x_n = b$, and Eq. (1) is approximated by

$$\sum_{i=1}^n K_{ji} w_i f_i = g_j + \epsilon_j \quad j = 1, \cdots, m, \quad (2)$$

where w_i are weights that depend on the quadrature formula chosen, $K_{ji} = K_j(x_j, x_i)$, $f_i = f(x_i)$, $g_j = g(x_j)$, $\epsilon_j = \epsilon(x_j)$ and x_1, x_2, \cdots, x_m the points at which g is measured. In order that the system of linear equations become meaningful, it is necessary to have $m \geq n$. Introducing the notation $\mathbf{A} = (w_i K_{ji})$, $\mathbf{f} = (f_i)$, $\mathbf{g} = (g_j)$, and $\boldsymbol{\epsilon} = (\epsilon_j)$, Eq. (2) can be written in the matrix form

$$\mathbf{A}\mathbf{f} = \mathbf{g} + \boldsymbol{\epsilon}. \quad (3)$$

The method used for the solution consists in finding the

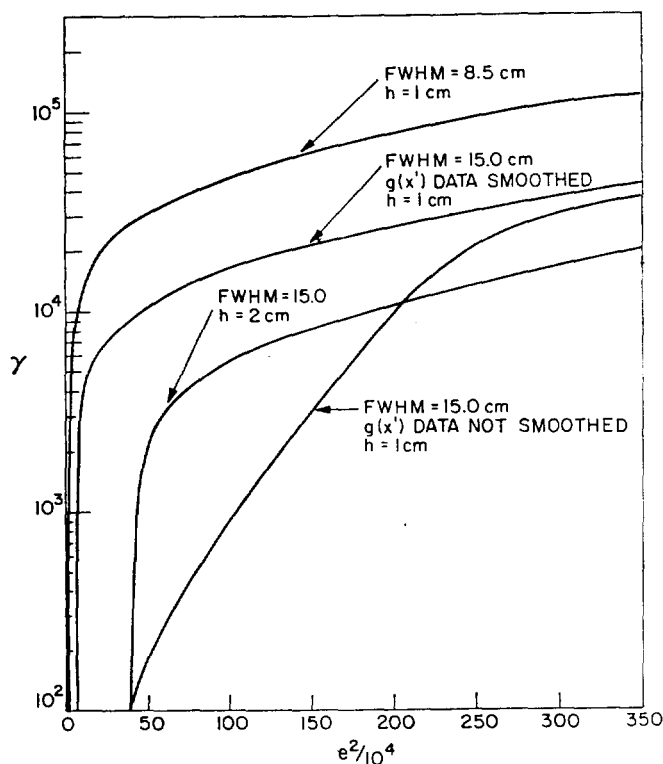


Fig. 70.—Representation of γ 's as a function of

$$e^2 = \sum_{i=1}^m \epsilon_i^2.$$

solution of Eq. (2) which minimizes

$$\sum_{j=1}^m p_j \epsilon_j^2 = \sum_{j=1}^m p_j \left(\sum_{i=1}^n a_{ji} f_i - g_j \right)^2,$$

where $a_{ji} = K_{ji}$ and p_j are appropriate weight. If there is no a priori evidence that some of the more accurate than others, then one may set, for all j . The minimization may be subject to constraint which arises when the total activity C is (see Section A below) and which has the discrete

$$\sum_{i=1}^n w_i f_i = C,$$

and to other constraints such as that of being sufficiently smooth.

A typical smoothness constraint is to minimize the sum of the squares of the second differences. The problem then is to minimize the function

$$\begin{aligned} H(f_1, \cdots, f_n, \lambda, \gamma) &= \sum_{j=1}^m p_j \left(\sum_{i=1}^n a_{ji} f_i - g_j \right)^2 \\ &+ 2\lambda \left(\sum_{i=1}^n w_i f_i - C \right) \\ &+ \gamma^2 \sum_{i=2}^{n-1} (f_{i+1} - 2f_i + f_{i-1})^2 + \gamma^2 (s_{11} f_1 \\ &+ s_{12} f_2)^2 \\ &+ \gamma^2 (s_{n,n-1} f_{n-1} + s_{nn} f_n)^2. \end{aligned}$$

The last two terms in the above equation contain conditions at the end points of the interval (a, b) . The factors λ and γ^2 are Lagrange multipliers. The smoothness of the solution depends on γ^2 , the factor given to minimize the second differences in the case. Four curves are plotted in Figure 70 (see comments in Section C), giving γ as a function of error

$$e^2 = \sum_{j=1}^m p_j \epsilon_j^2$$

for different cases.

Normally, in a given experiment a lower and an upper bound for the value of e^2 of Eq. (4) can be estimated. The γ to be chosen ought to be the one which gives an acceptable value of e^2 .

VARIATION OF THE EXPERIMENTAL PARAMETERS

A. The Knowledge of the Total Amount C of activity

The computer program yields both quantities $f(x)$ from the experimentally measured values of

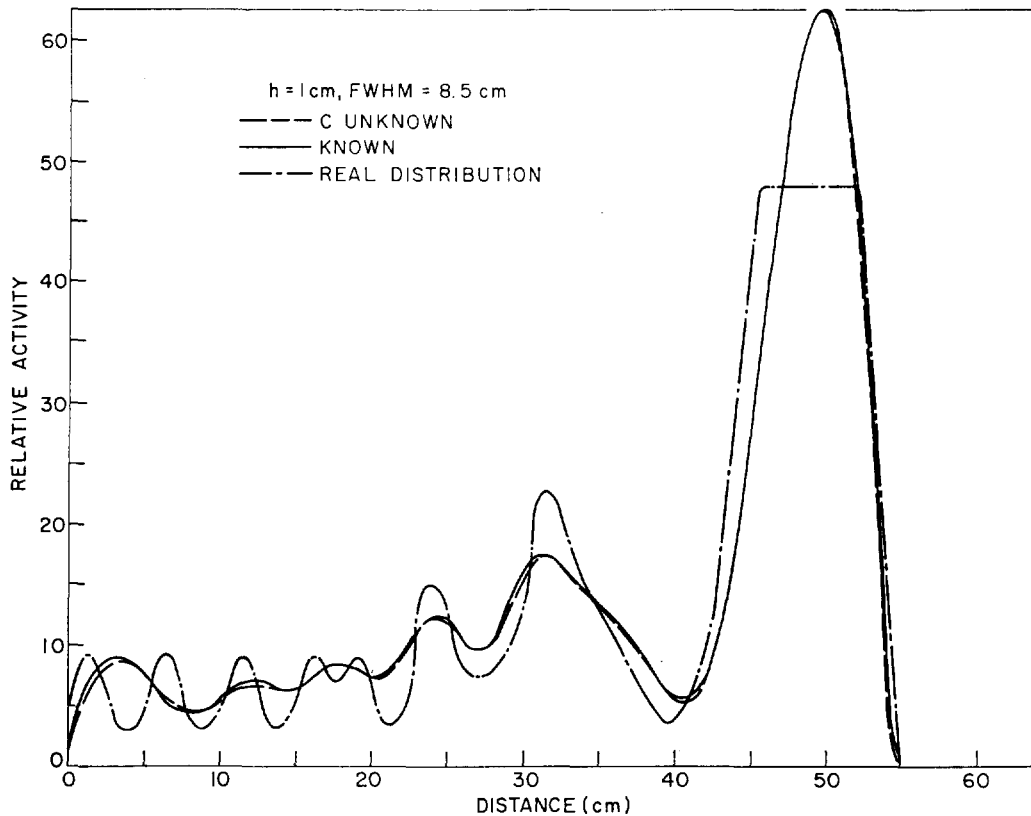


FIG. 71.—Variations in $f(x)$ caused by previous knowledge of C , $h = 1$ cm

The total amount of activity C can also be measured accurately by independent methods.⁽⁷⁾ Intuitively one would think that prior knowledge of the total activity C would lead to a more accurate determination of $f(x)$ and/or the net activities in certain subintervals of (a, b) . However, according to our mathematical method, the "a priori" condition

$$\int_a^b f(x) dx = C \quad (5)$$

is desirable only if (1) C is known to a high degree of accuracy, and (2) the best experimental choice of quadrature (the interval h between two readings) cannot be made a priori. In our calculations, we have elected to use the Simpson rule for quadrature and to take readings of $g(x)$ at equally spaced intervals of length $h = (b - a)/n$.

In Figures 71 and 72 are plotted the distributions $f(x)$ as computed in turn with C unknown and known, together with the actual $f(x)$, respectively for $h = 1$ cm and $h = 4$ cm in the cases of $K(x, x')$ with FWHM = 8.5 cm; Figure 73 gives the integrated activity over the three following intervals of the distribution: (a) 0–14 cm, where the density of activity is constant and low, (b) 14–44 cm, where the density of activity is widely

variable, and (c) 44–54 cm, where the density of activity is constant and high. From Figures 71 and 73 we see that for $1 \leq h \leq 3$ cm, previous knowledge of C does not yield better results; whereas when $h = 4$ (see Figure 72) one can clearly obtain improved results with such knowledge. These implications are also confirmed by using two other collimators whose point response functions have FWHM 11.0 cm and 15.0 cm respectively (Figure 74).

B. The FWHM of $K(x, x')$

The same distribution of activity was measured, using the three different point response functions $K(x, x')$ with FWHM of 15.0 cm, 11.0 cm, and 8.5 cm, respectively, plotted together in Figure 75. We assumed that $K(x, x') = K(|x - x'|)$, i.e., K constant and symmetric for every position x of the point source. This approximation is true if there is no absorber material between the distribution and the crystal, and if the backscattering due to the wall of the lead enclosing the entire apparatus is uniform all along the length of the distribution $f(x)$. The three computed values of the distribution $f(x)$ are plotted in Figure 76 together with the real distribution. The statistical errors are between 5%–10% in all cases for both $g(x')$ and $K(x, x')$. In Figure 74 are given

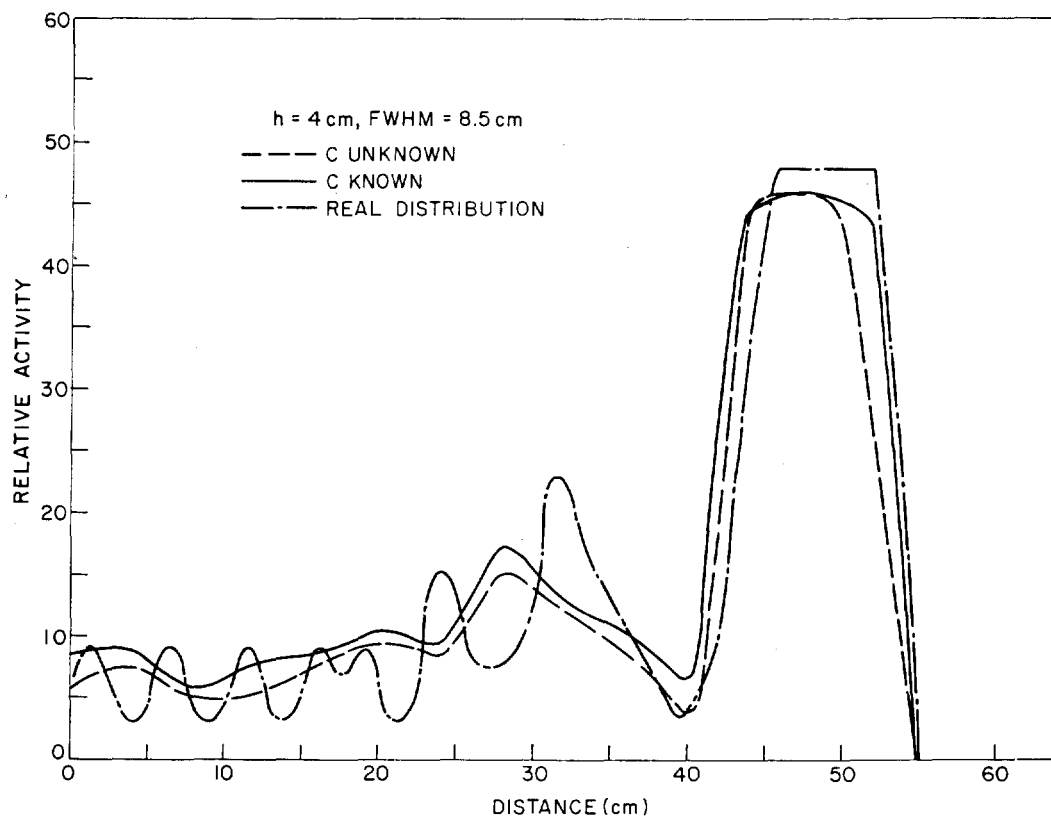


FIG. 72.—Variations in $f(x)$ caused by previous knowledge of C , $h = 4$ cm

Interval on $f(x)$ (cm)	Integrated Activity on $f(x)$ - FWHM = 8.5 cm								Experimental Value of the Activity $\pm 3\%$ (μCi)
	C Unknown				C = 8.5				
	h = 1	h = 2	h = 3	h = 4	h = 1	h = 2	h = 3	h = 4	
0-44	0.9	0.85	1.0	0.7	0.9	0.9	1.0	1.1	0.9
14-44	3.0	2.85	2.9	2.6	3.0	3.0	2.9	3.1	2.9
44-54	4.5	4.6	4.6	4.2	4.6	4.6	4.6	4.3	4.7
0-54	8.4	8.3	8.5	7.5	8.5	8.5	8.5	8.5	8.5

FIG. 73.—Integrated activities over various intervals of $f(x)$ for various h 's.

Interval on $f(x)$ (cm)	Integrated Activity on $f(x)$			Percent Error			Experimental Value of the Activity $\pm 3\%$ (μCi)
	FWHM = 15.0 cm $h = 2$ cm	FWHM = 11.0 cm $h = 2$ cm	FWHM = 8.5 cm $h = 2$ cm				
0-14	1.1	1.0	0.9	~22	~11	~0	0.9
14-44	3.2	2.7	3	~10	~7	~3.5	2.9
44-54	4.2	4.8	4.6	~10	~2	~2	4.7

FIG. 74.—Integrated activity with three different point response functions.

the integrated quantities and the percentage error for the three previously chosen intervals. The total integrated activity C is practically independent of the FWHM of $K(x, x')$. (See above for dependence on h .)

The results of Figures 74 and 76 suggest that the choice of the "best" collimator must be based on the following:*

- (a) the smallest interval Δx_s (larger than h) in the shape of the computed $f(x)$ should resemble the actual distribution, namely acceptable accuracy in the location of the peaks and magnitude of their slope; in our case $\Delta x_s \approx \text{FWHM}$;
- (b) the smallest interval Δx_E where the net (grated) activity

$$\int_{x_i}^{x_i + \Delta x_E} f(x) dx = C_i$$

should have acceptable error. (If $\Delta x_E > \text{FWHM}$, this condition is automatically satisfied.);

- (c) the efficiency of the collimator should be enough to minimize the statistical errors in feasible time intervals of measurement.

* These requirements are similar to those needed to detect and measure radioactivity in various organs of the body.

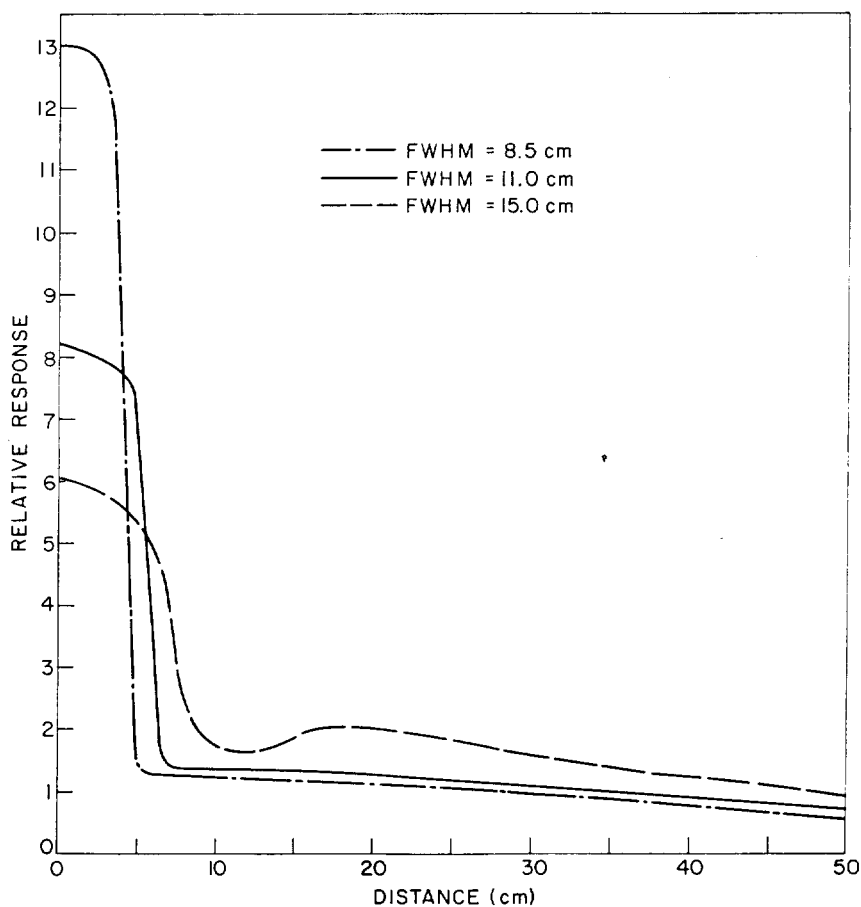


FIG. 75.—Point response function of the tested collimators

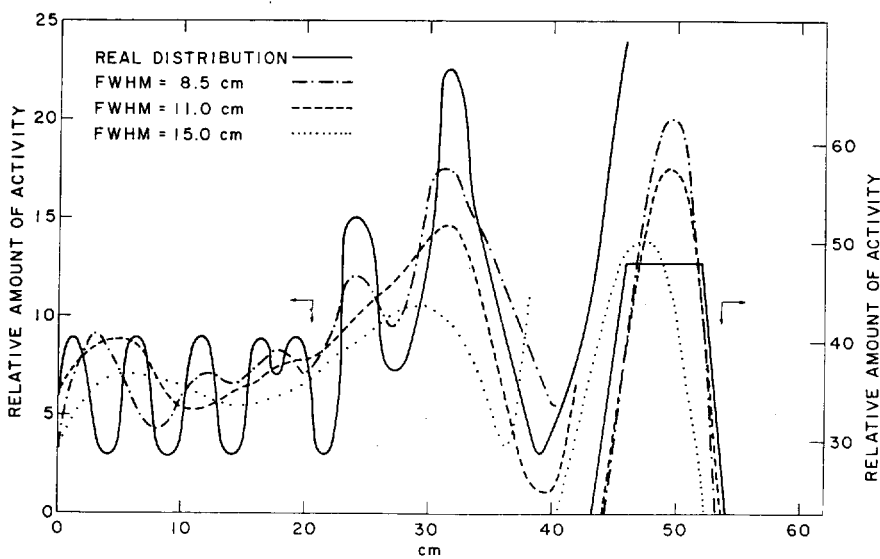


FIG. 76.—Influence of kernel $K(x, x')$ resolution

DOE AR 11000

C. Influence of the Errors in $g(x')$

Usually the selection of the collimation width is related to the limits of errors (statistical plus experimental) in $g(x')$ due to the structure of the system, the quantity of radioactivity available in the distribution, the natural background, and sometimes the limitations on the time available for performing the measurements.

Of significance in our mathematical method is the relationship between γ and the measure of the error

$$e^2 = \sum_{i=1}^m \epsilon_i^2$$

shown by the curves $\gamma(e^2)$ in Figure 70. The selection of the type of collimation and other parameters affects the shape of $\gamma(e^2)$ and consequently influences the determination of the computed distribution. In practice it is difficult to define a general rule concerning the error allowed in $g(x')$; hence it, is desirable to arrange the experimental parameters so as to have the acceptable values of the error e^2 fall in the region of $\gamma(e^2)$ where e^2 is a slowly varying function of γ .

A simple method to determine whether the experimental conditions are well chosen is to plot e^2 for a few different values of γ , as in Figure 70 and check whether: (1) the form of the curve $\gamma(e^2)$ is acceptable (as is the case in the three out of four curves in Figure 70, which have similar shape), and (2) the value of the error $e^2 = \sum_{i=1}^m \epsilon_i^2$ (experimental plus statistical) falls into the range of the curve which is insensitive to small variations in γ (e.g., in Figure 70 for FWHM = 8.5 cm the value of the e^2 should be less than 10^6). The underlying reason is that normally the value of e^2 is only roughly known and, with low sensitivity an error in the

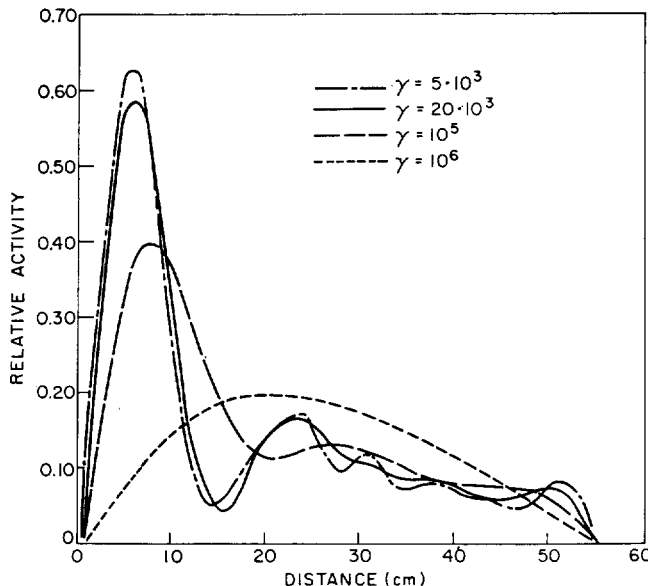


FIG. 77.—Effect of γ 's on $f(x)$

selection of γ by “guessing” at e^2 would not in the results unduly.

Various results for the distribution $f(x)$ obtained using different γ 's for the case FWHM = 8.5 shown in Figure 77; it is easily seen that for $5 \cdot 10^3 \leq \gamma \leq 20 \cdot 10^3$, the shape of $f(x)$ changes very little could be deduced from the corresponding curve (Figure 70), whereas for $\gamma \geq 20 \cdot 10^3$, the results are greatly influenced by the selection of γ and an error in estimation of the experimental value of e^2 could lead to a meaningless $f(x)$.

D. The Interval h between Successive Readings

When carrying out an experiment, the proper choice of the interval h between two consecutive readings $g(x')$ is important for obtaining acceptable results (see Section A above). We saw in Section A (Figure 7) the role played by h in the computation of the total activity under $f(x)$. Figures 78 and 79 show the distribution $f(x)$ obtained using different intervals h in the two extreme cases of FWHM = 8.5 cm and FWHM = 15.0 cm, respectively; these data show that acceptable results can be achieved only for a certain range of values of h . As a general rule, one may propose that the upper limit for h be kept around the FWHM of the point response function $K(x, x')$. The selection of its lower limit, on the other hand, should be strictly correlated with $\epsilon(x')$, namely with the magnitude of statistical noise superimposed on every reading in $g(x')$. In fact, if \bar{h} is less than h , the value of the error $e^2 = \sum_i \epsilon_i^2$ will eventually increase beyond acceptable levels. At such levels of e^2 the computation of the distribution $f(x)$ becomes sensitive to the choice of e^2 ; a wrong estimation of e^2 may make it difficult to obtain a satisfactory value. If a very narrow collimator is selected, and consequently a very small h , is selected, better values of $f(x)$ can be obtained by smoothing the experimental results* $g_i(x')$, namely by reducing the statistical oscillations of the experimental data. This effect, for the case of FWHM = 15.0 cm, $h = 1$, is shown in Figure 79. There, one sees that $e^2 = \sum_i \epsilon_i^2$ as a function of γ in the absence of data smoothing is very sensitive to a change in γ , which is an undesirable situation.

Smoothing the data instead moves the corresponding curve in Figure 70 to the left (reducing e^2), making it similar to the family of the other acceptable curves of e^2 as a function of γ .

E. Extension of Data Beyond the Limits of the Distribution

Intuitively, one expects that a certain improvement of the shape of $f(x)$ near the extremities should

* and $K(x, x')$ if the kernel also has significant statistical error.

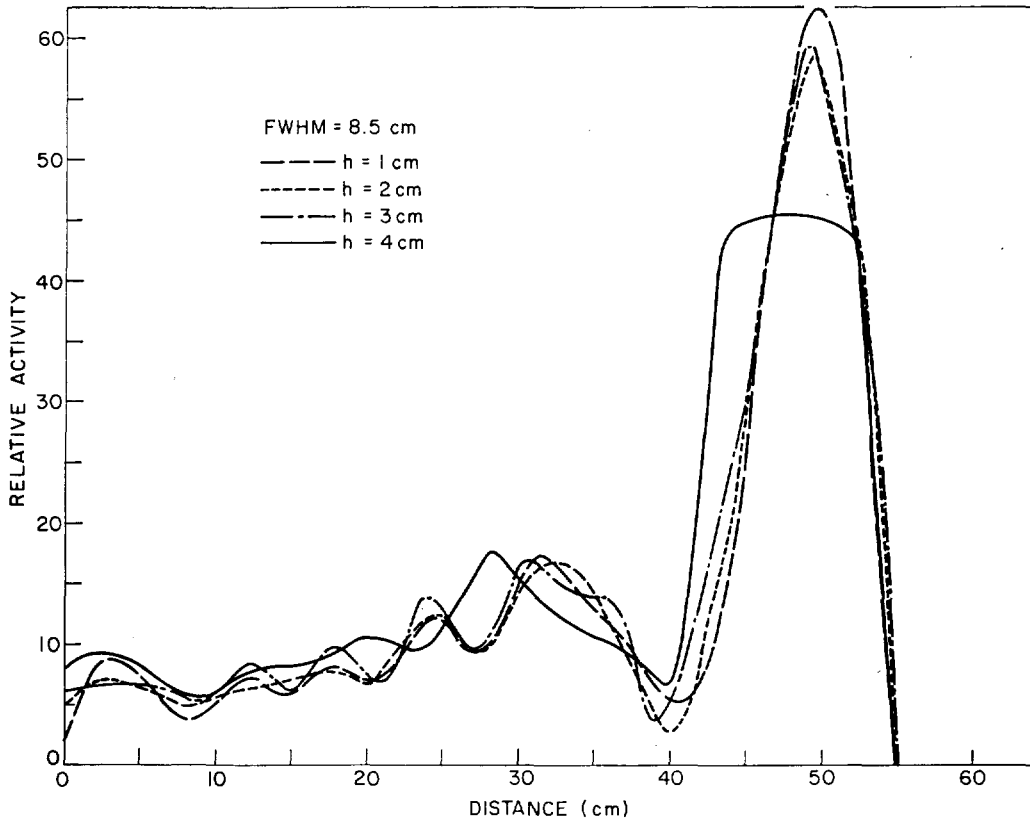


Fig. 78.—Variations in $f(x)$ according to detail in $g(x')$, FWHM = 8.5 cm

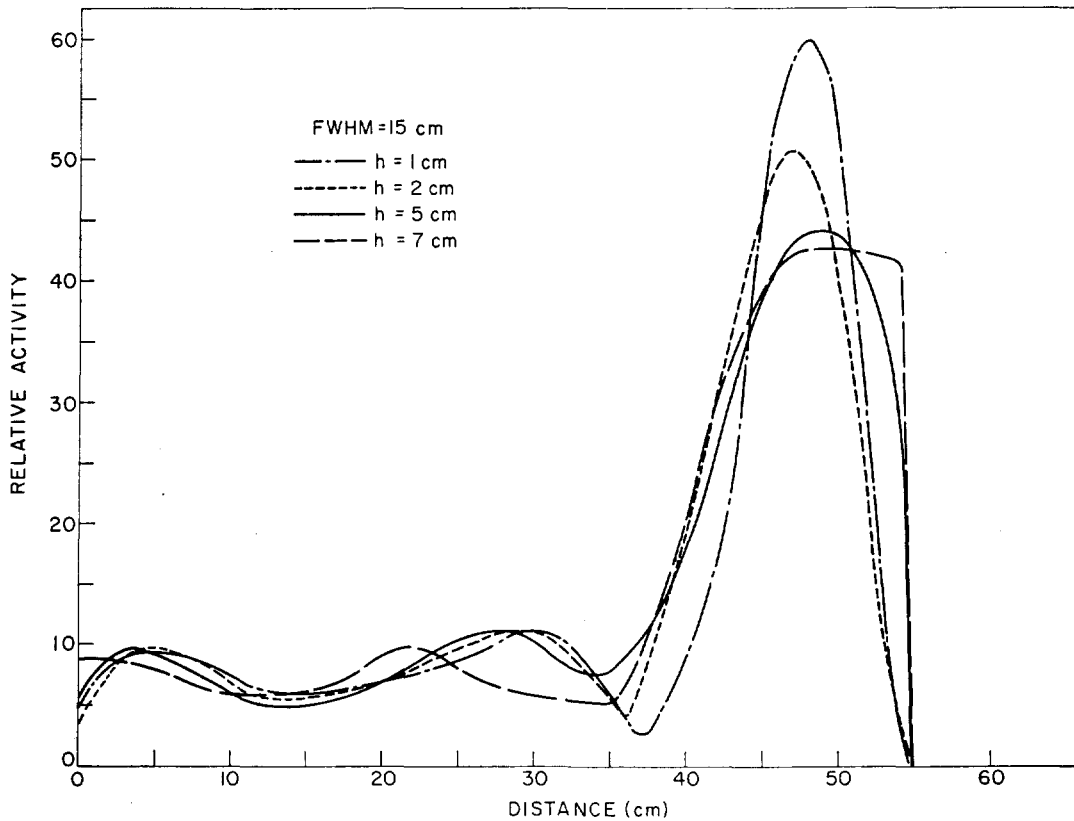


Fig. 79.—Variations in $f(x)$ according to detail in $g(x')$, FWHM = 15 cm

DOE REPORT 15

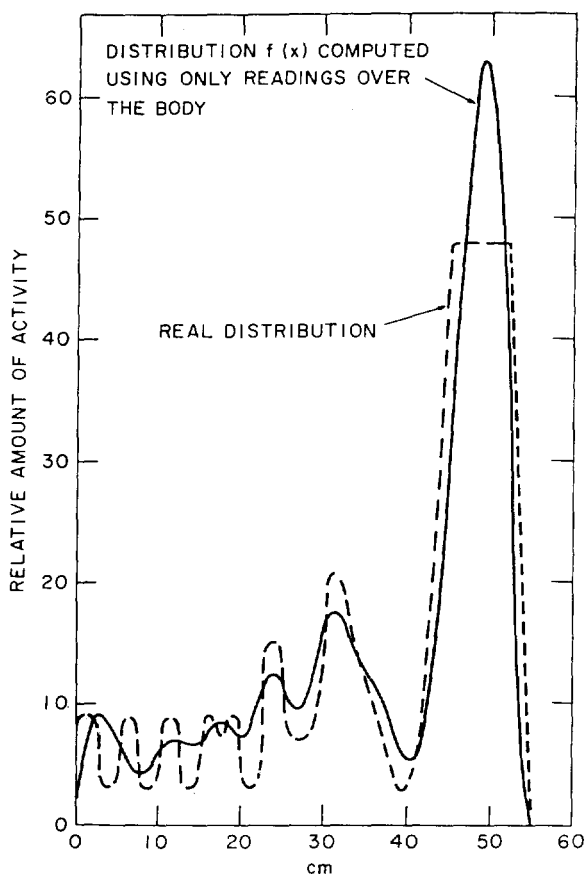


FIG. 80.—Distribution $f(x)$ computed using only readings over the body.

tained by taking readings beyond the interval (a,b) of the actual distribution, and by requiring $f(x)$ to vanish outside this interval. The results for $f(x)$ obtained with and without readings beyond the actual distribution are plotted respectively in Figures 80 and 81. These figures show a clear improvement of the shape of $f(x)$ in the interval 0–14 cm when additional values of $g(x)'$ are used.

F. Tests on the Iterative Technique

In order to establish whether the iterative technique reported elsewhere⁽³⁾ could lead to more accurate results in the case of the distribution $f(x)$ considered here and in the case of the experimental parameters described above, a program of calculations was undertaken for FWHM = 8.5 cm and $h = 1$ cm. The iteration was stopped when $f(x)$ became negative somewhere within the interval (a,b) , or when the error corresponding to $g(x)'$ reached the level of the expected error. The results were deemed unsatisfactory inasmuch as

- the approximations were not converging;
- the amplitudes varied more than in the true known distribution $f(x)$ —in other words, oscillations in the solution were not being dampened;

- the position of the peaks in the computed distribution were erroneous since they were related to those apparent in $g(x)'$; some of those in $g(x)'$ were due to statistical error.

In conclusion, the results were consistent with comments made elsewhere as to the experimental conditions suitable for the success of iterative techniques.

CONCLUSIONS

From the above, we now draw the following conclusions:

- For the distribution $f(x)$ considered here it is possible to obtain fairly accurate results (±3% of total activity, net (integrated) in a certain interval Δx and of the shape) if all the parameters involved in the problem (as collimation, etc., are properly chosen (text above). This is true even if statistical errors in $g(x)'$ and $K(x,x')$ are of the order of 5%.
- The FWHM of the kernel $K(x,x')$ does not seem to influence the calculation of the total (net (integrated) activity in subintervals). In practice, it is impossible to recognize small changes in the shape of $f(x)$ that are separated by distances less than the FWHM and to

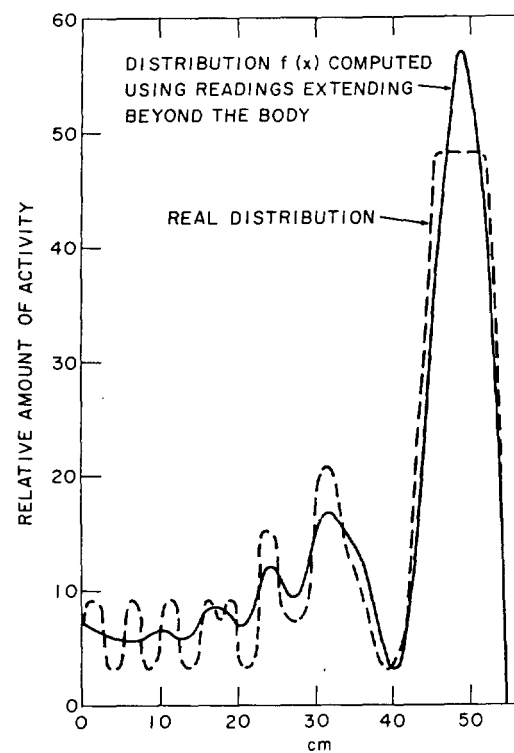


FIG. 81.—Distribution $f(x)$ computed using readings extending beyond the body.

the same time accurate results for the integration

$$\int_{x_i}^{x_i+\Delta x_E} f(x) dx = C_i$$

with $(\Delta x_E) < 2/3$ FWHM.

- (c) The limit on the errors pertinent to $g(x')$ is given not only by intrinsic properties of the instrument (efficiency, natural background, counting time, etc.), but also by the shape of the curve $\gamma(e^2)$. This means that if $\gamma(e^2)$ belongs to a certain family of curves, it may be possible to obtain optimal results on $f(x)$ even if the errors $\epsilon_1(x')$, superimposed on $g(x')$ are rather large (e.g., in Figure 70 for the FWHM = 8.5 cm, the rough value deduced from the experiment is $e^2 \simeq 5,000$; but we would obtain comparable accuracy for the computed $f(x)$ if the errors $\epsilon_1(x')$ were large enough to give a value of $e^2 \simeq 25 \cdot 10^4$, in which case we choose $\gamma \simeq 20 \cdot 10^3$).
- (d) The interval h between two consecutive readings on $g(x')$ can influence strongly the shape of $f(x)$ and consequently the net (integrated) activities C_i 's; good results can be obtained in practice with $h \leq 1/3$ FWHM.

- (e) Improvement in the shape of the computed $f(x)$ near the extremities of the interval (a,b) of the actual distribution can be obtained by taking readings $g(x')$ beyond the interval (a,b) and setting $f(x) = 0$ outside this interval.

The authors wish to acknowledge the technical help of Mr. Richard F. Selman.*

REFERENCES

1. Marinelli, L. D., Clemente, G. F., Abu-Shumays, I. K., and Steingraber, O. J. Argonne National Laboratory Radiological Physics Division Annual Report, July 1967-June 1968. ANL-7489, pp. 1-12.
2. Marinelli, L. D., Clemente, G. F., Abu-Shumays, I. K., and Steingraber, O. J. *Radiology* **92**, 167 (1969).
3. Iinuma, T. A. and Nagai, T. *Phys. Med. Biol.* **12**, 501-509 (1967).
4. DiPaolo, R., Albarède, P., Patau, J. P., and Tubiana, M. *Compt. Rend.* **263**, (Series D) 1160-1163 (1966).
5. Phillips, D. L. *J. Assoc. Comput. Mach.* **9**, 84-97 (1962).
6. Monahan, J. E. *Scintillation Spectroscopy of Gamma Radiation*, Ed. S. M. Shafroth. Gordon and Breach, New York, 1968, pp. 371-428.
7. Marinelli, L. D. Proc. XI Int. Congr. Radiology. Excerpta Medica Int. Congr. Series **105**, 1291-1301 (1966).

* Central Shops Department.

REGULARIZATION UNFOLDING FOR TWO DIMENSIONS: PROGRESS REPORT

I. K. Abu-Shumays*

A solution to a Fredholm equation of the first kind, relevant to a two-dimensional distribution of radioactivity is being sought by smoothing the experimental data by the use of appropriately weighted smoothing matrices. The kernel is assumed to be Gaussian.

In recent work^(1, 2) we have successfully adapted the regularization (smoothing) techniques for unfolding linear spectra,⁽³⁾ to determine unknown distributions of radioactivity per unit length of a one-dimensional phantom model. We report here an extension of the method to two dimensions, which meets both criteria of simplicity of form and considerable economy of computation time.

The distribution $f(x,y)$ of radioactivity in two dimensions is governed by the following Fredholm equations of the first kind

$$\int_a^b \int_c^d dx' \int_c^d dy' K(x, x', y, y') f(x', y') = g(x, y) + \epsilon(x, y), \quad (1)$$

where K is a known response kernel, $g(x', y')$ the measured spectrum and $\epsilon(x', y')$ † is the experimental and statistical error in the measurement of the spectra. We assume that $K = K_1(x, x')K_2(y, y')$, i.e., that the x and y components of the kernel are separable. This is justifiable, for example, whenever the kernel can be approximated by a Gaussian

$$K(x, x', y, y') \simeq C \text{Exp} \left\{ -\left[\frac{(x - x')^2}{4\sigma^2} + \frac{(y - y')^2}{4\sigma^2} \right] \right\}. \quad (2)$$

For numerical calculations, the domain of the distribution $f(x,y)$ and the range of the spectra $g(x', y')$ are covered with a hypothetical grid suitable for mathematical treatment. (For simplicity, we select a uniform grid with size up to 100×100 .)

If we neglect the error term, Eq. (1) is then transformed to the matrix equation

$$AFB = G, \quad (3)$$

† It is well known that without exact knowledge of the magnitude of the error term, Eq. (1) is a mathematically ill-posed problem for the distribution $f(x', y')$.

* Applied Mathematics Division.

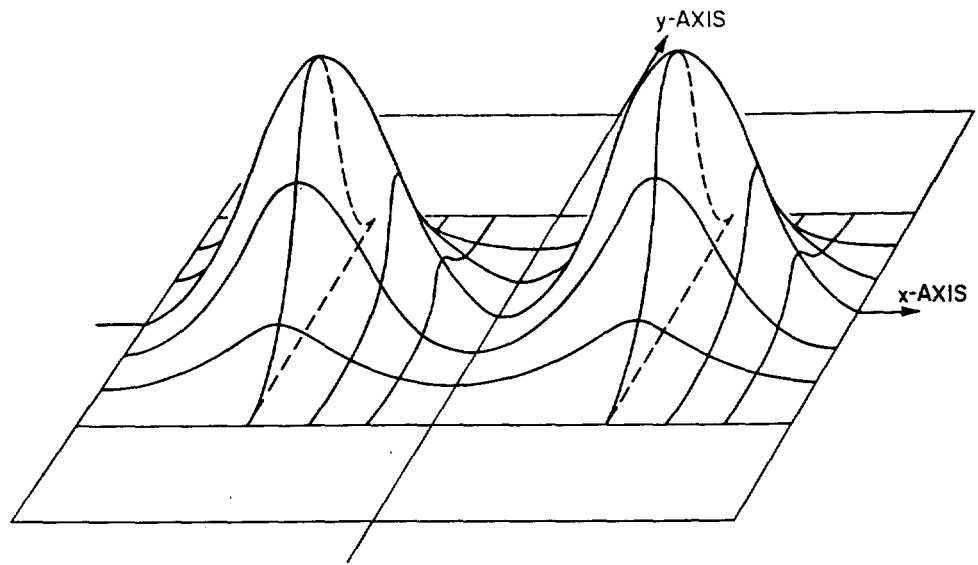


FIG. 82.—Example of a surface studied

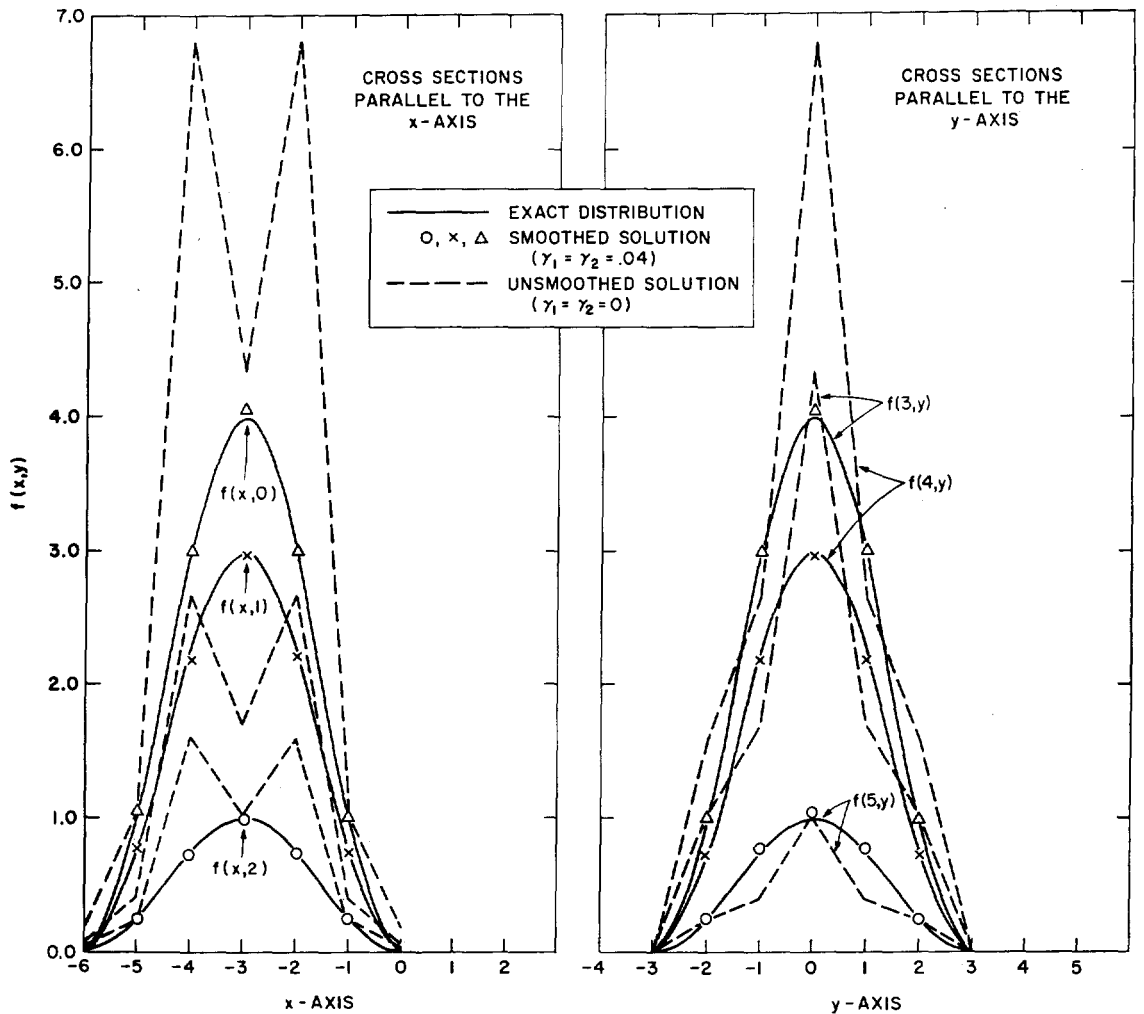


FIG. 83.—Comparison of both the unsmoothed solution and the smoothed solution with the exact distribution for two sets cross sections.

where the matrices A and B correspond to the components K_1 and K_2 of the response kernel, multiplied by appropriate quadrature weights. The regularization unfolding is based on the physically meaningful assumption that (except possibly at a few irregular locations) the magnitude of the activity $f(x,y)$ cannot change abruptly between one point and its immediate neighbors on the grid or between two adjacent grids; in other words, we require the surface $f(x,y)$ of the distribution to be sufficiently smooth. The solution of the matrix equation (3) subject to our smoothness requirements becomes

$$F = [A^T A + \gamma_1 S_1^T S_1]^{-1} A^T G B^T [B B^T + \gamma_2 S_2 S_2^T]^{-1}, \quad (4)$$

where S_1 and S_2 are appropriate smoothing matrices and γ_1 and γ_2 are corresponding weights. Usually it suffices to compute Eq. (4) for a few values of γ_1 and γ_2 in order to estimate the acceptable values of these weights γ_1 and γ_2 . The acceptable values of γ_1 and γ_2 are those which would lead to a new spectrum G' with an error comparable to the expected statistical and experimental error in the given spectrum.

Figure 82 shows a typical surface studied and Figure 83 compares both the usual (unsmoothed) solution ($\gamma_1 = \gamma_2 = 0$) and the smoothed solution ($\gamma_1 = \gamma_2 = 0.04$) with the exact distribution for two sets of three typical cross sections, each parallel to the x and y axis, respectively. Because of symmetry, the sets of Figure 83 correspond to only one of the peaks of Figure 82. The error in the spectra $g(x',y')$ in this case was between 24% and 28%.

A detailed analysis of the two dimensional regularization unfolding described above is currently being prepared for publication.

REFERENCES

1. Marinelli, L. D., Clemente, G. F., Abu-Shumays, I. K., and Steingraber, O. J. Argonne National Laboratory Radiological Physics Division Annual Report, July 1967-June 1968. ANL-7489, p. 1.
2. Clemente, G. F., Marinelli, L. D., and Abu-Shumays, I. K. This report.
3. Phillips, D. L. *J. Assoc. Comput. Mach.* **9**, 1 (1962).

METABOLISM OF ^{232}Th DECAY SERIES RADIONUCLIDES IN MAN AND OTHER ANIMALS FOLLOWING INTRAVASCULAR ADMINISTRATION OF THOROTRAST

R. M. Parr*, H. F. Lucas, Jr., and M. L. Griem†

The activities of ^{232}Th decay series radionuclides have been studied in tissue samples from 6 human patients and 9 experimental animals to whom Thorotrast had been administered intravascularly. In favorable cases where analyses could be commenced before extensive *in vitro* radioactive growth or decay had occurred, the *in vivo* activities of seven nuclides, ^{232}Th , ^{228}Ra , ^{228}Ac , ^{228}Th , ^{224}Ra , ^{212}Pb , and ^{212}Bi , were determined. The available information on the translocation of these nuclides within the body is reviewed, and current "best-estimates" are derived for the distribution of activities and consequent dose rates in the tissues of typical long-term Thorotrast patients. The anomalous behavior of ^{228}Ra , which is retained in the reticuloendothelial system in high concentrations, is explained by a model which postulates that atoms are trapped within the Thorotrast particles unless the recoil distance through which they move at the moment of their creation is sufficient to allow their escape.

INTRODUCTION

Thorotrast is a commercial preparation of colloidal thorium dioxide which was introduced as a contrast medium for radiography around 1931. Because of its

excellent contrast properties and its ease of administration, it was widely used for many years, mainly for angiography but also in other applications such as retrograde pyelography. Around 1945, however, it came into disrepute when the possibility was recognized of undesirable delayed sequelae resulting from its radioactivity and negligible excretion rate. Since then, its use in man has been largely discontinued.

Despite this diminished importance in radiography, interest in the metabolic characteristics of Thorotrast has tended to increase. As was pointed out by Marinelli,⁽¹⁾ the many thousands of patients to whom it was administered intravascularly during the years that it was in common usage now constitute an invaluable and irreplaceable potential source of data on the effects of low level and long-term irradiation in man. This is particularly the case for those patients to whom it was administered for cerebral angiography since they have a long life expectancy, and any observable effects are not likely to be related to the need for treatment.

Of fundamental importance in any study of the radiation effects of Thorotrast is, of course, the accurate

* Present address: Department of Research and Isotopes, International Atomic Energy Agency, Vienna.
† Argonne Cancer Research Hospital, Chicago.

TABLE 34. DECAY PARAMETERS OF THE ^{232}Th DECAY SERIES

Serial number of decay product	Nuclide	Half-life	Particle emitted and energy, MeV		Principal gamma-ray energies ^(a)
0 (parent)	^{232}Th	1.4×10^{10} y	α	4.10	
1	^{228}Ra	5.75 y	β	0.053	
2	^{228}Ac	6.13 h	β	1.55	0.34; 0.97; others up to
3	^{228}Th	1.91 y	α	5.42 (0.83)	
				5.33 (0.17)	
4	^{224}Ra	3.62 d	α	5.67	0.241 (weak)
5	^{220}Em	54.5 s	α	6.26	—
6	^{216}Po	0.16 s	α	6.77	—
7	^{212}Pb	10.6 h	β	0.36	0.239
8	^{212}Bi	60.5 m	α (0.337)	6.05	0.73 (weak)
			β (0.663)	2.20	
9	^{212}Po	0.14 μs	α	8.78	—
10	^{208}Tl	3.1 m	β	1.77	0.58; 2.62; and other

^(a) Only gamma rays greater than 0.10 MeV in energy and more than 1% abundant are listed.

determination of radiation dose. However, dosimetry in these cases is a problem of great complexity since energy is deposited within the tissues not only by the parent nuclide, ^{232}Th , but also by a long series of radioactive descendants (Table 34), each of which is translocated according to its own peculiar metabolic characteristics. Other problems also serve to complicate the dosimetry, such as the very nonuniform distribution of the colloid in the body and in any one organ, as well as the self-absorption of the radiation within aggregates of Thorotrast particles.

The general metabolic patterns of behavior of the longer lived nuclides ^{232}Th , ^{228}Ra , ^{228}Th and ^{224}Ra can be described in broad outline from the work of Rundo,⁽²⁻⁴⁾ Rotblat,⁽⁵⁾ Kaul⁽⁶⁻⁸⁾ and their coworkers in Europe, and of Hursh⁽⁹⁻¹⁰⁾ and Marinelli^(11, 12) and their collaborators in the United States. To a lesser extent, data are also available on the metabolism of the shorter-lived daughter products ^{220}Em ,^(10, 13, 14) ^{212}Pb , and ^{212}Bi .^(2, 6) However, much of this knowledge is based on a very small number of tissue measurements, which particularly for the shorter-lived daughter products, is very scanty indeed.

The present program of investigation was undertaken with the aims of (1) checking the validity of some of the currently accepted data on Thorotrast metabolism and (2) studying particularly the metabolism of the shorter-lived thorium daughter products, ^{228}Ac , ^{224}Ra , ^{212}Pb , and ^{212}Bi . On the basis of this knowledge it was hoped to obtain a better understanding of the factors on which the dosimetry of Thorotrast depends. This report also seeks to summarize the more important measurements of other workers in this field, and hence to derive the current "best estimates" of the radiation dose delivered to the tissues of Thorotrast patients.

MATERIALS AND METHODS

Sources of Tissue Samples Analyzed

The attainment of the main objectives of the investigation required a study of tissue samples from typical Thorotrast patients, most of whom received injections of the material 20 to 30 years previously. To this end, various small autopsy samples were obtained for analysis through the kind cooperation of several physicians who had an interest in the Thorotrast problem. However, it proved extremely difficult to gain access to more than a very small number of such specimens at a sufficiently early time after death for the study of the shorter-lived daughter products. For this reason—but also to obtain data on the metabolism of Thorotrast—the investigation of long-term Thorotrast patients was supplemented in several ways. Firstly, short-term studies were conducted on terminal cancer patients injected intravenously through a catheter with known amounts of Thorotrast. Selected tissue samples were examined promptly after death. Secondly, a series of animal experiments were performed using rats and dogs injected intravenously and then sacrificed after intervals up to about 2 weeks from the time of injection for prompt examination of the tissues. These animal experiments were important for the understanding they afforded of the behavior of the short-lived nuclides, ^{228}Ac , ^{212}Pb , and ^{212}Bi . In such cases could the measurements be commensurate at sufficiently early times after death (≤ 1 hr) to permit determination of the ^{212}Bi activities.

Radioactivity Measurements

Small samples of tissue weighing up to about 100 mg were used for the radioactivity determinations. The growth and decay of ^{228}Ac , ^{212}Pb , and ^{208}Tl were

followed by γ -ray spectrometry over the course of two or three weeks from the time of sampling,* and from the analysis of these data, the "zero-time" activities of ^{228}Ra , ^{228}Ac , ^{228}Th , ^{224}Ra , ^{212}Pb , and ^{212}Bi , were calculated. The activity of the parent isotope, ^{232}Th , was determined at a later time from a measurement by α -ray spectrometry in a Frisch grid ionization chamber. A more complete description of these analytical techniques can be found elsewhere.⁽¹⁵⁾ By these means, estimates were obtained of the *in vivo* activities of the above-mentioned thorium-series nuclides at the moment that biological activity ceased, i.e., generally at the moment of death.

The full utilization of these techniques required that measurements of the γ -ray spectra be commenced within an hour of the time of sampling. For obvious practical reasons this was not always possible, and hence the results for the shorter-lived daughter products, particularly ^{212}Bi , are not as extensive as for the other radionuclides.

Normalization of the Activity Measurements

The activities of the various thorium decay products in a tissue sample at the time of measurement are determined by two quite distinct processes. Firstly, in the living animal, there is the process of selective translocation of each respective nuclide from one organ to another or to the excreta. This may loosely be termed a "biological process," though it may depend on nothing more fundamental than the circulation of the blood. However, the important point is that it ceases to act at the moment of death, or, for a biopsy sample, at the time at which it is withdrawn. Secondly, there is the purely physical process of radioactive growth and decay, which continues regardless of whether the tissue sample exists *in vivo* or *in vitro*. It is the first of these two processes that we wish to understand, and the second is merely a physical phenomenon that complicates the calculations and interpretation of the measurements.

The method of measurement described above allows a correction to be applied for radioactive growth and decay occurring between the time of sampling and the time of measurement. However, this alone is not sufficient. In order to deduce correctly from the radioactivity data some measure of the mobility of each decay product within the body, it is necessary to take account of radioactive growth and decay *in vivo* between the time of injection and the time of sampling. A normalization procedure is, therefore, sought by which the steady state activity ratio for any daughter-

Also referred to as "zero-time," meaning in the case of autopsy samples, the time of death, and in the case of biopsy samples, the time of removal of the tissue from the body.

parent pair can be predicted from measurements at any time after injection, on the assumption that biological processes continue at an unchanged rate. Such a normalization allows a more meaningful comparison of biological transport parameters to be made in patients or animals injected with different batches of Thorotrast, or examined at different times after injection.

For the shorter-lived nuclides, ^{228}Ac , ^{224}Ra , ^{212}Pb , and ^{212}Bi , the normalization procedure presents no difficulty. The activity ratio for any daughter-parent pair reaches a steady state value (within $<2\%$) in about 6 half-lives of the daughter product concerned. Therefore, the steady state activity ratios, $^{228}\text{Ac}/^{228}\text{Ra}$, $^{224}\text{Ra}/^{228}\text{Th}$, $^{212}\text{Pb}/^{224}\text{Ra}$, and $^{212}\text{Bi}/^{212}\text{Pb}$, are given directly by the ratios of the observed activities, provided that the Thorotrast burden is of at least 3 weeks' standing (i.e., 6 half-lives of ^{224}Ra).

In the cases of ^{228}Ra and ^{228}Th , the problem is more complicated. *In vitro*, as may be seen from Figure 84, their activities relative to ^{232}Th continue to change significantly until about 50 years have elapsed from the time of manufacture of the Thorotrast. Moreover, during approximately the first 10 years, the ^{228}Th activity also depends on the initial value of the $^{228}\text{Th}/^{232}\text{Th}$ ratio. *In vivo*, therefore, the attainment of a radioactive steady state is likely to take many years, and until then, the expected steady state ratios, $^{228}\text{Ra}/^{232}\text{Th}$ and $^{228}\text{Th}/^{228}\text{Ra}$, can only be calculated by reference to their activities in the injection material. Even when these activities are known, the calculations can-

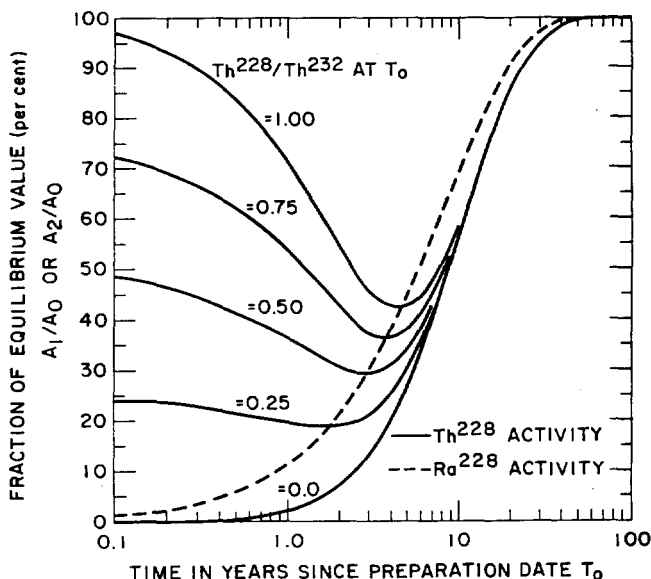


FIG. 84.—*In vitro* activities of ^{228}Ra and ^{228}Th in Thorotrast as a function of time since the preparation date. For ^{228}Th , the dependence of the activity on the initial $^{228}\text{Th}/^{232}\text{Th}$ ratio is shown.

TABLE 35. TISSUE DISTRIBUTION OF THOROTRAST^(a)

Animal	Age of burden	Code	Liver	Spleen	Kidney	Lung	Cortical bone	Bone ^(c) + marrow	Red bone marrow
Man	49d	02	100	258				8.4	
	49d	03	100	100				19.1	
								2.4	
	11y	66	100	134	0.5	0.9		1.9	
	26d	83	100	66	0.7	0.4	0.8	5.0	
	48d	85	100	65	1.0	1.1	1.3	5.8	14
	26y	166 ^(b)	100	604	0.2	0.5			11
Average			100	205	0.6	0.7	1.0	7.1	12.5
Rat	41d	67	100	175	0.4				
	35d	72	100	213	0.8				
	38d	73	100	580	0.9				
	18m	TH2 ^(b)	100	204					
	22m	TH3 ^(b)	100	441					
	12m	TH4 ^(b)	100	252					
	22m	TH5 ^(b)	100	316					
Average			100	312	0.7				

^(a) Concentration of thorium (²³²Th)/g of tissue as % of liver concentration.

^(b) Ratios are based on ²²⁶Ra activities assuming equal f_1 values for all the soft tissues.

^(c) Rib and vertebra, respectively.

TABLE 36. ORGAN DISTRIBUTION OF THOROTRAST IN MAN (²³²Th)^(a)

Organ	W, Organ wt in Standard Man, kg	C, Thorium conc. rel. to liver (from Table 35)	CW	% in organ (100 CW/227.5)
Liver	1.7	100	170.0	75
Spleen	0.15	205	30.8	13.6
Kidney	0.3	0.6	0.2	0.1
Lung	1.0	0.7	0.7	0.3
Cortical bone	7.0	1.0	7.0	3.1
Red bone marrow	1.5	12.5	18.8	8.3
Total			227.5	100
Bone + marrow	10.0	7.1	71 ^(b)	

^(a) The figures in the right hand column give the fractional retention of ²³²Th in the organ, relative to the amount in the whole body. Amounts of Thorotrast contained in organs other than those listed are assumed to be negligible. Thorotrast in lymph nodes, though probably not negligible, has been ignored because of inadequate data.

^(b) The danger in extrapolating from the figure for bone which contains marrow, is demonstrated. This value for the whole skeleton is approximately three times that obtained by extrapolating separately for cortical bone and red bone marrow.

not be carried out rigorously since they depend on metabolic parameters which are inadequately understood. For this reason a number of simplifying assump-

tions and approximations must be made. The mathematical model, and the one which assumes least about the physical and chemical properties of Thorotrast, is presented in an Appendix to this report. The following results have been obtained on the basis of the equations contained therein.

RESULTS AND DISCUSSION

Tissue distribution of Thorotrast (²³²Th)

Measurements were made of ²³²Th concentrations in various tissues from 6 humans and 7 rats. Average concentrations in the various organs are summarized in Table 35. All have been normalized with respect to the concentration in the liver, the organ which contains the major fraction of the total body burden. In this way some of the difficulties which arise in making extrapolations to the whole body can be minimized, e.g., those arising from a nonuniform distribution of activity in each organ. The uncertainty in the ratio between the weight of the sample measured and that of the whole organ (particularly in the case of bone marrow), and inaccuracies in the quoted amounts of Thorotrast injected. On this basis, no significant differences between man and the rat are evident in the extremely meager data.

Extrapolation from the data for man (Table 35) to the whole body has been made by assuming standard weights for the standard man in accordance with the recommendations of ICRP.⁽¹⁶⁾ The pattern of dis-

TABLE 37. ORGAN DISTRIBUTION OF ^{232}Th IN MAN FOLLOWING INTRAVASCULAR ADMINISTRATION OF THOROTRAST

Author	Hursh et al. ^(a)	Kaul	Rundo	ANL group	Parr et al.	Mean values (columns 2-6) <i>M</i>	Fraction of body burden in organ: ^(e) 100 <i>M</i> /144.7 percent
Reference	9	6	3	11, 17	This paper		
No. of cases	4	Several	9	2	6		
Duration	17d-19y	Long term	Long term (mean 12y)	18y, 26.5y	26d-26y		
Method of analysis	Spectro- chemistry	α -ray analysis	γ -ray analysis	α -ray analysis	α, γ -ray analysis		
Liver	100	(52) ^(b) 100	(71) ^(b) 100	100	100	100	69
Spleen	9	(17) 33	(17) 36		18	24	17
Red bone marrow	8	(30) 58	(≤ 12) ≤ 17		11	12 ^(d)	8
Lung	1.8				0.4	1.1	0.8
Skeleton	0.75	(0.8) 1.2		(0.55) ^(b) 0.8 ^(e)	4.1	1.7	1.2
Adrenal	0.003					0.003	0.002 ^(f)
Heart	0.07					0.07	0.05
Intestine	0.6					0.6	0.4 ^(f)
Kidney	0.18				0.13	0.15	0.1
Muscle	5					5	3.5 ^(f)
Pancreas	0.05					0.05	0.03 ^(f)
Thyroid	0.05					0.05	0.03 ^(f)
Total						144.7	100

^(a) Liver, spleen, red bone marrow and lung figures are from authors' "preferred values" for ^{232}Th concentrations in these organs, based on 4 patients (17d, 49d, 18y and 19y burdens). Other figures are based directly on quoted ^{232}Th concentrations (18 and 19y burdens). Organ weights in standard man assumed.

^(b) Quoted distribution as percent of whole-body burden.

^(c) Normalized with respect to the liver content assuming liver burden to be 70% of whole-body burden.

^(d) Weighted mean value, using weighting factor of 0.1 for results of Rundo and Kaul, which were not based directly on measurements of separated red bone marrow, and unit weighting factor otherwise.

^(e) Excluding organs not listed (particularly lymph nodes and perivascular deposits, which may contain a significant fraction of the injected Thorotrast).

^(f) Measurements to be interpreted with caution as they are based on only a single analysis.

tion of ^{232}Th among the various organs of the body, so revealed (Table 36) is in general agreement with the results of other workers. A comparison can be made on the basis of the data presented in Table 37, where, as for Table 35, normalized values relative to the concentration in the liver, are quoted. The results suggest that the major part of the Thorotrast (~95% of that contained in the organs listed) is taken up by the reticuloendothelial system, and that it is distributed between the liver, spleen, and bone marrow, approximately in the ratios 100:24:12.

It is important to note that the percentage values listed in Table 37, last column, refer only to those organs listed, and notably they neglect any consideration of the lymph nodes. Reliable data for the lymphatic system are almost completely lacking, but the activities quoted for patient 166 (Table 35) suggest that the ^{232}Th concentration in certain lymph nodes can exceed that in the liver by approximately a factor of 10. It would be not surprising, therefore, if a significant proportion of the whole-body burden of ^{232}Th

were to be found located in the whole lymphatic system.

Consideration has also been omitted from Table 37 of the activities located in perivascular deposits at the site of the injection. Such deposits are indicative of a poor injection technique. External measurements of Thorotrast patients in Vienna by whole-body profile scanning have shown that the proportion of the total-body radioactivity (of ^{208}Tl) so located, not uncommonly exceeds 50%. The perivascular deposits deserve a separate study.

Considerable caution is called for when using the results of Table 37 to predict the distribution of ^{232}Th in any one Thorotrast patient. Particularly for the liver and spleen, wide departures from these average values—showing no obvious correlations with variables such as the age of the burden—are commonly observed in individual cases. This is evident from the data of Table 35, though undoubtedly here, sampling problems were partly responsible. However, it is also certain that real differences exist. Thus, in a series of 15 patients,

Rundo⁽³⁾ observed that the estimated ^{232}Th content of the whole spleen varied between the wide limits of 8 and 75% of that of the whole liver. Experiments with dogs reported by Zilversmit et al.⁽¹⁸⁾ suggest that such differences are unlikely to be due to the use of Thorotrast batches of different mean particle sizes. It is more likely that the explanation can be found in the different pathological conditions from which these patients suffered, and which were, in part, the reason for the administration of the Thorotrast. As reported by Rankin et al.,⁽¹⁹⁾ wide variations in the relative uptake of colloidal material by liver, spleen and bone marrow, are observed in patients with liver disease.

The estimate of the thorium content of the whole marrow-free skeleton obtained in this investigation was 3.1% of the whole-body burden of ^{232}Th . This is somewhat higher than the values reported by other workers (Table 37, mean 0.6%). These discrepancies are not surprising since all the presently available estimates of skeletal burden are based on extrapolations from very small, and perhaps nonrepresentative, samples of bone and bone marrow. A more thorough investigation, embracing many different parts of the skeleton, is definitely required. Concerning its distribution in bone marrow, a recent autoradiographic study by Simmons⁽²⁰⁾ has shown that Thorotrast (^{232}Th) is deposited in rat bone marrow as a "hot line" at the time of injection and is not translocated further with subsequent bone growth.

The chemical form of the skeletal ^{232}Th is of some interest since it has a bearing on whether the distribution is likely to be diffuse or "hot spot", i.e. concentrated in colloidal particles. The observation by Hursh and his colleagues⁽⁹⁾ of a small but significant excretion

of ^{232}Th during the days immediately following administration of Thorotrast to two patients (0.1% of the administered dose in 17 days, and 0.1% in 10 days) can be taken as evidence that a small portion of the thorium in Thorotrast may exist in a soluble form. Thus, it may well be that the small skeletal burden of thorium in Thorotrast patients is derived from such a soluble pool, in which case, like ^{228}Ac , long times after injection,⁽²¹⁾ it would be expected to have a relatively diffuse distribution.

Tissue Distribution of ^{212}Pb

Many of the thorium daughter products are distributed throughout the body quite differently from the parent nuclide, ^{232}Th . This is the consequence of various mechanisms which operate to bring about selective translocation from one organ to another and into the excreta. The phenomenon is probably most marked for ^{212}Pb and the other daughter products which have low thoron in the decay series. Despite the 54 day half-life of thoron, its being an inert gas allows considerable translocation to occur, even to the extent that approximately 10% is exhaled.^(10, 13, 14)

^{212}Pb is of little direct significance in the dosimetry of Thorotrast since it emits only low energy β rays, and, therefore, contributes very little to the energy deposition within the tissues. Nevertheless, it is an interesting element to study, for reasons less obvious than that its activity happens to be measurable. In most of the tissues its biological half-life is considerably longer than its physical half-life of 10.6 hr.⁽¹⁶⁾ Therefore, there are good grounds for expecting that ^{212}Pb can be used to estimate the activities of its dosimetrically important precursors,

TABLE 38. TISSUE DISTRIBUTION OF ^{212}Pb ^(a)

Animal	Age of burden	Code	Liver	Spleen	Kidney	Lung	Cortical bone	Red bone marrow	Blood
Rat	35d	72	100	111	19				
	38d	73	100	200	32				
	41d	67	100	185	237				
	18m	TH2	100	120	40				
	22m	TH3	100	228	228				
	12m	TH4	100	—	311				
	22m	TH5	100	241	202				
Dog	21d	78	100	17	8 ^(b) 36 ^(c)		9		
Man	48d	85	100	59	8	35	8	30	2
Mean values			100	144	122	35	9	30	2

(a) Concentration of ^{212}Pb /g of tissue as % of liver concentration.

(b) Kidney medulla.

(c) Kidney cortex.

following and ^{210}Po . Additionally, in cases where no estimates of ^{212}Pb activity are available, the ^{212}Pb activity gives some indication of the doses to be expected from the daughter products which follow it in the decay series. Measurements are recorded in Table 38 of the distribution of ^{212}Pb throughout the organs of 7 rats, 1 dog, and 1 human patient. A method of normalization was employed similar to that of Table 35. The results for spleen and kidney in the one human patient who was examined do not appear to agree very well with the results from the experimental animals. The reason for this is not known.

If human kidneys contained ^{212}Pb in amounts comparable to those observed in rats (Table 38), a dose rate would be obtained which, taking account of the absence of any self-absorption of the radiation by Thorotrast particles, would be of comparable magnitude to dose rates in the reticuloendothelial system (RES). However, on present evidence it is unlikely that this is the case. Most, if not all, Thorotrast patients are long since past their youth. Therefore, it is significant that although lead (and bismuth) compounds may produce renal damage in children,^(22, 23) adult renal tissue appears to be relatively insusceptible. The inference that the adult kidneys do not concentrate these elements is strengthened by the observation in rats that a high dietary intake of lead produces high concentrations in the kidneys only in the young and young-adult animals.⁽²⁴⁾

As a consequence of these complicating factors, the data for the dog and rats contained in Table 38 can only be used to give a qualitative picture of the probable distribution of ^{212}Pb in man. Quantitative predictions of the distribution of ^{212}Pb in a Standard Man (Table 39) are, therefore, based solely on the results for patient code number 85. Even here the numbers are subject to large uncertainties. More reliable estimates,

TABLE 39. ORGAN DISTRIBUTION OF ^{212}Pb IN MAN

Tissue	W, Organ weight in standard man, kg	C, ^{212}Pb conc. rel. to liver (from Table 38)	CW	% in organ (CW/3.77) ^(a)
Liver	1.7	100	170	45
Spleen	0.15	50	7.5	2.0
Kidney	0.3	8	2.4	0.6
Lung	1.0	35	35	9.3
Cortical bone	7.0	8	56	14.9
Red bone marrow	1.5	30	45	12.0
Blood cells	2.1	29	61	16.2
Total			377	100

Percent only of those organs listed. Other soft tissues probably contain a significant activity of ^{212}Pb .

TABLE 40. ^{212}Pb ACTIVITIES IN BLOOD CELLS OF THOROTRAST PATIENTS 3 WEEKS AFTER I.V. ADMINISTRATION

Patient code	Thorotrast injected, ml	^{212}Pb activity, pCi/g cells	^{212}Pb in total blood, ^(a) % of whole body
85	48	36	24
83	48	28	19
71	24	20	27
Mean value			23

^(a) Based on (1) known ^{228}Th activity injected, (2) assumption of 4% body burden per day excretion of ^{224}Ra and 10% exhalation of thoron,⁽³⁰⁾ (3) 2100 g blood cells in whole body.

TABLE 41. ACTIVITY RATIOS IN BLOOD FROM ADULT BEAGLES INJECTED WITH ^{228}Th [AFTER STOVER ET AL.⁽²⁵⁾]^(a)

	^{228}Th	^{224}Ra	^{212}Pb	^{212}Bi
Cells	?	?	100	90
Plasma	0.21	5	≤2	10

^(a) The figures are normalized to refer to a volume of blood in which the ^{212}Pb activity of the cellular fraction is 100 (arbitrary units). The activities (same arbitrary units) of the other nuclides in the cellular and plasma fractions are then given by the numbers in the table.

based partly on additional arguments, are presented later in Table 51.

In addition to the autopsy samples referred to in Table 40, several blood samples from short-term Thorotrast patients were examined at 3 days, 1 week and 3 weeks after administration. ^{212}Pb was found in the cellular fraction of the blood, and was indeed the only radionuclide whose presence *in vivo* could be deduced with any certainty. The results of the measurements at three weeks following administration are listed in Table 40. The activities of ^{212}Pb in the blood at three days and seven days following administration were lower at values, respectively, of about 18% and 19% of the whole-body content. The activities in the blood of ^{212}Bi , and, with a larger uncertainty, those of ^{224}Ra and ^{228}Th , can probably be inferred approximately from the data of Stover et al.⁽²⁵⁾ on the metabolism of ^{228}Th in beagles (Table 41).

One of us (HFL) obtained 30 cc of whole blood from a Thorotrast case through the kindness of A. Grillmaier. This case had a whole-body content of 1.5×10^{-7} Ci ^{228}Ra and 1.3×10^{-7} Ci ^{228}Th . The ^{228}Th content in this blood sample was determined by the very sensitive method of Stehney,⁽²⁶⁾ and the ^{228}Ra was determined from the regrowth of ^{228}Th over a two-year period. The estimates of $4 \pm 3^* \times 10^{-16}$ Ci $^{228}\text{Th/g}$ and $4 \pm 15^* \times 10^{-16}$ Ci $^{228}\text{Ra/g}$ are not sta-

* 90% confidence interval.

TABLE 42. EQUILIBRIUM ACTIVITY RATIOS OF THORIUM DAUGHTER PRODUCTS IN LIVER

Batch No.	Animal	Code No.	Duration	$^{228}\text{Ra}/^{232}\text{Th}$	$^{228}\text{Ac}/^{228}\text{Ra}$	$^{228}\text{Th}/^{228}\text{Ra}$	$^{224}\text{Ra}/^{228}\text{Th}$	$^{212}\text{Pb}/^{224}\text{Ra}$	$^{212}\text{Bi}/^{212}\text{Pb}$
12878 (2y) ^(b)	Man	02	49d	0.30 ^(a)	—	—	0.59	—	—
	Man	03	49d	0.32 ^(a)	—	1.01 ^(a)	0.65	—	—
09940 (5-6y) ^(b)	Rat	72	35d	0.34 ^(a)	0.87	0.65 ^(a)	0.54	0.65	0.7
	Rat	73	38d	0.38 ^(a)	0.99	0.77 ^(a)	0.51	0.63	0.8
13098 (4y) ^(b)	Rat ^(c)	65	20d	0.25	1.1	0.97	0.31	1.4	0.5
	Rat	67	41d	0.19	0.98	0.86	0.38	0.37	0.3
	Dog	78	21d	0.18	0.96	0.87	0.55	0.34	—
	Man	83	26d	0.20	—	0.88	0.53	—	—
	Man	85	48d	0.19	—	0.88	0.59	0.63	—
	Rat	TH2	18m	0.30 ^(d)	—	—	0.51	0.54	1.0
	Rat	TH3	22m	0.24	0.94	—	0.52	0.34	0.9
	Rat	TH4	12m	0.25 ^(d)	0.9	—	0.51	0.38	0.8
Rat	TH5	22m	0.21 ^(d)	—	—	0.50	0.41	—	
?	Man	66	11y	0.36	—	1.00	—	—	—
?	Man	166	26y	~0.4 ^(e)	—	1.01	0.75	—	—
Weighted mean				0.27	0.97	0.89	0.53	0.48	0.7

^(a) Possibly an overestimate since no account was taken of the small amount of activity which may have been left absorbed on the walls of the Thorotrast ampoule.

^(b) Approximate time since manufacture, calculated from $^{228}\text{Ra}/^{232}\text{Th}$ ratio.

^(c) This animal was not typical in that, due to a poor injection, most of the Thorotrast was retained at the site of the injection in the tail.

^(d) Calculation based on an assumed $^{228}\text{Th}/^{228}\text{Ra}$ ratio of 0.9.

^(e) Measured by growth of ^{228}Ra γ -activity.

tistically different from zero, but do place an upper limit on the actual concentrations of these radionuclides in blood.

The proportion of ^{212}Pb in the blood observed at early times after administration (~23% of the whole-body burden at three weeks) seems surprisingly high, and it is difficult to account for the fact that it is higher after three weeks than after one day and seven days, respectively. Recent measurements in Vienna on patients with long-term Thorotrast burdens suggest that after several years the proportion is reduced to about 12%. Grillmaier in Germany, for similar patients, has reported values between 1.7% and 23.9%, with a mean of about 8%.⁽²⁷⁾

Steady State Activity Ratios of Thorium Daughter Products in Various Tissues

Steady state activity ratios for various pairs of daughter products have been calculated from the activity data and are presented in Table 42 for liver, in Table 43 for spleen, in Table 44 for kidney, in Table 45 for bone, and in Table 46 for various other tissues. Because of the possibility of a dependence on the batch of Thorotrast used, the results have, in general, been grouped according to the batch number. In a few

cases the ^{232}Th activities, and hence also the $^{228}\text{Th}/^{228}\text{Ra}$ activity ratios, f_1 , were not measured directly but were calculated from Eq. (3) (appendix) using an assumed value for the $^{228}\text{Th}/^{228}\text{Ra}$ activity ratio as indicated in the footnotes to the tables. To the extent that the assumption regarding f_2 is in error, it may also be the calculated value of f_1 be in error (probably <10%).

Mean values of the activity ratios are included in the tables. They were calculated using weighting factors of 0.1 for those measurements which were of inferior accuracy and unity otherwise. It must be remarked, however, that there are some obvious inconsistencies in the results which cannot be explained as arising simply from measurement errors or species differences (e.g., the $^{228}\text{Th}/^{228}\text{Ra}$ activity ratios), but which may depend on the batch of Thorotrast, its age, and the duration of the burden.

Recoil Model to Account for the Observed Activity Ratios

The high activities of most of the daughter products of ^{232}Th in the RES can only be regarded as anomalous unless it is assumed that these nuclides are physically trapped within the particulate material. Otherwise

TABLE 43. EQUILIBRIUM ACTIVITY RATIOS OF THORIUM DAUGHTER PRODUCTS IN SPLEEN

$^{212}\text{Bi}/^{212}\text{Pb}$	Batch No.	Animal	Code No.	Duration	$^{228}\text{Ra}/^{232}\text{Th}$	$^{228}\text{Ac}/^{228}\text{Ra}$	$^{228}\text{Th}/^{228}\text{Ra}$	$^{224}\text{Ra}/^{228}\text{Th}$	$^{212}\text{Pb}/^{224}\text{Ra}$	$^{212}\text{Bi}/^{212}\text{Pb}$
—	12878	Man	02	49d	0.32 ^(a)	—	—	0.74	—	—
—	2y ^(b)	Man	03	49d	0.32 ^(a)	—	0.97 ^(a)	0.74	—	—
0.72	09940	Rat	72	35d	0.23 ^(a)	0.97	0.47 ^(a)	0.44	0.57	0.72
0.88	5 (y) ^(b)	Rat	73	38d	0.20 ^(a)	0.94	0.41 ^(a)	0.38	0.54	0.65
0.55	13098	Rat ^(c)	65	20d	—	—	0.98	—	—	—
0.37	4y ^(b)	Rat	67	41d	0.24	0.94	—	0.28	0.50	0.59
—		Dog	78	21d	0.25	—	0.90	0.37	0.50	—
—		Man	83	26d	0.22	—	0.87	0.63	—	—
—		Man	85	48d	0.21	—	0.94	0.64	0.42	—
1.0		Rat	TH2	18m	0.25 ^(d)	—	—	0.43	0.41	1.0
0.93		Rat	TH3	22m	0.23 ^(d)	1.0	—	0.44	0.21	—
0.8		Rat	TH4	12m	0.22 ^(d)	1.1	—	0.37	<0.5	—
—		Rat	TH5	22m	0.19 ^(d)	—	—	0.36	0.43	—
—	?	Man	66	11y	0.36	—	0.97	—	—	—
—	?	Man	166	26y	~0.4 ^(e)	—	1.03	0.74	—	—
0.70	Weighted mean				0.25	0.97	0.84	0.51	0.45	0.66

^(a) Possibly an overestimate since no account was taken of the small amount of activity which may have been left absorbed on the walls of the Thorotrast ampoule.

^(b) Approximate time since manufacture, calculated from $^{228}\text{Ra}/^{232}\text{Th}$ ratio.

^(c) This animal was not typical in that, due to a poor injection, most of the Thorotrast was retained at the site of the injection in the tail.

^(d) Calculation based on an assumed $^{228}\text{Th}/^{228}\text{Ra}$ ratio of 0.9.

^(e) Measured by growth of ^{228}Ra γ -activity.

TABLE 44. EQUILIBRIUM ACTIVITY RATIOS OF THORIUM DAUGHTER PRODUCTS IN KIDNEY

Batch No.	Animal	Code No.	Duration	$^{228}\text{Ra}/^{232}\text{Th}$	$^{228}\text{Ac}/^{228}\text{Ra}$	$^{228}\text{Th}/^{228}\text{Ra}$	$^{224}\text{Ra}/^{228}\text{Th}$	$^{212}\text{Pb}^{(c)}/^{224}\text{Ra}$	$^{212}\text{Bi}/^{212}\text{Pb}$
09940	Rat	72	35d	1.03	1.4	2.5	0.64	3.5	1.5
5 (y)	Rat	73	38d	1.5	1.5	2.9	0.90	3.4	1.6
13098	Rat	65	20d	—	>1	0.91	—	>5	1.6
4y	Rat	67	41d	—	—	1.18	~1	>7	2.0
	Dog	78	21d	—	—	1.07	1.1	4.8	2.7 ^(a)
	Man	83	26d	—	—	0.94	~1	~2	<1 ^(b)
	Man	85	48d	—	—	0.95	—	—	—
	Rat	TH2	18m	—	—	0.98	~1	~1	—
	Rat	TH3	22m	—	—	—	~1	~3	2.3
	Rat	TH4	12m	—	—	—	~2	~6	1.9
	Rat	TH5	22m	—	—	—	~1	~7	1.8
	Man	66	11y	~0.2	—	~2	—	—	—
	Man	166	26y	—	—	~2	~1	—	—
Weighted mean				1.2	1.4	1.4	0.9	4.7	1.9

^(a) Kidney cortex.

^(b) Kidney medulla.

^(c) ^{212}Pb was generally readily measurable in kidney samples. However the values of $^{212}\text{Pb}/^{224}\text{Ra}$ ratio could only be determined approximately in most cases because of the low activities of ^{224}Ra , which could not be measured precisely.

TABLE 45. EQUILIBRIUM ACTIVITY RATIOS OF THORIUM DAUGHTER PRODUCTS IN BONE

Batch No.	Animal	Code No.	Duration	Sample	$^{228}\text{Ra}/^{232}\text{Th}$	$^{228}\text{Ac}/^{228}\text{Ra}$	$^{228}\text{Th}/^{228}\text{Ra}$	$^{224}\text{Ra}/^{228}\text{Th}$	$^{212}\text{Pb}/^{224}\text{Ra}$	$^{212}\text{Bi}/^{212}\text{Pb}$	
12878	Man	02	49d	Rib ^(a)	0.51 ^(b)	—	—	1.4	—	—	
				Vertebra ^(a)	0.43 ^(b)	—	—	0.8	—	—	
	Man	03	49d	Rib ^(a)	0.38	—	1.10	1.1	—	—	
				Vertebra ^(a)	1.2	—	1.03	1.3	—	—	
09940	Rat	72	35d	Long bones	6.1	1.1	1.8	1.0	2.2	—	
	Man	83	26d	Femur	1.7	—	1.16	—	—	—	
	Man	85	48d	Skull	—	—	1.06	—	—	—	
	Rat	TH2	18m	Long bones	>>1	0.9	—	1.3	0.8	~1	
	Rat	TH2	22m	Long bones	>>1	1.3	—	1.3	0.7	~1	
	Rat	TH4	12m	Long bones	>>1	0.8	—	1.6	0.7	~1	
	Rat	TH5	22m	Long bones	>>1	—	—	1.6	1	—	
	Man	66	11y	Rib ^(a)	0.53	—	0.9	—	—	—	—
				Vertebra ^(a)	0.45	—	0.9	—	—	—	—
	Man	166	26y	Femur	—	—	~1.0	1.7	—	—	
	Weighted means					2.7	1.0	1.4	1.8	0.9	1

^(a) Containing bone marrow.

^(b) Calculation based on an assumed $^{228}\text{Th}/^{228}\text{Ra}$ activity ratio of 1.00.

would be expected that many of them, and particularly ^{228}Ra , would be translocated to other organs or excreted. Since all the decay products are ultimately derived from ^{232}Th or ^{228}Th located within the particulate phase, there is no problem in explaining the fact that some of these decay-product atoms are physically confined within the particles. What *does* require an explanation, however, is the inference from the biological data that not all the decay-product atoms remain bound with the ^{232}Th in this way. It is probably significant in this connection that in experiments with Thorotrast samples from the same batch but in different animals and for different durations of the burden, the $^{228}\text{Ra}/^{232}\text{Th}$ ratios reported for the RES cover rather a narrow range of values (see for example Tables 42 and 43, batch 13098). The "retention" of ^{228}Ra therefore appears to be a property of the Thorotrast itself rather than the animal.

A plausible mechanism for the escape of radioactive daughter products from the Thorotrast particles might be thought to be diffusion. However, the physical half-life of a radionuclide would then be one of the most important parameters determining its fractional retention. Consideration of the available biological data for each thorium daughter product in relation to its physical half-life, renders this possibility unlikely (see Table 50). Particularly this is evident in the case of the two radium isotopes, ^{228}Ra (half-life 5.8 years; fractional retention at late times in the particles of the RES ~0.5) and ^{224}Ra (half-life 3.6 days; fractional retention in the particles of the RES ~0.7), since a

diffusion mechanism would require the fractionation to depend on the inverse square root of half-life.

A more plausible mechanism predicts that daughter products can escape from the particles by virtue of recoil energy which they gain at the moment of creation.⁽²⁸⁾ In the case of those nuclides which are formed concurrently with the emission of an α ray from the parent nucleus, this recoil energy is considerable (Table 47). By the application of standard energy relationships for heavy nuclei^(29, 30) it is calculated that a ^{228}Ra atom, for example, has a recoil range of approximately 60 Å in ThO_2 . The important consideration now is whether this is so long compared with the size of Thorotrast particles. From measurements of electron micrographs it appears that the particle size is not closely controlled, for it has been variously reported as 30 to 100 Å with a mean of 70 Å,⁽³¹⁾ 80 to 200 Å,⁽³²⁾ and 55 ± 25 Å.⁽³³⁾

Nevertheless, these are of the same order of magnitude as the calculated recoil ranges of several thorium decay products, and it is, therefore, to be expected that a substantial proportion of these daughter products would be able to escape from the particulate phase of the Thorotrast. In the case of atoms formed by β transitions, the recoil range is very much lower. Nevertheless, the recoil energy commonly exceeds that required for breaking chemical bonds (1–5 eV) and would thus be sufficient to allow some of the atoms to escape from surface locations on the particles to break free, even if the change in chemical state alone were not sufficient.

TABLE 46. EQUILIBRIUM ACTIVITY RATIOS OF THORIUM DAUGHTER PRODUCTS IN SELECTED TISSUES

Tissue	Animal	Code No.	Batch No.	Duration	$^{228}\text{Ra}/^{232}\text{Th}$	$^{228}\text{Ac}/^{228}\text{Ra}$	$^{228}\text{Th}/^{228}\text{Ra}$	$^{224}\text{Ra}/^{228}\text{Th}$	$^{212}\text{Pb}/^{224}\text{Ra}$	$^{212}\text{Bi}/^{212}\text{Pb}$
Red bone marrow (vert.) (vert.) (sternum)	Man	85	13098	48d	0.21	—	0.93	0.68	1.1	—
	Man	166	?	26y	—	—	1.0	0.58	—	—
	Man	166	?	26y	—	—	1.1	0.60	—	—
Weighted mean					0.21	—	1.0	0.6	1.1	—
Marrow (vert.) ^(a) Matrix (vert.) ^(b)	Man	85	13098	48d	0.29	—	0.89	1.02	0.82	—
	Man	166	?	26y	—	—	1.1	2.4	—	—
Weighted mean					0.29	—	1.0	1.7	0.8	—
Lung	Man	66	?	11y	~0.5	—	~1.0	—	—	—
	Man	83	13098	26d	—	—	0.86	—	—	—
	Man	85	13098	48d	—	—	0.86	~1	~18	—
	Man	166	?	26y	—	—	1.0	~2	—	—
Weighted mean					0.5	—	0.9	1.5	18	—
Lymph node	Man	166	?	26y	—	—	0.90	0.89	—	—
	Man	66	?	11y	0.25	—	~1.2	—	—	—
Weighted mean					0.25	—	0.9	0.9	—	—
Perivascular deposit ^(c)	Rat	65	13098	20d	—	0.96	—	0.97	—	—
	Rat	67	"	41d	1.47	0.89	1.08	1.08	0.94	0.71
	Rat	TH2	"	18m	>1	~1	—	~1	~1	~1
	Rat	TH3	"	22m	>1	~1	—	~1	~1	~1
	Rat	TH4	"	12m	—	~1	—	0.5	0.7	0.7
	Rat	TH5	"	22m	>1	—	—	1.05	0.8	—
	Rat	73	09940	38d	2.1	0.8	0.90	2.2	0.98	—
Rat	72	"	35d	1.7	1.06	0.96	2.2	0.81	0.82	
Weighted mean					1.7	0.9	0.98	1.3	0.9	0.8
Bile	Dog	78	13098	21d	—	—	—	—	~7	6

^(a) Spongy marrow matrix from which the red bone-marrow was extracted by pressure.

^(b) Spongy marrow matrix from which the red bone-marrow was completely extracted by means of a jet of water.

^(c) Rat tail at site of Thorotrast administration.

for this to happen. The size of the particles is such that a significant proportion of the atoms they contain could be in surface locations (~20%). Escape following a low energy recoil may therefore be an important mechanism, especially for ^{228}Th (vide infra).

According to the proposed recoil mechanism, the escape of recoiling atoms from the particles would be expected to depend strongly on the ratio of the particle size to the recoil range. The particles are reported to be irregular in shape and probably flat,⁽³¹⁾ and, therefore, we may provisionally regard them as being intermediate between a sphere and a plane. It is a fairly simple mathematical exercise to derive the relationships for the escape of recoiling atoms from particles of these two shapes, as illustrated in Figure 85. It is evident from either of the curves that the proportion of recoiling atoms expected to escape depends strongly

TABLE 47. RECOIL ENERGIES OF THORIUM SERIES NUCLIDES

Nucleus	Transition by which it is formed	Maximum recoil energy
^{228}Ra	α	70 keV
^{228}Ac	β, γ	0.1 eV
^{228}Th	β, γ	16 eV
^{224}Ra	α	97 keV
^{220}Em	α	103 keV
^{216}Po	α	116 keV
^{212}Pb	α	128 keV
^{212}Bi	β, γ	2.3 eV
^{212}Po	β, γ	19 eV
^{208}Tl	α	116 keV

on the particle size. In the case of ^{228}Ra , for example, the observed proportion was approximately 75% ($^{228}\text{Ra}/^{232}\text{Th} = 0.25$, Tables 42 and 43) which ob-

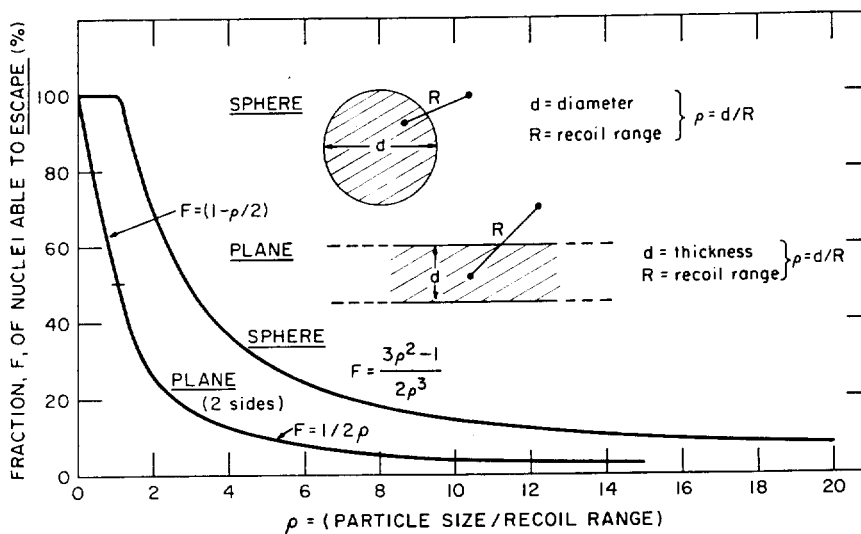


FIG. 85.—Theoretical escape of recoiling atoms from spherical and planar particles

TABLE 48. STEADY-STATE ACTIVITY RATIOS IN MAN (BURDENS $\gg 1$ YEAR)

Tissue	Author	Reference	Duration, years	$^{228}\text{Ra}/^{232}\text{Th}$	$^{228}\text{Th}/^{228}\text{Ra}$	$^{224}\text{Ra}/^{228}\text{Th}$	$^{212}\text{Pb}/^{224}\text{Ra}$
Liver	Rundo	2	13.5-14.5	0.62 (2) ^(a) [0.62-0.625]	0.76 (2) [0.73-0.80]	0.66 (2) [0.66-0.67]	0.42 (2) [0.39-0.45]
	Hursh	34	20	—	0.9 (1)	—	—
	Baserga	35	15	0.41 (1)	0.88 (1)	—	—
	Kaul	6, 7	long term (?)	0.46 (1)	0.90 (3) [0.87-0.92]	—	—
	Parr et al.	This paper	11-26	0.36 (1)	1.00 (2) [1.00-1.01]	0.75 (1)	—
Spleen	Rundo	2	13.5-14.5	0.69 (1)	0.83 (1)	0.75 (1)	0.17 (1)
	Hursh	34	20	0.48 (1)	0.96 (1)	—	—
	Kaul	6, 7	long term (?)	0.72 (3) [0.33-1.07]	0.91 (4) [0.85-0.96]	0.90 (3) [0.89-0.91]	0.57 (3) [0.44-0.84]
	Parr et al.	This paper	11-26	0.36 (1)	1.00 (2) [0.97-1.03]	0.74 (1)	—
Trabecular bone without marrow	Marinelli et al.	11	15-26.5	1.6 (1)	1.09 (7) [0.64-1.48]	—	—
	Kaul	6, 7	long term (?)	1.3 (5) [1.2-1.5]	1.2 (7) [1.1-1.7]	1.0 (1)	—
	Parr et al.	This paper	26	—	1.0 (1)	1.7 (1)	—
Red bone marrow	Kaul	6, 7	long term (?)	0.23 (3) [0.19-0.30]	1.12 (3) [1.08-1.18]	—	—
	Parr et al.	This paper	11-26	—	1.05 (2) 1.0-1.1	0.59 (2) [0.58-0.60]	—

^(a) Figures in round parentheses quote the number of measurements. Figures in square parentheses quote the range.

viously places this nuclide on a very sensitive part of the curve. Perhaps this accounts for some of the variability in results obtained with different batches of Thorotrast. It is also significant that at late times after Thorotrast administration, the particles are present in the form of aggregates, and the escape of ^{228}Ra appears to be further impeded. Thus, steady state activity ratios, $^{228}\text{Ra}/^{232}\text{Th}$, of the order of 0.5 are then reported

(see Table 48). Presumably this higher retention can be explained by the recoil of ^{228}Ra atoms from one particle into another in such a way that they continue to be trapped.

The interpretation of the estimated ^{228}Th steady state activity ratios, f_2 , presents considerable difficulties (see appendix). From the results of long term experiments, the calculated values of $(1 -$

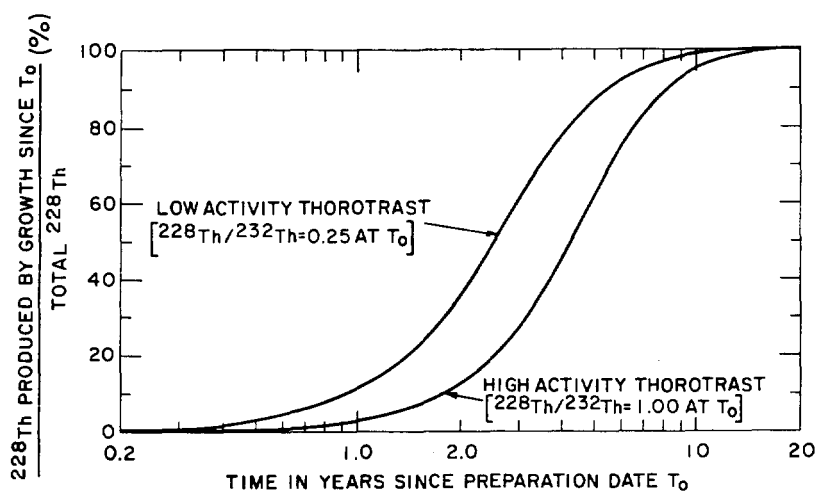


FIG. 86.—Proportion of ^{228}Th in Thorotrast produced *in vitro* since the date of preparation, relative to the total ^{228}Th activity.

TABLE 49. APPROXIMATE EXCRETION RATES OF THORIUM-SERIES NUCLIDES IN LONG-TERM THOROTRAST PATIENTS

Nuclide	% of total body burden excreted per day	Priority route of excretion	Consequent equilibrium ratio of activities in whole body	Reference for excretion rate
^{232}Th	$<10^{-3}$	Feces	—	9
^{228}Ra	0.03	Feces	$^{228}\text{Ra}/^{232}\text{Th} = 0.50$	6, 9
^{228}Th	<0.01	Feces (?)	$^{228}\text{Th}/^{228}\text{Ra} = 0.91-1.00$	6
^{224}Ra	1-2	Feces	$^{224}\text{Ra}/^{228}\text{Th} = 0.90-0.95$	6, 9
^{220}Em	— ^(a)	Breath	$^{220}\text{Em}/^{224}\text{Ra} = 0.90-0.92$	10, 13, 14
^{212}Pb	1	Urine and feces	$^{212}\text{Pb}/^{220}\text{Em} = 0.99$	6
Others	Negligible	—	—	—

^(a) On account of the short half-life of ^{220}Em it is not meaningful to express the excretion of this nuclide in the units of % body burden per day.

the RES probably reflect the proportion of ^{228}Th in the original injection solution which existed in an ionic or soluble form. In the Thorotrast ampoule prior to injection this proportion would be expected to grow with time in the manner of Figure 86. Since ^{228}Th grows from ^{228}Ra and there are no intermediate high energy recoil events, the maximum value of this proportion would be expected to approach the analogous figure of ^{228}Ra (i.e., ~75%). Some support for this theory can be found in the fact that the reported values of the $^{228}\text{Th}/^{228}\text{Ra}$ activity ratios in Tables 42 and 43 are larger for the "young" batches of Thorotrast, and smaller for the "old" batch of Thorotrast.

For Thorotrast burdens of many years standing, the values of $(1 - f_2)$ calculated for the RES probably reflect the proportion of ^{228}Th in a soluble form which has grown *in vivo* from the ^{228}Ra trapped within the particles. That is, unlike the original injection material, it does not include the ^{228}Th which grows from soluble ^{228}Ra , because the latter is largely excreted from the body (all but ~1% within its mean lifetime). Since there are no high energy recoil events to give rise to the direct escape of ^{228}Th from the particles,

the steady state activity ratios $^{228}\text{Th}/^{228}\text{Ra}$ would be expected to be close to unity. In the two long-term cases presented in Tables 42 and 43, this expectation is borne out. Nevertheless, other workers have reported a significant washout of ^{228}Th from the RES in long-term Thorotrast patients (~10%, see Table 49), and there have even been observations of ^{228}Th in the excreta.⁽⁶⁾ Thus, although there is clear evidence for the translocation of ^{228}Th at early times after administration, its later behaviour is uncertain.

The proposed recoil mechanism would lead to the prediction that, on account of the higher recoil energy (Table 47), the retention of ^{224}Ra atoms within the Thorotrast particles should be lower than that of ^{228}Ra . In fact the $^{224}\text{Ra}/^{228}\text{Th}$ steady state activity ratios turn out to be higher than the $^{228}\text{Ra}/^{232}\text{Th}$ ratios in the RES (e.g., in Tables 42 and 43, ~0.5 vs. ~0.3), but this is readily explained on the assumption that ^{224}Ra atoms which are not bound within the particles have a biological half-life in the RES of several days. ICRP quotes a figure of 10 days.⁽¹⁶⁾

The occurrence of several high-energy recoil events between ^{224}Ra and ^{212}Pb presumably implies that most

of the ^{212}Pb and ^{212}Bi atoms observed in the RES are not bound within the particles. The high activities of both these isotopes can be explained by the fact that their biological half-lives within the RES are much longer than their physical half-lives.⁽¹⁶⁾

Best Estimates of the Distribution of Activities throughout the Human Body and the Consequent Radiation Dose-Rates in Long-Term Thorotrast Patients.

There is unfortunately no completely objective way to combine the data reported here with those of other workers to obtain the current "best estimates" of the distribution of Thorotrast activities throughout the human body. Different investigators undoubtedly tend to attach different weighting factors to all the evidence that is available.

For the *whole body*, the most reliable estimates of the steady state activity ratios of the various thorium daughter products are probably derived from excretion measurements. The relations between percent excreted per day and activity ratio in the whole body are of the form shown for four of the thorium-series radionuclides in Figure 87. Steady state activity ratios calculated on this basis for the whole body are summarized in Table 49. It is to be noted in particular that the

$^{228}\text{Ra}/^{232}\text{Th}$ ratios come out somewhat higher than those implied by the figures of Tables 42 and 43, presumably because of the aggregation of Thorotrast particles that occurs at long times after administration.

For individual tissues at long times after Thorotrast administration, the steady state activity ratios observed by the present authors and those reported previously by other workers, are summarized in Table 49. On the basis of these data a collection of current "best estimates" (in the present authors' opinion) of steady state activity ratios has been assembled in Table 50. In cases where no human data were available for this table, the best estimates were derived from results of the animal experiments reported above. Data are quoted for the ratios $^{220}\text{Em}/^{224}\text{Ra}$. How from thoron breath analyses and calculations involving the circulation time of the blood, it is possible to get a rough estimate of the proportion of thoron daughter products generated within the major Thorotrast deposits in the RES which escape into the general circulation. Hursh⁽¹⁰⁾ calculated 16%, and Grillmaier et al.⁽¹¹⁾ concluded that it might even be as high as 20%. In tissues other than the RES, the expected thoron daughter activity ratios are more difficult to predict. From Stover's work on ^{212}Pb metabolism⁽³⁷⁾ there is some evidence

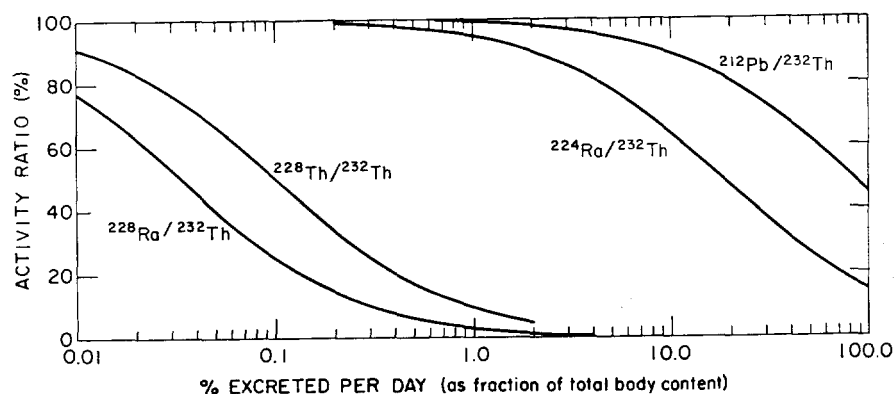


FIG. 87.—Relation between steady state activity ratios in the whole body and the excretion rates of four thorium series products.

TABLE 50. AUTHORS' "BEST ESTIMATES" OF STEADY STATE ACTIVITY RATIOS IN LONG-TERM THOROTRAST PATIENTS

Organ	$^{228}\text{Ra}/^{232}\text{Th}$	$^{228}\text{Ac}/^{228}\text{Ra}$	$^{228}\text{Th}/^{228}\text{Ra}$	$^{224}\text{Ra}/^{228}\text{Th}$	$^{212}\text{Pb}/^{224}\text{Ra}$	$^{212}\text{Bi}/^{212}\text{Pb}$	Source of
Liver	0.5	1.00	0.9	0.7	0.5	0.7	Table 48
Spleen	0.5	1.00	0.9	0.7	0.5	0.7	Table 48
Kidney	0.2	1.4 ^(b)	1.4 ^(b)	0.9 ^(b)	4.7 ^(b)	1.9 ^(b)	Table 44
Trabecular bone	1.3 ^(c)	(1.0) ^(d)	1.1	1.7	0.9 ^(b)	1.0 ^(b)	Tables 47
Red bone marrow	0.2	(1.0) ^(d)	1.1	0.6	≈ 1	(1) ^(d)	Tables 47
Lung	0.5	(1.0) ^(d)	1.0	~ 1	~ 18	(1) ^(d)	Table 46

(a) Except where indicated, the quoted values are based on measurements of tissues from actual long-term Thorotrast patients.

(b) Based on data obtained from experimental animals.

(c) Values much greater than one are observed in short-term animal experiments (Table 45).

(d) Assumed value in absence of actual measurement.

TABLE 51. THORIUM-SERIES ACTIVITIES AND MEAN DOSE RATES IN VARIOUS ORGANS
 (50 ML THOROTRAST INJECTED INTRAVASCULARLY)

Organ	Wet weight, g	Nanocuries in organ at steady state							α -ray dose from all isotopes, Rads/year
		^{232}Th	^{228}Ra	^{228}Th	^{224}Ra	^{220}Em and ^{216}Po	^{212}Pb	^{212}Bi	
Whole body	70,000	1,250	625	625	580	530	525	525	
Liver	1,700	860	430	390	270	215	135	90	71
Spleen	150	210	105	95	67	54	35	25	168
Red bone marrow	1,500	100	25	30	20	40	40	40	18
Lungs	1,000	10	5	3	3	30	30	30	13
Blood	5,400	0	0	0	3	100	55	55	6
Kidneys	300	1.3	0.3	0.6	0.5	0.4	2	4	3
Skeleton (marrow-free)	7,000	15	25	30	50	48	45	45	3

TABLE 52. SUMMARY OF ESTIMATED DOSE RATES TO ORGANS OF THOROTRAST PATIENTS

Author	Year	Mean organ dose rate ≥ 20 years after 50 ml Thorotrast intravenously, Rads/year ^(a)						
		Liver	Spleen	Red bone marrow	Kidney	Lung	Skeleton	Blood
Parr et al. (this paper)	1967	71	168	18	3	13	3	6
Hursh ⁽¹⁰⁾	1965					4-9		
Muth ⁽⁴⁰⁾	1965					4-7		
Kaul ^(6, 8)	1964, 1965	65	145	30			2	
Rundo ^(4, 13)	1958	68	178	14-61		5		1
Hursh et al. ⁽⁹⁾	1957	78	78	8		3		
Reynolds et al. ⁽¹²⁾	1957						4-9	

^(a) Dose rates reported by the different authors in most cases do not refer to 50 ml of Thorotrast. The values quoted here have been normalized on the assumption of proportionality between dose rates and volume of administered Thorotrast, though this is not strictly true because of differences in self-absorption of the radiation.

thoron concentrations in the blood may be approximately double those of ^{212}Pb .

The data of Tables 37, 39, and 50 have been combined in Table 51 to give a "balance sheet" for the distribution of activities throughout the whole body. This table is a slightly revised and recalculated version of one first prepared by Marinelli for presentation at an IAEA panel meeting in October 1965,⁽³⁸⁾ and since reproduced by Dudley.⁽³⁹⁾ The activities refer to 50 ml of Thorotrast administered intravenously 20-25 years previously. Such a dose probably exceeds the average volume administered, but is within the range of 10 to 75 ml that was most commonly employed. Mean dose rates (Rads/year) corresponding to these activities have been calculated and are recorded in the last column of Table 51. They take account only of the more important component of the dose, that deriving from the α -particles, which is of the order of 90% of the total dose. Corrections for self-absorption of the α -particles in the inert ThO_2 agglomerates have been applied according to the factor F quoted by Rundo⁽⁴⁾ in the form

$$F = 0.645 e^{-1.50A} + 0.355 e^{-0.047A},$$

where A is the concentration of ^{232}Th expressed as dpm/mm³. For the case considered in Table 51, F has values of 0.46, 0.31, and 0.87 for liver, spleen, and bone-marrow, respectively, and unity for the other tissues. However, in accordance with the "recoil-escape" model proposed above, these self-absorption corrections were not applied equally to all the thorium-series decay products, but only to that fraction of the activity of each nuclide thought to be bound within the ThO_2 agglomerates. The bound fraction in each case was estimated from the following argument. In the RES at late times after Thorotrast administration, the steady state activity ratio $^{228}\text{Ra}/^{232}\text{Th} = \sim 0.5$ is interpreted as meaning that the proportion of ^{228}Ra atoms ejected by recoil from the ThO_2 agglomerates is $\sim 50\%$. If it is then assumed that each subsequent α -decay within the agglomerates confers approximately the same 50% probability that the atom concerned will escape into the surrounding tissue, then the bound activity of each radionuclide can be readily inferred. Only to these bound activities have the Rundo self-absorption corrections been applied. If they had been

applied equally to the whole proportion of the activity of each radionuclide, the dose-rate estimates for liver, spleen, and bone marrow would have been reduced respectively to 55, 104 and 17 Rads/year from 50 ml of Thorotrast.

At earlier times than the 20–25 years considered in Table 51, the dose rates may be different on account of the different status of activities in the decay chain (Figure 84) and the different aggregation of particles within the tissues. However, these two effects partially compensate each other, and the quoted figures are probably reasonable measures of the average dose rates for Thorotrast burdens of long standing (>10 years). Further information on the expected time dependence of the dose rate has been given by Kaul.⁽⁶⁾

A comparison between the above best estimates of dose rates and those reported previously by other workers is contained in Table 52. Lest the apparently good agreement suggest that the dosimetry of Thorotrast no longer presents any problems, it should be pointed out that the present authors' calculations have, of course, relied extensively on measurements reported by previous workers in this field. The principal new point of interest is perhaps the dose to the lung since the present estimate is based on an actual activity measurement of lung tissue itself, while previous estimates have relied on calculations from the activity of thoron in the breath.

CONCLUDING REMARKS

Although the overall picture of Thorotrast metabolism presented here is unlikely to undergo major revision, there remain many important points of detail that need to be settled. Undoubtedly the greatest inadequacy in our current estimates of dose rate is their expression in the form of mean organ dose. On the microscopic scale, as shown by Rotblat et al.,⁽⁴¹⁾ it is to be expected that doses delivered to small regions of an organ may be a factor of ten or more higher than the average. The elucidation of these inhomogeneities remains one of the most challenging of the problems still to be solved. However, even if this problem is discounted, mean dose rates in the range of 3 to 100 Rads per year for a 50-ml Thorotrast injection are still disturbingly high. By comparison, the maximum permissible body burden of ²²⁶Ra (0.1 μ Ci), uniformly distributed in the skeleton, would yield a dose of about 3 Rads per year. It is clear, therefore, that Thorotrast patients constitute an important and unique population for the study of low-level and long-term irradiation in man. Their numbers are fast diminishing and within a few more years such studies will no longer be possible.

The authors wish to express their sincere thanks to

Mr. L. D. Marinelli, Radiological Physics D for his advice and encouragement in carrying out studies; to Dr. D. J. Simmons and Mr. J. E. F. for assistance with the animal experiments; and F. Markun for other technical assistance. On (RMP) would also like to thank Dr. R. A. (IAEA) for the benefit of many useful discussions for permission to quote the results for patient 1 was one of the IAEA series of patients.

REFERENCES

1. Marinelli, L. D. Trans. 9th Int. Congr. of Radiol. B. Rajewsky. Georg Thieme Verlag, Stuttgart, p. 1234.
2. Rundo, J. *Phys. Med. Biol.* **1**, 138 (1956).
3. Rundo, J. *Acta Radiol.* **47**, 65 (1957).
4. Rundo, J. Ph.D. Thesis, London, 1958.
5. Rotblat, J. and Ward, G. *Phys. Med. Biol.* **1**, 125 (1956).
6. Kaul, A. IAEA Symposium in Heidelberg on the *Measurement of Radioactivity in Man*, Proc. IAEA Symp., Heidelberg. Int. Atomic Energy Agency, Vienna, 1964, p. 491.
7. Stahlhofen, W. and Kaul, A. *Radiological Health and in Mining and Milling of Nuclear Materials*, Proc. Symp., Vienna. Int. Atomic Energy Agency, 1964, Vol. 2, p. 475.
8. Kaul, A. IAEA-WHO Panel Meeting on Dosimetry and Toxicity of Thorotrast, Vienna, October, 1968. Int. Atomic Energy Agency, Vienna, 1968, Tech. Rep. No. 106, pp. 30 and 69.
9. Hursh, J. B., Steadman, L. T., Looney, W. B., and Zin, M. *Acta Radiol.* **47**, 481 (1957).
10. Hursh, J. B. *Brit. J. Radiol.* **38**, 776 (1965).
11. Marinelli, L. D. and Lucas, H. F. *Some Aspects of Irradiation*, Proc. Symp. Heber, Utah. Pergamon Press, Oxford, 1962, pp. 499–516.
12. Reynolds, J. C., Gustafson, P. F., and Marinelli, L. D. Argonne National Laboratory Report. ANL-5689, pp. 1–43.
13. Rundo, J., Ward, A. H., and Jensen, P. G. *Phys. Med. Biol.* **3**, 101 (1958).
14. Muth, H. and Oberhausen, E. *Whole-Body Counting*, IAEA Symp., Vienna. Int. Atomic Energy Agency, Vienna, 1962, p. 267.
15. Parr, R. M. *Radioisotope Sample Measurement Techniques in Medicine and Biology*, Proc. IAEA Symp., Vienna. Int. Atomic Energy Agency, Vienna, 1965, p. 69.
16. *Recommendations of the International Commission on Radiological Protection*, ICRP Publication No. 2. Pergamon Press, Oxford, 1959.
17. Marinelli, L. D. and Stehney, A. F. Argonne National Laboratory Radiological Physics Division Semi-Annual Report, July–December 1958. ANL-5967, p. 105.
18. Zilversmit, D. B., Boyd, G. A., and Brucer, M. *Clin. Med.* **40**, 255 (1952).
19. Rankin, J. G., Playoust, M. R., and Beal, R. W. *Clin. Med.* **58**, 920 (1961).
20. Simmons, D. J., Cummins, H., and Nirdlinger, E. *Roentgenol.* **103**, 902 (1968).
21. Jee, W. S. S. *Assessment of Radioactivity in Man*, IAEA Symp., Heidelberg. Int. Atomic Energy Agency, Vienna, 1964, Vol. 1, p. 369.
22. Tange, J. D., Hayward, N. J., and Bremner, D. A. *A. Ann. Med.* **14**, 49 (1965).

23. Gryboski, J. D. and Gotoff, S. P. *New Eng. J. Med.* **265**, 1829 (1961).
24. Schroeder, H. A., Balassa, J. J., and Vinton, W. H. *J. Nutr.* **86**, 51 (1965).
25. Stover, B. J., Atherton, D. R., Buster, D. S., and Keller, N. *Radiat. Res.* **26**, 226 (1965).
26. Wallace, D. E., Stehney, A. F., and Ilciewicz, F. H. Argonne National Laboratory Radiological Physics Division. Semiannual Report January-June 1957. ANL-5755, p. 33.
27. Grillmaier, R. *Biophysikalische Untersuchungen an Personen mit Ablagerungen von Radionukliden der natürlichen Thoriumreihe*. Ph.D. Thesis, Homburg/Saar, 1964.
28. Parr, R. M. *Ann. N. Y. Acad. Sci.* **145**(3), 644 (1966).
29. Bohr, N. *Kgl. Danske Videnskab. Selskab, Mat.-fys. Medd.* **18**(8) (1948).
30. Nielson, K. O. *Electromagnetically Enriched Isotopes and Mass Spectrometry*, Ed. M. L. Smith. Butterworths, London, 1956, pp. 68-81.
31. Marinelli, L. D. Private communication.
32. Bensted, J. P. M. and Crookall, J. O. *Brit. J. Cancer* **17**(1), 62 (1963).
33. Hursh, J. B. Misbehavior of thorium daughters formed in Thorotrast. Paper presented at the 1st International Congress of the International Radiation Protection Association, Rome, Italy, 5-10 September, 1966.
34. Hursh, J. B. Personal communication quoted in Reference 11.
35. Baserga, R., Yokoo, H., and Henegar, G. C. *Cancer* **13**, 1021 (1960).
36. Grillmaier, R., Muth, H., and Oberhausen, E. IAEA Symposium on Assessment of Radioactivity in Man, Proc. IAEA Symp., Heidelberg. Int. Atomic Energy Agency, Vienna, 1964, Vol. 2, p. 473.
37. Stover, B. J. *Proc. Soc. Exptl. Biol. Med.* **100**, 269 (1959).
38. Marinelli, L. D. IAEA-WHO Panel Meeting on Dosimetry and Toxicity of Thorotrast, Vienna, October 1965. Int. Atomic Energy Agency, Vienna, 1968, Tech. Report **106**, p. 86.
39. Dudley, R. A. *Ann. N. Y. Acad. Sci.* **145**, 595 (1966).
40. Muth, H. and Grillmaier, R. IAEA-WHO Panel Meeting on Dosimetry and Toxicity of Thorotrast, Vienna, October, 1965. Int. Atomic Energy Agency, Vienna, 1968, Tech. Report **106**, p. 79.
41. Rotblat, J. and Ward, G. B. *Nature* **172**, 769 (1953).

APPENDIX

Calculation of the Steady State Activity Ratios
($^{228}\text{Ra}/^{232}\text{Th}$) and ($^{228}\text{Th}/^{228}\text{Ra}$) in vivo

A rigorous mathematical treatment of the ^{228}Ra and ^{228}Th activities *in vivo* is complicated by the fact that Thorotrast is a nonhomogeneous material in which the radioactivity is probably distributed throughout several different physical phases in proportions which are different for each nuclide. For this reason alone, and without regard to differences in physical half-life, it cannot be assumed that different isotopes of the same element will show the same pattern of tissue distribution *in vivo* (e.g., ^{228}Th and ^{232}Th , or ^{224}Ra and ^{228}Ra). Moreover, a thorough analysis of the problem even demands that distinctions be drawn between atoms of the same iso-

tope. In general, it is necessary to distinguish three types of atom; those which enter the circulation in the injection materials (type I), those which grow *in vivo* as daughters of injected atoms (type II), and those which grow *in vivo* as granddaughters of the injected atoms (type III). (In the present context, since we are dealing with growth and decay on a time scale long compared to the half-life of ^{228}Ac , the decay chain $^{232}\text{Th}:^{228}\text{Ra}:^{228}\text{Th}$ is visualized as a parent:daughter:granddaughter series). At the time of injection, therefore, all the ^{232}Th , ^{228}Ra , and ^{228}Th atoms are of type I. At any later time, ^{228}Th atoms are of types I, II, and III, ^{228}Ra atoms are of types I and II, and all the ^{232}Th atoms remain of type I.

For a Thorotrast body burden of very long standing (sufficiently long for essentially all the ^{228}Ra atoms of type I to have decayed away), we can write the following for the activities in any tissue sample and in the whole body. (See Table 53.)

TABLE 53. ACTIVITIES FOR A LONG-STANDING THOROTRAST BODY BURDEN

	^{232}Th (type I)	^{228}Ra (type II)	^{228}Th (type III)
Tissue sample activity	aA_0	$f_1[aA_0]$	$f_2[f_1aA_0]$
Whole body activity	A_0	\bar{f}_1A_0	$\bar{f}_2[\bar{f}_1A_0]$
Tissue/whole body	a	af_1/\bar{f}_1	$af_2\bar{f}_2/\bar{f}_1\bar{f}_2$

A_0 is the activity of ^{232}Th in the whole body (equally the activity of ^{232}Th in the total injection material) and a is the fraction of this administered material contained within the tissue sample.

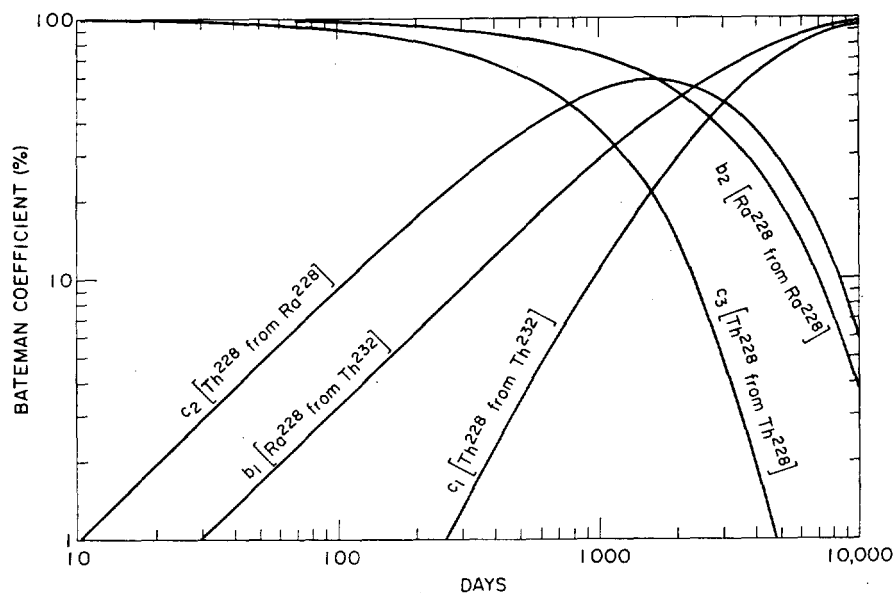
These expressions define the quantities f_1 and f_2 for the tissue sample, and \bar{f}_1 and \bar{f}_2 for the whole body, as the steady state activity ratios which it is desired to calculate. It follows that, of all the ^{228}Ra atoms born within the entire body which have not undergone decay by the time of sampling, a fraction \bar{f}_1 remains then within the body; and amongst the different tissues these retained atoms are distributed in the proportions af_1/\bar{f}_1 . Similarly for ^{228}Th , \bar{f}_2 measures the fraction retained in the whole body, and $af_2\bar{f}_2/\bar{f}_1\bar{f}_2$ measures the distribution of the retained atoms among the different tissues.

This discussion refers to a Thorotrast burden of such long standing that none of the type I ^{228}Ra atoms and none of the types I and II ^{228}Th atoms survive. At earlier times it is obviously necessary to consider the fates of the ^{228}Ra and ^{228}Th atoms contained within the administered Thorotrast. For ^{228}Ra it will be assumed that all type I atoms distribute themselves in the same proportions af_1/\bar{f}_1 among the different tissues as do the type II ^{228}Ra atoms referred to in Table 53 and that the whole-body retention is \bar{f}_1 . Similarly, the ^{228}Th atoms of type II will be assumed to distribute themselves in the

TABLE 54. SUMMARY OF DEFINITIONS USED IN NORMALIZATION PROCEDURE FOR ^{232}Th AND ^{228}Ra

Quantity	^{232}Th	^{228}Ra	^{228}Th
Activities in injection material at time of injection ^(a)	A_0	B_0	C_0
Activities in tissue sample at time t after injection	$A = aA_0$	B	C
Steady state activity ratio at $t = \infty$	—	$f_1 = \frac{^{228}\text{Ra}}{^{232}\text{Th}}$	$f_2 = \frac{^{228}\text{Th}}{^{228}\text{Ra}}$
Decay constants	λ_1	λ_2	λ_3
Bateman coefficients for growth and decay of ^{228}Ra (see Figure 88)	Growth from ^{232}Th of type II ^{228}Ra $b_1 = \lambda_2 \frac{e^{-\lambda_1 t} - e^{-\lambda_2 t}}{(\lambda_2 - \lambda_1)}$	Decay of type I ^{228}Th $b_2 = e^{-\lambda_2 t}$	—
Bateman coefficients for growth and decay of ^{228}Th (see Figure 88)	Growth from ^{232}Th of type III ^{228}Th $c_1 = \frac{\lambda_2 \lambda_3}{(\lambda_2 - \lambda_1)} \left(\frac{e^{-\lambda_1 t} - e^{-\lambda_2 t}}{\lambda_3 - \lambda_1} - \frac{e^{-\lambda_2 t} - e^{-\lambda_3 t}}{\lambda_3 - \lambda_2} \right)$	Growth from ^{228}Ra of type II ^{228}Th $c_2 = \lambda_3 \left(\frac{e^{-\lambda_2 t} - e^{-\lambda_3 t}}{\lambda_3 - \lambda_2} \right)$	Decay of type I ^{228}Th $c_3 = e^{-\lambda_1 t}$

^(a) This is taken to mean the material actually administered, which is not necessarily the same as the material in the amp or even the material in the syringe.

FIG. 88.—Bateman coefficients for the growth and decay of ^{228}Ra and ^{228}Th

same proportions $af_1f_2/\bar{f}_1\bar{f}_2$ among the tissues as do ^{228}Th atoms of type III, and with a whole-body retention of $\bar{f}_1\bar{f}_2$. Type I ^{228}Th atoms, however, must be treated somewhat differently since they do not grow *in vivo* from ^{228}Ra and, therefore, cannot depend on the ratio f_1/\bar{f}_1 . Thus it cannot be expected that type I ^{228}Th atoms will behave in the same manner as the atoms of types II and III; rather they bear an analogy with type I ^{228}Ra

atoms. In the case of ^{228}Ra , one is interested in the question: what fraction of the atoms in the injection material is carried by the Thorotrast particles? For ^{228}Th , exactly the same question arises. Therefore, in analogy with ^{228}Ra it will be assumed that the whole-body retention of type I ^{228}Th atoms is \bar{f}_2 and that the retained atoms are distributed among the tissues at the time of measurement in the proportions af_2/\bar{f}_2 .

It should be emphasized that this approach to the Thorotrast problem is not intended to accord very accurately with a metabolic model expressed in terms of compartments constrained by long biological half-lives, since this, in general, is not how Thorotrast behaves. The evidence is more in accord with a model which pictures the Thorotrast as a diphasic material containing a certain proportion of the activity trapped within the particles, and the remainder in a relatively rapidly metabolizing pool outside the particles. In such a case as this, the mathematical treatment presented here is a simple but not unreasonable approach to the problem, at least for the soft tissues. To the extent that it is oversimplified, its inadequacies should reveal themselves in the different values of the retention coefficients (or steady state activity ratios) f_1 and f_2 calculated from experiments of different durations.

In short-term experiments ($\ll 1$ year), most of the activity of ^{228}Ra and ^{228}Th is associated with atoms of type I, and, therefore, the calculated values of f_1 and f_2 should describe mainly the behavior of the injection material. At much later times ($\gg 2$ years), however, a significant proportion of the ^{228}Ra atoms are of type II, and most of the ^{228}Th atoms are of types II and III. In these cases, therefore, the calculated values of f_1 and f_2 should principally describe the behavior of the radioactive atoms generated *in vivo*. The quantitative interpretation of f_1 and f_2 is thus fraught with difficulty. Nevertheless, from a study of their values for different tissues, it should be possible to gain at least a reasonable qualitative picture of the overall metabolism of ^{228}Ra and ^{228}Th in the whole body, since values of f_1 and f_2 smaller than unity imply a "wash-out" of the daughter isotope concerned, while values in excess of unity imply a net gain or "wash-in" of that isotope from other tissues.

With the above qualifications in mind, and adopting the definitions given in Table 54, and from the variation of the coefficients of the Bateman equations with time (see Figure 88), we can write for the activity in a tissue sample at any time after administration of the Thorotrast:

$$\text{for } ^{232}\text{Th}: A = aA_0 \quad (1)$$

$$\text{for } ^{228}\text{Ra}: B = aA_0f_1b_1 + aB_0f_1b_2 \quad (2)$$

$$\text{for } ^{228}\text{Th}: C = aA_0f_1f_2c_1 + aB_0f_1f_2c_2 + aC_0f_2c_3 \quad (3)$$

Solving for f_1 , from Eq. (2) we obtain

$$f_1 = \left[\frac{A}{B} \right] \div \left[\frac{A_0b_1 + B_0b_2}{A_0} \right]$$

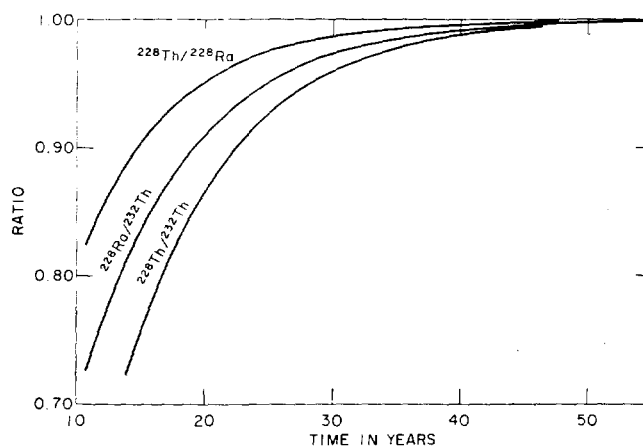


FIG. 89.—*In vitro* activity ratios $^{228}\text{Th}/^{228}\text{Ra}$: ^{228}Th in Thorotrast at different times after the preparation date.

$$\text{i.e.,} \quad f_1 = \left[\frac{^{228}\text{Ra}}{^{232}\text{Th}} \right]_S \div \left[\frac{^{228}\text{Ra}}{^{232}\text{Th}} \right]_T \quad (4)$$

The ratios of activities at the time of sampling are implied in this equation. The suffix S refers to the tissue sample, and the suffix T to a Thorotrast sample containing, at the time of injection, the same activities of ^{232}Th and its daughter isotopes as were actually administered. At very late times when $[^{228}\text{Ra}/^{232}\text{Th}]_T$ is equal to unity, f_1 has the desired property of expressing the $^{228}\text{Ra}/^{232}\text{Th}$ ratio in the tissue at the time of radioactive steady state.

Solving for f_2 , from Eq. (3) we obtain

$$f_2 = \frac{C/A}{\left[f_1c_1 + \frac{B_0}{A_0}f_1c_2 + \frac{C_0c_3}{A_0} \right]} \quad (5)$$

It should be noted that, at very early times when $c_1 \approx c_2 \approx 0$, and $c_3 \approx 1$, Eq. (5) can be expressed in a form similar to Eq. (4), i.e.,

$$f_2 = \left[\frac{^{228}\text{Th}}{^{232}\text{Th}} \right]_S \div \left[\frac{^{228}\text{Th}}{^{232}\text{Th}} \right]_T$$

At times greater than about 10 years when $c_3 \ll 1$, it is readily shown that f_2 can be expressed in the form

$$f_2 = \left[\frac{^{228}\text{Th}}{^{228}\text{Ra}} \right]_S \div \left[\frac{^{228}\text{Th}}{^{228}\text{Ra}} \right]_T \quad (6)$$

It is interesting to note that, from the time of manufacture of the Thorotrast, the ratio $[^{228}\text{Th}/^{228}\text{Ra}]_T$ takes many more than 6 half-lives of ^{228}Th to approach closely the value unity (Figure 89) and even after 20 years, is still about 5% below radioactive equilibrium. The ratio $[^{228}\text{Th}/^{228}\text{Ra}]_T$ in Eq. (6), therefore, remains a significant correction factor to the ratio $[^{228}\text{Th}/^{228}\text{Ra}]_S$ until many more than 20 years from the time of manufacture of the Thorotrast.

STRAIN DIFFERENCES IN THE RESPONSE OF THE MOUSE SKELETON TO EXTERNAL BETA IRRADIATION

D. J. Simmons, R. Hakim, and Helen Cummins*

Irradiation of mice with external $\text{Sr}^{90}\text{-Y}^{90}$ applicators provides a way to control the dose rate and time of exposure of the skeleton and other tissues to beta rays. Therefore, toxicity information may be obtained which is impossible to resolve by the use of internal emitters. This investigation concerns the skeletal changes that were produced by preliminary exposures of three strains of mice to body surface doses of 5000 to 7200 Rads. Several strain differences in response were found.

INTRODUCTION

The results from experiments which have measured the skeletal response to continuous whole-body x or gamma irradiation (100–200 Rads/day) or to single or multiple pulses of x rays (600–3000 Rads) administered over relatively short time periods suggest that radiation interferes with normal growth processes. Some of the end points studied have been total bone length,⁽¹⁻⁵⁾ the state of calcification,⁽⁶⁾ the histologic integrity of the cartilage plates,^(4, 7-10) the ability of cells in the cartilage and bone to sustain DNA synthesis,⁽¹¹⁾ the rate of fracture healing,⁽¹²⁾ and the changes in bone alkaline phosphatase concentrations, which are believed to measure (indirectly) the numbers of functional osteoblasts.^(4, 12, 13) With certain dose schedules, however, there has been tissue recovery.^(5, 7)

In an autoradiographic study of the kinetics of a heterogeneous population of osteogenic cells in the irradiated rat femur (1750 Rads), Kember⁽¹¹⁾ reported an initial decrease in the number of cells that could be flash-labeled with tritiated thymidine during the first two days, but full recovery on the sixteenth day. Recovery did not occur after a dose of 3000 Rads. In continuous irradiation studies (20 days), the reduction in the thymidine labeling indices became particularly severe as the dose was increased (84, 176, and 415 Rads/day); the time period of greatest damage occurred during the initial four days, but thereafter there was evidence that the degree of damage leveled off and that there was at least partial recovery. Adaptation to continuous irradiation has been noted for gut⁽¹⁴⁻¹⁶⁾ and marrow cell populations.⁽¹⁷⁾

Age, species, and the genetics of animals have also been shown to affect the ability of tissue cells to adapt to a particular dose level of irradiation. Thus, several laboratories have demonstrated strain differences in the normal incidence of bone tumors^(18, 19) in mice and rats, and the incidence of bone tumors in mice follow-

ing the parenteral administration of bone-seeking emitters such as ^{89}Sr ⁽²⁰⁾ and ^{90}Sr ⁽²¹⁾

This report is a preliminary study of the changes in the skeletons of three strains of Argonne C57 mice which had been subjected to partial-body irradiation from an external $^{90}\text{Sr}\text{-}^{90}\text{Y}$ beta source. This method has been employed by Auerbach and his associates⁽²⁾ to study epidermal cell population kinetics in mice irradiated with high doses at a slow rate. Interest has been focused upon the histologic changes in the epiphyseal growth plates and trabeculae in the primary spongy bone following irradiation and the time required for skeletal tissues to recover from the insult.

MATERIALS AND METHODS

Animals from three genetic strains of male C57 mice: black (HB = C57 BL/6 ANL [ANL 66]), and haired white (H), and haired analogues (HW), each 6 months old were exposed in a total-body surface irradiator ($^{90}\text{Sr}\text{-}^{90}\text{Y}$) designed by Auerbach and Brues.⁽²²⁾ The $^{90}\text{Sr}\text{-}^{90}\text{Y}$ source was in the form of ceramic microspherules embedded in polyurethane sheet. The sheet formed the inner lining of a 4" long aluminum tube placed inside a wooden box, which was shielded by a $\frac{5}{16}$ " thick fixed aluminum shield at one end and a similar but movable shield at the other. Irradiation was performed by inserting a mouse confined in a Lusteroid test tube within the source for 11 or 16 hr, but the head of the mouse was shielded from radiation by a 1" thick glass shield. Dosimetric studies using solid fluorid dosimeters in Lucite phantoms indicated a surface dose rate of 455 Rads/hr which increased to 68 Rads/hr at a 3-mm depth—well within the range of the surface tissues of the knee joint. For total-body surface doses, then, for 11-hr and 16-hr radiation periods were 5000 and 7200 Rads, respectively. The maximum dose rate delivered to the epiphyseal elements in the epiphyseal medullary cavity (about 5 mm from the surface) might be expected under optimal geometrical conditions to be on the order of 20–30 Rads/hr. However, it was difficult to estimate the actual doses delivered to the knee joints. We do not know, for instance, if the knee joints were in contact with the walls of the Lusteroid tube during the 11- to 16-hr exposure period. A few control animals, both stressed (restrained in the test tubes) and unstressed were included in this study, but they were sacrificed with the mice killed one day after irradiation to establish base line values.

* CSUI Honor Student, Spring, 1967. Present address: Harvard Biological Laboratories, Harvard University, Cambridge, Mass.



Fig. 90.—A photomicrograph of a longitudinal section from the tibia of an HB strain C57 mouse three days after partial whole-body irradiation with 7200 Rads. The proximal epiphyseal cartilage is perforated by a blood vessel to unite the epiphyseal and diaphyseal marrow spaces. Hematoxylin and eosin. 250X.

The hind legs of the mice were recovered at autopsy. They were fixed in 10% neutral formalin, decalcified in 10% EDTA, embedded in paraffin, and sectioned longitudinally at 5 μ . The sections were stained with hematoxylin and eosin.

RESULTS AND DISCUSSION

The histologic picture of the long bones from mice of strains H, HW, and HB suggests that they were not undergoing rapid growth in length. This would be consistent with the fact that the mice were 4 months old when the experiment began. There were some differences in the magnitude of the response of the bones to partial-body beta irradiation at surface doses of 5000 Rads and 7200 Rads, and the amount of damage observed and the pattern of healing also seemed to be dependent upon the strain.

The histologic damage observed in the cartilages of bones from the mice involved cartilage, marrow, and vascular anomalies similar to those previously described for rats.^(3, 4) Epiphyseal-diaphyseal fusion (Figure 90) occurred 1-3 days after irradiation with 5000 or 7200 Rads in strains HB and HW mice and was present in strain HB mice as late as 120 days. The

cartilages from strain H mice were similarly affected, but only after 7200 Rads at 14 days. We did not observe the postirradiation recovery clones of cells in cartilage as did Sams⁽⁴⁾ and Kember,^(9, 10) but this was probably due to the advanced age of the mice at the time of irradiation, as well as to the low bone dose. The data plotted in Figure 91 (strain HW) suggested that there might be a concomitant increase in the DNA synthetic indices and thicknesses of the growth carti-

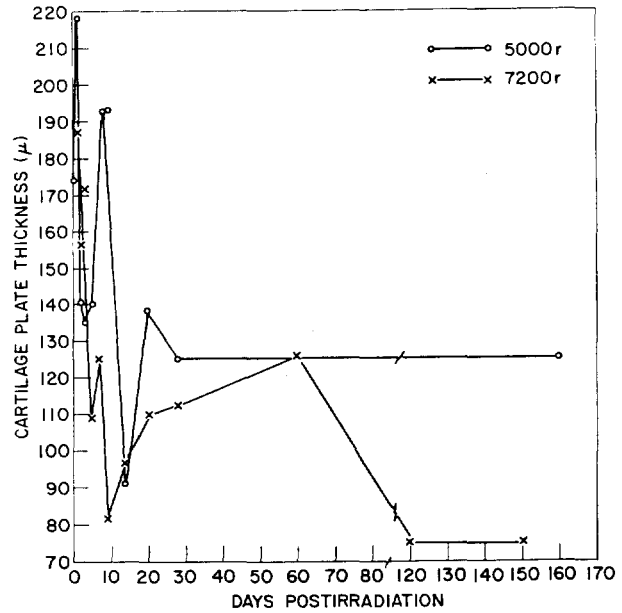


Fig. 91.—A plot of the thickness of the proximal tibial epiphyseal cartilages of strain HW C57 mice vs. time after partial whole-body irradiation with 5000 and 7200 Rads. The maximum reduction in cartilage thickness which occurred during the second week was interrupted by an earlier abortive attempt at recovery. The time periods required to thin the cartilages and to achieve partial recovery on the twentieth day were much longer than in the other strains (compare with Figures 92 and 93).

TABLE 55. DAYS TO ACHIEVE SUPPRESSION AND RECOVERY FROM IRRADIATION DAMAGE IN THE BONES OF THREE STRAINS OF C57 MICE

C57 strain	Total-body surface dose, Rads	Days post-irradiation to maximum reduction in cartilage plate thickness	Days post-irradiation to partial recovery of cartilage plate thickness	Days from maximum injury to partial recovery
H	5000	5	9	4
	7200	3	9	6
HW	5000	14	20	6
	7200	9	20	11
HB	5000	5	9	4
	7200	5	9	4

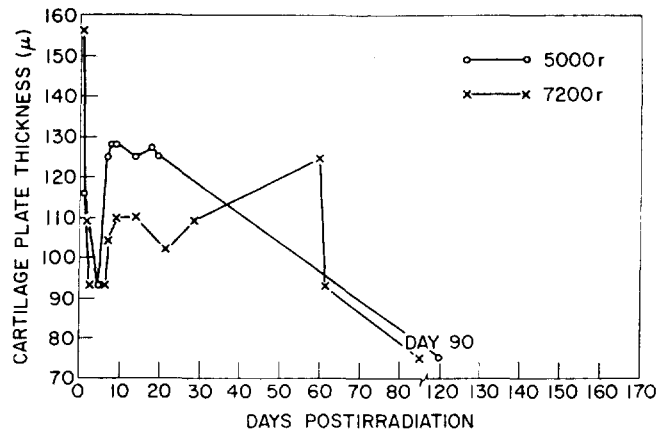


FIG. 92.—A plot of the thickness of the proximal tibial epiphyseal cartilages of strain H C57 mice vs. time after partial whole-body irradiation with 5000 and 7200 Rads. Irradiation initially produced thinner cartilages after 3 to 5 days followed by partial recovery on the ninth day. Less recovery was achieved following 7200 Rads than after 5000 Rads.

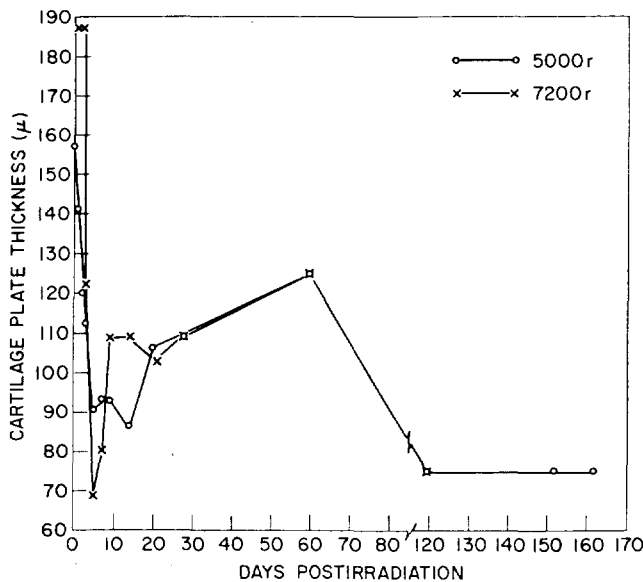


FIG. 93.—A plot of the thickness of the proximal tibial epiphyseal cartilages of strain HB C57 mice vs. time after partial whole-body irradiation with 5000 and 7200 Rads. While the thinning of the cartilages following 7200 Rads was more severe than after 5000 Rads (after 5 days), partial recovery had occurred in both groups by the ninth day.

lages during the first days following irradiation with 5000 Rads or 7200 Rads. The sharp decrease in plate thickness observed in strains H and HB during this time, 3–5 days postirradiation, fairly well correlated with histologic signs of chondroclastic activity in the metaphysis. Table 55 summarizes the essential information from the graphs (Figures 91–93). In these strains, recovery, measured by increased plate thickness, began 6 days after irradiation and was completed by the ninth day at both dose levels. The effects of

5000- or 7200-Rad surface doses on strain HW were substantially different from those on H and HB mice (Figures 91–93). First, the time required to grow the cartilage plates after irradiation was prolonged (9 days—7200 Rads; 14 days—5000 Rads). Second, recovery time following 7200 Rads was almost that observed after 5000 Rads. The graph (Figure 92) also suggests that strain HW cartilages attempt to recover 7–8 days after irradiation, but that this attempt was aborted. After partial recovery, it was impossible to distinguish one strain from the other on the basis of cartilage plate thickness. Recovery in strain HW, as noted above, was more dependent upon the timing of ossification patterns than on the ability of the cell populations in the cartilage to proliferate. There was a general decrease in cartilage plate thickness in all mice after 60 days, which may have been due to age changes.

Irregular endochondral ossification occurred as a result of both 5000 and 7200 Rads irradiation, and was due, in part, to the development of fibrillar and numerous foci of degenerate and probably permineralized plugs of matrix in the growth



FIG. 94.—A photomicrograph of the proximal tibial growth cartilage of an HW strain C57 mouse 2 days after partial whole-body irradiation with 5000 Rads. The cartilage plate shows degenerate plugs of acellular matrix and unresorbed islands of chondrocytes in the metaphysis, which suggest impaired processes of endochondral ossification. Hematoxylin and eosin, 250 ×.

HW mice and HB mice. In the first week after 5000 Rads, resorption of cartilage had proceeded so irregularly that numerous tongues and/or nodules of cartilage projected into the metaphysis and became partially ossified (Figure 94). That this change was delayed until the 4th week after irradiation with 7200 Rads (and only in strain H) again suggests that the higher dose level prolonged the postirradiation recovery period. The differences were undoubtedly related to the ability of the metaphyseal capillaries to invade the cartilage, and this process is known to be dependent upon the state of mineralization of the cartilage matrix.⁽²³⁾ Capillaries were found running parallel to, rather than perpendicular to, the face of the cartilage during the first week after both 5000 Rads and 7200 Rads, but while a few days were required in the 5000-Rad groups before normal invasion of the cartilage plate was reestablished, several weeks were required following 7200 Rads. In this respect, following 7200 Rads the bones from strain H mice had nodules of partially ossified cellular cartilage in the metaphysis as long as 120 days after irradiation. Remnants of cellular cartilage were never found after the second week in the metaphyses of mice irradiated with 5000 Rads. Ossification processes, while irregular and slow following 5000 Rads, always resulted in the formation of true endochondral bone. However, 7200 Rads appeared so disruptive to the normal processes of chondrocyte and tissue maturation in the growth plates that only simple lamellar bone was deposited on the subchondral surfaces (areas which were probably of normal mineral content) during the first two postirradiation weeks. Resumption of the normal cartilage metabolism and the formation of endochondral trabeculae were delayed until the third week. In view of the continuing formation of trabecular bone in all the mice, the population and function of osteoblasts seemed little affected by irradiation. A similar conclusion was reached by Kember.⁽¹⁰⁾ It is of interest that the trabeculae in mice of the HB strain were shorter at all postirradiation periods, but the significance of this is unknown since no unirradiated control animals of this strain and of the same age were available for comparison. However, it will be recalled that in this study HB strain mice also retained more medullary fat and sustained the more severe damage to their cartilages.

Because the mice were irradiated at an age when they normally begin to develop islands of degenerate cartilage in their growth plates, it was difficult to relate this change to the effects of irradiation. However, degenerate changes in the matrix became more severe with time at both dose levels. Small rents developed in the tissues following 7200 Rads, but only in one instance (strain H) did we observe amputation of a

middle segment of the femoral cartilage plate. Amputations are more frequently observed in mice after high exposures of radiation (2000 Rads) delivered at one sitting, and it usually involves separation of trabeculae from the growth apparatus.⁽⁴⁾

Marked strain differences were observed in the marrow. Two days after 5000 Rads the marrow cells were noticeably depopulated and increasing numbers of fat cells appeared toward the end of the first week in all strains. Marrow regeneration occurred during the second week, but it was slowest in strain HB mice. The time course for the development of fatty marrow was earlier after an exposure of 7200 Rads—at 2 days in strain HB mice and at 3 days in strain HW mice. Extravasation of red cells occurred at one day in strain H and at two days in strains HW and HB. Less fat was noted during the second week, and healing was completed by the third week—a delay of one week compared to the 5000-Rad groups.

SUMMARY

C57 mice of three strains received ⁹⁰Sr-⁹⁰Y partial body irradiation with a 5000- and 7200-Rad surface dose for a limit of 16 hr. In this preliminary study, the cartilages of strains H (hairless) and HB (haired black) mice responded similarly to the two doses. The cartilages were thinnest 5 days after irradiation owing to suppression of proliferative activity, but partial recovery was achieved earlier on the average in strain H. The time required to elicit these changes in strain HW (haired analogues) was extended. With the histologic observations, data suggested also that the recovery period in HW strain mice following 7200 Rads was somewhat longer than in the other two strains.

REFERENCES

1. Segale, G. C. Sull'azione biologica dei raggi Röntgen e del radium sulle cartilagini epiphysarie. *Rad. Med.* **7**, 234-247 (1920).
2. Hinkel, C. L. The effect of roentgen rays upon the growing long bones of albino rats. I. Quantitative studies on the growth limitation following irradiation. *Am. J. Roentgenol.* **47**, 439-457 (1942).
3. Hinkel, C. L. The effect of roentgen rays upon the growing long bones of albino rats. II. Histopathological changes involving endochondral growth centers. *Am. J. Roentgenol.* **49**, 321-347 (1943).
4. Sams, A. The effect of 2000 R of X-rays on the internal structure of the mouse tibia. *Int. J. Radiat. Biol.* **11**, 51-68 (1966).
5. Gall, E. A., Lingley, J. R., and Hilcken, J. A. Comparative experimental studies of 200 kilovolt and 1000 kilovolt roentgen rays. I. The biological effects on the epiphysis of the albino rat. *Am. J. Path.* **16**, 605-618 (1940).
6. Dahl, B. Effets des rayons x sur les os longs en développement étude radiographique et anatomique. *J. Radiol. et d'Electrol.* **18**, 131-140 (1934).

HW mice
and HB
d to nar-
prolonged
second, the
ost twice
figure 91)
mpted to
this was
ossible to
basis of
HW mice,
normal-
bility of
oliferate.
te thick-
ve been
ed as a
and this
r matrix
bly hy-
h carti-

growth
whole-
shows
ands of
1 proc-
eosin.

7. Brooks, B. and Hillstrom, H. T. Effect of roentgen rays on bone growth and bone irradiation. *Am. J. Surg.* **20**, 599-614 (1933).
8. Bloom, W. and Bloom, M. A. Histological changes after irradiation. *Radiation Biology*, Ed. A. Hollaender, McGraw-Hill Book Co., Inc., New York, 1954, pp. 1091-1114.
9. Kember, N. F. An *in vivo* cell survival system based on the recovery of rat growth cartilage from radiation injury. *Nature* **207**, 501-503 (1965).
10. Kember, N. F. Cell survival and radiation damage in growth cartilage. *Brit. J. Radiol.* **40**, 496-505 (1967).
11. Kember, N. F. Kinetics of population of bone forming cells in the normal and irradiated rat. *Some Aspects of Internal Irradiation*, Ed. T. F. Dougherty, W. S. S. Jee, C. W. Mays, and B. J. Stover. Pergamon Press, New York, 1962, pp. 309-316.
12. Regen, E. M. and Wilkins, W. E. The effect of large doses of x-rays on the growth of young bone. *J. Bone Jnt. Surg.* **18**, 61-68 (1936).
13. Woodard, H. Q. and Spiers, F. W. The effect of x-rays of different qualities on the alkaline phosphatase of living mouse bone. *Brit. J. Radiol.* **26**, 38-46 (1953).
14. Cairnie, A. B. Cell proliferation studies in the intestinal epithelium of the rat: Response to continuous irradiation. *Radiat. Res.* **32**, 240-264 (1967).
15. Lamerton, L. F. Cell proliferation under continuous irradiation. *Radiat. Res.* **27**, 119-138 (1966).
16. Wimber, D. R. and Lamerton, L. F. Cell population studies on the intestine of continuously irradiated rats. *Radiat. Res.* **18**, 137-146 (1963).
17. Lamerton, L. F., Partifex, A. H., Blackett, N. M., Adams, K. Effect of protracted irradiation on the bone forming organs of the rat. Part 1. Continuous exposure. *Brit. J. Radiol.* **33**, 287-301 (1960).
18. Pybus, F. C. and Miller, E. W. The gross pathology of spontaneous bone tumors in mice. *Am. J. Cancer* **47** (1940).
19. Pybus, F. C. and Miller, E. W. The histology of spontaneous bone tumors in mice. *Am. J. Cancer* **40**, 54 (1942).
20. Finkel, M. P., Bergstrand, P. J., and Biskis, B. O. Latent period, incidence, and growth of Sr⁹⁰-induced osteosarcomas in CF₁ and CBA mice. *Radiology* **77**, 281 (1961).
21. Finkel, M. P., Lisco, H., and Brues, A. M. Toxicity of Sr⁹⁰ in mice. Malignant bone tumors. Argonne National Laboratory Biological and Medical Research Division Quarterly Report, November and December 1954-January 1955. ANL-5378, p. 106.
22. Auerbach, H. and Brues, A. M. Total-body surface irradiation for mice. *Radiat. Res.* **27**, 37-38 (1966).
23. Trueta, J. The role of the vessels in osteogenesis. *J. Bone Jnt. Surg.* **45B**, 402-418 (1963).

THE DEVELOPMENT AND HEALING OF RICKETS IN RATS. II. STUDIES WITH TRITIATED PROLINE*

D. J. Simmons and A. S. Kunin†

One of the most dramatic modifications of skeletal mineralization occurs in rickets. The present investigation uses autoradiography of tritiated proline in rats in order to determine whether the failure of mineralization of cartilage in rachitic rats is related to change in the ability of cells to produce collagen. The results indicate that in bone the cellular production of collagen is normal, but that in cartilage the most mature cells do not produce significant amounts of collagen.

INTRODUCTION

Rickets readily develops in the skeleton of young growing rats fed a low phosphate, vitamin D-free diet. The resultant morphology is characterized in part by widened growth plates composed predominantly of unresorbed hypertrophic cells. In rachitic cartilage, the chondrocytes appear to mature normally⁽¹⁾ and the ultrastructure of the matrix seems unremarkable⁽²⁾; yet mineralization, a prerequisite for capillary invasion and cartilage resorption, fails to occur.

* This study was supported by the U. S. Atomic Energy Commission and a grant, AM-09632, awarded to Dr. Kunin from the National Institutes of Health.

† Departments of Medicine and Orthopedic Surgery, University of Vermont College of Medicine, Burlington, Vermont.

Biochemical studies on this relatively avascular tissue have revealed that carbohydrate metabolism in growth cartilage, as in bone, is predominantly glycolytic in character. However, when slices of rachitic cartilages are incubated *in vitro*, glycolysis is markedly increased over that of the normal. Dietary phosphate supplementation is probably more able to reverse this abnormality than vitamin D alone.^(3, 4) Others^(5, 6) have also remarked that vitamin D cannot by itself cure rickets in the rat in conjunction with increased glycolysis, the activity of the major glycolytic enzymes in rachitic cartilage is coordinately increased and can be coordinately reduced to normal levels by either dietary phosphate or vitamin D.⁽⁴⁾ Histochemical observations in parallel studies with this model system⁽⁷⁾ are in general accord with the biochemical data.

The role of dietary phosphate and vitamin D in the development and healing of rickets has also been investigated by high resolution autoradiographic techniques employing tritiated thymidine (³HTdR) as a marker for cells preparing to enter mitosis.⁽⁸⁾ These results indicate that the rapidity with which histologic rickets occurs initially is due to enhanced

TABLE 56. DIVISION OF RATS BY GROUP

Group	Dietary regimen	Number of rats sacrificed at	
		21 days	23 days
1	Purina Chow, <i>ad lib.</i>	3	3
2	Purina Chow, pair-fed with group 4	3	3
3	Rachitogenic diet fortified with phosphate and vitamin D ₂ <i>ad lib.</i>	3	3
4	Rachitogenic diet, 21 days, <i>ad lib.</i>	3	3
5	Rachitogenic diet (14 days) and phosphate (7-10 days)	3	3
6	Rachitogenic diet (14 days) and vitamin D ₂ (7-10 days)	3	3
7	Rachitogenic diet (14 days) and phosphate plus vitamin D ₂ (7-10 days)	3	3

study the ability of inorganic phosphate and vitamin D₂ to heal rickets, 3 groups of 6 rats each were raised on the basal rachitogenic ration for 14 days. Subsequently, these animals were maintained for an additional 7-10 days on diets which were selectively enriched with either NaH₂PO₄, vitamin D₂, or both, as outlined above. The division of rats by group is listed in Table 56.

On the 21st day of the experiment, all the animals were injected intraperitoneally with 2.0 μ Ci ³H-proline* per gram body weight in 0.1-0.3 ml 0.01 N HCl. Three rats from each group were sacrificed by cervical dislocation at 4 hr and 3 days after isotope injection. These time periods were chosen so that both the initial pattern of isotope uptake by chondrocytes and bone cells could be followed, as well as the subsequent rates of endochondral ossification and formation of new bone by osteoblasts. The tibias removed from the rats at autopsy were fixed in 10% neutral formalin, decalcified in 10% EDTA (pH 7.4-7.6), embedded in paraffin and sectioned with the bones oriented in their long axes on a rotary microtome at 4 μ . Slides bearing deparaffinized sections were autoradiographed by dipping in liquid Kodak NTB-2 emulsion. After a 9-week exposure period in a freezer, the slides were developed for 5 min in Kodak D-19 (20° C), fixed in acid fixer, washed thoroughly, and stained through the emulsion with hematoxylin and eosin.

Autoradiographic Studies

The pattern of silver grains developed in the emulsion was examined to determine which cell types in

* L-proline-3,4-³H, New England Nuclear Corporation, Lot No. 343-207, Specific Activity 5.86 Ci/mM.

proliferative activity of chondrocytes (percent labeled proliferative zone cells)—as well as to the inability of the tissue to calcify and undergo bony replacement. However, the autoradiographic studies with ³HTdR fail to delineate any specific cellular mechanism which, in the absence of deficient calcification, might explain why rickets occurs. With time, the proliferative capacity of chondrocytes decreases, but the ability of the competent cells to synthesize DNA seems normal. Rachitogenic diets enriched with phosphate were more effective than vitamin D alone in reversing the eventual decline in proliferative potential of rachitic cartilage.

The present autoradiographic investigation was undertaken to determine whether the abnormalities observed during the development of rickets in rats reflected an altered ability of cartilage and bone cells to produce the extracellular collagenous components of their respective matrices. We have used ³H-proline as a tracer based upon evidence that it is a selective marker for collagen formation.⁽⁹⁻¹²⁾ The intracellular pathway involving the Golgi apparatus by which protocollagen is synthesized in chondrocytes has been established by electron microscopic autoradiography.^(13, 14) The export of radioproline from chondrocytes and osteoblasts and its incorporation into collagen with time has been effectively demonstrated by light microscopic autoradiography,^(11, 15) and by experiments conducted *in vitro*.⁽¹⁶⁾ This study also permitted a further investigation of the capacity of dietary supplements of phosphate and/or vitamin D₂ to heal rickets, and the opportunity to evaluate the results from several other laboratories^(15, 17) which suggest that collagen formation is accelerated in rickets.

MATERIALS AND METHODS

The experimental protocol was essentially identical to that employed previously by Kunin and his coworkers.^(3, 7, 8) Rickets was produced in 6 male weanling Sprague-Dawley rats (40-50 g) utilizing a high calcium (1.2%), low phosphate (0.1%), vitamin D-free diet⁽¹⁸⁾ for 21-23 days. For comparison, littermates were fed either Purina Laboratory Chow (calcium, 1.42%; phosphorus, 0.96%) *ad libitum*, or pair-fed with this commercial preparation in amounts consumed daily by the rats on the rachitogenic diet. A third group was sustained on the basal rachitogenic diet which was supplemented with NaH₂PO₄ (calcium to phosphorus ratio = 1.4:1), and vitamin D₂ (10 I.U. per gram diet) *ad libitum*. Free access to deionized distilled water was permitted, and the colony was maintained under shielded incandescent lighting in constant temperature rooms at 22° C. In order to

the tissues had sequestered radioprolin during the initial 4 hr of the experiment. The number of silver grains over the cytoplasm of labeled osteoblasts in the periosteum, endosteum, and the endosteal surface in the area of the proximal tibial metaphysis was averaged for 30–50 cells to obtain a quantitative estimate of the utility of the tracer for bone matrix synthesis (*vide infra*). With the staining method employed, an osteoblast was defined as a basophilic cell with an eccentric nucleus, a prominent nucleolus and a juxtannuclear vacuole (Golgi apparatus) located on or close to a bone surface. The relative number of osteoblasts and their precursor cells, variously called reticular, mesenchymal, or osteoprogenitor cells, was not estimated in the primary spongiosa, although Rohr⁽¹⁵⁾ has indicated that the absolute

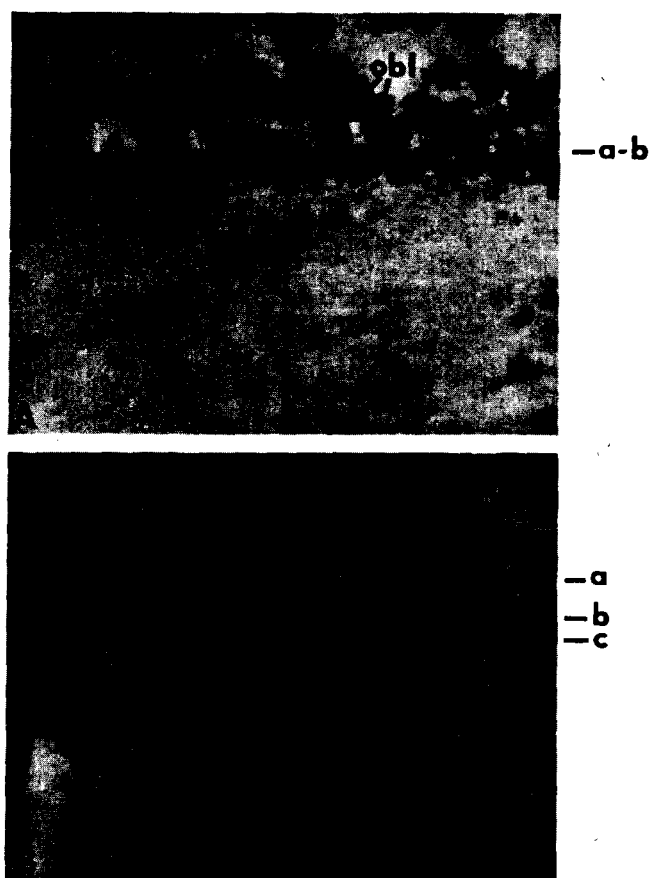


FIG. 95.—Autoradiographs of the articular surface of the transverse epiphyseal bone from rats sacrificed at two intervals of time after a single injection of ^3H -proline. A, a band of silver grains at a-b representing collagen newly formed by osteoblasts (obl) 4 hr after injection. The cytoplasm of the osteoblasts is lightly labeled. B, the position of the silver grains over labeled collagen lamellae 3 days postinjection. Interval a-c, thickness of lamellar bone formed in 3 days. Interval b-c, thickness of the band of silver grains. Note the trail of silver grains (interval a-b) due to reutilization of radioprolin. Hematoxylin and eosin. Original magnification 250 \times .

numbers of osteoblasts increase in rachitic rat this point, it should be noted first that Tom found peak uptake of radioprolin in the osteogenic cells of mice within 15–30 min after a ^3H -injection. Secondly, in concert with results from studies using radioglycine as a tracer for collagen formation,^(9, 10, 12) it is known that osteogenic cells report a large porportion of their tracer content to the surfaces of bone as an integral part of newly synthesized collagen molecules by 4 hr. However, proline is also an active metabolite and can be transformed via glutamic acid into other amino acids which are utilized for a number of other compounds, proteins and mucopolysaccharides. Thus the early grain count *per se* cannot be depended upon to measure only the rate of collagen synthesis by labeled osteoblasts.

The reliability of the initial grain counts was checked independently by measuring the position of the labeled matrical (collagen and mucopolysaccharide) band of silver grains buried within the cortex 30 days after radioprolin administration (Figure 96). The thickness of lamellar bone deposited by osteoblasts on the growing surfaces of the epiphyses (endosteal, periosteal) and transverse epiphyseal bone during this interval was calculated by measuring the total distance from the leading edge of the continuous band of labeled matrix to the anatomical surfaces. This was done in the center of approximately 60 adjacent high power fields (400 \times) with an ocular micrometer. This value was divided by 3 so that the rate of appositional bone growth could be expressed in microns per day. An estimation of the thickness of the band of labeled matrix was also attempted, for lack of definitive grain count data early after tracer administration, this measure should reflect accurately the rate at which the osteogenic cells on these surfaces were producing new structural collagen. The two sets of data were also expressed as an Osteoblast Activity Index (OAI), which is defined as the observed thickness of the ^3H -proline label divided by the observed apposition rate (microns/microns/day). It is unlikely that these data would be complicated at the light microscope level by any change in the catabolic rate of newly synthesized collagen molecules or differential packing of collagen fibers buried into the skeleton.^(8, 15) A ratio of 1 would suggest that the osteoblasts formed the labeled bone matrix in exactly 24 hours' time. Other values would be inversely proportional to the pace at which the osteogenic cells were performing. It was difficult to apply this type of analysis to trabecular bone, first because it is less well-oriented than compact bone and second, because our animals were not sacrificed at narrow time intervals.

TABLE 57. LINEAR AND APPositionAL BONE GROWTH DURING THE DEVELOPMENT AND HEALING OF RICKETS IN RAT TIBIAS (MEAN \pm S.E.)

Group	Linear growth, μ /day	Transverse epiphyseal bone			Periosteum			Proximal metaphyseal endosteum			Endosteum on shaft bone		
		Appositional growth, μ /day	Thickness of the ^3H -proline band of matrix, μ	OAI ^(a)	Appositional growth, μ /day	Thickness of the ^3H -proline band of matrix, μ	OAI ^(a)	Appositional growth, μ /day	Thickness of the ^3H -proline band of matrix, μ	OAI ^(a)	Appositional growth, μ /day	Thickness of the ^3H -proline band of matrix, μ	OAI ^(a)
Control: ad libitum-fed	222.4 \pm 13.4	3.98 \pm 0.15	4.3 \pm 0.31	1.08	6.73 \pm 0.96	6.71 \pm 0.82	0.99	5.98 \pm 0.48	4.40 \pm 0.10	0.74	4.73 \pm 0.21	4.54 \pm 0.16	0.96
Control: pair-fed	201.6 \pm 6.9	2.75 \pm 0.23	3.76 \pm 0.31	1.36	6.76 \pm 1.53	7.39 \pm 0.53	1.09	5.55 \pm 0.58	4.26 \pm 0.50	0.77	3.27 \pm 0.16	4.03 \pm 0.40	1.23
Rachitic (3 wk)	134.2 \pm 32.2	3.41 \pm 0.88	4.29 \pm 1.12	1.29	5.57 \pm 1.05	5.57 \pm 1.05	1.18	4.56 \pm 0.56	3.63 \pm 0.64	0.80	4.01 \pm 1.03	3.52 \pm 0.94	0.88
Rachitic + phosphorus (1 wk)	82.0 \pm 3.6	1.42 \pm 0.23	2.71 \pm 0.20	1.90	2.38 \pm 0.38	4.89 \pm 0.43	2.05	4.79 \pm 0.40	3.78 \pm 0.53	0.79	3.15 \pm 0.30	3.60 \pm 0.25	1.14
Rachitic + vitamin D (1 wk)	44.2 \pm 12.7	1.17 \pm 0.21	2.04 \pm 0.38	2.28	1.55 \pm 0.14	3.78 \pm 0.02	2.43	4.86 \pm 1.21	3.97 \pm 0.22	0.82	3.01 \pm 0.08	3.71 \pm 0.27	1.23
Rachitic + phosphorus and vitamin D (1 wk)	81.0 \pm 3.2	1.91 \pm 0.08	2.68 \pm 0.29	1.40	2.21 \pm 0.36	3.94 \pm 0.78	1.78	5.43 \pm 1.11	3.82 \pm 0.42	0.70	4.69 \pm 0.28	3.49 \pm 0.28	0.74
Control: Rachitic + phosphorus + vitamin D (3 wk)	96.9 \pm 11.9	1.34 \pm 0.18	2.67 \pm 0.38	1.99	2.17 \pm 0.27	4.37 \pm 0.33	2.01	4.39 \pm 0.10	3.02 \pm 0.41	0.69	2.95 \pm 0.17	2.88 \pm 0.26	0.97

^(a) Osteoblast activity index.

Estimates of the daily rate of endochondral ossification, i.e., linear growth of the tibias, were made by dividing the total distance (in microns) that the trabeculae labeled at time 0 had been displaced from the epiphyseal disc by the number (3) of days.

RESULTS

The weight gain, linear bone growth characteristics, and the appearance of the cartilage plates of the rats maintained on the various diets were comparable to those described previously.⁽⁸⁾ For the description of the pattern of labeling in cartilage, we have selected the terminology of Balogh and Kunin.⁽⁷⁾

Balogh and Kunin ⁽⁷⁾	Equivalent to Dodd's ⁽⁹⁾ classification
Upper layer	Zone 1—Narrow "reserve cell" zone adjacent to the bone and marrow spaces of the epiphysis.
Middle layer	Zone 2—Zone of cell proliferation composed of wedge-shaped or discoidal cells. Zone 3—Zone of cell enlargement.
Lower layer	Zone 4—Zone of cell hypertrophy.

The data relative to appositional growth rates of bone and OAI ratios have been tabulated in Table

TABLE 58. AVERAGE GRAIN COUNTS (³H-PROLINE) IN OSTEOBLASTS DURING DEVELOPMENT AND HEALING OF RICKETS IN RAT TIBIAS

Group	Post-injection time of sacrifice ^(a)	Periosteum	Shaft endosteum	Epiphyseal bone
Controls: ad libitum-fed	4h	13.1	10.9	10.9
	3d	5.4	6.5	5.1
Controls: pair-fed	4h	13.0	11.1	13.8
	3d	6.1	6.5	5.9
Rachitic (3 wk)	4h	12.4	12.5	15.0
	3d	5.5	5.0	6.2
Rachitic + phosphorus (1 wk)	4h	12.2	15.4	11.4
	3d	5.2	5.2	5.4
Rachitic + vitamin D (1 wk)	4h	7.6	10.3	10.1
	3d	4.96	6.5	6.2
Rachitic + phosphorus + vitamin D (1 wk)	4h	8.1	10.1	10.5
	3d	4.2	5.8	5.1
Control: Rachitic + phosphorus + vitamin D (3 wk)	4h	8.5	11.3	12.2
	3d	5.4	5.7	6.2

^(a) Average of 3 rats per time interval.

57. Osteoblast grain counts have been included in Table 58.

Control Animals Fed Commercial Laboratory Chow

At 4 hr after injection, silver grains were localized predominantly over the cells (nucleus and cytoplasm) and extracellular matrix in the middle layer of the cartilage (Figure 96). Perhaps only 2% of the cells in the upper layer were labeled. The matrix nuclei and cytoplasm of all the cells in the lower zone were labeled as well, but the intensity of the autoradiographs was much less than that noted in the middle layer. The cores of cartilage in the trabeculae of the primary spongiosa were not labeled at this early time. Radioprolin tagged the undifferentiated and differentiated cells in the metaphysis, and large concentrations of grains were found between the osteoblasts and bone trabecular surfaces. The osteoblasts were the most intensely labeled, and this general pattern was found on all periosteal and endosteal surfaces which were undergoing appositional bone growth at the time of injection. Newly buried osteocytes in the metaphysis and shaft were also marked by radioprolin, and the tracer was located at the edges of their lacunae. Only the cytoplasm of osteoclasts was labeled.

Significant labeling of the extracellular matrix of the cartilage plate was evident 3 days after tracer injection, but the tracer was concentrated in the middle and lower layers only. The intensity of the autoradiographs over the middle layer was less than at 4 hr, and somewhat increased over the lower layer. The remnants of the cartilage which had initially been labeled and had subsequently undergone endochondral ossification now projected from the plate into the metaphysis in trabeculae of the primary spongiosa, and lamellae of primary trabecular bone in this area were more diffusely labeled than the cores of cartilage. Distally, the trabeculae were very heavily labeled. This region quite obviously marked the juxta-epiphyseal zone labeled by radioprolin at 4 hr which had been displaced during the 3-day postinjection period by continued endochondral ossification and linear bone growth (200–220 μ /day). In this time, the trabeculae grew thicker by appositional bone growth and this process served to bury the heavily labeled lamellae under more diffusely labeled collagen matrix. The cytoplasm of the osteoblasts in this zone showed some 5–6 grains. It was impossible to measure the appositional rate of bone growth on these trabeculae owing to their irregular contours.

In the animals fed Purina Chow *ad libitum*, the daily apposition rate of lamellar bone measured on the periosteum, shaft endosteum, and transverse epi-

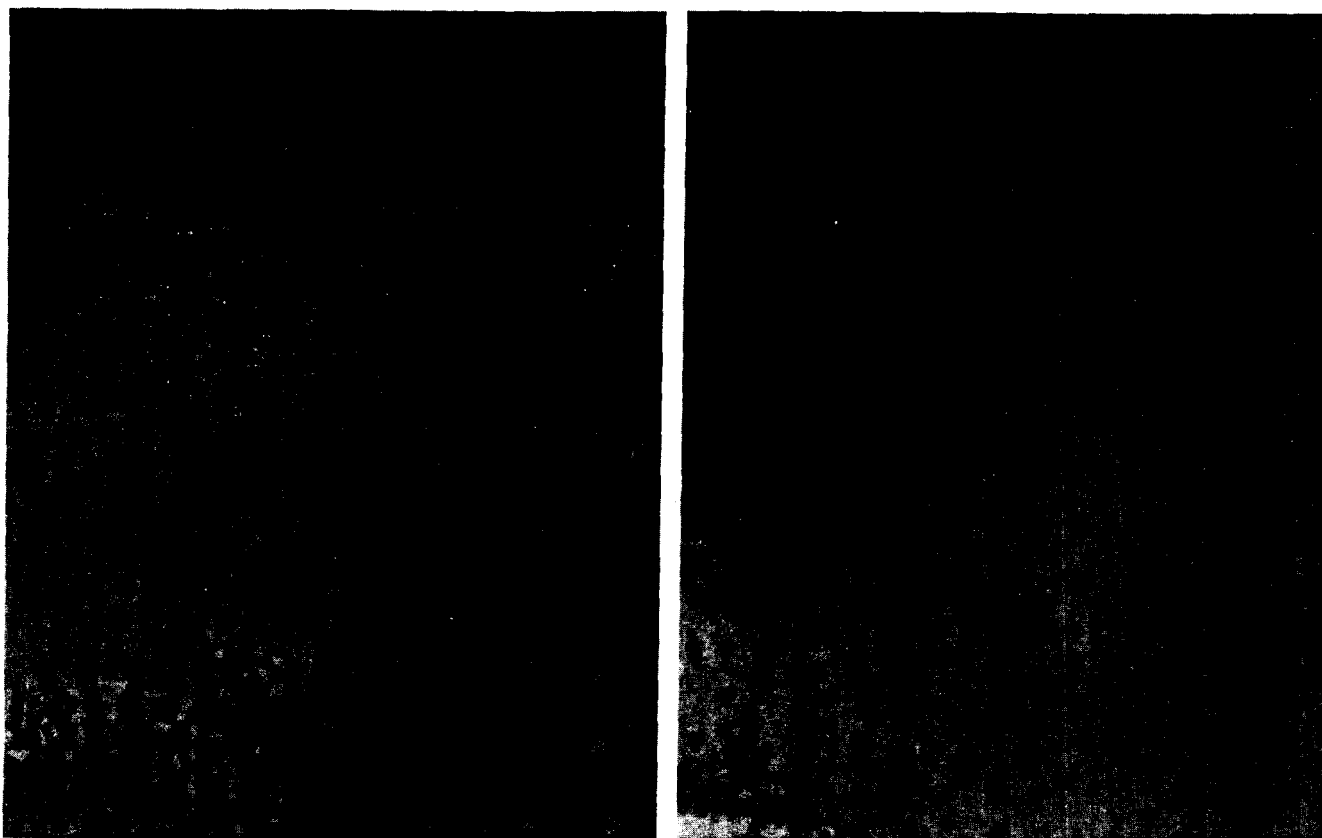


FIG. 96.—Autoradiographs of the proximal tibial cartilage of rats sacrificed 4 hr after a single intraperitoneal injection of ^3H proline. Left, control; right, rachitic. Note that the silver grains in the emulsion are distributed over the cells and extracellular matrix throughout the control cartilage, whereas the thickened lower zone of hypertrophic cells in the rachitic cartilage is unlabeled. Hematoxylin and eosin. Original magnification $250\times$.

physeal bone was $6.7\ \mu$, $4.7\ \mu$, and $3.9\ \mu$, respectively. In the pair-fed group, somewhat less bone growth was registered on the epiphyseal bone ($2.8\ \mu/\text{day}$), but otherwise there was no obvious effect due to dietary restriction. The thicknesses of the bands of labeled collagen were in fairly good agreement with these daily appositional growth rates, and the OAI ratios approximated a value of 1. In addition to the dense band of silver grains which moved away from the cells as new matrix was deposited (Figure 95), there was a diffuse distribution of grains in the matrix deposited during the second and third days. This has been described by Tonna⁽¹¹⁾ as a "trail" due presumably to reutilization of metabolized radioproline by the osteoblasts.

Rats fed the fully supplemental basal rachitogenic ratio for 2 weeks showed essentially the same pattern of radioproline uptake and retention. However, the rates of linear growth ($97\ \mu/\text{day}$) and lamellar bone apposition on periosteal and epiphyseal bone surfaces were substantially less than in the other control groups, and their OAI was approximately 2.

Only the rate of endosteal apposition was within normal limits (= pair-fed controls). The poor growth observed for this group may be due to voluntary reduction in food intake as the rats did not favor the diet and ate less.

Rachitic Rats

At 4 hr, the autoradiographs showed ^3H -proline retention in and around the cells in the upper and middle layers of the cartilage. In the lower layer, the label was found predominantly in the youngest hypertrophic cells—a distinct difference from the normal pattern. Little proline was detected in the older juxtametaphyseal chondrocytes (Figure 96). In the metaphysis, cortical and transverse epiphyseal bone, the early distribution of the isotope was similar to the controls, and the grain counts suggested that rachitic osteoblastic vigor was normal.

After 3 days, the middle and lower layers of the cartilage were uniformly labeled by radioproline, as were the remnants of the cartilage left by endochondral ossification in the primary spongiosa.

Distally, interposed between this newly formed endochondral bone and the heavily labeled trabeculae in the secondary spongiosa, there was a transitional zone characterized by trabeculae having unlabeled cores of cartilage and diffusely labeled bony lamellae. This pattern clearly reflected events accompanying linear bone growth ($134 \mu/\text{day}$) subsequent to labeling. The transitional zone represented the matrix around the juxtametaphyseal chondrocytes which had acquired the least radiopline 4 hr after injection. The grain counts in osteoblasts lining the trabeculae in the secondary spongiosa were essentially normal. The rates of appositional lamellar bone formation on the periosteum, endosteum, and epiphyseal bone were also normal, and the OAI approximated values obtained for the pair-fed control group.

Rachitic Rats Treated with Phosphorus

While the epiphyseal cartilages from rats fed the basal rachitogenic ration supplemented with inorganic phosphate were thinner than the rachitic plates and their cytoarchitecture was more nearly normal, the 4-hr pattern of labeling resembled that of the rachitic cartilage. In the upper and middle layers, radiopline was detected in the nucleus and cytoplasm of the cells and in their extracellular matrix. Only the first 1–2 hypertrophic cells per column in the lower layer were heavily labeled; matrical tracer deposition was very slight. No unusual patterns of labeling were detected in the metaphysis or in the periosteum and endosteum, but the cells and surfaces of the epiphyseal bone were only lightly marked.

Labeling of the cartilage and metaphyseal trabeculae 3 days after injection also resembled the pattern described for rats maintained on the rachitogenic diet. Linear growth was $80 \mu/\text{day}$. Compared to the normal and rachitic rats, little appositional bone growth ($1\text{--}2 \mu/\text{day}$) was registered on periosteal and epiphyseal bone surfaces. While dense bands of silver grains over labeled collagen lamellae were thinner than normal at these states, OAI values were nearly equivalent to those calculated for the bones of control rats fed the basal rachitogenic ration which had been supplemented with phosphorus and vitamin D. These criteria also indicated that endosteal apposition rates were normal (= pair-fed controls), and unchanged by the diet. The grain counts in osteoblasts were normal.

Rachitic Rats Treated with Vitamin D₂

The cartilage from vitamin D-treated rachitic rats was more normal than the rachitic in appearance, but the pattern of labeling resembled that described for the phosphate-supplemented group. Here, too, the

grain counts in periosteal osteoblasts were abnormally low 4 hr after injection.

Vitamin D treatment of the rachitic rats did not improve the rate of appositional bone growth on the periosteal and epiphyseal bone surfaces ($1.0\text{--}1.5 \mu/\text{day}$). In fact, the measurements were significantly less than those recorded for the phosphate-supplemented rats, but there was less difference between these two groups in terms of the thickness of the dense lines of silver grains developed in the emulsion above radiopline-rich collagen lamellae, OAI values, and the numbers of grains over osteoblasts. The bone growth provided by endosteal cells was equal to that of the pair-fed controls and rachitic rats. Whereas the bulk of the periosteal and epiphyseal bone activity remained in the surface lamellae, the endosteal hot lines were buried. Linear bone growth was approximately $44 \mu/\text{day}$.

Rachitic Rats Treated with Phosphorus and Vitamin D₂

The 4-hr and 3-day patterns of labeling in the bones of rachitic rats treated with both phosphate and vitamin D were not appreciably different from the effect of either partially enriched dietary supplement. Incomplete labeling of the lower layer of the cartilages produced, after 3 days' growth, the characteristic transitional zone in the metaphyseal trabeculae. Linear growth of the tibias was estimated to be $81 \mu/\text{day}$. Only the periosteal osteoblasts contained fewer than normal numbers of grains. However, appositional growth on periosteal and epiphyseal bone surfaces was more rapid than that observed for the animals supplemented with vitamin D or phosphorus alone. The ratio on the epiphyseal bone per se was normal (= pair-fed controls). Endosteal bone growth was particularly enhanced; the rate and OAI index approximated values achieved by controls fed the commercial chow *ad libitum*. The matrical band of silver grains was thinner than normal, but equivalent to that produced in the bones of the animals fed each of the supplements alone.

DISCUSSION

The results from this study confirm previous observations that rats maintained on a diet deficient in phosphorus and vitamin D are stunted in growth and develop rickets within 7 days.⁽⁸⁾ There appears to be some aspect of the artificial diet other than its Ca/P ratio and vitamin D content that prevents full restitution of growth potential when both these nutrients are replaced in amounts which in commercial feeds provide for good growth. This problem has also been encountered by other investigators

who have employed this diet^(1, 2) and the Steenbock-Black rachitogenic diet⁽²⁰⁾ as well, and it remains unresolved. However, in view of data indicating that the fully supplemented rachitogenic ration is utilized as effectively for growth as is Purina Laboratory Chow, disparate results from these control groups most probably reflect differences in daily food intake. In point of fact, since those rats fed the phosphate and vitamin D-supplemented ration for 3 weeks ate much less than the pair-fed controls, we do not believe that they are an adequate group against which to compare the effects of deficient diets. Parameters such as linear and appositional bone growth in this study, and epiphyseal cartilage thickness and cell DNA synthetic indices in the growth plate in a previous study, seemed to be most sensitive to the effects of what must be considered voluntary starvation.⁽⁸⁾

In most animals, irrespective of dietary treatment, the distribution of radioproline in chondrocytes, cartilage matrix, and bone 4 hr and 3 days after injection, was similar to that reported by Tonna, et al.⁽¹¹⁾ and corresponded with the pattern for radioglycine described by others.^(10, 12, 21, 23) Early, grains in the emulsion were found over the nucleus and cytoplasm of chondrocytes, osteoblasts, and undifferentiated mesenchymal cells, newly formed osteocytes, cartilage matrix, bone surfaces, and in the cytoplasm of osteoclasts. Three days after injection, radioproline was less heavily invested in the cells and was detected principally in the matrical proteins of bone and cartilage, suggesting that the bulk of radioactivity was destined for the synthesis and export of collagen by these cells. Most of the cells labeled initially retained a nuclear label after three days, presumably due to utilization of some tracer for structural nuclear protein synthesis as suggested by Carneiro and Leblond⁽²³⁾ and Revel and Hay.⁽¹³⁾ Thus, the progressive loss of label from the cytoplasm of cells and its burial deep within matrix provides direct evidence for the functional capacity of osteoblasts and chondrocytes. However, distributional changes in the initial tracer load and in the rate of bone matrix synthesis were observed in the treated rats.

Whereas, for instance, all the chondrocytes (upper, middle, and lower layers of the cartilage plates) in control tissues seemed able to synthesize and form collagen—albeit with less vigor as they matured—only a slight autoradiographic image was recorded over the mature juxtametaphyseal cells in either the rachitic cartilages or those from rachitic rats ostensibly healed by phosphorus and vitamin D. Thus, the efficacy of phosphate, in particular, and vitamin D to heal rickets histologically and correct the abnormal-

ities in enzyme activity^(3, 4, 7, 8) did not extend fully to the chondromucoprotein moiety of the cartilage matrix. An inability of the juxtametaphyseal cells in rachitic animals raised on the Steenbock-Black diet to incorporate radiosulfur was also reported by Hjertquist,⁽²⁴⁾ and this abnormality was not reversed by vitamin D and a return of these animals to a normal diet. On the other hand, the rate of ³⁵S uptake by cells in the cartilage is normally dependent upon vitamin D^(25, 26) which appears to be essential for the production of a calcifiable matrix. Thus these observations seem to suggest that the most mature cells in rachitic rat cartilage are not producing significant amounts of chondroitin sulfate and collagen, and that this basic cell deficit may account at least in part for the deficient calcification long observed in rachitic tissue. Implicit, also, is the possibility that the state or structure of the chondromucoproteins and other components of rachitic cartilage is too immature or abnormal for mineralization to proceed.⁽²⁷⁻²⁹⁾ These experiments, of course, do not contribute to the controversy about the dependent⁽³⁰⁾ or independent^(31, 32) cellular control for the secretion of procollagen and mucopolysaccharides in cartilage.

The findings in this study tend not to support the autoradiographic and biochemical evidence from other laboratories that the rate of bone formation in rachitic rats is excessive. Rohr⁽¹⁵⁾ reported that the rachitic rat metaphyses contained more osteoblasts than normal and that the export of radioglycine from these cells and matrix formation occurred more rapidly than normal. Parsons and Self⁽¹⁷⁾ reported a higher specific activity of labeled proline/hydroxyproline in rachitic rat metaphyses 48 hr after injection. But their data relative to bone turnover, i.e., normal urinary hydroxyproline specific activity and a fall in the specific activity of tibial bone 2-3 days post-injection compared to a significant rise in control tissue, suggest rather that the overall rate of bone formation in rickets is normal or slow. We observed regional differences in the rates of lamellar bone formation. But with the sole exception of a low rate of endosteal apposition along the margins of the metaphyseal cortex (Table 57), the pace of periosteal and endosteal osteogenesis in the compacta was within normal limits (= pair-fed controls). Frost⁽³³⁾ noted that the osteoblast birth rate in haversian bone of osteomalacic patients (adult rickets) was increased; however, while there were more cells, they showed decreased vigor, and bone formation rates were low.

Dietary supplements of phosphorus or vitamin D administered for at least 7 days to rachitic rats appeared to be without any great ameliorating influence on the rates of periosteal and epiphyseal bone apposi-

tion and linear bone growth. In fact, these rates were much lower than those calculated for the rachitic/pair-fed control animals, and the bone formation indices (OAI) suggested that the osteoblasts on these surfaces were functionally lethargic. Phosphate was statistically somewhat more effective than vitamin D on these parameters and it did cure rickets histologically and histochemically, but there was no overall improvement which could be attributed to either agent per se. In contrast, the pace of endosteal lamellar bone formation was quite independent of treatment, and osteoblast activity was normal at all times. It may be concluded, then, that thinning of the rachitic cortices is due to deficient periosteal bone formation. It is difficult to estimate the contribution of the partially or fully reconstituted diets to the observed stunting of bones. But it is known that the effects of undernutrition are much more severe if it occurs in young animals, and that if the nutritional insult is prolonged they may never attain the body weight or cell growth of animals reared on a normal diet.⁽³⁴⁾

The osteoblast activity indices reported in this study, based in part upon the thickness of the dense lines of matrical silver grains, are at the light microscope level of resolution unlikely to be influenced by changes in the ultrastructure of bone. Poorly oriented collagen fibers in rachitic osteoid have been described in dogs⁽³⁵⁾ and in rats⁽²⁾ by electron microscopy. It should be noted that the fine structure of the rachitic osteoblast is not entirely normal; broad cysternae have been observed which contain a moderately dense amorphous material that Robinson and Sheldon⁽³⁶⁾ suggest is collagen which is not yet polymerized to fibrillar form. There is little evidence from the present study to suggest that the ultrastructural changes contribute to the sharply decreased activity of osteoblasts following phosphorus and/or vitamin D supplementation. OAI values approximating 2 were also detected in the stunted bones from rats on the fully supplemented rachitogenic diet (Group 3). Nor is it likely that the instances where the rate of lamellar bone formation was depressed signal a parathyroid endocrinopathy, for serum calcium concentrations in these animals were normal or slightly high (vitamin D-treated) and the ultrastructure of the glands was normal.⁽³⁷⁾ Involvement of parathyroid activity might explain the very rapid osteogenesis reported by Rohr⁽¹⁵⁾ in the metaphyses of rachitic rats raised on a diet which was vitamin D-free and severely deficient in both calcium (hypocalcemic?) and phosphate. Parathyroid extract administered to rats and mice, for instance, elicits a biphasic response in bone—an initial inhibition and a secondary stimulation of bone cell amino acid transport and collagen synthesis.^(22, 38)

While the present studies do not necessarily contribute to our understanding of the basic biochemical lesions in cartilage and bone which produce histologic rickets, evidence has also been presented that the most mature cells in rachitic cartilage are not producing significant amounts of collagen (and presumably chondroitin sulfate) and that this basic cell defect accounts, at least in part, for deficient calcification of the tissue. The results from this study also suggest that the rate of bone matrix formation in rachitic bone is generally normal.

SUMMARY

³H-proline was administered intraperitoneally to young male rats with nutritional rickets produced by a low phosphate, vitamin D₂-free diet. Autoradiographs of the upper tibial epiphyseal cartilages from untreated control littermates showed tracer incorporation by the cells and extracellular matrix 4 hr and 3 days post-injection, respectively, and this occurred throughout the proliferative and hypertrophic cell zones. The pattern of tracer uptake was abnormal in the thickened cartilages from rachitic rats; the oldest juxtametaphyseal chondrocytes were unable to synthesize significant amounts of matrical protein and this effect could not be corrected thereafter by feeding rachitic rats nutritionally adequate supplements of phosphate and/or vitamin D.

The rate of bone formation was calculated from the displacement (burial) of the labeled lamellae of bone matrix from anatomical surfaces 3 days post-injection, as well as by the thickness of the linear bands of silver grains recorded in the photographic emulsion. Lamellar bone formation at the periosteum, endosteum and on the articular surface of the transverse epiphyseal bone was essentially normal in rats rendered rachitic by the deficient diet. Unexpectedly, the pace of appositional bone growth on the periosteum and transverse epiphyseal bone was depressed when rachitic rats were treated with phosphate and/or vitamin D, owing presumably to the functional lethargy of osteoblasts at these sites. Endosteal lamellar bone formation rates on the shaft and peripheral to the metaphysis were independent of treatment.

REFERENCES

1. Sheldon, H. and Robinson, R. A. Studies on rickets. II. The fine structure of the cellular components of bone in experimental rickets. *Z. Zellforsch.* **53**, 685-701 (1961).
2. Sheldon, H. and Robinson, R. A. Studies in rickets. I. The fine structure of uncalcified bone matrix in experimental rickets. *Z. Zellforsch.* **53**, 671-684 (1961).
3. Kunin, A. S. and Krane, S. M. The effect of dietary phosphorus on the intermediary metabolism of epiphyseal

- cartilage from rachitic rats. *Biochim. Biophys. Acta* **107**, 203-214 (1965).
4. Meyer, W. L. and Kunin, A. S. The inductive effect of rickets on glycolytic enzymes of rat epiphyseal cartilage and its reversal by vitamin D and phosphate. *Arch. Biochem. Biophys.*, in press.
 5. Ferguson, H. W. and Hartles, R. L. The effect of vitamin D on the bones of young growing rats receiving diets low in calcium and phosphorus. *Arch. Oral Biol.* **8**, 407-418 (1963).
 6. Shohl, A. T., Fan, C. H., and Farber, S. Effect of A. T. 10 (dihydroxytachysterol) on various types of experimental rickets. *Proc. Soc. Exptl. Biol. Med.* **42**, 529-534 (1939).
 7. Balogh, K., Jr. and Kunin, A. S. The effects of vitamin D₂ and dietary phosphorus on oxidative enzymes in the epiphyseal cartilage of rachitic rats. A histochemical study. *Lab. Invest.* **18**, 782-788 (1968).
 8. Simmons, D. J. and Kunin, A. S. The development and healing of rickets in rats. I. Nutritional considerations and studies with tritiated thymidine. To be published.
 9. Tonna, E. A., Cronkite, E. P., and Pavelec, M. A serial autoradiographic analysis of H³-glycine utilization and distribution in the femora of growing mice. *J. Histochem. Cytochem.* **11**, 720-733 (1963).
 10. Tonna, E. A. An autoradiographic evaluation of the aging cellular phase of mouse skeleton using tritiated glycine. *J. Gerontol.* **19**, 198-206 (1964).
 11. Tonna, E. A. Protein synthesis and cells of the skeletal system. *The Use of Radioautography in Investigating Protein Synthesis*, Ed. C. P. Leblond and K. B. Warren. Academic Press, New York, 1965, pp. 215-245.
 12. Young, R. W. Autoradiographic studies on postnatal growth of the skull in young rats injected with tritiated glycine. *Anat. Rec.* **143**, 1-13 (1962).
 13. Revel, J.-P. and Hay, E. D. An autoradiographic and electron microscopic study of collagen synthesis in differentiating cartilage. *Z. Zellforsch.* **61**, 110-144 (1963).
 14. Salpeter, M. M. H³-proline incorporation into cartilage: electron microscope autoradiographic observations. *J. Morph.* **124**, 387-422 (1968).
 15. Rohr, H.-P. Autoradiographische Untersuchungen über den Kollagenstoffwechsel bei der experimentellen Rattenrachitis. *Z. exp. Med.* **139**, 621-632 (1965).
 16. Flanagan, B. and Nichols, G., Jr. Metabolism studies of bone *in vitro*. IV. Collagen biosynthesis by surviving bone fragments *in vitro*. *J. Biol. Chem.* **237**, 3686-3692 (1962).
 17. Parsons, V. and Self, M. Urinary hydroxyproline excretion in phosphate depleted rachitic rats. *Nature* **217**, 551-552 (1968).
 18. Harrison, H. E. and Harrison, H. C. The uptake of radio-calcium by the skeleton: The effect of vitamin D and calcium intake. *J. Biol. Chem.* **185**, 857-867 (1950).
 19. Dodds, G. S. Row formation and other types of arrangements of cartilage cells in endochondral ossification. *Anat. Rec.* **46**, 385-395 (1930).
 20. Thomson, D. L. The effect of age and low phosphorus rickets on the metabolism of calcium-45 in rats. U.S. Atomic Energy Commission Report UCRL-2301 (1953), pp. 1-130.
 21. Carneiro, J. and Leblond, C. P. Role of osteoblasts and odontoblasts in secreting collagen of bone and dentin, as shown by radioautography in mice given tritium labeled glycine. *Exptl. Cell Res.* **18**, 291-300 (1959).
 22. Rosenbusch, J. P. and Nichols, G., Jr. Parathyroid hormone effects on amino acid transport into bone cells. *Endocrinology* **81**, 553-557 (1967).
 23. Carneiro, J. and Leblond, C. P. Continuous protein synthesis in nuclei, shown by radioautography with H³-labeled amino acids. *Science* **129**, 391-392 (1959).
 24. Hjertquist, S.-O. Autoradiographic study of the epiphyseal cartilage and bone tissue in normal and rachitic rats after administration of radiosulphate. *Biochim. Biol. Sper.* **2**, 126-140 (1961).
 25. Bescol-Liversac, J., Bassanetti, F., Dupuis, Y., and Guillem, C. Le ³⁵SO₄Na₂ et le ⁴⁵CaCl₂ dans l'étude du rachitisme expérimental chez le rat. *Radioisotopes in Animal Nutrition and Physiology*, Int. Atomic Energy Agency, Vienna, 1965, pp. 463-485.
 26. Dziewiatkowski, D. D. Vitamin D and endochondral ossification in the rat as indicated by the use of sulfur-35 and phosphorus-32. *J. Exptl. Med.* **100**, 25-32 (1954).
 27. Howell, D. S. Histologic observations and biochemical composition of rachitic cartilage with special reference to mucopolysaccharides. *Arthritis and Rheumatism* **8**, 337-354 (1965).
 28. Howell, D. S., Marquez, J. F., and Fita, J. C. The nature of phospholipids in normal and rachitic costochondral plates. *Arthritis and Rheumatism* **8**, 1039-1046 (1965).
 29. Kuhlman, R. E. and Stamp, W. G. Biochemical biopsy evaluation of the epiphyseal mechanism in a patient with Vitamin D-resistant rickets. *J. Lab. Clin. Med.* **64**, 14-20 (1964).
 30. Roskova-Cmucalova, B. and Bentley, J. P. Relation of collagen synthesis to chondroitin sulfate synthesis in cartilage. *Biochem. Pharmacol. (Suppl.)* **315**, 315-328 (1968).
 31. Bhatnager, R. S. and Prockop, D. J. Dissociation of the synthesis of sulphated mucopolysaccharide and the synthesis of collagen in embryonic cartilage. *Biochim. Biophys. Acta* **130**, 383-392 (1966).
 32. Juva, K., Prockop, D. J., Cooper, G. W., and Lash, J. W. Hydroxylation of proline and the intracellular accumulation of a polypeptide precursor of collagen. *Science* **152**, 92-94 (1966).
 33. Frost, H. M. The dynamics of human osteoid tissue. *Osteomalacie*, Ed. D. J. Hioco. Masson et Cie, Paris, 1967, pp. 3-18.
 34. Winick, M. and Noble, A. Cellular response in rats during malnutrition at various ages. *J. Nutr.* **89**, 300-306 (1966).
 35. Engfeldt, B. and Zetterström, B. Biophysical studies of the bone tissue of dogs with experimental rickets. *Arch. Path.* **59**, 321-331 (1955).
 36. Robinson, R. A. and Sheldon, H. Crystal-collagen relationships in healing rickets. *Calcification in Biological Systems*, Ed. R. F. Sognnaes. Am. Assoc. Advan. Sci., Washington, 1960, pp. 261-279.
 37. Roth, S. I., Au, Y. K. W., Kunin, A. S., Krane, S. M., and Raisz, L. G. Effect of dietary deficiency in vitamin D, calcium and phosphorus on the ultrastructure of the rat parathyroid gland. *Am. J. Path.* **53**, 631-650 (1968).
 38. Nichols, G., Jr., Flanagan, B., and Woods, J. F. Parathyroid influences on bone biosynthetic mechanisms. *The Parathyroid Glands*, Ed. P. J. Gaillard, R. V. Talmage and A. M. Budy. University of Chicago Press, Chicago, 1965, pp. 243-260.

CHICAGO AIR POLLUTION SYSTEM MODEL EXPERIMENTAL STUDIES

J. E. Carson

The city of Chicago's Department of Air Pollution Control and the Argonne National Laboratory's Meteorology Group have joined forces to obtain certain meteorological measurements needed for a proper understanding of diffusion rates over the city; these data are not available from other sources, such as the U. S. Weather Bureau. Fifteen flights, using both helicopters and light planes, have been made to measure the vertical and horizontal variations of temperature, humidity, and sulfur dioxide. Temperature sensors are being placed 1200 feet above street level on the TV support towers on the roof of the John Hancock Building. These data will result in continuous measure of the stability of the atmosphere over the city. Preliminary results using the sulfur hexafluoride (SF₆) tracer technique are discussed. The data show that background levels of this gas, at least near Argonne, are alarmingly high.

INTRODUCTION

Argonne National Laboratory, with the cooperation of the Chicago Department of Air Pollution Control (DAPC) and the support of the Department of Health, Education, and Welfare's National Air Pollution Control Administration (NAPCA), is developing a numerical model to predict air pollution levels (specifically, sulfur dioxide concentrations) from forecast meteorological and stack emission data. If a numerical model can be formulated which accurately forecasts SO₂ levels, it will then be possible to design air pollution abatement strategies which are effective with the least amount of cost and disruption to industry.

Complete information on the Argonne diffusion model can be found in the progress reports issued to date.⁽¹⁻⁴⁾

CHICAGO URBAN METEOROLOGICAL EXPERIMENTS

In order to predict SO₂ concentrations in an urban area accurately, it is necessary to know how the atmosphere transports and dilutes effluents ejected into it. That is, we must know how the diffusive capacity of the atmosphere over Chicago varies in time and space and from one meteorological regime to another. The diffusion parameters can be indirectly, but not very accurately, estimated from standard meteorological data, such as wind speed and cloud cover.

Four experimental programs to obtain additional meteorological measurements in Chicago and to measure dispersion rates over the uneven terrain of the city have been initiated. These projects are giving

a better understanding of urban flow patterns and how the city itself affects the structure of the atmosphere.

The four experimental programs in which Argonne is involved are: (1) helicopter sounding program, (2) instrumentation of tall buildings in the city, (3) tracer studies, and (4) fuel switch tests. In an earlier report of this series,⁽⁵⁾ the projected experimental programs were discussed in considerable detail. This paper will spell out the progress that has been made to implement and improve these projects.

AIRCRAFT SOUNDING PROGRAMS

Approximately fifteen flights have been made by DAPC and Argonne personnel to measure vertical sulfur dioxide and temperature profiles in and near Chicago. Both helicopters and light airplanes have been used.

The primary objective of this sounding program is to evaluate atmospheric and diffusion conditions (such as the horizontal and temporal variations of the urban lapse rate; the height, base, and thickness of inversions; the depth and extent of penetration of lake breeze circulation; and the altitudes of maximum SO₂ concentration) for a number of typical weather situations. Argonne's role in this program is to design the flight program and to analyze the resultant data inventory. The accomplishments during the fiscal year are discussed in the next article.

INSTRUMENTATION OF TALL BUILDINGS

The helicopter is an ideal sensor platform for obtaining data over large areas rapidly and at moderate cost. Unfortunately, neither helicopters nor radiosonde balloons permit continuous observations to be made at heights well above the surface.

The Chicago Department of Air Pollution Control has obtained permission to locate one aspirated temperature sensor on each of the two television towers on the roof of the John Hancock Building in Chicago. These sensors will be about 365 meters (1200 feet) above ground level and about 30 meters above the roof of the structure. Another sensor will be located about 45 meters (150 feet) above street level on the nearby Chicago Water Tower. DAPC will shortly begin discussions with the operator of one or two inter-

mediate-sized buildings in the area to obtain sites for additional sensors, so that temperature profiles up to 365 meters can be measured on a continuous basis. It is recognized that it may not be possible to obtain exact temperature profiles in this manner because of heat from buildings, obstructions to wind flow, and the fact that the sensors are not placed vertically; but for the purpose of diffusion analysis, information on the lapse rate class (inversion, isothermal, near neutral, or unstable) is probably adequate.

The accuracy of building sensor data can be tested by having the instrumented helicopter fly at the height of the sensor but away from the building heat. If these building-mounted sensors prove useful and accurate, a significant advance in city meteorological observations will have been achieved. Similar observations could be made at other locations in Chicago, as well as in other cities, at low cost.

FUEL SWITCH TESTS

The second in a series of fuel switch tests was conducted in Chicago between June 16 and July 4, 1968. A paper published in one of the progress reports⁽⁴⁾ and presented at the 62nd Annual Meeting of the Air Pollution Control Association,⁽⁶⁾ discusses the design of the experiment and results obtained. An extended abstract of this experiment appears elsewhere in this publication.

The third fuel switch test was conducted by DAPC and Argonne between May 20 and May 30, 1969. Realistic pollution abatement procedures were used in this test. Analysis of the resulting fuel use, air quality, and meteorological data is continuing.

SULFUR HEXAFLUORIDE TRACER STUDIES

In a previous report of this series,⁽⁴⁾ a series of tracer studies using SF_6 as the tracer material was proposed to learn more about diffusion rates in Chicago.

The SO_2 concentration observed at any location is the sum of the contributions by many individual sources and, with certain assumptions, to estimate their group of sources is unknown. For pollution abatement in general, but especially during serious pollution episodes, control authorities must know the relative contribution of each source in the area. Otherwise, effective and economical abatement is not possible.

Tracers give one the ability to "see" individual sources and, with certain assumptions, to estimate its contribution to the total SO_2 levels at the location. Thus, in a given weather situation, we can tag a suspected source and see whether the tracer reaches the sensor, and if so, in what amounts. Several experiments under different weather conditions, using differ-

ent kinds of sources, should tell a lot about the relative importance of different individual sources and classes of sources, and test the ability of the diffusion equations to accurately simulate nature.

The analysis system developed by the Department of Health, Education and Welfare's National Air Pollution Control Administration in Cincinnati for this tracer gas will be used.^(7, 8) The ultrasensitive detectability of this material results from the high response characteristics of electron capture detectors to halogenated materials. Much of the experimental work to date has been to optimize procedures so that very high sensitivities can be realized. Gas is released at a rate of about 3.5 to 7.0 g/sec (1 to 2 cfm) and is collected in plastic bags using samplers borrowed from NAPCA. These samplers contain a small battery-driven pump which fill 16-liter bags at a rate of about 120 ml/min. Instantaneous air samples are also collected in evacuated 1-liter metal cylinders.

Argonne's Industrial Hygiene and Safety Division has modified one of its gas chromatographs to determine concentrations of this tracer material. A Model GC 1500 Micro-Tek unit is being used.

The system initially chosen was that designated "System B" by Saltzman, Coleman, and Clemons.⁽⁷⁾ The column consists of a 1.2-meter section of 40 to 60-mesh 3A molecular sieve which is used to remove interfering water, followed by a 4.2-meter section of 1/8-inch tubing containing 40 to 60-mesh Baymal. The latter material is a colloidal alumina which is particularly useful for halogenated hydrocarbons. The standard inlet in the chromatograph was replaced with a 7-port valve containing a 0.25-ml sample loop. The carrier gas is high purity nitrogen which is cleaned with two 5A molecular sieves. The scavenger gas is 5% hydrogen in argon. A polarizing power supply and a nanoammeter were constructed by Argonne's IHS instrument group. A one-millivolt recorder is used to record the chromatograms. The air in the sample bag is flushed through the sampling loop until approximately 100 ml have passed through. A 0.25-ml sample is then retained and the SF_6 concentration measured. The system will be calibrated using standard gas mixtures supplied by NAPCA.

A sensitivity better than 0.05 ppb (vol/vol) of SF_6 in air has been achieved with this system; it is possible to improve this to 0.01 ppb using minor changes.

The sensitivity of the system is being greatly increased to better than reported geophysical background levels, one part SF_6 in 10^{12} parts air, by using changes that have been developed and tested by R. K. Stevens and others in the Cincinnati NAPCA chemistry group. These changes include:

- (1) using a Nickel-63 detector,

- (2) operating the detector at 280° C rather than at room temperature,
- (3) using a pulsed power supply,
- (4) using a larger volume (2 ml) for the sample loop,
- (5) using pure helium as the carrier gas, and
- (6) using alumina as the column material.

Additional work to insure the absolute accuracy and repeatability of the system and to refine analysis procedures will continue.

BACKGROUND SF₆ MEASUREMENTS

On February 27, 1969, six samples of air were collected at the Argonne site and analyzed for background levels of SF₆. No gas was released during the collection period. The weather conditions at Argonne during the collection periods (about 1030 to 1130 CST) were: east winds at 10 mph, clear skies, temperature 23° F, very unstable air. In other words, the winds brought in polluted air from the City of Chicago, and very rapid dilution was occurring.

Two of the six samplers were placed upwind of all Argonne buildings, and two were placed downwind of two Argonne buildings known to contain large quantities of SF₆: the Tandem Van de Graaff accelerator building and the Zero Gradient Synchrotron. In 1968, 15,000 lbs of SF₆ leaked from the Van de Graaff machine. One sampler was placed near each building, the second about 300 meters further downwind.

Five of the six samplers showed SF₆ concentrations below 0.20 ppb, the maximum sensitivity of the detector system at that time; the sample taken just outside the Van de Graaff building contained 0.78 ppb. Since projected changes in the analysis system will result in sensitivities of one part in 10¹², this background level and leak rate are disturbing.

Sixteen more background samples were collected at Argonne during the morning of April 23, 1969; two of these were found to have measurable levels of SF₆ (>0.05 ppb). These two were located downwind of the Van de Graaff building.

Additional background air samples were collected in Chicago on May 27 and 28, 1969, during the third fuel switch test. Strong WSW to SW winds carried air from Argonne into the city. For this reason, most of the air samples were collected along Lake Shore Drive and in the Loop; any large SF₆ sources in the city would have been detected.

Twelve instantaneous air samples were collected on May 27, eighteen more the next day. None showed SF₆ concentrations greater than the limit of detectability (again 0.05 ppb). Two samples yielded readings in the vicinity of the limit of detectability; it is believed that these represent baseline excursions rather than the positive results.

Four of the NAPCA continuous sample collectors were placed along Lake Shore Drive in Chicago, from 31st Street to Lincoln Park, on May 28. Samples were collected between 1135 and 1400 CST; none showed measurable SF₆ levels. In addition, a sampler was placed on the roof of the DAPC building, 320 North Clark Street. Four one-hour samples were collected between 1100 and 1500 CST; none was positive.

It is clear that many more background samples must be collected and analyzed when the improved SF₆ detector system is completed and operational.

SF₆ RELEASE EXPERIMENTS

Three SF₆ tracer gas experiments were made at the Argonne site in order to gain experience with the total system: release, collection, and analysis. The gas release rate was about 3.5 g/sec.

The first of these releases was made between 1030 and 1100 CST on February 28, 1969. At the time the SF₆ tank and the samplers were located, the winds at Argonne were straight east (90°).

The actual conditions during the release period were: wind ENE (70°) at 13 mph, clear skies, temperature 34° F, very unstable surface layer. The six samplers were placed along an east-west road 45, 135, 300, 550, 750, and 950 meters downwind of the release point. Just as the releases began, the winds backed to ENE; as a result, only the two closest samplers were in the plume. The nearest sampler measured 342 ppb, the next one 5.65 ppb. The remaining four were below 0.2 ppb.

Another release was made at Argonne between 1518 and 1550 CST on March 3, 1969. The weather during this release period was: wind NNE (30°) 14 mph, sky clear, temperature 40° F, very unstable surface layer, (a sigma meter showed a standard deviation of the horizontal wind direction of 11°; for the vertical component, 5.5°). Seven samplers were placed in an arc about 450 meters downwind of the source. One failed to collect any gas due to a poor connection between the pump and the sample bag; the other six showed concentrations between 5.6 and 23.0 ppb. The results of this release are not shown in figure form since the absolute accuracy of the system was not known. A simple diffusion calculation (Turner⁽⁹⁾) for class "D" stability yields a center-line concentration of 18.2 ppb, somewhat lower than the 23.0 observed.

The final release was made between 1145 and 1220 CST on April 17, 1969, with the tracer gas being emitted from the 34-meter Argonne experimental stack. Seven samplers were placed in an arc 1500 meters downwind. Weather conditions during the release were: wind SE (140°) at 11 mph, cumulus overcast at 1500 meters, temperature, 19° C. A light shower dropped 0.01 inches of rain during the release.

The highest SF₆ value measured was 0.60 ppb, with values about half as large as 10° on either side of the plume centerline. One sample again failed to collect any air.

PROPOSED SF₆ PROGRAM, SUMMER AND FALL 1969

More SF₆ experiments will be made at Argonne, using both ground level and stack releases. These will continue until the system is operational. Simultaneously, additional SF₆ background measurements will be made both in Chicago and at Argonne. Some of the Argonne releases will be made from the Argonne heating plant.

If these tests are satisfactory, and if background levels are acceptably low and uniform, full-scale releases in Chicago will begin. Arrangements have been made to introduce the SF₆ into one of the stacks of the Commonwealth Edison Company's Crawford and Will County plants. Gas samplers will be placed next to the TAM SO₂ sensor inlets to determine the relative contribution of this one stack to total SO₂ levels. A series of gas collectors will also be placed across the expected plume axis one or more miles downwind to define the plume center-line and to measure actual dispersion coefficients (sigmas) in the urban environment. Other experiments are being planned, including the use of other power plant stacks and ground and roof-level releases.

REFERENCES

1. Croke, E., Carson, J. E., Clark, F., Kennedy, A., and Roberts, J. Chicago Air Pollution System Model, First Quarterly Progress Report. Argonne National Laboratory Report ANL/ES-CC-001 (February 1968).
2. Croke, E. J., Carson, J. E., Gatz, D. F., Moses, H., Clark, F. L., Kennedy, A. S., Gregory, J. A., Roberts, J. J., Carter, R. P., and Turner, D. B. Chicago Air Pollution System Model, Second Quarterly Progress Report. Argonne National Laboratory Report ANL/ES-CC-002 (May 1968).
3. Croke, E. J., Carson, J. E., Gatz, D. F., Moses, H., Kennedy, A. S., Gregory, J. A., Roberts, J. J., Croke, K., Anderson, J., Parsons, D., Ash, J., Norco, J., and Carter, R. P. Chicago Air Pollution System Model, Third Quarterly Progress Report. Argonne National Laboratory Report ANL/ES-CC-003 (October 1968).
4. Croke, E. J., Carson, J. E., Gatz, D. F., Moses, H., Kennedy, A. S., Norco, J. E., Roberts, J. J., Croke, K. G., Anderson, J. B., Nelson, D. M., Ash, J. E., Carter, R. P., Lin, J.-W., and Votruba, R. J. Chicago Air Pollution System Model, Fourth Quarterly Progress Report. Argonne National Laboratory Report ANL/ES-CC-004 (March 1969).
5. Carson, J. E. and Gatz, D. F. Chicago Air Pollution Meteorological Studies. Argonne National Laboratory Radiological Physics Division Annual Report, July 1967-June 1968 ANL-7489, pp. 87-93.
6. Carson, J. E., Votruba, R. J., and Lin, J.-W. Chicago's Air Pollution Incident Control Test, Summer 1968. Paper presented at 62nd Annual Meeting, Air Pollution Control Association, New York City, June 25, 1969.
7. Saltzman, B. E., Coleman, A. I., and Clemons, C. A. Halogenated Compounds as Meteorological Tracers. *Anal. Chem.* **38**, 753-758 (1966).
8. Niemeyer, L. E. and McCormick, R. A. Some Results of Multiple Tracer Diffusion Experiments at Cincinnati. *J. Air Pollution Control Assoc.* **18**, 403-405 (1968).
9. Turner, D. B. Workbook of Atmospheric Dispersion Estimates. Public Health Service Publication, No. 999-AP-26, Environmental Health Series, Department of Health, Education and Welfare, 1967.

CHICAGO'S AIR POLLUTION INCIDENT CONTROL TEST, SUMMER 1968*. †

J. E. Carson, R. J. Votruba‡§ and J.-W. Lin‡

One method for reducing pollution concentrations during periods of weak winds and poor diffusion conditions without turning industry off is to convert as many of the large sources to alternate fuels as possible. Sulfur dioxide is a major pollutant in Chicago; unfortunately, sufficient supplies of low-sulfur fuels are not available to replace the usual fuels at all times.

The City of Chicago's Department of Air Pollution Control, in cooperation with Argonne National Laboratory, is developing an air pollution abatement strategy to use the limited

quantities of low-sulfur fuels with maximum effect on air quality. This technique consists of asking major SO₂ producers to convert to such fuels during periods of poor ventilation, especially those sources within and upwind of the polluted areas and population centers.

A full-scale dress rehearsal of this technique was tested during a three-week period in June and July, 1968. This paper discusses the results of this outdoor experiment, including changes of air quality due to fuel switches.

* Summary of paper presented at the 62nd Annual Meeting, Air Pollution Control Association, June 25, 1969, New York City.

† This work was partially supported by the Chicago Department of Air Pollution Control and the National Air Pollution Control Administration, Department of Health, Education and Welfare.

‡ Department of Air Pollution Control, City of Chicago.

§ Deceased, October 16, 1969.

The second in a series of fuel-switch tests was conducted in the City of Chicago between 16 June and 6 July 1968. Industry and the power generating plants cooperated with the city's Department of Air Pollution Control (DAPC) in conducting this unique and valuable experiment in air quality control.

Chicago is the first and to date the only major city

in the U.S.A. (and perhaps the entire world) to deliberately vary the rate of production of an atmospheric pollutant (sulfur dioxide) on a city-wide basis on a schedule designed to tell more about diffusion and transport over a large urban area.

The incident control test discussed in this report represents a joint effort conducted by the Chicago Department of Air Pollution Control, the Atomic Energy Commission, and the National Air Pollution Control Administration of the Department of Health, Education and Welfare.

The Chicago Department of Air Pollution Control was responsible for program direction and for handling the mechanics of the fuel-switch test. DAPC personnel were to contact each plant, secure their cooperation and provide the appropriate plant officials with details of the test schedule, objectives, etc. DAPC also provided the necessary forms for logging fuel consumption data. A total of 76 plants, which produce on an annual basis 85% of the city's SO₂, were asked to participate; forty-nine plants did.

Scientists from the Reactor Engineering and Radiological Physics Divisions of Argonne cooperated with DAPC in the planning phases of this simulated "pollution incident control test." Except for the starting date, the schedule which resulted was about as close to a controlled laboratory experiment as one could hope to conduct in an area as large and diversified as the City of Chicago.

This city-wide pollution experiment had three primary objectives: (1) to act as a trial run for establishing procedures for implementing effective SO₂ abatement procedures during a forecast period of air pollution buildup, (2) to observe changes in air quality due to fuel changes and to compare these changes with those computed from the diffusion equations, and (3) to provide Argonne scientists with detailed air quality, meteorological, and SO₂ emission data during a short period to aid in the development of better methods for predicting air pollution levels.

This city-wide experiment did bring into sharper focus the practical actions that industry can and cannot realistically take to reduce or curtail SO₂ output during pollution episodes. Any air pollution abatement strategy must, of course, be based on accurate assessments of the availability of low sulfur fuels and industrial-commercial operating procedures, so that no undue burden will be placed on industry by air pollution control operations. Communications channels between DAPC and the operating engineers of the various plants were established and used; the test showed that improvements are needed.

The third objective of the test was to provide the air quality and emission data needed by Argonne sci-

entists in their efforts to develop a mathematical model to forecast air pollution levels (specifically, SO₂ concentrations) in Chicago from meteorological and emission data. Input data for this model include existing hourly air quality (SO₂ concentrations), wind speed, and wind direction at each of the eight TAM (Telemetered Air Monitoring) stations in Chicago, standard hourly weather data at five additional locations, hourly SO₂ emission data from as many as possible of the large industrial, commercial and residential point sources, and estimated hourly emissions from area sources due to space heating and small industrial sources. This computer model, if able to predict future SO₂ levels accurately, will be used to develop effective abatement procedures at minimal costs and minimal disruption to industry whenever an air pollution incident occurs or is forecast.

There is only one way to reduce air pollution levels during a period of poor ventilation conditions: reduce the rate of emission of the pollutants. In Chicago, sulfur dioxide is a major pollutant (but not the only one). One could turn off SO₂ sources during an air pollution episode, but this would be economically and politically difficult. Or, the sources could convert to low sulfur fuels during the episode. In Chicago, an optimal abatement strategy for SO₂ basically consists of determining the best use of the available supply of natural gas and other low-sulfur fuels.

The procedures used during the Summer 1968 fuel-switch test were as follows: Those industries with single-fuel capacity (coal or oil) were asked to collect and submit to DAPC detailed hourly fuel and sulfur consumption data for the entire test period, 16 June through 6 July 1968. Plants with dual-fuel capacity were also asked to maintain hourly fuel use records for the same period; they were further requested to burn their usual fuel for that season during the first week of the test, and to convert to maximum use of high-sulfur fuel between 0700 and 1100 CST on both June 24th and July 1st, 1968. During the week of June 23rd, Commonwealth Edison was asked to convert its plants to minimum use of high-sulfur fuels after 24, 48, or 72 hours on coal, with industry converting 1 day later; the exact date was determined by the weather forecast. It was hoped that fairly steady weather conditions would prevail for 48 hr or more after the 24th so that the SO₂ concentrations observed at each of the eight TAM stations could be compared with consecutive periods of similar weather but different SO₂ emission patterns. These conditions did not occur during the first week of the test, and little useful air quality data was obtained. Again on the morning of July 1st, all plants with dual-fuel capacity were

asked to convert to maximum use of high-sulfur coal or oil. During this week, industry was asked to recon-vert to minimum-sulfur fuels on a date selected on the basis of the weather forecast, with the Edison Company following one day later. Fortunately, the weather did cooperate this week.

When the city converted to maximum use of high-sulfur fuels on July 1st, four of the eight TAM stations reported rapid and large increases in SO₂ values (from 0.00 to 0.23 ppm in 15 min at one site, for example). Fluctuations during the balance of the day can be related to changes of wind direction. Very low ground-level SO₂ concentrations were often observed at night and early morning during the high SO₂ output period with light winds and strong, ground-level inversions, showing that the pollutants were trapped above the stable layer and did not reach the surface.

On July 3rd, when a lake breeze circulation covered the city, a SO₂ concentration of 0.47 ppm was observed at one station. This occurred several hours after the lake breeze front passed the station, showing that the SO₂ was trapped in the relatively cool, stable air moving in from the lake. No high SO₂ levels were observed at any station in the zone of convergence along the lake breeze front.

The data show that sources outside of the city are often responsible for high SO₂ levels inside the city.

The third fuel-switch test in this series was conducted between May 19th and May 30th, 1969. During this experiment, the dual-fueled plants and the electrical generating plants were asked to convert to high sulfur fuels on May 20th and May 26th. The conversions to low sulfur fuels were made one or two days later using a *selective* abatement strategy; that is, only a limited number of plants changed to low-sulfur fuels. The abatement strategy used depended on the actual and forecast weather conditions, observed and forecast SO₂ levels, location of dual-fuel plants with respect to the SO₂ observing sites, diffusion calculations, and the availability of natural gas. Only those sources contributing to areas of high SO₂ concentrations were asked to convert to gas. The strategy employed in this test is quite similar to that which would be used during a real air pollution episode. The observed changes in SO₂ levels indicated that fuel switches were effective in lowering SO₂ concentrations in the affected areas, and that the decreases were consistent with those computed by the diffusion model. A complete analysis of this experiment in pollution abatement is in progress.

CHICAGO AIRCRAFT SOUNDING PROGRAM

J. E. Carson and D. M. Nelson

Atmospheric stability, as measured by the vertical temperature distribution, is an important meteorological factor controlling diffusion rates. Until recently, no measurements of this parameter were being made in or near Chicago. The Chicago Department of Air Pollution Control has purchased a flight package to measure vertical profiles of air temperature and sulfur dioxide. Both helicopters and light airplanes have been used; Argonne and city scientists have made flights with the system. About fifteen flights were made during the period of this report; features of several of the more interesting flights are presented.

Until recently, two types of meteorological measurements needed to accurately estimate diffusion conditions over Chicago were not being made. These are the vertical temperature gradient and winds in the zone of mixing and transport. The vertical temperature gradient (lapse rate) determines the atmospheric stability and (combined with wind speed and surface roughness) the intensity and spectrum of turbulence. The depth of the mixing layer (that is, the volume of air in which the pollutants can be mixed) is determined by the height above ground and intensity of stable layers (inversions) aloft; it is very difficult if

not impossible to estimate this critical pollution parameter without direct measurements.

The low-level lapse rate varies with time and height as well as horizontally in an urban area such as Chicago with its mixture of tall and low buildings, roads, parks, lake, etc. In dispersion calculations, the lapse rate in the first several hundred feet above ground is usually estimated from standard weather observations (wind speed, cloud cover, time of day, etc.) using objective techniques, such as those proposed by Gifford⁽¹⁾ and Pasquill.⁽²⁾ Unfortunately, these procedures cannot be used to provide accurate estimates of the mixing depth.

Techniques to extrapolate the observations from the two nearest U. S. Weather Bureau radiosonde stations (Peoria, Illinois, 140 miles southwest of the Loop and Green Bay, Wisconsin, 180 miles north) have been developed at Argonne and by a local private meteorological forecasting service (See Reference 3, p. 129). These procedures cannot be expected to be sufficiently accurate or detailed always to represent conditions over Chicago.

Since vertical lapse rate data are so important in pollution work, the City of Chicago Department of Air Pollution Control purchased an airborne instrument package designed to measure SO_2 , pressure altitude, and wet bulb depression and temperature. The instrument was purchased from Sign X Laboratories, Inc., Essex, Connecticut. This package, mounted on a Chicago Fire Department helicopter, has been used to measure SO_2 and temperature profiles over the city since March 1969. Several examples of the types of information that can be obtained from this system are given below. DAPC personnel operate the equipment on most flights.

The U. S. Weather Bureau, using funds from NAPCA, began a balloon program in Chicago in April 1969 to provide wind and temperature data from the surface to 10,000 feet. Slow-rising radiosondes are used to obtain temperature and humidity data; the balloons are followed optically to give wind speed and direction. An over-inflated 100-g pilot balloon is used to lift the package. Two flights are made each normal work day at 0500 CST and 1000 CST (none on weekends or holidays).

As originally planned, the helicopter system was to be used both to obtain routine vertical temperature and SO_2 soundings and to study in detail these profiles in the city and how they vary horizontally and with time during "typical" weather and pollution situations. The balloon program frees the helicopter from

routine observations. The balloons also give wind information in the zone of transport over the city, data not observable from the helicopter.

The first helicopter flight using this instrument was made on March 5, 1969. On this flight, only the Midway temperature profile was complete and showed an adiabatic lapse rate to the top of the sounding at 2600 ft above ground at 1045 CST. The winds were southwest at 8 to 10 mph. Clouds at Midway were thin, broken cirrus above 20,000 feet with scattered cumulus at 900 meters.

By far the most interesting of the helicopter flights was made on March 19, 1969. The 0600 CST weather map on this date showed an east-west stationary front across Wisconsin, Lake Michigan, and Michigan just to the north of Chicago. Winds were mostly light and variable south of the front and weak north to north-east behind it. This frontal zone pushed to the south during the morning hours, passing Meigs Airport *before* the helicopter started its flight program and Argonne *after* the sounding there. The three temperature soundings are shown in Figure 97.

All three soundings show the same temperature at 2600 ft (MSL) and above; it is assumed that all three soundings were made in the same air mass above this level. The data indicate that the fresh polar air mass behind the front was still very shallow at Meigs and Midway.

The Meigs temperature profile was made at 1030

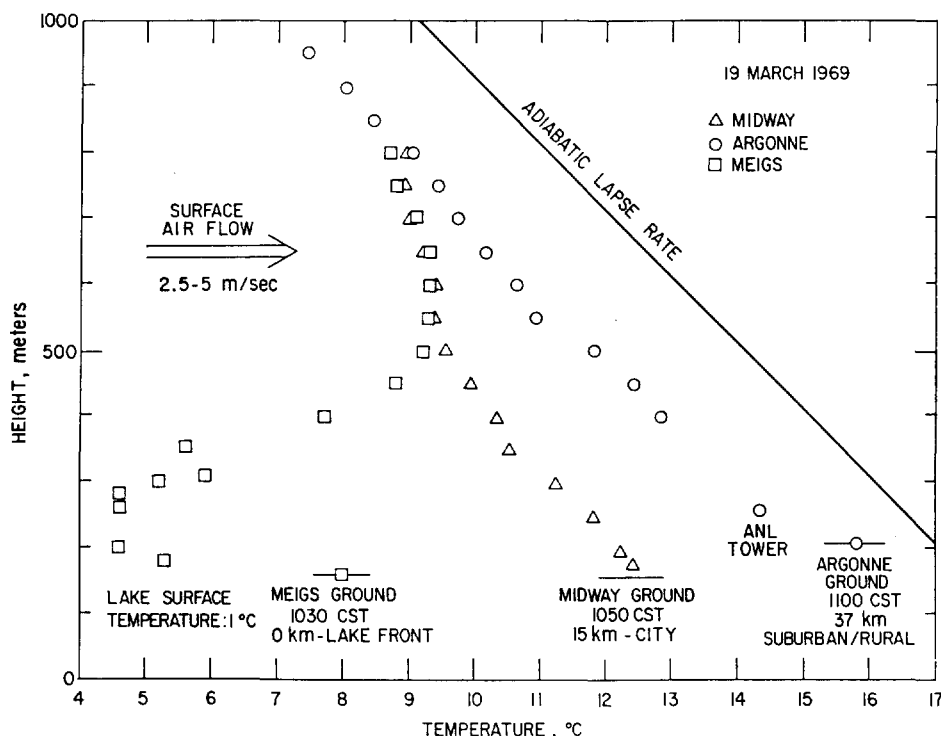


FIG. 97.—Vertical temperature profiles, Meigs and Midway Airports and Argonne National Laboratory, March 19, 1969

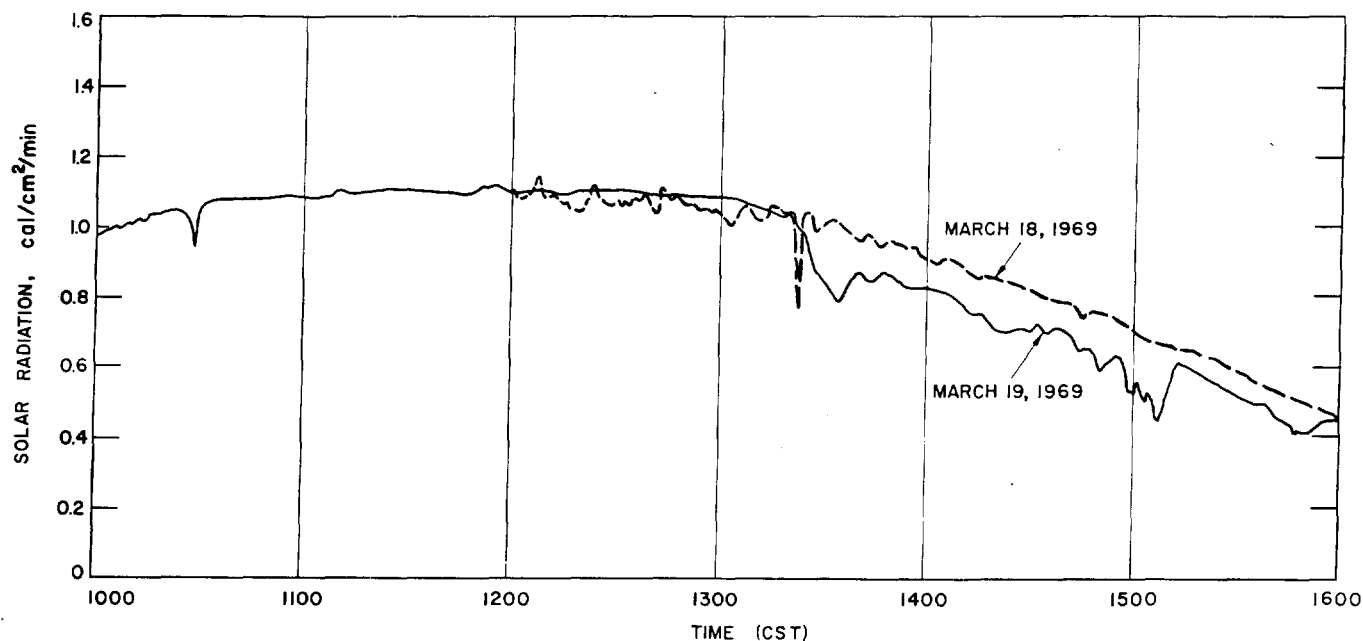


Fig. 98.—Solar radiation data at Argonne National Laboratory, March 18 and 19, 1969

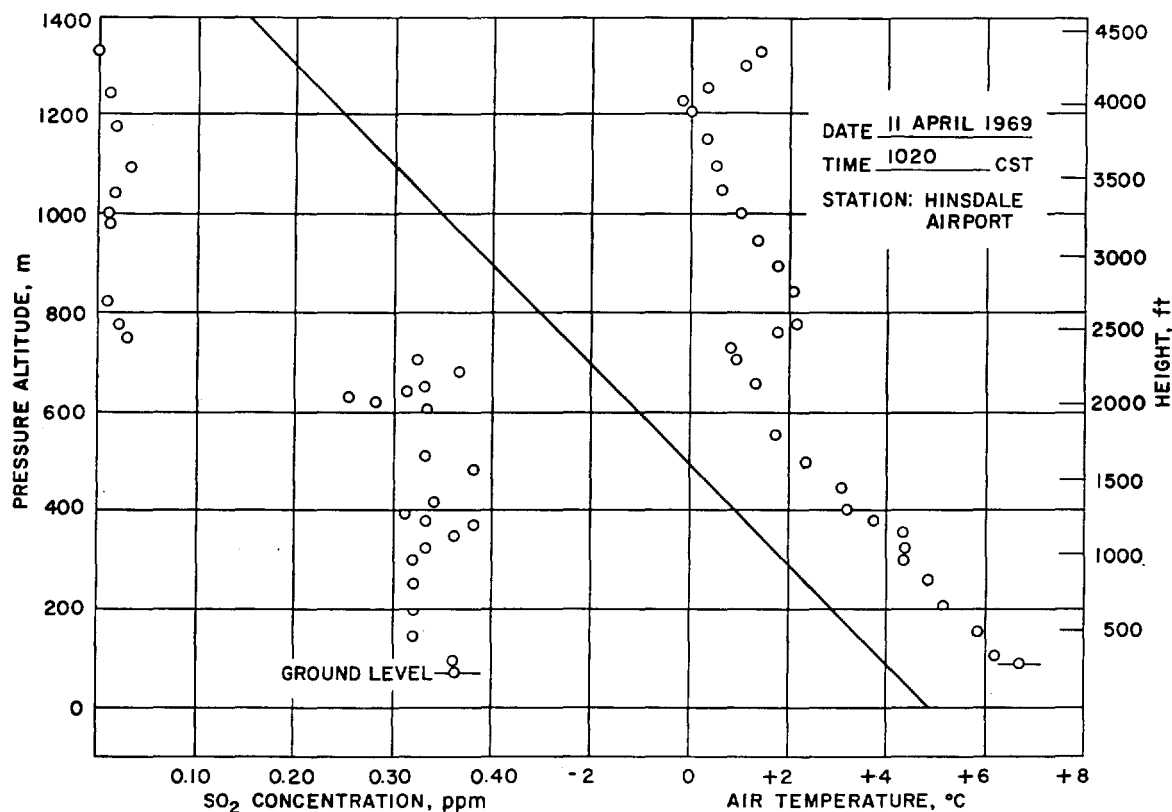


Fig. 99.—Vertical SO_2 and temperature profiles, Hinsdale Airport, April 11, 1969, 1020 CST

CST, when north winds at 14 mph were reported and the temperature of the water in Lake Michigan was near 0°C . This trajectory, of course, brought fresh, clear air across the very cold lake over the lake-front airport into the city. A very thin superadiabatic layer

is observed at ground level. The air at Meigs a short distance above the surface was 10°C cooler than the air inland. This temperature difference is due to both the change of air mass and cooling by the lake.

Midway reported NNE (10°) winds at 7 mph at

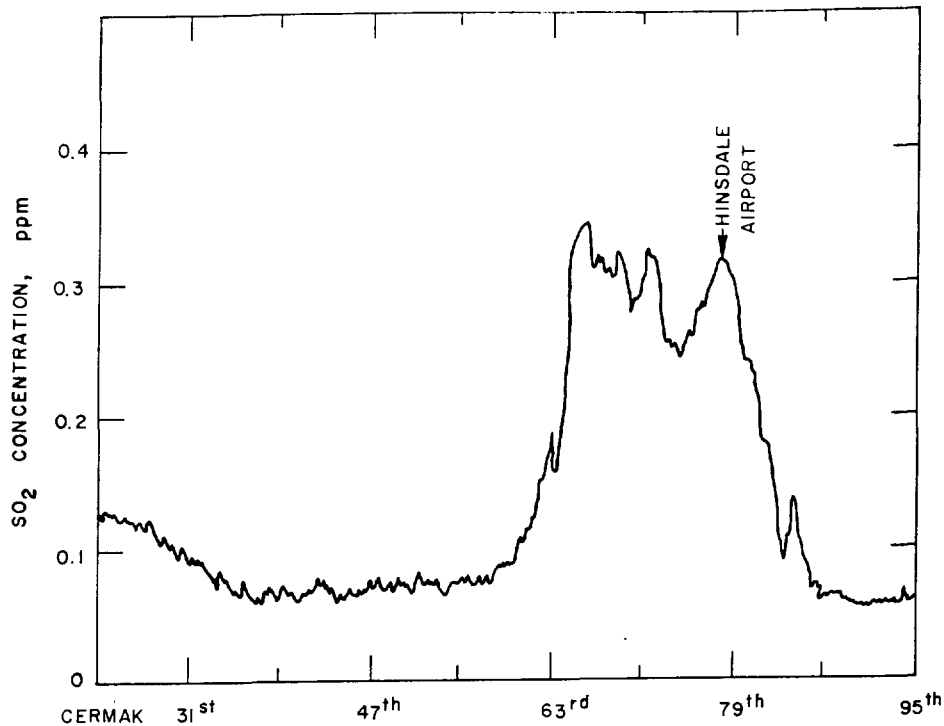


Fig. 100.—SO₂ concentrations observed during horizontal traverse along County Line Road, 250 meters above ground level, April 1, 1969.

1000 CST, ENE (80°) at 10 mph at 1100. The Midway sounding was made at 1050 CST, after the frontal passage. The cool air behind the front was considerably moderated by the time it reached Midway Airport; a dry adiabatic layer about 1300 ft thick had been generated, with a stable layer above.

The front did not pass Argonne until 1320 CST. The weather before the air mass change was very good: clear skies and light winds mostly from the north at 3 to 5 mph. The maximum temperature was 19° C (66° F), reached just before the frontal passage. After the frontal passage, the winds became ENE at 9 to 11 mph and the skies remained clear.

The Argonne sounding, made at 1100 CST, showed an adiabatic layer to the top of the sounding at 3300 ft. (The lowest two points on this sounding are from the Argonne weather tower and show the usual super-adiabatic surface layer.)

The pall of pollution brought to Argonne was easily visible; there was enough dust in the air to reduce solar radiation intensity about 15 to 20%. Figure 98 shows the solar radiation data at Argonne on this date; data for May 18th, also a clear day, are included to show the reduction of insolation due to polluted air. These data show that the pollutants were within the new air mass, not ahead of it.

Wind data at Argonne show that the intensity of

turbulence in the new air mass was quite low; for example, the standard deviation of the vertical wind direction (as measured by a bivane and sigma meter) 37.5 ft above the ground changed from 13° before the lake air arrived to 6° after. The standard deviation of the azimuth angle changed from 40° to 10°. These data show the reduced turbulence levels in cold air mass.

By far the best SO₂ and temperature profile data collected by the helicopter to date were obtained between 0940 and 1100 CST on April 11, 1969. The flight path and sounding locations were selected using existing weather conditions and modified during the flight itself to obtain maximum useful information.

On April 11, a large cold high pressure area was centered over the upper peninsula of Michigan, moving ESE. The sky was mostly clear with a few scattered middle clouds. Winds were ENE at 7 to 9 mph. This flow concentrated the pollutants emitted by the complex of industries and power plants along the Stevenson Expressway into a single visual plume. The flight pattern was altered to take advantage of this concentration of pollutants. The original plan was to make vertical soundings at Meigs and Midway Airports and at Argonne, the standard flight schedule. A decision was made while in the air to make a detour to Hinsdale Airport in order to make an additional sounding

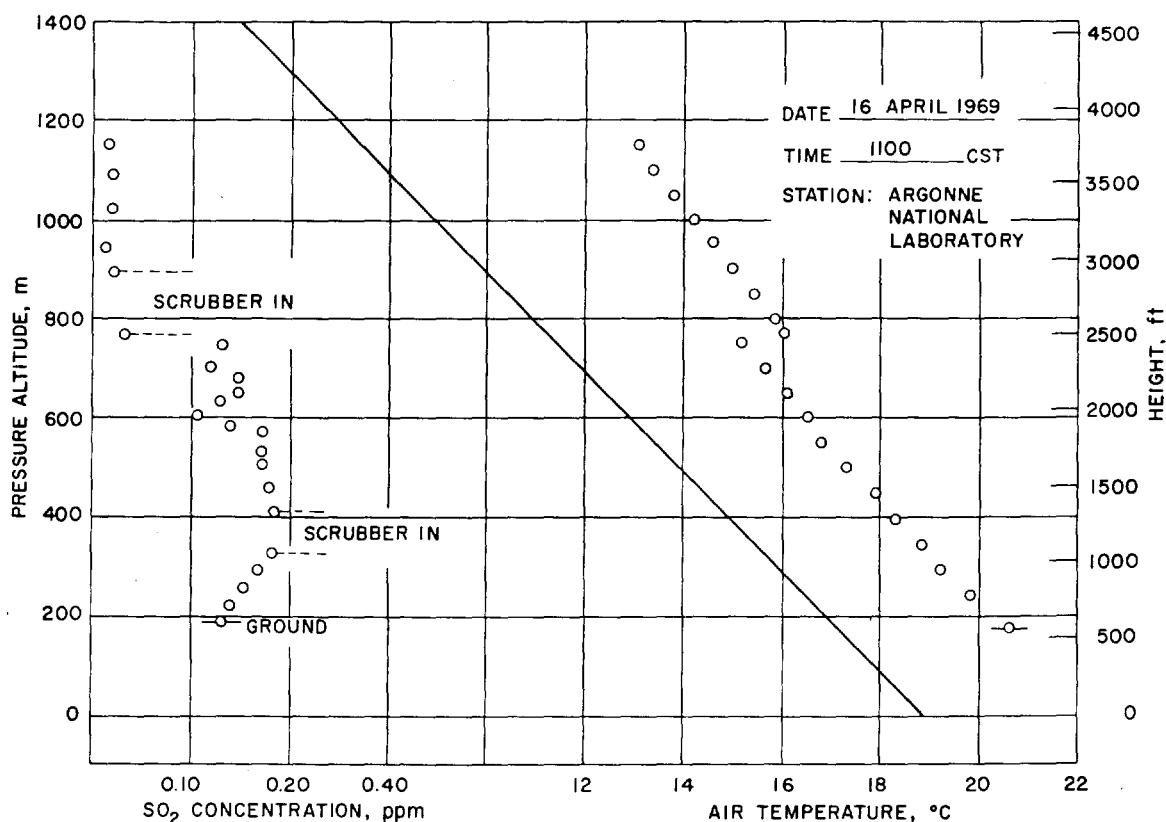


FIG. 101.—Vertical SO_2 and temperature profiles, Argonne National Laboratory, April 16, 1969, 1100 CST

near the center of the visible smoke plume moving to the SSW along the Expressway. Most of the plume seemed to the observer in the aircraft to originate in the Ridgeland Power Station and the Chicago Sanitary District Plant in Stickney. This airport is about 10 miles from these sources. The SO_2 and temperature profiles at this airport are shown in Figure 99. A dry adiabatic lapse rate 2000 ft thick was observed just below a weak inversion. The SO_2 data show that SO_2 levels were high and rather uniformly mixed in this layer, with a very rapid decrease to background levels above the base of the inversion. This figure rather convincingly demonstrates the importance of the mixing layer concept and how even a weak inversion aloft can act as a lid to dispersion and vertical mixing.

The temperature profiles at Midway and Argonne were quite similar to that of Figure 99; SO_2 concentrations below the inversion were considerably lower than those observed at Hinsdale Airport. The soundings at Meigs show near zero SO_2 at all heights, with a cool surface layer caused by on-shore winds.

One leg of the return flight was going north at constant levels (980 ft, MSL) along County Line Road from 95th Street (Des Plaines River) to Cernak Road

(2200 South). (County Line Road runs N-S along the boundary between Cook and DuPage Counties.)

The SO_2 recorder trace for this leg is shown in Figure 100. SO_2 levels were quite high (0.25 to 0.33 ppm) in the visible plume, much lower on either side. The figure shows that valuable pollution information can be gained on horizontal as well as vertical flights.

The ragged nature of the interesting SO_2 cross section may be due to incomplete horizontal mixing from several large point sources. A simple diffusion calculation, using typical SO_2 outputs from the two plants mentioned above, the Gifford⁽¹⁾ diffusion parameters, and the observed weather information, shows that most of the observed SO_2 concentration at Hinsdale Airport could have originated at these two sources. Not too much should be inferred from this calculation, as the real SO_2 emission rates were not known and the SO_2 contributions from all the other possible sources were ignored.

Figure 101 shows the SO_2 and temperature profiles at Argonne on April 16, 1969 at 1100 CST. South winds at 8 mph with clear skies were present when the sounding was made. The temperature data show the expected adiabatic layer with a weak ($\sim 1^\circ\text{C}$) inversion at 2000 ft. Even this inversion was enough to

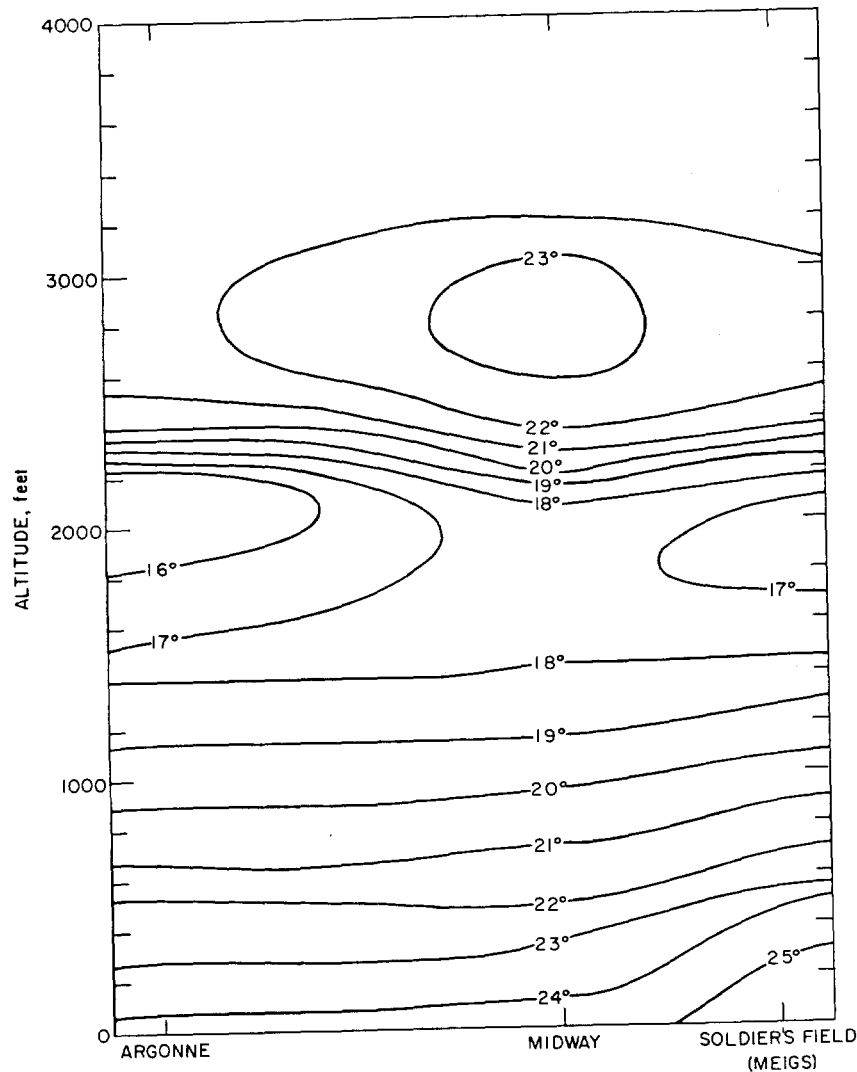


FIG. 102.—Vertical temperature cross section over Chicago, December 16, 1968

limit mixing. Profiles at the other airports were similar. (The SO_2 sensor on the flight package uses the David conductivity method. It is unable to distinguish between SO_2 and CO_2 ; a scrubber is used to eliminate the SO_2 before the conductivity is measured. The CO_2 contribution is then subtracted from the CO_2 plus SO_2 reading. In Figure 101, the periods when the scrubber was in operation are shown.)

Several other flights have also been made using a very simple thermistor bridge combination furnished by the National Air Pollution Control Administration. This package has been flown both on a helicopter and on a light airplane. The thermistor, inside an aluminum radiator shield, was mounted at the forward end of the landing skid of the helicopter or on a strut of the airplane. The thermistor resistance was measured by manually nulling a Wheatstone bridge having the

thermistor as one resistance element and a 10-turn potentiometer as another. Temperatures were then determined from a resistance vs. temperature calibration chart. Heights were taken directly from the aircraft altimeter.

The first of these flights was made on December 16, 1968, when vertical temperature profiles were observed over Meigs (lakefront) and Midway (urban) Airports in Chicago and over Argonne (rural), using a Chicago Fire Department helicopter.

Figure 102 shows the variation of temperature with height between Meigs Airport on the lakefront and Argonne. The three profiles are very similar, showing adiabatic lapse rates up to a strong inversion layer at about 2000 ft. Some of the horizontal differences may be due to the fact that the sounding at Meigs was made at 1000 CST, at Midway at 1015, and at 1100

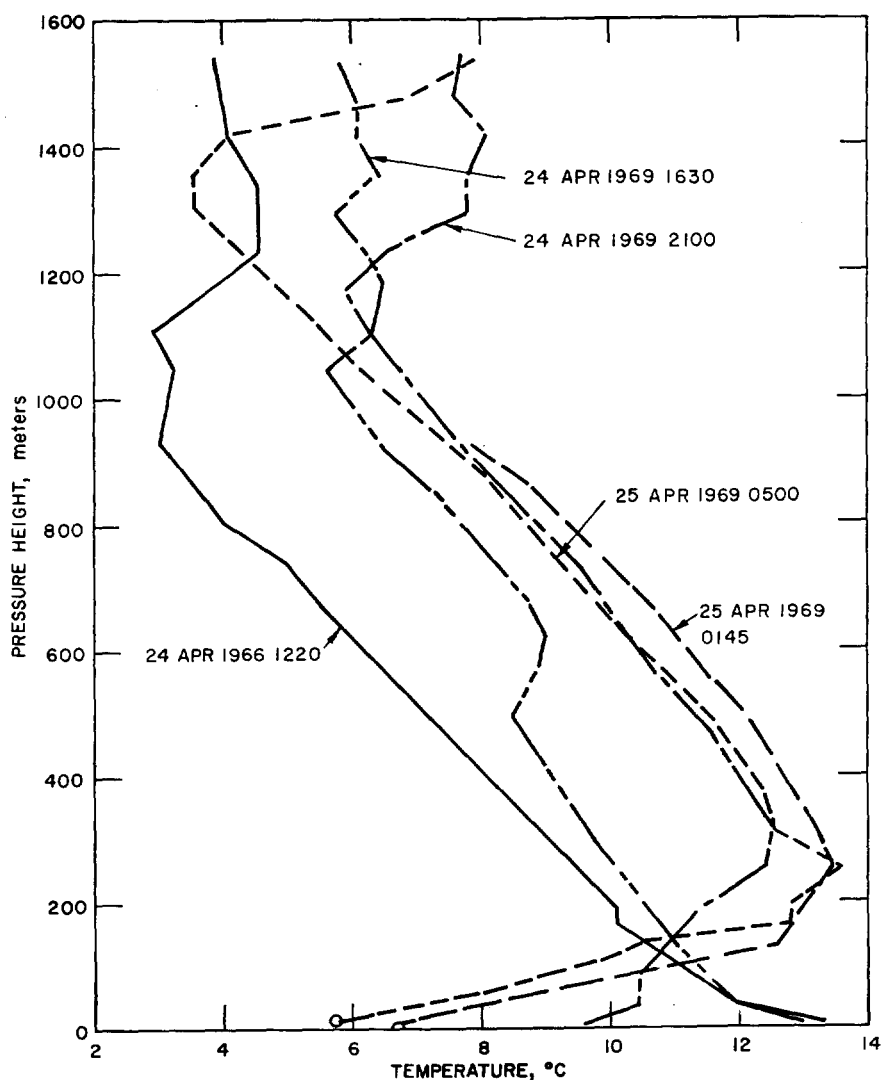


FIG. 103.—Vertical temperature profiles, Midway Airport, April 24–25, 1969

CST at Argonne. The winds were southwest at 8 to 10 mph. Clouds were broken at 10,000 feet with a 0.9 cloud cover at Midway.

The Cincinnati thermistor system was flown on January 14, 1969 by Argonne personnel in a rented light plane (Cherokee 140). An adiabatic lapse rate was observed up to the solid cloud layer at 1400 feet over the Lewis Lockport Airport.

The airplane flights conducted between 1200 CST on April 24th and 0600 CST on April 25th are illustrative of how an aircraft can be used to measure both the space *and* time variability of lapse rate in the area. The thermistor-bridge system was used every four to five hours to make profile measurements at Lewis Airport in Lockport, Illinois (a rural area), Midway Airport (a city location) and Meigs Airport

(a lakefront site). A few soundings were made at other locations.

A large, strong, high pressure area was moving from NW to SE across Chicago during the flight program. As the center of the high pressure passed, the winds veered from north at 8 mph at the start of the program through ESE at 5 mph at 2100 CST on the 24th, through S at 4 mph at midnight to SE at 4 mph by the end of the period. The sky remained clear.

The time variability of lapse rate at Midway is shown in Figure 103. Considerable warm advection occurred above 1300 ft between 1220 and 2100 CST. The mixing depth decreased from 2900 ft to 1640 ft between 1220 and 1630 on the 24th. The surface nocturnal inversion extended to 980 ft by 2100 CST; the intensity but not the depth of the inversion increased

during the nighttime hours. The data show that the mixing depth on the 25th was much deeper than on the previous day.

REFERENCES

1. Gifford, F. A. Uses of routine meteorological observations for estimating atmospheric dispersion. *Nucl. Safety* **2**, (4), 45-51 (1961).
2. Pasquill, F. The estimation of dispersion of windblown material. *Meteorol. Mag.* **90**, (1063), 33-49 (1961).
3. Croke, E. J., Carson, J. E., Gatz, D. F., Moses, H., Kennedy, A. S., Norco, J. E., Roberts, J. J., Croke, K. G., Anderson, J. B., Nelson, D. M., Ash, J. E., Carter, R. P., Lin, J.-W., and Votruba, R. J. Chicago Air Pollution System Model, Fourth Quarterly Progress Report. Argonne National Laboratory, ANL/ES-CC-004 (March 1969).

PROJECT ITREX—A COOPERATIVE THUNDERSTORM TRACER EXPERIMENT

D. F. Gatz

The Illinois Tracer Experiment (ITREX) is a cooperative field research program to study the removal of dust and pollutants from the air by rain. Three research groups are participating in the study, which utilizes two types of tracer materials: some already present in the atmosphere, and some specifically added by the experimenters. The research program runs for several weeks during the summer in a 40-mile-square rain gauge network near Champaign, Illinois.

"ITREX" stands for Illinois TRacer EXperiment. It is the code name for the largest field study ever attempted on how rain cleans pollutants from the atmosphere. In some experiments, artificial tracers are released into thunderstorms. Argonne scientists comprise one of three groups participating in the study, which was scheduled for central Illinois during spring and summer 1969. The other groups are from the University of Michigan and the University of Illinois—Illinois State Water Survey. An aircraft from Weather Science, Inc., Norman, Oklahoma, will participate during the first of two scheduled operational periods. During the second period, an aircraft from the National Center for Atmospheric Research (NCAR), Boulder, Colorado, will participate.

Participation in ITREX is a first step in the development of a program in precipitation chemistry at Argonne. This new program, as now planned, will measure the chemical content of rain, air, and airborne particles. Such information will aid the study of two different but related problems of great interest today: air pollution and weather modification. The application to air pollution comes from a desire for a better understanding of the way rain and snow clean the atmosphere. The application of weather modification stems from the need to understand how nature makes rain so that man can find ways of modifying the natural processes for his benefit. These two areas are related because of the very real possibility that pollutants can interfere with natural processes to produce more—or less—rainfall.

The field location for project ITREX (Figure 104)

is central Illinois in an area northwest of Champaign-Urbana, where the State Water Survey maintains a network of 196 rain gauges and rain samplers. The field station of the University of Michigan group is located near Clinton. An Argonne automatic rain collector (AARC) will also be located near Clinton, about 1.5 miles from the University of Michigan station. The AARC is an automatic device to collect up to 72 separate 500-ml samples sequentially from rains of up to 1.6 inches. The Water Survey weather radars are at the University of Illinois Willard Airport, five miles south of Champaign. Both the Michigan and Water Survey groups have radio-dispatched mobile units that carry roof-top and basket-type rain samplers.

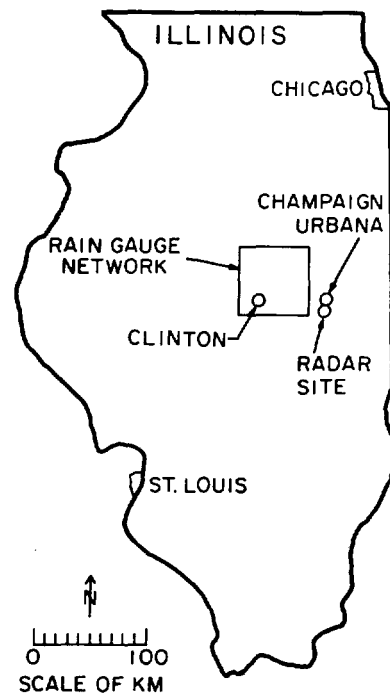


FIG. 104.—Map showing field location of Project ITREX

Five separate types of experiments are planned by the cooperating groups. For the most part, these are being done jointly by two or more investigators. Some of the experiments have definite goals; others are pilot, or exploratory in nature. The experiments and the cooperating groups are listed in Table 59.

In experiment 1, several hundred grams of indium will be released from a burning pyrotechnic flare by an aircraft flying below the cloud base in a thunderstorm updraft. Rain from that storm will be collected by the network of samplers on the ground and analyzed for the tracer by neutron activation. Total deposition of indium by the storm over the network will be calculated and divided by the known amount of indium released to obtain the removal efficiency.

Experiment 2 has similar objectives, but in addition will compare results between tracers to see if the different materials are removed at different rates.

Experiment 3 is based on the recognition that the elements present in rain were once borne by one or more of the following: soluble particles, insoluble particles, large particles, small particles, condensation nuclei, and ice nuclei. Besides, oxygen and hydrogen isotopes are present in rain water. These different particles and water tracers may follow different pathways through the precipitation process, depending on their size and chemical nature. Sometimes different pathways result in different concentration-versus-time curves (concentration "profiles") between two tracers observed at the same station. For example, we know (Dingle and Gatz⁽¹⁾) that gross airborne dust, artificial radioactivity, and plant pollen concentrations in rain usually have an inverse relationship to rainfall rate, whereas ice nuclei (Vali⁽²⁾) usually have a direct relationship.

We want to see if a number of different characteristic profiles occur, and whether each can be identified with a particular pathway through the precipitation process. If so, one could tell how precipitation scavenges a given particle or element (i.e., what its pathway is) by observing its concentration profile in rain.

In this experiment we will look for different tracer profiles in two series of rain samples from the same storm at two stations 2 km apart. The tracer materials, rain collection sites, and analyst groups are listed in Table 60. Some analyses will be done by cooperating specialists at the U. S. Geological Survey, Denver, Colorado, and The University of Wyoming, Laramie.

Experiment 4 is an attempt to trace thunderstorm downdrafts from their theoretical middle-level (3-6 km) origin to ground level, using gaseous SF₆ first developed for air pollution tracing. Such deep downdrafts could be important transport mechanisms for

TABLE 59. PROJECT ITREX EXPERIMENTS AND PARTICIPATING GROUPS

Experiment	Groups participating ^(a)
1. Indium tracer budget	UM, SWS
2. Indium, lithium, silver tracer comparison	SWS, UM
3. Chemical analysis of serial rain samples	ANL, UM
4. Sulfur hexafluoride downdraft tracing	ANL, SWS
5. Pollutant scavenging efficiency	ANL, SWS

^(a) UM, University of Michigan; SWS, Illinois State Water Survey; ANL, Argonne National Laboratory.

TABLE 60. SERIAL RAIN WATER SAMPLE COLLECTION AND ANALYSIS, PROJECT ITREX

Tracer material	Collection site ^(a)		Analyst group ^(a)
	UM	ANL	
Lead, lead-210	X	X	ANL, UM
Oxygen-18, deuterium	X	X	ANL, USGS
Ice nuclei	X	X	UW
Several elements by atomic absorption		X	ANL
Pollens, beta radioactivity	X		UM

^(a) UM, University of Michigan; SWS, Illinois State Water Survey; ANL, Argonne National Laboratory; USGS, U. S. Geological Survey; UW, University of Wyoming.

bringing bomb-debris radioactivity from aloft to the surface.

Experiment 5 is similar to the first experiment, but uses tracers that are naturally available instead of introduced. In this case, the tracer input to the storm is not controlled and must be measured. This is done by taking a filter sample of the aerosols entering the storm from a plane flying in the updraft. The air and moisture inputs are measured at the same time. Deposition is measured over a network of rain collectors and divided by input to find the removal efficiency for each storm sampled.

In summary, Project ITREX is a cooperative study to learn more about the mechanisms and efficiencies of aerosol scavenging by rain, using natural and artificial tracers. We are also using techniques of trace analysis to understand the basic circulations, microphysics, and chemistry of convective storm precipitation.

REFERENCES

1. Dingle, A. N., and Gatz, D. F. Air cleansing by convective rains. *J. Appl. Meteorol.* 5(2), 160-168 (1966).
2. Vali, G. Freezing-nucleus content of hail and rain in Alberta. Preprints of papers presented at the Sixth Conference of Severe Local Storms, Chicago, Illinois, 8-10 April, 1969, pp. 270-274 (unpublished).

CITY OF CHICAGO POLLUTION INCIDENTS: CASE STUDIES*

D. F. Gatz and E. W. Klappenbach†

Chicago weather phenomena and SO₂ pollution sources interact in a number of different ways to produce episodes of severe pollution. The three high-pollution case studies presented in this paper were a first step in our study of the weather associated with Chicago pollution. This information

through the city may have caused the unusually high pollution of that day. The two remaining cases involved winds off Lake Michigan. One was a lake breeze, with the land warmer than the lake surface. The other involved a shift to east winds over the whole region in response to a pressure gradient

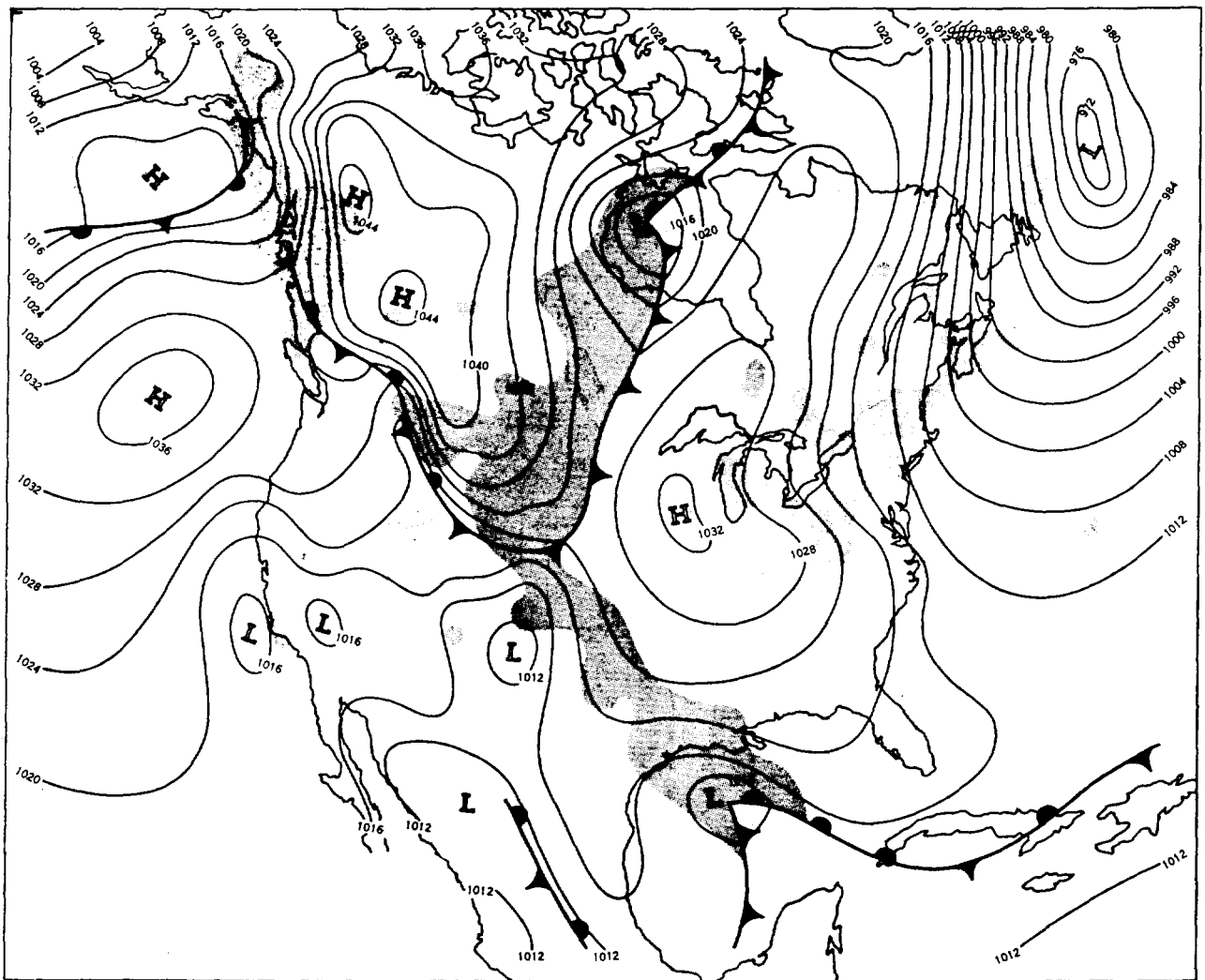


FIG. 105.—19 January 1966 surface weather map, 1200 CST

is crucial to our efforts to build an SO₂ prediction model for the city.

The first case examined was evidently a heat-island circulation. Winds converged over the axis of the city heat island from northwest and northeast on a clear, cold, nearly calm winter afternoon. There is evidence that recirculation of air

* This paper was prepared for presentation at the Air Pollution Control Association Annual Meeting, New York, June 24, 1969.

† Senior Meteorologist, City of Chicago Department of Air Pollution Control.

reorientation. In this case, the lake surface was warmer than the land. In both cases, observed pollution conditions were generally consistent with theoretical expectations.

INTRODUCTION

Argonne National Laboratory scientists are developing an SO₂ pollution prediction model for Chicago. To be useful, the model must be able to predict high concentrations accurately. For the model to predict high concentrations accurately we must provide it

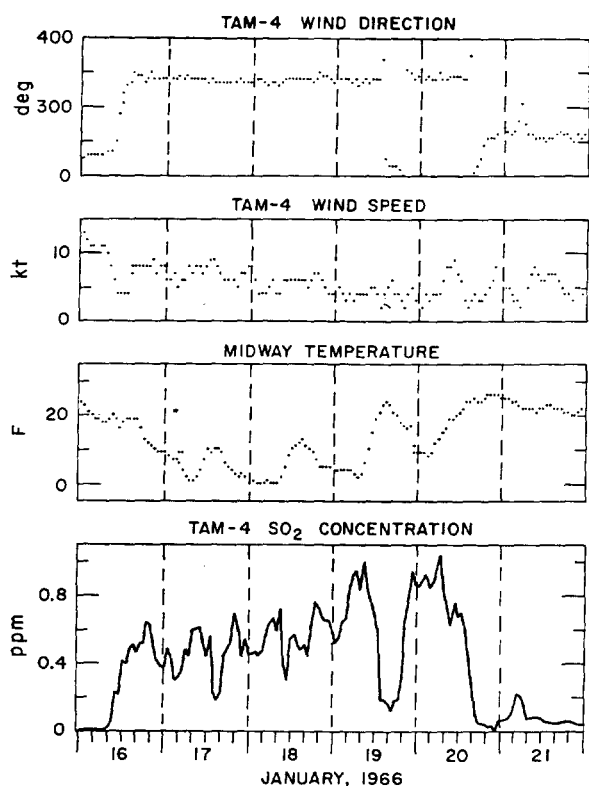


FIG. 106.—TAM-4 winds and SO₂ and Midway temperature, 16-20 January 1966.

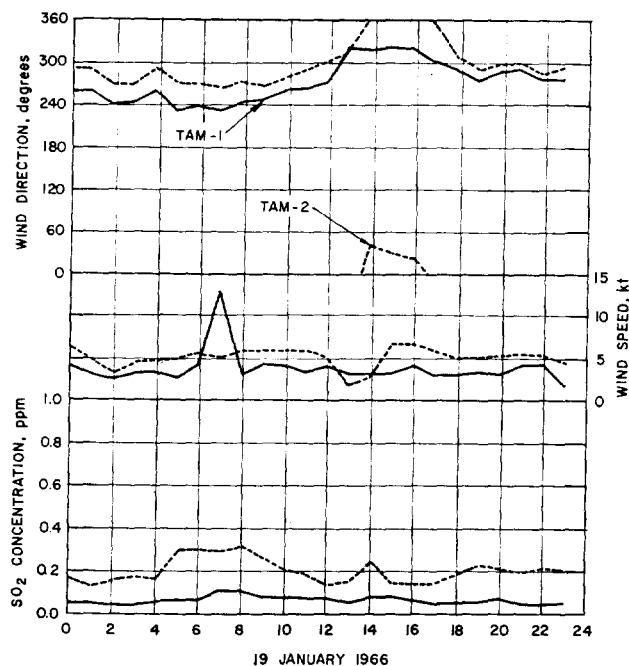


FIG. 108.—Winds and SO₂ at TAM-1 and 2, 19 January 1966.

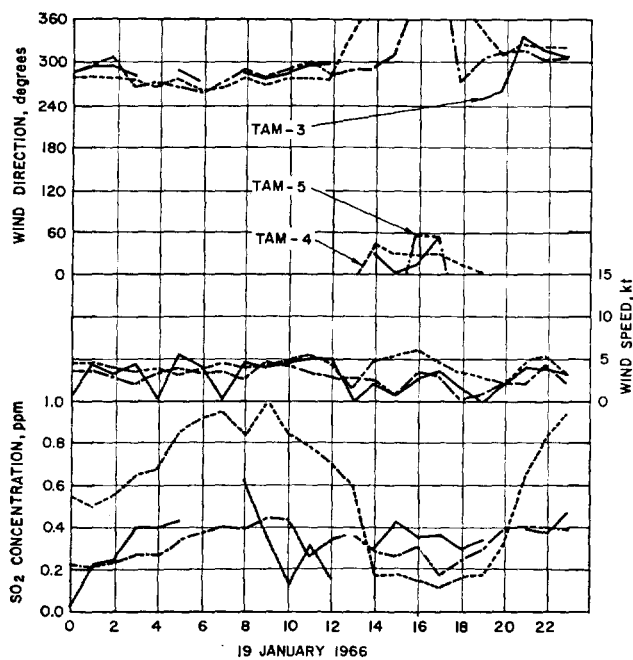


FIG. 107.—Winds and SO₂ at TAM-3, 4, and 5, 19 January 1966.

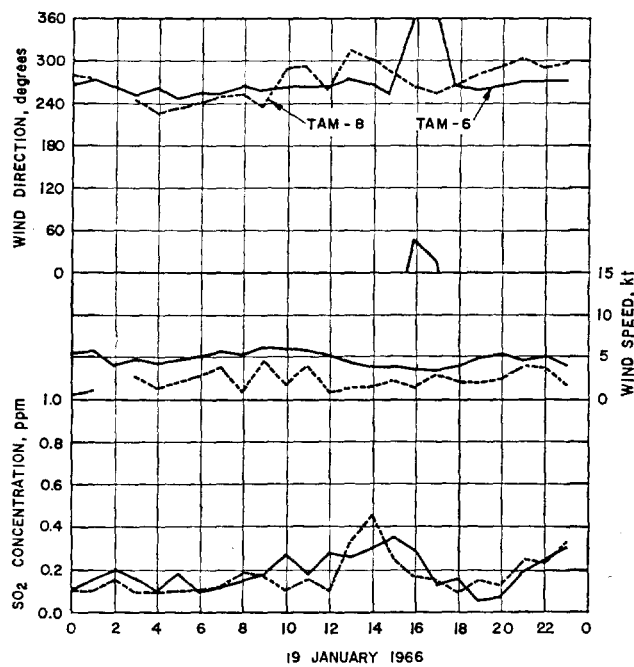


FIG. 109.—Winds and SO₂ at TAM-6 and 8, 19 January 1966.

with as much information as possible about the meteorological processes involved in pollution episodes. Chicago weather phenomena and SO₂ pollution sources interact in a number of different ways to produce episodes of severe pollution. The case studies presented in this paper are a first step in our study of these events.

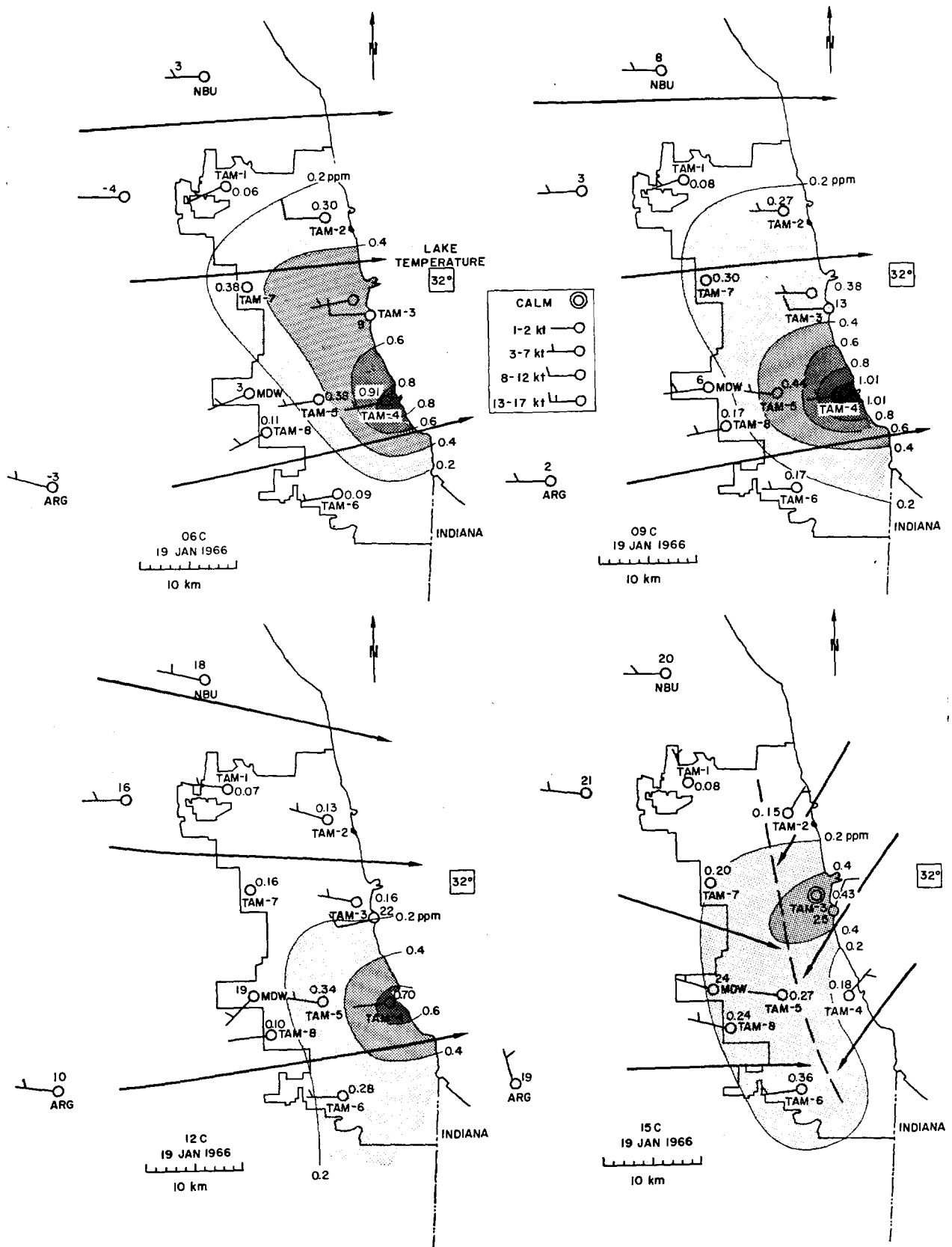


FIG. 110.—Weather and pollution maps for Chicago area, 19 January 1966

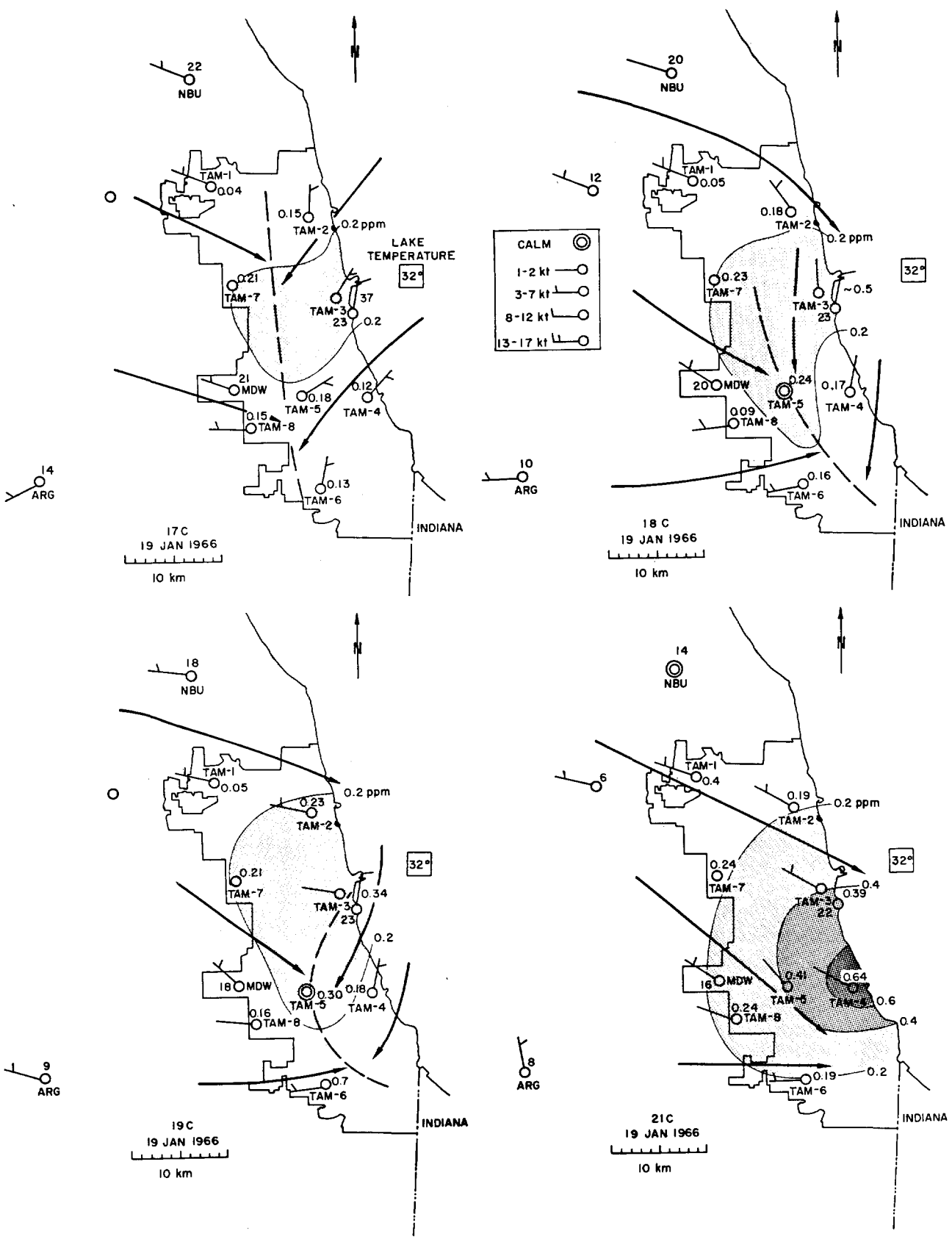


FIG. 111.—Weather and pollution maps for Chicago area, 19 January 1966

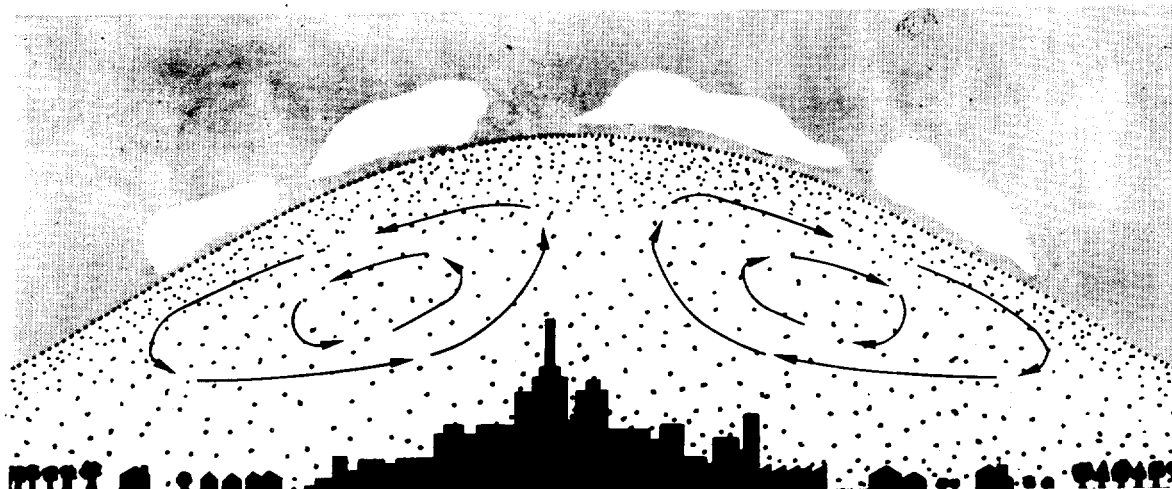


FIG. 112.—Schematic diagram of heat-island circulation (redrawn from Lowry⁽¹⁾)

DATA AND PROCEDURES

We studied each case using three graphical aids: (1) a surface weather map for the day; (2) time sections of SO₂ concentrations and winds at selected stations; and (3) meso-scale charts showing winds, temperatures and SO₂ concentrations over the Chicago area.

The weather maps show the broad scale framework of each specific local event. The time sections show the hour-to-hour relationships between SO₂ and winds. These relationships are clearest in smoothed data; therefore, we plotted hourly averaged winds and SO₂ concentrations on the time sections. The purpose of the meso-scale charts is to show instantaneous distributions of SO₂, winds, and temperature over Chicago. Thus the winds on these charts are 1- to 5-min averages, and temperatures are instantaneous. SO₂ values are still 1-hr averages, though, to insure that plotted values represent real effects and not nearby sources.

We drew SO₂ isopleths and shaded areas progressively darker with increasing concentration to show pollution patterns at a glance. These are general patterns only—they are not meant to give details. For example, where data were sparse, uniform concentration gradients were drawn. This is an obvious simplification. Others may be evident as we look at the three cases in detail.

RESULTS AND DISCUSSION

19 January 1966: A Possible Heat-Island Circulation Case

The 1200 CST* surface weather map (Figure 105) shows an anticyclone covering the Midwest. Its center

* All times in this paper are CST.

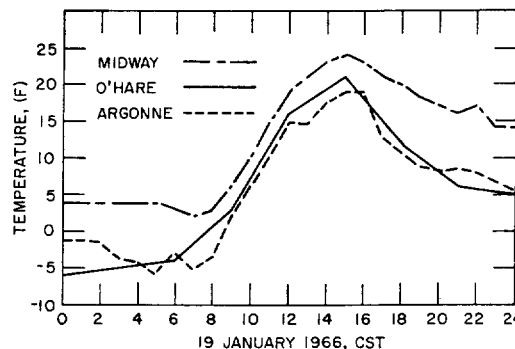


FIG. 113.—Diurnal temperature changes at Argonne, Midway, and O'Hare, 19 January 1966.

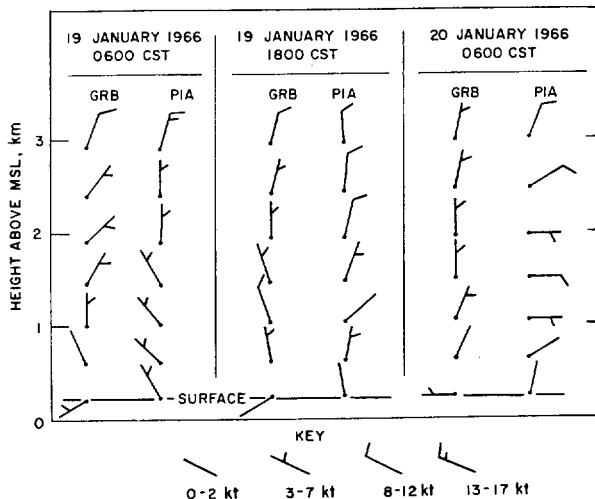


FIG. 114.—Winds aloft at Peoria and Green Bay, 19-20 January 1966.

was just west of Chicago. The pressure gradient over Chicago was weak; hence winds were light. The 19th was the third consecutive day that Chicago was in-

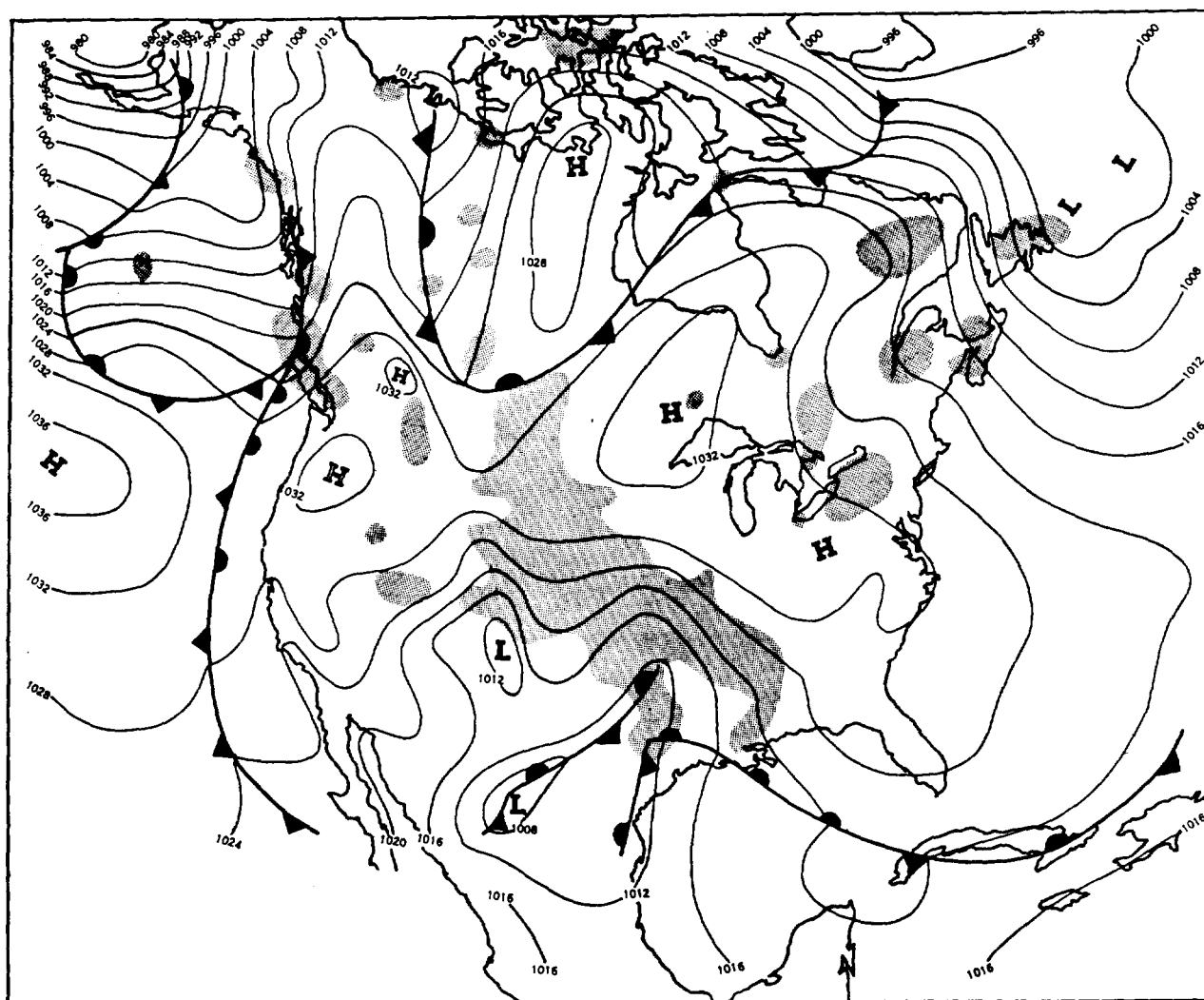


FIG. 115.—27 December 1966 surface weather map, 1200 CST

fluenced by the same high pressure area and had light winds.

The 19th was not an isolated day of high pollution, but the third or fourth of a series. Between 16 and 20 January, hourly averaged SO_2 values were above 0.4 ppm most of the time at station 4 of the City of Chicago Department of Air Pollution Control Network of Telemetered Air Monitoring (TAM) Stations. (TAM station locations are shown in Figure 110). The hourly SO_2 and wind averages at TAM-4 are given in Figure 106. We see that the wind speed was always less than 10 kt, often less than 5 kt, during this period. Wind direction was very constant from the northwest. The figure also shows typical sunny day temperature variation on 17, 18, and 19 January.

Figure 106 shows some interesting details of the SO_2 concentrations during this period. The generally high levels, the gradual increase with time, and the extremely high concentrations at TAM-4 on the 19th

and 20th are all significant, but the temporary drop in SO_2 levels with northeast winds, especially pronounced at TAM-4, is particularly interesting. A drop in SO_2 with a shift to northeasterly winds is not surprising, especially at a lakefront station, because these winds bring in clean air from over Lake Michigan. What is surprising is that a temporary shift to northeast winds occurred over part of the city. Such occurrences are common in warm seasons because of lake breeze effects, but this situation developed during the middle of January on a day when the high temperature at Midway was 24°F .

When comparing Chicago temperatures to those of its surroundings during winter, it is important to consider carefully the condition of the lake surface. The temperature and heat transfer properties of a solid ice surface are much different from those of a water surface. Mr. Ivan Brunk of the ESSA Weather Bureau in Chicago reports (1969) that some ice was present in

Lake Michigan off Chicago from the middle of January to the end of February, 1966, and that reports from Dunn crib, a city water intake facility in the lake off Chicago's south shore, indicate that "pancake ice" (floating pieces) was present on 19 January and several days before. There was also a report of "slush ice" at 1800 on the 19th.

Lake water temperatures of 32° F were measured several feet below the surface at Dunn crib on the 19th. This does not indicate either the presence or absence of ice. However, the absence of a long period of extremely cold weather, and westerly winds on several days preceding the 19th add to the evidence above that the lake surface was essentially liquid and 32° F.

Therefore, the observed easterly winds are clearly not the usual kind of lake breeze because the land was colder than the lake. Figures 107-109 show details of SO₂ and wind behavior at individual TAM stations on the 19th. Temporary winds shifts occurred at some stations, but not all.

A better way to evaluate these events on an hour to hour basis is to examine the meso-scale maps. Figures 110 and 111 show winds, SO₂, and temperatures in the Chicago area for 8 selected hours on 19 January. The 0600, 0900, and 1200 maps show a westerly flow, at low speeds, over the Chicago area. At 1500, convergence over the city was very clear, with north-east winds at the three TAM stations along the lake shore and westerly or northwesterly winds inland. The

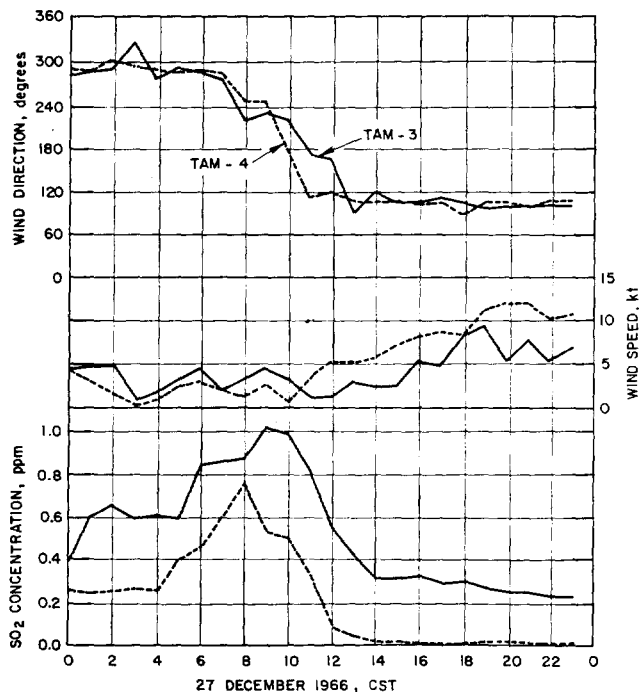


FIG. 116.—Winds and SO₂ at TAM-3 and 4, 27 December 1966.

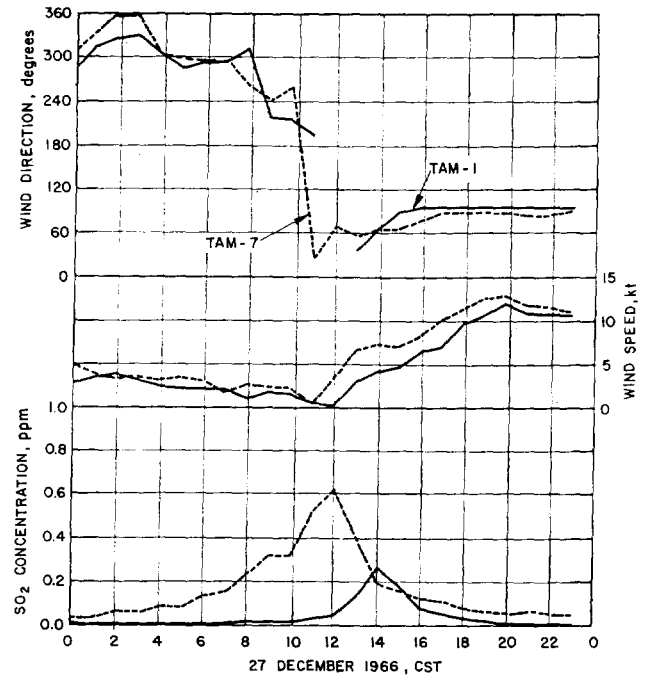


FIG. 117.—Winds and SO₂ at TAM-1 and 7, 27 December 1966.

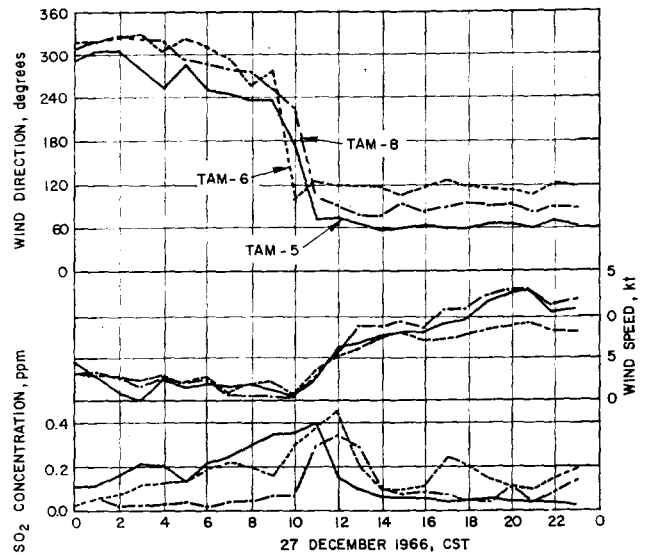


FIG. 118.—Winds and SO₂ at TAM-5, 6, and 8, 27 December 1966.

circulation was still strong over the south end of the city at 1700 and the convergence line had retreated east of TAM-5 and -6 once more and disappeared in the north end of the city. The circulation continued to weaken during the next hour; the 1900 map shows northeasterly winds only at TAM-4 and Meigs Field (CGX). By 2100 winds were northwesterly over the whole area once again.

The city wind pattern is clear; it shows that winds converged over the center of the city for several hours.

These observed wind patterns suggest that we may have found a heat-island circulation much like that described by Lowry⁽¹⁾ and pictured schematically in Figure 112.

Two conditions are usually required for city-rural circulations to begin. The first is a temperature excess in the city; the second is sufficiently light ambient winds. A plot of hourly temperatures at Midway, O'Hare, and Argonne (Figure 113) shows a definite temperature excess at Midway Airport (in the city) relative to O'Hare Airport and Argonne (essentially rural sites). Figures 110 and 111 show that surface winds were light in the Chicago area on the 19th, and Figure 114 shows light winds aloft at Peoria, Illinois and Green Bay, Wisconsin—the two rawinsonde stations nearest* to Chicago. Therefore, favorable temperature and wind conditions for a city-rural circulation did exist.

The available data suggest a city-rural circulation somewhat different than the classical form. The classical case is for a somewhat circular city. The corresponding circulation is a ring vortex, with air rising in the center of the doughnut, flowing outward aloft, and returning to the surface at the outer perimeter. Chicago's topography and demography are not classical because the city lies along a lake shore. The heat island is not circular, but is instead a north-south band. Thus, heat island circulations in Chicago may have an *axis* of symmetry, rather than a *center* of symmetry.

For analysis of this episode, we must also consider possible interactions with the synoptic scale air flow. This point is not clear; perhaps the outside air simply flows around or over the city air "dome" with little interaction between the two. There is some evidence that interaction did occur in this case, however. The wind fields at 1500 and 1700 (Figures 110 and 111) show definite northerly components in both converging currents. This suggests that momentum is being transferred downward from the northerly winds aloft† (Figure 114). The Chicago circulation observed on 19 January 1966 appears to have had the following basic characteristics:

1. Relatively warm city air rose over the axis of the heat island;
2. To preserve continuity, air from the edges of the city was drawn inward;

* Peoria is 210 km southwest and Green Bay is 300 km north of Chicago.

† It is necessary to verify that the circulation reaches high enough altitudes to interact with the northerly winds. The depth of penetration of the rising city air was estimated from the 0600 temperature sounding at Peoria and the Midway high temperature of 24. The depth of penetration was about 1 km. This is high enough for the rising air to encounter north winds.

3. At the upper limit of convection, the rising air began to spread outwards, to the east and west, at the same time gaining momentum from northerly winds in this region;
4. The air was thus carried to the outer limits of the circulation, perhaps 10–20 km away, and reached ground level at a point south of where it ascended;
5. From this point, it was drawn back into the city, where it was repolluted. If this circulation pattern prevailed, air could have been recycled through the city several times before finally leaving at the south end of the metropolitan area.

One additional item of evidence to support the existence of this kind of circulation is found in the recorded SO₂ concentration of air arriving at TAM-4 from the northeast. Figure 107 shows concentrations near 0.20 ppm in the northeast winds. These are unusually high concentrations for winds off the lake. This is evidence of a recirculation of once-polluted air back into the city.

One curious aspect of this episode is that the circulation died (about 1900) as the city-rural temperature difference increased. Theory predicts the opposite—the strength of the circulation should increase in proportion to the temperature difference. The explanation probably lies with some change in the external conditions (especially winds) that permit such local circulations.

There is considerable latitude for speculation here, of course, but one thing is clear: an unusual circulation prevailed in Chicago on 19 January 1966. This event was associated with severe air pollution in Chicago, and as far as we know, has not been described for this city before.

From only one case, one should not try to identify critical parameters or their threshold values for heat island circulations in Chicago; however, two points are worth noting:

1. Surface winds outside the city were mostly less than 5 kt between 18 and 20 January. Winds aloft at Peoria and Green Bay were mostly less than 10 kt up to 700 mb on the day of the circulation.
2. The city-rural temperature difference ranged from 3 to 10° F on January 19. The larger values occurred at night.

27 December 1966: A Wind Off Lake Michigan

The surface weather map for 1200 on the 27th is given in Figure 115. The ridge line has just passed Chicago. This movement caused a surface wind shift to easterly. The storm over Oklahoma developed rapidly and moved toward Chicago during the after-

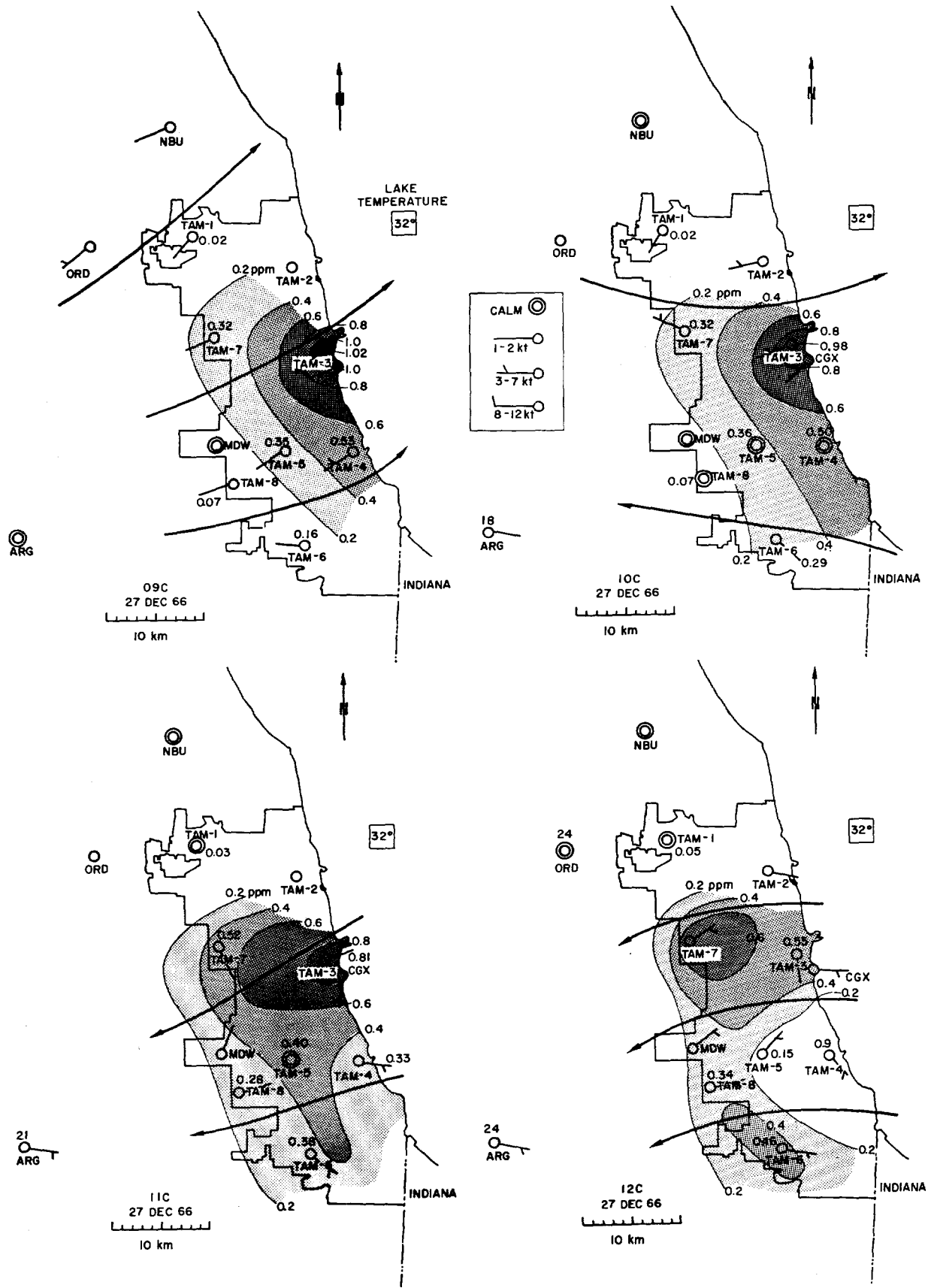


FIG. 119.—Weather and pollution maps for Chicago area, 27 December 1966

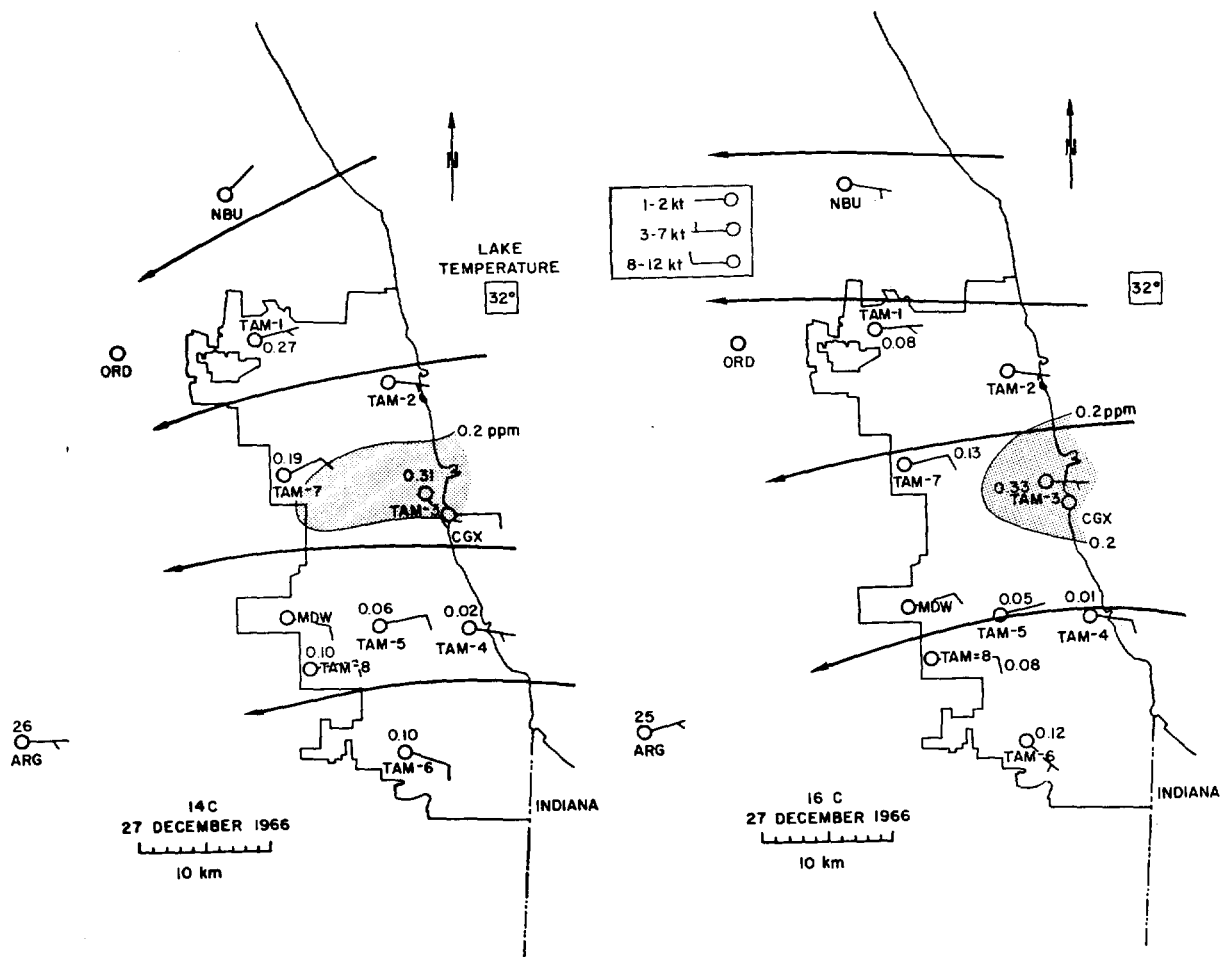


FIG. 120.—Weather and pollution maps for Chicago area, 27 December 1966

UNCLASSIFIED

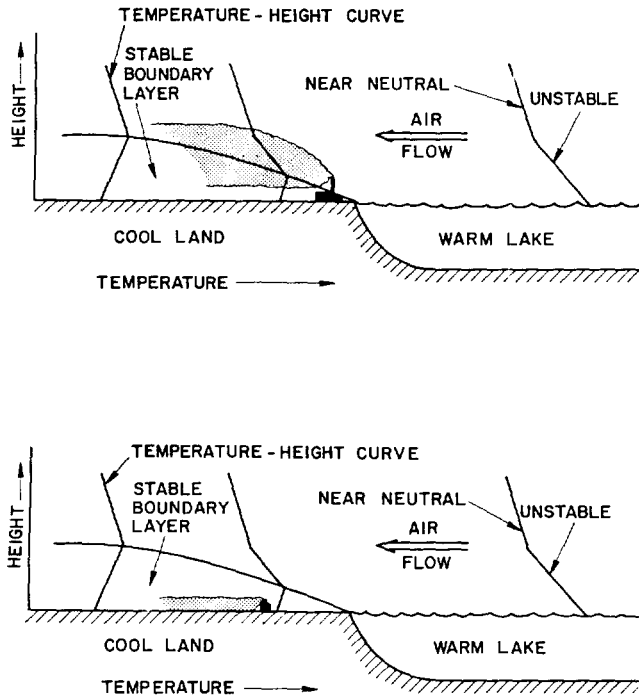


FIG. 121.—Schematic diagram of stability regimes for on-shore flow from a warm lake. Top tall stack; bottom, short stack.

noon, tightening the pressure gradient and thus increasing the wind speed.

Figures 116–118 show the wind shifts at the TAM stations and the wind speed and SO_2 changes that occurred with them. Two different relationships were observed. Figure 116 shows that very high concentrations were observed at lake front stations 3 and 4 with southwest winds during the morning. At inland stations 1 and 7, the peak concentrations occurred in the east wind, as shown in Figure 117. The same is true for inland stations 5, 6, and 8 as shown in Figure 118.

The meso-scale charts (Figures 119 and 120) show another view of these events. At 0900 winds over the whole region were light from the southwest. Highest SO_2 concentrations occurred along the lake shore. At 1000 winds at the southern stations had switched to easterly. The northern stations still had southwesterly or westerly winds, and there was a calm zone between. The SO_2 pattern remained about the same. By 1100 winds were more generally from the east, and the SO_2 had begun to move inland. It is clear from comparisons of 1000 and 1100 SO_2 readings at individual stations that concentrations were dropping at lake front stations and increasing inland. This trend continued, as shown on the 1200 map. Stations 6, 7, and 8, at the outer perimeter of Chicago, all had higher SO_2 con-

centrations than the hour before, while lake front concentrations dropped even lower. The clean air had reached TAM-5 also, and SO_2 decreased sharply there from the 1000 reading. At 1400 and 1600 the whole city was quite clean, except for readings of about 0.3 ppm in the downtown area, undoubtedly from local sources.

This is a case of a large morning SO_2 buildup. It was 14°F at Midway most of the night, so residential sources were undoubtedly strong. Winds were light and skies clear during the night, so a nighttime radiation inversion was likely. This stable layer and the light surface winds probably caused the observed high SO_2 concentrations through the accumulation of SO_2 in a shallow surface layer. Breakup of the radiation inversion after sunrise could have brought additional SO_2 to the surface from plumes aloft. As winds swung to easterly and became stronger, this pollution pall was blown west and diluted somewhat, so stations on the west side of the city observed smaller peaks one or two hours after the wind shift.

There is no evidence for any effects other than advection for the high concentrations observed on the west side after the wind shift. This may be compared with the model for onshore flow from a warm lake shown in Figure 121. If a stable boundary layer were present, it would inhibit the downward transport of SO_2 from plumes aloft. As the figure shows, SO_2 from low-level sources should remain concentrated near the ground. High concentrations were not observed after the morning pollution blew away, perhaps because of a reduced source strength in the afternoon and the stronger east winds.

9–10 May 1967: A Lake Breeze

The surface weather map for 1200 on the 9th (Figure 122) shows a high-pressure ridge line west of Chicago. The pressure gradient over Chicago was fairly tight in this case; winds were northwest at about 10 kt. The lake water temperature was 48°F , in contrast to a midmorning (1000) reading of 54°F at Midway. Increasing inland temperatures apparently caused convection and initiated the lake breeze soon after 1000.

Wind direction shifts during the day at six TAM stations are shown in Figures 123–125, together with simultaneous variations of wind speed and SO_2 concentration. These figures show that the pollution peaks occurred *behind* the lake breeze front, but not until several hours after the front passed.

The 1000 CST map (Figure 126) shows moderate northwest winds over the whole region with SO_2 concentrations less than 0.10 ppm at all stations. By 1000

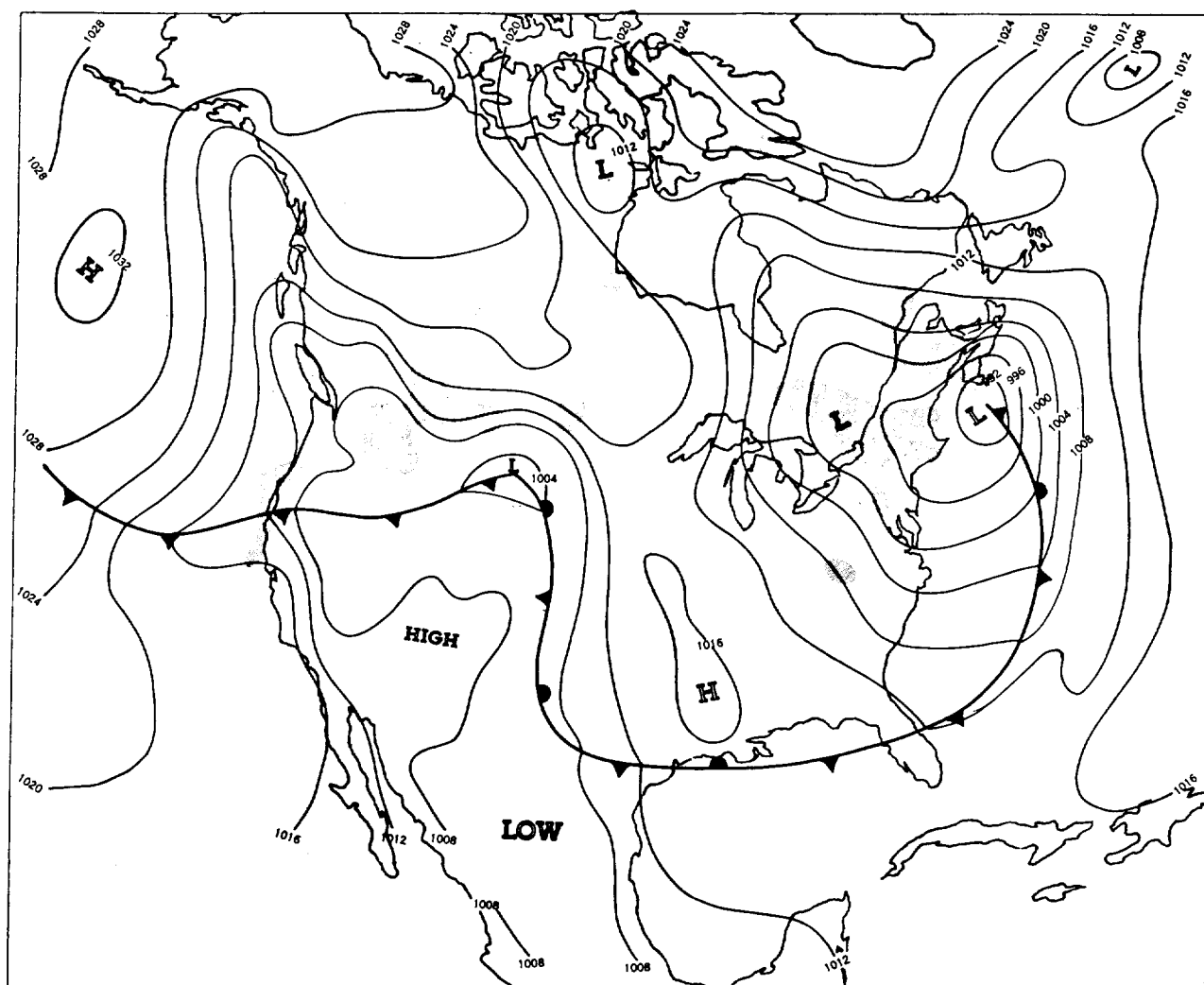


FIG. 122.—9 May surface weather map, 1200 CST

the lake breeze had already passed the three lake front stations. All stations still had low SO_2 readings. The 1400 and 1800 maps show the penetration of the lake breeze many kilometers inland. The first high SO_2 values were observed at station 6 at 1800. An hour later (Figure 127) the lake breeze front had passed Argonne. Winds behind the front were southeasterly, and station 7 also had an increase in SO_2 . The reading at station 6 had dropped from 0.38 to 0.27 ppm. The next map (2000) shows continued veering of the wind to southerly and a jump in SO_2 at station 8. Two hours later (2200), winds were southwest and SO_2 concentrations were 0.3 ppm or more at all stations except 5 and 6. At 0200 on the 10th, winds were light and variable and SO_2 concentrations were lower at all stations. The highest levels appeared in a band along the lake shore.

This case may be summarized as follows: A lake breeze developed between 1000 and 1100 and pene-

trated inland as far as Argonne by 1900. High pollution levels appeared first at 1800 well behind the lake breeze front in easterly winds at TAM-6. The pollution moved to the northwest, north, and then east; it was detected next at station 8, then 7, and then almost simultaneously at 2, 3, and 4. The fact that the pollution first appeared at station 6 in easterly winds suggests a source between TAM-6 and the lake shore. We traced the trajectory of TAM-2 pollution backwards from 2200 and arrived at the same area.

Theoretically an onshore wind from a cool lake should behave as shown in Figure 128, with the formation of an unstable boundary layer that deepens with distance from the shore. When this unstable layer intersects plumes aloft, contaminants will mix downward to the surface in high concentrations.

Circumstances in this case suggest that SO_2 from the South Chicago-Northwest Indiana industrial complex may have been brought to the surface in this way

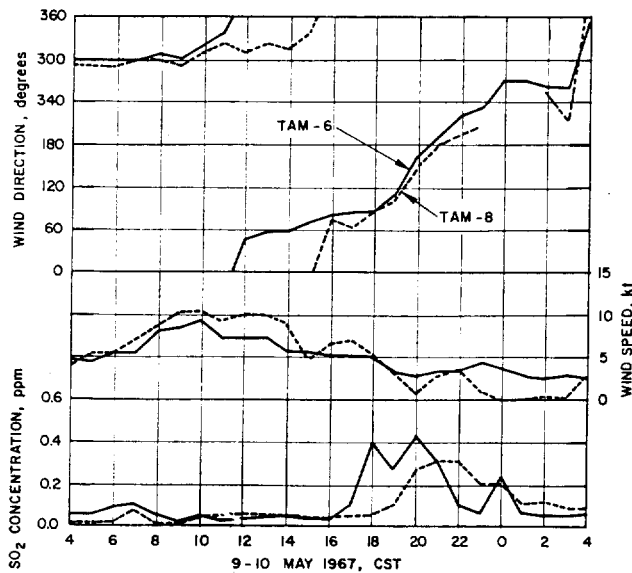


FIG. 123.—Winds and SO₂ at TAM-6 and 8, 9-10 May 1967

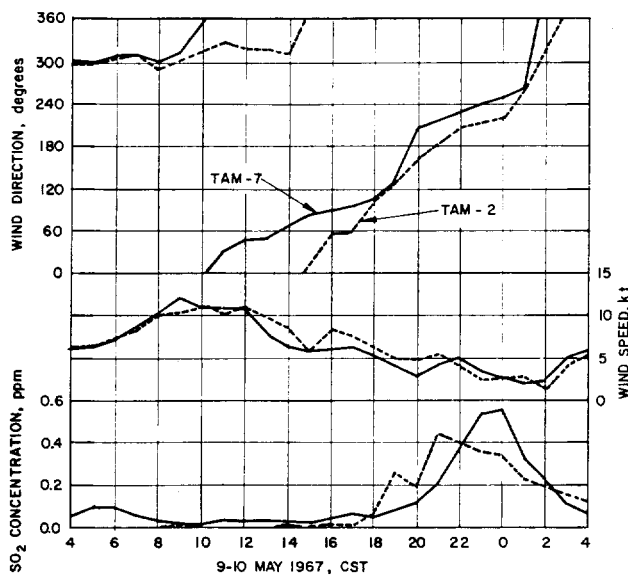


FIG. 124.—Winds and SO₂ at TAM-2 and 7, 9-10 May 1967

and subsequently blown about the city by shifting surface winds.

Frequencies of Occurrence

Each of the three cases examined involved high SO₂ readings at several stations. Thus we know that the weather phenomena involved can produce high pollution levels. Therefore, they deserve more attention. One important aspect to consider is how often they occur. Table 61 shows frequencies of occurrence for the three weather processes examined in this paper, namely heat island circulations, winds off the lake in response to the regional pressure gradient, and lake breezes.

The frequency of 1-2 per month for heat-island circulations is a preliminary figure based on a search of two years of data in the Argonne air pollution data file. The frequencies for offlake winds were determined from a search of Chicago local climatological data for 1965, 1966, and 1967.

An offlake wind day is defined as a day when the prevailing direction was between 40 and 120 degrees. To qualify as a "lake warmer" case, the lake temperature had to be at least 3° F warmer than the maximum daily temperature at Midway; and vice versa for the "land warmer" cases.

Table 61 shows that several potential pollution-producing events normally occur each month throughout the year. Beside the three pollution phenomena dealt with here, there are others that add to the monthly totals. The highest frequencies in Table 61 come during summer. Fortunately, SO₂ emissions are lowest then. There is little residential heating, and many Chicago industries find it cheaper to burn natural gas in summer.

SUMMARY AND CONCLUSIONS

Three high pollution cases involving different meteorological events were examined in detail using air quality and weather data taken near the surface.

On a cold, nearly calm day in winter, when the city was several degrees warmer than the surrounding rural land area, an internal "heat-island" circulation apparently developed. Winds converged from east and west near the north-south axis of the city. Continuity indicated rising air over this axis and return flow to the east and west aloft. Measured SO₂ concentrations of 0.2 ppm in air arriving at shoreline

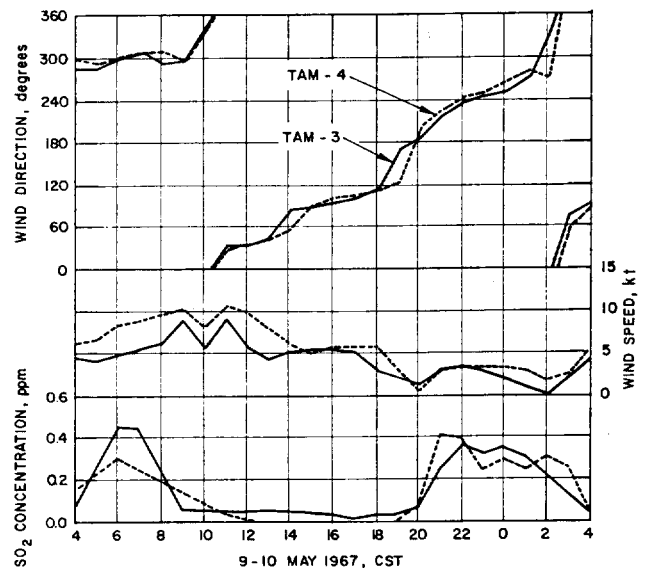


FIG. 125.—Winds and SO₂ at TAM-3 and 4, 9-10 May 1967

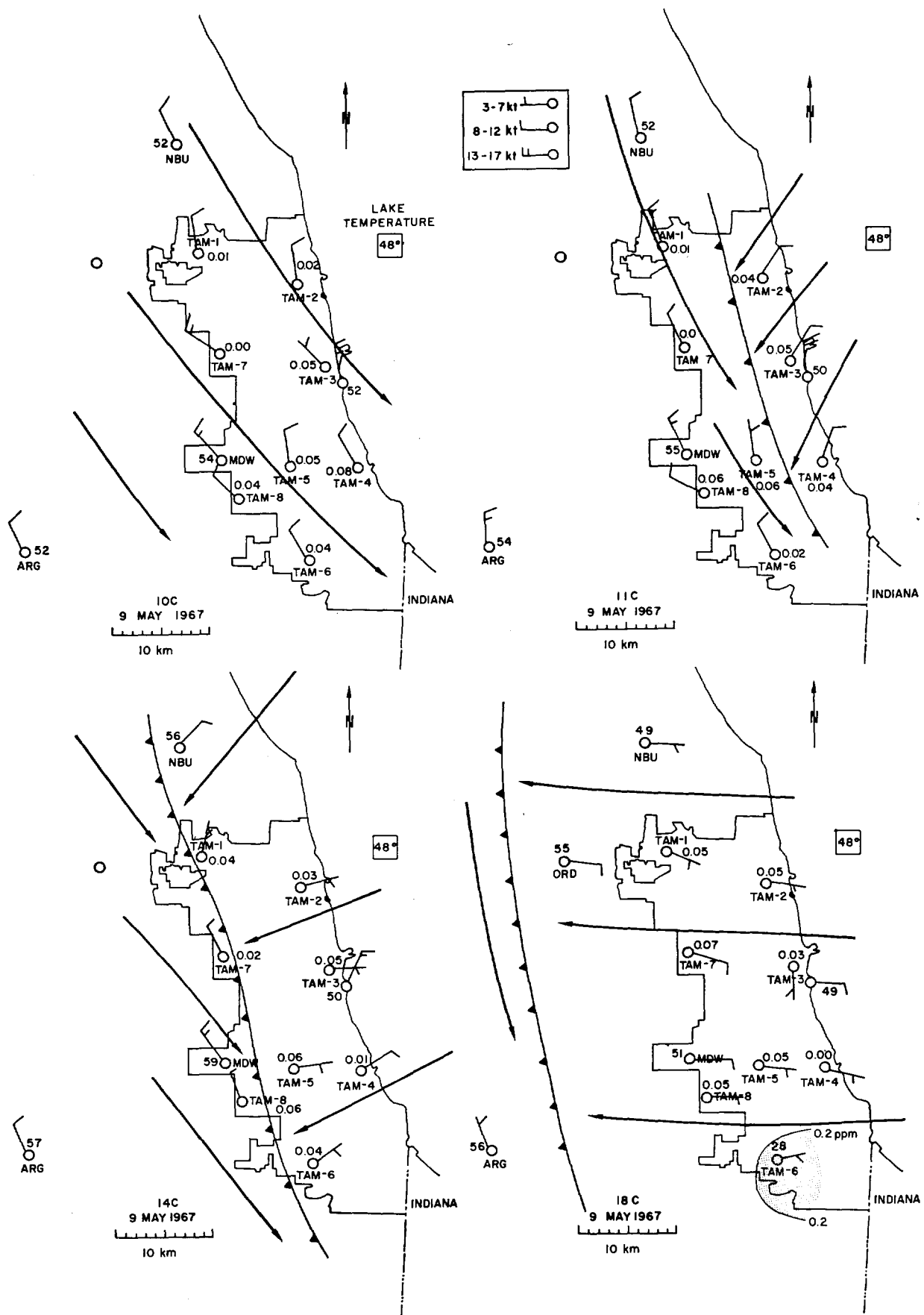


FIG. 126.—Weather and pollution maps for Chicago area, 9 May 1967

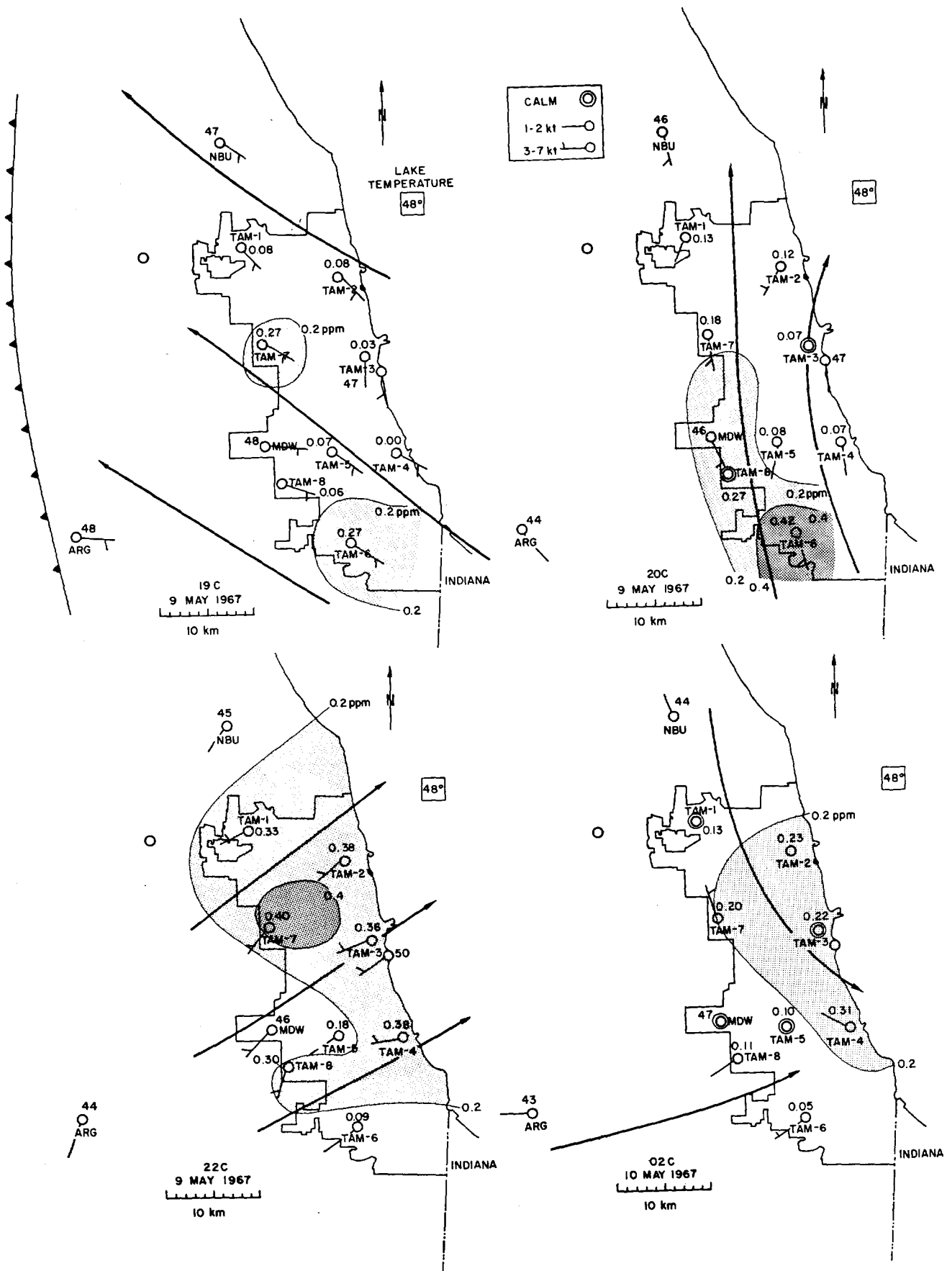


FIG. 127.—Weather and pollution maps for Chicago area, 9-10 May 1967

stations from over the lake strongly suggests that this circulation was recirculating air through the city. This may account for the very high concentrations of SO_2 observed that day.

Two cases of winds off Lake Michigan were also examined. In one case, the lake was warmer than the land; in the other the land was warmer. Observed pollution patterns generally agree with those expected theoretically. However, more cases must be studied before we can draw firm conclusions.

Two other possible meteorological pollution phenomena, namely nocturnal inversion trapping and morning inversion breakup fumigation may also have occurred in one of the cases. This shows that the me-

TABLE 61. FREQUENCIES OF OCCURRENCE OF SOME WEATHER PHENOMENA IMPORTANT TO CHICAGO AIR POLLUTION

Event	Frequency	Reference
Heat-island circulation	1-2 per month during fall and winter (preliminary)	This study
Offlake winds		
Lake warmer	1 per month, September through April	This study
Land warmer*	8 per month, March through September	This study
	2 per month, October through February	This study
Lake breeze	3 per month reach Midway, May through September	Murray and Trettel, Inc. ⁽³⁾

* Some of these may be lake breezes.

eteorological cause for any given pollution episode may be highly complex and involve several different physical processes.

More study of these and other phenomena are needed. Extensive observations in four dimensions would be desirable, of course, but these case studies offer hope that important information can come from data on hand now.

We thank Mr. Ivan Brunk for information on Lake Michigan ice conditions on 19 January 1966, and Mr. Harry Moses for helpful discussions of the case.

REFERENCES

1. Lowry, W. O. The climate of cities. *Sci. Am.* **217**(2), 15-23 (1967).
2. Hewson, E. S. and Olsson, L. E. Lake effects on air pollution dispersion. *J. Air Poll. Control Assoc.* **17**(11), 757-761 (1967).
3. Murray and Trettel, Inc. The climatology of air pollution in northeastern Illinois. Report prepared for The Northeastern Illinois Metropolitan Area Planning Commission. Murray and Trettel, Inc., Northfield, Illinois, February 1966.

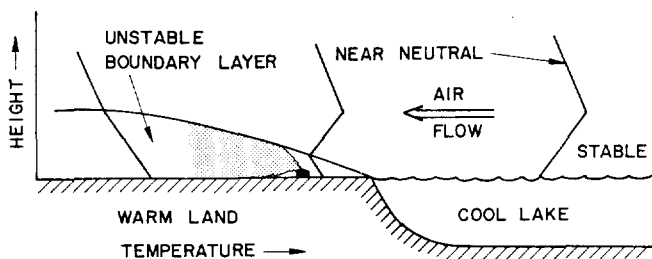
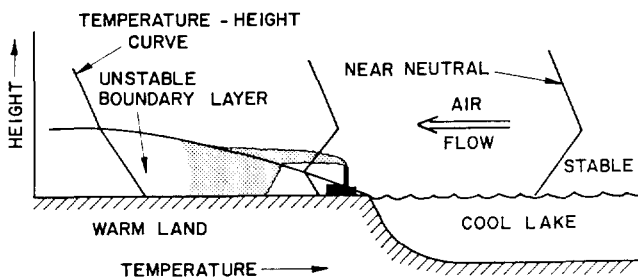


FIG. 128.—Schematic diagram of stability regimes for on-shore flow from a cool lake. Top, tall stack; bottom, short stack. (After Hewson and Olsson.⁽²⁾)

MATHEMATICAL URBAN AIR POLLUTION MODELS*

Harry Moses

This paper provides a review of the use of mathematical models for urban air pollution problems. Discussed are the major contributions in this field beginning with the early work of Frenkiel to those of

modern day operational models. To allow an assessment of work in this area, five tables are presented including the locations of the studies, types of tracers, sizes of the monitoring and meteorological networks, amounts of data collected, and the mathematical equations used.

The urban air pollution model is considered as having four components. These are (1) the source in-

* Summary of a paper presented at the 67th Annual Meeting of the Air Pollution Control Association, New York, June 26-29, 1969.

ventory, including point as well as area sources; (2) the network of meteorological stations; (3) the network of pollutant monitoring stations; and (4) the mathematical algorithm which describes the processes which transform the concentrations at the source to those observed at the receptor. Also, a substantial amount of attention is devoted to verification procedures.

Two general categories of mathematical models are discussed. The first is the source-oriented model characterized by the work of Turner. In this model, the concentration at a particular point is determined by the superposition of the contributions from each of the sources upwind. The second is the receptor-oriented model of which there are three types: the first is that described by Clarke, in which the pollutant concentrations at a particular monitoring station are analyzed in a manner similar to that of the source-oriented model. Second, there is the regression model, in which

regression equations are developed relating observed concentrations at a receptor with meteorological variables; and third, the tabulation prediction scheme in which combinations of meteorological variables are arranged in an ordered sequence. For each combination, the probability distribution of pollutant concentration is given along with other statistical parameters, such as the interquartile range, the mean, and the standard deviation of the distributions. With the tabulation prediction scheme, one may look up the meteorological conditions just as one looks up a name in a telephone book or a word in a dictionary and read off the probability distribution of concentrations.

A summary of verification techniques is given with examples of how other workers in the field have verified their models. These include scatter diagrams, correlation coefficients, and isopleth comparisons. The weaknesses and strengths of validation techniques are discussed.

THE USE OF PYRHELIOMETERS FOR CONTINUOUS MEASUREMENTS OF AN EFFECTIVE AIR POLLUTION MIXING DEPTH

*Harry Moses and D. N. Eggenberger**

Information on the magnitude of the mixing depth is important for forecasting levels of pollutant concentrations over a given area. To date, mixing depth information has been obtained by means of sensors mounted in an aircraft or carried aloft by balloons. At best, the information provided has been sporadic.

This paper describes techniques using combinations of either pyrheiliometers or pyranometers to provide continuous recordings of the mixing depth. Various techniques are described for obtaining these measurements. The most attractive of these consists of two pairs of pyrheiliometers on equatorial mounts; one pair is located on a tall building and another pair near the ground. One instrument of each pair has a 4000–4500 Å filter and the other, a 5500–6000 Å filter. By considering ratios of the solar radiation recorded by combinations of these pyrheiliometers, it is possible to determine the depth of the aerosol mixing layer under the assumption that the aerosol concentration is approximately uniformly mixed within the mixing layer and drops to a very small value above it. Variations from this aerosol distribution can be handled when three or four pairs of instruments are used at various heights with the greatest height approaching 1000 ft.

The correlation technique involving the crossing of two pyranometer fields of view is also discussed. In this method, one pyranometer has a conical field of view of about ½ degree directed upward. The second pyranometer, also with a narrow field of view, is located about 1000 to 2000 ft away. The fields of view of the two pyranometers are made to intersect. The second pyranometer is designed to scan by changing its elevation angle so that the height of a common volume of the two intersecting fields of view varies from a level

near the ground to several thousand feet. The covariance between the signals recorded by the two instruments would change as the common volume passed from air with a high concentration of aerosol to clean air. By noting the height at which the changes occur, it should be possible to determine both the height of the aerosol mixing layer and also the presence of aerosol layers above the primary ground base layers.

INTRODUCTION

When one approaches an industrialized urban area either by aircraft or by automobile, a pall of pollution is readily discernible. The emission of pollutants into the urban atmosphere coupled with meteorological processes such as diffusion, transport, or convection controls the height of this pollution or atmospheric mixing layer. One may consider the mixing layer in different ways: (a) the vertical distribution of pollutants, (b) the vertical distribution of temperature, or (c) the vertical wind profile. During steady state conditions, one expects agreement among these three types of measurements. During dawn or dusk—transitional periods—appreciable differences may be observed because of different adjustment rates or system time constants.

If the mixing depth is small, levels of pollutant concentrations are high since the pollutants are mixed with air confined to a narrow layer; with a large mixing

* Electronics Division.

depth, pollutants are diluted by mixing with air over a thicker layer resulting in lower ground concentrations.

When one examines vertical temperature soundings taken over land in the early morning during clear skies and winds less than about 10 mph, a ground based inversion is normally found. As this inversion begins to dissipate shortly after sunrise, the vertical temperature gradient approaches or exceeds the adiabatic lapse rate over an increasingly thicker layer. As a result, the lowermost layer is unstable but is capped by an inversion. Pollutants in this unstable layer from the ground upward are uniformly mixed. Equation (1) describes the concentration of pollutants within such a layer resulting from a continuous point source located below the inversion lid

$$x = \frac{Q}{\sqrt{2\pi} u \sigma_y H} \exp \left\{ -\frac{y^2}{2\sigma_y^2} \right\} \quad (1)$$

- x = concentration gr/m³
- Q = emission rate of pollutants gr/sec
- u = wind speed downwind of source meters/sec
- H = mixing depth in meters
- y = crosswind distance in meters
- σ_y = the perpendicular distance in meters from centerline of the plume in the horizontal direction to the point where the concentration falls to 0.61 times the centerline value

As the ground based inversion is dissipated and the lower unstable layer increases to the level at which a particularly strong source is located (the chimney top) the material is brought to the ground in high concentrations and a condition known as fumigation results. Equation (1) may be used under fumigation conditions.

Thus, the mixing depth must undergo diurnal variations. Information on the behavior of the mixing depth is useful in forecasting air pollution levels or devising strategies for incident control. Continuous measurements of the mixing depth over rural as well as urban areas or during pronounced convection would assist in gaining a fundamental insight into those meteorological processes of importance to the air pollution problems.

The normal constituents of the atmosphere, oxygen, nitrogen, water vapor, ozone, carbon dioxide, and aerosols attenuate solar radiation. Attenuation is caused to some extent by absorption but to a larger extent by scattering.

Measurements of the attenuation of solar radiation within a given layer may be determined by comparing the radiation readings at the top and bottom of the layer. Three or four pyrhemometers at different levels would provide information on the variation of attenuation with height, which in turn would be related to the vertical distribution of aerosol.

If we assume that in the lower layers above ground

the pollutant is approximately uniformly mixed or changes slowly with height up to the top of the mixing layer, but then falls sharply, we can determine the effective height of the mixing layer from the readings of pyrhemometers at two or three levels. Several techniques for doing this are described below.

THE CASE OF UNIFORM MIXING OR CONSTANT DENSITY OF POLLUTANTS

Technique for Obtaining Mixing Depths with Two Pyrhemometers and Two Solar Zenith Distances

In this method, one pyrhemometer is located at the ground and the other on the rooftop of a building a feet tall. (See Figure 129.) Readings are taken about one hour apart; it is assumed that the mixing depth has changed little during this period. This assumption, of course, is not valid during transitional periods; it may be tolerable during the middle of the day.

The intensity of the solar beam passing from the top of the atmosphere to the top of the building on which the upper pyrhemometer is mounted may be given by

$$I_T(\theta_1) = I_0(\theta_1) \exp \{-\mu L(\theta_1)\}, \quad (2)$$

where

$I_T(\theta_1)$ = intensity of all band solar radiation at top of building with the sun's zenith distance θ_1

θ_1 = solar zenith distance in radians at initial time

$I_0(\theta_1)$ = intensity of normal incidence solar radiation at top of atmosphere with the sun's zenith distance θ_1

T = subscript representing instrument on rooftop of building serving as a platform

μ = attenuation coefficient in meters⁻¹. This coefficient is the sum of the absorption and scattering coefficients.

$L(\theta_1)$ = length of solar beam from top of mixing layer to uppermost pyrhemometer with solar zenith distance, θ_1 .

For a solar zenith angle of θ_2 , the equation becomes

$$I_T(\theta_2) = I_0(\theta_2) \exp \{-\mu L(\theta_2)\}. \quad (3)$$

Similar equations for pyrhemometers at ground level are

$$I_B(\theta_1) = I_0(\theta_1) \exp \{-\mu[L(\theta_1) + L_a(\theta_1)]\} \quad (4)$$

$$I_B(\theta_2) = I_0(\theta_2) \exp \{-\mu[L(\theta_2) + L_a(\theta_2)]\} \quad (5)$$

where

B = subscript which refers to the bottom of the building

$L_a(\theta_1)$ and $L_a(\theta_2)$ = length of solar beam from top to bottom of building

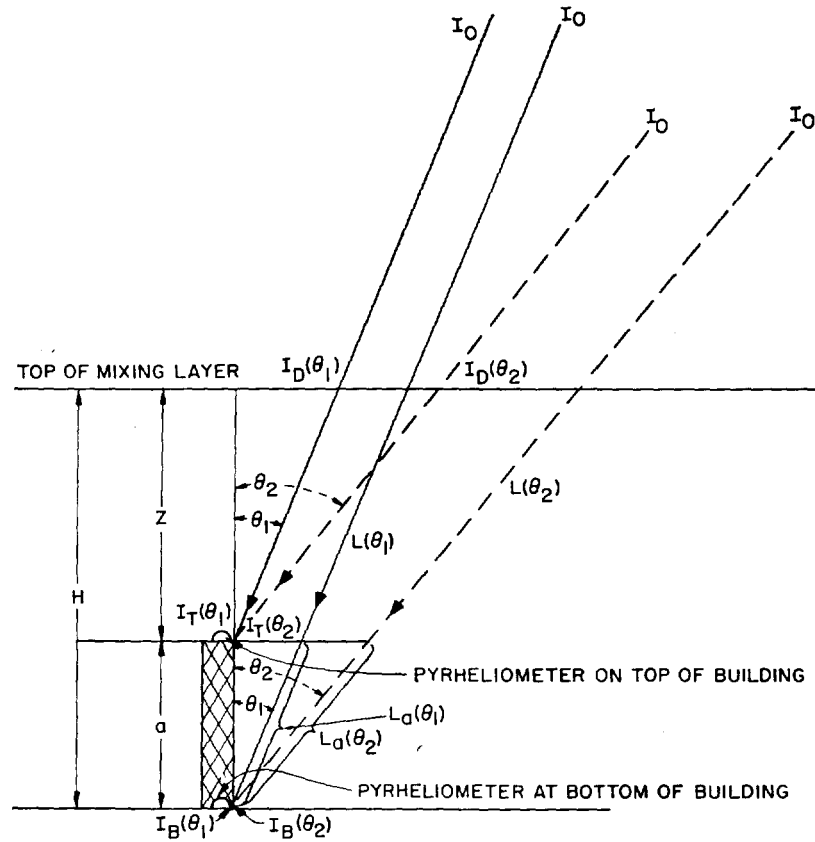


FIG. 129.—Measurement of mixing depth with two pyrheliometers and two solar zenith distances. Unfiltered solar radiation used.

$$L_a(\theta_1) = a \sec \theta_1$$

$$L_a(\theta_2) = a \sec \theta_2$$

Dividing Equation (2) by Equation (4) we have

$$\frac{I_T(\theta_1)}{I_B(\theta_1)} = \frac{I_0(\theta_1)}{I_0(\theta_1)} \exp \{ \mu a \sec \theta_1 \} \quad (6)$$

or

$$\mu = \frac{\ln [I_T(\theta_1)/I_B(\theta_1)]}{a \sec \theta_1} \quad (7)$$

Dividing Equation (4) by Equation (5) we have

$$\frac{I_B(\theta_1)/I_B(\theta_2)}{I_0(\theta_1)/I_0(\theta_2)} = \exp \{ -\mu [L(\theta_1) + L_a(\theta_1) - L(\theta_2) - L_a(\theta_2)] \} \quad (8)$$

Since $I_0(\theta_1) = I_0(\theta_2)$ and $L(\theta_1) + L_a(\theta_1)$ and $L(\theta_2) + L_a(\theta_2)$ are $H \sec \theta_1$ and $H \sec \theta_2$ respectively, we have

$$\ln \frac{I_B(\theta_1)}{I_B(\theta_2)} = -\mu H (\sec \theta_1 - \sec \theta_2), \quad (9)$$

where H is the effective height of the mixing depth.

Combining Equations (7) and (9) and solving for H we have

$$H = \frac{a \sec \theta_1 \ln I_B(\theta_1) - \ln I_B(\theta_2)}{\sec \theta_2 - \sec \theta_1 \ln I_T(\theta_1) - \ln I_B(\theta_1)} \quad (10)$$

Technique for Obtaining Mixing Depth with Pairs of Pyrheliometers at Each of Two Levels Using Two Wave Bands

Through the use of filters, it is possible to measure the received solar radiation in a prescribed band. With two pyrheliometers at each of two levels, one operating at 400–450 nanometers and the other at 550–600 nanometers, it is possible to determine the height of the mixing depth at a single zenith distance of the sun. (See Figure 130.) In other words, nearly instantaneous measurements of the mixing depth are obtained. In selecting the two bands, it is desired that attenuation in one band be as large as possible and in the other as small as possible so that the difference $\mu(\lambda_1) - \mu(\lambda_2)$ is at a maximum.

Using an argument similar to that above we have

$$I_T(\lambda_1, \theta_1) = I_0(\lambda_1, \theta_1) \exp \{ -\mu(\lambda_1) L(\theta_1) \} \quad (11)$$

Since we are dealing with a single zenith angle the θ 's will be omitted and we have

$$I_T(\lambda_1) = I_0(\lambda_1) \exp \{ -\mu(\lambda_1) L \} \quad (12)$$

The λ_1 refers to the first wave band used. See Figure 130.

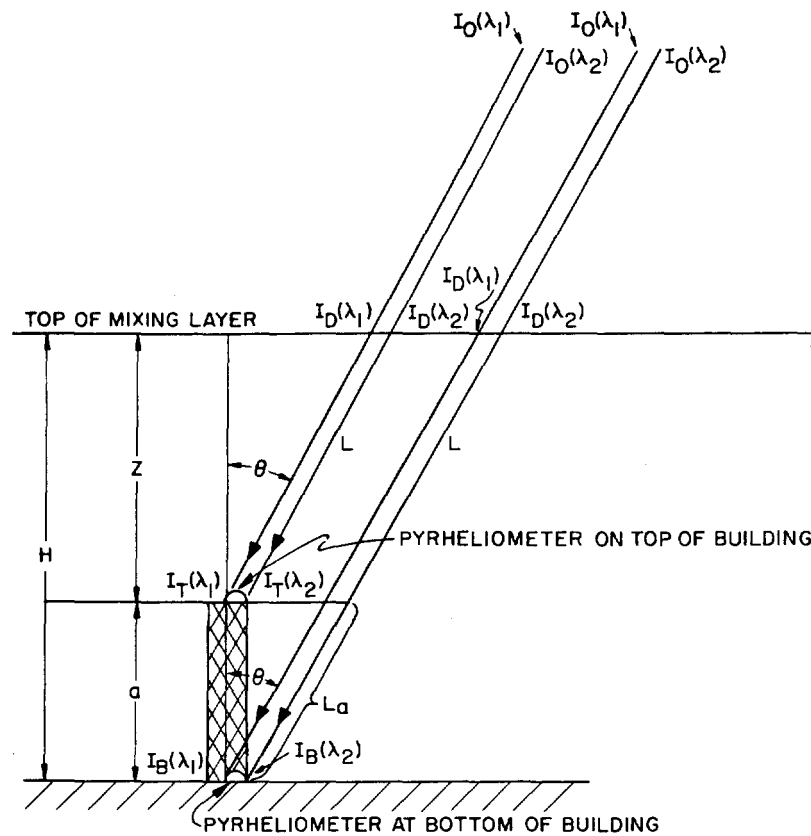


FIG. 130.—Measurement of mixing depth with pairs of pyrhemometers at each of two levels. One pyrhemometer of each pair operates in a 500 \AA band centered at $\lambda_1 \text{ \AA}$ and the other in a 500 \AA band centered at $\lambda_2 \text{ \AA}$.

Equations corresponding to Equations (3), (4), and (5) are

$$I_T(\lambda_2) = I_0(\lambda_2) \exp \{-\mu(\lambda_2)L\} \quad (13)$$

$$I_B(\lambda_1) = I_0(\lambda_1) \exp \{-\mu(\lambda_1)(L + L_a)\} \quad (14)$$

$$I_B(\lambda_2) = I_0(\lambda_2) \exp \{-\mu(\lambda_2)(L + L_a)\}. \quad (15)$$

Dividing Equation (12) by Equation (14) and taking the logarithm of both sides we have

$$\therefore \ln \frac{I_T(\lambda_1)}{I_B(\lambda_1)} = \mu(\lambda_1) a \sec \theta \quad (16)$$

or

$$\mu(\lambda_1) = \frac{\ln \frac{I_T(\lambda_1)}{I_B(\lambda_1)}}{a \sec \theta}. \quad (17)$$

Similarly,

$$\mu(\lambda_2) = \frac{\ln I_T(\lambda_2)/I_B(\lambda_2)}{a \sec \theta}, \quad (18)$$

where λ_2 represents the solar radiation in band 2.

Dividing Equation (14) by Equation (15) and taking the logarithms of both sides, we have

$$\ln I_B(\lambda_1)/I_B(\lambda_2) = \ln I_0(\lambda_1)/I_0(\lambda_2) - [\mu(\lambda_1) - \mu(\lambda_2)](L + L_a) \quad (19)$$

or

$$\ln I_B(\lambda_1)/I_B(\lambda_2) - \ln I_0(\lambda_1)/I_0(\lambda_2) = [\mu(\lambda_2) - \mu(\lambda_1)] H \sec \theta \quad (20)$$

Solving for H and making use of Equations (17) and (18) we have

$$\therefore H = \frac{a(\ln I_B(\lambda_1)/I_B(\lambda_2) - \ln I_0(\lambda_1)/I_0(\lambda_2))}{\ln I_T(\lambda_2)/I_B(\lambda_2) - \ln I_T(\lambda_1)/I_B(\lambda_1)}. \quad (21)$$

Thus H , the effective height is determined from known or measured quantities. The ratio $I_0(\lambda_1)/I_0(\lambda_2)$ is, of course, the ratio of the energy in the two selected wave bands and is given in Physical Tables.

Figure 131 shows a schematic circuit diagram for providing a continuous reading of the mixing depth.

LINEAR VARIATION OF POLLUTANT WITH HEIGHT

The attenuation coefficient, μ , varies directly with the mass of pollutant traversed per unit cross section or the concentration. If the concentration varies linearly with height, then the attenuation coefficient will also vary this way. Let us assume that

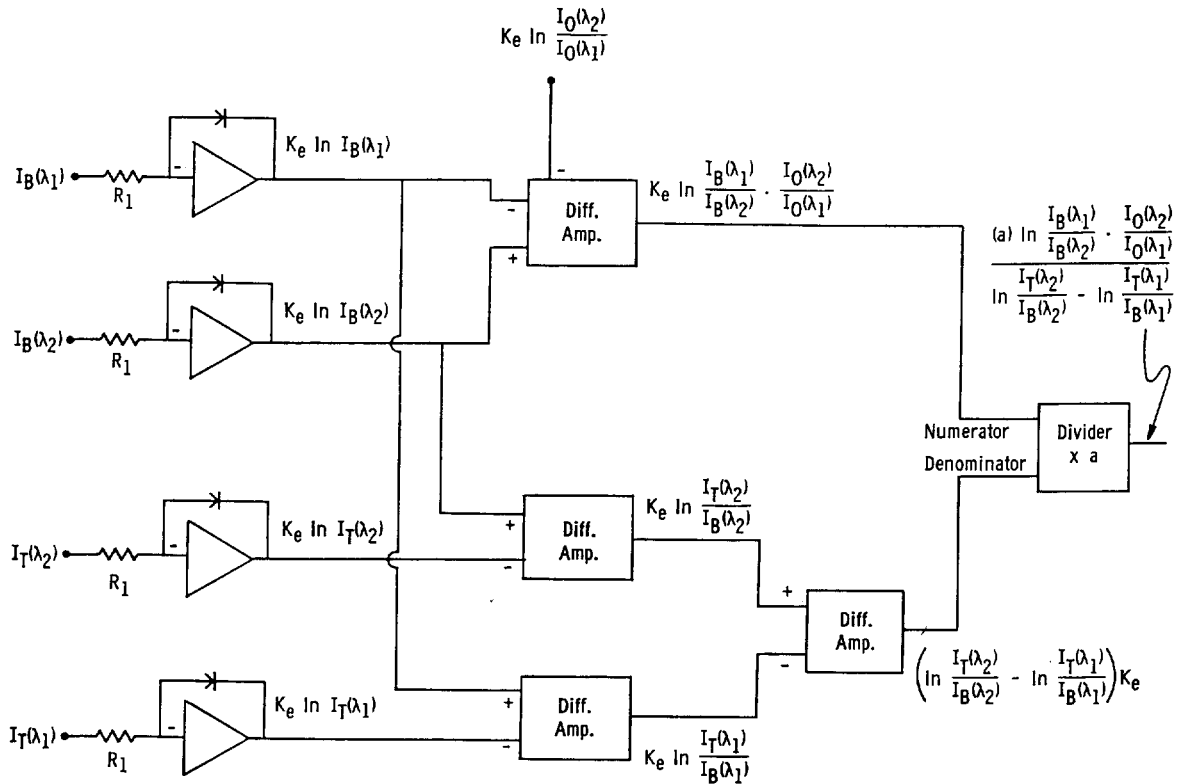


FIG. 131.—Circuit diagram for providing a continuous reading of the mixing depth in the case of uniform mixing using two pairs of pyrhelimeters, with one of the two pyrhelimeters in each pair operating in one wave band and the other in a different wave band.

$$\mu = kz,$$

where k is a constant and z is measured in the vertical direction with positive upward.

The basic differential equation then becomes (see Figure 129)

$$\frac{dI}{I} = -\mu dL = -kz dL = -kz \sec \theta dz. \quad (22)$$

Integrating between the limits of the top of the building and the top of the mixing layer we have

$$\int_D^T \frac{dI}{I} = -k \sec \theta \int_0^z z dz$$

$$\ln \frac{I_T}{I_D} = \frac{-k \sec \theta}{2} z^2$$

or

$$I_T = I_D \exp \left\{ \frac{-k \sec \theta}{2} z^2 \right\}, \quad (23)$$

where I_D = intensity of solar radiation at top of the mixing layer and z is measured from the top of the layer.

If we express

$$I_D = I_0 e^{-\alpha}$$

where I_0 = the solar constant for all-band radiation, and α is a constant, we have

$$I_T = I_0 e^{-\alpha} e^{-(k/2) \sec \theta z^2}$$

$$= I_0 \exp \left\{ -\alpha - \frac{k}{2} (\sec \theta) z^2 \right\}. \quad (24)$$

Three Pyrhelimeters at One Wave Band and One Zenith Distance

If we use three pyrhelimeters, each at a different level, it is possible to determine an effective height of the mixing layer instantaneously and without filters under the assumption that the concentration decreases linearly with height. If we are dealing with a tall building, we may place one pyrhelimeter at the ground denoted by subscript B ; one at an intermediate level (M); and one at the top (T). (See Figure 132.)

We may then write

$$I_T = I_0 \exp \left\{ -\alpha - \frac{k \sec \theta}{2} z^2 \right\} \quad (25)$$

or

$$I_T = I_0 \exp \left\{ -\alpha - \frac{k}{2} (\cos \theta) L^2 \right\} \quad (26)$$

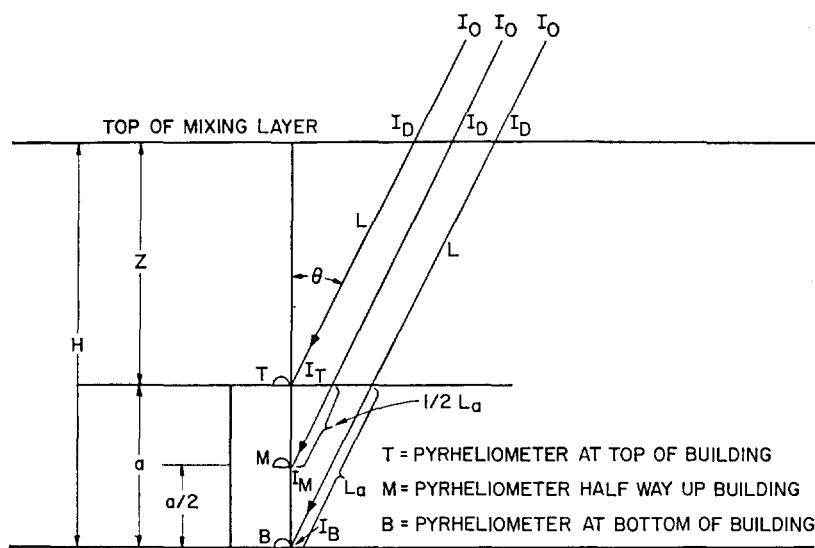


FIG. 132.—Three pyrheliometers at one wave band and one zenith distance to provide mixing depth information where pollutant concentration is distributed linearly with height.

$$I_B = I_0 \exp \left\{ -\alpha - \frac{k}{2} (\cos \theta) (L + L_a)^2 \right\} \quad (27)$$

$$I_M = I_0 \exp \left\{ -\alpha - \frac{k}{2} (\cos \theta) \left(L + \frac{L_a}{2} \right)^2 \right\} \quad (28)$$

$$\ln \frac{I_T}{I_B} = \frac{k}{2} (\cos \theta) (2L \cdot L_a + L_a^2) = P \quad (29)$$

$$\ln \frac{I_T}{I_M} = \frac{k}{2} (\cos \theta) \left(L \cdot L_a + \frac{L_a^2}{4} \right) = Q \quad (30)$$

$$\frac{k}{2} (\cos \theta) (2L \cdot L_a + L_a^2) = P \quad (31)$$

$$\frac{k}{2} (\cos \theta) (4L \cdot L_a + L_a^2) = 4Q \quad (32)$$

Solving Equations (31) and (32) for k we have

$$k = \frac{4P - 8Q}{\cos \theta L_a^2} \quad (33)$$

And solving for L we have

$$L = L_a \frac{4Q - P}{4P - 8Q} \quad (34)$$

$$L = L_a \frac{4 \ln I_T/I_M - \ln I_T/I_B}{4 \ln I_T/I_B - 8 \ln I_T/I_M} \quad (35)$$

But $L = z \sec \theta$ and $L_a = a \sec \theta$

$$z = a \frac{4 \ln I_T/I_M - \ln I_T/I_B}{4 \ln I_T/I_B - 8 \ln I_T/I_M} \quad (36)$$

$$H = z + a = a + a \frac{4 \ln I_T/I_M - \ln I_T/I_B}{4 \ln I_T/I_B - 8 \ln I_T/I_M}$$

or

$$H = \frac{a}{4} \frac{3 \ln I_T/I_B - 4 \ln I_T/I_M}{\ln I_T/I_B - 2 \ln I_T/I_M} \quad (37)$$

All of the quantities are measurable.

Two Pairs of Pyrheliometers at Two Levels and Two Wave Bands

As previously, we shall assume that the wave bands λ_1 and λ_2 are 400–450 and 550–600 nanometers. The same notation as above is used.

$$I_T(\lambda_1) = I_0(\lambda_1) \exp \left\{ -\alpha - \frac{k(\lambda_1)}{2} L^2 \cos \theta \right\} \quad (38)$$

$$I_T(\lambda_2) = I_0(\lambda_2) \exp \left\{ -\alpha - \frac{k(\lambda_2)}{2} L^2 \cos \theta \right\} \quad (39)$$

$$I_B(\lambda_1) = I_0(\lambda_1) \exp \left\{ -\alpha - \frac{k(\lambda_1)}{2} (L + L_a)^2 \cos \theta \right\} \quad (40)$$

$$I_B(\lambda_2) = I_0(\lambda_2) \exp \left\{ -\alpha - \frac{k(\lambda_2)}{2} (L + L_a)^2 \cos \theta \right\} \quad (41)$$

From Equations (38) and (39)

$$\ln \left(\frac{I_T(\lambda_1)}{I_T(\lambda_2)} \cdot \frac{I_0(\lambda_2)}{I_0(\lambda_1)} \right) = \frac{k(\lambda_2) - k(\lambda_1)}{2} (\cos \theta) L^2 \quad (42)$$

From Equations (40) and (41)

$$\ln \frac{I_B(\lambda_1)}{I_B(\lambda_2)} \cdot \frac{I_0(\lambda_2)}{I_0(\lambda_1)} = \frac{k(\lambda_2) - k(\lambda_1)}{2} \cos \theta (L + L_a)^2 \quad (43)$$

Dividing Equation (42) by Equation (43) we have

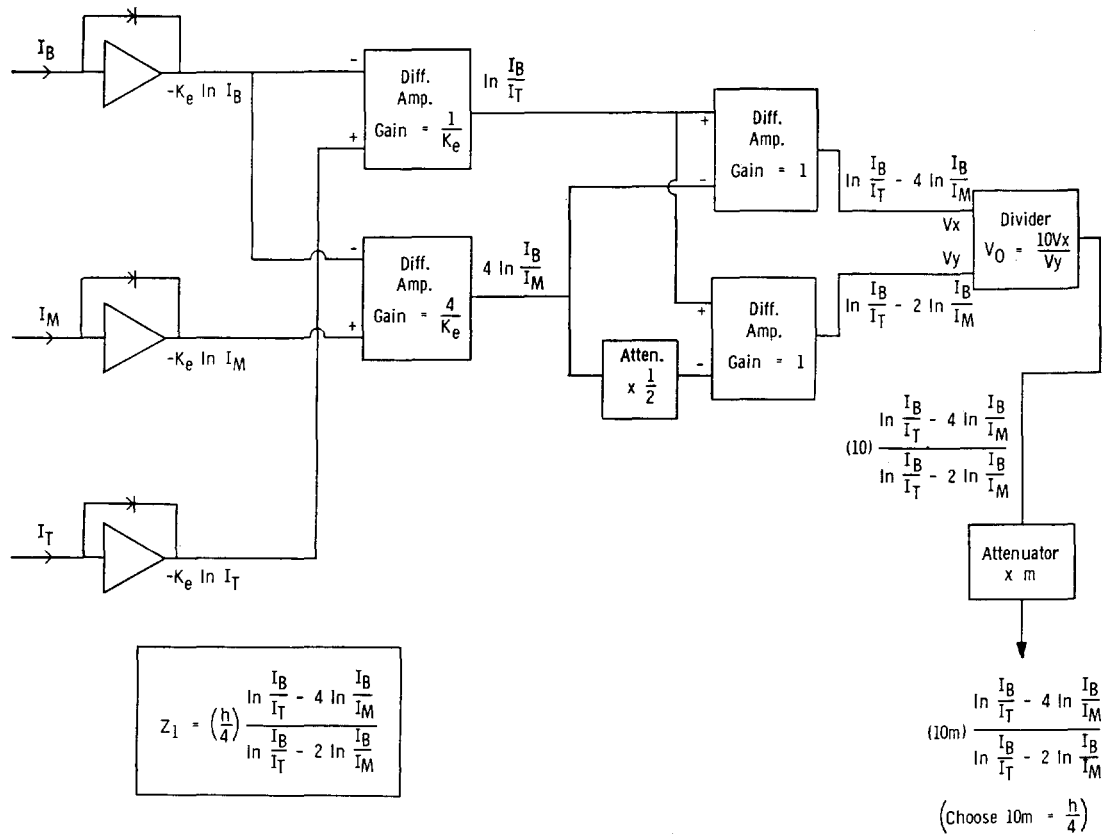


FIG. 133.—Circuit diagram for providing a continuous reading of the mixing depth in the case of linear variation of pollutant with height. Three pyrheliometers at one wave band and one zenith distance are used.

$$\frac{\ln \left(\frac{I_T(\lambda_1)}{I_T(\lambda_2)} \cdot \frac{I_0(\lambda_2)}{I_0(\lambda_1)} \right)}{\ln \left(\frac{I_B(\lambda_1)}{I_B(\lambda_2)} \cdot \frac{I_0(\lambda_2)}{I_0(\lambda_1)} \right)} = S = \frac{L^2}{(L + L_a)^2} \quad (44)$$

Therefore,

$$\frac{L}{L + L_a} = S^{1/2} \quad (45)$$

and

$$L = \frac{L_a S^{1/2}}{1 - S^{1/2}} \quad (46)$$

One must exercise care to see that the square root is taken of positive numbers only.

$$z + a = H = a + \frac{aS^{1/2}}{1 - S^{1/2}} = \frac{a - aS^{1/2} + aS^{1/2}}{1 - S^{1/2}} = \frac{a}{1 - S^{1/2}} \quad (47)$$

$$H = \frac{a \left[\ln \left(\frac{I_B(\lambda_1)}{I_B(\lambda_2)} \cdot \frac{I_0(\lambda_2)}{I_0(\lambda_1)} \right) \right]^{1/2}}{\left[\ln \left(\frac{I_B(\lambda_1)}{I_B(\lambda_2)} \cdot \frac{I_0(\lambda_2)}{I_0(\lambda_1)} \right) \right]^{1/2} - \left[\ln \left(\frac{I_T(\lambda_1)}{I_T(\lambda_2)} \cdot \frac{I_0(\lambda_2)}{I_0(\lambda_1)} \right) \right]^{1/2}} \quad (48)$$

Thus, H , the mixing layer depth is determined from measured quantities for the case when the extinction coefficient varies linearly with height.

Figure 133 gives a circuit diagram for providing a continuous reading of the mixing depth.

CONCLUDING REMARKS

Vertical Distribution of Pollutants

The preceding development is based on an atmosphere in which the pollutants are distributed in height either uniformly or linearly. Under these conditions, it is possible to use pyrheliometers to determine the thickness of the mixing layer. In every case, it was assumed that the instruments measuring solar radiation were on an equatorial mount and, therefore, pointing at the sun. All of the equipment discussed, including the equatorial mounts, is available commercially off the shelf.

Work of other investigators has indicated that at times the vertical distribution of pollutants may be exponential.⁽¹⁾ A development similar to that above for the exponential distribution has been carried out by J. Gilroy and D. N. Eggenberger.⁽²⁾

The question arises on how to determine the distribution of pollutant concentration with height in order to

know which formula to apply. Solar radiation measurements will be made at four levels above ground up to about 1000 feet or greater. These will provide the distribution within the layer of measurement. Extrapolation techniques for determining the mixing depth may be developed by a series of comparison measurements using helicopter and balloon data and the pyrhelimeter measurements. These measurements will consist of vertical profiles of temperature and particulates in addition to those of other atmospheric constituents such as SO₂ or water vapor. A check on the system is, of course, essential before operational reliability can be established.

Aerosols may occur in layers varying from 10's to 100's of feet in thickness above the primary mixing layer near the ground.⁽³⁾ Should this condition prevail, then the method as described here will be ineffective in determining the true mixing depth. However, work is currently in progress which will allow a determination of the position and thickness of such layers. This involves a passive system using two pyranometers separated by a baseline of about 2000 feet. The covariance of the solar radiation flux observed by the two instruments involving a common volume arising from two intersecting cones of view is computed continuously. The height and extent of aerosol layers may be determined from the covariance measurements as the common volume is allowed to change its elevation above ground. The pyranometer system also requires validation by independent means such as by aircraft or balloons.

Advantages of the Pyrhelimeter System for Measuring Mixing Depth

The technique described here is essentially a passive remote probe, but it would work best during cloudless

daytime conditions. During cloudy conditions or during the night, it may be necessary to develop an active system in which a source of electromagnetic energy is used.

When conditions of severe pollution exist, an extensive anticyclone is generally present. With extensive high pressure areas, atmospheric subsidence is likely, with the result that little cloudiness is present. One may, therefore, expect to find that this system works well when needed during high pollution situations.

As indicated in the schematic diagrams, Figures 131 and 133, the information obtained from the pyrhelimeters may be passed through an electronic circuit in which the output represents the height of the mixing depth. This output may be transmitted to a central control point, such as an air pollution control office, where a recording meter provides continuous readings of the height of the mixing depth.

The pyrhelimeter technique represents distinct advantages over the systems currently available for measuring the mixing depth, such as those with helicopters, fixed winged aircraft, or balloons. At best under current systems, only a few measurements per day can be obtained. With a system such as described in this paper, continuous measurements are provided. These, of course, would be invaluable for not only providing a better insight into meteorological processes, but as a valuable tool for incident control.

REFERENCES

1. McCormick, R. A. and Kurfis, K. R. Vertical diffusion of aerosols over a city. *Quart. J. Roy. Meteorol. Soc.* **92**(393), 392-396 (1966).
2. Gilroy, John. Private Communication, 1969.
3. Davidson, Ben. A summary of the New York urban air pollution dynamics research program. *J. Air Pollution Control Assoc.* **17**(3), 154-158 (1967).

THE TABULATION TECHNIQUE FOR FORECASTING CONCENTRATIONS OF URBAN AIR POLLUTANTS

Harry Moses, J. B. Anderson, and D. F. Gatz

An urban air pollution model can be of considerable use to a municipality for incident control, for the siting of new plants, and for assessing the effectiveness of abatement procedures. Two types of urban air pollution models are available: 1) the source-oriented model, and 2) the receptor-oriented model.

In the tabulation prediction technique, combinations of meteorological variables are arranged in an ordered sequence in tabular form. For each combination of meteorological variables, a cumulative percentile distribution of the concentrations of a selected pollutant, e.g., SO₂, is presented. Also included are relevant statistical parameters such as the interquartile range, the mean, or the number of cases.

The development of a tabulation prediction technique requires a number of preliminary analyses. These include test-

ing meteorological variables for their relative importance in influencing the pollutant concentrations, selecting optimum class intervals of the weather elements, and deciding the most effective arrangement of the independent variables in the tabulation.

These are examined in a discussion of the construction of this technique. The paper also discusses the continual upgrading of the tabulation prediction technique and its use in source surveillance. An example is given of the tabulation prediction technique as applied to the city of Chicago.

When material is injected into the atmosphere, whether it be from a distributed area source or a point source, the meteorological conditions determine the

bution of SO₂ concentrations for this combination of meteorological variables.

To develop the Tabulation Prediction Technique, values of SO₂ concentrations, wind speed, and wind direction were obtained from the appropriate Telemetered Automatic Monitoring (TAM) Station operated by the City of Chicago; values of other meteorological variables were obtained either from the Chicago Midway Airport or from the Argonne Meteorology Laboratory.

THE INFLUENCE OF METEOROLOGICAL VARIABLES ON AIR POLLUTANT CONCENTRATIONS

Since the Tabulation Prediction Scheme depends on the relations between observed SO₂ concentrations at a receptor and the ambient meteorological variables, it is necessary to understand the principles underlying the meteorological processes. Each of the meteorological variables, wind speed, wind direction, temperature, relative humidity, stability, net solar-terrestrial radiation flux, mixing depth, ceiling, or visibility, may play an important role. The relationships may be substantially nonlinear.

The role played by meteorological variables in processes which affect SO₂ concentration levels is briefly discussed.

Wind Speed

The wind speed determines the urban ventilation rate. Further, the effluent from a point or distributed source is mixed with a large volume of air per unit time if the winds are strong and with a relatively small volume if the winds are light. Therefore, near the source, the low wind condition gives rise to high concentrations. In general, concentration levels vary inversely with the wind speed.

The situation, however, is not as simple as it appears. During clear nights with strong inversions, there is a decoupling of the air motions in the lower layers, i.e., several hundred feet above the ground. Under these conditions, the surface winds are very light and the effluent from a stack 200 or 300 feet high will remain aloft. Therefore, such stacks contribute little to the concentrations observed near the ground even though the wind speed is low. Effluents from low stacks (a few feet to tens of feet above the building) are caught in the turbulent wake of the building; high ground-level pollution concentrations result. With clear skies during the daytime and light winds, looping may occur, bringing high concentrations to the ground. Therefore, with light winds, the observed SO₂ concentrations would be very high or low, depending on the meteorological conditions.

The concentration at the ground is affected both by

plume rise and eddy mixing. There exists a critical wind speed which results in a maximum concentration near the ground. Thus, there are a number of considerations one has to take into account in evaluating the effect of wind speed on resulting levels of pollutant concentration.

Wind Direction

The effect of wind direction on a given receptor is obvious. If the wind blows directly from a strong source to the receptor, the concentrations will be high and vice versa. It should be pointed out, however, that even if the sources were uniformly distributed with respect to direction, there might still be a pronounced direction effect due to variations in ground roughness.

Temperature

The primary importance of temperature is its effect on the amount of fuel used, especially for space heating. There are secondary effects which one would have to take into account for long trajectories, i.e., exceeding three or four hours. Since SO₂ undergoes chemical reaction, especially oxidation, and since reaction rates double for every 10° C rise in temperature, the removal rate is a function of temperature. With a 4-hr residence time for SO₂ (probably at about 50° F) this effect has to be considered.

Although at first sight it may appear that the SO₂ concentrations and temperature or degree-hours are linearly related, this appears not to be the case as indicated by Roberts,⁽¹⁾ who points out that for temperatures above 32° F, the slope of the SO₂ vs. temperature curves differs from that below 32° F.

Another point worthy of note is the wind chill factor. With low temperatures and brisk winds cooling is enhanced, resulting in greater use of fuel with higher SO₂ concentrations.

Relative Humidity

Ordinarily, one might expect that relative humidity is not an important variable in the diffusion process. However, there are factors of which one must be aware; with high humidity, i.e., exceeding 90%, condensation of water droplets or ice crystals may occur which may scavenge SO₂. Oxidation rates are influenced by the ambient relative humidity since the oxidation rates of SO₂ in aqueous solution differ from those in the gaseous state. The oxidation of SO₂ yields SO₃, which reacts with water to form sulfuric acid. Further, chemical and physical action in the presence of metals or salts leads to the formation of sulfate particles.

Not only is relative humidity of importance in determining levels of concentration, but high values

of relative humidity for particular values of SO₂ concentration may have an important physiological effect on people as well as plants and animals. One must, therefore, always be aware of relative humidity levels in assessing the severity of an air pollution incident.

Mixing Depth

From a physical standpoint, the height of the mixing depth is important since it determines the volume in which the contaminants will be mixed.

The Vertical Temperature Gradient

The vertical temperature gradient represents a direct measure of the stability of the atmosphere. These measurements should be made in the urban area. Measurements several miles outside of the city in a rural area may be relevant, especially during extreme conditions when strong inversions are present. However, for optimum results, stability measurements should be made in the same area that predictions of pollution levels are made.

Net Radiation Flux

This measurement represents the difference between the sum of incoming solar and sky radiation and the outgoing terrestrial radiation. It provides information on characteristic weather regimes relevant to the diffusive capacity of the atmosphere. For example, during clear sunny conditions, there is a surplus of incoming radiation. As a result, the ground surface warms, and convection increases resulting in pronounced vertical mixing. The readings are strongly positive. During a clear night with strong outgoing radiation, the readings are invariably negative. This indicates a strong inversion, which results in a marked suppression of vertical motions. These data may also be used to indicate the degree of cloudiness.

Visibility

Visibility is directly related to the amount of particulate matter located in the lower layers of the atmosphere. Particle size is also an important factor in determining visibility. Not counting fog or other hydrometeors, low visibility denotes high concentrations of pollutants. At times, the pollutants are brought in from an external source such as the combustion products emanating from a forest fire even hundreds of miles away. More often, the particulates originate within the city and accumulate in the air because of poor diffusion conditions. Thus, visibility may be an indicator of pollutant concentration.

The Previous Hourly Reading of SO₂ Concentration

The meteorological variables selected for the Tabulation Prediction Technique are those which are most influential in controlling the levels of SO₂ concentration. It is conceivable that at times there are conditions which are not accounted for by the selected variables resulting in concentration values different from those expected. Examples are pronounced shear in the lower layers or lack of information on the height of the mixing depth. If it is assumed that persistence of concentration levels is appreciable from one hour to the next, the SO₂ concentration level would serve as a useful parameter.

There are conditions, of course, when abrupt changes do occur in the weather conditions, such as when a front is passing over the station and the usual pronounced wind direction change occurs. Further, during some parts of the day and under some weather regimes, both rapid meteorological and source strength changes are likely.

Ceiling Height

With relatively low ceilings, those formed essentially by stratus clouds, the base of the clouds is related to the height of the mixing layer and thus provides a useful measure of pollution levels to be expected. Intermediate or high cloudiness, for example cloudiness over 7000 feet, also influences SO₂ concentration levels. These clouds affect the intensity of solar radiation and consequently the magnitude of convection in the lower layer which strongly influences the atmospheric diffusion rates. The ceiling height is, therefore, a related variable.

Time of Day

The time of day is important for several reasons. First, a maximum occurs in the early morning hours, primarily because the source strengths are increased during these hours. When people arise in the morning, they turn their thermostats up or put several shovels of coal into the furnace. A secondary maximum occurs shortly before sunset, due to increased use of sulfur-bearing fuel and to a decrease in the diffusive capacity of the atmosphere. Since there are substantial differences in concentration between the maximum and minimum values during a given day, the time of day must be seriously considered.

SELECTION OF VARIABLES

The relationships between SO₂ concentration and the meteorological variables are not linear, and some

are monotonic while others are not. Wind direction and time of day are non-monotonic. In order to treat these two variables, plots are made of SO_2 concentration vs. wind direction and SO_2 concentration vs. time of day. Examples of these charts are shown in Figures 134-137. In each of these figures, the 50th, 90th, and 95th percentile values as well as the maximum are presented. These charts and a tabulation of the data on which the charts are based were used to select time bands and wind direction bands in which the variation of SO_2 concentration was relatively small. The Tabulation Prediction Scheme was developed for the TAM Stations. The bands for time of day and wind direction selected for each of the TAM stations are presented in Table 63.

Many interesting features are brought out by these charts which may be useful in practice to forecast SO_2 concentrations. The relative positions of clean areas or pollution sources with respect to the TAM stations are indicated. In Figure 137, showing the time of day vs. SO_2 concentration for TAM 6, the usual peaks of the early morning hours as well as those of the late afternoon or early evening hours are shown in the 90th and 95th percentile curves. Note that the morning peak shows up in the 90th and 95th percentile curves, but is barely perceptible in that of the 50th percentile. This suggests that the peak is due to relatively infrequent events that can produce unusually high concentrations in the morning, possibly inversion breakup fumigations.

There is more evidence here pertinent to fumigations. In Figures 136 and 137, the highest values observed (i.e., the highest values of each MAX curve) occur at 0600, 0700, or 0800 at six of the eight TAM stations. These are the hours during which fumigations may be expected. The wind direction associated with the SO_2 peaks are those associated with the highest peaks of the MAX curves in Figures 136 and 137.

TAM 7 is a good example. The highest SO_2 value occurred at 0700 with a wind from 195 degrees. The joint occurrence of a very high SO_2 value at a morning hour from the direction of known high stack sources in the industrial corridor is consistent with the inversion breakup fumigation process. This example gives just a hint about how SO_2 percentile plots can be used to investigate meteorological events.

Also of interest is the early afternoon peak in the TAM 6 maximum value. An examination of Figure 135, showing wind direction vs. SO_2 concentration for TAM 6, shows that the peak occurred with an east wind off the lake. (Figure 135 shows an actual case of high SO_2 concentration at TAM 6 during a lake breeze.) Strong SO_2 sources are located between

TAM 6 and the Lake Michigan shore. The joint occurrence of time and direction make it very likely that a lake breeze causes this high SO_2 value. Additional interesting relationships may be observed from an examination of the other charts.

The interquartile range is a measure of the dispersion of the measurements for each combination of meteorological measurements. The amount of noise or uncertainty in the prediction is shown by the magnitude of the interquartile range. Similarly, the difference between the 95th and 75th percentile values represents the amount of skewness present. Since the distributions approximate the log normal function, one would expect appreciable skewness.

Before a final choice is made of the meteorological variables used in the Tabulation Prediction Scheme, each must be examined. This may be done in a number of ways, one of which is to plot the percentile values of SO_2 concentration vs. each meteorological variable and examine the relationships. The 50, 90, and 95 percentile and maximum curves could be plotted for this purpose in the same format as shown in Figures 134 and 135.

Where a network of stations is available, such as exists in New York City, Los Angeles, Washington, or Chicago, the receptor-oriented techniques may be applied to each of the stations to obtain isopleths of concentrations similar to that obtained in the source-oriented model.

CONSTRUCTION OF THE TABLES

Meteorological variables recommended for the construction of a Tabulation Prediction Scheme are (1) wind direction, (2) ceiling height, (3) wind speed, (4) temperature, and (5) hour of the day. The relevance of each of these variables has been given above.

The importance of atmospheric stability has been noted, but such data are usually unavailable. A substitute is provided by the choice of the variables: ceiling height, hour of the day, and wind speed. Combinations of these are closely related to stability. For example, during high winds, e.g., near 15 knots, the stability is usually neutral. This is true during the day or night. During unlimited ceilings with light winds, an inversion is highly likely at night, but unstable conditions are to be expected during the day.

Class intervals for the variables, ceiling height, wind speed and temperature are shown in Table 64. As a first step the data are stratified by season and by the presence or absence of precipitation. An intermediate tabulation is prepared in which wind direction and hour of day are listed as Band I, Band II, and

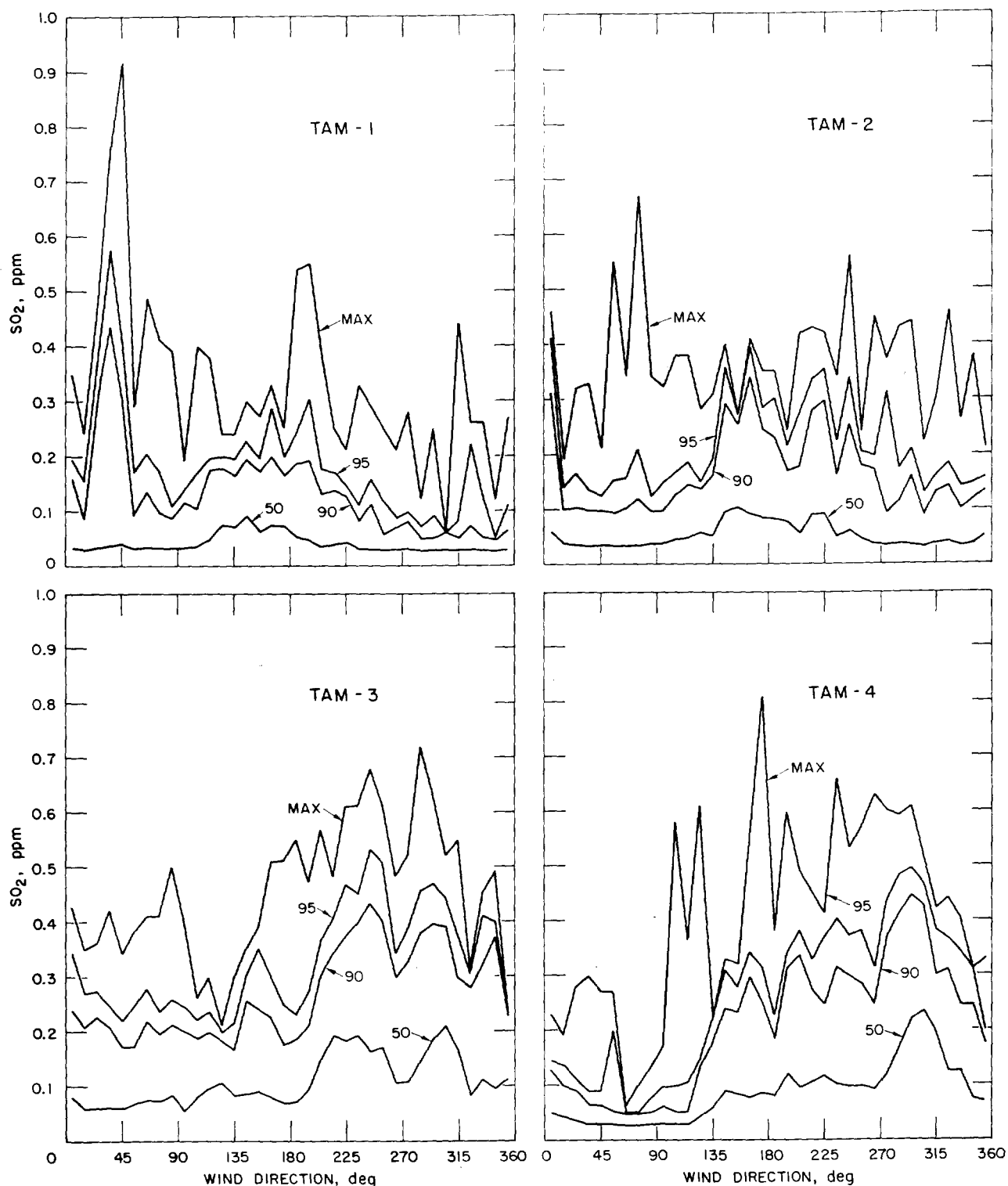


FIG. 134.—Selected percentile curves relating SO₂ concentrations to wind direction at TAM Stations 1-4

so on as shown in Table 63. The final form of the tabulation should substitute actual values of wind direction and hour in numerical order as shown in Table 65. For example, for TAM station 1, the wind

directions 5-15, 55-105, 205-355 are under category I. The percentile distribution corresponding to category I in combination with the appropriate variables will be presented for wind direction in each

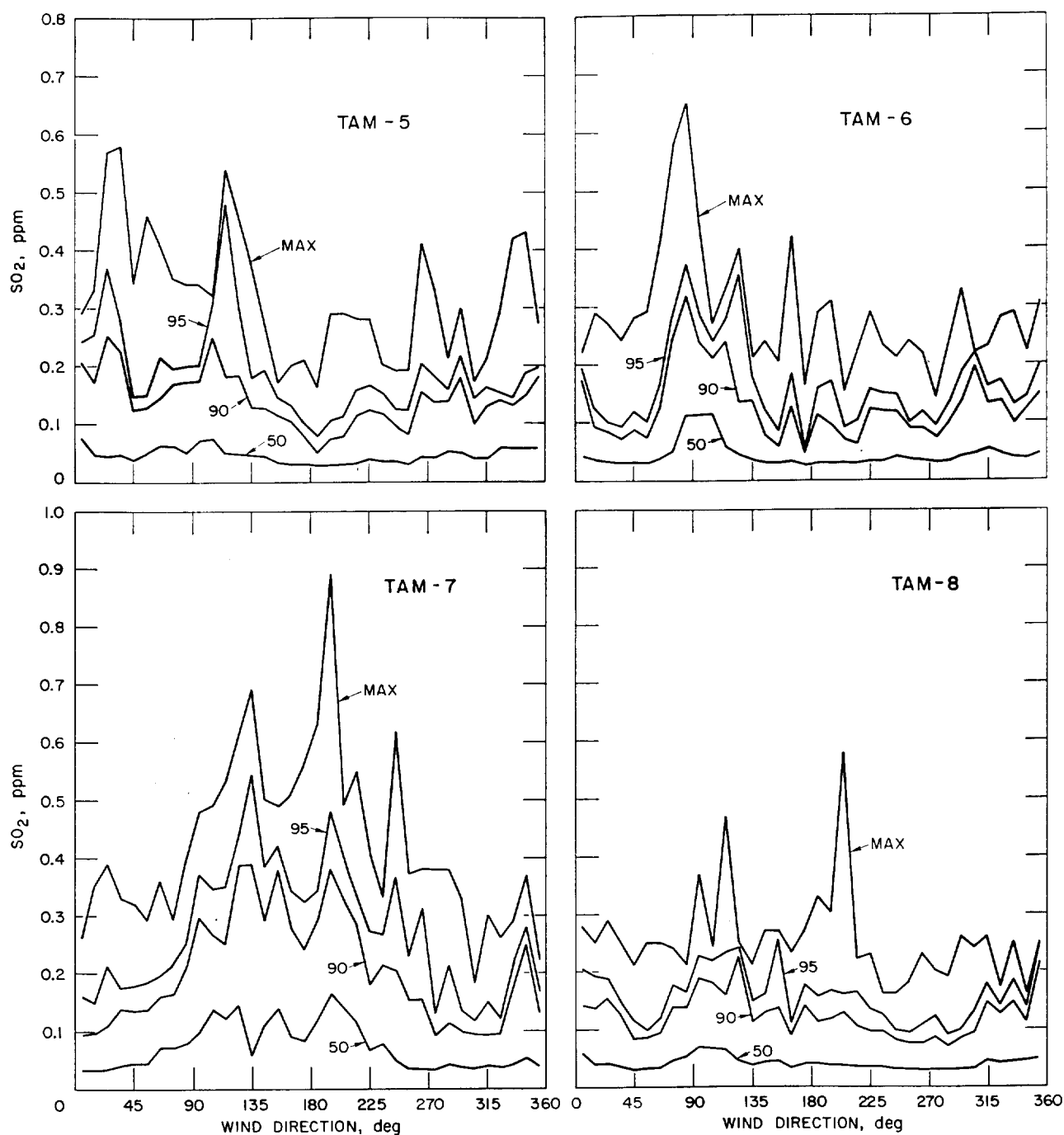


FIG. 135.—Selected percentile curves relating SO_2 concentrations to wind direction at TAM Stations 5-8

of these ranges. Thus, if the wind directions are listed for every ten degrees, the percentile values will be repeated as often as necessary.

The order of the variables in the columns should be arranged so that the last column represents the variable which influences the SO_2 concentrations the least and the first column the most. Further, wind speed and temperature should be presented in de-

scending order since lowest values of each correspond to highest SO_2 concentration. (Table 62 is a sample of an intermediate provisional table where the temperature is shown in increasing order. In the final tables temperatures will appear in decreasing order.) Ideally, the tabular arrangement should show a steady increase in values of SO_2 concentration as one reads down from the top of the table.

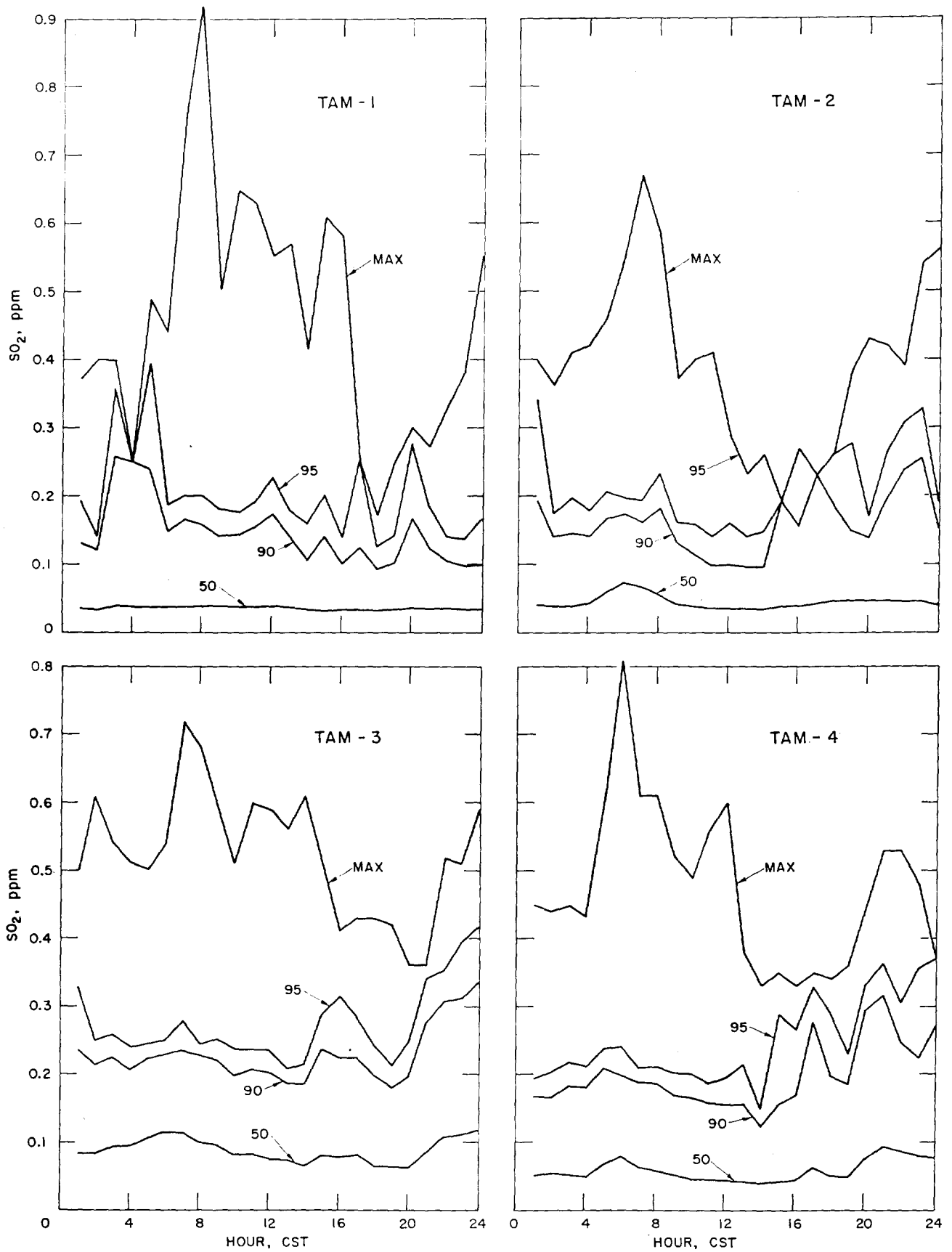


FIG. 136.—Selected percentile curves relating SO₂ concentration with time at TAM Stations 1-4

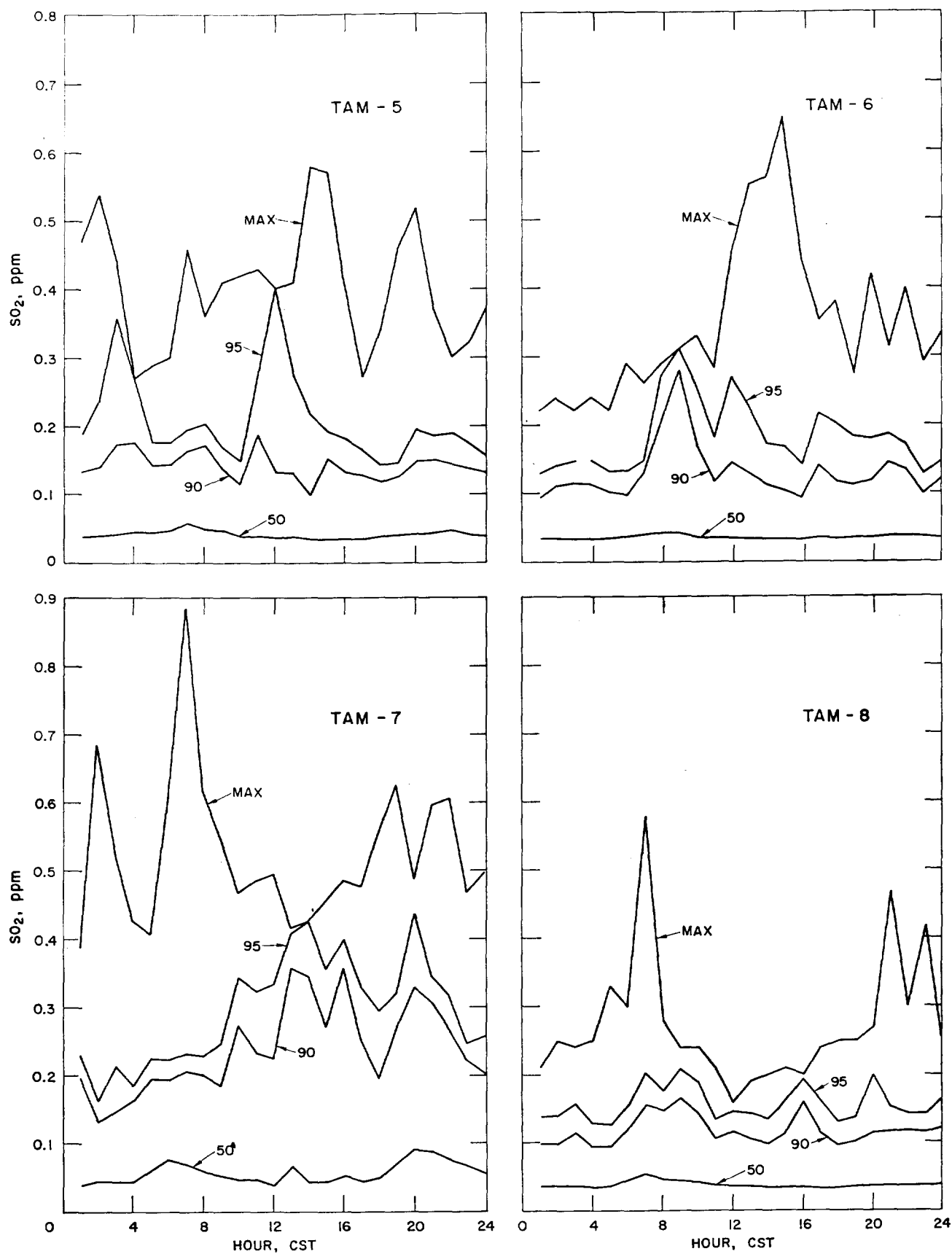


FIG. 137.—Selected percentile curves relating SO_2 concentration with time at TAM Stations 5-8

TABLE 63. STRATIFICATION TABULATION PREDICTION TECHNIQUE BANDS FOR WIND DIRECTION AND HOUR OF DAY

TAM station number	Wind direction, degrees			Hour (CST)		
	I	II	III	I	II	III
1	55-105 205-355 5-15	115-195	25-45	1-2 18-24	6-17	3-5
2	15-135 275-355	145-265 5		9-14	1-8 15-24	
3	355 5-195	205-345		2-20	1 21-24	
4	5-135	145-265 335-355	275-325	1-4	5-16	17-24
5	165-205 245-255	45-95 135-155 215-235 265-355	5-45 105-125	1-3 5-6 9-10 12-24	4 7-8 11	
6	15-55 145-285 335-345	5 295-325 355	65-135	1-7 23-24	14-22	8-13
7	5-65 275-325 355	225-265 335-345	75-215	2-4	1 5-9 17-18 23-24	10-16 19-22
8	45-65 135-305	5-35 75-125 315-355		1-6 11-15 17-24	7-10 16	

APPLICATION OF TABULATION PREDICTION SCHEME TO DAILY OPERATIONS

Since the variables used in the Tabulation Prediction Scheme are wind direction, wind speed, temperature, ceiling heights, and hour of day, these are the variables (except of course the hour of day) for which forecasts are required. The forecasts should be made for each hour and the range of the group interval, e.g., a wind speed forecast over the range of 4-7 miles per hour, should correspond to the ranges in the Tabulation Prediction Scheme.

The forecast for the day should preferably be made between 0700 and 0800 so that the severity of the early morning pollution peak will be covered. Forecasts for 12 to 24 hours are reasonably routine. These forecasts may be issued every 6, 12, or 24 hours, depending on the local needs. Of course, during potential or actual severe pollution conditions, constant surveillance is necessary.

A format for recording the forecasts and the computed and observed pollution concentrations is shown

in Figure 138. This form has been in use in test operations with Murray and Trettel, Inc. providing the hourly forecasts and the Argonne National Laboratory and the City of Chicago Department of Air Pollution Control adapting the forecasts for operational use.

More variables are indicated than were actually used because of the developmental nature of this work; but a municipality may use this form as a guide in tailoring one to its own needs. The symbol Prb stands for the probability estimate of the forecast verification.

After the forecast values are received, a clerk may use the 50 percentile entry of the Tabulation Prediction Scheme Tables to enter the predicted SO₂ concentration or those of another pollutant of interest and present these to the meteorologist.

Ordinarily, municipal air pollution control agencies will find it uneconomical to employ a complete forecasting staff. Hourly forecasts will, therefore, be obtained from an organization like the U. S. Weather Bureau or a private meteorological firm. The services of one or two meteorologists employed by the air pollution control agency would be used to interpret the forecasts of both the weather and pollutant concentration for action by appropriate officials.

The municipal meteorologist would determine whether an air pollution incident was probable within the forecast period. His access to the latest upper air and surface weather charts enables him to judge whether (1) a land-sea breeze will develop, (2) a thunderstorm is likely, (3) precipitation or fog will appear, (4) a frontal system will pass, or (5)

TABLE 64. UNITS AND GROUP INTERVALS FOR VARIABLES USED IN THE TABULATION PREDICTION SCHEME

1. Wind speed	Unit: miles per hour Group interval: 0-3, 4-7, 8-12, 13-18, 19-24, >24
2. Wind direction	Unit: degrees Group interval: 10-degree grouping: 5-14, 15-24, 25-35, etc., or according to band widths of Table 63.
3. Temperature	Unit: °F Group interval: -20--11, -10--1, 0-9, 10-19, 20-29, 30-39, 40-49, 50-59, 60-69, 70-79, 80-89, 90-99
4. Ceiling height	Unit: feet Group interval: 0-999, 1000-2499, 2500-6999, ≥7000
5. Hour of day	Unit: one hour Group interval: one hour intervals centered on the hour; or according to band width of Table 63.

TABLE 65. TABULATION PREDICTION TECHNIQUE

Wind direction, degrees	Hour of day (CST)	Wind speed, mph	Temperature, °F	Stability, °C/100 m	Percentile values of SO ₂ concentrations, ppm										No. of cases
					Min.	10	25	50	75	90	95	98	99	Max.	
300-350	08-11	4-7	20-29	>2	0.05	0.10	0.12	0.15	0.20	0.30	0.35	0.40	0.50	0.70	92
300-350	08-11	4-7	20-29	1.9-0.0	0.05	0.08	0.10	0.11	0.12	0.15	0.15	0.20	0.25	0.35	81
300-350	08-11	4-7	10-19	>2	0.10	0.12	0.15	0.20	0.35	0.50	0.85	1.00	1.20	1.50	85
300-350	08-11	4-7	10-19	1.9-0.0	0.08	0.10	0.13	0.15	0.30	0.40	0.70	0.90	1.10	1.20	90

Season: December, January, February. (Data taken in 1966 and 1967.)

Precipitation: No.

TAM Station No. 4.

a lowering of the mixing depth is probable because of pronounced subsidence. Any one of the above or similar phenomena markedly affects the pollution potential. The municipal meteorologist may issue forecasts such as a 24-hour air pollution index for the entire urban complex or the maximum levels for selected areas where special forecasts are warranted.

With the availability of on-line computer facilities, some functions may be facilitated. For example, the hourly forecast may be entered into the computer and a printout received in proper format of the 50 percentile values based on the Tabulation Prediction Scheme Tables stored on a disc or tape memory. It is possible for the computer to print out maps of the area with plotted values of pollutants and weather variables. This is being done at the Argonne National Laboratory. The printout of maps with machine-drawn isopleths of variables has been accomplished by other meteorological organizations. Although the use of automatic machine-drawn maps appears to be a sophisticated operation, the availability of the computers and necessary software makes such maps quite feasible.

The Tabulation Prediction Scheme is a new development in air pollution forecasting. There are a number of areas in which improvement is possible, but the improvements must be based on the individual needs. For example, the municipal meteorologist should conduct investigations to determine the conditions under which high values of pollutant concentrations occur, e.g., such as are found in the 90 to 100 percentile range. Case studies, especially of high pollution episodes, should be made. The results of these may well be applied to optimize the use of the Tabulation Prediction Scheme. Further, an investigation involving the persistence of high pollution levels should be

made in each city desiring a high caliber pollution warning capability. The percentile value of the SO₂ concentration at the beginning of the forecast period may be a good indicator of the probability of the concentration values exceeding the 50 percentile value.

ADVANTAGES AND DISADVANTAGES OF THE TABULATION PREDICTION SCHEME

Some of the advantages are

1. It is easy to use and does not require on-line, real-time access to a computer.
2. It provides for rapid prediction of pollution concentration.
3. It provides the entire percentile distribution of pollutant concentrations to allow a forecaster to "fine tune" his predictions on the basis of synoptic situations.
4. It takes into account nonlinearities in the relationship between meteorological variables and pollution concentrations.
5. It is an effective method for analyzing and displaying air quality and relevant meteorological data.

Disadvantages of the method are

1. It is necessary to use a large digital computer to construct the tables.
2. At least several years of historical data are necessary.
3. Changes in the emission sources degrade the tables, which must, therefore, be updated every one or two years.

GENERAL APPLICABILITY OF THE TABULATION PREDICTION TECHNIQUE

For general application, it appears that there is less work in applying the Tabulation Prediction Scheme

DATE: _____
 TIME: _____
 GIVEN BY: _____
 RECEIVED BY: _____

CONTROL POINT:
 MIDWAY AIRPORT:

HOUR	1. SURFACE WIND DIRECTION		2. SURFACE WIND SPEED		3. MIXING HEIGHT INDEX		4. DRY BULB TEMPERATURE (SURFACE)		5. CEILING BELOW 7,000		6. RELATIVE HUMIDITY		7. CLOUD COVER		8. CEILING HEIGHT		9. PRECIPITATION (OVER A TRACE)		10. VISIBILITY		11.
	Prb.	(MPR)	Prb.	(MKT)	Prb.	(°F)	Prb.	(YES/NO)	Prb.	(%)	Prb.	Prb.	(ft.)	Prb.	(YES/NO)	Prb.	(mi.)	Prb.			
NOON																					
1 pm																					
2 pm																					
3 pm																					
4 pm																					
5 pm																					
6 pm																					
7 pm																					
8 pm																					
9 pm																					
10 pm																					
11 pm																					
MIDNIGHT																					
1 am																					
2 am																					
3 am																					
4 am																					
5 am																					
6 am																					
7 am																					
8 am																					
9 am																					
10 am																					
11 am																					

HOUR	TAM SO ₂ PREDICTIONS AND ACTUAL READINGS - PROBABILITIES ARE FOR SO ₂ > 0.1															
	1		2		3		4		5		6		7		8	
	PROB.	ACT.	PROB.	ACT.	PROB.	ACT.	PROB.	ACT.	PROB.	ACT.	PROB.	ACT.	PROB.	ACT.	PROB.	ACT.
NOON																
1 pm																
2 pm																
3 pm																
4 pm																
5 pm																
6 pm																
7 pm																
8 pm																
9 pm																
10 pm																
11 pm																
MIDNIGHT																
1 am																
2 am																
3 am																
4 am																
5 am																
6 am																
7 am																
8 am																
9 am																
10 am																
11 am																

Fig. 138.—Format for recording the computed and observed pollution concentrations and the forecast weather elements influencing these.

than in developing a source-oriented model. In a source-oriented model, it is necessary to calibrate the urban terrain by determining the variation of σ_y and σ_z with distance for a number of direction bands. Surface roughness affects these relationships. In addition, it is essential to make a detailed source inventory. With a receptor-oriented model, based on a Tabulation Prediction Scheme, a detailed source inventory is not necessary. However, one must know whether or not changes are occurring.

It appears possible to develop a Tabulation Prediction Scheme which would have the advantages of both the source-oriented and receptor-oriented models. By maintaining surveillance over the addition or subtraction of sources within the urban area, a modification to the tabulation may be made just as the new sources come on line. In addition, by applying significance tests to these tabulations on a monthly basis, it appears likely that the addition or subtraction of new sources in the area could be detected and the tables updated accordingly. In fact by triangulation techniques (using two or more stations) the tabulation technique can be used to delineate the area which shows a change in source strength. Thus, a skillful use of the Tabulation Prediction Technique may be used to monitor the distribution of sources.

The Tabulation Prediction Scheme is a technique which cannot be constructed blindly; it must be a dynamic system in which changes are continuously made. Similarly, a source-oriented model must be a dynamic system sensitive to the addition or subtraction of sources. By applying the diffusion algorithms of the source-oriented type, the receptor-oriented tabulation prediction may be updated frequently. Of course, each station of the network would have to be updated. Such a hybrid technique may provide a superior system for forecasting air pollution levels based on meteorological variables.

REFERENCE

1. Roberts, J. J., Reactor Engineering Division, Argonne National Laboratory. Private communication.

RADIATION PHYSICS

FURTHER STUDIES ON FLUORESCENCE POLARIZATION

W. R. Anderson and I. B. Berlman

Polarization studies of several compounds in solution have been made and the results are reported. For 1,3,6,8-tetra-phenyl pyrene, the polarization values start to become negative at about 3100 Å in agreement with other findings that the transition moment for absorption in this region is in a different direction from that of fluorescence. In the case of substituted binaphthyls, an absorption band associated with a weak transition can be located at 3300 Å.

INTRODUCTION

In a previous report⁽¹⁾ the reasons were given for interest in these studies, the polarimeter used was described, the theory involved was outlined, technical difficulties were discussed, and information obtained to that point was tabulated. The reasons for undertaking the studies are, in summary, the following:

1. To obtain information on the electronic transitions; more specifically, to look for hidden transitions; and
2. To study the effect of intrinsic viscosity on the degree of polarization.

The principle involved in the first of these is as follows: In general, the absorption band associated with a given electronic transition overlaps that of others. Because of this, a weak and, therefore, seemingly narrow band within the span of a strong band may be obscured in an ordinary absorbance scan, but may be disclosed if changes in the degree of polarization of the fluorescent emission are noted during the scan, provided a 90° angular shift between absorbing and emitting oscillators exists for one, but not both, of the transitions. Suppose that for a particular molecule the electronic transition representing the change to the first excited level happens to be $^1A \rightarrow ^1L_a$ ⁽²⁾ and that to the second excited level $^1A \rightarrow ^1L_b$. The states 1L_a and 1L_b represent oscillators at 90° to each other. Fluorescence takes place from the lower of the two and is represented by $^1L_a \rightarrow ^1A$; therefore, the molecules originally excited to the 1L_b state undergo a 90° oscillator shift in dropping to the 1L_a state through internal conversion before emission.

TABLE 66. POLARIZATION IN HEAVY MINERAL OIL AT $-4 \pm 1^\circ\text{C}$

Compound	Band edge, $m\mu$	Upper line: $\lambda, m\mu$ Lower line: polarization (P), %							
		3. <i>p</i> -Bis[2-(5-phenyloxazolyl)]benzene ("POPOP")	395	375 +43	360 +43	340 +43	320 +42	321 +26	300 +11
6. 4,4'-Di(undecyloxy ^(a) -1)-1,1'-binaphthyl	360	350 +41	240 +38	330 +25	320 +33	310 +33	300 +32	290 +32 ^(b)	
7. 9,12-Di(<i>n</i> -octadecyloxy)benz[e]-acephenanthrylene	440	410 +41	395 +32	375 +32	355 +28	340 +24	320 +13	300 +11	290 +17 ^(b)
8. Diphenyl stilbene	390	370 +45	340 +45	300 +43					
9. Tetraphenyl ethylene	380	350 +41	330 +38	310 +35	300 +31	290 +20 ^(b)			
10. 1,8-Diphenyl-1,3,5,7-octatetraene	430	400 +41	378 +40	360 +40	345 +41	330 +38	300 +26		
11. Trans-1-(4-biphenyl)-2-(1-naphthyl)-ethylene	390	380 +44	365 +45	350 +44	335 +44	320 +43	305 +40		
12. Trans-1-(4-biphenyl)-2-phenyl-ethylene	365	350 +42	335 +43	325 +43	305 +42	290 +39 ^(b)			
13. 1,3,6,8-Tetraphenylpyrene	425	400 +42	380 +41	370 +40	350 +35	330 +28	320 +18	310 -15	300 -19

^(a) or butyloxy or octyloxy.

^(b) at 290 $m\mu$, absorption by the solvent is appreciable ($A = 0.3$). Whether this affects the result is conjectural.

Theory shows that if no depolarization takes place between absorption and emission, and if there is no mixing of types, the degree of polarization P of emission is (a) +50% when absorbing and emitting oscillators are parallel, and (b) $-33\frac{1}{3}\%$ when perpendicular to each other. If there is overlap, the result will be somewhere between the two extremes. Depolarization (the result of rotation during the lifetime of the excited state), of course, reduces the (absolute) value of the polarization, but its effect is easily distinguished from that being discussed. Depolarization affects the *whole* absorption spectrum, whereas the effect being discussed is a function of wavelength.

A principal difficulty encountered originally, especially as it affected the viscosity-effect study, was temperature instability. Through modifications of the apparatus, improved, though not completely satisfactory, temperature control has been obtained. A hollow jacket, thermally insulated on the outside, was added surrounding the cell chamber. The jacket, filled with an antifreeze solution, has in it also copper tubing coiled around the chamber. The cold nitrogen gas, which originally was allowed to

flow directly into the chamber, now flows first through the copper tubing in the jacket before entering the chamber, thus tending to bring the surroundings of the chamber into temperature equilibrium with the gas in the chamber. Rapid temperature fluctuations in the chamber have been eliminated, but the aim of holding the temperature invariant has not been realized. It was thought that creation of slush in the jacket would assure constancy; however, it was found that even then there is a temperature gradient in the jacket. The possibility of using more effective insulation is being investigated.

A distinct improvement has been made in connection with the solvent used. A heavier mineral oil has been obtained (Fisher Paraffin Oil #0-120), of Saybolt 335/350, and an unexpected bonus has been its transparency. Because of the improvement in the latter, the range in which meaningful results can be obtained has been extended downwards to about 290 $m\mu$. The absorbance of this oil in the 1-cm cell does not reach 1.0 until 285 $m\mu$. The increased viscosity has lessened the depolarization so that higher values of polarization are now realized. The limita-

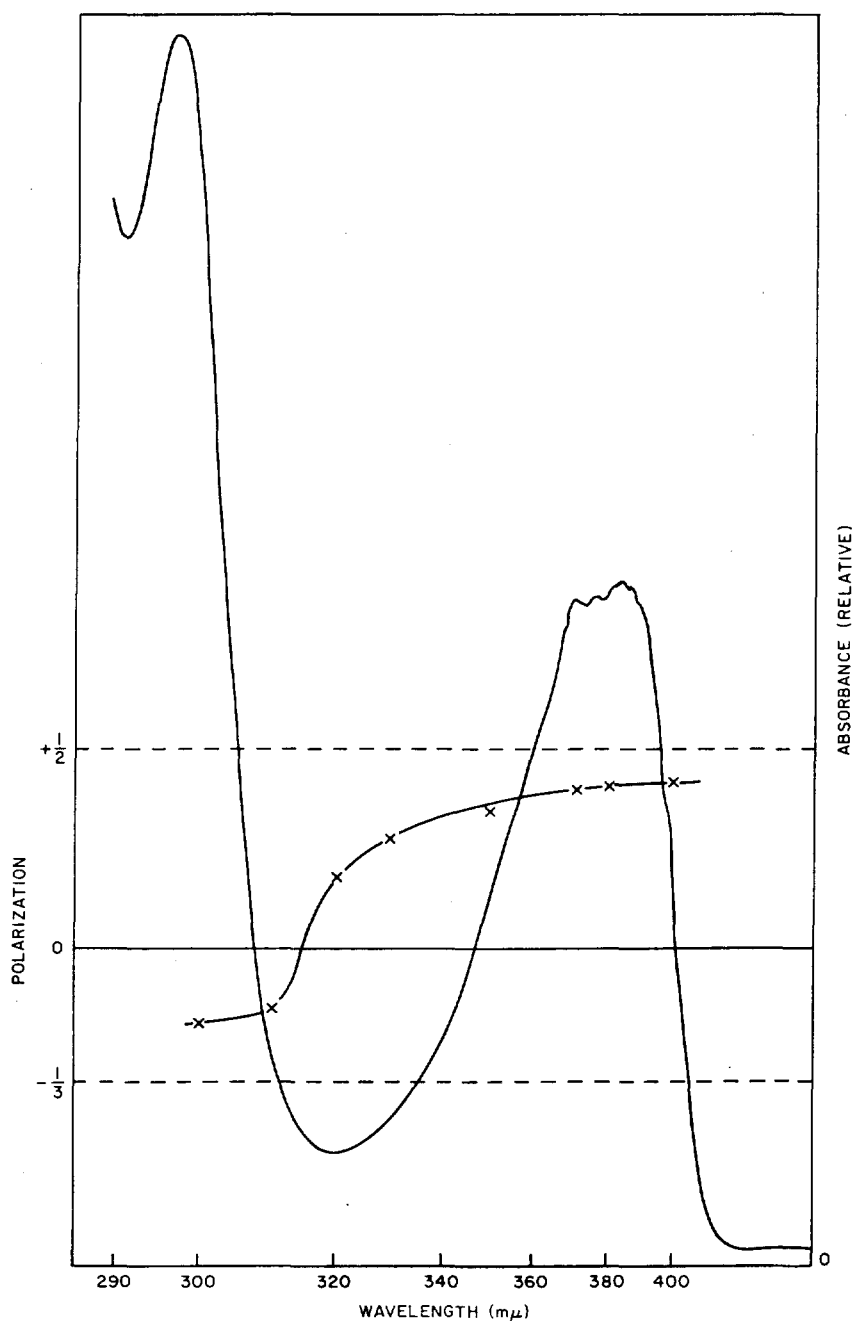


FIG. 139.—Absorbance of 1,3,6,8-tetraphenyl pyrene and corresponding polarization of emission

tion at the long-wavelength end of the range is that of the grating, 410 $m\mu$.

SEARCH FOR HIDDEN LEVELS

Several additional compounds have been studied; also, some of those studied previously have been re-studied for more complete information. As pointed out previously,⁽¹⁾ in general it has been found not worth while to study a compound in a liquid medium

unless the compound has a very short fluorescence decay time of the order of one nanosecond) because otherwise depolarization reduces the values to the point where trends are obscured. Table 66 gives the additional results to date. The long-wavelength edge of the first absorption band is given to provide orientation for the reader. Also, to aid in the visualization of the results, curves are given in Figure 139 of absorption and corresponding polarization of emission

for one of the compounds. Compounds 3, 6, and 7 were studied previously, but have been restudied in order to obtain more complete and accurate data. The numbers used to designate these correspond with those used in the previous report. Numbers 8 through 13 are additional compounds. Except as indicated below, the wavelengths which could be studied are in the first absorption band of the compound.

Some experimental details are as follows: To achieve maximum spectral purity, monochromator slits were kept very narrow, 0.9 and 0.5 mm, respectively, for entrance and exit slits; this corresponds to a half-intensity band width of only 1.6 $m\mu$. In all cases signals were sufficiently large to permit use of such narrow slits. No set rule was followed concerning the number of times a measurement was to be repeated; however, enough repetition was carried out to make a result convincing, especially where it seemed crucial. In general, because of the great variations in absorbance of a solution at the different wavelengths, more than one concentration of solution was needed in covering each spectrum.

In the first report, mention was made that (for the particular geometry of our apparatus) calculations showed that maximum signal would result when the absorbance is 0.9. However, it was found that solutions somewhat more dilute than this gave stronger signals. In the cell chamber is a reflector (inadvertently omitted from the polarimeter diagram of the first report) which sends the incident beam back through the cell. Evidently this is more effective than was assumed.

A test was performed to learn something of the magnitude of the signal, produced by incident light scattered in the cell, reaching the photomultiplier after attenuation by the appropriate fluorescent-beam filter. The polarimeter was operated with the solvent alone in the cell (fluorescent solute missing) and signals recorded for each filter used at each incident-light wavelength used. Because of xenon-source instability, mentioned in the first report, readings taken at different times have been found to vary considerably; however, if the values obtained in this test were to be used as signal corrections, the effect on P (expressed as percent) would be to change it (negatively) by only 0.1 in 70% of the instances and by no more than 1 in any instance. Considering this and other possibilities for error, the total uncertainty in P is perhaps no greater than 2 [that is, $P = 41\%$ means $P = (41 \pm 2)\%$, etc].

Certain features of the results in Table 66 are of particular interest. First, in every instance, the polarization drops as one moves from the long- toward the

short-wavelength end of the first absorption band. Two possible explanations suggest themselves, either or both of which could be involved in a given instance. (a) Broadly speaking, the shorter the wavelength absorbed, the higher the vibrational state to which the molecule is raised and the greater the excitation energy involved in the instantaneous (10^{-12} second) vibrational-relaxation process which follows. If the molecules having had the greater excitation energy now end up with greater *rotational* energy, which they retain during the period preceding emission, then greater depolarization would be observed for them. (b) There may be a region of overlap between the first and second absorption bands, and if the second band is of the opposite type (as regards 90° shift or no shift) the two opposite polarizations will tend to cancel each other. For compound 13 (see also Figure 139), it was possible to extend the measurements into the second absorption band, and explanation (b) seems to be confirmed, although (a) may be involved as well. Second, hidden transitions seem likely or possible in two of the compounds—in compound 6 at about 330 $m\mu$ and in compound 7 at about 320 $m\mu$.

It might be added at this point that both positive and negative polarizations were observed, that the most positive and most negative values (+45 and -19%, respectively) were reasonably close to the theoretical limits (+50 and -33½%, respectively), and that, therefore, the observations attest to the reliability of the apparatus.

INTRINSIC VISCOSITY STUDIES

Tests in which depolarizations of the three binaphthyl derivatives⁽¹⁾ are compared are continuing, but as yet, because of our inability to secure sufficiently precise and reproducible results, no conclusion has been reached as to whether there are or are not differences among them. Tentatively, one might conclude that if there are effects, they are of small magnitude. Temperature control is no longer a major problem; other factors appear to interfere and need to be investigated. A slight change in the position of the cell or in the level of the liquid in it may affect the results enough to obscure the effect. Also, certain observations have suggested that the compounds used may undergo a photochemical reaction when exposed to the UV radiation.

REFERENCES

1. Anderson, W. R., Berlan, I. B., and Wirth, H. O. Argonne National Laboratory Radiological Physics Division Annual Report, July 1966–June 1967. ANL 7360, pp. 1–4.
2. Platt, J. R. *J. Chem. Phys.* **17**, 484–495 (1949).

ON THE FLUORESCENCE CHARACTERISTICS OF THE *p*-OLIGOPHENYLENES AND THEIR SUBSTITUTED ANALOGS

I. B. Berlman and O. J. Steingraber

The *p*-oligophenylenes have very desirable fluorescence characteristics, such as high quantum yields and short decay times, that make them very useful as scintillators. A systematic investigation has been made of the fluorescence characteristics of variously substituted and bridged compounds with the hope of understanding better the relationship between molecular structure and these characteristics. When large alkyl chains are employed as substituents to enhance the solubility of a compound, it is important that these substituents be positioned in the proper place. When alkyl substituents are placed on the *para* or *meta* positions of *terminal* rings, the effect on the fluorescence characteristics is minimal; but if the substituents are placed on other positions, the characteristics are adversely affected by steric crowding. Moreover, an alkyloxy group substituted on the *para* position will enhance the dipole moment of the ground and first excited state, as well as the molar extinction coefficient.

INTRODUCTION

In a previous publication⁽¹⁾ it was shown that the *p*-oligophenylenes (see Table 67) are a most useful set of compounds possessing very fast fluorescence decay times. It was reported that as the number of phenyl rings in the basic chromophor was increased, the molar extinction coefficient ϵ was increased, the natural fluorescence lifetime decreased, and both the absorption and fluorescence spectra shifted toward longer wavelengths. An experimental problem that arises when the molecular length is increased is that the solubility of these compounds in aromatic solvents is drastically decreased. Wirth, et al.⁽²⁾ have demonstrated that by adding large alkyl chains to the *p*-oligophenylenes, their solubility is dramatically enhanced. For example, the solubility of *p*-quaterphenyl in toluene at room temperature is about 0.1 g/l, whereas that of tetramethyl-*p*-quaterphenyl (VII) is over 500 g/l. Substituents not only change the solubility of a compound, but they may also interfere with the planarity of the chromophor or affect its dipole moment in either the ground state or first excited state or both. The effect of various types of substituents, their number, and positions on the chromophor on the fluorescence characteristics have been systematically investigated; the data are tabulated in Table 67 and some of the spectra are shown in Figures 140-158.

The procedures employed in measuring the absorption and fluorescence spectra, the fluorescence decay time, natural lifetime, and quantum yield, Stokes loss, and the full width at reciprocal epsilon

(FWRE) of the maximum value of the spectra have been explained elsewhere.^(3, 4) Compound IV (Table 67) was kindly sent to us by Prof. Dr. W. Ried* and the remaining compounds except for I and V were generously given to us by Dr. H. O. Wirth.†

RESULTS

Unsubstituted *p*-oligophenylenes such as *p*-terphenyl (I) and *p*-quaterphenyl (V)⁽⁵⁾ and some of the substituted compounds such as 3,3'-dimethyl-*p*-terphenyl (II) display band structure in their fluorescence spectra but not in their absorption spectra as shown in Figure 140. It is believed that the absorption curve is structureless because a planar configuration in the ground state is impeded by steric crowding. In the excited state the essential bonds, those bonds joining adjacent phenyl rings, acquire some double bond character, thus becoming stronger and more effective in forcing the phenyl rings into a more planar configuration. Supporting evidence for the above contentions may be found in the observation that the values of the FWRE of the fluorescence spectra are much less than those of the absorption spectra (Table 67). As discussed below, analogous compounds with substituents that interfere with the planarity of the chromophor do not have fluorescence spectra with structure.

It has been known for some time⁽²⁾ that the maximum value of the molar extinction coefficient ϵ_{\max} of the *p*-oligophenylenes increases monotonically with the number of phenyl rings. Since the value of the natural fluorescence lifetime τ_0 can be approximated⁽¹⁾ by integrating over the long wavelength absorption bands as follows

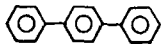

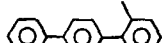

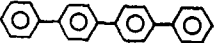
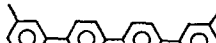
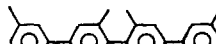



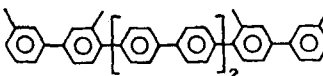
$$\frac{1}{\tau_0} = A\nu_0^2 \int \epsilon d\nu$$

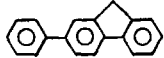
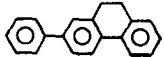
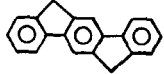
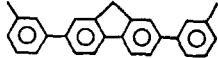
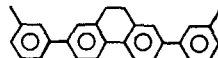
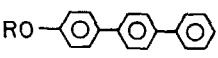
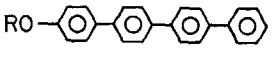
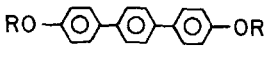
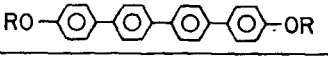
where ν_0 is the wave number of the line of mirror symmetry between the absorption and fluorescence spectra and ϵ is the molar extinction coefficient (liter mole⁻¹ cm⁻¹), it is apparent that the longer the chain of rings the shorter is the computed lifetime. It has already been pointed out⁽¹⁾ that the *p*-oligophenylenes have the added advantage of having their emission spectra at relatively short wavelengths (large ν_0 values) as compared to other conjugated

* Goethe University, Frankfurt, Germany.

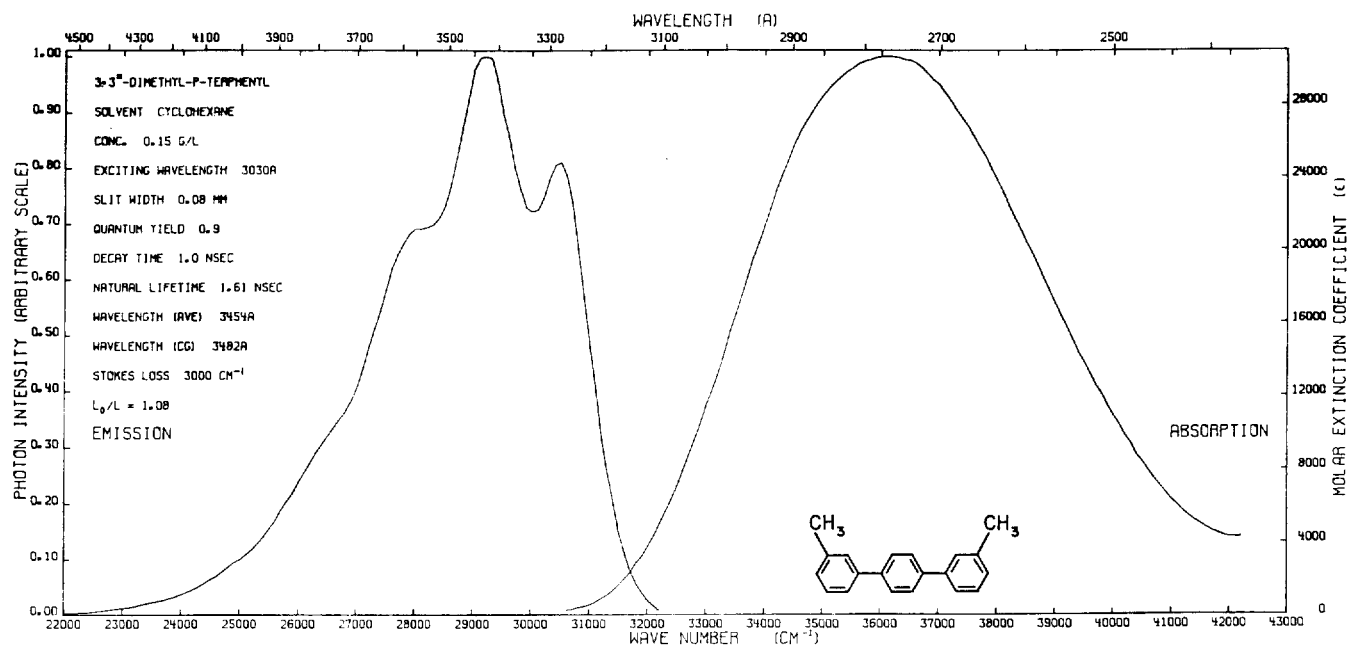
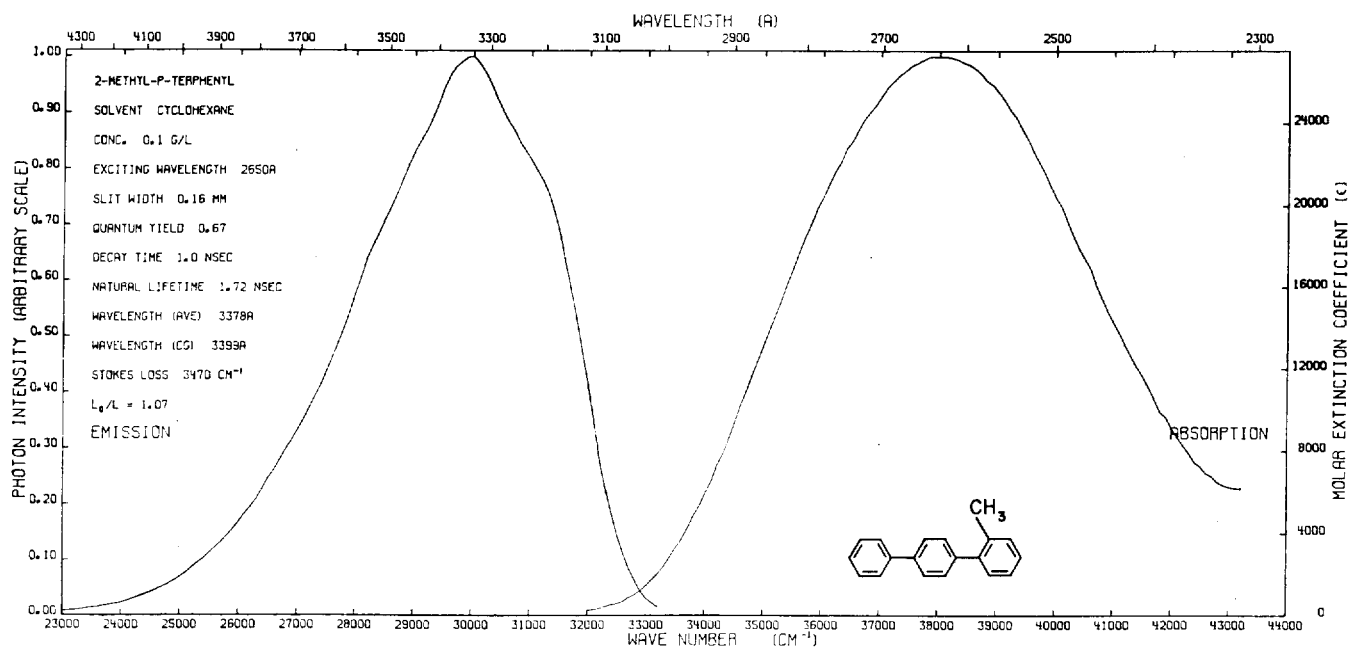
† Present address: Deutsche Advance Produktion GMBH, 6140 Marienberg, Post Bensheim, Germany.

TABLE 67. EFFECT OF SUBSTITUENTS ON FLUORESCENCE CHARACTERISTICS OF VARIOUS COMPOUNDS

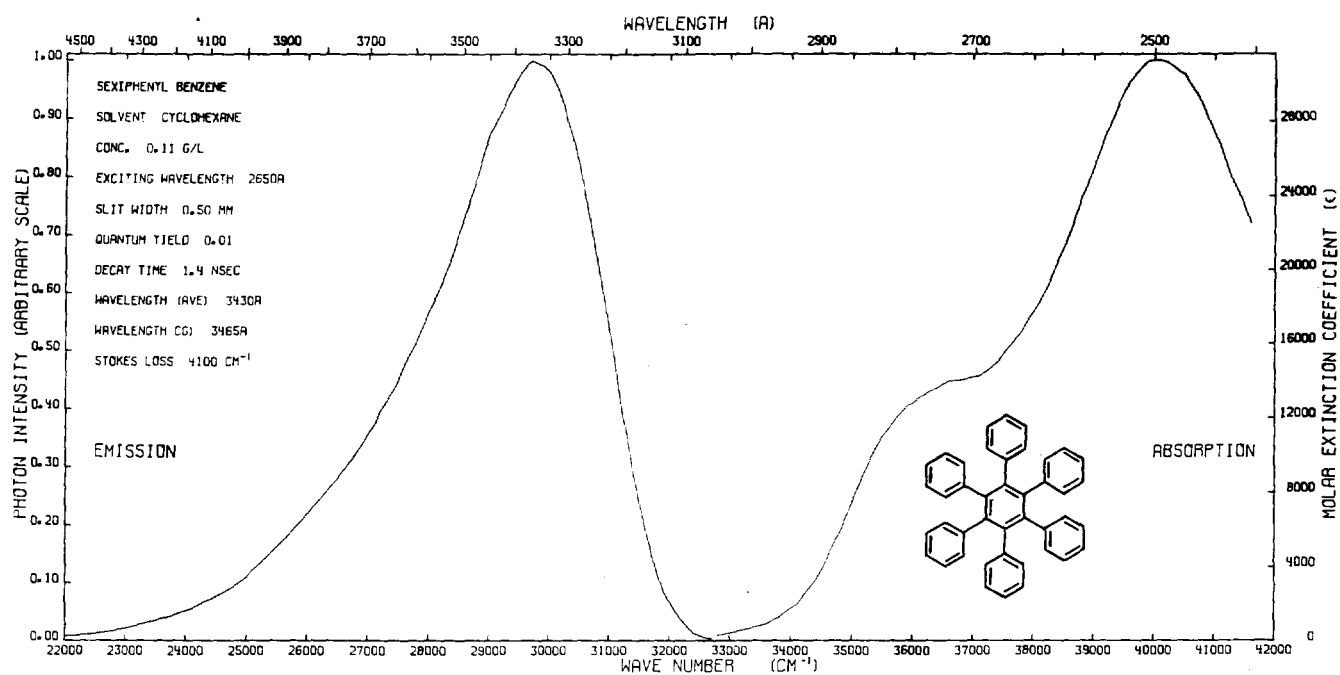
Compound	τ_0 , nsec	τ , nsec	Q.Y.	Stokes loss, cm^{-1}	FWRE		ϵ_{max} , $\text{l mole}^{-1} \text{cm}^{-1}$	λ_{avg} (Fl), \AA
					(Fl), cm^{-1}	(Abs), cm^{-1}		
 I. <i>p</i> -terphenyl	1.45	1.05	0.93	2,960	4,400	6,600	32,000	3,420
 II. 3,3'-dimethyl- <i>p</i> -terphenyl	1.61	1.0	0.9	2,980	4,400	6,900	30,600	3,455
 III. 2-methyl- <i>p</i> -terphenyl	1.72	1.0	0.67	3,470	4,500	7,200	27,400	3,380
 IV. sexiphenyl benzene		1.4	0.01	4,100	4,150			3,430
 V. <i>p</i> -quaterphenyl	1.40	0.85	0.89	2,900	4,400	6,400		3,656
 VI. dimethyl- <i>p</i> -quaterphenyl	1.39	0.85	1.0	3,000	4,350	6,650	44,000	3,700
 VII. tetramethyl- <i>p</i> -quaterphenyl	1.36	0.9	0.73	4,100	5,000	7,200	43,300	3,545
 VIII. di(3-ethylheptyl)- <i>p</i> -quinquephenyl	1.05	0.80	1.0	2,900	4,150	6,350	63,200	3,838
 IX. diethyl- <i>p</i> -quinquephenyl	1.04	0.88	0.92	3,200	4,500	6,700	57,700	3,720
 X. tetramethyl- <i>p</i> -sexiphenyl	0.95	0.76	0.94	3,350	4,500	7,100	62,500	3,775
 XI. tetramethyl- <i>p</i> -octaphenyl	0.84	0.65		3,000	4,300		76,300	3,960

	XII. 2,2'-methylene- <i>p</i> -terphenyl	(1.4)	1.5	0.91	2,200	3,800	7,100	30,500	3,430
	XIII. 2,2'-ethylene- <i>p</i> -terphenyl	(1.58)	1.4	0.84	2,500	4,100	7,000	31,700	3,515
	XIV. 2,2'-methylene, 5',6''-methylene- <i>p</i> -terphenyl		2.3	0.9	1,480	3,100		55,700	3,515
	XV. 3,3'''-dimethyl-2',2''-methylene- <i>p</i> -quaterphenyl	(1.1)	1.05	1.0	2,300	4,100	6,400	47,000	3,690
	XVI. 3,3'''-dimethyl-2',2''-ethylene- <i>p</i> -quaterphenyl	(1.30)	1.08	0.75	2,700	4,200	8,200	44,000	3,790
	XVII. 4-(3,3-dimethylbutoxy)- <i>p</i> -terphenyl	1.61	1.05	0.89	2,860	4,500	6,700	34,000	3,550
	XVIII. 4-(5-ethylhexoxy)- <i>p</i> -quaterphenyl	1.43	0.85		2,900	4,200	6,505	46,100	3,765
	XIX. 4,4''-dihexahydrofarnesoxy- <i>p</i> -terphenyl	1.48	0.95	0.97	2,780	4,100	6,650	41,000	3,600
	XX. 4,4''-di(2-butyloctoxy)- <i>p</i> -quaterphenyl	1.1	0.9	0.93	2,800	4,200	6,600	54,200	3,800

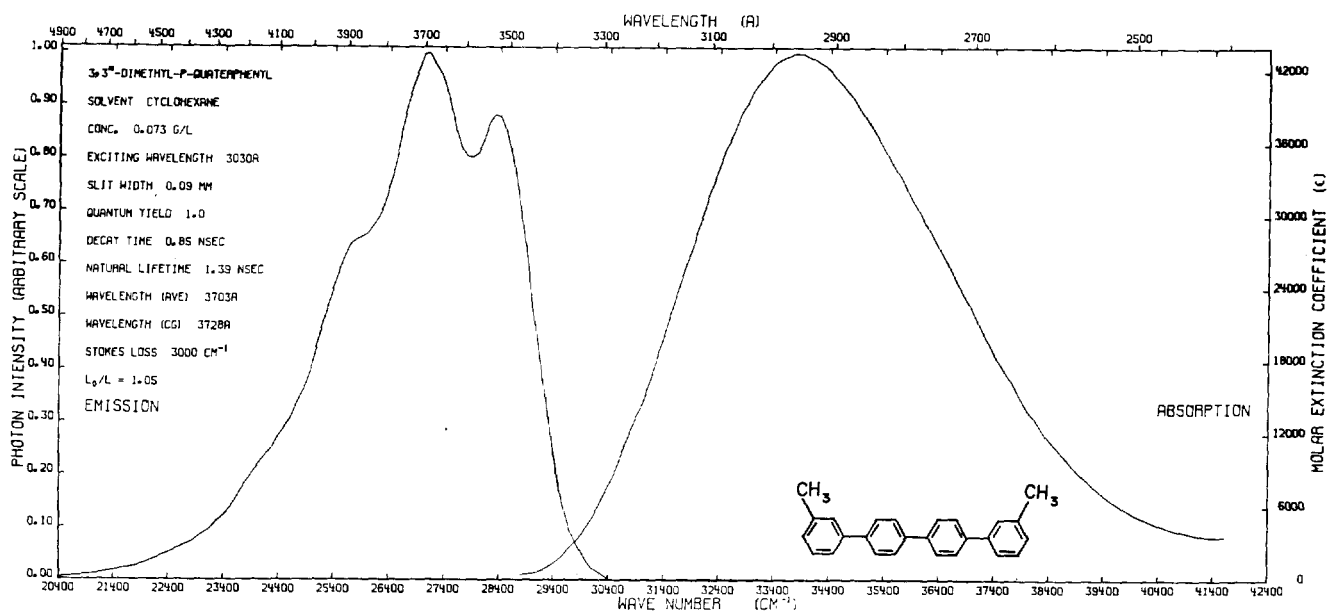
(*) Values for these compounds are for benzene solutions.

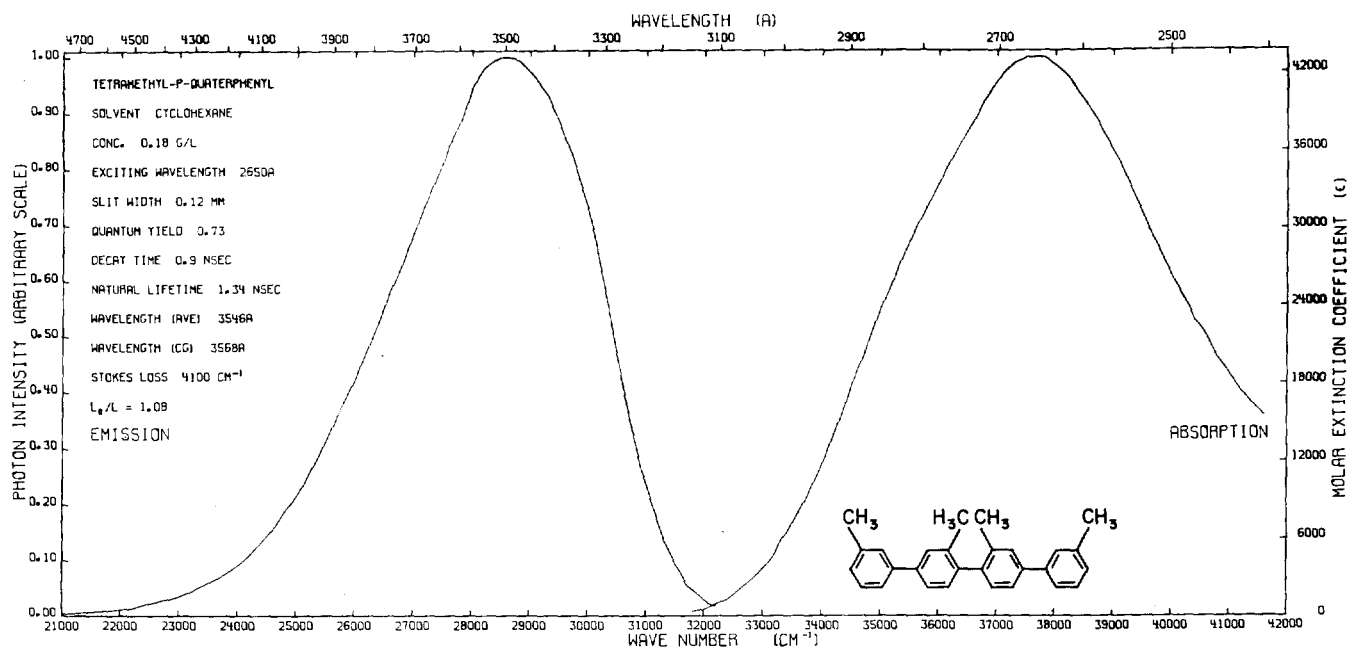
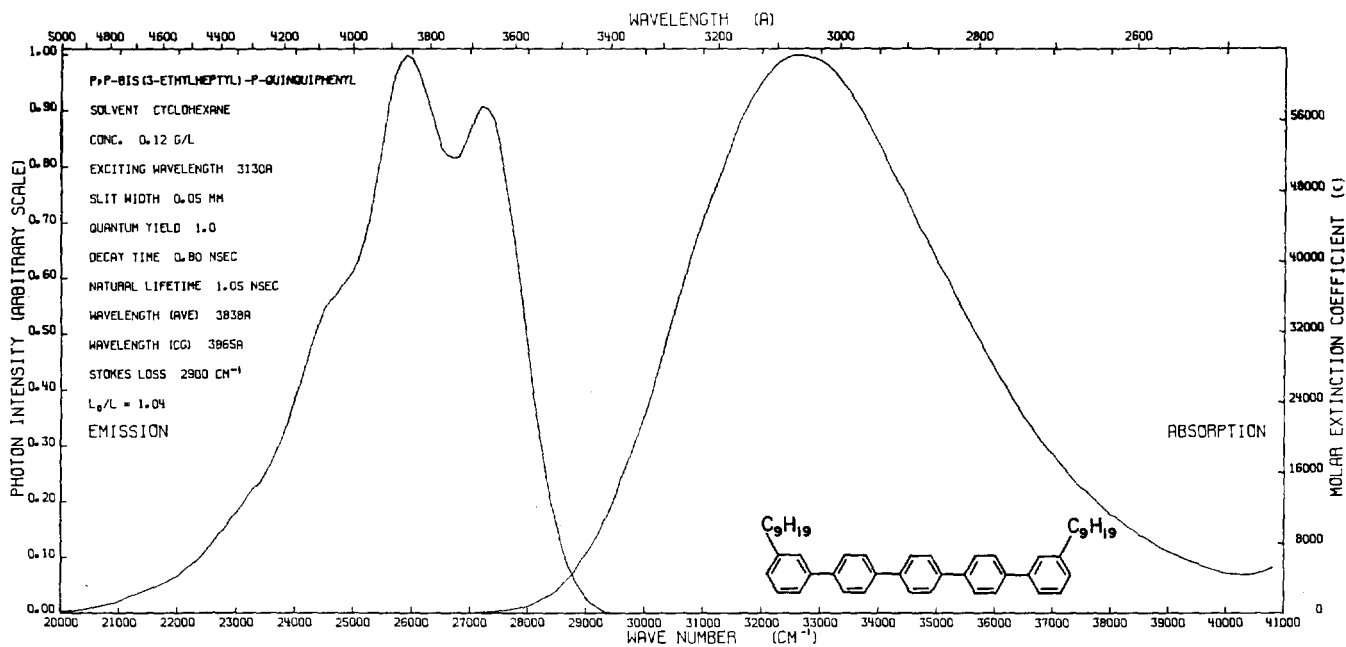
Fig. 140.—Compound II, 3,3'-dimethyl-*p*-terphenyl141.—Compound III, 2-methyl-*p*-terphenyl

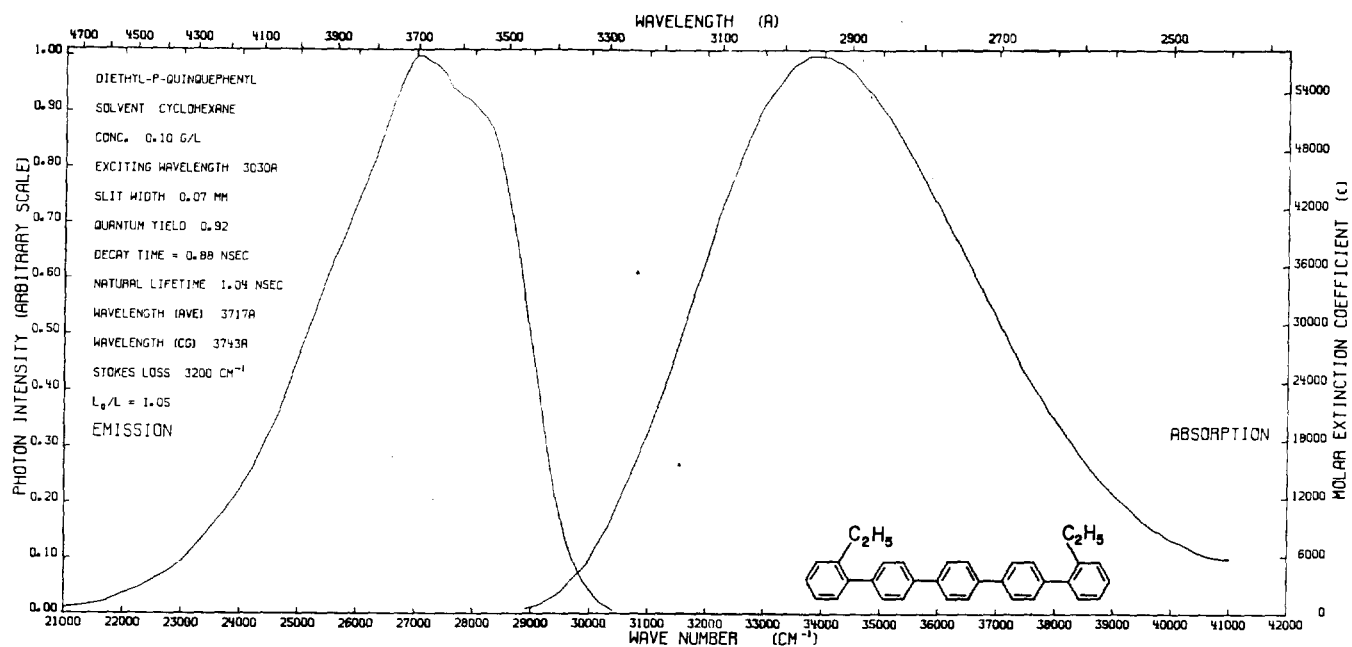
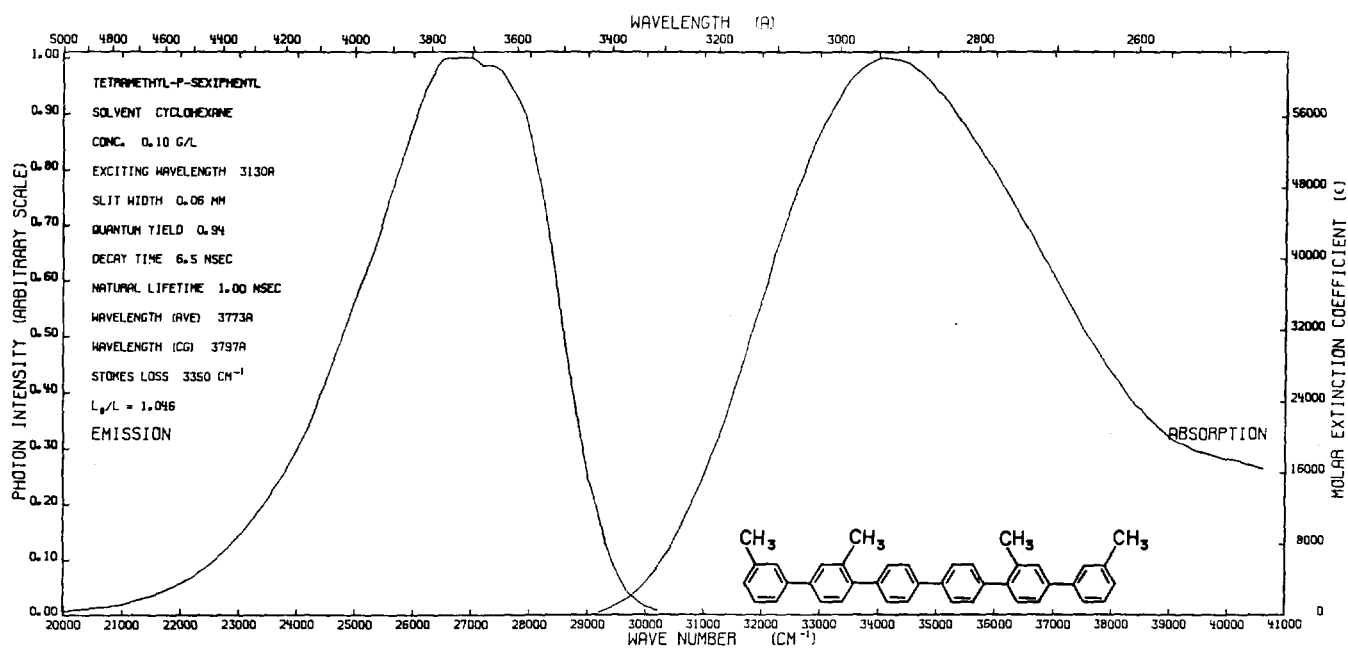
DOI-10.1002

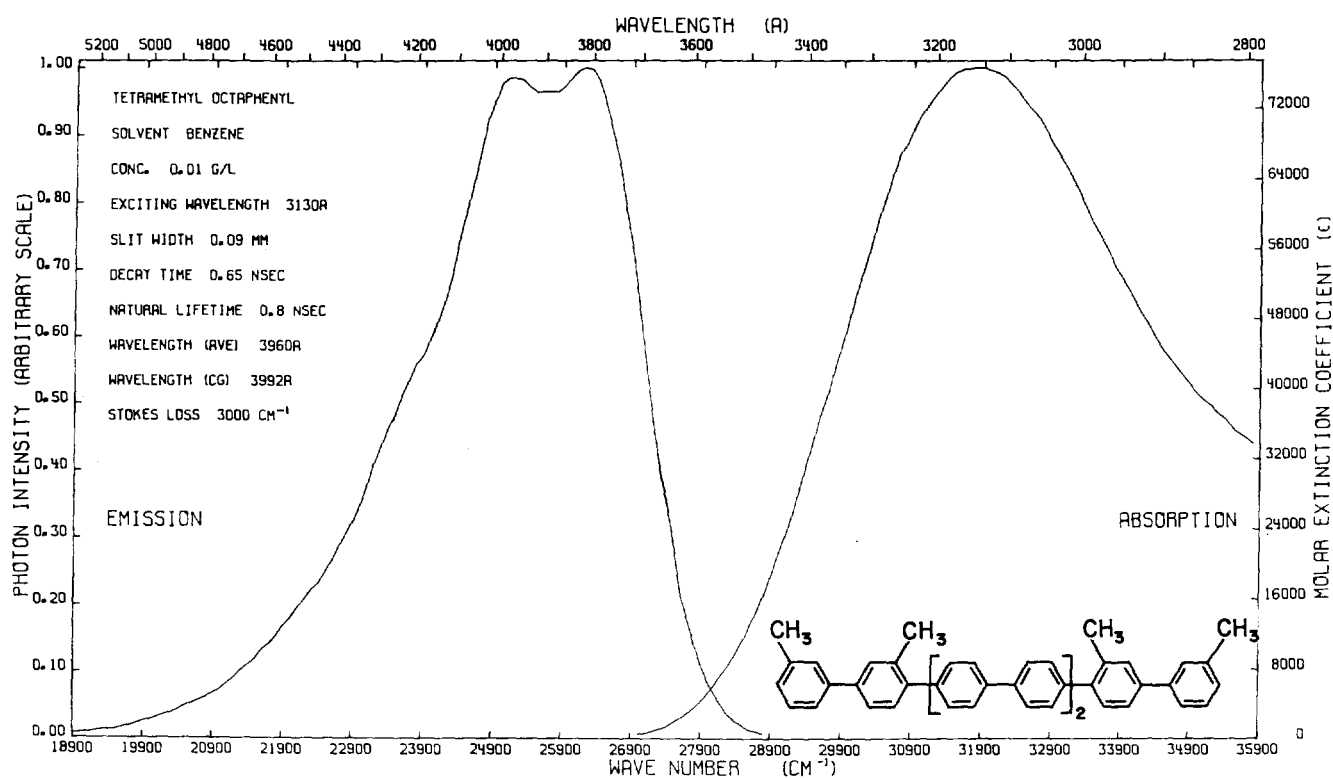
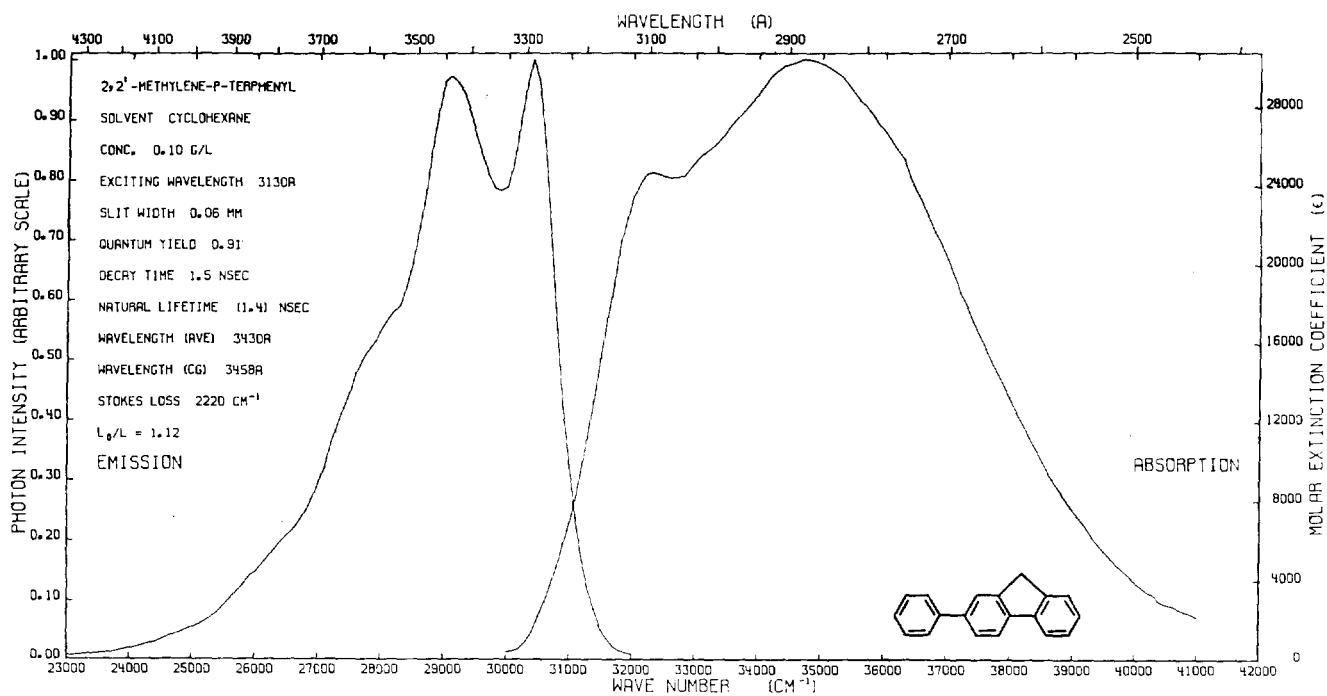


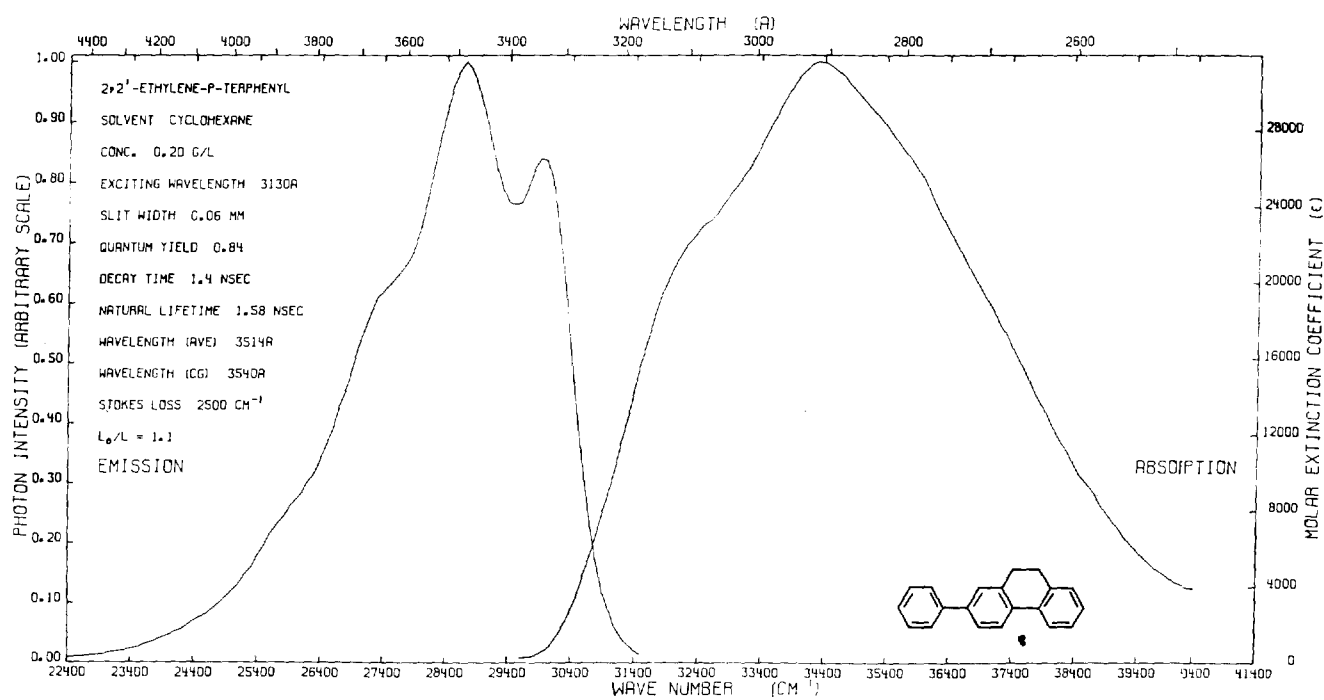
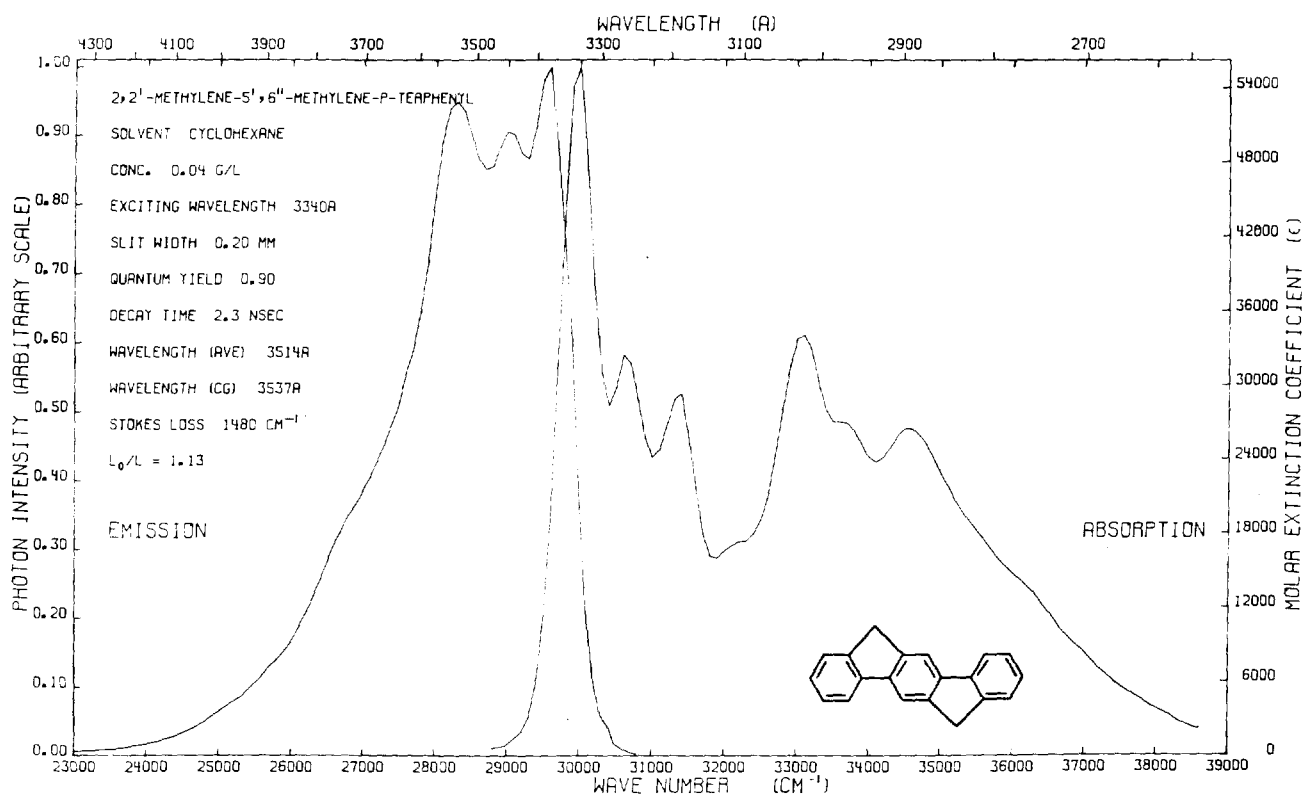
142.—Compound IV, sexiphenyl benzene

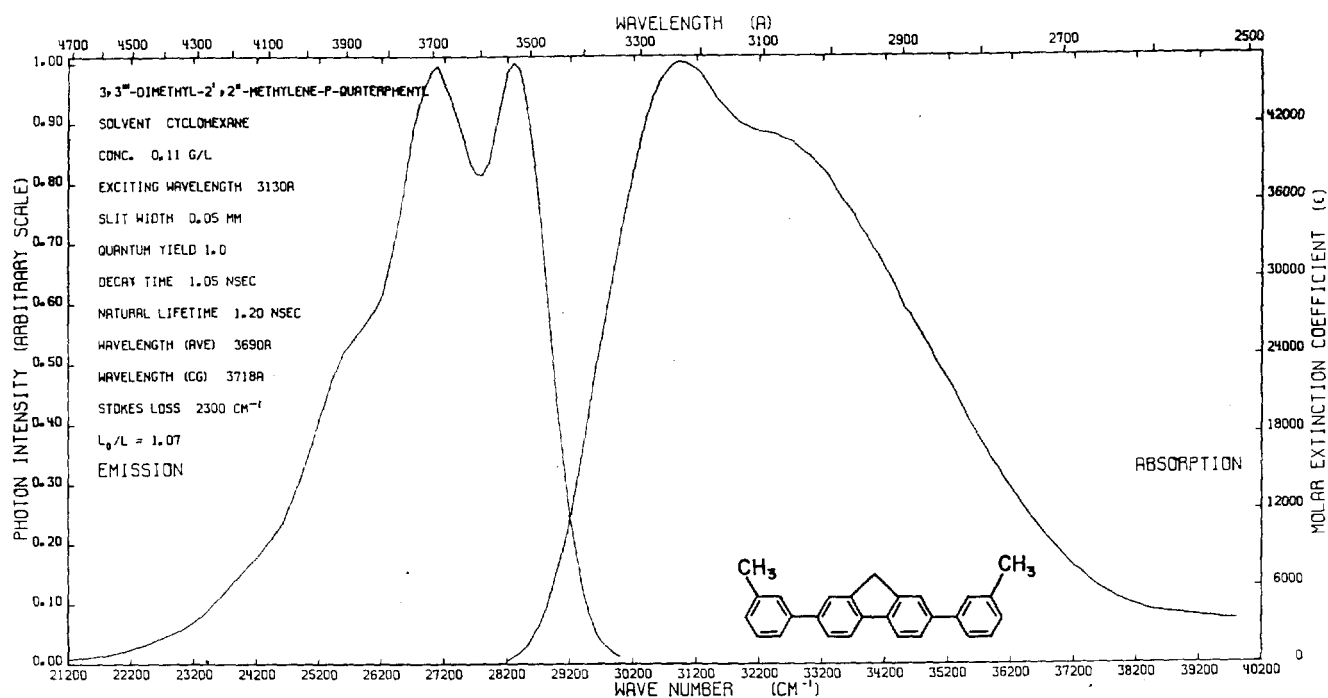
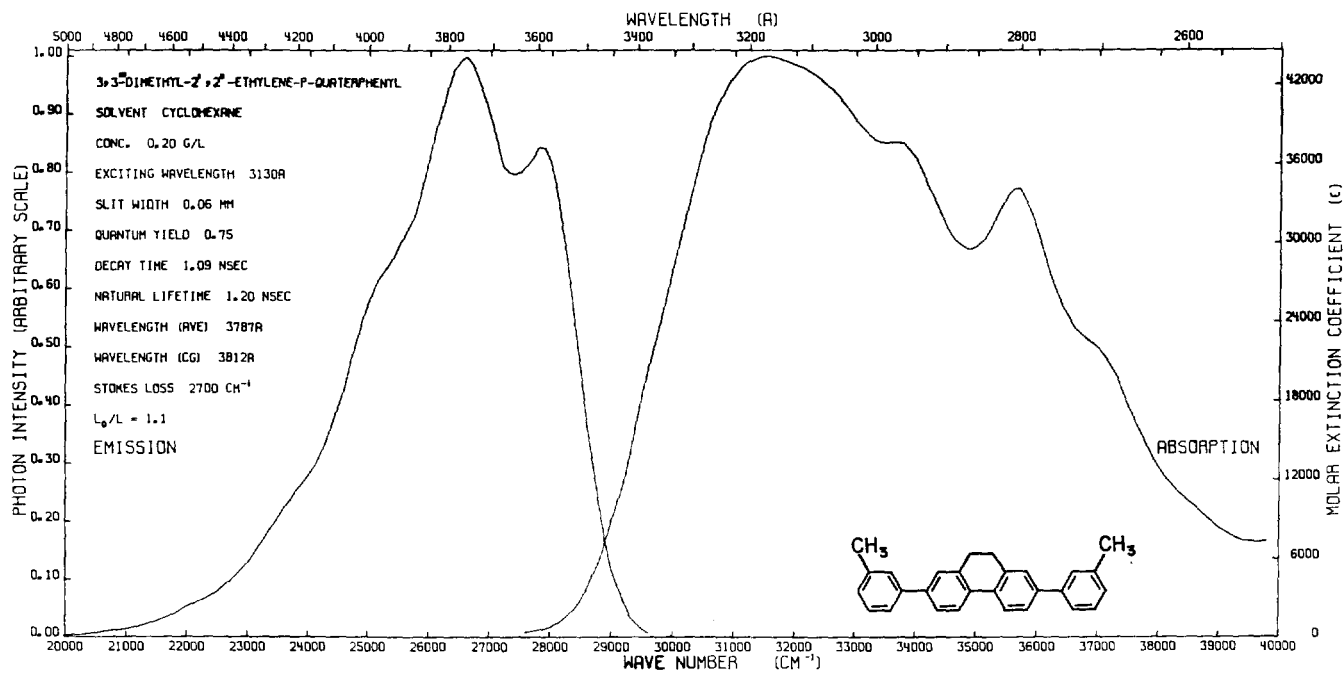
143.—Compound VI, dimethyl-*p*-aterphenyl

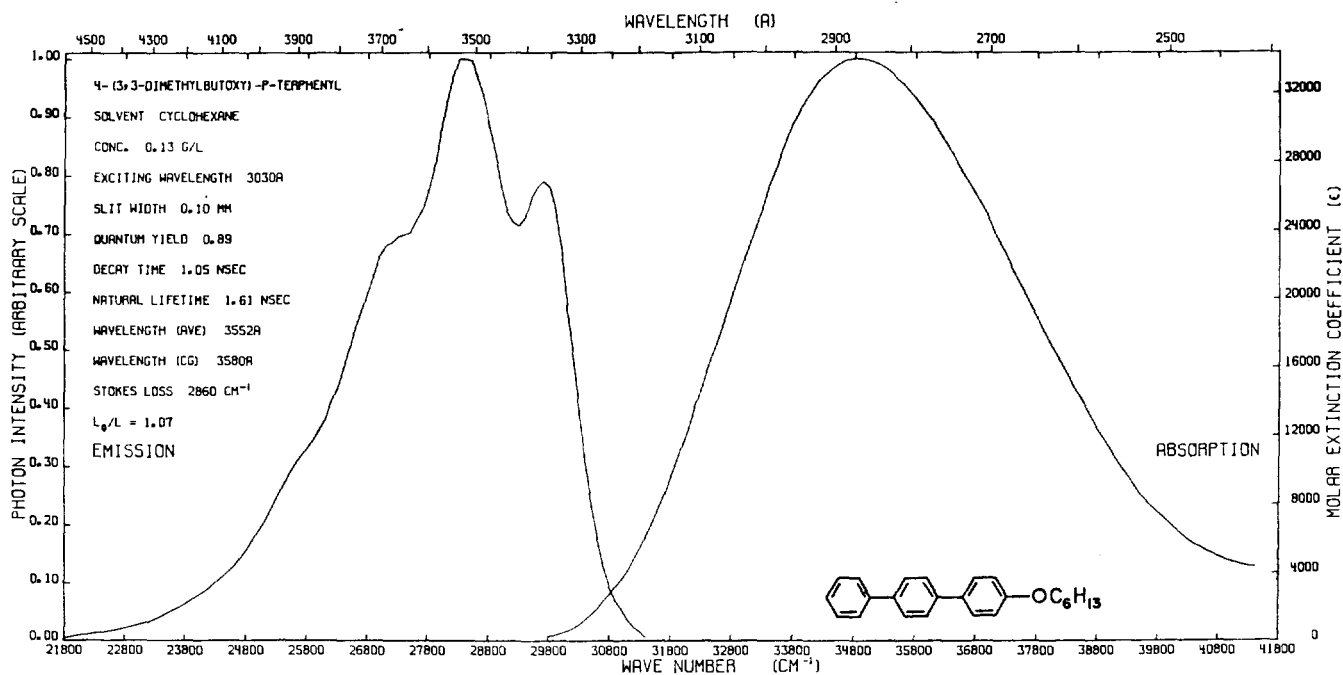
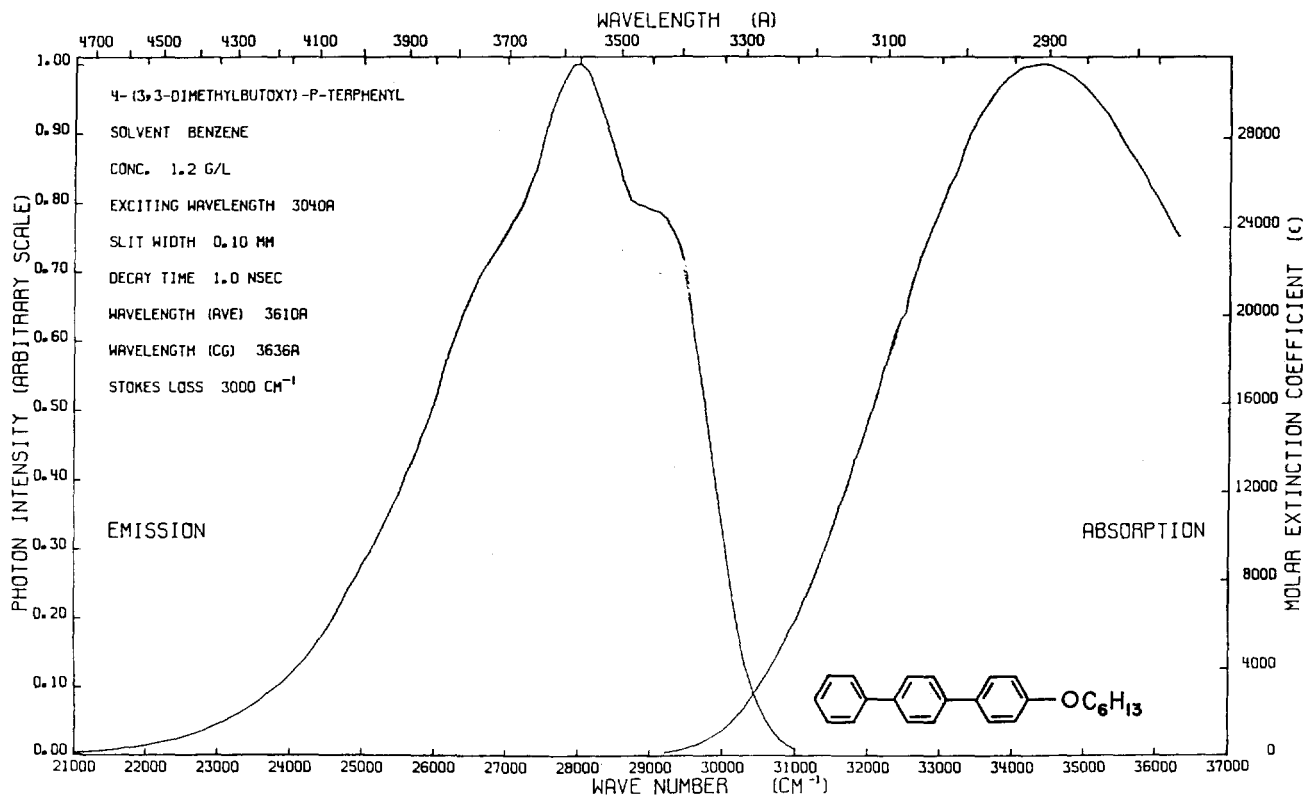
144.—Compound VII, tetramethyl-*p*-quaterphenyl145.—Compound VIII, di(3-ethylheptyl)-*p*-quinquephenyl

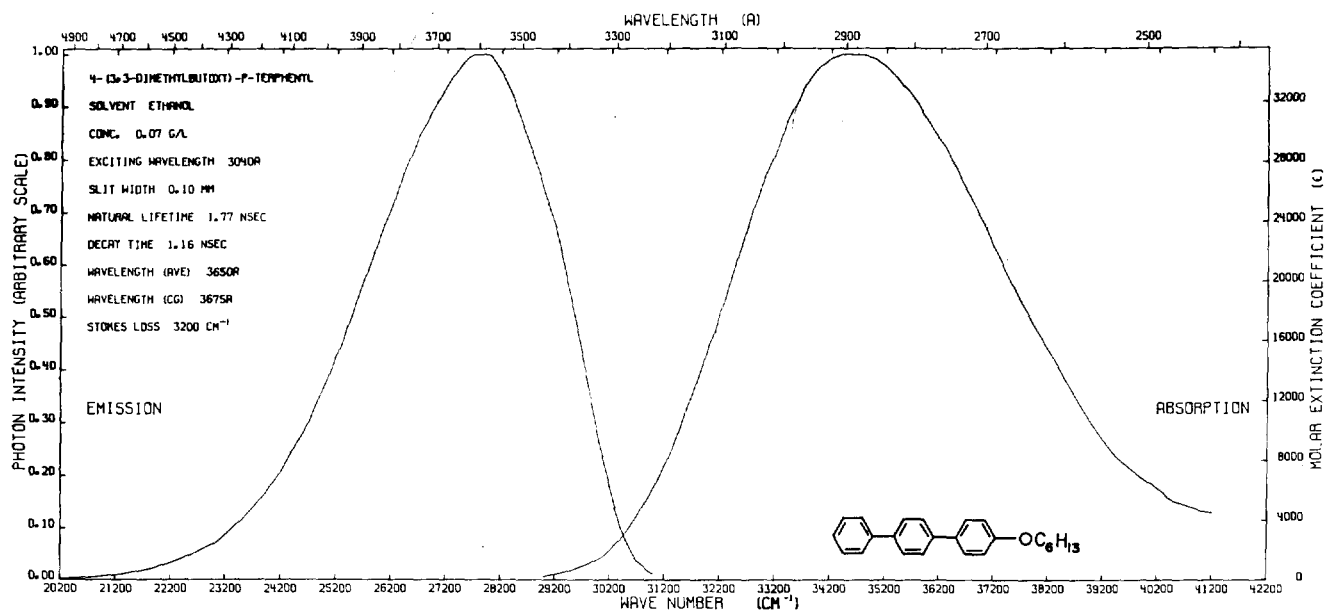
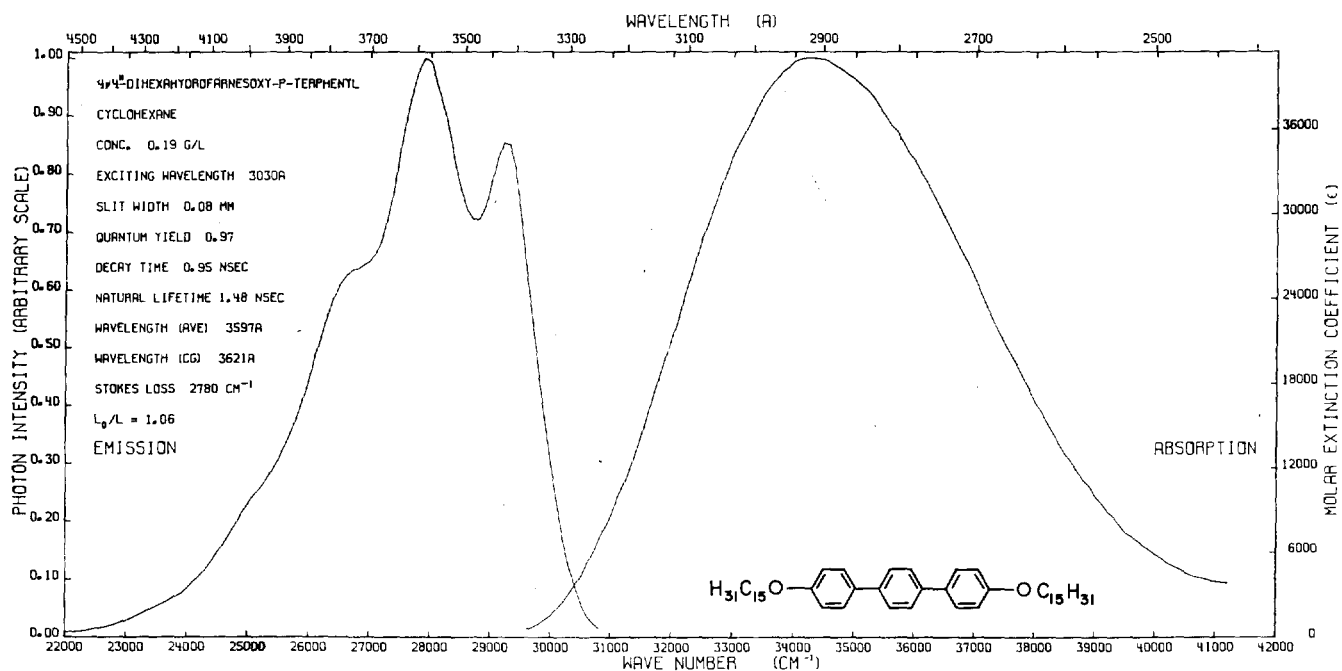
146.—Compound IX, diethyl-*p*-quinquephenyl147.—Compound X, tetramethyl-*p*-sexiphenyl

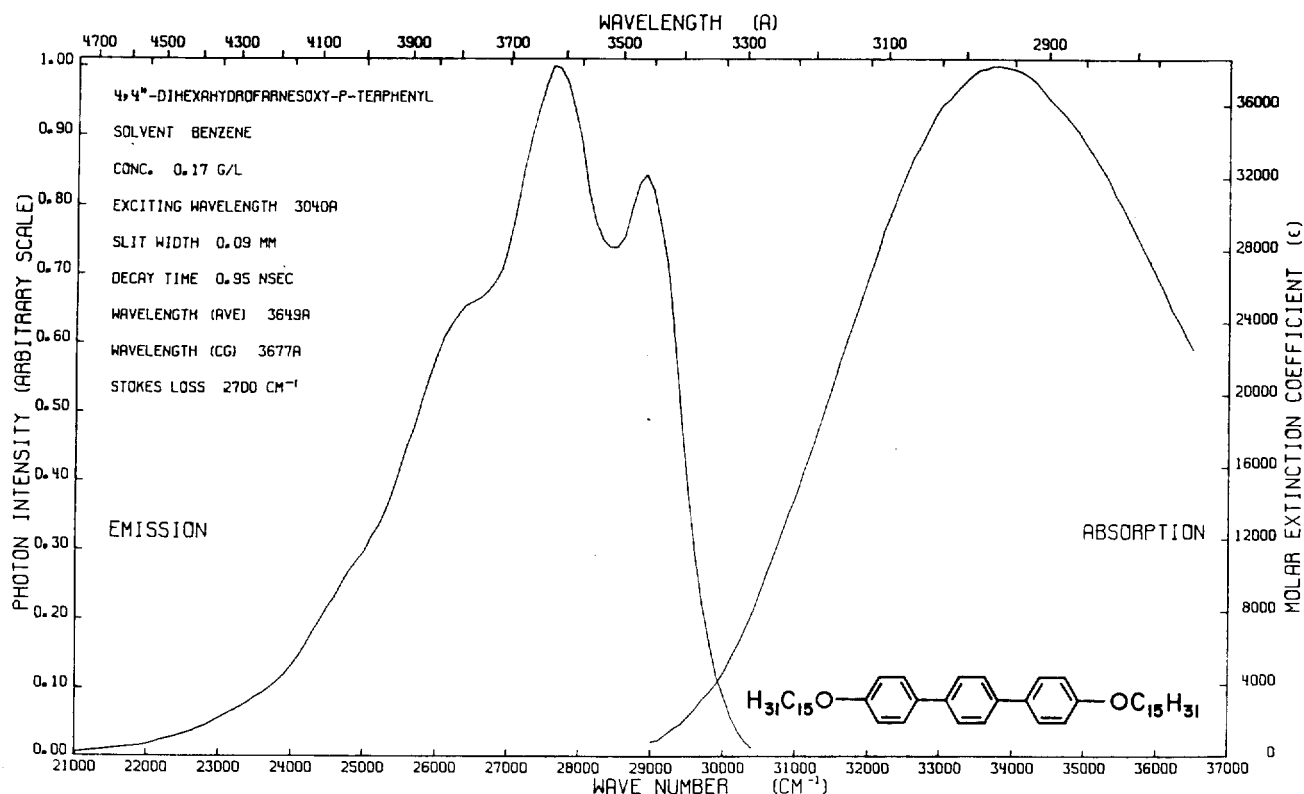
148.—Compound XI, tetramethyl-*p*-octaphenyl149.—Compound XII, 2,2'-methylene-*p*-terphenyl

150.—Compound XIII, 2,2'-ethylene-*p*-terphenyl151.—Compound XIV, 2,2'-methylene,5',6''-methylene-*p*-terphenyl

152.—Compound XV, 3,3''-dimethyl,2',2''-methylene-*p*-quaterphenyl153.—Compound XVI, 3,3''-dimethyl,2',2''-ethylene-*p*-quaterphenyl

154.—Compound XVII, 4-(3,3-dimethylbutoxy)-*p*-terphenyl, solvent cyclohexane155.—Compound XVII, 4-(3,3-dimethylbutoxy)-*p*-terphenyl, solvent benzene

156.—Compound XVII, 4-(3,3-dimethylbutoxy)-*p*-terphenyl, solvent ethanol157.—Compound XIX, 4,4'-dihexahydrofarnesoxy-*p*-terphenyl, solvent cyclohexane



158.—Compound XIX, 4,4'-dihexahydrofarnesoxy-*p*-terphenyl, solvent benzene

systems of the similar size. Among the compounds tested, XI is the longest molecule and, as expected, has the shortest computed lifetime, 0.8 nsec.

It has been postulated by Suzuki⁽⁶⁾ that the larger the *p*-oligophenylene, the more planar is the chromophor in the ground state. In support of this assumption, the FWRE values of the absorption spectra become smaller as the chromophor becomes larger as shown in Table 67 for compounds II, VI, and VIII.

Alkyl chains substituted in the *para* and *meta* positions of *terminal* rings are effective in increasing the solubility of the compound and yet do not affect the planarity of the chromophor or the strength of the transition. For these reasons, these substituted compounds possess characteristics very similar to those of the unsubstituted compounds. On the other hand, if these same substituents are positioned on the *ortho* position of the end rings or on *meta* or *ortho* positions of phenylene rings, the planarity of the basic chromophor is disturbed, and its fluorescence characteristics are affected in the following manner: The long wavelength absorption band is shifted toward shorter wavelengths, the value of ϵ_{\max} is reduced, the value of FWRE of the absorption curve is increased, the fluorescence spectrum becomes less structured, the value of Stokes loss is increased, and the quantum yield is reduced. These effects of steric hindrance are

readily noted in comparing the data for II with III, VI with VII, and VII with IX, as shown in Table 67 and Figures 140, 141, and 143–146. If it were not for steric crowding by the substituents with the hydrogen atoms on the basic chromophor in VII, X (Figure 147) and XI (Figure 148), the natural fluorescence lifetimes would be even shorter than those tabulated. IV (Figure 142) can be considered as tetraphenyl-*p*-terphenyl and is an illustration of an extreme case of steric hindrance. For this latter compound the quantum yield is very small, the intense transition that is the hallmark of the *p*-oligophenylenes is shifted toward shorter wavelengths, and Stokes loss is very large. Surprisingly FWRE (F_1) is abnormally small. This result may be explained by the fact that the six phenyl rings make large angles with the central benzene rings so that there is no effective conjugation between the rings and the fluorescence characteristics correspond to a ${}^1L_b - {}^1A$ transition of the basic chromophor, the central benzene ring.

The angle between successive phenyl rings can be held fixed by means of a bridging group as in XII, XIII, XIV, XV, and XVI, Figures 149–153, respectively. This added planarity is responsible for the structure in both the absorption and fluorescence spectra, and their shift toward longer wavelengths, for the increase in the value of ϵ_{\max} , and for the de-

crease in the values of Stokes loss and FWRE (F1). These effects of bridging can be noted in comparison of the data and figures of bridged and unbridged compounds, i.e. XV and XVI versus V. Compounds XII and XIII also possess the characteristics of planar compounds. In comparing effects on the fluorescence characteristics by a methylene group versus an ethylene group, it is noted that the quantum yield is smaller and the values of Stokes loss and FWRE (F1) are larger when an ethylene group is employed. Since XII and XIII can be called 2-phenyl-fluorene and 2-phenyl-9,10-dihydrophenanthrene, respectively, it is apparent that information as to the structure of these compounds can be obtained from studies on fluorene and 9,10-dihydrophenanthrene. From x-ray data on these latter compounds in the crystalline state, it is concluded that fluorene is planar⁽⁷⁾, whereas in the case of 9,10-dihydrophenanthrene the planes containing the phenyl rings are estimated to be at an angle of about 20° with respect to each other.⁽⁸⁾ On comparing the spectroscopic data on these latter compounds, it is found that the fluorescence quantum yield of fluorene is larger and the values of Stokes loss and FWRE (F1) are smaller than those of 9,10-dihydrophenanthrene.⁽⁹⁾ From these results on comparing bridging by a methylene chain vis-a-vis an ethylene chain, it is concluded that phenyl rings are held in a more planar conformation when bridged by a methylene chain, and the fluorescence characteristics are optimized better.

It is apparent from looking at the absorption spectra of the bridged oligophenylenes that the long wavelength absorption bands are produced by two separate transitions. In the case of the most planar compound tested, XIV, the absorption spectrum is very structured and the bands due to the two transitions are well separated. Since τ_0 for each of the compounds in Table 67 is computed by integrating over the whole absorption curve and since a meaningful value of τ_0 is obtained only when the integration is performed over the bands corresponding to the transition leading to fluorescence, the τ_0 values for the bridged compounds are questionable. Therefore, these values are bracketed. The absorption spectra of all the other compounds may possibly contain, also, bands lying at shorter wavelengths than the main band, but in these cases the secondary bands are not readily apparent. Such a masked band in an absorption spectrum would contribute to the very large measured values of FWRE, yet the transition responsible for this band

would not interfere with the measured fluorescence characteristics.

An alkyloxy substituent when in the *para* position as in XVII (Figure 154) and XVIII is effective in increasing the value of ϵ_{\max} and the static dipole moment of the ground and first excited singlet state. As noted in Figures 154-156, the fluorescence spectra become more diffuse and are shifted toward the red in polar solvents such as ethanol. Even in benzene most of the structure in the fluorescence spectrum is lost. This spectral shift and the loss of structure are interpreted by Eisinger and Navon⁽¹⁰⁾ as being produced by an interaction between the dipole moment of the solute and that of the solvent. On the other hand, when two alkyloxy substituents are positioned at opposite *para* positions of the chromophor as in XIX and XX, the dipole moment becomes negligibly small but ϵ_{\max} becomes larger, almost as large as that produced by an additional phenyl group. These effects are also shown in Table 67 and Figures 157 and 158. Benzene has little effect on this compound. Since XIX is practically insoluble in ethanol, no figure is available for this solution. It is believed that the alkyloxy substituent is particularly effective in affecting the value of ϵ_{\max} and the dipole moment when substituted on the *para* position because the transition moment is along the long axis of the molecule.

In conclusion, efficiency and speed are two useful features of a good scintillator and both of these characteristics depend on large values of the molar extinction coefficient. Not only are a large number of rings desirable, but they should be in a linear and planar conformation. When substituents and bridging groups are employed, they should be so positioned so as to enhance, not interfere, with this arrangement.

REFERENCES

- Berlman, I. B. *Mol. Cryst.* **4**, 157 (1968).
- Wirth, H. O., Herrmann, F. U., Herrmann, G., and Kern, W. *Mol. Cryst.* **4**, 321 (1968).
- Berlman, I. B. *Handbook of Fluorescence Spectra of Aromatic Molecules*. Academic Press Inc., New York, 1965, p. 13-26.
- Berlman, I. B. *Chem. Phys. Letters* **3**, 61 (1969).
- Berlman, I. B. *Handbook of Fluorescence Spectra of Aromatic Molecules*. Academic Press, Inc., New York, 1965, pp. 138 and 141.
- Suzuki, H. *Bull. Chem. Soc. Japan* **33**, 109 (1960).
- Burns, M. D., and Iballs, J. *Proc. Roy. Soc. (London)* **A227**, 200 (1955).
- Beaven, G. H., Hall, D. M., Leslie, M. S., and Turner, E. *J. Chem. Soc.* **854**, (1952).
- Berlman, I. B. Unpublished data.
- Eisinger, J. and Navon, G. *J. Chem. Phys.* **50**, 2069 (1969).

TOTAL CROSS SECTIONS FOR INELASTIC SCATTERING OF CHARGED PARTICLES BY ATOMS AND MOLECULES. III. ACCURATE BETHE CROSS SECTION FOR IONIZATION OF HELIUM*

Mitio Inokuti and Y.-K. Kim

The Bethe cross section σ_i for ionization of He by fast charged particles is accurately evaluated by a subtraction $\sigma_i = \sigma_{\text{tot}} - \sigma_{\text{ex}}$, where σ_{tot} is the total inelastic-scattering cross section and σ_{ex} the sum of all discrete-excitation cross sections. Our earlier work has given a highly precise value of σ_{tot} , and recent results on discrete excitations enable one to determine σ_{ex} . The

* Abstract of a paper published in *Phys. Rev.* **186**, 100 (1969).

resulting "counting" ionization cross section for a particle of charge ze and velocity $v = \beta c$ is

$$\sigma_i = \frac{8\pi a_0^2 z^2}{mv^2 R} \left\{ 0.489 \left[\ln \left(\frac{\beta^2}{1 - \beta^2} \right) - \beta^2 \right] + 5.526 \right\},$$

where m is the electron mass, a_0 the Bohr radius, and R the Rydberg energy. Among numerous measurements, the electron-impact data by Smith are most consistent with our result and suggest a gradual attainment of the Bethe asymptotic behavior near 1 keV incident electron energy.

ELECTRO-OPTICAL TECHNIQUES FOR ULTRASENSITIVE RADIOPHOTOLUMINESCENT DOSIMETRY*

Jacob Kastner, R. K. Langs, B. A. Cameron, Michael Paesler and George Anderson

The factor which has limited the sensitivity of photoluminescent dosimetry has been the "pre-dose" or matrix fluorescence background which is stimulated during readout by the usual continuous ultraviolet exposure. The signal-to-noise ratio has only been partially optimized by selective choice of filters and optical geometry.

A microdosimetric system was conceived and investigated which is potentially capable of sensing extremely low radiation dosages (in the order of micro-

* Abstract of a paper given at the Second Int. Conf. on Luminescence Dosimetry, Gatlenburg, Tenn., September 23-26, 1968, and published in U. S. Atomic Energy Commission Report CONF-680920.

rads). This system depends on the little-known fact that the decay time for the visible luminescence, which is a measure of the absorbed dose, is at least ten times longer than the decay of the indistinguishable visible fluorescence (to UV) which is an inherent characteristic of unexposed silver phosphate glasses.

The principle was confirmed some time ago using an ultraviolet laser and was reported elsewhere. In the hope of simplifying the reader, experiments have been carried out using an electro-optical Pockels shutter and much cheaper and less complex UV sources. To date we have been successful in obtaining a 2-to-1 signal-to-noise ratio from a Toshiba fluord exposed to 10 mR.

SPECTRAL ANALYSIS OF THERMOLUMINESCENT GLOW CURVES*

B. G. Oltman, Jacob Kastner and C. M. Paden

An effort has been made to correlate the spectrum of the light from thermoluminescent materials, in-

* Abstract of a paper presented at the Second Int. Conf. on Luminescence Dosimetry, Gatlenburg, Tenn., September 23-26, 1968 and published in CONF-680920.

cluding the far UV, with various kinds of ionizing radiations. An apparatus is described which has been designed and constructed to provide well-controlled heating ramps and monochromator scanning capability. Results are given for such analysis for various inorganic thermoluminescent materials.

ENVIRONMENTAL NEUTRON MEASUREMENTS WITH SOLID STATE TRACK RECORDERS

J. H. Roberts, R. A. Parker,* F. J. Congel, Jacob Kastner, and B. G. Oltman*

The suitability of using ^{10}B and ^6LiF in contact with cellulose acetate butyrate (CAB) for the measurement of slow neutron densities has been investigated. The upper energy threshold of clear Diacel cellulose nitrate (CN) and of the CAB have also been measured. The CAB in good contact with thick ^{10}B or ^6LiF sources offers good promise for the detection of slow neutrons. For the actual CAB samples used, the CAB- ^{10}B combination had an efficiency of 1.3×10^{-3} tracks per thermal neutron incident in a 2π solid angle. The corresponding number for the CAB- ^6Li combination is 5.6×10^{-3} tracks per thermal neutron.

INTRODUCTION

The measurement of low level slow neutron densities with highly efficient and stable detection systems with low background is important for neutron dosimetry in a variety of environmental conditions. The suitability of cellulose nitrate (clear Diacel CN) and cellulose acetate butyrate (CAB) for registration of alpha and ^7Li particles from $^{10}\text{B}(n,\alpha)$ and of alpha particles from $^6\text{Li}(n,\alpha)$ has been studied. These studies have included a measurement of the upper energy threshold of these materials for alpha track registration.

The motivation for the present studies is an application to the measurement of slow neutron levels over land and water due to cosmic radiation. These studies are now being undertaken.

ETCHING PROCEDURES

A 6.25 N NaOH solution was used to etch both types of plastic. This is nearly that suggested by Fleischer et al for CN.⁽¹⁾ For the clear Diacel CN a room temperature etch of 2 hr gave excellent track quality. However, by increasing the temperature to 40° C the etching time could be reduced to 19 min without any significant increase in etch damage. Following a suggestion of G. R. Ringo⁽²⁾ it was found that good track quality in the CAB was obtained by etching for 2.5 hr at 62° C.

Typical alpha tracks in the CAB are shown in Figures 159 and 160. The etched damage in the CAB resulting from alpha particle bombardment was more like circular pits than tracks. These etch pits are distinctive and readily distinguished from surface damage produced by the etchant in the unirradiated surface. When the surface was irradiated with alpha particles from a thick source, very short tracks in the

Diacel CN were hard to distinguish from surface imperfections. Thus the CAB was found to be much more promising for this application.

THRESHOLD STUDIES

Measurements of the upper energy threshold for alpha particles were carried out with a thin ^{241}Am source. Two methods, one involving keeping the source-recorder distance fixed and varying the air pressure (Diacel CN), and the other, involving varying the source-recorder distance in air at constant pressure (CAB) were used.

For the Diacel CN the source-recorder distance was 5.65 cm. The angle of incidence of the alpha particles on the plastic was $\sim 45^\circ$. The source-recorder combination was placed inside a chamber so that the air pressure could be regulated as desired. The main group of alpha particles from ^{241}Am have an energy of 5.48 MeV. The source used had an activity of 2×10^5 disintegrations/min. Strips of CN were exposed for 90 min at 26° C and pressures of 30.5, 33.0, 35.6, 38.1, 40.6, 43.2, and 45.7 cm of Hg. These correspond to incident alpha particle energies at the CN surface of 3.0, 2.8, 2.5, 2.2, 1.9, 1.5, and 1.1 MeV respectively.† Good tracks were obtained up to an alpha energy of 1.9 MeV, and no tracks were visible at all above 2.5 MeV.

For the CAB, similar measurements indicated that the diameter of the etch pits decreased with increasing particle energy and were no longer visible for alpha particles above ~ 1.6 MeV. It is planned to refine these measurements on both the Diacel CN and the CAB.

SLOW NEUTRON DETECTION EFFICIENCY OF CELLULOSE ACETATE BUTYRATE IN CONTACT WITH THICK ^{10}B AND ^6LiF SOURCES

Source-recorder combinations were irradiated with slow neutrons in the standard sigma pile at the Argonne National Laboratory. Calibrations were made by sandwiching a disk of CAB between a gold foil and a ^6LiF or ^{10}B source. These sources had a smooth flat surface so that good contact was possible. The ^6LiF crystals were square, 2 cm on a side and 2 mm thick. The ^{10}B was in the form of circular disks, 8 mm in diameter and 2 mm thick. Both sources were "black" to slow neutrons, and were infinitely thick

* Northwestern University.

† Based on the range-energy curve given by M. S. Livingston and H. A. Bethe.⁽³⁾

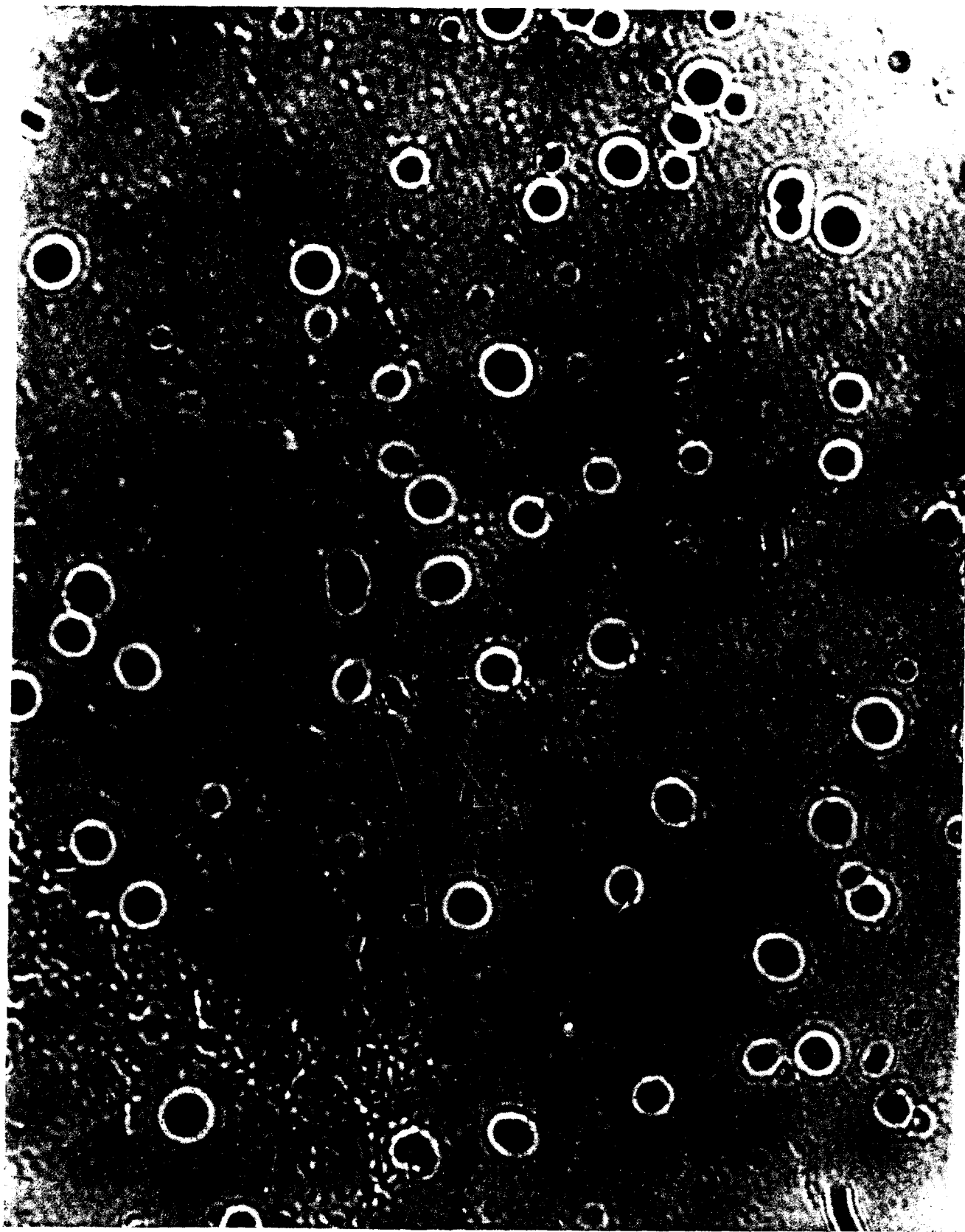


FIG. 159.—Etch pits produced in CAB by alpha particles. The focal plane of the microscope objective is slightly above the plastic surface.

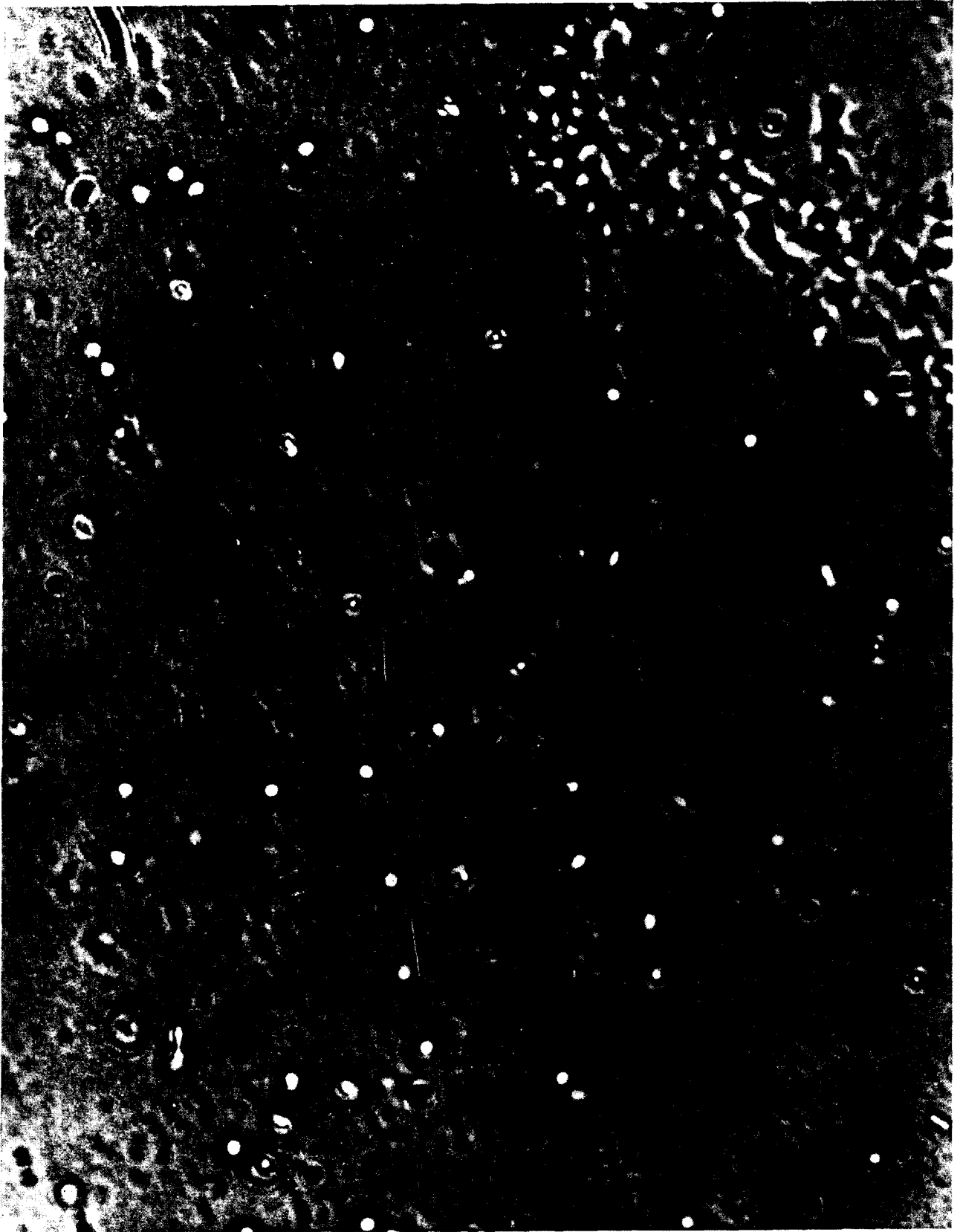


FIG. 160.—The same etch pits in CAB as in Figure 159 except that the focal plane of the microscope is now slightly below the plastic surface. Slight changes in focus are an aid in distinguishing etch pits from imperfections.

relative to the range of all charged particles produced by slow neutron capture in ${}^6\text{Li}$ or ${}^{10}\text{B}$. The recorder-source combinations were placed in aluminum holders under pressure supplied by a thin layer of sponge rubber to insure good surface contact. In some exposures the packages were placed in Cd boxes so that a correction for epithermal neutrons could be made.

The unperturbed thermal neutron flux in the standard pile at the position where the packages were placed was assumed* to be 4100 ± 200 neutrons/cm² sec. The ratio of the Au activity for a given exposure time with and without the ${}^6\text{LiF}$ was 0.42 ± 0.02 . The corresponding ratio for the ${}^{10}\text{B}$ was 0.50 ± 0.01 . The lack of flux depression in the case of the ${}^{10}\text{B}$ is due to its small mass. Thus, the thermal neutron flux at the ${}^6\text{LiF}$ surface was 1720 ± 100 neutrons/cm² sec, and the corresponding flux at the ${}^{10}\text{B}$ was 2050 ± 100 neutrons/cm² sec.

The track recording rate for the ${}^6\text{LiF}$ was 9.65 ± 0.23 tracks/cm² sec in the neutron flux of 1720 neutrons/cm² sec. The detection efficiency is thus $(5.6 \pm 0.3) \times 10^{-3}$ tracks per thermal neutron. The corresponding numbers for the ${}^{10}\text{B}$ are (26.7 ± 1.1) tracks/cm²·sec in the thermal neutron flux of 2050, or $(1.30 \pm 0.08) \times 10^{-2}$ tracks/thermal neutron.

The above calculated efficiencies are for thermal neutrons incident over a 2π solid angle. For thermal neutrons incident isotropically, the above values should be divided by two, since all neutrons incident

* Based on a measurement carried out by Harvey Casson in 1961 with gold foils. The flux is being redetermined with gold foils and natural uranium-mica combinations.⁶

PERMANENT DAMAGE OF ${}^7\text{LiF}$ THERMOLUMINESCENT DOSIMETERS BY FAST NEUTRONS

Jacob Kastner, Keith Eckerman,* B. G. Oltman, and Pete Tedeschi

It has been postulated that lattice heating may be the mechanism for the effects of fast neutrons on the gamma-ray response of TLD-700. In the experiment to be described, LiF was exposed to neutron energies of 6-14 MeV. The observed decrease in thermoluminescent response was established to be due in part to permanent damage of the dosimeter and definitely not attributable to lattice heating.

INTRODUCTION

That there was an effect of fast neutron exposure on the ${}^7\text{LiF}$ thermoluminescent response to gamma rays was reported earlier.⁽¹⁾ The decrease in thermoluminescent response observed seemed to be independent of the total neutron exposure and neutron energies

* Civil Engineering Department, Environmental Health Division, Northwestern University, Evanston, Illinois.

on the back side of the ${}^6\text{LiF}$ and ${}^{10}\text{B}$ sources are absorbed without producing tracks.

CONCLUSIONS

The full energy of the alpha particles from ${}^6\text{Li}(n,\alpha)$ induced by slow neutrons is 2.0 MeV. Most of the alpha particles from ${}^{10}\text{B}(n,\alpha)$ will have a maximum energy of 1.5 MeV. For thick ${}^{10}\text{B}$ and ${}^6\text{LiF}$ sources most of the alpha particles entering the CAB surface will be below its threshold ~ 1.6 MeV. For the ${}^{10}\text{B}$ sources the ${}^7\text{Li}$ recoil nuclei will also produce tracks. Thus, the ${}^{10}\text{B}$ is especially well suited for thermal neutron detection when used with the CAB plastic.

Whereas the research reported here indicates that the CAB ${}^{10}\text{B}$ or ${}^6\text{Li}$ combinations offer great promise for slow neutron detection, further studies are needed to put the results on a completely quantitative basis. Anyone planning to use the CAB should carry out his own calibrations. The threshold, detection efficiency, etc., depend upon the manufacturing process of the actual material used and may even vary from batch to batch from the same manufacturer.

The authors are indebted to Harvey Casson for helpful discussions on the thermal neutron flux measurements.

REFERENCES

1. Fleischer, R. L., Price, P. B., and Walker, R. M. *Ann. Rev. Nucl. Sci.* **15**, 1 (1965).
2. Ringo, G. R. Private communication.
3. Livingston, M. S., and Bethe, H. A. *Rev. Mod. Phys.* **9**, 245 (1937).
4. Gold, R., Armani, R. J., and Roberts, J. H. *Nucl. Sci. Eng.* **34**, 13 (1968).

below 1 MeV. Furthermore, as no permanent damage was observed, it was postulated that neutrons of less than 1.0 MeV may be introducing lattice vibrations giving effects similar to the thermal effects of a TLD heater.

In order to verify this hypothesis, it was decided to investigate this phenomenon at neutron energies of 6 to 14 MeV. The following is an account of this study and its results.

EXPERIMENTAL PROCEDURE

The gamma-ray responses of TLD 700 dosimeters[†] were determined with radium gamma rays using a

[†] Extruded rods, $1.4 \times 1.4 \times 6$ mm, Harshaw Chemical Co., Cleveland, Ohio.

modified reader of the research type described elsewhere.⁽²⁾ The glow curves were recorded on a strip chart, and the area under the glow curve peak was obtained with a mechanical integrator. Each dosimeter was weighed after readout and the weight recorded to the nearest 0.1 mg. The responses of the dosimeters were expressed as area/mg/Rad (precalibration). The dosimeters were then annealed at 400° C for 1 hr and 85° C for 18 hr.

Two sets of these dosimeters were used. One set, referred to as the predosed dosimeters, were exposed to radium gamma rays before the fast neutron irradiation, and a second set, referred to as postdosed dosimeters, were exposed to radium gamma rays after the fast neutron irradiation. Both sets were exposed to 4 R of radium gamma rays.

The dosimeters were packaged in cadmium holders, which consisted of two square cadmium plates 6 mm square and 1 mm thick. Each holder contained 4 predosed dosimeters, 4 postdosed dosimeters, and 3 background dosimeters.

The exposure to fast neutrons was obtained by using the ${}^7\text{Li}(p,n){}^6\text{Be}$ reaction from an 18-MeV tandem accelerator. At these energies there is the possibility that the residual nucleus, ${}^7\text{Be}$, could be left in an excited state as well as the ground state.⁽³⁾ Consequently, the resulting neutrons would not necessarily be monoenergetic. However, the cross section for this event proved negligible.

Exposures were made by placing the dosimeters at 20° with respect to the beam and 20 cm from the target. A ${}^{238}\text{U}$ fission counter was placed symmetrically with respect to the dosimeters and the beam. Exposures were made over several hours for a fluence of approximately 10^8 neutrons/cm² as determined by the fission counter. After exposure and readout (observed area per mg), all dosimeters were annealed at 400° C for 1 hr and 85° C for 18 hr. The responses to

radium gamma rays were redetermined (postcalibration area/mg/Rad).

The gamma background exposure during neutron irradiation was determined from the background dosimeters. The expected response was calculated using the calibration values. The damage factor was computed as the ratio of the observed response to the expected response.

Since the background dosimeters also suffered a decrease in thermoluminescent response, the background gamma exposure had to be corrected. The initially determined factor was used to correct the background data and the results applied in an iterative manner until there was less than a 20% change in the background correction.

RESULTS AND DISCUSSION

Tables 68 and 69 give the results obtained for the predose and postdose dosimeters respectively.

A comparison of the precalibration (Col. 5) and the postcalibration areas (Col. 6) showed that the dosimeters suffered a decrease in gamma sensitivity. The glow curves, however, exhibited no marked changes. Furthermore, this damage was established to be permanent, because there was no recovery of gamma sensitivity with further annealing in the manner described above.

The ratio of the precalibration to postcalibration, i.e., the irreversible or permanent damage factor (Col. 7), failed to account fully for the observed decrease in thermoluminescence. This can be seen by comparing the total damage factor (Col. 4) with the irreversible damage factor. There is a residual temporary loss of response or a reversible damage.

In speculating about the mechanism which would account for this reversible damage, one has to rule out lattice heating owing to the presence of this factor in both the predosed and postdosed dosimeters. It ap-

TABLE 68. FAST NEUTRON EFFECT ON PREDOSED TLD-700

Neutron energy (1)	Total damage			Irreversible damage			Reversible
	(2)	(3)	(4) [(3)/(2)]	(5)	(6)	(7) [(6)/(5)]	(8) [(4)/(7)]
MeV	Calc. area/ mg	Obs. area/ mg		Precalib. area/ mg × Rad	Postcalib. area/ mg × Rad		
6.2	224.8	126.9	0.570	34.0	28.1	0.83	0.68
7.2	170.9	47.8	0.30	14.4	11.5	0.78	0.40
8.2	312.6	216.7	0.65	26.1	21.1	0.84	0.78
9.2	263.3	148.0	0.54	19.8	15.4	0.76	0.71
10.1	346.1	136.2	0.38	16.3	13.3	0.77	0.52
11.1	328.2	123.4	0.40	16.6	12.4	0.70	0.58
12.1	152.2	91.5	0.60	8.6	8.2	0.96	0.63
14.1	391.2	196.8	0.49	16.0	10.6	0.70	0.73

TABLE 69. FAST NEUTRON EFFECT ON POSTDOSED TLD-700

Neutron energy (1)	Total damage			Irreversible damage			Reversible
	(2)	(3)	(4) [(3)/(2)]	(5)	(6)	(7) [(6)/(5)]	(8) [(4)/(7)]
MeV	Calc. area/ mg	Obs. area/ mg		Precalib. area/ mg × Rad	Postcalib. area/ mg × Rad		
6.2	59.4	33.5	.57	9.0	8.0	0.89	0.64
7.2	114.5	42.5	.38	10.4	8.0	0.78	0.48
8.2	185.4	98.6	.49	15.5	12.4	0.78	0.62
9.2	139.7	64.4	.47	10.5	7.1	0.69	0.68
10.1	228.4	84.7	.37	10.8	7.7	0.73	0.52
11.1	211.9	80.9	.38	10.7	7.8	0.73	0.54
12.1	199.1	89.9	.45	11.3	7.1	0.63	0.71
14.1	244.0	111.2	.46	10.0	8.3	0.84	0.54

pears necessary to attribute the irreversible and reversible damage to the same mechanism, the differences in these factors being due only to the annealing process. At the neutron energies present in this experiment, 6 to 14 MeV, the deformation of the crystal by collision processes appears to be the mechanism for the damage.

CONCLUSIONS

The effect of fast neutrons on the gamma ray response of ${}^7\text{LiF}$ has been investigated. The dosimeters were found to suffer a marked damage, part of which is reversible with the annealing procedure employed. The results from this experiment indicate that ${}^7\text{LiF}$

should not be used in the presence of fast neutrons to monitor gamma radiation.

We wish to thank Prof. Herman Cember, Civil Engineering Department, Northwestern University, for his encouragement and cooperation.

One of us (K.E.) carried out this work under a fellowship from the U.S. Public Health Services.

REFERENCES

1. Kastner, J., Oltman, B. G., Tedeschi, P., and Beggs, J. N. *Health Phys.* **13**, 918 (1967).
2. Kastner, J., Ramesh, Hukkoo, Oltman B. G., and Dayal, Y. *Radiat. Res.* **32**, 625 (1967).
3. Lauritsen T., and Ajsenberg-Selove, F. Energy Levels of Light Nuclei. To be published.

ULTRASONIC EXCITATION OF THERMOLUMINESCENT LITHIUM FLUORIDE*

Jacob Kastner, R. H. Selner, C. M. Paden, and B. G. Oltman

Ultrasonic excitation of luminescence has been proposed to eliminate the black-body radiation background noise inevitably associated with thermoluminescent dosimeter readout.

Studies have been carried out with single LiF crystals bonded directly to piezoelectric transducers. The transducers were driven with a continuous radiofrequency generator over a range of frequencies from 4 to 10 megacycles/sec (MHz).

Glow peaks were observed at 10 MHz. After observing a rise in the transducer-LiF temperature, we duplicated the temperature ramp with our normal thermoluminescent readout apparatus. The recorded glow peaks were identical with the luminescence produced by the ultrasonic excitation, verifying the latter's essentially thermal character and thus eliminating the hope that ultrasonics might provide real advantages as a readout technique.

* Abstract of paper published in *Health Phys.* **16**, 803 (1969).

NEUTRON EXPOSURE TO LUNAR ASTRONAUTS

Jacob Kastner, B. G. Oltman, Yehuda Feige,* and Raymond Gold†

The flux and energy distribution of neutrons generated by cosmic rays in lunar material has been inferred from a knowledge of the situation at the earth's surface. It is suggested that lunar astronauts may suffer significant exposure to thermal neutrons so that their tissue sodium could well be activated to sodium-24. It would be very informative for the future assessment of risks to personnel on the moon to subject lunar astronauts to whole-body counting.

The flux and energy distribution of neutrons generated by cosmic rays in lunar material can be inferred from knowledge of neutrons generated by cosmic rays in the earth's atmosphere and at the air-ground interface.⁽¹⁻⁴⁾

A number of factors will enhance the neutron flux at the moon's surface. The total flux will be greater because of the vastly higher cosmic-ray intensity resulting from the lack of a shielding atmosphere and magnetic field. Also, the higher average atomic mass of lunar materials will result in a greater neutron yield and lower slowing down so more of the neutrons can leak out into space.

The number of thermal or slow neutrons will be relatively even greater because of the lack of nitrogen to act as a sink (for the production of ^{14}C ⁽⁵⁾). Furthermore, the moon's gravity will trap most thermal neutrons (especially on the night side, where the moon's escape velocity of 2.4 km/sec is certainly greater than the mean neutron speed). Finally, the neutron decay ($\tau = 13$ min) will restrict the slow neutrons to within about one or two moon radii of the lunar surface.

We have derived the theoretical distributions at an air-SiO₂ interface for various energy groups of neutrons using a modification of an Argonne reactor code. Figures 161 and 162 are a presentation of the situation for two widely different energy groups. At the moon's surface, (vacuum-matter interface) the flux would, of course, be considerably less than half of the maximum intensity within the lunar crust. This factor could be as much as 10, thus reducing the derived fluxes by a factor of 5.

From flights at 20,000 ft over Florida, we have confirmed the mean free path for cosmic ray protons in our atmosphere to be 145 g/cm². Thus, our atmosphere (1 kg/cm²) reduces the incident cosmic-ray proton flux by a factor of $\exp(-1000/145)$ or about

10^{-3} . One would, therefore, expect the thermal neutron flux at the moon's surface to be greater than on the earth by the factors, 1000 (lack of atmosphere) \times 2 (lack of magnetism) \times 2 (atomic mass yield) \times 2 (gravity turn around), i.e., greater by a factor of 8000. If the hydrogen content of the lunar surface is significant, the leakage of thermal neutrons will be even greater.⁽¹⁾

The thermal neutron flux at an air-land interface (Argonne) has been measured by its $^{14}\text{N}(n,p)^{14}\text{C}$ reaction to be 3.7×10^{-3} n/cm²/sec.⁽⁵⁾ Thus, at the moon's surface we estimate between 20 and 30 n/cm²/sec for thermal neutrons.

Our measurement of the fast neutron flux between 1 and 10 MeV gives a numerically similar value of 4×10^{-3} n/cm²/sec at the land-air interface. The gravity and decay effect are, of course, irrelevant; thus the flux will be relatively constant at 10-15 n/cm²/sec to a distance of about 2-3 moon radii before geometry begins to play a part.

As far as we can tell, none of the neutron leakage due to galactic protons striking the lunar surface is severe enough to produce significant dosage problems, at least as compared with the risk of solar flares. However, the thermal neutron cross section (varying as $1/v$) will be very great at or near the altitude of low-flying astronauts, e.g., 100-mile-high orbits. On the cold night side, for example, the astronaut tissue sodium could well be activated to ^{24}Na . It would be very informative for the future assessment of risk to personnel on the moon to count lunar astronauts in a whole-body counter. Resonant foils should accompany the expeditions; or at the very least, gold plating on electronic components can serve as thermal neutron detectors.

For future lunar projects, however, thermal neutrons are so easily shielded by a few millimeters of ^6LiF or ^{10}B that we see no reason at all to expose personnel to slow neutrons.

REFERENCES

1. Lingenfelter, R. E., Canfield, E. H., and Hess, W. N. *J. Geophys. Res.* **66**, 2665 (1961).
2. Kastner, J., Oltman, B. G., Marinelli, L. D., and Klems, J. Argonne National Laboratory Radiological Physics Division Annual Report, July 1963-June 1964. ANL-6938, p. 71.
3. Gold, R. *Phys. Rev.* **165**, 1406 (1968).
4. Spergel, M. *Health Phys.* **13**, 845 (1967).
5. Gold, R. *Phys. Rev.* **165**, 1411 (1968).

* Present address: Health Physics Division, Israel Atomic Energy Commission, Soreq, Israel.

† Reactor Physics Division.

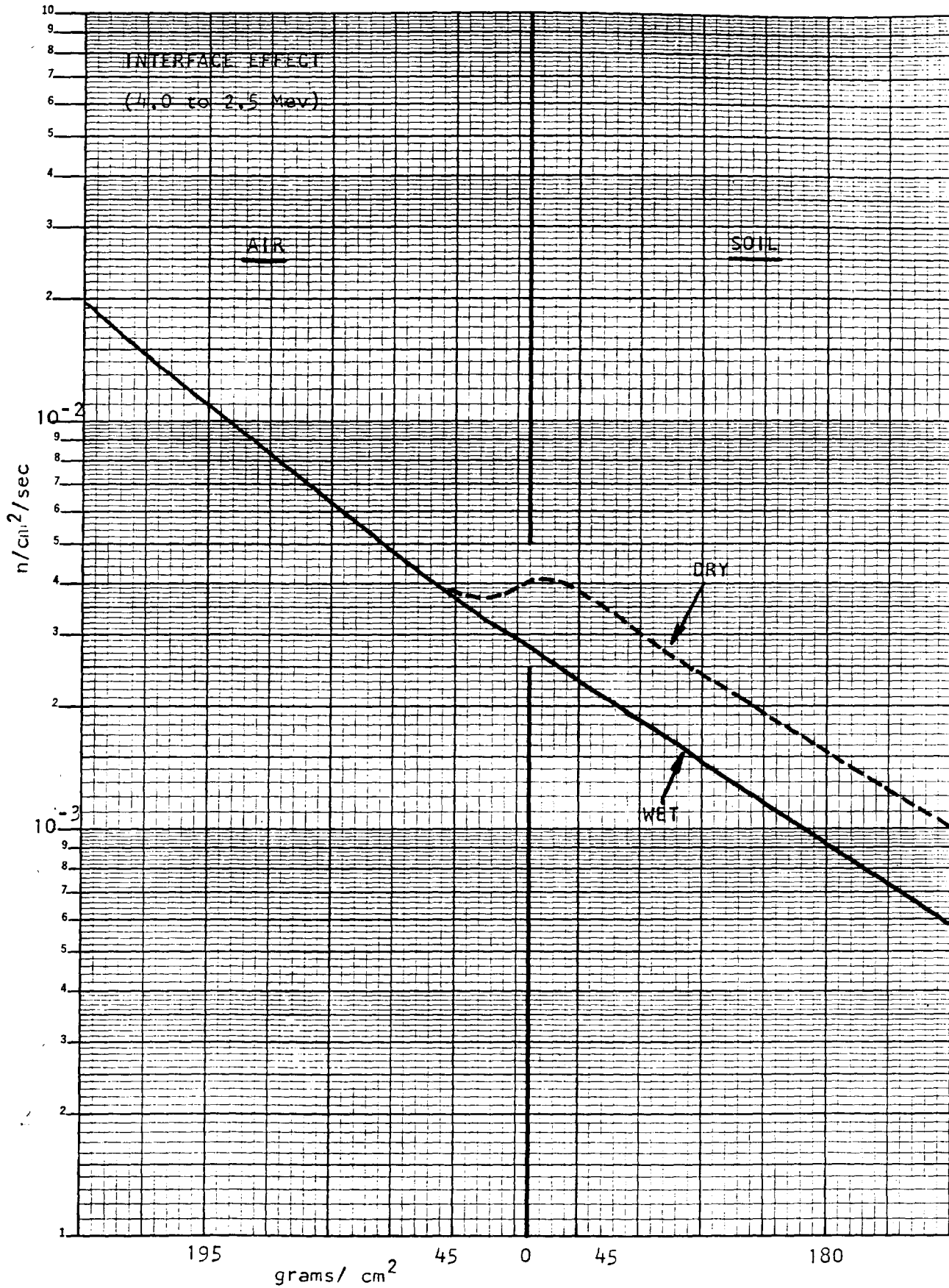


FIG. 161.—Effect of air-land interface on fast neutrons generated by cosmic-ray protons

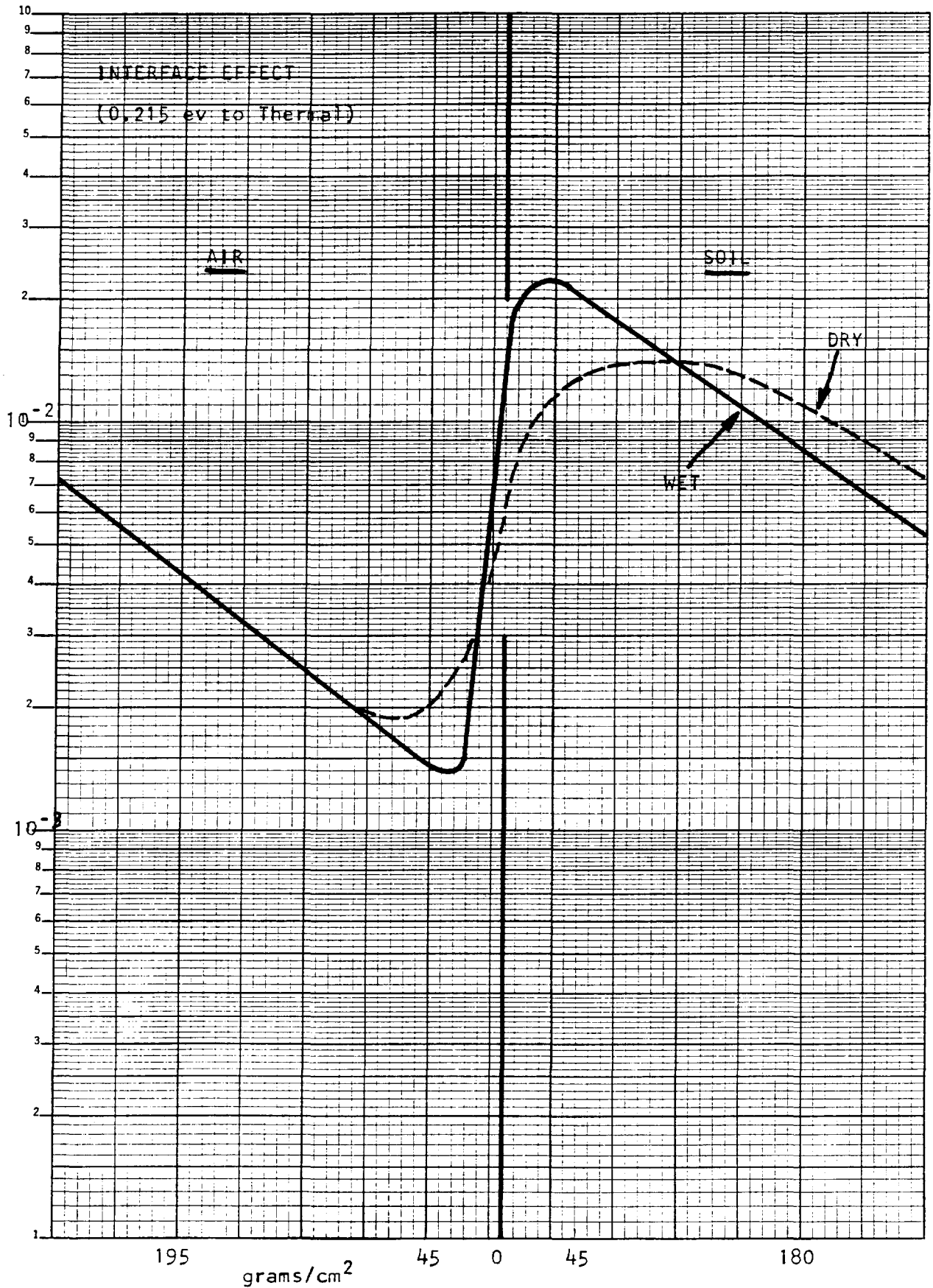


FIG. 162.—Effect of air-land interface on slow (thermal) neutrons generated by cosmic-ray protons

INELASTIC-SCATTERING CROSS SECTIONS OF FAST CHARGED PARTICLES BY Li^+ *

Y.-K. Kim and Mitio Inokuti

The cross sections for some important discrete excitations and for the total inelastic scattering of fast charged particles by Li^+ are evaluated directly from correlated wave functions and other data in the literature according to the Bethe procedure and related sum rules. Cross sections for other discrete excitations are determined by extrapolating their dependence on the effective quantum numbers. The ionization cross section is then obtained by subtracting the sum of all discrete excitation cross sections from the total inelastic scattering cross section, thus avoiding the direct use of any continuum wave functions. The resulting ionization cross section is reliable, and agrees very well with the experiment by Peart and Dolder.

The total inelastic-scattering cross section σ_{tot} for sufficiently fast charged particles of charge ze and velocity v is given by^(1, 2)

$$\sigma_{\text{tot}} = \frac{8\pi a_0^2 z^2}{mv^2/R} \left\{ M_{\text{tot}}^2 \left[\ln \left(\frac{\beta^2}{1 - \beta^2} \right) - \beta^2 \right] + C_{\text{tot}} \right\}, \quad (1)$$

where a_0 is the Bohr radius, m the electron mass, R the Rydberg energy, and $\beta = v/c$, c being the speed of light. The constants M_{tot}^2 and C_{tot} can be evaluated from the ground-state wave function and the optical (dipole) oscillator strength distribution of the target system.⁽²⁾ The ground-state wave function of Li^+ computed by Weiss⁽³⁾ leads to $M_{\text{tot}}^2 = 0.2860$, in complete agreement with a more accurate result of Pekeris.⁽⁴⁾ The value $I_1 - I_2 = 0.6280$ (in the notation of Reference 2) obtained from the Weiss wave function should, therefore, be very reliable. Furthermore, a value of $L(-1) = 0.526 \pm 0.015$ [see Reference 2 for the definition of $L(-1)$] was adopted on the basis of the oscillator-strength distribution in the literature.⁽³⁻⁷⁾ The value of $C_{\text{tot}} = -2L(-1) + I_1 - I_2 + M_{\text{tot}}^2 \ln(2mc^2/R)$ is given in Table 70.

The Bethe cross sections for discrete excitations are also given by⁽⁸⁾

$$\sigma_n = \frac{8\pi a_0^2 z^2}{mv^2/R} \left\{ M_n^2 \left[\ln \left(\frac{\beta^2}{1 - \beta^2} \right) - \beta^2 \right] + C_n \right\} \quad (2)$$

for an (optically) allowed transition, and

$$\sigma_n = \frac{8\pi a_0^2 z^2}{mv^2/R} b_n \quad (3)$$

for a forbidden transition. The constants M_n^2 , C_n and b_n

TABLE 70. PARAMETERS FOR THE BETHE CROSS SECTIONS OF Li^+

	M^2	C
Total	0.2860	2.787
Discrete excitation	0.1414	1.224
Ionization	0.1446	1.563

can be calculated from wave functions directly (see Sec. 5 of Reference 8).

Weiss⁽³⁾ calculated for Li^+ very accurate wave functions not only for the ground state but also for the 2^1S , 2^1P , 3^1S , 3^1P and 3^1D states, and Perkins⁽⁹⁾ computed correlated wave functions for the 4^1S , 5^1S , 6^1S and 7^1S states with similar accuracy. From these wave functions one can evaluate accurate Bethe cross sections for the excitations to the above-mentioned discrete states and eventually to higher discrete states by extrapolation.

The values of M_n^2 , C_n and b_n are listed in Table 71. The sum of all discrete (single) excitation cross sections σ_{exc} can be expressed in the form similar to Eq. (1) with two constants M_{exc}^2 and C_{exc} . These constants are defined as

$$M_{\text{exc}}^2 = \sum (\text{discrete}) M_n^2, \quad (4)$$

and

$$C_{\text{exc}} = \sum (\text{discrete}) [C_n + b_n], \quad (5)$$

respectively. The results thus obtained are given in Table 70.

Once the values of M^2 and C are known for σ_{tot} and σ_{exc} , one can evaluate the "counting" ionization cross section σ_{ion} by subtraction:

$$\begin{aligned} \sigma_{\text{ion}} &\equiv \sigma_{\text{tot}} - \sigma_{\text{exc}} \\ &= \frac{8\pi a_0^2 z^2}{mv^2/R} \left\{ M_{\text{ion}}^2 \left[\ln \left(\frac{\beta^2}{1 - \beta^2} \right) - \beta^2 \right] + C_{\text{ion}} \right\}. \quad (6) \end{aligned}$$

This method leads to an accurate ionization cross section without calculating the continuum wave functions directly. The same method was applied successfully to He as explained elsewhere in this report.⁽¹⁰⁾ The values of M_{ion}^2 and C_{ion} are listed in Table 70.

The uncertainty in σ_{exc} is about the same as that in σ_{tot} .[†] When appropriate values of the constants are substituted, one gets

[†] The generalized oscillator strengths of Li^+ computed from the Weiss and Perkins wave functions in the length and velocity formulas agree with each other within 1% or better.

* Principal results of this work presented at the VIth International Conference on the Physics of Electronic and Atomic Collisions (VI ICPEAC), Cambridge, Massachusetts, July 28-Aug. 2, 1969.

$$\sigma_{\text{tot}} = \frac{z^2}{\beta^2} \left\{ 0.536 \left[\ln \left(\frac{\beta^2}{1 - \beta^2} \right) - \beta^2 \right] + 5.22 \pm 0.03 \right\} \times 10^{-20} \text{ cm}^2, \quad (7a)$$

$$\sigma_{\text{exc}} = \frac{z^2}{\beta^2} \left\{ 0.265 \left[\ln \left(\frac{\beta^2}{1 - \beta^2} \right) - \beta^2 \right] + 2.29 \pm 0.03 \right\} \times 10^{-20} \text{ cm}^2, \quad (7b)$$

and

$$\sigma_{\text{ion}} = \frac{z^2}{\beta^2} \left\{ 0.271 \left[\ln \left(\frac{\beta^2}{1 - \beta^2} \right) - \beta^2 \right] + 2.93 \pm 0.06 \right\} \times 10^{-20} \text{ cm}^2. \quad (7c)$$

These cross sections—actually $\sigma\beta^2/z^2$ —are plotted against $\ln [\beta^2/(1 - \beta^2)] - \beta^2$ in Figure 163, along with the Bethe cross section for the 2^1P excitation.

TABLE 71. PARAMETERS FOR THE BETHE CROSS SECTIONS FOR DISCRETE EXCITATION OF Li^+

n	Allowed transition (n^1P)		Forbidden transition ^(a)	
	M_n^2	C_n	$b(n^1S)$	$b(n^1D)$
2	0.0998	0.835	0.022	
3	0.0216	0.183	0.005	0.002
4	0.0082	0.069	0.002	0.001
$n \geq 5^{(b)}$	$\frac{0.461}{(n^*)^3} + \frac{1.09}{(n^*)^5}$	$\frac{3.95}{(n^*)^3} + \frac{8.04}{(n^*)^5}$	$\frac{0.105}{(n^*)^3} + \frac{0.148}{(n^*)^5}$	$\frac{0.0752}{(n^*)^3} + \frac{0.135}{(n^*)^5}$
$\sum_{n \geq 5}$	0.0118	0.100	0.003	0.002
$\sum_{\text{all } n}$	0.1414	1.187	0.032	0.005

^(a) The sum of $b(n^1F)$ and higher excitations is estimated at $\sim 1\%$ of $\sum b(n^1D)$, and is neglected in evaluating C_{exc} .

^(b) $n^* = n + \delta$, where $\delta = -0.074, 0.0136$ and -0.001 for the $^1S, ^1P$ and 1D states, respectively.

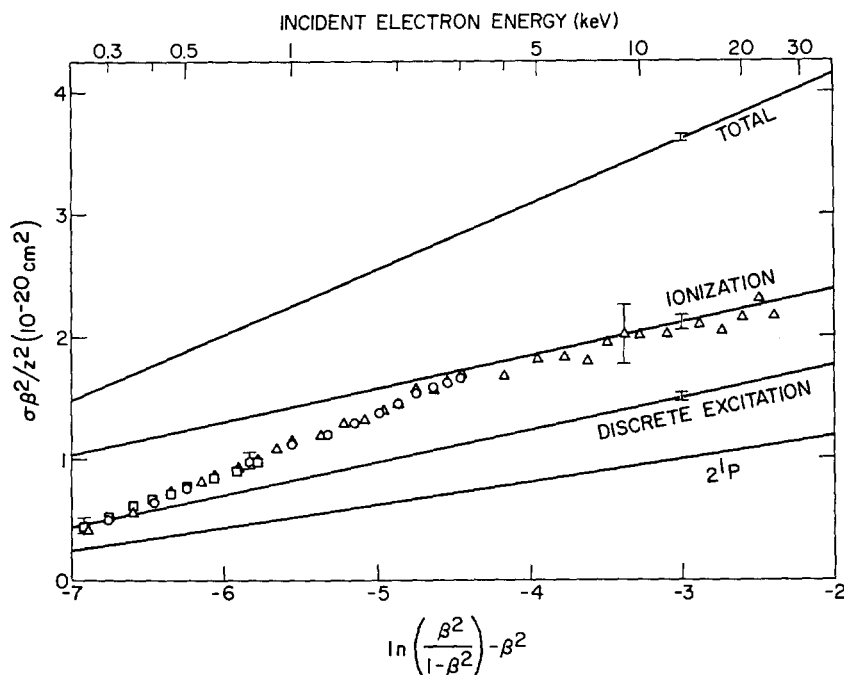


FIG. 163.—The Bethe cross sections of Li^+ . The ordinate is the cross section $\times (\beta/z)^2$, where $\beta = v/c$ is the velocity in units of the speed of light and ze is the charge of the incident particle. The squares are the experimental data by Lineberger, Hooper, and McDaniel,⁽⁴¹⁾ the circles are those by Peart and Dolder,⁽⁴²⁾ and the triangles are more recent data also by Peart and Dolder.⁽⁴³⁾ Only representative error limits are shown for the experimental data. The error limits for the theoretical cross sections given at $\ln [\beta^2/(1 - \beta^2)] - \beta^2 = -3$ are independent of incident energy, contrary to the tendency in experiment.

There are four sets of experimental ionization cross sections of Li^+ , all measured by crossed beam methods.⁽¹¹⁻¹⁴⁾ These experiments measure the absolute cross section for single ionization only, but the double ionization cross section is negligible.* Figure 163 shows that the theory and experiment agree very well in the asymptotic region (incident electron energy $\gtrsim 5$ keV).

A more detailed account of this work is being prepared for publication elsewhere.

The authors would like to express their gratitude to Dr. A. W. Weiss of the National Bureau of Standards and to Dr. J. F. Perkins of the Redstone Arsenal for providing the wave functions. The authors are also indebted to Dr. K. Dolder of the University of Newcastle upon Tyne for communicating prior to publication the experimental data quoted in References 14 and 15.

* The cross section for double ionization is at least two orders of magnitude smaller than the single ionization cross section for the incident electron energy of $\gtrsim 500$ eV.⁽¹⁵⁾

FORM FACTORS OF H^- , He , AND Li^+

Y.-K. Kim

Atomic form factors and incoherent scattering functions are necessary in evaluating the cross sections for the coherent and incoherent scattering of photons as well as those for the elastic and inelastic scattering of charged particles by atoms and molecules. Accurate atomic form factors, incoherent scattering functions, and the Born elastic electron scattering factors for the ground states of H^- , He , and Li^+ have been computed from correlated wave functions. The data presented are in good agreement with those evaluated from less accurate wave functions, and confirm the expectation that the electron correlation affects the values of incoherent scattering functions more than those of atomic form factors. Values of some integrals which are used in the sum rule for the Bethe cross sections are also tabulated.

This report is an extension of earlier ones^(1, 2) on the atomic form factors $F(K)$ and incoherent-scattering functions $S_{\text{inc}}(K)$ of H^- and He . Similar data on Li^+ are also presented.

The functions $F(K)$ and $S_{\text{inc}}(K)$ for an atom or ion with N electrons are defined as

$$F(K) = \sum_{j=1}^N \langle \exp(i\mathbf{K} \cdot \mathbf{r}_j) \rangle, \quad (1)$$

and

$$S_{\text{inc}}(K) = N^{-1} \left\{ \sum_{j,k=1}^N \langle \exp[i\mathbf{K} \cdot (\mathbf{r}_j - \mathbf{r}_k)] \rangle - |F(K)|^2 \right\}, \quad (2)$$

REFERENCES

1. Bethe, H. *Ann. Physik* **5**, 325 (1930).
2. Inokuti, M., Kim, Y.-K., and Platzman, R. L. *Phys. Rev.* **164**, 55 (1967).
3. Weiss, A. W. *J. Res. Natl. Bur. Std.* **71A**, 163 (1967).
4. Pekeris, C. L. *Phys. Rev.* **126**, 143 (1962).
5. Stewart, A. L. and Webb, T. G. *Proc. Phys. Soc. (London)* **82**, 532 (1963).
6. Bell, K. L., and Kingston, A. E. *Proc. Phys. Soc. (London)* **90**, 337 (1967).
7. Dalgarno, A., and Parkinson, E. M. *Proc. Roy. Soc. (London)* **A301**, 253 (1967).
8. Kim, Y.-K., and Inokuti, M. *Phys. Rev.* **175**, 176 (1968).
9. Perkins, J. F. *Phys. Rev.* **151**, 80 (1966).
10. Inokuti, M., and Kim, Y.-K. Total Cross Sections for Inelastic Scattering of Charged Particles by Atoms and Molecules. III. Accurate Bethe Cross Section for Ionization of Helium. This report.
11. Lineberger, W. C., Hooper, J. W., and McDaniel, E. W. *Phys. Rev.* **141**, 151 (1966).
12. Wareing, J. B., and Dolder, K. T. *Proc. Phys. Soc. (London)* **91**, 887 (1967).
13. Peart, B., and Dolder, K. T. *J. Phys.* **B1**, 872 (1968).
14. Peart, B., and Dolder, K. T. Private communication (1969).
15. Peart, B., and Dolder, K. T. Private communication (1969).

TABLE 72. TOTAL ENERGIES AND EXPECTATION VALUES OF r_1^2 AND r_{12}^2 COMPUTED FROM THE WEISS AND PEKERIS WAVE FUNCTIONS IN ATOMIC UNITS

Property	Atom		
	H^-	He	Li^+
Total energy			
Weiss ⁽⁴⁾	-0.5277475	-2.903724	-7.279913
Pekeris ⁽⁵⁻⁷⁾	-0.5277510	-2.903724	-7.279913
$\langle r_1^2 \rangle$			
Weiss	11.928	1.19348	0.446279
Pekeris	11.914	1.19348	0.446279
$\langle r_{12}^2 \rangle$			
Weiss	25.239	2.51643	0.927065
Pekeris	25.202	2.51644	0.927065

respectively, where $\langle \rangle$ denotes an expectation value in the ground state, $\mathbf{K}\hbar$ the momentum transfer, and \mathbf{r}_j the coordinate vector of the j th electron from the nucleus. Furthermore, in the Born approximation, the elastic electron scattering factor $f_{\text{el}}(K)$, which is defined by

$$f_{\text{el}}(K) = [Z - F(K)] / (Ka_0)^2, \quad (3)$$

where a_0 is the Bohr radius, is closely related to the differential cross section $d\sigma_{\text{el}}$ for the elastic scattering of electrons by an atom of nuclear charge Ze . [See

Reference 1, Eqs. (3)-(6) for various cross sections related to the functions defined above.] In addition, knowledge of $S_{\text{inc}}(K)$ enables one to evaluate integrals I_1 and I_2 defined by Eqs. (18) and (19) of Reference 3. These integrals are required in the evaluation of the total inelastic-scattering cross section.⁽³⁾ For the evaluation of $F(K)$ and $S_{\text{inc}}(K)$, accurate ground-state wave functions for H^- , He, and Li^+ computed by Weiss⁽⁴⁾ have been used. The Weiss wave functions compare very favorably with more elaborate ones cal-

TABLE 73. ATOMIC FORM FACTOR, INCOHERENT SCATTERING FUNCTION, AND ELASTIC ELECTRON SCATTERING FACTOR OF H^- , COMPUTED FROM THE 39-TERM WEISS WAVE FUNCTION^(a)

$(Ka_0)^2$	$F(K)^{(b)}$	$2S_{\text{inc}}(K)$	$[1 - F(K)]/(Ka_0)^2$
0.01	1.96127D 00	7.18329D-02	-9.61272D 01
0.02	1.92450D 00	1.37988D-01	-4.62251D 01
0.03	1.88951D 00	1.99110D-01	-2.96504D 01
0.04	1.85616D 00	2.55751D-01	-2.14040D 01
0.05	1.82432D 00	3.08390D-01	-1.64864D 01
0.06	1.79388D 00	3.57446D-01	-1.32314D 01
0.07	1.76472D 00	4.03279D-01	-1.09246D 01
0.08	1.73677D 00	4.46207D-01	-9.20965D 00
0.09	1.70993D 00	4.86508D-01	-7.88813D 00
0.10	1.68413D 00	5.24426D-01	-6.84132D 00
0.20	1.47071D 00	8.10130D-01	-2.35356D 00
0.30	1.31270D 00	9.95089D-01	-1.04234D 00
0.40	1.18901D 00	1.12837D 00	-4.72529D-01
0.50	1.08852D 00	1.23125D 00	-1.77044D-01
0.60	1.00465D 00	1.31434D 00	-7.75300D-03
0.70	9.33213D-01	1.38352D 00	9.54103D-02
0.80	8.71396D-01	1.44234D 00	1.60755D-01
0.90	8.17216D-01	1.49312D 00	2.03094D-01
1.00	7.69230D-01	1.53743D 00	2.30770D-01
2.00	4.76417D-01	1.78725D 00	2.61792D-01
3.00	3.34143D-01	1.88564D 00	2.21952D-01
4.00	2.50139D-01	1.93209D 00	1.87465D-01
5.00	1.95288D-01	1.95662D 00	1.60942D-01
6.00	1.57109D-01	1.97067D 00	1.40482D-01
7.00	1.29306D-01	1.97922D 00	1.24385D-01
8.00	1.08359D-01	1.98469D 00	1.11455D-01
9.00	9.21484D-02	1.98833D 00	1.00872D-01
10.00	7.93263D-02	1.99083D 00	9.20674D-02
20.00	2.64176D-02	1.99754D 00	4.86791D-02
30.00	1.25867D-02	1.99830D 00	3.29138D-02
40.00	7.00331D-03	1.99848D 00	2.48249D-02
50.00	4.20556D-03	1.99855D 00	1.99159D-02
60.00	2.60660D-03	1.99858D 00	1.66232D-02
70.00	1.60776D-03	1.99859D 00	1.42627D-02
80.00	9.42350D-04	1.99860D 00	1.24882D-02
90.00	4.76910D-04	1.99861D 00	1.11058D-02
100.00	1.38660D-04	1.99861D 00	9.99861D-03

^(a) See Eqs. (1)-(3) of text for definitions.

^(b) FORTRAN notation is used, i.e., 1.38660D-04 = 1.38660×10^{-4} .

TABLE 74. ATOMIC FORM FACTOR, INCOHERENT SCATTERING FUNCTION, AND ELASTIC ELECTRON SCATTERING FACTOR OF He, COMPUTED FROM THE 53-TERM WEISS WAVE FUNCTION^(a)

$(Ka_0)^2$	$F(K)^{(b)}$	$2S_{\text{inc}}(K)$	$[2 - F(K)]/(Ka_0)^2$
0.0	2.0	0.0	3.97826D-01
0.01	1.99603D 00	7.50431D-03	3.97161D-01
0.02	1.99207D 00	1.49676D-02	3.96503D-01
0.03	1.98812D 00	2.23900D-02	3.95847D-01
0.04	1.98419D 00	2.97721D-02	3.95193D-01
0.05	1.98027D 00	3.71139D-02	3.94540D-01
0.06	1.97637D 00	4.44158D-02	3.93889D-01
0.07	1.97247D 00	5.16780D-02	3.93240D-01
0.08	1.96859D 00	5.89010D-02	3.92594D-01
0.09	1.96472D 00	6.60849D-02	3.91949D-01
0.10	1.96087D 00	7.32300D-02	3.91306D-01
0.20	1.92300D 00	1.42608D-01	3.84986D-01
0.30	1.88634D 00	2.08396D-01	3.78857D-01
0.40	1.85084D 00	2.70835D-01	3.72909D-01
0.50	1.81643D 00	3.30146D-01	3.67136D-01
0.60	1.78308D 00	3.86534D-01	3.61530D-01
0.70	1.75074D 00	4.40184D-01	3.56084D-01
0.80	1.71937D 00	4.91272D-01	3.50792D-01
0.90	1.68892D 00	5.39955D-01	3.45647D-01
1.0	1.65936D 00	5.86383D-01	3.40643D-01
2.0	1.40544D 00	9.52267D-01	2.97278D-01
3.0	1.20998D 00	1.19565D 00	2.63340D-01
4.0	1.05559D 00	1.36569D 00	2.36103D-01
5.0	9.31046D-01	1.48910D 00	2.13791D-01
6.0	8.28811D-01	1.58143D 00	1.95198D-01
7.0	7.43639D-01	1.65222D 00	1.79480D-01
8.0	6.71777D-01	1.70760D 00	1.66028D-01
9.0	6.10480D-01	1.75165D 00	1.54391D-01
10.0	5.57690D-01	1.78721D 00	1.44231D-01
20.0	2.74195D-01	1.93738D 00	8.62902D-02
30.0	1.65370D-01	1.97403D 00	6.11543D-02
40.0	1.11224D-01	1.98696D 00	4.72194D-02
50.0	8.01375D-02	1.99258D 00	3.83973D-02
60.0	6.05662D-02	1.99539D 00	3.23239D-02
70.0	4.74192D-02	1.99693D 00	2.78940D-02
80.0	3.81503D-02	1.99785D 00	2.45231D-02
90.0	3.13653D-02	1.99843D 00	2.18737D-02
100.0	2.62469D-02	1.99882D 00	1.97375D-02

^(a) See Eqs. (1)-(3) of text for definitions.

^(b) FORTRAN notation is used, i.e., 2.62469D-02 = 2.62469×10^{-2} .

culated by Pekeris⁽⁵⁻⁷⁾ in terms of the total energies, as well as some other expectation values (Table 72).

In Tables 73, 74, and 75, we present $F(K)$, $S_{\text{inc}}(K)$, and $f_{\text{el}}(K)$ computed from the Weiss wave functions for H^- , He, and Li^+ , respectively. Numerical data in Tables 73-75 are given to six significant figures to allow for reliable interpolation. The values of the integrals I_1 and I_2 are given in Table 76.

TABLE 75. ATOMIC FORM FACTOR, INCOHERENT SCATTERING FUNCTION, AND ELASTIC ELECTRON SCATTERING FACTOR OF Li^+ , COMPUTED FROM THE 53-TERM WEISS WAVE FUNCTION^(a)

$(Ka_0)^2$	$F(K)^{(b)}$	$2S_{\text{inc}}(K)$	$[3 - F(K)]/(Ka_0)^2$
0.01	1.99851D 00	2.85738D-03	1.00149D 02
0.02	1.99703D 00	5.70916D-03	5.01486D 01
0.03	1.99555D 00	8.55538D-03	3.34818D 01
0.04	1.99406D 00	1.13960D-02	2.51484D 01
0.05	1.99258D 00	1.42311D-02	2.01483D 01
0.06	1.99111D 00	1.70607D-02	1.68149D 01
0.07	1.98963D 00	1.98848D-02	1.44339D 01
0.08	1.98816D 00	2.27034D-02	1.26481D 01
0.09	1.98668D 00	2.55164D-02	1.12591D 01
0.10	1.98521D 00	2.83240D-02	1.01479D 01
0.20	1.97060D 00	5.61020D-02	5.14701D 00
0.30	1.95615D 00	8.33466D-02	3.47949D 00
0.40	1.94188D 00	1.10071D-01	2.64530D 00
0.50	1.92777D 00	1.36288D-01	2.14446D 00
0.60	1.91382D 00	1.62010D-01	1.81030D 00
0.70	1.90003D 00	1.87248D-01	1.57138D 00
0.80	1.88640D 00	2.12014D-01	1.39199D 00
0.90	1.87293D 00	2.36319D-01	1.25230D 00
1.00	1.85961D 00	2.60174D-01	1.14039D 00
2.00	1.73430D 00	4.76156D-01	6.32852D-01
3.00	1.62191D 00	6.57074D-01	4.59363D-01
4.00	1.52069D 00	8.09871D-01	3.69829D-01
5.00	1.42914D 00	9.39891D-01	3.14171D-01
6.00	1.34605D 00	1.05129D 00	2.75658D-01
7.00	1.27037D 00	1.14735D 00	2.47090D-01
8.00	1.20122D 00	1.23065D 00	2.24848D-01
9.00	1.13784D 00	1.30329D 00	2.06907D-01
10.00	1.07959D 00	1.36695D 00	1.92041D-01
20.00	6.86344D-01	1.72002D 00	1.15683D-01
30.00	4.78842D-01	1.85253D 00	8.40386D-02
40.00	3.54802D-01	1.91336D 00	6.61299D-02
50.00	2.74256D-01	1.94508D 00	5.45149D-02
60.00	2.18770D-01	1.96316D 00	4.63538D-02
70.00	1.78812D-01	1.97417D 00	4.03027D-02
80.00	1.49023D-01	1.98124D 00	3.56372D-02
90.00	1.26190D-01	1.98597D 00	3.19312D-02
100.00	1.08283D-01	1.98925D 00	2.89172D-02

^(a) See Eqs. (1)–(3) of text for definitions.

^(b) FORTRAN notation is used, i.e., 1.08283D-01 = 1.08283×10^{-1} .

H^-

The 39-term Weiss wave function for H^- is somewhat less accurate than the 444-term Pekeris wave function⁽⁵⁾, judging from the expectation values (Table 72), and the reliability of the data in Table 73 is expected to be of the order of 1%.

The data in Table 73 agree well ($\sim 1\%$ or better) with those presented in Appendix I of Reference 2, which were computed from the 20-term Hylleraas wave function by Hart and Herzberg.⁽⁸⁾ An interesting fea-

ture in $f_{e1}(K)$ of H^- is the node near $(Ka_0)^2 = 0.6$. In the Born approximation, this type of node should be present in $f_{e1}(K)$ of all negative ions, and the node results in a zero-minimum in $d\sigma_{e1}$. For H^- , however, the minimum occurs in the forward direction where the Born approximation may not be applicable because of the large polarization effect when the incident electron energy is moderate. The present values of I_1 and I_2 confirm the extrapolated value of $I_1 - I_2$ used in Reference 2. The present result also agrees very well with slightly more accurate values of the integrals computed by Rotenberg and Stein.⁽⁹⁾ The new result reduces the uncertainty of the total inelastic-scattering cross section in Reference 2 by about one third.

He

As can be seen from the expectation values of He in Table 72, the 53-term Weiss wave function for He is, for all practical purposes, as good as the 1078-term Pekeris wave function.⁽⁶⁾

The data in Table 74 agree very well ($\sim 0.1\%$ or better) with those (see Tables I–III of Reference 1) computed from the 20-term Hylleraas wave function by Hart and Herzberg.⁽⁸⁾ The reliability of the data in Table 74 is expected to be of the order of 0.1%. The integrals (Table 76) from the Weiss wave function are only slightly different from the values used in Reference 3.

Li^+

The Li^+ ion is more hydrogenic than H^- and He, and one expects $F(K)$ and $S_{\text{inc}}(K)$ of Li^+ to be less sensitive to the choice of wave functions. The 53-term Weiss wave function for Li^+ is, as can be seen from Table 72, almost as precise as the 444-term wave function by Pekeris,⁽⁷⁾ and the data in Table 75 are expected to be correspondingly accurate. The values of $F(K)$

TABLE 76. VALUES OF I_1 AND I_2 ^(a) COMPUTED FROM VARIOUS WAVE FUNCTIONS

	H^-	He	Li^+
I_1			
Present work	1.787	1.0811	0.6549
From 20-term Hylleraas ^(2, 3)	1.788	1.0811	
I_2			
Present work	12.386	0.1850	0.0269
From 20-term Hylleraas	11.153	0.1849	
$I_1 - I_2$			
Present work	-10.598	0.8961	0.6280
From 20-term Hylleraas	-9.365	0.8962	
Extrapolation ^(2, 3)	-10.5	0.8962	
Rotenberg and Stein ⁽⁹⁾	-10.665		

^(a) Defined by Eqs. (18) and (19) of Reference 3.

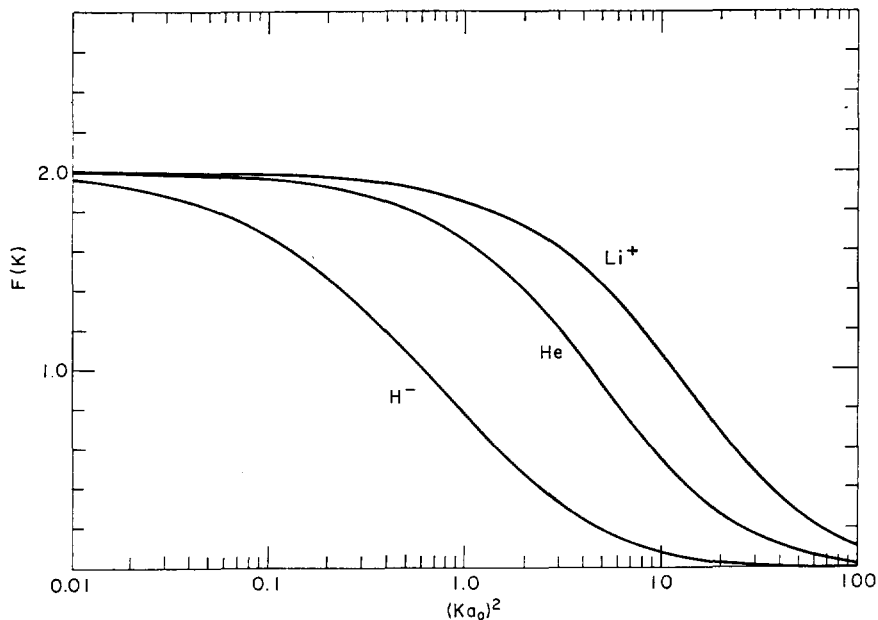


FIG. 164.—Atomic form factors of H^- , He, and Li^+ [see Eq. (1) of the text] versus the square of momentum transfer in atomic units.

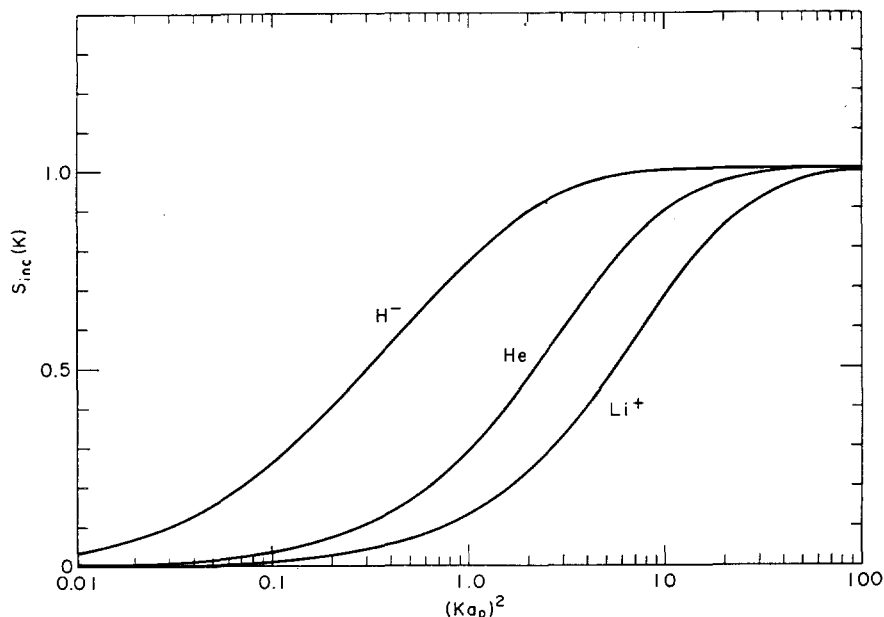


FIG. 165.—Incoherent scattering functions of H^- , He, and Li^+ [see Eq. (2) of the text] versus the square of momentum transfer in atomic units.

computed from a 3-term Hylleraas wave function by Hurst⁽¹⁰⁾ are in good agreement with those in Table 75, confirming the expectation that the electron correlation is less important in the evaluation of $F(K)$.⁽¹⁾ The values of $S_{inc}(K)$ for Li^+ calculated by Freeman⁽¹¹⁾ are larger than those in Table 75 by $\sim 5\%$ in the region $5 \lesssim (Ka_0)^2 \leq 50$, but agree reasonably well for $(Ka_0)^2 \lesssim 5$. In He, we found that a larger deviation is found toward smaller K . Freeman⁽¹¹⁾ used a simple self-consistent-field wave function by Fock and Petra-

shen.⁽¹²⁾ The integrals for Li^+ in Table 76 have been used in the determination of total inelastic-scattering cross section reported elsewhere.⁽¹³⁾

The functions $F(K)$ and $S_{inc}(K)$ are plotted in Figures 164 and 165, respectively. As is clear from Figure 165, $S_{inc}(K)$ for H^- is large, resulting in a large inelastic scattering cross section [see Eq. (6) of Reference 1], and vice versa for Li^+ . The figures show that H^- has a "soft" and Li^+ a "hard" electronic structure compared to that of He.

The author is indebted to Dr. A. W. Weiss for providing the wave functions, and to Dr. M. Inokuti for many helpful discussions.

REFERENCES

1. Kim, Y.-K., and Inokuti, M. *Phys. Rev.* **165**, 39 (1968).
2. Inokuti, M., and Kim, Y.-K. *Phys. Rev.* **173**, 154 (1968).
3. Inokuti, M., Kim, Y.-K., and Platzman, R. L. *Phys. Rev.* **164**, 55 (1967).
4. Weiss, A. W. *J. Res. Natl. Bur. Std.* **71A**, 163 (1967).
5. Pekeris, C. L. *Phys. Rev.* **126**, 1470 (1962).
6. Pekeris, C. L. *Phys. Rev.* **115**, 1216 (1959).
7. Pekeris, C. L. *Phys. Rev.* **126**, 143 (1962).
8. Hart, J. F. and Herzberg, G. *Phys. Rev.* **106**, 79 (1957).
9. Rotenberg, M. and Stein, J. *Phys. Rev.* **182**, 1 (1969).
10. Hurst, R. P. *Acta Cryst.* **13**, 634 (1960).
11. Freeman, A. J. *Acta Cryst.* **13**, 190 (1960).
12. Fock, V. and Petrashen, M. J. *Phys. Z. Sowjet.* **8**, 547 (1935).
13. Kim, Y.-K. and Inokuti, M. Inelastic-Scattering Cross Sections of Fast Charged Particles by Li^+ . This report.

THE NUMBER OF BOUND STATES IN ION-ATOM SYSTEMS

Smio Tani* and Mito Inokuti

The knowledge of the number of bound states and density of states of a molecular ion is very useful in the analysis of molecular spectra and also in the study of ion-atom scattering at low incident energy. The WKB approximation in quantum mechanics has been used to estimate the total number of bound states and the density of states for the ion-atom complex represented by a simple parameter.

The purpose of this work is to provide, in a quick estimate, parameters concerning bound states of an ion with a neutral atom. Accordingly, we assume that the polarization (r^{-4}) potential plays the most essential role,⁽¹⁾ and extend it to a distance which is a sum of effective radii of the ion and the atom. Inside we assume an infinitely high repulsive potential (hard core) for the sake of mathematical simplicity. The parameters we deal with are (1) the number of bound states for each rotational quantum number, (2) the density of bound states per unit energy interval, and (3) the radius of the largest classical orbit. In the above-mentioned simplified model, the polarizability α of the neutral atom,⁽²⁾ the reduced mass μ of the system, and the ionic and the atomic radii⁽³⁾ a_{ion} and $a_{\text{neutr.}}$ will appear only in a combination of the form

$$z = \sqrt{a\mu}/(a_{\text{ion}} + a_{\text{neutr.}}),$$

where all quantities will be expressed in atomic units. Therefore, a handy tabulation of the results is possible by using values of z as indices.

The zero-energy resonances in this model can be determined from the zeros of a Bessel function.⁽⁴⁾ We consider the rotational quantum number (J) as a continuously varying parameter.† When the parameter z

introduced above is known, the upper limit of J will be determined for each vibrational quantum number (v). The results will be presented in the form of an extensive table, and we can estimate the possible number of bound states straightforwardly. Besides being of direct help in the spectroscopy of molecular ions, the location of such resonances for variable J (Regge poles) is greatly relevant to the study of ion-atom scattering at very low energies. This is so because, as energy is raised above zero, these resonances continue to exist with a complex value of angular momenta, and some of them may be significant as a cause of a rainbow or a glory.*

Both quantum numbers, J and v , can take large values. Then, the situation is semiclassical. Namely, an estimate based on classical mechanics is quite close to the rigorous result, and the WKB approximation is valid. Therefore, we shall use this method in the evaluation of the density of the states. Since the problem is characterized by a single parameter z in the case of $J = 0$, we shall investigate this case in detail. It turns out that only a small correction is necessary for a non-vanishing value of J , unless J is very large. The orbital radius for a high lying level is large. If other atoms or ions are encountered along such a large orbit, the spectral line of a high lying level will be shifted. The density effect of the same kind in which an electron is orbiting instead of an ion was first discussed by Fermi.⁽⁶⁾ It is planned to derive an effective value of the largest orbital radius, which will serve as a critical parameter in the shift of spectral lines of high lying levels.

* Visiting Scientist for the period of July–August, 1969; permanent address: Physics Department, Marquette University, Milwaukee, Wisconsin, 53233.

† A resonance considered as a function of angular momentum is called a Regge pole and is well studied in scattering theory. (See, for example, Reference 5.)

* The quantal effect of the $\text{Li}^+\text{-He}$ scattering was studied by Weber and Bernstein;⁽⁶⁾ in the case of H-H , in which the potential behaves like r^{-9} at a large distance, an extensive tabulation and drawing of graphs was made by Waech and Bernstein;⁽⁷⁾ although there is a difference between the nature of their problem and ours, presentation of the final result has certain common aspects in these two cases.

REFERENCES

1. Vogt, E. and Wannier, G. H. *Phys. Rev.* **95**, 1190 (1954).
2. Dalgarno, A. *Adv. in Phys.* **11**, 281 (1962).
3. Pauling L. *The Nature of Chemical Bond*, Cornell Univ., Press, 1960, 3rd. ed., Ch. 13; also Hirschfelder, J. O., Curtiss, C. F., and Bird, R. B. *Molecular Theory of Gases and Liquids*. Wiley, New York, 1964.
4. O'Malley, T. F., Spruch, L., and Rosenberg, L. *J. Math. Phys.* **2**, 491 (1961).
5. Newton, R. *Scattering Theory of Particles and Waves*. McGraw-Hill, New York, 1966.
6. Weber, G. G. and Bernstein, R. B. *J. Chem. Phys.* **42**, 2166 (1965).
7. Waech, T. G. and Bernstein, R. B. *J. Chem. Phys.* **46**, 4905 (1967).
8. Fermi, E. *Nuovo cimento* **11**, 157 (1934); for further references, see Breene, R. G., Jr. *The Shift and Shape of Spectral Lines*. Pergamon Press, New York, 1961, Ch. 7.

GENERALIZED OSCILLATOR STRENGTHS OF THE HELIUM ATOM. III. TRANSITIONS FROM THE GROUND STATE TO THE 3^1D AND 4^1P STATES*

Y.-K. Kim and Mitio Inokuti

The generalized oscillator strengths of He for the $1^1S \rightarrow 3^1D$ and 4^1P transitions have been calculated with correlated wave functions, according to both the length and velocity formulas. The agreement between

the two alternative results is within 3% or less for moderate values of the momentum transfer. The resulting Born cross sections for charged-particle impact are also given. Compared with our values, available experimental data on the 3^1D excitation are substantially larger, while for the 4^1P excitation they agree within $\pm 50\%$.

* Abstract of an article published in *Phys. Rev.* **184**, 38-43 (August 5, 1969).

SPECIFIC PRIMARY IONIZATION

F. F. Rieke and William Prepejchal

Primary ionization cross sections have been measured for 16 additional gases. Present and previous results are summarized in graphical form. New measurements show that high-energy positrons and electrons have primary ionization cross sections that are equal within one percent.

Primary ionization cross sections have been measured for 16 new gases, supplementing work reported earlier⁽¹⁾. The results are given in the first 16 lines of Table 77.

Early in the investigation, measurements were made on several gases with positrons as primaries; these measurements were in the nature of absolute determinations. The results indicated that the cross sections for positrons might be slightly greater than for electrons, but the excess was well within the uncertainty of the absolute determinations. We have recently made some relative measurements that afford a much more accurate comparison. For these measurements, a source was prepared to contain suitable activities of both Co^{56} for positrons and $\text{Ce}^{144}\text{-Pr}^{144}$ for electrons. With such a mixed source, it was possible by simply reversing the current in the magnetic analyzer to measure counter efficiencies for positrons and for electrons alternately while maintaining exactly constant counting conditions. To avoid uncertainties in analyzer calibration with field reversed,

the field strength was monitored throughout with a gaussmeter. Comparisons were made with argon at primary energies where the positrons and electrons gave comparable counting rates. The results are given in Table 78; they indicate that at high energies the ionization cross sections for positrons and for electrons differ by less than a percent. It seems unprofitable to carry the comparison further.

In line with our aim of determining cross sections as accurately as is feasible, we have reviewed our older results and made adjustments where they appeared to be indicated.

The procedure for obtaining the constants M^2 and C from the observed counter efficiencies by the method of least squares has been simplified in that wall effects are represented by one adjustable constant instead of two. The solution now used amounts to assuming that the observed efficiencies η can be expressed by the relation

$$-\ln(1 - \eta) = NL\sigma(E)(P - P_0),$$

where P_0 represents wall effects and is independent of primary energy E ; $\sigma(E)$ follows the Bethe formula. A small systematic error has been eliminated by taking into account scattering of the primary electrons by the

TABLE 77. M^2 AND C FOR VARIOUS GASES

Gas	Pressure range, torr	M^2	C
1. H ₂ S	2-11	5.0	42.2
2. CF ₄	1.3-11	10.3	84.0
3. PH ₃	2-12	4.6	45.9
4. C ₂ H ₂	9-27	5.2	53.8
5. CH ₃ OH	5-20	6.2	66.4
6. C ₂ H ₅ OH	4-12	9.9	97.7
7. (CH ₃) ₂ O	3-14	10.2	105.2
8. (CH ₃) ₂ CO	3-10	11.9	118.0
9. <i>cyclo</i> C ₃ H ₆	3-12	10.6	106.2
10. (CH ₃)CH	2.3-9	14.2	141.9
11. <i>n</i> C ₃ H ₁₂	1.9-8	18.4	184.8
12. (CH ₃) ₄ C	1.1-8	19.6	182.9
13. C ₆ H ₆	1.0-4	17.5	162.4
14. <i>cyclo</i> C ₆ H ₁₂	1.5-9	22.0	213.2
15. <i>n</i> C ₆ H ₁₄	1.9-6	23.0	223.4
16. <i>n</i> C ₇ H ₁₆	1.0-6	25.1	256.2
17. Xe	2.4-14	8.0	72.4
18. C ₂ H ₄	2.4-18	6.8	68.8
19. H ₂ O	4-12	3.2	32.3

$$\sigma(\text{cm}^2) = 1.874 \times 10^{-20} (M^2x_1 + Cx_2)$$

$$x_1 = \frac{1}{\beta^2} \ln \frac{\beta^2}{1 - \beta^2} - 1, \quad x_2 = \frac{1}{\beta^2}$$

$$\beta = (\text{velocity of primary electron})/(\text{velocity of light}).$$

entrance window of a gas-filled counter. Calculations showed that at 0.1 MeV the average path of primaries between entrance and exit windows is 1½% greater than the distance between the windows; the difference becomes negligible for energies above 0.5 MeV. Previously reported results can be corrected for this effect by increasing M^2 by 4% and decreasing C by ¾%; the correction has been applied to all values quoted in this report.

The results for CO₂ reported previously were obtained by Geiger Mueller counting. When we learned that proportional counting could be used with this gas, a new set of measurements with this mode of counting were carried out to provide a cross check. The results originally reported, corrected for scattering, are

$$M^2 = 6.14 \pm 0.4, \quad C = 55.7 \pm 0.6.$$

The same data, reevaluated and reduced according to our current criteria and method, yield the values

$$M^2 = 5.75 \pm 0.10, \quad C = 55.9 \pm 0.4.$$

The new data, with proportional counting, give the result

$$M^2 = 5.75 \pm 0.07, \quad C = 57.9 \pm 0.3.$$

The uncertainties indicated are the standard deviations as given by the least squares solutions, each involving about forty data points, and indicate the degree of internal consistency of the data. We believe the last

results quoted above to be the most reliable, but the uncertainty in the absolute values is not indicated. Limits of error will be discussed in the following section of this report.

Our previous measurements on Xe and C₂H₄ were less self-consistent than we would like, so new sets of data for them were obtained and analyzed. The data for H₂O are reanalyzed. The results, given in the last three lines of Table 77, supplant the results reported earlier.

LIMITS OF ERROR

Errors may best be discussed in relation to the Bethe formula, which has been used as the basis for smoothing and averaging our observations. On theoretical grounds, the formula should be expected to describe accurately the energy dependence of cross sections throughout and well beyond the range of our measurements; within their limits, the measurements conform to this expectation. The formula may be written

$$\sigma = (1.874 \times 10^{-20} \text{ cm}^2) C[(M^2/C)x_1 + x_2].$$

Its form is illustrated in Figure 166, where σ/C is plotted against $\log E$ for the values of $M^2/C = 0.08, 0.10,$ and 0.12 . Among our results, values of C range from 7 to 250,

TABLE 78. COMPARISON OF IONIZATION CROSS SECTIONS OF ELECTRONS AND POSITRONS ON ARGON

$E, \text{ MeV}$	σ^+/σ^-
0.77	$0.9960 \pm 0.0057^{(a)}$
1.10	1.0075 ± 0.0059
Average	1.0015 ± 0.0041

(a) Relative standard deviation, based on counted numbers.

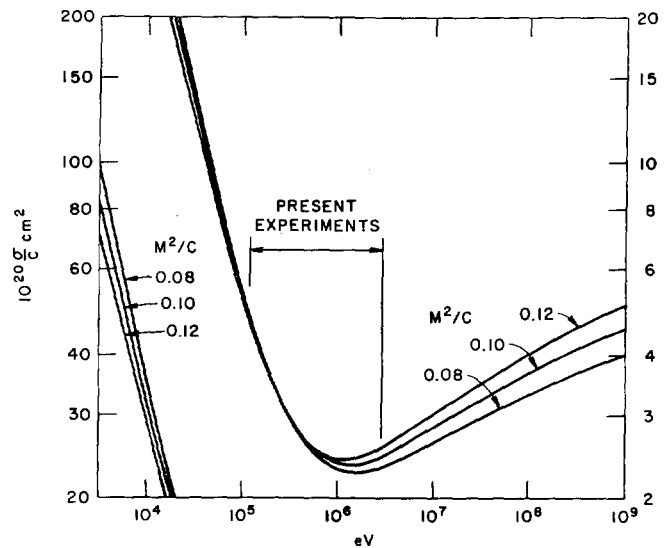


FIG. 166.—Bethe formula σ/C as a function of primary energy, E , with M^2/C as a parameter.

while M^2/C is confined to the limits 0.086–0.123. C may be regarded as the scale factor and M^2/C as the shape parameter for the curve. Generally speaking, C represents an average over all data points, and its value is rather insensitive to errors in individual points. On the other hand, M^2/C is determined by the ratio (cross section at high energy)/(cross section at low energy). Taking cross sections at the two limits of our energy range, the ratio is 0.453 for $M^2/C = 0.092$ and 0.502 for $M^2/C = 0.123$. From these numbers it is evident that M^2/C is very sensitive to errors toward either end of the energy range and can be determined only with a much lower relative precision than can C . Conversely, given an accurate value of C , cross sections can be computed quite accurately and extrapolated over a wide energy range in spite of a relatively large uncertainty in M^2/C .

For each gas studied, values of M^2 and C are derived from a collection of thirty or more data points. A quantitative estimate of the limits of errors is necessarily rather complicated and tedious; the method will be sketched only briefly.

The quantities involved are connected by the relation

$$y = QL[M^2x_1(\rho) + Cx_2(\rho)](P - P_0), \quad (1)$$

where

$$y \simeq -\ln(1 - \eta).$$

y is the average number of ionization acts per transit of a primary electron

Q is a known numerical constant

L is the path length of the primary electron

ρ is the momentum of the primary electron (in units

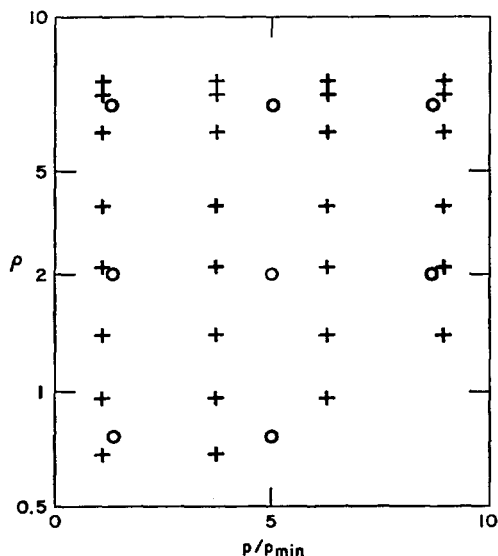


FIG. 167.—Distribution of data points: +, experiments; O, calculation of errors.

of m_0c) and is directly proportional to the magnetic field strength in the analyzer

P is the pressure of gas in the gas-filled counter.

It is convenient to write Eq. (1) in the form

$$x_1 = \left(1 + \frac{1}{\rho^2}\right) \ln \rho^2 - 1, \quad x_2 = 1 + \frac{1}{\rho^2}$$

$$y/(1 - \epsilon) = \left[\frac{M^2}{C_0} x_1 + \frac{C}{C_0} x_2 \right] QLC_0 P_{\min} \frac{P}{P_{\min}} + [0.1x_1 + x_2]P_0, \quad (2)$$

where the term in P_0 is approximated by the last term. The approximation is permissible because the term is always small and M^2/C is never very different from 0.1; ϵ represents the probability that the counting mechanism fails to register a valid ionization act.

Suppose that the true values of M^2 and C are M_0^2 and C_0 and that during the measurements the actual values of ρ and P differ from those given by the meter readings and calibrations by $\Delta\rho$ and ΔP , and that ϵ is not zero, though small. When the observed values are put into a least squares solution for M^2 and C , values differing from the true ones by ΔM^2 and ΔC are obtained. We wish to find how $\Delta C/C_0$ and $\Delta(M^2/C)$ are related to the ϵ , $\Delta\rho/\rho$ and $\Delta P/P$.

SYSTEMATIC ERRORS

Systematic errors are those that result from errors of calibration for L , ρ , and P and from nonideal counting conditions for ϵ .

The case of L is trivial; the uncertainty in the path length is not greater than $\frac{1}{2}\%$; it contributes 0.005 to $\Delta C/C$ and zero to $\Delta(M^2/C)$.

The systematic errors in ρ may be different for different values of ρ , but do not vary from data point to data point taken at the same ρ . We estimate the maximum magnitude of $\Delta\rho/\rho$ to be 0.01. Similarly for P , we estimate the error in calibration of the W & T gauge to be not greater than 0.05 torr. Counting conditions vary from gas to gas and from pressure to pressure for the same gas. Conditions are tested for each combination of gas and pressure by observing y at successively higher counter voltages with ρ near the value for minimum ionization. Conditions are considered satisfactory when the variation with voltage does not exceed the statistical uncertainty in y ; counting is continued until the standard deviation in y , based on counted numbers, is 0.01 (absolute, not relative, deviation). We conclude that ϵ must lie between zero and 0.02 except perhaps in a few difficult cases.

The data points from an actual experiment are distributed generally as indicated by the crosses in Figure 167. The effects of systematic errors must depend upon the area from which the points come, so one can

TABLE 79. LIMITS OF ERROR SYSTEMATIC

P_{\min}	$\Delta C/C$		$\Delta(M^2/C)$	
	Max	Min	Max	Min
1 torr	0.04	-0.06	0.016	-0.020
10 torr or more	0.02	-0.04	0.011	-0.015

make the calculations tractable by basing them upon the eight points indicated by circles. Each point represents an area; the points at the intermediate value of ρ are given double weight because they represent the middle half of the field.

By partial differentiation of Eq. (2), dy can be computed for any combination of $d\rho/\rho$, $d\epsilon/\epsilon$, and dP/P for the individual points. As shown below, one can then find out how the LS solution relates, through the dy 's, the values of dC/C and $d(M^2/C)$ to any small variation of ρ , ϵ , and P . Because of the correlations of the errors, it is convenient to label the y 's with indices i, j to represent momentum i , pressure j . Because ϵ is correlated with P , it also carries the index j .

The least squares method (LS) expresses M^2 and C as linear functions of the y_{ij} :

$$C = \sum A_{ij} y_{ij} \quad M^2 = \sum B_{ij} y_{ij},$$

where A_{ij} and B_{ij} are independent of the y_{ij} . Thus A_{ij} and B_{ij} can be evaluated by comparing two LS solutions that are exactly the same except for a variation in y_{ij} . (A set of nine such solutions required 18 seconds of computing time.) The numerical work was carried out for $M_0^2/C_0 = 0.105$, a median value, and with $QLC_0 P_{\min}$ so chosen as to yield a typical range of the y_{ij} . (The range tends to be much the same for all

experiments.) One can arrange to work with relative values, so the calculation need be carried out only once.

From the expression

$$\frac{dC}{C} = \frac{1}{C} \sum_{ij} \frac{\partial C}{\partial y_{ij}} \left[\rho_i \frac{\partial y_{ij}}{\partial \rho_i} \frac{d\rho_i}{\rho_i} + P_j \frac{\partial y_{ij}}{\partial P_j} \frac{dP_j}{P_j} - y_{ij} \epsilon \right] \quad (3)$$

one can compute the error $\Delta C/C$ that results from any combination of the errors $\Delta\rho_1/\rho_1$, $\Delta\rho_2/\rho_2 \dots \epsilon_2, \epsilon_3$; the limit of error is found by choosing the combination of signs that maximizes the magnitude of $\Delta C/C$. A relation analogous to (3) for dM^2 can be written, and from

$$d(M^2/C) = \frac{1}{C} \left(dM^2 - M^2 \frac{dC}{C} \right)$$

$\Delta(M^2/C)$ can be evaluated. The results of the calculation are given in Table 79.

RANDOM ERRORS

The term random errors is generally applied to errors that arise from truly capricious aspects of an experiment such as noise, statistical errors in counting, and chance errors in reading instruments. According to the theory of the method of least squares, the uncertainty in our values for M^2 and C should be given by multiplying the root mean square deviation of the individual y 's by certain coefficients that come out of the least squares solution. The uncertainty due to random errors should then be added to that due to systematic errors. Such a procedure in our case, however, is not completely valid, inasmuch as some of the errors we have treated as systematic can also contribute to the RMS deviation of the data points.

Our standard practice has been to accumulate counts until y has been determined with a statistical accuracy

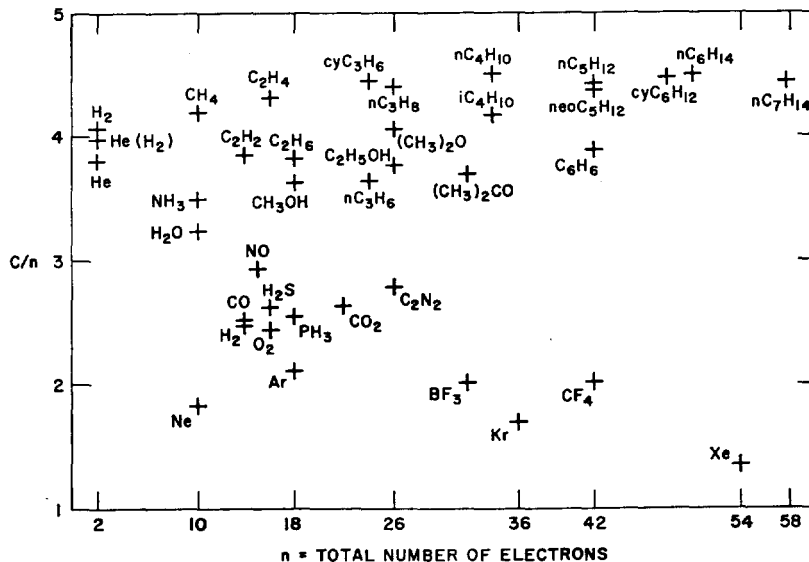


FIG. 168.—Experimental results for C

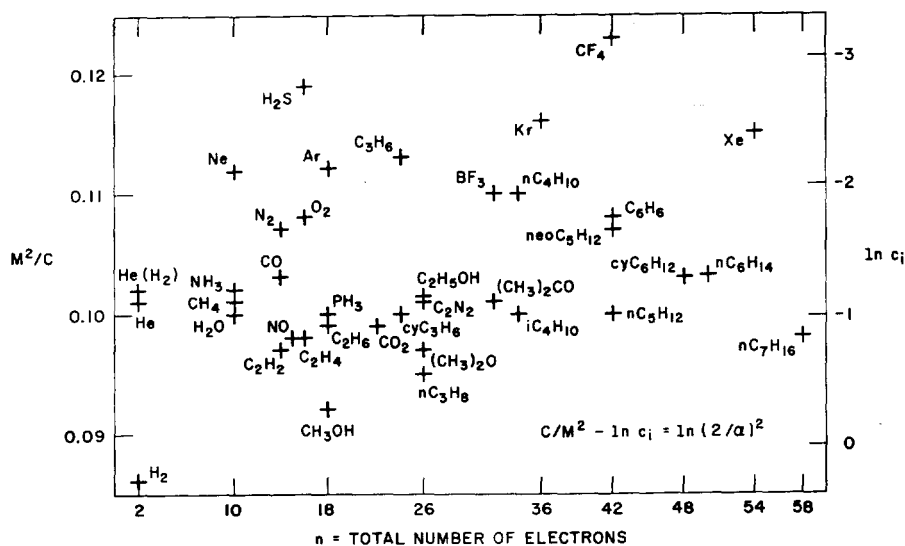


FIG. 169.—Experimental results for M^2/C

of 0.01. Points of that or better accuracy are given unit weight in the LS solution; points of less accuracy are given appropriately smaller weight. In some cases, the RMS deviation turns out to be very nearly 0.01; in others, as much as $2\frac{1}{2}$ times as great. The difference cannot be attributed to genuinely random effects; we attribute it to variations in ϵ , which have been treated as systematic error. We conclude that the true random error in our experiments can be estimated reasonably well by multiplying the coefficients from the LS solution by 0.01. It is the random error so obtained that should be added to the systematic errors indicated in Table 79. The coefficients vary from experiment to experiment, since they depend upon the number and distribution of

the data points. They lead to magnitudes of $\Delta C/C$ ranging from 0.002 to 0.012. For $\Delta(M^2/C)$, the magnitudes range from 0.0015 to 0.004.

SUMMARY

All the results obtained to date are summarized graphically in Figures 168 and 169. With the aid of values taken from these plots and Figure 166, cross sections at any energy where the Bethe formula is applicable can be obtained by simple multiplication.

REFERENCE

1. Rieke, F. F. and Prepejchae, William. Argonne National Laboratory Radiological Physics Division Annual Report, July 1967–June 1968. ANL-7489, p. 99.

TABLES OF ABSORPTION CROSS SECTIONS, PHOTOIONIZATION YIELDS, AND PHOTOIONIZATION CROSS SECTIONS FOR SEVERAL GASES

J. C. Person and P. P. Nicole

Tables of absorption cross sections, photoionization yields, and photoionization cross sections are presented for acetylene, propyne, propene, methanol, ethanol, and methyl bromide, and also for the perdeuterated analogues of these gases. For each gas, the data are reported for energies ranging from a value below the ionization potential up to 11.78 eV.

This report gives the data in tabular form for results that will be presented and discussed elsewhere. The data were collected using an experimental apparatus and procedure that were essentially the same as previously described.^(1, 2) The data for acetylene, propyne,

propene, methanol, ethanol, and methyl bromide are labelled with a subscript H; while the data for the perdeuterated analogues of these gases are labelled with a subscript D. Each table gives the wavelength and the energy, E , of the monochromatic ($\approx 1 \text{ \AA}$ bandwidth) exciting light. The absorption cross sections, σ , were determined from measurements using n gas pressures; and the deviations from a weighted least squares fit of the data to Beer's law were used to estimate the 90% confidence limits as $(\sigma - \delta\sigma)$ to $(\sigma + \delta\sigma)$. In addition to this statistical error, the systematic error in the σ

measurements is estimated to be 4% or less for $10.85 < E < 11.0$ eV and $E > 11.4$ eV, and 2% or less for other E values. The photoionization yield, η , is the probability that photon absorption produces ionization. For some gases the measured η values were pressure dependent in the energy region just below the ionization potential,^(2, 3) and in these cases footnotes indicate the

pressures used. The η values for a given E have a relative uncertainty of approximately (2% of the η value) + 0.002, but the absolute $\eta(E)$ values are more uncertain because of the uncertainties in the $\eta(E)$ values for acetone,⁽²⁾ which was used as a secondary standard. The photoionization cross sections, σ_i ($\sigma_i \equiv \eta\sigma$), are also given in the tables.

TABLE 80. ABSORPTION CROSS SECTIONS, PHOTOIONIZATION YIELDS, AND PHOTOIONIZATION CROSS SECTIONS FOR ACETYLENE AND ACETYLENE- d_2

Wave-length, Å	E , eV	σ_H , Mb ^(a)	$\delta\sigma_H$, Mb	η_H	σ_D , Mb	$\delta\sigma_D$, Mb	η_D	η_H	η_D	σ_{iH} , Mb	σ_{iD} , Mb
1052.4	11.78	27.56	1.31	10	27.15	0.68	10	0.864	0.893	23.80	24.24
1055.6	11.75	27.13	0.67	10	27.21	0.52	10	0.859	0.906	23.29	24.66
1058.6	11.71	27.70	0.62	9	27.98	0.46	10	0.870	0.880	24.10	24.61
1061.7	11.68	28.17	0.56	10	27.60	0.35	10	0.873	0.873	24.59	24.10
1065.2	11.64	29.08	0.50	10	29.09	0.54	10	0.836	0.868	24.32	25.25
1069.9	11.59	25.47	0.54	10	27.74	0.43	10	0.710	0.706	18.07	19.59
1072.8	11.56	27.10	0.36	10	26.20	0.37	10	0.676	0.721	18.33	18.90
1076.8	11.51	28.32	0.43	10	28.05	0.21	10	0.641	0.668	18.16	18.75
1079.7	11.48	27.86	0.38	10	25.78	0.42	10	0.652	0.660	18.17	17.03
1081.6	11.46	28.30	0.51	10	26.78	0.26	10	0.621	0.702	17.56	18.81
1084.5	11.43	22.58	0.40	12	28.51	0.34	10	0.667	0.650	15.06	18.52
1088.7	11.39	35.20	0.26	10	27.31	0.27	10	0.154 ^(b)	0.121 ^(b)	5.41 ^(b)	3.29 ^(b)
1090.0	11.37	20.76	0.31	12	35.45	0.50	10	0.040 ^(b)	0.029 ^(b)	0.82 ^(b)	1.04 ^(b)
1092.4	11.35	31.02	0.49	10	18.13	0.36	12	0.012	0.038	0.39	0.69
1094.7	11.33	20.60	0.29	12	20.67	0.26	12	0.018	0.011	0.38	0.23
1098.1	11.29	22.71	0.40	12	54.80	1.19	7	0.002	0.002	0.05	0.09
1099.5	11.28	13.52	0.58	14	17.66	0.92	13	0.001	0.005	0.02	0.08
1102.0	11.25	44.42	0.48	10	11.83	0.40	12	0.000	0.004	0.02	0.05

^(a) 1 Mb = 10^{-18} cm².

^(b) Pressure ~ 0.2 torr.

TABLE 81. ABSORPTION CROSS SECTIONS, PHOTOIONIZATION YIELDS, AND PHOTOIONIZATION
 CROSS SECTIONS FOR PROPYNE AND PROPYNE- d_4

Wave-length, Å	E , eV	σ_H , Mb ^(a)	$\delta\sigma_H$, Mb	η_H	σ_D , Mb	$\delta\sigma_D$, Mb	η_D	η_H	η_D	σ_{iH} , Mb	σ_{iD} , Mb
1052.4	11.78	56.37	3.11	5	57.82	1.28	5	0.674	0.697	37.99	40.31
1055.6	11.75	57.80	1.09	5	57.48	1.37	5	0.672	0.694	38.86	39.88
1058.6	11.71	57.65	1.17	5	57.98	0.74	5	0.677	0.699	39.03	40.50
1061.7	11.68	56.93	2.41	5	57.73	3.27	5	0.682	0.701	38.83	40.49
1065.2	11.64	57.43	1.57	5	58.35	2.07	5	0.687	0.704	39.43	41.07
1069.9	11.59	57.67	2.12	5	58.30	3.16	5	0.694	0.711	40.00	41.45
1072.8	11.56	57.59	2.58	5	58.69	1.75	5	0.696	0.713	40.11	41.86
1076.8	11.51	57.99	1.45	5	58.81	2.17	5	0.710	0.729	41.18	42.86
1079.7	11.48	57.86	1.27	5	58.70	2.22	5	0.712	0.730	41.22	42.84
1081.6	11.46	57.72	1.37	5	58.32	2.08	5	0.713	0.731	41.16	42.64
1084.5	11.43	58.14	1.12	5	59.86	1.21	5	0.714	0.732	41.53	43.79
1088.7	11.39	59.18	1.25	5	60.06	2.16	5	0.723	0.740	42.78	44.47
1090.0	11.37	59.33	1.02	5	60.63	1.70	5	0.722	0.738	42.86	44.77
1092.4	11.35	59.56	1.83	5	59.86	1.17	5	0.717	0.732	42.73	43.80
1094.7	11.33	59.51	1.87	5	60.25	1.40	5	0.721	0.737	42.94	44.40
1098.1	11.29	60.04	2.28	5	60.85	1.04	5	0.729	0.741	43.75	45.11
1099.4	11.28	59.96	1.73	5	61.29	2.79	5	0.728	0.741	43.68	45.43
1102.0	11.25	61.31	1.21	5	62.47	2.07	5	0.730	0.743	44.76	46.39
1104.4	11.23	61.54	1.44	5	62.86	1.98	5	0.728	0.740	44.82	46.50
1107.2	11.20	60.94	1.20	9	62.86	1.85	9	0.720	0.731	43.89	45.97
1110.3	11.17	61.48	1.49	9	63.29	1.95	9	0.720	0.730	44.26	46.22
1115.0	11.12	62.19	0.95	5	63.98	0.90	5	0.718	0.727	44.66	46.49
1119.1	11.08	62.07	1.40	5	62.88	2.36	5	0.707	0.720	43.86	45.29
1121.2	11.06	62.86	1.23	5	63.44	1.97	5	0.705	0.717	44.30	45.52
1123.9	11.03	62.87	2.11	5	63.44	2.81	5	0.696	0.713	43.77	45.25
1127.3	11.00	62.99	2.35	5	63.83	4.42	5	0.700	0.715	44.09	45.66
1132.9	10.94	63.17	2.88	5	63.16	4.81	5	0.689	0.715	43.51	45.19
1135.3	10.92	64.37	2.22	5	63.62	5.20	5	0.676	0.700	43.53	44.55
1137.4	10.90	64.57	2.70	5	63.59	4.08	5	0.685	0.700	44.23	44.51
1144.4	10.83	63.81	1.99	5	62.80	2.79	5	0.652	0.683	41.64	42.88
1145.9	10.82	64.44	1.74	5	62.35	2.83	5	0.649	0.684	41.84	42.63
1148.5	10.79	64.44	1.95	5	61.65	2.87	5	0.633	0.683	40.82	42.14
1150.9	10.77	63.88	1.65	5	61.79	2.60	5	0.630	0.674	40.24	41.67
1159.9	10.69	64.01	2.48	5	60.83	2.83	5	0.599	0.645	38.34	39.25
1161.3	10.68	65.93	2.46	5	60.92	3.16	5	0.585	0.634	38.55	38.63
1163.8	10.65	63.19	1.96	5	59.30	3.07	5	0.595	0.626	37.61	37.15
1166.1	10.63	63.84	1.72	5	59.77	2.98	5	0.572	0.614	36.53	36.69
1172.2	10.58	60.42	1.77	5	57.27	2.28	5	0.471	0.512	28.44	29.31
1174.5	10.56	66.35	2.12	5	58.74	2.72	5	0.419	0.479	27.82	28.14
1175.9	10.54	64.54	1.93	5	60.08	3.04	5	0.416	0.461	26.84	27.68
1178.3	10.52	62.49	1.06	9	62.38	2.02	9	0.411	0.435	25.70	27.13
1180.4	10.50	58.48	1.13	9	58.49	1.86	9	0.439	0.436	25.67	25.51
1182.7	10.48	57.95	1.64	5	55.68	1.49	5	0.410	0.429	23.78	23.91
1188.0	10.44	67.05	1.67	5	62.11	1.26	5	0.311	0.333	20.83	20.70
1189.4	10.42	69.03	1.59	5	63.85	1.09	5	0.304	0.300	21.00	19.16
1191.7	10.40	61.53	1.49	5	57.09	1.47	5	0.321	0.322	19.78	18.38
1193.3	10.39	63.84	1.42	5	65.37	1.74	5	0.307	0.259	19.62	16.95
1198.0	10.35	49.85	1.33	5	49.20	1.31	5	0.062	0.036	3.09	1.77
1201.8	10.32	63.77	1.68	5	63.62	1.82	5	0.011 ^(b)	0.010 ^(b)	0.71 ^(b)	0.64 ^(b)
1205.1	10.29	68.76	1.94	5	72.80	2.13	5	0.004 ^(b)	0.004 ^(b)	0.29 ^(b)	0.32 ^(b)
1206.6	10.27	64.78	1.98	5	55.43	2.60	4	0.003	0.004	0.20	0.24
1209.1	10.25	46.22	1.29	5	47.18	1.86	5	0.003	0.004	0.15	0.17
1211.4	10.23	50.71	2.55	4	63.56	2.23	5	0.002	0.002	0.11	0.15

(a) 1 Mb = 10^{-18} cm².(b) Pressure ≈ 0.1 torr.

TABLE 82. ABSORPTION CROSS SECTIONS, PHOTOIONIZATION YIELDS, AND PHOTOIONIZATION CROSS SECTIONS FOR PROPENE AND PROPENE- d_6

Wave-length, Å	E, eV	σ_H , Mb ^(a)	$\delta\sigma_H$, Mb	n_H	σ_D , Mb	$\delta\sigma_D$, Mb	n_D	η_H	η_D	σ_{iH} , Mb	σ_{iD} , Mb
1052.4	11.78	57.74	3.21	6	55.28	1.97	6	0.245	0.258	14.15	14.27
1055.6	11.75	57.09	2.37	6	54.07	2.26	6	0.240	0.251	13.70	13.59
1058.6	11.71	55.85	1.44	6	54.12	1.28	6	0.236	0.248	13.21	13.42
1061.7	11.68	56.03	2.35	6	54.46	0.39	6	0.236	0.247	13.21	13.43
1065.2	11.64	56.04	2.13	6	54.93	1.07	6	0.234	0.245	13.09	13.47
1069.9	11.59	55.52	1.87	6	54.73	1.24	6	0.234	0.244	13.01	13.38
1072.8	11.56	55.34	1.80	6	54.01	0.91	6	0.235	0.246	13.01	13.29
1076.8	11.51	54.61	1.70	6	53.50	0.86	6	0.237	0.248	12.92	13.29
1079.7	11.48	53.74	1.81	6	52.64	0.97	6	0.239	0.251	12.83	13.21
1081.6	11.46	53.66	1.60	6	52.51	1.22	6	0.239	0.252	12.84	13.25
1084.5	11.43	53.08	1.88	6	52.24	1.43	6	0.239	0.252	12.66	13.18
1088.7	11.39	52.45	1.59	6	51.68	1.11	6	0.242	0.255	12.71	13.18
1090.0	11.37	52.28	1.25	6	51.53	0.80	6	0.244	0.259	12.78	13.35
1092.4	11.35	51.92	1.09	6	50.96	0.98	6	0.243	0.257	12.59	13.09
1094.7	11.33	51.33	1.48	6	50.21	0.54	6	0.243	0.261	12.46	13.12
1099.4	11.28	50.88	1.24	6	49.93	0.96	6	0.248	0.266	12.64	13.30
1102.0	11.25	50.80	1.11	6	49.59	0.50	6	0.247	0.267	12.57	13.22
1104.4	11.23	50.94	1.32	6	49.85	1.00	6	0.250	0.268	12.75	13.38
1107.2	11.20	50.41	0.82	6	49.57	0.81	6	0.252	0.270	12.70	13.37
1110.3	11.17	50.02	1.20	6	49.24	0.94	6	0.253	0.271	12.63	13.34
1115.0	11.12	49.70	0.69	6	49.37	0.40	6	0.255	0.274	12.66	13.53
1119.1	11.08	49.10	1.01	6	48.56	0.83	6	0.257	0.274	12.60	13.30
1121.2	11.06	48.87	0.79	6	48.36	0.48	6	0.256	0.273	12.51	13.20
1123.9	11.03	48.73	1.14	6	47.97	0.66	6	0.256	0.274	12.45	13.13
1127.3	11.00	47.57	1.17	6	47.00	0.79	6	0.256	0.271	12.16	12.75
1132.9	10.94	47.05	1.22	6	46.30	1.15	6	0.258	0.271	12.15	12.56
1135.3	10.92	47.06	1.40	6	45.66	0.76	6	0.257	0.272	12.09	12.43
1137.4	10.90	46.89	1.54	6	45.94	0.99	6	0.257	0.273	12.06	12.54
1144.4	10.83	47.11	1.40	6	45.95	1.09	6	0.258	0.275	12.17	12.63
1145.9	10.82	46.71	1.13	6	45.55	1.16	6	0.258	0.276	12.07	12.57
1148.5	10.79	46.22	0.67	11	44.29	1.03	12	0.261	0.277	12.07	12.27
1150.9	10.77	45.85	0.70	11	43.58	0.99	12	0.262	0.278	12.00	12.14
1159.9	10.69	43.55	0.58	6	40.73	0.80	7	0.269	0.287	11.70	11.70
1163.8	10.65	42.16	0.42	6	39.11	0.72	7	0.272	0.291	11.49	11.39
1166.1	10.63	41.67	0.41	6	38.57	0.75	7	0.274	0.294	11.44	11.34
1172.2	10.58	40.03	0.36	6	37.28	0.84	7	0.281	0.299	11.26	11.16
1174.5	10.56	39.54	0.28	6	36.82	0.80	7	0.281	0.300	11.11	11.05
1178.3	10.52	38.87	0.61	6	36.17	1.06	7	0.285	0.302	11.09	10.92
1180.4	10.50	38.28	0.26	6	36.11	1.00	7	0.286	0.303	10.96	10.94
1182.7	10.48	37.99	0.79	6	36.08	0.87	7	0.289	0.303	10.98	10.94
1188.0	10.44	37.75	0.59	6	36.07	0.83	7	0.290	0.301	10.94	10.86
1191.7	10.40	37.21	0.42	6	36.00	0.93	7	0.290	0.299	10.78	10.77
1193.3	10.39	37.39	1.03	6	36.17	0.98	7	0.290	0.298	10.83	10.78
1198.0	10.35	37.27	0.55	6	36.49	0.59	7	0.286	0.293	10.67	10.68
1201.8	10.32	37.51	0.81	6	36.52	0.94	7	0.284	0.289	10.67	10.54
1205.1	10.29	38.20	0.36	6	37.42	0.41	7	0.277	0.283	10.60	10.57
1209.1	10.25	38.03	1.23	6	37.07	1.09	7	0.271	0.274	10.31	10.16
1211.4	10.23	38.02	1.09	6	37.13	1.09	7	0.266	0.269	10.10	10.00
1217.4	10.18	38.66	0.41	6	37.67	0.67	7	0.253	0.258	9.80	9.72
1219.0	10.17	38.71	0.48	6	37.63	0.66	7	0.251	0.254	9.70	9.58
1221.2	10.15	38.91	0.45	6	38.22	0.95	7	0.246	0.250	9.59	9.57
1223.5	10.13	38.95	0.39	6	37.78	0.84	7	0.242	0.244	9.41	9.24
1228.3	10.09	39.00	0.42	6	37.79	0.88	7	0.226	0.226	8.81	8.53
1230.0	10.08	39.01	0.50	6	37.67	0.94	7	0.218	0.219	8.50	8.25
1232.0	10.06	38.82	0.53	6	37.39	1.17	7	0.208	0.212	8.09	7.92
1234.1	10.05	38.59	0.50	6	36.96	1.33	7	0.201	0.204	7.74	7.53
1238.0	10.01	38.62	0.33	6	37.12	0.87	7	0.189	0.190	7.31	7.07
1241.4	9.99	38.13	0.68	6	36.64	1.17	7	0.180	0.179	6.88	6.57
1243.5	9.97	38.23	0.39	6	36.63	1.28	7	0.174	0.171	6.67	6.25
1247.5	9.94	37.69	0.40	6	36.62	1.22	7	0.161	0.148	6.07	5.44

TABLE 82—Continued

Wave-length Å	E , eV	σ_H , Mb ^(a)	$\delta\sigma_H$, Mb	n_H	σ_D , Mb	$\delta\sigma_D$, Mb	n_D	η_H	η_D	σ_{iH} , Mb	σ_{iD} , Mb
1251.6	9.91	37.64	0.33	6	36.88	0.87	7	0.132	0.116	4.96	4.28
1253.6	9.89	37.45	0.52	6	37.09	1.04	7	0.114	0.107	4.28	3.97
1257.0	9.86	37.59	0.51	6	36.90	0.96	7	0.095	0.094	3.59	3.47
1261.8	9.83	37.39	0.51	6	37.45	1.17	7	0.082	0.076	3.08	2.85
1264.0	9.81	36.98	0.90	6	37.10	1.40	7	0.078	0.071	2.87	2.65
1265.8	9.79	37.41	0.78	6	36.80	1.57	7	0.070	0.064	2.63	2.35
1269.0	9.77	37.33	0.66	6	38.12	1.20	7	0.062	0.051	2.31	1.93
1271.3	9.75	37.81	0.57	6	37.68	1.19	7	0.054	0.029	2.06	1.09
1276.7	9.71	38.65	0.56	6	38.59	1.24	7	0.008	0.004	0.30	0.17
1279.3	9.69	38.80	0.52	6	37.87	1.22	7	0.003	0.002	0.12	0.09
1281.0	9.68	39.04	0.56	6	37.91	0.99	7	0.002	0.002	0.07	0.07
1283.2	9.66	38.78	0.53	6	38.33	1.05	7	0.001	0.001	0.05	0.05
1286.7	9.64	39.11	0.78	6	37.89	1.33	7	0.001	0.001	0.03	0.03

(a) 1 Mb = 10^{-18} cm².TABLE 83. ABSORPTION CROSS SECTIONS, PHOTOIONIZATION YIELDS, AND PHOTOIONIZATION CROSS SECTIONS FOR METHANOL AND METHANOL- d_4

Wave-length, Å	E , eV	σ_H , Mb ^(a)	$\delta\sigma_H$, Mb	n_H	σ_D , Mb	$\delta\sigma_D$, Mb	n_D	η_H	η_D	σ_{iH} , Mb	σ_{iD} , Mb
1052.4	11.78	35.28	0.31	6	35.79	1.25	6	0.310	0.332	10.94	11.89
1055.6	11.75	34.90	0.50	6	35.35	0.88	6	0.309	0.332	10.77	11.75
1058.6	11.71	33.84	0.74	6	34.11	0.43	6	0.309	0.336	10.47	11.45
1061.7	11.68	33.47	0.66	6	33.46	0.42	6	0.313	0.339	10.48	11.34
1065.2	11.64	32.88	0.40	6	32.62	0.32	6	0.315	0.342	10.36	11.16
1069.9	11.59	31.57	0.34	6	31.29	0.31	6	0.319	0.348	10.06	10.89
1072.8	11.56	30.86	0.58	6	30.34	0.27	6	0.322	0.352	9.94	10.69
1076.8	11.51	30.08	0.62	6	28.65	0.62	6	0.326	0.358	9.81	10.27
1079.7	11.48	29.31	0.76	6	27.92	0.93	6	0.329	0.363	9.64	10.13
1081.6	11.46	28.46	1.25	6	27.21	1.42	6	0.332	0.367	9.44	9.98
1084.5	11.43	27.63	1.04	6	26.53	0.90	6	0.336	0.369	9.28	9.78
1088.7	11.39	26.75	0.39	5	25.27	0.46	7	0.332	0.366	8.87	9.26
1090.0	11.37	26.32	0.28	6	24.92	0.37	7	0.332	0.366	8.75	9.13
1092.4	11.35	25.55	0.33	7	24.18	0.34	7	0.331	0.365	8.46	8.82
1094.7	11.33	24.91	0.31	7	23.71	0.44	7	0.334	0.366	8.32	8.68
1098.1	11.29	24.18	0.33	7	22.99	0.30	7	0.335	0.365	8.09	8.39
1099.4	11.28	23.89	0.31	7	22.70	0.32	7	0.334	0.364	7.98	8.27
1102.0	11.25	23.39	0.18	7	22.21	0.26	7	0.329	0.359	7.70	7.98
1104.4	11.23	22.79	0.20	7	21.70	0.23	8	0.325	0.355	7.41	7.70
1107.2	11.20	22.30	0.12	7	21.19	0.19	8	0.320	0.347	7.14	7.36
1110.3	11.17	21.79	0.12	8	20.66	0.17	8	0.313	0.335	6.83	6.91
1115.0	11.12	21.38	0.25	8	19.84	0.17	8	0.291	0.315	6.23	6.24
1119.1	11.08	20.46	0.05	8	19.04	0.11	9	0.275	0.285	5.62	5.43
1121.2	11.06	20.30	0.13	8	18.74	0.17	9	0.261	0.268	5.30	5.02
1123.9	11.03	19.77	0.09	9	18.29	0.12	9	0.247	0.249	4.89	4.56
1127.3	11.00	19.18	0.14	9	17.61	0.19	9	0.223	0.218	4.28	3.84
1132.9	10.94	18.26	0.10	9	16.77	0.14	10	0.162	0.140	2.96	2.34
1135.3	10.92	17.89	0.17	9	16.51	0.22	10	0.136	0.115	2.43	1.90
1137.4	10.90	17.65	0.19	9	16.22	0.20	10	0.120	0.100	2.12	1.63
1139.8	10.88	17.40	0.14	9	15.93	0.20	10	0.108	0.074	1.88	1.18
1141.8	10.86	17.24	0.47	10	15.70	0.32	10	0.093	0.043	1.61	0.68
1144.4	10.83	16.93	0.07	10	15.56	0.11	10	0.051	0.015	0.86	0.24
1145.9	10.82	16.64	0.04	10	15.60	0.08	10	0.029	0.008	0.48	0.12
1148.5	10.79	16.51	0.08	15	15.17	0.09	15	0.009	0.004	0.15	0.06

TABLE 83—Continued

Wave-length, Å	E , eV	σ_H , Mb ^(a)	$\delta\sigma_H$, Mb	n_H	σ_D , Mb	$\delta\sigma_D$, Mb	n_D	η_H	η_D	σ_{iH} , Mb	σ_{iD} , Mb
1150.9	10.77	16.13	0.06	15	14.98	0.09	15	0.003	0.003	0.05	0.04
1153.7	10.75	16.38	0.11	15	14.88	0.17	15	0.002	0.002	0.03	0.04
1157.2	10.71	15.67	0.13	15	14.60	0.14	15	0.001	0.002	0.02	0.02
1159.9	10.69	15.91	0.13	6	14.74	0.23	6	0.001	0.001	0.01	0.01
1161.3	10.68	15.72	0.10	6	14.50	0.19	6	0	0.001	0.01	0.01
1163.8	10.65	15.39	0.19	6	14.45	0.38	6	0	0.001	0.01	0.01
1166.1	10.63	15.59	0.18	6	14.24	0.19	6	0	0.001	0	0.01
1168.8	10.61	14.72	0.56	6	14.68	0.43	6	0	0.001	0	0.01
1170.5	10.59	15.14	0.48	6	14.39	0.40	6	0	0.001	0.01	0.01
1172.2	10.58	15.58	0.23	6	13.68	0.21	6	0	0.001	0	0.01
1174.5	10.56	15.08	0.15	6	14.10	0.16	6	0	0	0	0.01
1175.9	10.54	15.03	0.14	6	13.70	0.21	6	0	0.001	0	0.01
1178.3	10.52	14.39	0.20	6	13.39	0.28	6	0	0	0	0.01
1180.4	10.50	13.83	0.18	6	13.96	0.23	6	0	0	0	0
1182.7	10.48	14.48	0.31	6	13.42	0.27	6	0	0	0	0.01
1188.0	10.44	14.15	0.23	6	13.42	0.15	6	0	0	0	0
1189.4	10.42	14.64	0.20	6	13.96	0.19	6	0	0	0	0
1191.7	10.40	14.56	0.23	6	13.32	0.28	6	0	0	0	0
1193.3	10.39	14.33	0.25	6	13.68	0.32	6	0	0	0	0
1198.0	10.35	13.10	0.22	6	13.33	0.35	6	0	0	0	0
1201.8	10.32	13.96	0.28	6	13.87	0.50	6	0	0	0	0
1205.1	10.29	14.03	0.19	6	13.87	0.20	6	0	0	0	0
1206.6	10.27	13.94	0.18	6	13.95	0.24	6	0	0	0	0
1209.1	10.25	14.64	0.37	6	14.35	0.34	6	0	0	0	0
1211.4	10.23	13.86	0.36	6	14.14	0.47	6	0	0	0	0
1217.4	10.18	13.00	0.14	6	13.97	0.18	6	0	0	0	0
1219.0	10.17	13.45	0.22	6	15.00	0.21	6	0	0	0	0
1221.2	10.15	14.46	0.33	6	15.38	0.36	6	0	0	0	0
1223.5	10.13	14.76	0.14	6	15.06	0.38	6	0	0	0	0
1228.3	10.09	14.66	0.20	6	14.85	0.27	6	0	0	0	0
1230.0	10.08	14.23	0.06	6	15.06	0.13	6	0	0	0	0
1232.0	10.06	15.22	0.20	6	15.34	0.32	6	0	0	0	0
1234.1	10.05	14.81	0.36	6	15.42	0.34	6	0	0	0	0
1235.6	10.03	14.53	0.30	6	15.78	0.38	6	0	0	0	0
1238.0	10.01	15.03	0.22	6	16.15	0.31	6	0	0	0	0
1241.4	9.99	16.28	0.24	6	15.26	0.35	6	0	0	0	0
1243.5	9.97	15.40	0.26	6	14.59	0.43	5	0	0	0	0

(a) 1 Mb = 10^{-18} cm².

TABLE 84. ABSORPTION CROSS SECTIONS, PHOTOIONIZATION YIELDS, AND PHOTOIONIZATION
 CROSS SECTIONS FOR ETHANOL AND ETHANOL- d_6

Wave-length, Å	E , eV	σ_H , Mb ^(a)	$\delta\sigma_H$, Mb	η_H	σ_D , Mb'	$\delta\sigma_D$, Mb	η_D	η_H	η_D	σ_{iH} , Mb	σ_{iD} , Mb
1052.4	11.78	47.32	2.01	9	46.49	3.29	10	0.247	0.251	11.71	11.66
1055.6	11.75	47.53	1.04	9	45.97	1.42	10	0.239	0.243	11.38	11.15
1058.6	11.71	47.29	0.94	9	45.79	1.69	10	0.234	0.236	11.07	10.83
1061.7	11.68	47.32	1.00	9	46.22	1.76	10	0.227	0.230	10.73	10.64
1065.2	11.64	47.43	0.54	9	46.04	0.96	10	0.221	0.225	10.47	10.34
1069.9	11.59	47.30	0.80	9	45.95	1.23	10	0.215	0.221	10.19	10.14
1072.8	11.56	47.29	0.79	9	46.18	1.18	10	0.212	0.216	10.01	9.98
1076.8	11.51	47.15	0.77	9	45.92	1.12	10	0.210	0.216	9.89	9.91
1079.7	11.48	47.01	1.06	9	45.81	1.28	10	0.208	0.215	9.80	9.83
1081.6	11.46	47.37	0.58	9	45.88	1.04	10	0.207	0.214	9.79	9.81
1084.5	11.43	47.06	0.80	9	46.39	1.23	10	0.205	0.212	9.65	9.83
1088.7	11.39	46.44	0.78	9	45.18	1.60	10	0.201	0.212	9.36	9.60
1090.0	11.37	46.45	0.59	9	45.18	1.13	10	0.202	0.213	9.38	9.61
1092.4	11.35	46.23	0.90	9	44.62	2.33	10	0.199	0.212	9.20	9.45
1094.7	11.33	45.80	0.63	9	44.10	1.59	10	0.199	0.212	9.12	9.35
1099.4	11.28	45.17	0.96	9	43.34	1.52	10	0.200	0.214	9.04	9.27
1102.0	11.25	44.80	0.66	9	42.98	0.93	10	0.200	0.213	8.96	9.17
1104.4	11.23	44.41	0.54	9	42.64	0.85	10	0.200	0.213	8.87	9.07
1107.2	11.20	43.91	0.56	9	42.09	0.90	10	0.199	0.213	8.75	8.96
1110.3	11.17	43.31	0.70	9	41.31	1.02	10	0.198	0.212	8.58	8.77
1115.0	11.12	42.49	0.38	9	40.64	0.59	10	0.197	0.211	8.39	8.56
1119.1	11.08	41.50	0.60	9	39.64	0.73	10	0.195	0.207	8.08	8.21
1121.2	11.06	41.14	0.42	9	39.44	0.68	10	0.193	0.205	7.93	8.08
1123.9	11.03	40.74	0.62	9	38.92	0.86	10	0.190	0.202	7.72	7.85
1127.3	11.00	39.92	0.69	9	38.09	0.79	10	0.186	0.199	7.43	7.57
1132.9	10.94	38.93	0.60	9	37.73	1.10	10	0.181	0.191	7.05	7.20
1135.3	10.92	38.92	0.97	9	37.57	1.18	10	0.177	0.185	6.88	6.96
1137.4	10.90	38.79	1.13	9	37.77	0.87	10	0.174	0.180	6.73	6.81
1144.4	10.83	38.40	0.56	9	37.59	0.90	10	0.157	0.162	6.03	6.11
1145.9	10.82	38.25	0.42	9	37.28	0.76	10	0.153	0.158	5.86	5.89
1148.5	10.79	37.98	0.34	13	37.42	0.62	14	0.147	0.150	5.59	5.63
1150.9	10.77	37.76	0.23	13	37.19	0.63	14	0.141	0.143	5.32	5.31
1159.9	10.69	36.83	0.17	5	36.42	0.32	5	0.110	0.106	4.06	3.86
1163.8	10.65	36.42	0.23	5	35.90	0.35	5	0.095	0.088	3.46	3.17
1166.1	10.63	36.09	0.22	5	35.56	0.27	5	0.086	0.078	3.10	2.77
1172.2	10.58	35.20	0.38	5	34.46	0.49	5	0.059	0.048	2.07	1.66
1174.5	10.56	34.97	0.14	5	34.16	0.18	5	0.048	0.038	1.68	1.31
1178.3	10.52	34.34	0.17	5	33.30	0.38	5	0.035	0.026	1.19	0.86
1180.4	10.50	33.90	0.15	5	32.88	0.16	5	0.027	0.019	0.93	0.62
1182.7	10.48	33.63	0.38	5	32.30	0.15	4	0.022	0.013	0.73	0.42
1188.0	10.44	32.44	0.22	5	30.83	0.26	4	0.008	0.004	0.27	0.14
1191.7	10.40	31.45	0.35	5	29.99	0.18	5	0.003	0.002	0.11	0.06
1193.3	10.39	31.02	0.24	5	29.56	0.45	5	0.002	0.002	0.08	0.05
1198.0	10.35	29.81	0.15	5	28.69	0.57	5	0.001	0.001	0.02	0.02
1201.8	10.32	29.24	0.41	5	27.98	0.41	5	0	0	0.01	0.01

(a) 1 Mb = 10^{-18} cm².

TABLE 85. ABSORPTION CROSS SECTIONS, PHOTOIONIZATION YIELDS, AND PHOTOIONIZATION CROSS SECTIONS FOR METHYL BROMIDE AND METHYL BROMIDE- d_2

Wave-length, Å	E, eV	σ_H , Mb ^(a)	$\delta\sigma_H$, Mb	η_H	σ_D , Mb	$\delta\sigma_D$, Mb	η_D	η_H	η_D	σ_{iH} , Mb	σ_{iD} , Mb
1052.4	11.78	65.75	5.29	6	66.21	3.48	6	0.700	0.700	46.05	46.34
1055.6	11.75	64.29	4.13	6	65.20	4.02	6	0.698	0.693	44.85	45.20
1058.6	11.71	63.06	2.52	6	63.99	1.59	6	0.695	0.687	43.81	43.94
1061.7	11.68	63.14	1.66	6	63.66	1.94	6	0.692	0.684	43.66	43.56
1065.2	11.64	62.83	1.67	6	62.97	1.69	6	0.687	0.679	43.14	42.78
1069.9	11.59	61.49	1.99	6	62.36	1.45	6	0.685	0.677	42.13	42.23
1072.8	11.56	61.57	1.12	6	62.24	1.58	6	0.683	0.677	42.06	42.11
1076.8	11.51	61.05	0.74	6	61.83	1.46	6	0.683	0.678	41.67	41.94
1079.7	11.48	60.66	1.81	6	61.52	0.89	6	0.685	0.680	41.56	41.86
1081.6	11.46	61.06	2.39	6	61.73	1.06	6	0.686	0.683	41.86	42.16
1084.5	11.43	61.24	0.92	6	61.59	1.23	6	0.687	0.685	42.09	42.21
1088.7	11.39	60.99	0.81	6	61.64	0.72	6	0.683	0.685	41.64	42.20
1090.0	11.37	61.46	0.90	6	61.39	0.55	6	0.684	0.689	42.06	42.27
1092.4	11.35	61.72	2.20	6	61.95	0.53	6	0.680	0.685	41.99	42.41
1094.7	11.33	61.99	1.24	6	61.59	0.84	6	0.686	0.695	42.51	42.81
1098.1	11.29	62.11	1.09	6	61.66	0.54	6	0.692	0.705	43.00	43.49
1099.4	11.28	62.84	1.07	6	61.49	0.72	6	0.693	0.707	43.54	43.45
1102.0	11.25	62.41	0.87	6	61.74	0.75	6	0.693	0.708	43.25	43.73
1104.4	11.23	63.02	0.52	6	62.31	0.55	6	0.692	0.714	43.63	44.46
1107.2	11.20	63.13	0.40	6	62.39	0.86	6	0.691	0.715	43.62	44.59
1110.3	11.17	63.60	1.04	6	62.73	0.89	6	0.692	0.720	44.01	45.18
1115.0	11.12	64.69	0.65	6	62.88	0.69	6	0.694	0.728	44.91	45.81
1119.1	11.08	64.58	0.51	6	62.42	0.88	6	0.693	0.729	44.78	45.53
1121.2	11.06	64.66	0.49	6	62.31	0.78	6	0.688	0.728	44.47	45.38
1123.9	11.03	64.96	0.61	6	62.87	0.64	6	0.688	0.728	44.70	45.80
1127.3	11.00	65.01	0.64	6	62.48	0.86	6	0.671	0.725	43.59	45.30
1132.9	10.94	64.52	0.81	6	62.24	0.83	6	0.668	0.702	43.08	43.70
1135.3	10.92	64.94	1.65	6	61.69	0.35	6	0.641	0.692	41.61	42.69
1137.4	10.90	64.45	2.17	6	60.93	0.67	6	0.620	0.689	39.96	42.00
1139.8	10.88	65.62	3.11	4	61.11	0.85	4	0.615	0.625	40.34	38.18
1141.8	10.86	65.17	5.30	4	60.40	0.73	4	0.597	0.546	38.91	32.97
1144.4	10.83	63.27	0.48	8	65.11	0.87	8	0.463	0.534	29.30	34.76
1145.9	10.82	63.39	0.57	8	59.58	0.78	8	0.460	0.531	29.16	31.61
1148.5	10.79	65.48	0.52	9	64.01	0.67	9	0.436	0.508	28.53	32.51
1150.9	10.77	61.95	0.44	9	65.83	0.61	9	0.451	0.469	27.93	30.89
1153.7	10.75	65.96	1.10	7	66.04	1.15	7	0.434	0.471	28.65	31.09
1157.2	10.71	60.10	2.11	7	77.48	0.48	7	0.412	0.437	24.77	33.87
1159.9	10.69	70.72	0.54	6	49.14	0.35	7	0.372	0.500	26.34	24.55
1161.3	10.68	57.40	0.53	6	65.40	0.62	6	0.364	0.472	20.89	30.86
1163.8	10.65	63.34	0.64	6	51.39	0.71	7	0.395	0.406	25.00	20.88
1166.1	10.63	66.35	0.69	6	54.47	0.45	7	0.299	0.383	19.86	20.86
1168.8	10.61	53.34	1.17	4	77.82	1.15	4	0.358	0.364	19.07	28.30
1170.5	10.59	54.58	1.79	4	60.84	1.33	4	0.382	0.336	20.84	20.47
1172.2	10.58	79.26	0.67	6	46.97	0.63	8	0.310	0.345	24.61	16.21
1174.5	10.56	57.67	0.44	6	53.48	0.25	7	0.304	0.339	17.55	18.15
1175.9	10.54	58.07	0.33	6	51.50	0.49	7	0.296	0.310 ^(b)	17.18	15.98 ^(b)
1178.3	10.52	55.14	0.64	6	55.17	0.67	6	0.067 ^(b)	0.032 ^(b)	3.68 ^(b)	1.75 ^(b)
1180.4	10.50	55.40	0.60	6	83.13	0.70	6	0.012 ^(b)	0.006 ^(b)	0.64 ^(b)	0.49 ^(b)
1182.7	10.48	69.44	1.11	6	52.76	0.80	7	0.005	0.007	0.35	0.39
1188.0	10.44	43.10	0.22	8	80.87	0.81	6	0.002	0.002	0.10	0.13
1189.4	10.42	45.76	0.28	8	48.14	0.47	8	0.002	0.002	0.10	0.10
1191.7	10.40	72.81	1.19	6	40.11	0.34	8	0.002	0.001	0.14	0.06
1193.3	10.39	42.72	0.12	8	53.01	0.52	7	0.002	0.001	0.08	0.08
1198.0	10.35	43.97	0.23	8	47.58	0.44	8	0.002	0.001	0.08	0.06
1201.8	10.32	58.10	0.60	6	74.39	0.78	6	0.002	0.001	0.10	0.08
1205.1	10.29	95.46	0.71	6	45.40	0.44	8	0.001	0.001	0.11	0.03
1206.6	10.28	48.85	0.13	7	76.37	0.63	6	0.001	0.001	0.06	0.04
1209.1	10.25	93.81	1.41	6	35.37	0.43	9	0.002	0.001	0.17	0.04
1211.4	10.24	36.28	0.35	8	33.66	0.22	9	0.001	0.001	0.05	0.03
1217.4	10.18	53.02	0.21	7	48.48	0.34	8	0.001	0.001	0.05	0.02

TABLE 85—Continued

Wave-length, Å	E , eV	σ_H , Mb ^(a)	$\delta\sigma_H$, Mb	n_H	σ_D , Mb	$\delta\sigma_D$, Mb	n_D	η_H	η_D	σ_{iH} , Mb	σ_{iD} , Mb
1219.0	10.17	58.32	0.23	6	57.23	0.65	6	0.002	0.000	0.09	0.02
1221.2	10.15	146.06	1.71	4	73.58	1.81	6	0.002	0.001	0.25	0.05
1223.5	10.13	49.47	0.37	7	52.59	0.37	7	0.002	0.001	0.08	0.04
1228.3	10.09	46.35	0.38	8	51.59	0.55	7	0.001	0.001	0.05	0.04
1230.0	10.08	49.12	0.12	7	37.38	0.37	8	0.002	0.001	0.08	0.02

(a) 1 Mb = 10^{-18} cm².

(b) Pressure ≈ 0.1 torr.

REFERENCES

- Person, J. C. and Nicole, P. P. *J. Chem. Phys.* **49**, 5421 (1968).
- Person, J. C. and Nicole, P. P. Argonne National Laboratory, Radiological Physics Division Annual Report, July 1967 through June 1968. ANL-7489, p. 105.
- Person, J. C. Collision-Induced Ionization of Highly Excited Rydberg Levels of Polyatomic Molecules. With International Conference on the Physics of Electronic and Atomic Collisions. Cambridge, Massachusetts, July 28-August 2, 1969. Book of Abstracts, p. 990.

ISOTOPE EFFECTS IN THE PHOTOIONIZATION YIELDS AND THE ABSORPTION CROSS SECTIONS FOR ETHYLENE AND *n*-BUTANE*

J. C. Person and P. P. Nicole

The absorption cross section, σ , and the photoionization yield, η (the probability that photon absorption produces ionization), are reported for C₂H₄ and C₂D₄ at 44 photon energies between 10.44 and 11.78 eV, and they are reported for *n*-butane and *n*-butane-*d*₁₀ at 37 photon energies between 10.56 and 11.78 eV. For

* Abstract of paper published in *J. Chem. Phys.* **49**, 5421 (1968).

ethylene, the nature of the isotope effects on η , σ , and the photoionization cross sections, σ_i ($\sigma_i = \eta\sigma$), indicates that the increase in η upon deuteration is not the result of a simple competition between preionization processes and atomic rearrangement processes in the superexcited states. The isotope effects for *n*-butane and the implications of the results for radiation chemistry are also discussed.

A METHOD FOR ESTIMATING THE RELATIVE IMPORTANCE OF THE PLATZMAN COMPETITIVE IONIZATION PROCESS FROM ISOTOPE EFFECTS IN MOLECULAR PHOTOIONIZATION

J. C. Person

A graphical method is presented for estimating the minimum contribution to the total ionization of the Platzman competitive ionization process from data on the ionization yield, η , for deuterated (η_D) and protonated (η_H) molecules. The method assumes that one may use the simple kinetic model proposed by Platzman in which the ionization occurs either by direct ionization or by the preionization of superexcited states in competition with atomic rearrangement processes leading to neutral products. It is also assumed that deuteration does not change the part of the ionization yield that results from direct ionization. The results are given in a figure which shows the curves (for the different values of η_H) giving the maximum fraction of the ionization due to direct ionization as functions of a variable determined by the ratio of the observed η_D/η_H ratio to

the maximum possible η_D/η_H ratio. Another figure plots the maximum η_D/η_H ratio for each value of η_H .

This paper presents a graphical method of analyzing data on the changes in ionization resulting from deuteration. The purpose is to estimate a lower limit of the contribution to the total ionization from the preionization of superexcited states that are in competition with atomic rearrangement processes leading to neutral products (e.g., dissociation). The method is based on the simple kinetic model proposed by Platzman.⁽¹⁻³⁾ In this model the ionization yield, $\eta(E)$ (the probability that

excitation with an energy, E , leads to ionization), is given by^(2, 3)

$$\eta = \delta + (1 - \delta)[1 + (k_2' \mu^{-1/2})/k_1]^{-1}, \quad (1)$$

where δ is the fraction of excitations leading to direct ionization, k_1 is the rate constant for the preionization of the superexcited states, $k_2' \mu^{-1/2}$ is the rate constant for the atomic rearrangement processes leading to neutral products, and μ is the reduced mass for the motion leading to a point in coordinate space subsequent to which preionization is impossible. Platzman assumes that k_1 is approximately independent of the isotopic composition of the molecule; and we shall make the further assumption that δ is also independent of isotopic composition. One can then write

$$\eta_D = \delta + (1 - \delta)[1 + k_2'/(k_1 \mu_D^{1/2})]^{-1} \quad (2)$$

and

$$\eta_H = \delta + (1 - \delta)[1 + k_2'/(k_1 \mu_H^{1/2})]^{-1}, \quad (3)$$

where the subscripts D and H refer to the deuterated and the protonated molecules, respectively. The maximum value of the η_D/η_H ratio will then occur when $\delta = 0$. Elimination of k_2'/k_1 from equations (2) and (3) with $\delta = 0$ gives

$$\begin{aligned} \left(\frac{\eta_D}{\eta_H}\right)_0 &= \frac{1}{\eta_H + (1 - \eta_H)(\mu_H/\mu_D)^{1/2}} \\ &= \frac{(\mu_D/\mu_H)^{1/2}}{1 + \eta_H[(\mu_D/\mu_H)^{1/2} - 1]}, \end{aligned} \quad (4)$$

where the subscript zero indicates that the ratio is for $\delta = 0$. The $(\eta_D/\eta_H)_0$ values will be largest for the largest values of $(\mu_D/\mu_H)^{1/2}$ and the largest μ_D/μ_H ratios are for motions involving one hydrogen atom moving against the rest of the molecule. The maximum $(\mu_D/\mu_H)^{1/2}$ value depends on the molecule, but a typical value is about 1.4 (for example, it is 1.38 and 1.39 for light molecules like H_2O and C_2H_2 , and it would be 1.414 for a molecule of infinite mass). Figure 170 shows a plot of $(\eta_D/\eta_H)_0$ vs. η_H for $(\mu_D/\mu_H)^{1/2} = 1.40$.

The experimental observation of an η_D/η_H ratio smaller than the $(\eta_D/\eta_H)_0$ value at the experimental value of η_H could mean that direct ionization is making a contribution ($\delta \neq 0$), or it could mean that the effective value of $(\mu_D/\mu_H)^{1/2}$ is less than 1.4. However, it is possible to estimate an upper limit to the relative contribution of direct ionization by comparing the observed η_D/η_H ratio with η_D/η_H ratios calculated assuming $(\mu_D/\mu_H)^{1/2} = 1.4$ and $\delta \neq 0$. The calculation is done by eliminating k_2'/k_1 from equations (2) and (3), dividing by η_H , and rearranging to give

$$\frac{\eta_D}{\eta_H} = \frac{\delta(1 - \eta_H) + (\mu_D/\mu_H)^{1/2}(\eta_H - \delta)}{\eta_H[(\mu_D/\mu_H)^{1/2}(\eta_H - \delta) + 1 - \eta_H]}. \quad (5)$$

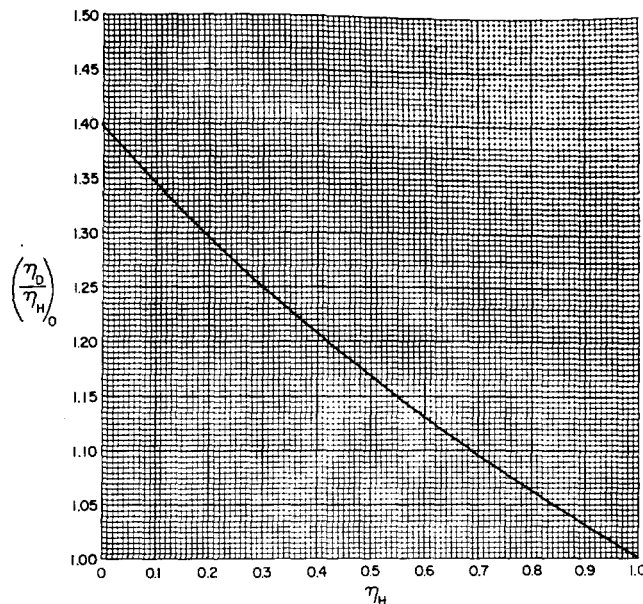


FIG. 170.—The ratio of the ionization yield for the deuterated molecule (η_D) to the ionization yield for the protonated molecule (η_H) when there is no direct ionization ($\delta = 0$) as a function of η_H . The square root of the ratio of the reduced masses $(\mu_D/\mu_H)^{1/2}$ is taken as 1.40.

The results are presented more compactly by defining a term, R , by

$$R = \frac{(\eta_D/\eta_H) - 1}{(\eta_D/\eta_H)_0 - 1}, \quad (6)$$

where the η_D/η_H ratio in the numerator is from equation (5). The R values are functions of $(\mu_D/\mu_H)^{1/2}$, δ , and η_H . Figure 171 is a plot of δ/η_H vs. R , giving nine curves for the values of η_H from 0.1 to 0.9, all calculated for $(\mu_D/\mu_H)^{1/2} = 1.4$. Actually, the curves for (δ/η_H) vs. R are not very sensitive to the choice of $(\mu_D/\mu_H)^{1/2}$, provided that the same value of $(\mu_D/\mu_H)^{1/2}$ is used in equation (4) as in equation (5). Thus, for $(\mu_D/\mu_H)^{1/2} = 1.36$, the δ/η_H value at a given value of R would be slightly smaller (<0.01 smaller) than the value in Figure 171, and for $(\mu_D/\mu_H)^{1/2} = 1.08$, the δ/η_H value would be smaller (<0.05 smaller) than the value in Figure 171.

To illustrate the use of the method consider an example where $\eta_D/\eta_H = 1.07$ and $\eta_H = 0.25$. From Figure 170 we find that $(\eta_D/\eta_H)_0 = 1.273$, so that $R = 0.07/0.273 = 0.256$. From Figure 171 we find that $\delta/\eta_H \approx 0.81$. This would indicate that at least 19% of the ionization in this example was from the Platzman competitive ionization process.

One should use this method with care, however, as there are some difficulties. One difficulty is the problem of how to handle energy level shifts,⁽⁴⁾ which may be real shifts caused by differences in the zero-point energies or may be apparent shifts caused by unfavorable Franck-Condon factors. One method of handling these

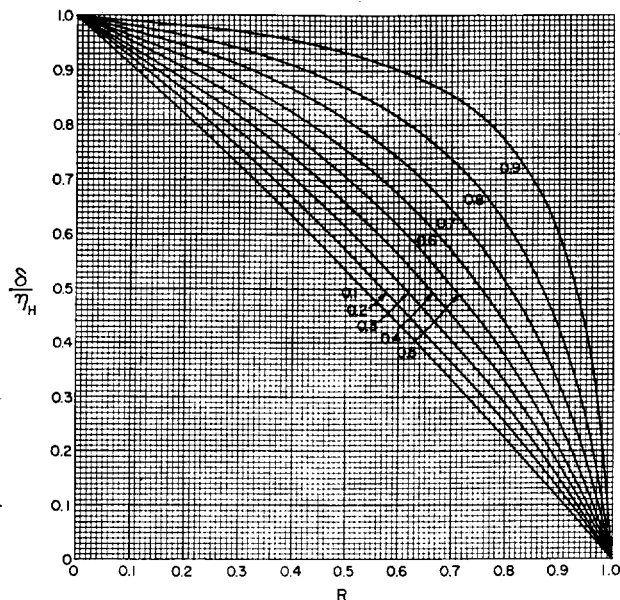


FIG. 171.—The maximum fraction of the ionization produced by direct ionization for the protonated molecule (σ/η_H) as a function of R . See equation (6) for the definition of R . The nine separate curves are each labelled with the η_H value for that curve.

THE EFFECT OF PRESSURE UPON IONIZATION IN PURE RARE GASES

H. A. Schultz

Components of the ion chambers designed to measure the effect of pressure upon the ionization of pure rare gases were cleaned, assembled, and checked for satisfactory operation. Several portions of the apparatus were modified because they were unsatisfactory in their original form.

A fast particle traversing a medium produces ionization and excitation within the material. If the medium is a pure rare gas, the value of W , the average energy lost by the particle per ion pair produced, can be expected to vary with gas pressure; this is because rare gas atoms that are excited to certain high energy levels can release their excess energy through two competing processes: photon emission and associative ionization. The latter is a collision process in which an excited atom combines with an atom in the ground state to yield a diatomic positive ion and a free electron. This reaction is often called the Hornbeck-Molnar effect. At sufficiently high pressures the collision process will be more probable than the emission process, and at lower pressures the reverse will

be true; this implies that W must decrease with increasing pressure. The previous report⁽¹⁾ described briefly an apparatus designed to utilize two ionization chambers of similar geometry but different dimensions to measure the effect of pressure upon W for neon and argon. After the stainless steel chambers had been fabricated in the shops, they were disassembled in the laboratory, cleaned carefully with solvents to remove foreign materials that had been picked up on the surfaces, then reassembled. It is possible that trace quantities of gaseous impurities desorbed by surfaces inside the chambers will produce relatively few spurious ions, or a relatively great number; it will depend upon the ionization potential of the impurity and, to a very great extent, upon the decay scheme associated with the photon emission processes of the rare gas atoms. The effect of small traces of impurities can be small if all the excitation energy of a rare gas atom is lost in

REFERENCES

1. Platzman, R. L. *J. Phys. Radium* **21**, 853 (1960); *Radiat. Res.* **17**, 419 (1962); *J. Chem. Phys.* **38**, 2775 (1963).
2. Platzman, R. L. *Vortex* **23**, 372 (1962).
3. Jesse, W. P. and Platzman, R. L. *Nature* **195**, 790 (1962).
4. Person, J. C. and Nicole, P. P. *J. Chem. Phys.* **49**, 5421 (1968).
5. Johnson, P. M. and Rice, S. A. *J. Chem. Phys.* **49**, 2734 (1968).
6. Krauss, M., Walker, J. A., and Dibeler, V. H. *J. Res. Natl. Bur. Std.* **72A**, 281 (1968).

a single emission step, or if there are successive steps that involve only states of ordinary lifetimes (i.e., of the order of 10^{-8} sec). On the other hand, the effect of the same concentration of impurity can be much greater if the emission scheme involves a metastable state, or a state with a long effective lifetime because of radiation trapping, and if the ionization potential of the impurity is less than the energy of excitation of this state. Then the Jesse effect will be in competition with the associative ionization process; each process will yield an ion, and the two kinds of ions will be indistinguishable to an ionization chamber. Until it is proved otherwise, it is reasonable to assume that both types of radiative decay, the fast and the slow, will occur for the states involved in the associative ionization of the rare gases.

After the various parts of the ionization chamber had been cleaned, a great deal of filing and polishing was required before they could be reassembled, because clean stainless steel surfaces in intimate contact tend to "gall" or "cold weld." The design of the shutter in front of the alpha source of the large chamber was modified for the same reason. It had operated satisfactorily until after the chamber had been completely assembled for use with the alpha source in place.

Most of the gas leaks that were found by checking the entire apparatus were of types that can be repaired easily and permanently, e.g. by resoldering a pinhole or retightening a flange. In general, leaks

that occur in components that are to be stressed from time to time, or that may possibly be stressed, are much more serious. Modifications were made in the apparatus to reduce the probability of having recurring leaks in the shutter manipulator of the large chamber, in the flexible connection between the small chamber and the gas supply and evacuation system, and in the connection between the precision pressure gage and the gas system.

Carbon films of $50 \mu\text{g}/\text{cm}^2$ and 6.60 mm diameter were found to be too fragile for the intended use as a filter for atomic or aggregate particles ejected from the alpha source in the large chamber. A search revealed that films of nickel and of alumina with stopping power similar to that of the carbon could be obtained readily at the Laboratory. Either type of film appeared to have much better mechanical strength than the carbon type. A nickel film of 0.10μ thickness was chosen because the filter forms part of the wall of the ionization chamber, and, therefore, high electrical conductivity is desirable.

At this writing, all components of the equipment have been checked, everything is ready for the final assembly and the measurement of ion currents early in the new fiscal year.

REFERENCE

1. Schultz, Harvey A. Argonne National Laboratory Radiological Physics Division Annual Report, July 1967-June 1968. ANL-7489, pp. 100-101.

BIO-ENVIRONMENTAL STUDIES

BEHAVIOR OF FALLOUT ^{137}Cs IN AQUATIC AND TERRESTRIAL ENVIRONMENTS

P. F. Gustafson, S. S. Brar, D. M. Nelson, and S. E. Muniak

Fallout ^{137}Cs in terrestrial systems was found to be highly dependent upon fallout rate, where total deposition seems more important in the aquatic case. In both situations a general downward trend has been evident since 1964-1965.

The biological importance of ^{137}Cs was first noted in 1955 by Miller and Marinelli,⁽¹⁾ who detected this radionuclide in human subjects serving as controls for the whole-body counting portion of the Argonne Radium Toxicity Program. The metabolic activity of cesium stems from its chemical similarity to potassium, a necessary nutrient element. Like potassium,

cesium goes to soft tissue in man, primarily muscle, and, therefore, has a relatively short biological half-time (~ 100 days in adults).

Over the years since 1955, ^{137}Cs has been examined in a wide variety of media: air, precipitation, soil, plants, animals, and man. Empirical relationships between atmospheric inventory, deposition, and uptake by man have led to the construction of mathematical fallout models for both ^{137}Cs and ^{90}Sr . These models have shown a reasonable capability for predicting the radiological consequences of nuclear debris globally dispersed from a stratospheric source.

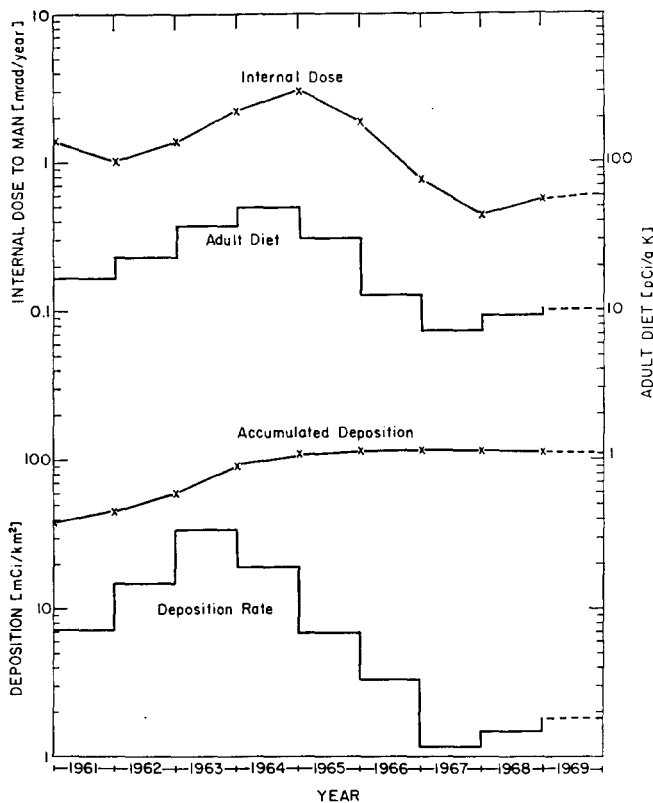


FIG. 172.— ^{137}Cs in the Chicago area 1961–1969; deposition rate, accumulated deposition, concentration in diet, internal dose to man.

Properly modified, such models may also be useful in assessing the dosimetric aspects of other modes of environmental release of ^{137}Cs and ^{90}Sr , and by extension may be applied to other contaminants.

Fairly extensive measurements of ^{137}Cs in air, soil, food, and man have been made routinely at Argonne for a number of years. These data allow the observation of temporal trends and indicate something of the transport through the environment of this particular substance. Indeed, it is the transport and environmental persistence of ^{137}Cs which justifies continuation of these studies.

The pulse of ^{137}Cs generated by the large scale nuclear weapons testing in 1961–1962 serves as an illustration. The duration of this pulse is indicated in Figure 172, where the deposition rate is shown to reach a maximum in 1963 and has a half-width of ~ 4 years. The fine structure of annual deposition is characterized by maximal deposition rates in the spring and early summer due to the higher levels of airborne activity coinciding with high precipitation. From 1963 through 1967 the deposition rate decreased with a half-time of about 12 months, which is in accord with the observed half-residence time for fallout ^{137}Cs in the stratosphere.

Figure 172 also shows that the concentration of ^{137}Cs in the diet closely parallels the course of fall-out rate, but is delayed essentially one year in reaching its maximum level. This delay is due to the lag between the growth and actual marketing of many food items. Throughout the time interval considered, the accumulated deposition of ^{137}Cs is either increasing or remaining at a nearly constant maximum level. The primary dependence of the ^{137}Cs in the diet upon fallout rate rather than accumulated radioactivity is clearly evident, and reflects the fact that foliar and stem uptake far outweighs root uptake in the case of ^{137}Cs under most circumstances. It should be pointed out, however, that recent work in Florida⁽²⁾ has shown fairly constant dietary levels of ^{137}Cs , presumably due to root uptake caused by local soil characteristics.

The effective half-time for ^{137}Cs in the Chicago diet shown in Figure 172 is about 18 months, and the half-time in man is closely the same, as illustrated by the internal dose curve. The slight increases in deposition rate, diet ^{137}Cs , and resultant dose in the last two years is attributed to the input of new nuclear debris from Chinese and French testing.

Most of the foodstuffs in the diet considered are terrestrially produced; hence we may presume that the relatively rapid decrease in ^{137}Cs concentration ob-

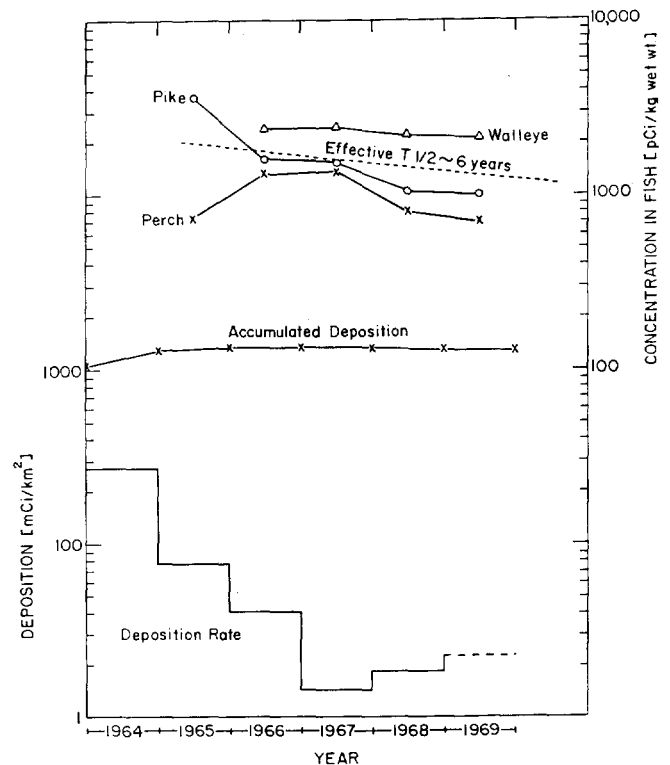


FIG. 173.— ^{137}Cs in the Red Lakes, Minnesota area 1964–1969; deposition rate, accumulated deposition, concentration in perch, northern pike, and walleye.

served is generally true for the terrestrial case (though bearing in mind the anomalous Florida situation). The behavior of ^{137}Cs in the aquatic case is somewhat different as illustrated by data from Red Lakes, Minnesota, shown in Figure 173. Again, the deposition rate and total accumulation are indicated along with annual (June-September) levels of ^{137}Cs in perch, northern pike, and walleye. These were all adult fish caught commercially. The effective half-time for ^{137}Cs in these fish is appreciably longer than that exhibited by the fallout rate, and for the average of the three species amounts to about a six-year half-time. The persistence of ^{137}Cs under aquatic conditions may be due to recycling or to the continuing biological availability of this radionuclide in a water environment. In any event, this behavior suggests further study of the fate of radiocesium released in water.

In summary, a comparison between the total internal dose from ^{137}Cs experienced by a typical Chicago

adult and a member of the Red Lakes band of Chipewewa Indians eating Red Lakes fish might be of interest. In 1965, on the basis of examining the $^{137}\text{Cs}/\text{K}$ ratio in urine specimens, it was determined that the fish-consuming Red Lakes people had three times the body burden of ^{137}Cs that prevailed in Chicago.⁽³⁾ Using the observed decrease in ^{137}Cs content of fish shown in Figure 173 and summing the internal doses given in Figure 172 for the interval 1965-1968, it appears that while a Chicago resident received ~ 3.6 mRads, the Red Lakes individual accumulated ~ 19 mRads.

REFERENCES

1. Miller, C. E. and Marinelli, L. D. *Science* **124**, 122 (1956).
2. Roessler, G. S., Dunavant, B. G., and Roessler, C. E. *Health Phys.* **16**, 673 (1969).
3. Gustafson, P. F. Radioecological Concentration Processes. Proc. Int. Symp. held in Stockholm, 25-29 April 1966. Pergamon Press, Oxford, 1966, p. 853.

ARTICLES PUBLISHED BY THE RADIOLOGICAL PHYSICS DIVISION STAFF JULY 1968-JUNE 1969

PUBLICATIONS

- Berlman, I. B., C. R. Goldschmidt, Y. Tomkiewicz, and A. Weinreb. Energy Transfer from Pyrene to Perylene at High Excitation Intensity. *Chem. Phys. Letters* **2**(8), 657-658 (December 1968).
- Goldschmidt, C. R., Y. Tomkiewicz, and I. B. Berlman. An Intermolecular Interaction of Excited States in Crystals and Liquids. *Chem. Phys. Letters* **2**(8), 520-522 (December 1968).
- Goldschmidt, C. R., Y. Tomkiewicz, and I. B. Berlman. A Saturation of Excimer Formation. *Chem. Phys. Letters* **2**(8), 536-538 (December 1968).
- Berlman, I. B. Evidence of Intramolecular Hydrogen Bonding from Spectrographic Data. *Chem. Phys. Letters* **3**, 61 (1969).
- Brar, S. S. and D. M. Nelsen. Cs^{137} In Various Chicago Foods. Health and Safety Laboratory Quarterly, U.S. Atomic Energy Commission Report, HASL-197, pp. III-64-III-67 (July 1968); HASL-200, pp. III-18-III-21 (October 1968); HASL-204, pp. III-2-III-5 (January 1969); HASL-207, pp. III-2-III-5 (April 1969).
- Brar, S. S., D. M. Nelsen, et al. Thermal Neutron Activation Analysis of Airborne Particulate Matter in Chicago Metropolitan Area. *Modern Trends in Activation Analysis*. U. S. Dept. Commerce, Natl. Bur. Std. Spec. Publ. 312, June 1969, Vol. 1, pp. 43-54.
- Croke, E. J., J. E. Carson, D. F. Gatz, H. Moses, A. S. Kennedy, J. A. Gregory, J. J. Roberts, K. Croke, J. L. Anderson, D. Parsons, James Ash, J. E. Norco, and R. P. Carter. Chicago Air Pollution System Model. Third Quarterly Progress Report. Argonne National Laboratory Report ANL/ES-CC-003 (October 1968).
- Croke, E. J., J. E. Carson, D. F. Gatz, H. Moses, A. S. Kennedy, J. E. Norco, J. J. Roberts, K. Croke, J. B. Anderson, D. M. Nelson, J. E. Ash, R. P. Carter, D. Parsons, J.-W. Lin, and R. J. Votruba. Chicago Air Pollution System Analysis Program. Fourth Quarterly Report. Argonne National Laboratory Report ANL ES-CC-004 (March 1969).
- Carson, J. Carson, J. E., R. J. Votruba, and J.-W. Lin. Chicago's Air Pollution Incident Control Test. Summer 1968. Informal Report (April 1969).
- Gustafson, P. F. Cesium-37 in Freshwater Fish during 1945-1965. *Symposium on Radioecology*, Proc. 2nd Natl. Symp., Ann Arbor, Michigan, May 15-17, 1968. U. S. Atomic Energy Commission Report CONF-670503 (1969), pp. 249-257.
- Gustafson, P. F. Gross Gamma-Ray Activity Profiles over Northern Chile. Health and Safety Laboratory Quarterly, U. S. Atomic Energy Commission Report HASL-204 (August-October, 1968), pp. 163-174.
- Gustafson, P. F., S. S. Brar, and D. M. Nelson. Possible Evidence of Radioactivity from Southern

- Hemisphere Nuclear Tests in Surface Air over the Central United States. Health and Safety Laboratory Quarterly, U. S. Atomic Energy Commission Report HASL-204 (August-October, 1968), pp. 175-177.
- Holtzman, R. B. ^{226}Ra and the Natural Airborne Nuclides ^{210}Pb and ^{210}Po in Arctic Biota. *Radiation Protection*, Proc. 1st Int. Congr., Rome, September 5-10, 1966. Pergamon Press, Oxford, 1968, pp. 1087-1096.
- Holtzman, R. B. Concentrations of the Naturally Occurring Radionuclides ^{226}Ra , ^{210}Pb , and ^{210}Po in Aquatic Fauna. *Symposium on Radioecology*, Proc. 2nd Natl. Symp., Ann Arbor, Michigan, May 15-17, 1968. U. S. Atomic Energy Commission Report CONF-670503 (1969), pp. 535-546.
- Gustafson, P. F., S. S. Brar, and D. M. Nelson. Summary of ^{137}Cs in the Chicago Area, 1965-1968. Health and Safety Laboratory Quarterly, U. S. Atomic Energy Commission Report HASL-204 (August-October 1968), pp. 178-180.
- Gustafson, P. F. and J. E. Miller. The Significance of ^{137}Cs in Man and His Diet. *Health Phys.* **16**, 167-183 (1969).
- Inokuti, M. and Yong-Ki Kim. Total Cross Sections for Inelastic Scattering of Charged Particles by Atoms and Molecules. II. Negative Hydrogen Ions. *Phys. Rev.* **173**, 154-160 (1968).
- Kim, Yong-Ki and M. Inokuti, G. E. Chamberlain, and S. R. Mielczarek, Minima of Generalized Oscillator Strengths. *Phys. Rev. Letters* **21**, 1146-1148 (1968).
- Kim, Yong-Ki and M. Inokuti. Generalized Oscillator Strengths of the Helium Atom. I. *Phys. Rev.* **175**, 176-188 (1968).
- Kim, Yong-Ki and M. Inokuti. Generalized Oscillator Strengths of the Helium Atom. II. Transitions from the Metastable States. *Phys. Rev.* **181**, 205-214 (1969).
- Oltman, B. G., J. Kastner, and C. Paden. Spectral Analysis of Thermoluminescence Glow Curves. Proc. 2nd Int. Conf. on Luminescence Dosimetry, Gatlinburg, Tenn., September 23-26, 1968. U. S. Atomic Energy Commission Report CONF-680920 (1969), pp. 623-631.
- Kastner, J., R. K. Langs, B. A. Cameron, M. A. Paesler, and G. Anderson. Electro-Optical Techniques for Ultrasensitive Radiophotoluminescent Dosimetry. Proc. 2nd Int. Conf. on Luminescence Dosimetry, Gatlinburg, Tenn., September 23-26, 1968. U. S. Atomic Energy Commission Report CONF-680920 (1969), pp. 670-676.
- Kastner, J., R. H. Selner, C. M. Paden, and B. G. Oltman. Ultrasonic Excitation of Thermoluminescent Lithium Fluoride. *Health Phys.* **16**(6), 803-804 (1969).
- Kline, J. R., J. E. Foss, and S. S. Brar. Lanthanum and Scandium Distribution in Three Glacial Soils of Western Wisconsin. *Soil Sci. Soc. Am. Proc.* **33**(2), 287-291 (March-April 1969).
- Kline, J. R. and S. S. Brar. Instrumental Analysis of Neutron Irradiated Soils. *Soil Sci. Soc. Am. Proc.* **33**, 234-238 (March-April 1969).
- Gatz, Donald F., A. N. Dingle, and J. W. Winchester. Detection of Indium as an Atmospheric Tracer by Neutron Activation. *J. Appl. Meteorol.* **8**(2), 229-235 (1969).
- Dingle, A. N., D. F. Gatz, and J. W. Winchester. A Pilot Experiment Using Indium as Tracer in a Convective Storm. *J. Appl. Meteorol.* **8**(2), 236-240 (1969).
- Lucas, H. F., Jr., and D. N. Edgington. Computer Analysis of Gamma-Ray Spectra: Validity of the Results. *Modern Trends in Activation Analysis*, Ed. J. R. DeVoe and P. D. LaFleur. U. S. Dept. Commerce, Natl. Bur. Std. Spec. Publ. 312, 1969, Vol. **2**, pp. 1207-1214.
- Marinelli, L. D. A Revised Estimate of Maximum Permissible Burden for ^{90}Sr . *Delayed Effects of Bone-Seeking Radionuclides*, Ed. C. W. Mays et al. University of Utah Press, Salt Lake City, 1969, pp. 409-416.
- Marinelli, L. D. Dosimetry in Relation to Epidemiology. *Guidelines to Radiological Health*. Public Health Service Publication No. 999-RH-33, September 1968, pp. 128-136.
- Marinelli, L. D. The Doses from Thorotrast and Migrated Descendants: Status, Prospect and Implications. *The Dosimetry and Toxicity of Thorotrast*. IAEA Technical Report 106. Int. Atomic Energy Agency, Vienna, 1968, pp. 86-99.
- Marinelli, L. D. A Review of the Radiosensitivity of the Tissues in Bone. ICRP Publication No. 11. Pergamon Press, Oxford, 1968, pp. 1-36.
- Rosenthal, M. W., J. H. Marshall and Arthur Lindenbaum. Autoradiographic and Radiochemical Studies of the Effect of Colloidal State of Intravenously Injected Plutonium on Its Distribution in Bone and Marrow. *Diagnosis and Treatment of Deposited Radionuclides*, Symp. Richland, Washington, May 15-17, 1967. Excerpta Medica Foundation, Amsterdam, 1968, pp. 73-80.
- Marshall, J. H. The Retention of Radionuclides in Bone. *Delayed Effects of Bone-Seeking Radionuclides*, Ed. C. W. Mays et al. University of Utah Press, Salt Lake City, 1969, pp. 7-27.

- Moses, Harry and J. E. Carson. Stack Design Parameters Influencing Plume Rise. *J. Air Pollution Control Assoc.* **18**(7), 454-458 (July 1968).
- Moses, H., Elmer Robinson, M. E. Smith, G. C. Gill, C. R. Dickson, and E. C. Wilkins. Meteorological Instruments for Use in the Atomic Energy Industry. *Meteorology and Atomic Energy. Meteorology and Atomic Energy 1968*, Ed. David H. Slade. U. S. Atomic Energy Commission, Oak Ridge, July 1968, TID-24190, Ch. 6, pp. 257-300.
- Moses, Harry. Mathematical Urban Air Pollution Models. Argonne National Laboratory Report ANL/ES-RPY-001 (April 1969).
- Person, James C. and Paul P. Nicole. Isotope Effects in the Photoionization Yields and the Absorption Cross Sections for Ethylene and *n*-Butane. *J. Chem. Phys.* **49**, 5421-5426 (December 1968).
- Rose, John E. and Francis R. Shonka. Calculated Calibrations for Ion Chambers Fabricated from Plastics Simulating Air and Muscle: Determination of W and k_{Ra} . *Radiat. Res.* **36**, 384-395 (December 1968).
- Simmons, D. J., Helen Cummins, and Edwin Nirdlinger. Observations on the Deposition of Thorotrast in Rat Tissue. *Am. J. Roentgenol.*, **103**, 902-918 (August 1968).
- Simmons, D. J. and Helen Cummins. Effect of the Acetophenone-Derivative of 16 alpha, 17 alpha-Dihydroxyprogesterone (Deladroxone) and Estrogen (Dihydroxyprogesterone Acetophenid) on Sr^{85} Retention in Rats and Mice. *Proc. Soc. Exptl. Biol. Med.* **128**, 1102-1106 (September 1968).
- Simmons, D. J. and Helen Cummins. Effect of the Acetophenide Derivative of 16 α , 17 α -Dihydroxyprogesterone and Estradiol on the Skeletons of Rats and Mice. *Am. J. Obstet. Gynecol.* **103**(7), 1002-1018 (April 1969).
- ABSTRACTS**
- Failla, P. M. Recovery from Radiation-Induced Division Delay in Sea Urchin Eggs. *Radiat. Res. Soc. Mtg.*, Houston, Texas, April 21-25, 1968. *Radiat. Res.* **35**, 514 (August 1968).
- Kim, Yong-Ki and M. Inokuti. Accurate Generalized Oscillator Strengths of He. *Bull. Am. Phys. Soc.* **14**, 610, 1969.
- Inokuti, M. and Y.-K. Kim. Accurate Cross Section for Ionization of Helium by Fast Charged Particles. 6th Int. Conf. on the Physics of Electronic and Atomic Collisions, Cambridge, Mass., July 28-August 2, 1969. M.I.T. Press, 1969, Cambridge, Mass., pp. 5-9; pp. 10-12.
- Dedolph, R. R., R. B. Holtzman, H. F. Lucas, and G. L. Ter Haar. The Sources of Lead in Perennial Ryegrass and Radishes. Abstracts of papers of the 157th Natl. Mtg. American Chemical Society, April 13-18, 1969. Abstract INDE-1.
- Marinelli, L. D., G. F. Clemente, I. K. Abu-Shumays, and O. J. Steingraber. Localization of Scintillations in Gamma-Ray Cameras by Time-of-Flight Techniques. Linear Resolutions Attainable in Long Fluorescent Rods. *Radiology* **92**, 167 (January 1969).
- Simmons, D. J. and Helen Cummins. Retention of Sr^{85} in Rats and Mice Treated with an Acetophenone Derivative of 16, 17-Dihydroxyprogesterone (Deladroxone) and Estradiol (Deladroxate). *3rd Intern. Congr. of Endocrinology, 1968*. Excerpta Medica Foundation, Amsterdam, 1968, Abstract No. 224.
- ACCEPTED PAPERS**
- Carson, J. E. and Harry Moses. The Validity of Several Plume Rise Formulas. *J. Air Pollution Control Assoc.*
- Failla, P. M. Recovery and Modification of Radiation-Induced Division Delay in Developing Sea Urchin Eggs. *Radiology*.
- Kim, Yong-Ki and M. Inokuti. Generalized Oscillator Strengths of the Helium Atom. III. Transitions from the Ground State to the 3^1D and 4^1P States. *Phys. Rev.*
- Inokuti, M. and Y.-K. Kim. Total Cross Sections for Inelastic Scattering of Charged Particles by Atoms and Molecules. III. Accurate Bethe Cross Section for Ionization of Helium. *Phys. Rev.*
- Ter Haar, G. L., R. R. Dedolph, R. B. Holtzman and H. F. Lucas, Jr. The Lead Uptake by Perennial Ryegrass and Radishes from Air, Water and Soil. *Environmental Res.*
- Lucas, H. F., Jr., J. H. Marshall, and L. A. Barrer. The Level of Radium in Human Blood Forty Years after Ingestion. *Radiat. Res.*
- Marshall, J. H., J. Rundo, and G. E. Harrison. Retention of Radium in Man. *Radiat. Res.*
- Rowland, R. E. and J. Farnham. The Deposition of Uranium in Bone. *Health Phys.*
- Simmons, D. J. and Arthur S. Kunin. The Development and Healing of Rickets in Rats. I. Nutritional Considerations and Studies with Tritiated Thymidine. *Clin. Orthopaed.*
- Simmons, D. J. and Arthur S. Kunin. The Development and Healing of Rickets in Rats. II. Studies with Tritiated Proline. *Clin. Orthopaed.*